

NanoScience and Technology

Anqi Zhang  
Gengfeng Zheng  
Charles M. Lieber

# Nanowires

Building Blocks for Nanoscience and  
Nanotechnology

 Springer

# **NanoScience and Technology**

## **Series editors**

Phaedon Avouris, Yorktown Heights, USA

Bharat Bhushan, Columbus, USA

Dieter Bimberg, Berlin, Germany

Klaus von Klitzing, Stuttgart, Germany

Cun-Zheng Ning, Tempe, USA

Roland Wiesendanger, Hamburg, Germany

The series NanoScience and Technology is focused on the fascinating nano-world, mesoscopic physics, analysis with atomic resolution, nano and quantum-effect devices, nanomechanics and atomic-scale processes. All the basic aspects and technology-oriented developments in this emerging discipline are covered by comprehensive and timely books. The series constitutes a survey of the relevant special topics, which are presented by leading experts in the field. These books will appeal to researchers, engineers, and advanced students.

More information about this series at <http://www.springer.com/series/3705>

Anqi Zhang · Gengfeng Zheng  
Charles M. Lieber

# Nanowires

Building Blocks for Nanoscience  
and Nanotechnology

 Springer

Anqi Zhang  
Department of Chemistry and Chemical  
Biology  
Harvard University  
Cambridge, MA  
USA

Charles M. Lieber  
Department of Chemistry and Chemical  
Biology  
Harvard University  
Cambridge, MA  
USA

Gengfeng Zheng  
Department of Chemistry, Collaborative  
Innovation Center of Chemistry  
for Energy Materials  
Fudan University  
Shanghai  
China

and  
Harvard John A. Paulson School  
of Engineering and Applied Sciences  
Harvard University  
Cambridge, MA  
USA

ISSN 1434-4904  
NanoScience and Technology  
ISBN 978-3-319-41979-4  
DOI 10.1007/978-3-319-41981-7

ISSN 2197-7127 (electronic)  
ISBN 978-3-319-41981-7 (eBook)

Library of Congress Control Number: 2016945143

© Springer International Publishing Switzerland 2016

This work is subject to copyright. All rights are reserved by the Publisher, whether the whole or part of the material is concerned, specifically the rights of translation, reprinting, reuse of illustrations, recitation, broadcasting, reproduction on microfilms or in any other physical way, and transmission or information storage and retrieval, electronic adaptation, computer software, or by similar or dissimilar methodology now known or hereafter developed.

The use of general descriptive names, registered names, trademarks, service marks, etc. in this publication does not imply, even in the absence of a specific statement, that such names are exempt from the relevant protective laws and regulations and therefore free for general use.

The publisher, the authors and the editors are safe to assume that the advice and information in this book are believed to be true and accurate at the date of publication. Neither the publisher nor the authors or the editors give a warranty, express or implied, with respect to the material contained herein or for any errors or omissions that may have been made.

Printed on acid-free paper

This Springer imprint is published by Springer Nature  
The registered company is Springer International Publishing AG Switzerland

# Preface

Dimensionality plays a critical role in determining the properties of materials due to, for example, the different ways that electrons interact in 3D, 2D and 1D structures. 1D nanowires (NWs), with diameters reaching to the molecular or quantum regime, have been the focus of research for two decades and today remain at the forefront of both scientific research and developing nanotechnologies. In particular, semiconductor NWs represent one of the most important and versatile nanometer-scale structures. In contrast to other classes of 1D nanostructures, such as carbon nanotubes, semiconductor NWs can be rationally and predictably synthesized in single crystal forms with all key parameters controlled, including chemical composition, diameter, length, doping and electronic properties. Thus, semiconductor NWs represent one of the best-defined classes of nanoscale building blocks, and the precise control over key variables has correspondingly enabled a wide range of devices, assembly strategies and integrated nanosystems to be pursued, as well as opening new directions at the interface with other fields. This book provides an overview of this vibrant area of nanoscience and nanotechnology research starting from early efforts that recognized the importance and began to develop this class of building blocks through to state-of-the-art directions today, including quantum devices, energy technology and interfacing to biological systems.

Chapter 1 will introduce the emergence of the semiconductor NW research platform, including the concept and importance, synthetic challenges and initial design, and the development of vapor-liquid-solid crystal growth mechanism, as well as other nanofabrication-based approaches explored in the early years of this field.

In Chap. 2, we will overview major bottom-up strategies for the synthesis of semiconductor NWs, including vapor phase, templated, and solution-based methods. Chapter 3 will further expand upon the basic synthetic methods to yield controlled growth of a host of semiconductor NWs with modulated morphologies and structures, including axial and radial heterostructures, kinked, branched, and/or

modulated doped structures, where the increased complexity in the NWs can enable unique functional properties.

To utilize these NW building blocks for nanoscale devices through integrated systems, such as in electronics and photonics, requires controlled and scalable assembly of NWs on either rigid or flexible substrates. In Chap. 4, we will summarize advances in large-scale NW assembly by organizing pre-grown NWs onto target substrates and the direct growth of aligned NWs on substrates.

Electronics obtained through the bottom-up approach of molecular-level control of material composition and structure can lead to devices and fabrication strategies, as well as new architectures not readily accessible or even possible within the context of the top-down driven industry and manufacturing infrastructure. Chapter 5 will present a summary of advances in basic nanoelectronics devices, basic circuits and nanoprocessors assembled by semiconductor NWs.

In Chap. 6, we will review the advantages of the sub-wavelength diameters of NW structures and tunable energy band gaps for investigating generation, detection, amplification and modulation of light. The rational design and synthesis of NW structures together with the capability of controlling and manipulating these structures on surfaces to form single devices and networks has been crucial for realizing NW-based photonic circuitry. Progress in the area of NW photonic devices, including waveguides, light-emitting diodes, lasers, and photodetectors, will be reviewed.

When the dimensions of the NWs become comparable to the electron characteristic lengths, the fundamental quantum properties of charge carriers can dominate the charge transport and new device properties become possible. Chapter 7 will summarize studies over the past decade where quantum properties are critical to the observed behavior, including quantum dot systems in semiconductor NWs, hybrid superconductor-semiconductor NW devices, and NW topological insulators.

Substantial recent scientific effort has been focused on efficient energy storage and conversion of renewable energy sources, where semiconductor NWs represent attractive candidates since their composition, size and other factors that determine basic electronic and optical properties can be synthetically manipulated in complex ways. In Chaps. 8 and 9, the advantages of NW structures for efficient energy storage and conversion will be illustrated and discussed.

Chapter 10 will introduce research advances exploiting NWs configured as field-effect transistors for biomolecule analysis, as one of the most promising and powerful platforms for label-free, real-time, and sensitive electrical detection based upon the electrostatic gating effect on the surface. Representative examples of semiconductor NW sensors will be described, including sensitive detection of proteins, nucleic acids, viruses and small molecules.

The interface between nanosystems and biosystems is emerging as one of the broadest and most dynamic areas of science and technology, bringing together researchers and ideas from biology, chemistry, physics and many areas of engineering, biotechnology and medicine. These efforts are leading to many advances, for example, the creation of new and powerful tools that enable direct, sensitive and rapid analysis of biological species and cellular activities. Research at the interface

between nanomaterials and biology could yield breakthroughs in fundamental science and lead to revolutionary technologies. In Chap. 11, we will introduce studies focused on building interfaces between NWs with cells and tissues, including extracellular and intracellular signal recording, synthetic cyborg tissues and in vivo recording.

Finally, in Chap. 12, we will conclude this book and look into the future of the exciting opportunities of NW science and technology moving forward.

We thank Yongjie Hu (University of California, Los Angeles), Wei Lu (University of Michigan) and Yat Li (University of California, Santa Cruz) for reviewing early drafts of several chapters.

Cambridge  
Shanghai  
Cambridge  
Jun 2016

Anqi Zhang  
Gengfeng Zheng  
Charles M. Lieber



# Contents

<b>1</b>	<b>Emergence of Nanowires</b>	1
1.1	Introduction: Motivation for Nanowires	1
1.1.1	Importance of One-Dimensional Materials	2
1.1.2	Synthetic Challenges and Initial Design	4
1.1.3	Top-Down and Bottom-Up Nanotechnology	5
1.2	Micron-Scale Whiskers: VLS Concept	6
1.2.1	Concept and Key Results	6
1.2.2	Limitations	8
1.3	Other Early Works	8
1.3.1	Top-Down Lithography-Based Si Nanopillars	8
1.3.2	Carbide Nanorods	9
1.3.3	Nanowiskers by Vapor Phase Epitaxy	9
1.4	Beginning of Rapid Growth: Vapor-Phase Nanocluster Catalyzed Growth	10
	References	11
<b>2</b>	<b>General Synthetic Methods</b>	15
2.1	Introduction	15
2.2	Vapor Phase Growth	16
2.2.1	Laser-Assisted Catalytic Growth	16
2.2.2	Chemical Vapor Deposition	18
2.2.3	Chemical Vapor Transport	20
2.2.4	Molecular Beam Epitaxy	21
2.2.5	Vapor-Solid-Solid Growth	22
2.2.6	Vapor-Solid Growth	22
2.2.7	Oxide-Assisted Growth	23
2.3	Templated Growth	24
2.3.1	Formation Inside Nanopores	24
2.3.2	Templating Against Self-assembled Structures	25
2.3.3	Construction on Existing Nanostructures	25
2.3.4	Superlattice Nanowire Pattern Transfer	26

2.4	Solution-Based Methods . . . . .	27
2.4.1	Solution-Liquid-Solid Growth . . . . .	27
2.4.2	Supercritical Fluid-Liquid-Solid Growth . . . . .	28
2.4.3	Solvothermal/Hydrothermal Synthesis . . . . .	29
2.4.4	Directed Solution Phase Growth. . . . .	30
2.5	Future Directions and Challenges. . . . .	31
	References . . . . .	32
<b>3</b>	<b>Structure-Controlled Synthesis . . . . .</b>	<b>39</b>
3.1	Introduction. . . . .	39
3.2	Homogeneous Nanowires . . . . .	40
3.3	Axial Modulated Structures. . . . .	42
3.3.1	Early Work . . . . .	42
3.3.2	Semiconductor Heterojunctions . . . . .	43
3.3.3	Metal-Semiconductor Heterostructures . . . . .	43
3.3.4	<i>p-n</i> Homojunctions. . . . .	45
3.3.5	Ultrashort Morphology Features. . . . .	48
3.4	Radial/Coaxial Modulated Structures . . . . .	48
3.4.1	Semiconductor Radial Structures . . . . .	49
3.4.2	Coaxial Modulated Structures . . . . .	52
3.5	Branched/Tree-Like Structures. . . . .	53
3.5.1	Sequential Catalyst-Assisted Growth. . . . .	54
3.5.2	Solution Growth on Existing Nanowires . . . . .	56
3.5.3	Phase Transition Induced Branching . . . . .	56
3.5.4	One-Step Self-catalytic Growth . . . . .	58
3.5.5	Screw Dislocation Driven Growth . . . . .	58
3.6	Kinked Structures . . . . .	60
3.6.1	Undersaturation/Supersaturation-Induced Kinking. . . . .	60
3.6.2	Confinement-Guided Kinking . . . . .	62
3.7	Future Directions and Challenges. . . . .	63
	References . . . . .	64
<b>4</b>	<b>Hierarchical Organization in Two and Three Dimensions . . . . .</b>	<b>69</b>
4.1	Introduction. . . . .	69
4.2	Post-growth Assembly . . . . .	70
4.2.1	Fluidic Method . . . . .	70
4.2.2	Langmuir-Blodgett Method . . . . .	72
4.2.3	Blown Bubble Method . . . . .	77
4.2.4	Chemical Interactions for Assembly . . . . .	78
4.2.5	Assembly at Interfaces . . . . .	79
4.2.6	Electric/Magnetic Field-Based Methods. . . . .	81
4.2.7	PDMS Transfer Method . . . . .	82
4.2.8	Printing. . . . .	85
4.2.9	Nanocombing-Based Assembly . . . . .	87
4.2.10	Other Assembly Methods . . . . .	89

- 4.3 Patterned Growth . . . . . 90
  - 4.3.1 Epitaxial Growth from Patterned Nanocluster Catalysts . . . . . 90
  - 4.3.2 Substrate-Step-Directed Growth . . . . . 95
- 4.4 Future Directions and Challenges . . . . . 97
- References . . . . . 97
- 5 Nanoelectronics, Circuits and Nanoprocessors . . . . . 103**
  - 5.1 Introduction and Historical Perspective . . . . . 103
  - 5.2 Basic Nanoelectronic Devices . . . . . 104
    - 5.2.1 Field-Effect Transistors . . . . . 104
    - 5.2.2 p-n Diodes . . . . . 112
  - 5.3 Simple Circuits . . . . . 115
    - 5.3.1 Logic Gates . . . . . 115
    - 5.3.2 Ring Oscillators . . . . . 120
    - 5.3.3 Demultiplexers . . . . . 121
    - 5.3.4 Nonvolatile Memory . . . . . 122
  - 5.4 Nanoprocessors . . . . . 129
    - 5.4.1 Logic Tiles . . . . . 129
    - 5.4.2 Arithmetic Logic . . . . . 131
    - 5.4.3 Sequential Logic . . . . . 132
    - 5.4.4 Basic Nanocomputer . . . . . 133
  - 5.5 Future Directions and Challenges . . . . . 136
  - References . . . . . 137
- 6 Nanophotonics . . . . . 143**
  - 6.1 Introduction . . . . . 143
  - 6.2 Optical Phenomena . . . . . 144
    - 6.2.1 Photoluminescence from Nanowire Structures . . . . . 144
    - 6.2.2 Nonlinear Processes . . . . . 146
  - 6.3 Photonic Devices . . . . . 152
    - 6.3.1 Nanowire Waveguides . . . . . 152
    - 6.3.2 Nanoscale Light-Emitting Diodes . . . . . 153
    - 6.3.3 Optically-Pumped Nanowire Lasers . . . . . 156
    - 6.3.4 Electrically-Pumped Nanowire Lasers . . . . . 166
    - 6.3.5 Photodetectors . . . . . 167
  - 6.4 Future Directions and Challenges . . . . . 168
  - References . . . . . 169
- 7 Quantum Devices . . . . . 177**
  - 7.1 Introduction . . . . . 177
  - 7.2 Quantum Dot Systems in Semiconductor Nanowires . . . . . 179
    - 7.2.1 Configurations of Quantum Dot Systems in Nanowires . . . . . 179
    - 7.2.2 Basic Electronic Properties of Quantum Dots . . . . . 181

7.2.3	Single Quantum Dots in Nanowires . . . . .	182
7.2.4	Coupled Quantum Dots in Nanowires . . . . .	184
7.2.5	$g$ -Factor and Spin-Orbit Interaction . . . . .	187
7.3	Hybrid Superconductor-Semiconductor Devices . . . . .	192
7.3.1	Josephson Junctions . . . . .	192
7.3.2	Majorana Fermions . . . . .	194
7.4	Topological Insulators . . . . .	196
7.5	Future Directions and Challenges . . . . .	197
	References . . . . .	198
<b>8</b>	<b>Nanowire-Enabled Energy Storage . . . . .</b>	<b>203</b>
8.1	Introduction . . . . .	203
8.2	Lithium-Ion Batteries . . . . .	204
8.2.1	Anodes . . . . .	205
8.2.2	Cathodes . . . . .	211
8.3	Electrochemical Capacitors . . . . .	214
8.4	Sodium-Ion Batteries . . . . .	219
8.5	Future Directions and Challenges . . . . .	219
	References . . . . .	220
<b>9</b>	<b>Nanowire-Enabled Energy Conversion . . . . .</b>	<b>227</b>
9.1	Introduction . . . . .	227
9.2	Photovoltaics . . . . .	228
9.2.1	Nanowire Arrays for Enhanced Light Absorption . . . . .	229
9.2.2	Radial Junction Nanowires for Enhanced Carrier Separation . . . . .	233
9.2.3	Tuning Band Gaps of III-V Compounds . . . . .	236
9.3	Photoelectrochemical Conversion/Photocatalysis . . . . .	238
9.3.1	Si Nanowire-Based Photoelectrochemical Water Splitting . . . . .	239
9.3.2	Dual-Band Gap Artificial Photosynthesis . . . . .	240
9.4	Thermoelectrics . . . . .	244
9.5	Piezoelectric Effects . . . . .	246
9.6	Future Directions and Challenges . . . . .	248
	References . . . . .	248
<b>10</b>	<b>Nanowire Field-Effect Transistor Sensors . . . . .</b>	<b>255</b>
10.1	Introduction . . . . .	255
10.2	Fundamental Principles of Field-Effect Transistor Sensors . . . . .	256
10.3	Examples of Nanoelectronic Sensors . . . . .	258
10.3.1	Protein Detection . . . . .	258
10.3.2	Nucleic Acid Detection . . . . .	260
10.3.3	Virus Detection . . . . .	261
10.3.4	Small Molecule Detection . . . . .	262

- 10.4 Methods for Enhancing the Sensitivity of Nanowire Sensors . . . . . 263
  - 10.4.1 3D Branched Nanowires for Enhanced Analyte Capture Efficiency . . . . . 263
  - 10.4.2 Detection in the Subthreshold Regime . . . . . 263
  - 10.4.3 Reducing the Debye Screening Effect . . . . . 265
  - 10.4.4 Electrokinetic Enhancement . . . . . 267
  - 10.4.5 Frequency Domain Measurement . . . . . 267
  - 10.4.6 Nanowire–Nanopore Sensors . . . . . 269
  - 10.4.7 Double-Gate Nanowire Sensors . . . . . 270
  - 10.4.8 Detection of Biomolecules in Physiological Fluids . . . . . 270
- 10.5 Future Directions and Challenges . . . . . 271
- References . . . . . 272
- 11 Nanowire Interfaces to Cells and Tissue . . . . . 277**
  - 11.1 Introduction . . . . . 277
  - 11.2 Nanowire/Cell Interfaces and Electrophysiological Recording . . . . . 278
    - 11.2.1 Traditional Extracellular Electrophysiological Recording . . . . . 278
    - 11.2.2 Nanowire Transistors for Extracellular Recording . . . . . 280
    - 11.2.3 Intracellular and Intracellular-like Electrophysiological Recording . . . . . 284
  - 11.3 Nanowire-Tissue Interfaces and Electrophysiological Recording . . . . . 290
    - 11.3.1 Acute Brain Slice Studies with Nanowire Transistors . . . . . 291
    - 11.3.2 Cardiac Tissue Studies with Nanowire Transistors . . . . . 291
    - 11.3.3 3D Nano–Bioelectronic Hybrids . . . . . 293
    - 11.3.4 Injectable Electronics . . . . . 298
  - 11.4 Future Directions and Challenges . . . . . 300
  - References . . . . . 301
- 12 Conclusions and Outlook . . . . . 307**
  - References . . . . . 309
- Curriculum Vitae . . . . . 311**
- Index . . . . . 315**

# Chapter 1

## Emergence of Nanowires

**Abstract** The design, development and understanding of synthetic materials, with at least one dimension below 100 nm, have been driving a broad range of research in the scientific community for a number of years given the potential of such materials to substantially impact many areas of science and technology. In particular, one-dimensional nanowires, with diameters reaching to the molecular or quantum regime, have been a focus of research over the past two decades. The underlying principles for synthesis of one-dimensional materials have been investigated in different contexts for almost half a century ago, although significant challenges existed in developing the critical understanding to control (i) diameters to the deep nanoscale dimensions as well as (ii) structure and composition in the axial and radial coordinates as necessary for the synthesis of materials with designed and tunable functionality. In this chapter, the emergence of the nanowire research platform is introduced, including the concept and importance, synthetic challenges and initial design, and the development of vapor-liquid-solid crystal growth mechanism. In addition, other nanofabrication based approaches explored in the early years of this field will be briefly introduced.

### 1.1 Introduction: Motivation for Nanowires

“Nano” has become a nearly ubiquitous prefix used today in science and technology, and also one widely recognized by the general public. But what is the science that can build nanotechnologies and may make nanotechnology a unique field of endeavor that revolutionizes many other areas? Indeed, nanometer scale structures represent an exciting, intellectually-challenging and rapidly expanding area of research that crosses the borders between many areas of the physical sciences and engineering [1, 2]. Nanostructures can be defined as systems in which at least one dimension is less than 100 nm. That is, reducing 1, 2 or 3 dimensions (D) of a bulk material to the nanometer scale produces nanometer thick 2D layers, 1D nanowires (NWs), or 0D nanoclusters, respectively. Interest in nanometer scale structures has been driven by fascinating questions and the potential to impact basic

science and technology. Three questions at the heart of basic chemistry and physics research of nanomaterials are: (1) how can nanostructures that have controlled dimensionality be synthesized or fabricated; (2) what are the intrinsic and potentially unique physical properties of these synthesized nanostructures; and (3) how can nanostructures with tailorable properties contribute to and even create breakthroughs in fields, including but not limited to, electronics, photonics, energy conversion and storage, and the life sciences? Before delving in detail to these questions in subsequent chapters of the book, an abbreviated history of the development of the unique 1D nanostructure now known as NWs is reviewed.

### *1.1.1 Importance of One-Dimensional Materials*

Dimensionality plays a critical role in determining the properties of materials due to, for example, the different ways that electrons interact in 3D, 2D and 1D structures [3–5]. The study of dimensionality has a long history in chemistry and physics, although this has been primarily with the prefix “quasi” added to the description of materials. That is, quasi-1D solids, including square-planar platinum chain and metal trichalcogenide compounds [6, 7], and quasi-2D layered solids, such as metal dichalcogenides and copper oxide superconductors [3, 5, 8, 9]. The anisotropy inherent in quasi-1D and -2D systems is central to the unique properties and phases that these materials exhibit, although the small but finite interactions between 1D chains or 2D layers in bulk materials have made it difficult to address the interesting properties expected for the pure low-dimensional systems [10, 11].

The focus on nanometer scale wires is motivated by basic scientific and technology questions. How can atoms or other building blocks be rationally assembled into structures with nanometer size diameters but much longer lengths? By the end of the 20th century, there had been relatively well developed methods for the synthesis of 0D nanoclusters via arrested precipitation [12] and the growth of 2D layers using molecular beam epitaxy (MBE), although general methods for the growth of 1D structures with diameters less than 10 nm had not been available. In addition, 1D structures with nanometer diameters, such as NWs, have great potential for testing and understanding fundamental concepts about the roles of dimensionality and size on physical properties. For instance, 1D systems should exhibit density of states singularities, can have energetically discrete molecular states extending over large distances, and may show more exotic phenomena, such as spin-charge separation predicted for a Luttinger liquid [13]. There are also many applications where 1D NWs can be exploited, including (i) functional nanostructure materials, (ii) novel probe microscopy tips, (iii) nanoelectronics, (iv) nanophotonics, (v) quantum devices, (vi) energy storage, (vii) energy conversion, (viii) chemical and biological sensing, and (ix) nano-bio interfaces. To realize these and other exciting uses of 1D nanostructures, however, requires an understanding of the fundamental chemistry and physics questions raised above [11, 14].

Semiconductor NWs represent arguable the most important and versatile nanometer-scale wire structures. In contrast to another classes of 1D nanostructures, such as carbon nanotubes (CNTs) [10, 11], semiconductor NWs can be rationally and predictably synthesized in single crystal forms with all key parameters controlled, including chemical composition, diameter and length, and doping and electronic properties. Thus, semiconductor NWs represent one of the best-defined classes of nanoscale building blocks, and this precise control over key variables has correspondingly enabled a wide range of devices and assembly/integration strategies to be pursued [15]. For example, early work showed that semiconductor NWs could be assembled into functional electronic devices, including crossed NW  $p$ - $n$  diodes, crossed NW-FETs, nanoscale logic gates and computation circuits, as well as optoelectronic devices such as nanoscale light-emitting diodes (LEDs) and lasers. In addition, it is possible to combine distinct NW building blocks in ways not possible in conventional electronics, and to leverage the knowledge base that exists for the chemical modification of inorganic surfaces to produce semiconductor NW devices that achieve new function and correspondingly lead to unexpected device and system concepts [14, 16, 17]. In the past 20 years, the research community has witnessed a substantial increase in development of NW research with a near exponential increase in publications, which reached over 20,000 new publications per year in 2014 (Fig. 1.1). Nonetheless, significant challenges existed at the very early days when people started to explore the methodologies for 1D NW synthesis.

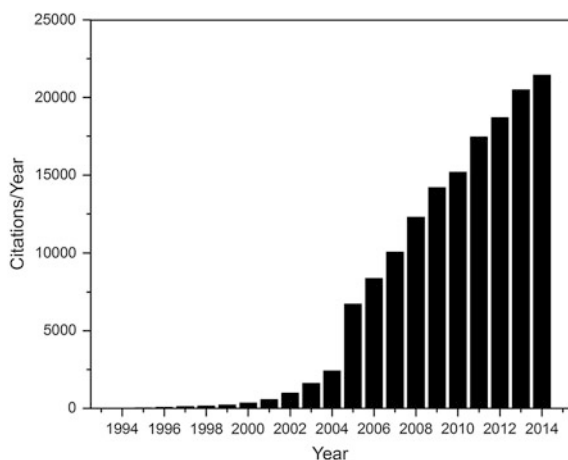


**Fig. 1.1** Histogram of citations by year to “nanowire(s)” (Search performed on 7th July 2015 with Web of Science)



### 1.1.2 Synthetic Challenges and Initial Design

How can atoms or other building blocks be rationally assembled into structures with nanometer size diameters but much longer lengths? Answering this question is central to the preparation of 1D nanostructures, and correspondingly, research had pursued several strategies to synthesize CNTs and NWs. For example, multiple-walled CNTs had been prepared via the condensation of hot carbon plasmas. The growth mechanism producing these 1D nanostructures is, however, specific to the tubular structures of  $sp^2$ -bonded carbon and isostructural hexagonal boron nitride. It is also possible to favor the formation of single-walled CNTs from carbon plasmas by adding certain metals [18]. These metals appeared to function as catalysts, although a sufficiently good understanding of the growth mechanism needed to control the diameter and helicity of SWCNTs had not been available by the end of last century.

In general, the growth of 1D nanostructures requires two dimensions to be restricted to the nanometer regime, while the third dimension extends to a much greater length scale [10, 19]. This overall requirement is considerably more difficult to achieve than the corresponding constraints needed for successful growth of 0D and 2D structures [20]. For example, many important semiconductor materials adopt a cubic zinc blende structure, and thus when growth is stopped at an early stage, the resulting nanoscale structures are nanocrystals with various polyhedron shapes but not 1D NWs. To achieve 1D growth in systems, where atomic bonding is relatively isotropic, requires that the growth symmetry be broken rather than simply arresting growth at an early stage.

By the end of the last century, considerable efforts had been placed on the bulk synthesis of NWs, and various strategies had been developed to break the growth symmetry either “physically” or “chemically”. A common theme in many of these studies had been the use of linear templates, including the edges of surface steps [21], nanofibers [22, 23], and porous membranes [24], to direct chemical reactions and material growth in 1D. Although a promising and conceptually simple technique, template mediated growth generally produces polycrystalline materials with diameters greater than 10 nm. Hence, it was unclear based on these previous studies, whether a general method for the growth of single crystalline NWs with diameters less than 10 nm existed [10, 11].

In order to understand the intrinsic behavior of 1D structures in a size regime where quantum effects produce new phenomena, the first goal should be to develop a general and predictive method for preparing compositionally diverse single-crystal materials with nanometer to tens of nanometer diameters. From the outset it was believed that a catalytic approach, in which the catalyst is used to direct growth in a highly anisotropic or 1D manner, would enable one to meet this overall goal [11]. Depending on the phases involved in the reaction, this approach is typically defined as vapor-liquid-solid (VLS) [25, 26], solution-liquid-solid (SLS) [27] or vapor-solid (VS) [28, 29] growth, which will be introduced in more details later in this chapter and the following chapter.

### ***1.1.3 Top-Down and Bottom-Up Nanotechnology***

Nanotechnology aims to be a revolution, not an evolution, in science and technology. It distinguishes itself from all previous scientific and industrial revolutions in three major aspects [30]. For the first time in human history, one can (i) change the fundamental properties (such as band gaps and luminescence) of matter as well as make materials with desirable attributes; (ii) observe and manipulate nanoscale objects (such as atoms and molecules); and (iii) fabricate and build single-NW/nanotube single-electron/photon nanodevices. The first characteristic is due to the so-called quantum-size effects whereby the properties of a material change with its size in the nanometer regime. The second is made possible by the invention of high-resolution transmission electron microscopy (HRTEM) and scanning probe microscopy (SPM), including scanning tunneling microscopy (STM) and atomic force microscopy (AFM). The third is the result of the developments of various nanofabrication techniques (such as nanoimprint and electron beam lithography) as well as due to a physical phenomenon known as “quantum confinement” in the nanorealm. It is quite possible that the nano-revolution will ultimately impact most aspects of human activities, not just in science and technology.

How can this revolution be realized? There are, in principle, two approaches to nanotechnology: the bottom-up and the top-down strategies [31, 32]. The bottom-up strategy focuses on building or assembling nanodevices from atomic or molecular components. The top-down one seeks to fabricate nanodevices on silicon or other semiconductor chips directly using increasingly high resolution lithography [33]. It is widely held that present top-down semiconductor technology has not exploited the chemistry and physics (e.g., quantum-size effects) of nanomaterials, and also not taken advantage of the development of bottom-up nanotechnology [30, 32]. Many reasons come to mind. First, nanomaterials and their properties in the nanorealm, especially at the interface, are not well understood and/or still under investigation. Second, the fabrication techniques, both at the materials level and at the device stage, are not well-defined or fully developed. Third, connection to the macroscopic world remains a real problem. Finally, even if all these problems can be overcome, they are not at present mass producible and/or cost competitive enough to challenge the existing semiconductor technology. For a stand-alone bottom-up nanodevice to challenge the top-down nanodevice, it must overcome these hurdles.

Thus, while each approach has its advantages and disadvantages, it is generally believed that future development of nanotechnology will encompass both approaches with their relative contributions depending upon specific applications and taking into account pros and cons associated with factors such as performance enhancement and materials improvement. In other words, application-specific nanodevices can be fabricated using a combination of the two approaches. For example, nanodevices can be made via the bottom-up strategy and assembled in situ or “grown in place” on a nanochip fabricated via the top-down lithography

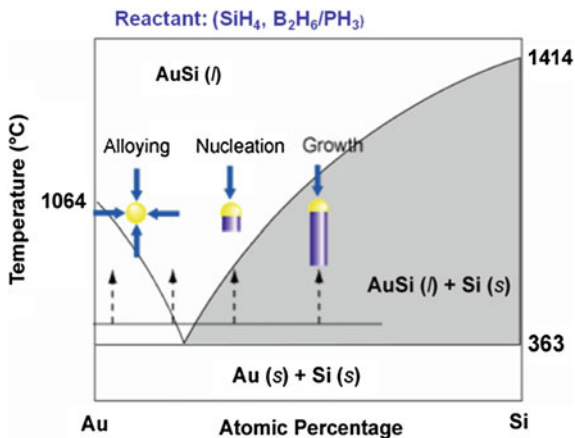
techniques, which enable straightforward interfacing to the outside world. Such hybrid nanotechnologies would allow the exploitation of advantageous attributes of both approaches. In this book, we will focus on the developments of the bottom-up synthesis strategy and NW structures and their characteristics that arise from this bottom-up approach.

## 1.2 Micron-Scale Whiskers: VLS Concept

### 1.2.1 Concept and Key Results

In general, the preparation of wires requires that the addition of material during the growth process be constrained to occur along only one direction. This is conveniently accomplished by taking advantage of ideas from vapor–liquid–solid (VLS) growth [25, 26, 34, 35] (Fig. 1.2). In this mechanism, a metal catalyst, such as a gold (Au) nanoparticle, forms a liquid metal–semiconductor eutectic alloy at an elevated temperature by adsorbing the vapor reactant, such as silicon resulting from silane ( $\text{SiH}_4$ ) decomposition. Continuous incorporation of the semiconductor material in the alloy through the vapor/liquid interface ultimately results in supersaturation of the semiconductor material, and this supersaturated state leads to precipitation of the semiconductor material and formation of a liquid–solid interface to achieve minimum free energy. Accordingly, the 1D crystal growth begins via the transfer of the semiconductor material from the vapor reactant at the vapor/liquid interface into the eutectic, followed by atom (e.g., Si atoms) addition at the liquid/solid interface. In addition, because the gold nanoparticle remains at the tip of the NW during VLS growth, it can define the diameter of the 1D NW as long as all reactant addition is through the liquid/solid interface. An important feature of this concept is that it readily provides the intellectual underpinning needed for the

**Fig. 1.2** VLS growth mechanism of Si wires



prediction of good catalysts and synthesis conditions. First, one uses equilibrium phase diagrams to choose a catalyst that can form a liquid alloy with the NW material of interest. The phase diagram is then used to choose a specific composition (catalyst: NW material) and synthesis temperature so that there is a coexistence of liquid alloy and solid NW material. Second, the liquid catalyst alloy cluster serves as a preferential site for absorption of reactant (i.e., there is a much higher sticking probability on liquid vs. solid surfaces) and, when supersaturated, the nucleation site for crystallization. Preferential 1D growth occurs in the presence of reactant as long as the catalyst remains liquid [11, 36].

The first successful synthesis of Si wires, or filamentary Si crystals with macroscopic dimensions, was reported in 1957 for the synthesis of Si whisker with  $\langle 111 \rangle$  orientation [37]. In 1961, Greiner et al. [38] reported that silicon nanoribbons were made by reacting silicon pellets with iodine and hydrogen in a closed tube in a temperature gradient. Arsenic-doped silicon pellets with resistivity from 0.001 to 0.005  $\Omega$ -cm produced ribbons, in which the silicon source of 0.002  $\Omega$ -cm resistivity gave optimum yields. The arsenic content of this silicon source material was estimated to be  $4 \times 10^{19}$  atoms/cm<sup>3</sup>. Several years later, the illuminating work performed by Wagner and Ellis [25, 26] established the mechanism of the Si whisker growth, well recognized as the VLS mechanism, which until today still represents the most important bottom-up approach to synthesize silicon nanowires (SiNWs) [39, 40]. In these and subsequent studies, Si whiskers were grown by the disproportionation of SiI<sub>2</sub> or by hydrogen reduction of SiCl<sub>4</sub>. Three important facts emerged: (a) silicon whiskers do not contain an axial screw dislocation; (b) an impurity, such as Au, is essential for whisker growth; and (c) a small globule is present at the tip of the whisker during growth. In this VLS mechanism, the role of the impurity is to form a liquid alloy droplet of relatively low melting temperature. Thus, the liquid droplet is a preferred site for deposition from the vapor, which causes the liquid to become supersaturated with Si.

Typical of this early work, a small particle of Au was placed on a  $\{111\}$  surface of a Si wafer and heated to 950 °C, forming a small droplet of Au-Si alloy [25, 26]. A mixture of hydrogen and SiCl<sub>4</sub> was introduced. The liquid alloy acts as a preferred sink for arriving Si atoms, that is, as a catalyst for the chemical process involved. The Si enters the liquid and freezes out, with a very small concentration of Au in solid solution, at the interface between solid Si and the liquid alloy. Continuation of this process results in the displacement of the alloy droplet from the substrate crystal atop the growing whisker. The growth direction is  $\langle 111 \rangle$ , and the side facets of the whisker are usually  $\{211\}$  and sometimes  $\{110\}$ . The whisker grows in length by this mechanism until the Au is consumed or until the growth conditions are changed. Similar results were obtained with Pt, Ag, Pd, Cu or Ni, either by replacing a particle on the Si substrate or co-deposition [25, 26]. VLS growth of twinned Si ribbons having a  $\langle 211 \rangle$  or a  $\langle 110 \rangle$  growth direction and  $\{111\}$  main faces were also observed [25, 26].

## 1.2.2 Limitations

The primary products identified in these early studies were micrometer to millimeter diameter Si whiskers or wires [25, 26]. Within the framework of the VLS mechanism, one can readily imagine synthesizing NWs of many different materials and diameters, if catalyst clusters of nanometer dimensions are available. This raises an important point, because equilibrium thermodynamics can be used to define the minimum radius,  $r_{\min}$ , of a liquid metal cluster as:

$$r_{\min} = 2\sigma_{LV}V_L/RT \ln \sigma$$

where  $\sigma_{LV}$  is the liquid-vapor surface free energy,  $V_L$  is the molar volume,  $R$  is the ideal gas constant,  $T$  is the absolute temperature, and  $\sigma$  is the vapor phase supersaturation [11]. Substituting typical values into the above equation yields a minimum radius on the order of 0.2  $\mu\text{m}$ , and thus under equilibrium conditions, one does not expect to be able to grow NWs with sufficiently small diameters to exhibit interesting new properties. Indeed, previous studies using a growth process similar to that described above, termed VLS growth, had only yielded micrometer diameter whiskers [25]. The large micrometer diameter clusters at the ends of these whiskers suggested strongly that the constraint imposed by the above equation led to the lower diameter limit in these previous studies. This constraint from equilibrium thermodynamics were overcome rationally by employing laser ablation and condensation, which has been studied extensively in the past [41], to generate nanometer diameter clusters. We will go into details of this breakthrough in Chap. 2.

## 1.3 Other Early Works

### 1.3.1 Top-Down Lithography-Based Si Nanopillars

In 1993, Chou and coworkers [42] reported the fabrication and preliminary photoluminescence study of free-standing Si pillars with diameters as small as about 10 nm and aspect ratio greater than 15. The pillars were fabricated using electron-beam lithography (EBL), chlorine-based reactive ion etching (RIE), and subsequent hydrofluoride (HF) wet etching. Photoluminescence with a peak at 720 nm was repeatedly observed from an array of nanoscale pillar with  $\sim 20$  nm diameters, although the origin of such photoluminescence was not clear. They further presented the fabrication of sub-50 nm Si pillars, ridges, and trenches using ultrahigh resolution EBL and chlorine based RIE [43].

On the other hand, Chen and Ahmed [44] reported the fabrication of high aspect ratio, sub-10 nm size structures in silicon without any wet chemical etching. A 50-nm thick double layer of low and high molecular weight polymethylmethacrylate

(PMMA) resist was exposed to an 80 kV electron beam with a beam diameter smaller than 5 nm. After exposure, the resist was developed and a 5-nm-thick AuPd film was deposited and sub-10 nm AuPd dots were obtained by liftoff. These dots served as a RIE etch mask on the Si substrate, yielding silicon nanocolumns with 5–7 nm diameters about 7:1 aspect ratios. Similarly, about 15 nm silicon nanopillars were fabricated using gold colloidal nanoparticles as the etch mask [45].

### 1.3.2 Carbide Nanorods

In 1995, the Lieber group [22] reported an alternative approach to the synthesis of nanoscale structures based on nanotubes, in which the carbon nanotubes were used as templates and converted to carbide rods by reacting with volatile oxide and/or halide species. In this way they were able to prepare solid carbide nanoscale rods of TiC, NbC, Fe<sub>3</sub>C, SiC and BC<sub>x</sub> in high yield with typical diameters of between 2 and 30 nm and lengths of up to 20 μm. Preliminary studies showed that these rods shared the properties of the bulk materials, such as magnetism and superconductivity, suggesting that they might allow the investigation of the effects of confinement and reduced dimensionality on such solid-state properties. This was especially important as it articulated the key importance of controlling composition—not being limited to simply Si or C—to enable unique functional properties.

Systematic temperature-dependent growth studies of TiC nanorods produced from spatially separated Ti metal and carbon nanotubes in the presence of iodine showed that reaction proceeds initially via the formation of a thin, uniform carbide coating and that further reaction proceeds via inward growth of this coating with a concomitant consumption of the carbon nanotube until a solid nanorod is formed [46]. The coatings and nanorods were polycrystalline, cubic TiC. Similar results were also obtained in growth studies of NbC nanorods from Nb metal and carbon nanotubes. These data showed that the growth of TiC and NbC nanorods involves a template mechanism in which the carbon nanotubes define the overall morphology and furthermore demonstrated that new TiC and NbC nanotubes could be prepared by controlling the growth conditions.

### 1.3.3 Nanowiskers by Vapor Phase Epitaxy

In 1992, Yazawa et al. [47] showed that selective heteroepitaxy of nanometer-scale InAs whiskers on SiO<sub>2</sub>-patterned GaAs substrates was induced by surface contamination with Au resulting from the fluorocarbon plasma etching process used to etch the SiO<sub>2</sub> mask. It was demonstrated that high-density ( $\sim 10^{10}/\text{cm}^2$ ) InAs nanowiskers with 20–30 nm in diameter could be epitaxially grown on InAs (111)B substrates onto which 1 monolayer of Au atoms had been deposited. This pillar-like

growth yielded primarily tapered or cone-like structure and appeared to be induced by ultrafine alloy droplets generated by the reaction between Au-nanoclusters and InAs substrates. Later, these researchers [48, 49] demonstrated the growth of GaAs cone-like structures with diameters of 15-100 nm and lengths up to 2  $\mu\text{m}$  on a GaAs substrate by metal-organic vapor-phase epitaxy. It was found that the growth direction was parallel to the [111] arsenic dangling-bond direction and were controlled by the crystallographic orientation of the GaAs substrate surface. It was further found that the whisker/cone-like structures were zinc-blende type for the growth temperature range of 460–500  $^{\circ}\text{C}$ , but changed to the wurtzite type at 420  $^{\circ}\text{C}$  and temperatures higher than 500  $^{\circ}\text{C}$ . These studies represents important steps forward in extending conventional substrate-based epitaxial growth to out-of-plane structures, but faced many of the same limitations of conventional 2D processing that general synthesis of NWs with arbitrary structure and composition that was needed to realize the potential promise as building blocks for nanotechnology.

#### 1.4 Beginning of Rapid Growth: Vapor-Phase Nanocluster Catalyzed Growth

It has long been recognized that metal vaporization can be easily accomplished by irradiation with pulsed high-power lasers [50], much earlier than its use in the growth of 1D nanostructures. For instance, Smalley and coworkers [41] combined the laser vaporization technique with the pulsed supersonic nozzle technology for generating nanometer-sized metal nanoclusters. In 1997 and 1998, the Lieber group [34, 51] introduced a laser ablation method for VLS growth of Si and germanium (Ge) NWs in truly nanoscopic dimensions. Specifically, laser ablation was used to prepare nanometer-diameter catalyst clusters that define the size of wires produced by VLS growth. This approach was used to prepare bulk quantities of uniform single-crystal SiNWs with diameters of 6–20 nm, and germanium NWs with diameters of 3–9 nm, respectively. The lengths of these NWs ranged from 1 to 30  $\mu\text{m}$ . Studies carried out with different conditions and catalyst materials confirmed the central details of the growth mechanism and suggested that well-established phase diagrams can be used to rationally predict catalyst materials and growth conditions for the preparation of NWs.

In 1998, Lee and coworkers [52] also reported a high-temperature laser-ablation method for the preparation of SiNWs, although a distinct oxide catalyzed NW growth mechanism was proposed. The growth rate was measured as 10–80  $\mu\text{m}/\text{h}$ . TEM investigation showed that the NWs were crystalline Si, and had diameters ranging from 3 to 43 nm and lengths up to a few hundreds of microns. Twins and stacking faults were observed in the Si core of the NWs. The lattice structure and constant of the NWs were nearly identical to those of bulk Si, although the relative XRD peak intensities were different from those of randomly oriented Si crystallites.

Raman scattering from the NWs showed an asymmetric peak at the same position as that of bulk crystalline silicon.

These two independent efforts immediately opened up a new era with substantial opportunities in this research field [36]. Significant progress has been achieved subsequently in controlling the morphology, size, composition and doping, on length scales ranging from the atomic and up [17, 53]. In the next chapter, we will focus on the metal nanocluster catalyzed VLS-growth as a representative method for the bottom up approach.

## References

1. M.H. Devoret, D. Esteve, C. Urbina, Single-electron transfer in metallic nanostructures. *Nature* **360**(6404), 547–553 (1992)
2. A.P. Alivisatos, Semiconductor clusters, nanocrystals, and quantum dots. *Science* **271**(5251), 933–937 (1996)
3. C.M. Lieber, X.L. Wu, Scanning tunneling microscopy studies of low-dimensional materials: probing the effects of chemical substitution at the atomic level. *Acc. Chem. Res.* **24**(6), 170–177 (1991)
4. H. Dai, C. Lieber, Scanning tunneling microscopy studies of low-dimensional materials: charge density wave pinning and melting in two dimensions. *Annu. Rev. Phys. Chem.* **44**(1), 237–263 (1993)
5. C.M. Lieber, J. Liu, P.E. Sheehan, Understanding and manipulating inorganic materials with scanning probe microscopes. *Angew. Chem. Int. Ed.* **35**(7), 686–704 (1996)
6. V. Emery, J. Devreese, R. Evrard, V. Van Doren, *Highly conducting one-dimensional solids* (Plenum, New York, 1979)
7. C. Schlenker, J. Dumas, J. Rouxel, *Crystal chemistry and properties of materials with quasi-one-dimensional structures* (Reidel, Boston, 1986)
8. H. Dai, C.M. Lieber, Scanning tunneling microscopy studies of low-dimensional materials: charge density wave pinning and melting in two dimensions. *Annu. Rev. Phys. Chem.* **44**(1), 237–263 (1993)
9. J.A. Wilson, F. Di Salvo, S. Mahajan, Charge-density waves and superlattices in the metallic layered transition metal dichalcogenides. *Adv. Phys.* **24**(2), 117–201 (1975)
10. C.M. Lieber, One-dimensional nanostructures: chemistry, physics & applications. *Solid State Commun.* **107**(11), 607–616 (1998)
11. J. Hu, T.W. Odom, C.M. Lieber, Chemistry and physics in one dimension: synthesis and properties of nanowires and nanotubes. *Acc. Chem. Res.* **32**(5), 435–445 (1999)
12. C. Murray, C. Kagan, M. Bawendi, Self-organization of CdSe nanocrystallites into three-dimensional quantum dot superlattices. *Science* **270**(5240), 1335–1338 (1995)
13. C. Kane, L. Balents, M.P. Fisher, Coulomb interactions and mesoscopic effects in carbon nanotubes. *Phys. Rev. Lett.* **79**(25), 5086–5089 (1997)
14. C.M. Lieber, Z.L. Wang, Functional nanowires. *MRS Bull.* **32**(02), 99–108 (2007)
15. Y. Huang, C.M. Lieber, Integrated nanoscale electronics and optoelectronics: exploring nanoscale science and technology through semiconductor nanowires. *Pure Appl. Chem.* **76**(12), 2051–2068 (2004)
16. C.M. Lieber, Semiconductor nanowires: a platform for nanoscience and nanotechnology. *MRS Bull.* **36**(12), 1052–1063 (2011)
17. A. Zhang, C.M. Lieber, Nano-bioelectronics. *Chem. Rev.* **116**(1), 215–257 (2016)
18. A. Thess, R. Lee, P. Nikolaev, H. Dai, P. Petit, J. Robert, C. Xu, Y.H. Lee, S.G. Kim, A.G. Rinzler, Crystalline ropes of metallic carbon nanotubes. *Science* **273**(5274), 483–487 (1996)



19. X. Duan, C.M. Lieber, General synthesis of compound semiconductor nanowires. *Adv. Mater.* **12**(4), 298–302 (2000)
20. C.B. Murray, D.J. Norris, M.G. Bawendi, Synthesis and characterization of nearly monodisperse CdE (E = sulfur, selenium, tellurium) semiconductor nanocrystallites. *J. Am. Chem. Soc.* **115**(19), 8706–8715 (1993)
21. F. Himpsel, T. Jung, A. Kirakosian, J.-L. Lin, D. Petrovykh, H. Rauscher, J. Viernow, Nanowires by step decoration. *MRS Bull.* **24**(8), 20–24 (1999)
22. H. Dai, E.W. Wong, Y.Z. Lu, S. Fan, C.M. Lieber, Synthesis and characterization of carbide nanorods. *Nature* **375**(6534), 769–772 (1995)
23. W. Han, S. Fan, Q. Li, Y. Hu, Synthesis of gallium nitride nanorods through a carbon nanotube-confined reaction. *Science* **277**(5330), 1287–1289 (1997)
24. C.R. Martin, Nanomaterials: a membrane-based synthetic approach. *Science* **266**(5193), 1961–1966 (1994)
25. R.S. Wagner, W.C. Ellis, Vapor-liquid-solid mechanism of single crystal growth. *Appl. Phys. Lett.* **4**(5), 89–90 (1964)
26. R. Wagner, W. Ellis, The vapor-liquid-solid mechanism of crystal growth and its application to silicon. *Trans. Met. Soc. AIME* **233**, 1053–1064 (1965)
27. T.J. Trentler, K.M. Hickman, S.C. Goel, A.M. Viano, P.C. Gibbons, W.E. Buhro, Solution-liquid-solid growth of crystalline III-V semiconductors: an analogy to vapor-liquid-solid growth. *Science* **270**(5243), 1791–1794 (1995)
28. P. Yang, C.M. Lieber, Nanorod-superconductor composites: a pathway to materials with high critical current densities. *Science* **273**(5283), 1836–1840 (1996)
29. Z.W. Pan, Z.R. Dai, Z.L. Wang, Nanobelts of semiconducting oxides. *Science* **291**(5510), 1947–1949 (2001)
30. B.K. Teo, X. Sun, Silicon-based low-dimensional nanomaterials and nanodevices. *Chem. Rev.* **107**(5), 1454–1532 (2007)
31. W. Lu, C.M. Lieber, Semiconductor nanowires. *J. Phys. D Appl. Phys.* **39**(21), R387–R406 (2006)
32. R.G. Hobbs, N. Petkov, J.D. Holmes, Semiconductor nanowire fabrication by bottom-up and top-down paradigms. *Chem. Mat.* **24**(11), 1975–1991 (2012)
33. M. van den Brink, Continuing to shrink: Next-generation lithography—Progress and prospects, in *IEEE International Solid-State Circuits Conference*, (IEEE, 2013), pp. 20–25
34. A.M. Morales, C.M. Lieber, A laser ablation method for the synthesis of crystalline semiconductor nanowires. *Science* **279**(5348), 208–211 (1998)
35. Y. Cui, L.J. Lauhon, M.S. Gudiksen, J. Wang, C.M. Lieber, Diameter-controlled synthesis of single-crystal silicon nanowires. *Appl. Phys. Lett.* **78**(15), 2214–2216 (2001)
36. X. Duan, C.M. Lieber, Semiconductor nanowires: rational synthesis, in *Dekker Encyclopedia of Nanoscience and Nanotechnology*, ed. by J.A. Schwarz (Marcel Dekker, Inc., New York, 2005)
37. R. Treuting, S. Arnold, Orientation habits of metal whiskers. *Acta Met.* **5**(10), 598 (1957)
38. E.S. Greiner, J.A. Gutowski, W.C. Ellis, Preparation of silicon ribbons. *J. Appl. Phys.* **32**(11), 2489–2490 (1961)
39. R.S. Wagner, Growth of whiskers by vapor-phase reactions, in *Whisker technology*, ed. by A. P. Levitt (Wiley, New York, 1970), pp. 15–119
40. E. Givargizov, Fundamental aspects of VLS growth. *J. Cryst. Growth* **31**, 20–30 (1975)
41. T.G. Dietz, M.A. Duncan, D.E. Powers, R.E. Smalley, Laser production of supersonic metal cluster beams. *J. Chem. Phys.* **74**(11), 6511–6512 (1981)
42. P.B. Fischer, K. Dai, E. Chen, S.Y. Chou, 10 nm Si pillars fabricated using electron-beam lithography, reactive ion etching, and HF etching. *J. Vac. Sci. Technol., B* **11**(6), 2524–2527 (1993)
43. P.B. Fischer, S.Y. Chou, Sub-50 nm high aspect-ratio silicon pillars, ridges, and trenches fabricated using ultrahigh resolution electron beam lithography and reactive ion etching. *Appl. Phys. Lett.* **62**(12), 1414–1416 (1993)

44. W. Chen, H. Ahmed, Fabrication of high aspect ratio silicon pillars of <10 nm diameter. *Appl. Phys. Lett.* **63**(8), 1116–1118 (1993)
45. P.A. Lewis, H. Ahmed, T. Sato, Silicon nanopillars formed with gold colloidal particle masking. *J. Vac. Sci. Technol., B* **16**(6), 2938–2941 (1998)
46. E.W. Wong, B.W. Maynor, L.D. Burns, C.M. Lieber, Growth of metal carbide nanotubes and nanorods. *Chem. Mat.* **8**(8), 2041–2046 (1996)
47. M. Yazawa, M. Koguchi, A. Muto, M. Ozawa, K. Hiruma, Effect of one monolayer of surface gold atoms on the epitaxial growth of InAs nanowhiskers. *Appl. Phys. Lett.* **61**(17), 2051–2053 (1992)
48. K. Hiruma, M. Yazawa, K. Haraguchi, K. Ogawa, T. Katsuyama, M. Koguchi, H. Kakibayashi, GaAs free-standing quantum-size wires. *J. Appl. Phys.* **74**(5), 3162–3171 (1993)
49. T. Sato, K. Hiruma, M. Shirai, K. Tominaga, K. Haraguchi, T. Katsuyama, T. Shimada, Site-controlled growth of nanowhiskers. *Appl. Phys. Lett.* **66**(2), 159–161 (1995)
50. J.F. Ready, *Effects of high-power laser radiation* (Academic Press, New York, 1971)
51. C. Lieber, A. Morales, P. Sheehan, E. Wong, P. Yang, One-dimensional nanostructures: Rational synthesis, novel properties and applications, in *Proceedings of the Robert A. Welch Foundation 40th Conference on Chemical Research: Chemistry on the Nanometer Scale* (1997), pp. 165–187
52. Y.F. Zhang, Y.H. Tang, N. Wang, D.P. Yu, C.S. Lee, I. Bello, S.T. Lee, Silicon nanowires prepared by laser ablation at high temperature. *Appl. Phys. Lett.* **72**(15), 1835–1837 (1998)
53. Y. Wang, T. Wang, P. Da, M. Xu, H. Wu, G. Zheng, Silicon nanowires for biosensing, energy storage, and conversion. *Adv. Mater.* **25**(37), 5177–5195 (2013)

## Chapter 2

# General Synthetic Methods

**Abstract** Over the past two decades, remarkable progress has been made in research focused on the synthesis of 1D NWs leading to the rational design and synthetic control of key properties, where the capability of design and control of NWs has opened up the potential for revolutionary advances in diverse areas ranging from electronics and photonics to energy and healthcare. Scaling NW diameters to the deep nanometer and even molecular regime, as well as controlling their morphology, composition and structure represents fundamental challenges critical to exploiting NWs for applications in science and technology. In this chapter, we overview major bottom-up strategies for the synthesis of NWs, including vapor phase, templated, and solution-based methods. The advantages and challenges of different methods will be discussed, with representative examples illustrated.

### 2.1 Introduction

Semiconductor NWs can be prepared by a variety of methods, which can be generally categorized as either top-down or bottom-up approaches [1–6]. In the top-down approach, the NW features are patterned at the surface of bulk materials, typically single crystal semiconductor wafers, by a combination of lithography, doping, etching and deposition. An advantage of top-down methods is that lithographically-defined NWs are formed at well-defined locations that facilitate integration into systems. While developments continue to push the resolution limits of the top-down approaches, these improvements in resolution are accompanied by two limitations. First, lithography-based patterning yields surface roughness that can become substantial fraction of the total NW diameter, and second, there is a near-exponential increase in cost associated with each new level of manufacturing facilities. These material and economic limitations of top-down strategies have motivated efforts worldwide the past two decades to search for new paradigms to meet the demand for nanoscale structures. Bottom-up approaches, in which functional structures are assembled from well-defined chemically/physically synthesized nanoscale building blocks, represent an alternative yet powerful scenario to

conventional top-down methods. The bottom-up strategy has the potential to go far beyond the limits and functionality of top-down technology by defining key nanometer-scale metrics through synthesis and subsequent assembly [1, 6, 7]. Moreover, it is highly likely that the bottom-up approaches will enable entirely new device concepts and functional systems, and thereby create technologies that people have not yet imagined. In this chapter, we will focus on the bottom-up fabrication methods, which can be divided into three categories: vapor phase growth, templated growth and solution-based methods. Several reviews on NW synthetic methods have appeared [3, 5, 6].

## 2.2 Vapor Phase Growth

The most widely used NW synthetic methods have focused on vapor phase growth since these have yielded NWs with high crystallinity, monodispersity, as well as and controlled morphology and electrical properties. This section introduces vapor phase growth strategies, such as the dominant nanocluster-catalyzed vapor-liquid-solid (VLS) approach, and other related schemes, including vapor-solid-solid and oxide-assisted growth.

### 2.2.1 *Laser-Assisted Catalytic Growth*

In 1997 and 1998, the Lieber group [8, 9] reported a method combining laser ablation cluster formation and VLS growth for the synthesis of semiconductor NWs. This method, termed as “laser-assisted catalytic growth (LCG)”, which was capable of producing nanometer scale clusters [10] required to nucleate and direct the growth of NWs, was used to prepare single-crystal silicon and germanium NWs with diameters of 6–20 and 3–9 nm, respectively, and lengths ranging from 1 to 30  $\mu\text{m}$ . The NW growth was readily achieved by laser ablation of a composite target containing the metal catalyst and NW material in a heated flow tube (Fig. 2.1a). The background pressure within the flow reactor was used to control condensation of the ablated material and thereby cluster size, while the temperature is varied to maintain the catalyst cluster in the liquid state for VLS growth. When the laser-generated clusters become supersaturated with the desired NW material, a nucleation event occurs to produce a NW solid-liquid (NW-catalyst alloy) interface. To minimize the interfacial free energy, subsequent solid growth/crystallization occurs at this initial interface, which thus imposes a highly anisotropic growth constraint that leads to 1D nanoscale wires. This approach was shown early on to be general for the synthesis of NWs of most important semiconductor materials, including group IV elemental (Si, Ge) and alloys (SiGe), group III–V (GaAs, GaP, GaAsP, InAs, InP, InAsP), II–VI (ZnS, ZnSe, CdS, CdSe), and IV–VI (PbTe) compound semiconductor NW materials [11–14].

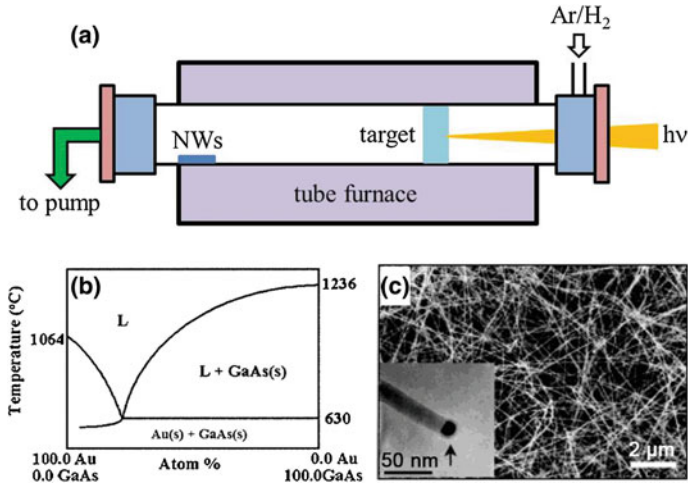


**Fig. 2.1** **a** Schematic of a laser-based NW growth apparatus. **b** Pseudobinary phase diagram of the GaAs-Au system. **c** SEM image of GaAs NWs produced by LCG. Reproduced from [11]. Copyright 2000 John Wiley and Sons

A key feature of the VLS growth approach for NW synthesis is that equilibrium phase diagrams can be used to predict the catalyst material, chemical composition, and growth conditions, thus enabling rational and predictable synthesis of new NW materials. For example, binary phase diagrams have been used to predict the composition and growth temperatures for the synthesis of elemental semiconductor NW materials such as silicon and germanium NWs [9]. Predictable catalytic growth of compound NWs is more challenging than that of Si and Ge NWs, due to the complexity of ternary or higher ordered phase diagrams. However, such complexity can be greatly simplified by considering pseudo-binary phase diagrams for the catalyst and compound semiconductor of interest. For example, the pseudo-binary phase diagram of Au-GaAs (Fig. 2.1b) shows that Au-Ga-As liquid and GaAs solid are the principle phases above 630 °C in the GaAs-rich region of the phase diagram [15]. This information implies that Au can serve as a catalyst to grow GaAs NWs by the LCG method, if the target composition and growth temperature are chosen to be within this region of the phase diagram. Indeed, LCG growth of GaAs NWs using Au as the catalyst produced samples consisting primarily of wire-like structures with diameters on the order of 10 nm, and lengths extending up to tens of micrometers [11, 16] (Fig. 2.1c).

Gold has been used extensively as a catalyst for growth of a number of NWs of III–V and II–VI material. However, Au exhibits poor solubility of N and thus is not ideal for GaN NW growth. Instead, analysis of phase diagrams showed that Fe and Ni can dissolve both gallium and nitrogen, but do not form a more stable compound than GaN. Subsequent LCG using Fe and Ni as catalysts led successfully to the growth of GaN NW [13].

## 2.2.2 Chemical Vapor Deposition

Chemical vapor deposition (CVD) is now one of the most widely applied methods to synthesize semiconductor NWs. For example and in the case of SiNWs, a volatile gaseous precursor, such as  $\text{SiH}_4$  or  $\text{SiCl}_4$ , serves as the silicon source for growth. The gaseous precursor, which may partially decompose in a heated reactor, is transported by inert carrier gases, typically Ar or  $\text{H}_2$ , to the surface of metal catalyst. At the nanocluster catalyst sites the precursor decomposes into its elemental (i.e., Si) constituent. In 2001, Cui et al. [17] first demonstrated CVD-based nanocluster-catalyzed VLS growth of SiNWs (Fig. 2.2a). Figure 2.2b shows SEM images of the SiNWs produced from 10-nm Au nanoclusters. The NW density was comparable to the nanocluster density, suggesting that the SiNW nucleation was dominated by these clusters. TEM image (Fig. 2.2b, bottom inset) further showed that the Au particle at the NW end controlled the NW diameters.

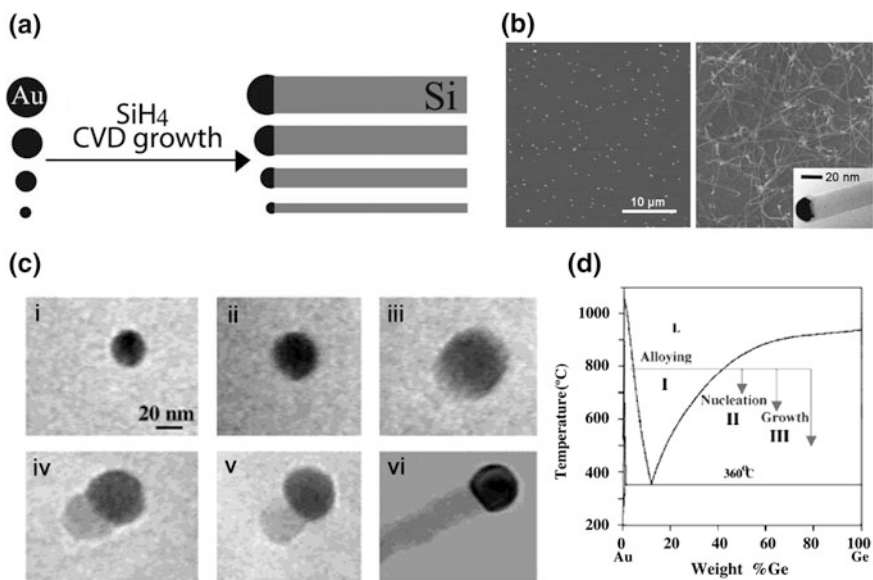


**Fig. 2.2** a Schematic illustrating size-controlled synthesis of SiNWs from Au nanoclusters. b AFM image of 10 nm Au nanoclusters dispersed on the substrate (*left*) and FESEM image of SiNWs grown from the nanoclusters (*right*). The *inset* is a TEM image of a SiNW with a gold catalyst at the end. Reproduced from [17]. Copyright 2001 AIP Publishing LLC. c In situ TEM images recorded during the process of NW growth. *i* Au nanoclusters in solid state at 500 °C; *ii* alloying initiates at 800 °C, at this stage Au exists in mostly solid state; *iii* liquid Au/Ge alloy; *iv* the nucleation of Ge nanocrystal on the alloy surface; *v* Ge nanocrystal elongates with further Ge condensation and eventually (*vi*) a wire forms. d Au-Ge binary phase diagram including (I) alloying, (II) nucleation, and (III) axial growth. Reproduced from [18]. Copyright 2001 American Chemical Society

In the same year, Wu et al. [18] reported the first real-time observation of semiconductor NW CVD growth in a high-temperature TEM, which unambiguously demonstrated the validity of the nanocluster-catalyzed VLS growth mechanism. Figure 2.2c shows a sequence of TEM images during the growth of a GeNW in situ. Three stages, including the alloying process, the nucleation, and the subsequent axial growth, are clearly identified. (1) Alloying process (i–iii). With the increasing amount of Ge vapor condensation and dissolution, Ge and Au form an alloy and liquefy. The volume of the alloy droplets increases, due to dilution of the heavy metal Au with the lighter element Ge, while the alloy composition crosses sequentially, from left to right, a biphasic region (solid Au and Au/Ge liquid alloy) and a single-phase region (liquid) (Fig. 2.2d). (2) Nucleation (iv–v). When the composition of the alloy crosses the second liquidus line, it enters another biphasic region (Au/Ge alloy and solid Ge), which starts the NW nucleation. (3) Axial growth (iv–vi). Once the Ge nanocrystal nucleates at the liquid/solid interface, further condensation/dissolution of Ge vapor into the system increases the amount of Ge crystal precipitation. The existing interface then moves forward to form a NW.

During VLS growth, SiNWs are formed in near-equilibrium condition, and the growth processes can thus be considered primarily thermodynamically driven. As a result, the preferred growth direction is the one that minimizes the total free energy. Wu et al. [19] and Schmidt et al. [20] found that the growth directions of intrinsic SiNWs can be influenced by the diameters of the NWs. The larger intrinsic SiNWs with diameters above  $\sim 20$  nm exhibit a dominant  $\langle 111 \rangle$  growth direction, whereas NWs with smaller diameters (3–10 nm) tend to grow along the  $\langle 110 \rangle$  direction, and  $\langle 112 \rangle$  NWs are obtained in the transition region. These results can be understood as arising from the increasing contribution of the silicon/vacuum surface energy to the total free energy in smaller NWs. In addition, system pressure during growth and doping level can play an important role in determining NW growth orientations [5, 21, 22], and represents an area for further study in the future.

In the case of compound semiconductor NWs, atomic-level precision growth requires better control of the conditions. By growing GaP NWs in a TEM, the Ross group [23] measured the local kinetics in situ as each atomic plane is added at the nanocluster catalyst-NW growth interface by the VLS process. During growth of GaP NWs at typical V/III ratios, they found surprising fluctuations in the growth rate, even under steady-state growth conditions, though these variations can be suppressed by switching to growth conditions with a low V/III ratio. The authors derived a growth model showing that this unexpected variation in local growth kinetics reflects the very different supply pathways of the V and III species. The model explains under which conditions the growth rate can be controlled precisely at the atomic level.

Generally, a CVD process requires a temperature sufficiently high to initiate decomposition of the precursor, while there are a number of methods to achieve low temperature CVD [5]. Hence, the choice of precursors can be important in achieving growth close to the minimum temperature predicted by phase diagrams for formation of the nanocluster catalyst/semiconductor liquid solution necessary for VLS growth. For example, disilane ( $\text{Si}_2\text{H}_6$ ), which decomposes at low temperature than  $\text{SiH}_4$ ,

enables growth of SiNWs at lower temperature [24, 25]. Another approach to achieving lower temperature growth involves using plasma-enhanced CVD (PECVD) [26, 27], where the plasma in the NW synthesis reactor facilitates precursor decomposition at temperature lower than a purely thermal process.

### 2.2.3 Chemical Vapor Transport

Chemical vapor transport (CVT) provides another approach for conveniently yielding volatile precursors for nanocluster-catalyzed VLS growth of NWs. When a condensed phase, typically a solid, has an insufficient vapor pressure for growth, the effective vapor-phase concentration can be increased by utilizing a thermodynamically reversible reaction with the gaseous transport species to form a discrete volatile complex. There is a long history of CVT, often using halogens, to grow crystals [28, 29].

In 2000, the Yang group [30] reported the synthesis of GeNWs by nanocluster-catalyzed VLS growth, where the Ge reactant was generated by the CVT in a sealed-tube. In their experiments, a mixture Ge and  $\text{GeI}_4$  was put at one end of a quartz tube, and a gold-coated Si (001) substrate was put at the opposite end of the tube. The temperature gradient between the source material and the substrate was 100–200 °C to enable transport of the volatile  $\text{GeI}_2$  complex, and GeNWs were collected on the Si substrate surface. Later, the same research group applied CVT to generate reactant species for nanocluster-catalyzed VLS growth of several different composition NWs, including ZnO [31, 32], B [33] and GaN/AlGaIn core-shell heterostructures [34].

Song et al. [35] reported the large-scale synthesis of ultralong  $\text{Ni}_2\text{Si}$  NWs iodine CVT of  $\text{Ni}_2\text{Si}$  powder as the source material, where Ni was assumed to be the catalyst for VLS growth. The reaction was carried out in a continuous flow CVT reactor tube as illustrated in Fig. 2.3a. At the higher temperature ( $T_1 = 1000$  °C),

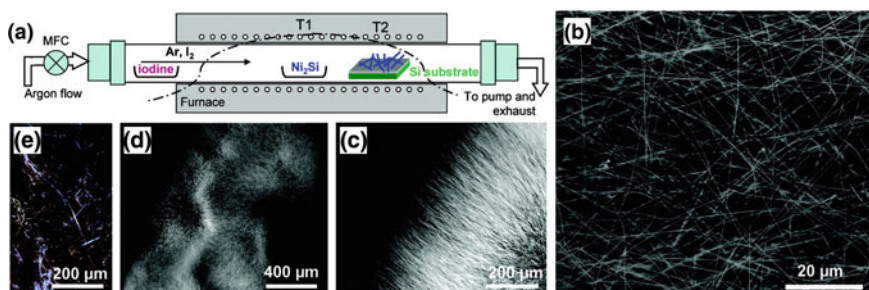


**Fig. 2.3** a Schematic setup for the synthesis of  $\text{Ni}_2\text{Si}$  NWs using CVT. b–d Representative SEM images of  $\text{Ni}_2\text{Si}$  NWs found on substrates at various magnifications. e Dark field optical image of  $\text{Ni}_2\text{Si}$  NWs dispersed on a silicon substrate highlighting up to 1 mm NW length. Reproduced from [35]. Copyright 2007 American Chemical Society



iodine reacts with the  $\text{Ni}_2\text{Si}$  powder to produce gaseous  $\text{NiI}_2$  and  $\text{SiI}_4$  and are transported downstream by the inert argon carrier gas flow to the lower temperature ( $T_2 \approx 850$  °C)  $\text{Ni}_2\text{Si}$  NW growth zone. Representative SEM images and dark field optical image are shown in Fig. 2.3b–e.

### 2.2.4 Molecular Beam Epitaxy

Since 2000, molecular beam epitaxy (MBE) techniques have been employed to synthesize Si [36–38], II–VI [39] and III–V [40, 41] compound semiconductor NWs based on the nanocluster-catalyzed VLS growth mechanism [3, 5]. The MBE technique provides an ideal clean growth environment, where the atomic structure, doping and junctions (or heterostructures) can in principle be well controlled. Different from other synthesis techniques, MBE is carried out under ultra-high vacuum conditions, where the mean-free-path of atomic/molecular species is generally longer than the separation between reactant source and growth substrates. In this regime, reactant atoms or molecules will travel line-of-sight from sources to substrate since there are no collisions. MBE-based nanocluster-catalyzed VLS growth has several advantages, including that the atomic reactants do not require elevated temperatures to decompose prior to incorporation in metal nanocluster catalysts like many molecular precursors. On the other hand, the line-of-site delivery of reactants represents a serious limit to reactant flux/concentration at the nanocluster catalysts, which direct growth, although surface diffusion of reactants collected on the substrate to these growth tips can alleviate this issue.

To exemplify MBE NW growth consider the case of SiNWs [37]. Elemental Si, instead of a chemical Si compound such as  $\text{SiH}_4$ , serves as the source for growth. SiNW growth is achieved by evaporating Si atoms onto a catalyst covered substrate (Fig. 2.4). Prior to initiating NW growth, Au is deposited onto a clean single-crystal

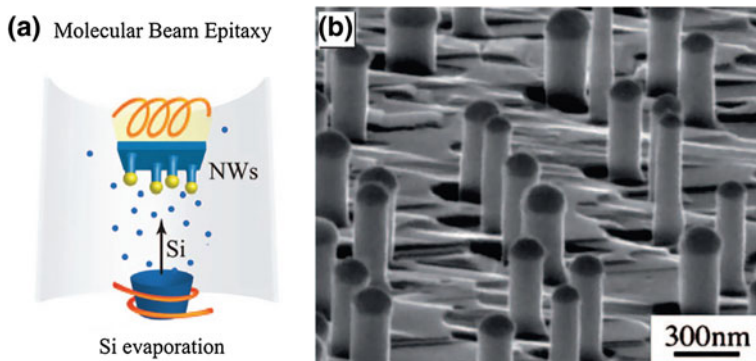


**Fig. 2.4** **a** Schematics of MBE SiNW growth. **b** SEM image of Au-catalyzed SiNWs on Si  $\langle 111 \rangle$ . Reproduced from [5]. Copyright 2010 American Chemical Society

Si-substrate and annealed above the Au–Si eutectic temperature to form nanosized particles that serve as the nanocluster catalysts for the subsequent VLS SiNW growth. During MBE NW growth, Si evaporated onto the substrate surface diffuses until it either crystallizes directly or dissolves into a gold nanocluster catalyst droplet. Because the MBE growth strongly relies on Si surface diffusion, growth temperatures are typically higher than 500 °C to facilitate this diffusion process. Doping of NWs during MBE growth can be carried out by co-evaporation of dopants such as B or Sb along with Si to yield SiNWs with well controlled doping profiles [38]. If additional evaporation sources, such as Ge, are available, then axial NW heterostructures can be achieved by sequential switching of the elemental sources [37].

### 2.2.5 Vapor-Solid-Solid Growth

In 2004, Persson et al. [42] proposed a modified mechanism for NW growth termed vapor-solid-solid (VSS), where the nanocluster catalyst remains in a solid versus liquid state. Their VSS proposal was based on electron diffraction measurements of Au nanocluster-catalyzed GaAs NW growth showing that the Au particle did not melt in the temperature range used for growth. Using in situ TEM, Kodambaka et al. [43] showed that for the classic Ge/Au system, the nanocluster catalysts can be either liquid or solid below the eutectic temperature ( $T_e$ ), depending on thermal history. NWs grow in both VLS and VSS processes, although at different rates with much slower rates observed for VSS. The catalyst state depends on  $\text{Ge}_2\text{H}_6$  pressure as well as temperature. The supersaturation of Ge in the alloy during growth appears to be essential in stabilizing the liquid below  $T_e$ . Subsequent reports on real-time observations of VSS growth of Cu-catalyzed SiNWs [44] and Ni-induced GaN NWs [45] further confirmed this observation. In 2015, Cui et al. [46] demonstrated a step-flow kinetics model for the VSS growth and performed a kinetic analysis taking into account the steady-state atom transport kinetics with three surfaces and one slow interfacial diffusion processes. Their model fit the step-flow behavior at the interface between the NW and catalyst, and revealed that the cyclical change of atom concentration was responsible for the successive side-to-side ledge flow. These theoretical results also described the growth kinetic process with growth rate as a function of temperature and pressure, and length and diameter of SiNWs.

### 2.2.6 Vapor-Solid Growth

There have been numerous reports on 1D nanostructure formation from vapor phase precursors in the absence of a metal catalyst or obvious VLS mechanism. A model

that can lead to 1D material structures without a metal catalyst particle has been termed vapor-solid (VS) growth [2, 3, 47, 48]. Using thermodynamic and kinetic considerations, the formation of NWs can be achieved through an anisotropic VS growth mechanism [48–50]. In addition, 1D growth can be realized in the context of defect-induced growth models [51, 52] and self-catalytic VLS growth [2, 3, 53–56].

Anisotropic growth mechanism [48–50]. The anisotropic properties of different surfaces in a crystal can lead to preferential reactivity and binding of reactants (on specific surface facets), and thereby wire- or rod-like shapes. The typical anisotropic properties of crystals are, however, insufficiently large to obtain length to diameter ratios greater than 100 [3].

Defect-induced growth models [51, 52]. Screw dislocations can significantly enhance the crystal growth of metals and some molecular materials [57]. This classical mechanism is based on the fact that the growth of a crystal proceeds by adding atoms at the kink sites of a surface step. Kink sites always exist on the steps even at the thermal equilibrium state. Due to the advance of the kink along the surface by the addition of atoms, the crystal grows perpendicularly to the surface.

Self-catalytic VLS [53–55]. NW growth has been achieved without nanocluster catalysts on the growth substrate or catalyst material in the source. In these cases, the nanocluster nuclei necessary for VLS growth of NWs can form through internal chemical reactions. This mechanism is considered to be a self-catalytic VLS growth. For example, Zn metal forms from disproportionation of ZnO in vacuum, and serves as the catalyst for subsequent ZnO NW growth [53].

### 2.2.7 *Oxide-Assisted Growth*

Lee’s group [58] first reported a metal catalyst-free “oxide-assisted growth (OAG)” method to obtain SiNWs. The growth process involved thermal evaporation of either mixed powders of SiO<sub>2</sub> and Si to produce SiO vapor [58, 59] or a pure SiO powder [60, 61]. The powders and Si wafers are placed inside a heated alumina tube, where nucleation of SiNWs occurs from SiO vapor on the substrates due to disproportionation. The disproportionation reaction also leads to a thick SiO<sub>x</sub> shell, with  $x$  values between 1.5 and 2, on the SiNWs. Figure 2.5 highlights a comparison between OAG and VLS. In the OAG approach, SiNW growth is proposed to be assisted by “semi-liquid” SiO<sub>x</sub>, while the solid SiO<sub>2</sub> shell can prevent lateral growth during elongation [62]. While useful for growth of intrinsic SiNWs, it remains unclear whether this OAG approach can be used to introduce dopants in a controlled and/or modulated manner, which is critical for most electronic and opto-electronic applications of SiNWs, and whether the method could be used more generally (like VLS) to prepare NWs of other materials.

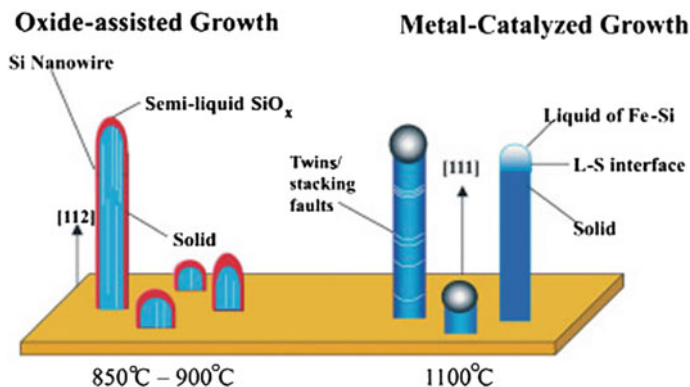


**Fig. 2.5** A schematic diagram comparing the OAG (*left*) and VLS growth (*right*). Reproduced from [62]. Copyright 2003 John Wiley and Sons

## 2.3 Templated Growth

Template-based growth of 1D nanostructures can be achieved using both vapor- and solution-based process [63, 64]. The diameter, density and length of NWs and nanorods can be conveniently controlled, based on the pre-formed template dimensions. The template-based synthetic approach also has limitations, including (i) fabrication of templates with desired pore channel diameters and lengths, (ii) typical polycrystalline (vs. single crystalline) NWs obtained during synthesis, and (iii) post-synthesis removal of templates without compromising the integrity of the NWs. This section focuses on template based approaches used to synthesize NWs, including nanopores, self-assembled surfactants, existing nanostructures and superlattices.

### 2.3.1 Formation Inside Nanopores

Porous anodic aluminum oxide (AAO) [40, 65–70], zeolites [71, 72], track-etched polymer membranes [73, 74], or other types of porous structures can serve as templates for NW synthesis [63, 64]. There are two approaches to guide 1D growth using such templates. The first approach is to use the template to deposit metal dots on a substrate surface with the size and spacing defined by the template, and grow NW arrays (Sect. 4.3.1.3) [40, 65, 66]. The second approach is direct formation of NWs inside the nanopores of the template, where we discuss studies of AAO as a representative example [67–70]. Porous AAO is one of the most commonly used and commercially available templates. The membranes produced by anodization of aluminum foils in acidic solutions contain hexagonally arranged 2D parallel arrays of cylindrical pores with a uniform size. Porous template-based growth of NW

arrays can be achieved using well-established techniques such as electrochemical deposition, electrophoretic deposition and template filling in AAO. Then, the NWs can be released from the templates by selective removal of the host matrix. Accordingly, free-standing NW arrays integrated on a large surface area are obtained. Various inorganic materials, including metals, metal oxides and semiconductors, have been synthesized within AAO templates [64, 75]. One intrinsic advantage of AAO templates regarding NW synthesis is that different materials can be deposited successively to produce axial modulated structures [69, 70]. Qin et al. [76] and Liu et al. [77] have extended these structures by “on-wire lithography” (OWL) in which one component of the modulated structure is preferentially etched.

### ***2.3.2 Templating Against Self-assembled Structures***

It is well-known that surfactant molecules can spontaneously organize into rod-shaped micelles when their concentration reaches a critical value [78]. These self-assembled structures provide another class of versatile templates for generating 1D nanostructures. Based on this principle, Yu et al. [79] reported the synthesis of Au nanorods on micelles formed by cetyltrimethylammonium bromide (CTAB) and another much more hydrophobic cationic surfactant (e.g., tetraoctylammonium bromide, TOAB). Kwan et al. [80] also studied the synthesis of BaWO<sub>4</sub> nanorods with uniform dimensions using this approach. In another demonstration, Li et al. [81] synthesized single crystalline tungsten NWs by templating WO<sub>4</sub><sup>2-</sup> ions against the lamellar phase of CTAB, followed by pyrolysis in vacuum.

Meso-phase structures self-assembled from surfactants are able to generate NWs on a large scale. This method has several challenges, however, such as non-uniform pore filling in high aspect-ratio structures, template degradation during extended synthetic procedures, and poor crystallinity of the resulting NWs.

### ***2.3.3 Construction on Existing Nanostructures***

Existing nanostructures can be used as physical or chemical templates to generate NWs. As physical templates, carbon nanotubes (CNTs) can be applied to confine the reaction, resulting in GaN nanorods having a diameter similar to that of the original NTs [82]. In another case, CNTs are used as substrates for deposition of various metals (Au, Pd, Fe, Al, and Pb) by evaporation [83]. He et al. [84] demonstrated that pre-synthesized NWs could serve as substrates for epitaxial growth of another material to produce bilayer nanotapes with sharp interfaces. As a proof of concept, TiO<sub>2</sub>, Co<sub>0.05</sub>Ti<sub>0.95</sub>O<sub>2</sub>, or BaTiO<sub>3</sub> were deposited onto a collection of SnO<sub>2</sub> nanoribbons to yield composite nanotapes. The Belcher group [85–87] reported the directed synthesis of NWs based on virus templates, followed by

annealing of the virus-particle assemblies into high aspect ratio crystalline NWs through oriented aggregation-based crystal growth. Lee et al. [88] showed that inorganic NWs of gold(I) cyanide can grow directly on pristine graphene, aligning themselves with the zigzag lattice directions of the graphene. The NWs are formed through a self organized growth process in aqueous solution at room temperature, which indicates that the inorganic material spontaneously binds to the pristine graphene surface. First-principles calculations suggest that this assembly originates from lattice matching and  $\pi$  interaction to gold atoms.

A more important and seminal example of using nanostructures in NW synthesis is their application as chemically reactive templates [33, 89, 90]. For example, Dai et al. [89] obtained carbide nanorods via the reaction of carbon nanotubes with volatile transition-metal and main group halide or oxide species. Gates et al. [90] converted selenium NWs with triangular cross-sections into single crystalline NWs of  $\text{Ag}_2\text{Se}$  by the reaction of SeNWs with aqueous  $\text{AgNO}_3$  solutions at room temperature. In another demonstration, Wu et al. [33] transformed boron NWs into  $\text{MgB}_2$  NWs by reacting with Mg vapor.

### 2.3.4 Superlattice Nanowire Pattern Transfer

Superlattice nanowire pattern transfer (SNAP), a technique based on translating thin film growth thickness control into planar wire arrays, is capable of producing ultrahigh-density arrays of aligned metal and semiconductor NWs [91]. The SNAP synthetic procedure is illustrated in Fig. 2.6a. A GaAs/ $\text{Al}_{0.8}\text{Ga}_{0.2}\text{As}$  superlattice

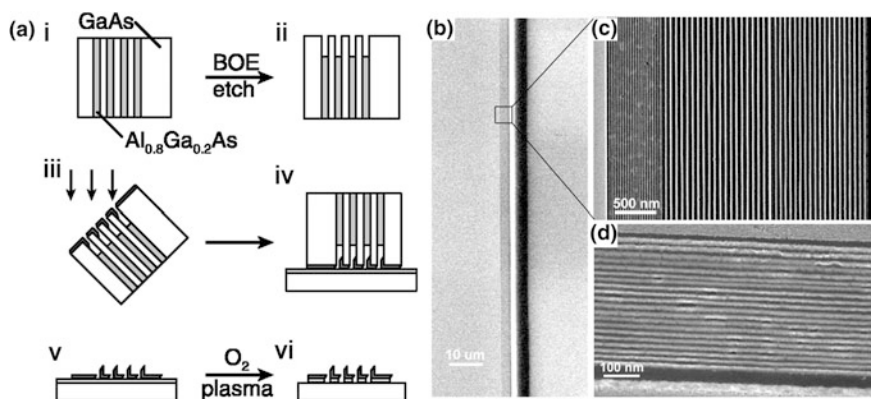


**Fig. 2.6** a Process diagram to create small pitch wires. *i* The GaAs/ $\text{AlGaAs}$  superlattice, *ii* after selectively etching the  $\text{AlGaAs}$ , *iii* metal deposition while tilted at  $36^\circ$ , *iv* contact of superlattice onto adhesive layer, *v* release of metal wires by etching GaAs oxide, and *vi* after optional  $\text{O}_2$  plasma to remove adhesive layer. **b-d** SEM images of a NW array showing Pt wires created by SNAP technique. Reproduced from [91]. Copyright 2003 the American Association for the Advancement of Science

was grown on the [92] surface of a GaAs substrate by MBE techniques. A dilute mixture of buffered hydrofluoric acid was used to selectively etch the AlGaAs layers roughly 20–30 nm deep. Metal wires were then evaporated onto the top of the GaAs template layers, by orienting the superlattice at  $36^\circ$  with respect to the evaporative flux within the vacuum chamber of an electron beam metal evaporation system. This tilt caused the metal to be deposited only on the GaAs layers because of their elevation relative to the etched AlGaAs layers. The wire widths were defined by the thickness of the GaAs layers, and the separation between wires was defined by the thickness of the AlGaAs layers. Wires deposited with this technique were uniform and continuous over the 2- to 3-mm length of the GaAs superlattices, with remarkably few defects (Fig. 2.6b–d).

## 2.4 Solution-Based Methods

Compared with the vapor-phase growth process, solution-based synthetic routes have advantages, such as relatively low reaction temperatures, low cost, and composition/surface chemistry control. These features make solutions-based approaches promising for large-scale and environmentally benign synthesis of NWs [93, 94]. In this section, we introduce several representative solution-phase NW growth approaches. The synthetic routes are mainly classified into four categories, solution-liquid-solid (SLS) growth, supercritical fluid-liquid-solid (SFSL) growth, solvothermal/hydrothermal synthesis and directed solution-based growth.

### 2.4.1 *Solution-Liquid-Solid Growth*

In the mid-1990s, the initial discovery of solution-liquid-solid (SLS) growth was reported by the Buhro group [95], where a solution synthesis of crystalline III–V semiconductor NWs at low temperature was reported. The SLS mechanism, by analogy to the VLS growth, is a solution-based nanocluster catalyzed growth mechanism in which nanometer-scale metallic droplets catalyze the decomposition of metallo-organic precursors with resultant crystalline NW growth (Fig. 2.7a, b) [96, 97].

In the SLS mechanism, the NW diameter is controlled by liquid-metal droplets, similar to the case of VLS growth. Because of the limited temperature stability of most organic solvents, it is necessary to prepare mono-dispersed catalyst clusters with low melting point, such as Bi [96]; moreover, the chosen metal must have a eutectic point with the semiconductor of interest that is lower than the solvent boiling point. The SLS growth method has been applied to the synthesis of several types of NWs, including III–V (GaP, GaAs, InP, InAs) and II–VI (CdSe, CdTe, ZnTe) [92, 98–101]. For example, by using nearly monodispersed Bi nanoparticles as catalysts, CdSe NWs were synthesized from cadmium stearate and  $n$ -R<sub>3</sub>PSe

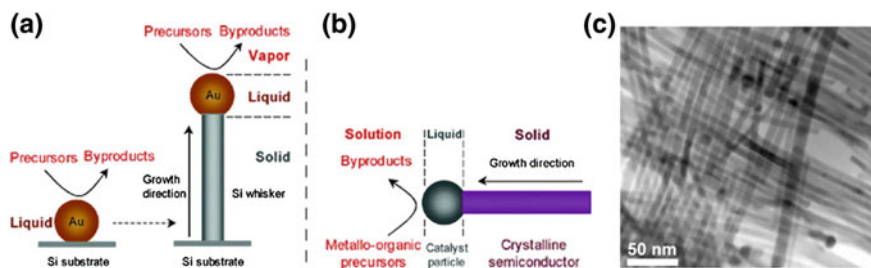


**Fig. 2.7** **a** VLS mechanism for NW growth. **b** SLS mechanism for analogous growth from solution. Reproduced from [96]. Copyright 2006 American Chemical Society. **c** TEM images of SLS-grown CdSe NWs. Reproduced from [92]. Copyright 2003 American Chemical Society

(R = butyl or octyl) in trioctylphosphane oxide (TOPO) at 240–300 °C [92]. The diameter of NWs was controlled by controlling the size of Bi nanoparticles and the reaction temperature. From these procedures, crystalline CdSe NWs with a diameter of 5–20 nm were obtained (Fig. 2.7c). In another case, Grebinski et al. [101] reported the synthesis of CdSe NWs by using Au/Bi nanoparticles as catalyst, CdO and TOPSe as precursors, and octanoic acid as Cd-coordinating surfactant, providing good control over the growth kinetics of NWs. Both straight and branched NWs were synthesized by varying the Cd/Se precursor ratio and the excess amount of TOP ligand. All of resulting crystalline NWs had diameters below 10 nm with lengths of 1–10  $\mu\text{m}$ .

In comparison with the VLS method, the SLS method has synthesized crystalline NWs using low-melting-point metal catalysts at a lower growth temperatures (<350 °C); in principle the same metal and low growth temperatures should be possible for VLS growth, if suitable gas-phase reactants with comparable decomposition temperatures are used.

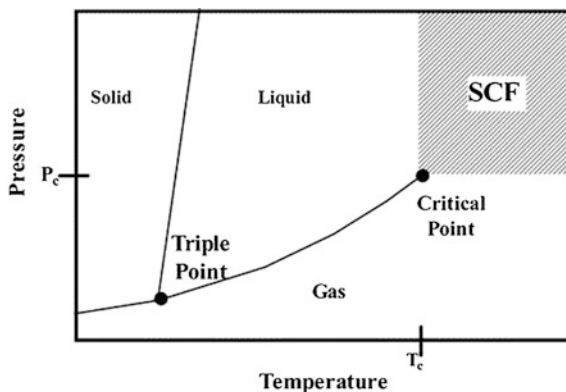
## 2.4.2 Supercritical Fluid-Liquid-Solid Growth

At temperatures and pressures beyond the critical point in the vapor-liquid coexistence curve (at  $T > T_c$  and  $P > P_c$ ), only a single-phase fluid (supercritical fluid, SCF) exists (Fig. 2.8). In this single-phase region of the phase diagram, the density, viscosity and diffusivity are intermediate between those of liquids and gases, and vary continuously from gas-like to liquid-like with modest changes in temperature and pressure. During the past decade, the use of solvents heated and pressurized to their SCF regions has been explored for nanocrystal and NW synthesis, stabilization, and processing [102].

Supercritical fluid-liquid-solid (SFLS) NW growth, which has been described by the Korgel group [103], is analogous to the VLS mechanism. Specifically, they have used colloidal metal nanocluster catalysts and semiconductor precursor in a reactor with organic solvent in its SCF region. In their initial experiments,



**Fig. 2.8** Schematic of pressure-temperature phase diagram showing the triple point, the critical point and the supercritical region. Reproduced from [102]. Copyright 2004 American Chemical Society



diphenylsilane,  $\text{SiH}_2(\text{C}_6\text{H}_5)_2$ , was used as the Si precursor along with gold nanoparticles and hexane in a high pressure reactor. At pressures of 200–270 bar and a temperature of 500 °C, SiNWs were observed as the product [103].

SCF solvents provide access to high temperatures (350–600°C) that are well above the boiling points of conventional solvents. Although, as compared with the SLS method, the synthetic conditions of the SFLS method are somewhat hazardous due to the high temperature and pressure, smaller monodispersed metal nanoparticles are available as catalysts. Because metal nanoparticles are protected by an organic monolayer, the size of nanoparticles is maintained even at the reaction temperature. Thus, the SFLS method has yielded very small diameter crystalline semiconductor NWs, including highly covalent materials, such as Si [103] and Ge [104, 105].

In an alternative approach aimed at the reduction of seed particle agglomeration, monodispersed Au nanocrystals were covalently-linked to a substrate, and served as the catalysts for SiNW growth [106]. This approach, which is analogous to the procedures used in many VLS studies, has two distinct advantages. First, undesired byproducts are easily removed from the synthesized NWs. Second, a continuous flow approach allows the precursor concentration in the reactor to be maintained at a controlled value, thereby enabling the study of the critical kinetic growth factors involved in NW nucleation and growth. The supply rate of Si to the seed particle can be easily adjusted by changing the flow rate or concentration of the precursor solution, or by tuning the decomposition kinetics through changes in the synthesis temperatures.

### 2.4.3 Solvothermal/Hydrothermal Synthesis

In a sealed vessel, solvents can be heated to temperatures well above their boiling points due to the increase of pressure with heating. Chemical reactions under such

conditions are referred to as solvothermal or, in the case of water as solvent, hydrothermal. In the past decade, considerable advances have been made in the solvothermal/hydrothermal synthesis of 1D semiconductor NWs with controlled size and morphology, although the products usually suffer from low purity and poor uniformity in size and morphology, and the growth mechanism remain largely unclear due to the inherent complexity of the process [94, 107, 108].

For example, in a mixed solvent of ethylenediamine and dodecanethiol, high-yield CdS NWs with an average diameter of 25 nm and lengths of 20–40  $\mu\text{m}$  were synthesized [109]. Time-dependent examination revealed that the formation process of CdS NWs involved two sequential processes: a short-period solid-solid transformation process in the initial stage, and a subsequent long-period Ostwald ripening process.

Furthermore, 1D metal oxide nanostructures can also be synthesized via solvothermal/hydrothermal method. Wang et al. [110] reported the hydrothermal synthesis of 1D  $\text{MnO}_2$  nanostructures through oxidation of  $\text{Mn}^{2+}$  by  $\text{S}_2\text{O}_8^{2-}$ :  $\alpha$ - $\text{MnO}_2$  with diameters of 5–20 nm and lengths ranging between 5 and 10  $\mu\text{m}$ , and  $\beta$ - $\text{MnO}_2$  with diameters of 40–100 nm and lengths ranging between 2.5 and 4.0  $\mu\text{m}$ . In another case, Liu and Aydil [111] reported a hydrothermal method to grow oriented, single-crystalline rutile  $\text{TiO}_2$  nanorod films on fluorine-doped tin oxide (FTO) substrates. The diameter, length, and density of the nanorods were varied by changing the growth parameters, such as growth time, growth temperature, initial reactant concentration, acidity, and additives. Control experiments showed that the small lattice mismatch between the FTO substrate and rutile  $\text{TiO}_2$  plays a key role in driving the nucleation and growth of the rutile  $\text{TiO}_2$  nanorods on FTO.

#### 2.4.4 Directed Solution Phase Growth

The shape of a crystal can be considered in terms of growth kinetics, by which the fastest growing planes should disappear and leave behind the slowest growing planes as the facets of the products [63, 112, 113]. Therefore, the shape of a crystal can be controlled by introducing capping agents with specific binding effects. For example, Sun et al. [114] reported a solution-phase method that generates Ag NWs, by reducing silver nitrate with ethylene glycol in the presence of poly(vinyl pyrrolidone) (PVP). Pt or Ag nanoparticles serve as seeds for the heterogeneous nucleation and growth of Ag NWs because of their close match in crystal structure and lattice constants. In another report, gold seeds were synthesized and added to a solution containing more metal salt, a weak reducing agent (e.g., ascorbic acid), and a structure-directing surfactant (CTAB). Preferential binding of the surfactant CTAB to a single-crystal face led to the unidirectional growth of the gold NWs [115].

In addition to capping agents, the formation of NWs may also be directed by kinetic control of diffusion and hydrolysis rates of precursors. For example, Zhang et al. [116] reported the in-solution synthesis of silica NWs directed by reverse micelles via a solution-solution-solid (SSS) mechanism (Fig. 2.9a, b). Specifically, highly

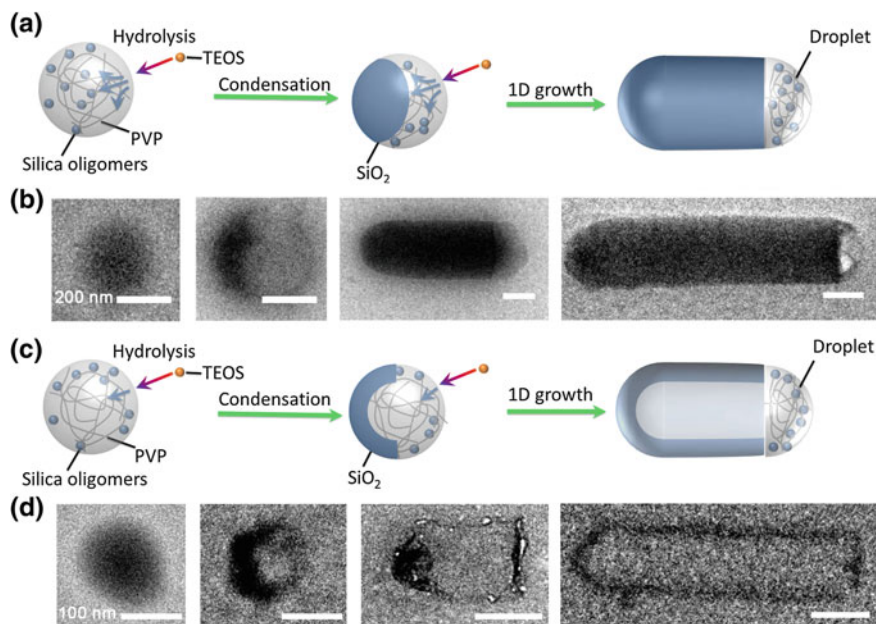


**Fig. 2.9** **a** Schematic illustration of the growth of silica NWs by a condensation-controlled process. **b** Evolution of silica NWs by TEM records during growth after 0, 10, 30 and 60 min, respectively. **c** Schematic illustration of the growth of silica tubes by a diffusion-controlled process. **d** Evolution of silica tubes by TEM records during growth after 0, 10, 20 and 40 min, respectively. Reproduced from [116]. Copyright 2014 IOP Publishing Ltd.

concentrated PVP chains in reverse micelles tend to aggregate in the core of the droplet, leaving an aqueous outer layer. Tetraethyl orthosilicate (TEOS) is then introduced, immediately hydrolyzed and spontaneously polymerized at the droplet surface, forming silica oligomers. The hydrolyzed TEOS species with strong hydrophilicity diffuse into the reverse micelle and are polymerized into larger silica particles. In addition, by accelerating the hydrolysis, the growth is controlled by the diffusion rate. Thus, once hydrolyzed TEOS molecules are formed on the droplet surface, they are deposited immediately as solid silica before reaching the droplet center, resulting in a ring-shaped condensation front and a tubular structure (Fig. 2.9c, d).

## 2.5 Future Directions and Challenges

The continued scaling of devices on a chip has created a landscape that provided an initial driving force for the mass production of NWs with high uniformity and controllability. Today, many other directions and applications of these materials are

emerging, and it is likely that several of these may be more important than the original goal of replacing the top-down computer chip. Various synthetic methods have been investigated extensively in the past decades. Semiconductor NWs, created by rational synthesis, can realize unprecedented structural and functional complexity as nanoscale building blocks. Nonetheless, considerable challenges still exist and remain to be accomplished. In particular, one major challenge is to ultimately control the NW synthesis to achieve chemical composition modulation and doping with atomic accuracy. Thereby, consideration of a number of techniques may be required when developing a NW growth process, and the benefits and drawbacks of each technique should be carefully weighed against one another so as to identify the technique best suited for synthesis of the desired complex NW products. Furthermore, the synthetic methods should be compatible with the subsequent assembly steps, which will be discussed in Chap. 4.

## References

1. C.M. Lieber, Nanoscale science and technology: building a big future from small things. *MRS Bull.* **28**(07), 486–491 (2003)
2. M. Law, J. Goldberger, P. Yang, Semiconductor nanowires and nanotubes. *Annu. Rev. Mater. Res.* **34**, 83–122 (2004)
3. N. Wang, Y. Cai, R. Zhang, Growth of nanowires. *Mater. Sci. Eng., R* **60**(1), 1–51 (2008)
4. V. Schmidt, J.V. Wittemann, S. Senz, U. Gösele, Silicon nanowires: a review on aspects of their growth and their electrical properties. *Adv. Mater.* **21**(25–26), 2681–2702 (2009)
5. V. Schmidt, J. Wittemann, U. Gosele, Growth, thermodynamics, and electrical properties of silicon nanowires. *Chem. Rev.* **110**(1), 361–388 (2010)
6. R.G. Hobbs, N. Petkov, J.D. Holmes, Semiconductor nanowire fabrication by bottom-up and top-down paradigms. *Chem. Mat.* **24**(11), 1975–1991 (2012)
7. C.M. Lieber, Z.L. Wang, Functional nanowires. *MRS Bull.* **32**(02), 99–108 (2007)
8. C. Lieber, A. Morales, P. Sheehan, E. Wong, P. Yang, One-dimensional nanostructures: rational synthesis, novel properties and applications, in *Proceedings of the Robert A. Welch Foundation 40th Conference on Chemical Research: Chemistry on the Nanometer Scale* (1997), pp. 165–187
9. A.M. Morales, C.M. Lieber, A laser ablation method for the synthesis of crystalline semiconductor nanowires. *Science* **279**(5348), 208–211 (1998)
10. T.G. Dietz, M.A. Duncan, D.E. Powers, R.E. Smalley, Laser production of supersonic metal cluster beams. *J. Chem. Phys.* **74**(11), 6511–6512 (1981)
11. X. Duan, C.M. Lieber, General synthesis of compound semiconductor nanowires. *Adv. Mater.* **12**(4), 298–302 (2000)
12. X. Duan, J. Wang, C.M. Lieber, Synthesis and optical properties of gallium arsenide nanowires. *Appl. Phys. Lett.* **76**(9), 1116–1118 (2000)
13. X. Duan, C.M. Lieber, Laser-assisted catalytic growth of single crystal GaN nanowires. *J. Am. Chem. Soc.* **122**(1), 188–189 (2000)
14. Q. Wei, C.M. Lieber, Synthesis of single crystal bismuth-telluride and lead-telluride nanowires for new thermoelectric materials. *MRS Online Proc. Libr.* **581**, 219–223 (1999)
15. M.B. Panish, Ternary phase diagram of GaAs-M (M-Cu, Ag, Au) system. *J. Electrochem. Soc.* **114**, 517 (1969)
16. Y.F. Zhang, Y.H. Tang, N. Wang, D.P. Yu, C.S. Lee, I. Bello, S.T. Lee, Silicon nanowires prepared by laser ablation at high temperature. *Appl. Phys. Lett.* **72**(15), 1835–1837 (1998)

17. Y. Cui, L.J. Lauhon, M.S. Gudiksen, J. Wang, C.M. Lieber, Diameter-controlled synthesis of single-crystal silicon nanowires. *Appl. Phys. Lett.* **78**(15), 2214–2216 (2001)
18. Y. Wu, P. Yang, Direct observation of vapor-liquid-solid nanowire growth. *J. Am. Chem. Soc.* **123**(13), 3165–3166 (2001)
19. Y. Wu, Y. Cui, L. Huynh, C.J. Barrelet, D.C. Bell, C.M. Lieber, Controlled growth and structures of molecular-scale silicon nanowires. *Nano Lett.* **4**(3), 433–436 (2004)
20. V. Schmidt, S. Senz, U. Gösele, Diameter-dependent growth direction of epitaxial silicon nanowires. *Nano Lett.* **5**(5), 931–935 (2005)
21. A. Lugstein, M. Steinmair, Y. Hyun, G. Hauer, P. Pongratz, E. Bertagnolli, Pressure-induced orientation control of the growth of epitaxial silicon nanowires. *Nano Lett.* **8**(8), 2310–2314 (2008)
22. B. Tian, P. Xie, T.J. Kempa, D.C. Bell, C.M. Lieber, Single-crystalline kinked semiconductor nanowire superstructures. *Nat. Nanotechnol.* **4**(12), 824–829 (2009)
23. Y.-C. Chou, K. Hillerich, J. Tersoff, M. Reuter, K. Dick, F. Ross, Atomic-scale variability and control of III-V nanowire growth kinetics. *Science* **343**(6168), 281–284 (2014)
24. S. Kodambaka, J. Tersoff, M. Reuter, F. Ross, Diameter-independent kinetics in the vapor-liquid-solid growth of Si nanowires. *Phys. Rev. Lett.* **96**(9), 096105 (2006)
25. W.I. Park, G. Zheng, X. Jiang, B. Tian, C.M. Lieber, Controlled synthesis of millimeter-long silicon nanowires with uniform electronic properties. *Nano Lett.* **8**(9), 3004–3009 (2008)
26. M.K. Sunkara, S. Sharma, R. Miranda, G. Lian, E. Dickey, Bulk synthesis of silicon nanowires using a low-temperature vapor–liquid–solid method. *Appl. Phys. Lett.* **79**(10), 1546–1548 (2001)
27. S. Hofmann, C. Ducati, R. Neill, S. Piscanec, A. Ferrari, J. Geng, R. Dunin-Borkowski, J. Robertson, Gold catalyzed growth of silicon nanowires by plasma enhanced chemical vapor deposition. *J. Appl. Phys.* **94**(9), 6005–6012 (2003)
28. H. Schäfer, H. Jacob, K. Etzel, *Chemische Transportreaktionen. I. Über den Transport des Bodenkörpers im Temperaturgefälle mit Hilfe heterogener Gleichgewichte. Z. Anorg. Allg. Chem.* **286**(1–2), 27–41 (1956)
29. H. Schäfer, *Chemical Transport Reactions* (Academic Press, New York, 1964)
30. Y. Wu, P. Yang, Germanium nanowire growth via simple vapor transport. *Chem. Mat.* **12**(3), 605–607 (2000)
31. M.H. Huang, Y. Wu, H. Feick, N. Tran, E. Weber, P. Yang, Catalytic growth of zinc oxide nanowires by vapor transport. *Adv. Mater.* **13**(2), 113–116 (2001)
32. P. Yang, H. Yan, S. Mao, R. Russo, J. Johnson, R. Saykally, N. Morris, J. Pham, R. He, H.-J. Choi, Controlled growth of ZnO nanowires and their optical properties. *Adv. Funct. Mater.* **12**(5), 323 (2002)
33. Y. Wu, B. Messer, P. Yang, Superconducting MgB<sub>2</sub> nanowires. *Adv. Mater.* **13**(19), 1487–1489 (2001)
34. H.-J. Choi, J.C. Johnson, R. He, S.-K. Lee, F. Kim, P. Pauzauskie, J. Goldberger, R. J. Saykally, P. Yang, Self-organized GaN quantum wire UV lasers. *J. Phys. Chem. B* **107**(34), 8721–8725 (2003)
35. Y. Song, A.L. Schmitt, S. Jin, Ultralong single-crystal metallic Ni<sub>2</sub>Si nanowires with low resistivity. *Nano Lett.* **7**(4), 965–969 (2007)
36. L. Schubert, P. Werner, N. Zakharov, G. Gerth, F. Kolb, L. Long, U. Gösele, T. Tan, Silicon nanowhiskers grown on  $\langle 111 \rangle$  Si substrates by molecular-beam epitaxy. *Appl. Phys. Lett.* **84**(24), 4968–4970 (2004)
37. N. Zakharov, P. Werner, G. Gerth, L. Schubert, L. Sokolov, U. Gösele, Growth phenomena of Si and Si/Ge nanowires on Si (111) by molecular beam epitaxy. *J. Cryst. Growth* **290**(1), 6–10 (2006)
38. P. Das Kanungo, N. Zakharov, J. Bauer, O. Breitenstein, P. Werner, U. Goesele, Controlled in situ boron doping of short silicon nanowires grown by molecular beam epitaxy. *Appl. Phys. Lett.* **92**(26), 263107–263107-3 (2008)

39. Y. Chan, X. Duan, S. Chan, I. Sou, X. Zhang, N. Wang, ZnSe nanowires epitaxially grown on GaP (111) substrates by molecular-beam epitaxy. *Appl. Phys. Lett.* **83**(13), 2665–2667 (2003)
40. Z. Wu, X. Mei, D. Kim, M. Blumin, H. Ruda, Growth of Au-catalyzed ordered GaAs nanowire arrays by molecular-beam epitaxy. *Appl. Phys. Lett.* **81**(27), 5177–5179 (2002)
41. M. Björk, B. Ohlsson, T. Sass, A. Persson, C. Thelander, M. Magnusson, K. Deppert, L. Wallenberg, L. Samuelson, One-dimensional heterostructures in semiconductor nanowhiskers. *Appl. Phys. Lett.* **80**(6), 1058–1060 (2002)
42. A.I. Persson, M.W. Larsson, S. Stenström, B.J. Ohlsson, L. Samuelson, L.R. Wallenberg, Solid-phase diffusion mechanism for GaAs nanowire growth. *Nat. Mater.* **3**(10), 677–681 (2004)
43. S. Kodambaka, J. Tersoff, M. Reuter, F. Ross, Germanium nanowire growth below the eutectic temperature. *Science* **316**(5825), 729–732 (2007)
44. C.-Y. Wen, M. Reuter, J. Tersoff, E. Stach, F. Ross, Structure, growth kinetics, and ledge flow during vapor–solid–solid growth of copper-catalyzed silicon nanowires. *Nano Lett.* **10**(2), 514–519 (2010)
45. C. Cheze, L. Geelhaar, A. Trampert, O. Brandt, H. Riechert, Collector phase transitions during vapor–solid–solid nucleation of GaN nanowires. *Nano Lett.* **10**(9), 3426–3431 (2010)
46. H. Cui, Y. Iv, G. Yang, Y. Chen, C. Wang, Step-flow Kinetics model for the vapor-solid-solid Si nanowires growth. *Nano Lett.* **15**, 3640–3645 (2015)
47. Z.W. Pan, Z.R. Dai, Z.L. Wang, Nanobelts of semiconducting oxides. *Science* **291**(5510), 1947–1949 (2001)
48. Y.-J. Hsu, S.-Y. Lu, Vapor-solid growth of Sn nanowires: Growth mechanism and superconductivity. *J. Phys. Chem. B* **109**(10), 4398–4403 (2005)
49. Y. Jiang, X.-M. Meng, W.-C. Yiu, J. Liu, J.-X. Ding, C.-S. Lee, S.-T. Lee, Zinc selenide nanoribbons and nanowires. *J. Phys. Chem. B* **108**(9), 2784–2787 (2004)
50. D. Moore, Z.L. Wang, Growth of anisotropic one-dimensional ZnS nanostructures. *J. Mater. Chem.* **16**(40), 3898–3905 (2006)
51. X. Peng, G. Meng, J. Zhang, X. Wang, Y. Wang, C. Wang, L. Zhang, Synthesis and photoluminescence of single-crystalline  $\text{In}_2\text{O}_3$  nanowires. *J. Mater. Chem.* **12**(5), 1602–1605 (2002)
52. Y. Liang, S. Li, L. Nie, Y. Wang, In situ synthesis of  $\text{In}_2\text{O}_3$  nanowires with different diameters from indium film. *Appl. Phys. Lett.* **88**(19), 193119–193119-3 (2006)
53. Z.L. Wang, X. Kong, J. Zuo, Induced growth of asymmetric nanocantilever arrays on polar surfaces. *Phys. Rev. Lett.* **91**(18), 185502 (2003)
54. Y. Chen, X. Cui, K. Zhang, D. Pan, S. Zhang, B. Wang, J. Hou, Bulk-quantity synthesis and self-catalytic VLS growth of  $\text{SnO}_2$  nanowires by lower-temperature evaporation. *Chem. Phys. Lett.* **369**(1), 16–20 (2003)
55. E.A. Stach, P.J. Pauzaukie, T. Kuykendall, J. Goldberger, R. He, P. Yang, Watching GaN nanowires grow. *Nano Lett.* **3**(6), 867–869 (2003)
56. Z.R. Dai, Z.W. Pan, Z.L. Wang, Novel nanostructures of functional oxides synthesized by thermal evaporation. *Adv. Funct. Mater.* **13**(1), 9–24 (2003)
57. W. Burton, N. Cabrera, F. Frank, Role of dislocations in crystal growth. *Nature* **163**(4141), 398–399 (1949)
58. N. Wang, Y. Tang, Y. Zhang, C. Lee, S. Lee, Nucleation and growth of Si nanowires from silicon oxide. *Phys. Rev. B* **58**(24), R16024 (1998)
59. N. Wang, Y. Tang, Y. Zhang, C. Lee, I. Bello, S. Lee, Si nanowires grown from silicon oxide. *Chem. Phys. Lett.* **299**(2), 237–242 (1999)
60. W. Shi, H. Peng, Y. Zheng, N. Wang, N. Shang, Z. Pan, C. Lee, S. Lee, Synthesis of large areas of highly oriented, very long silicon nanowires. *Adv. Mater.* **12**(18), 1343–1345 (2000)
61. Z. Pan, Z. Dai, L. Xu, S. Lee, Z. Wang, Temperature-controlled growth of silicon-based nanostructures by thermal evaporation of  $\text{SiO}$  powders. *J. Phys. Chem. B* **105**(13), 2507–2514 (2001)

62. R.-Q. Zhang, Y. Lifshitz, S.-T. Lee, Oxide-assisted growth of semiconducting nanowires. *Adv. Mater.* **15**(7–8), 635–640 (2003)
63. Y. Xia, P. Yang, Y. Sun, Y. Wu, B. Mayers, B. Gates, Y. Yin, F. Kim, H. Yan, One-dimensional nanostructures: synthesis, characterization, and applications. *Adv. Mater.* **15**(5), 353–389 (2003)
64. G. Cao, D. Liu, Template-based synthesis of nanorod, nanowire, and nanotube arrays. *Adv. Colloid Interface Sci.* **136**(1), 45–64 (2008)
65. H. Chik, J. Liang, S. Cloutier, N. Kouklin, J. Xu, Periodic array of uniform ZnO nanorods by second-order self-assembly. *Appl. Phys. Lett.* **84**(17), 3376–3378 (2004)
66. H.J. Fan, W. Lee, R. Scholz, A. Dadgar, A. Krost, K. Nielsch, M. Zacharias, Arrays of vertically aligned and hexagonally arranged ZnO nanowires: a new template-directed approach. *Nanotechnology* **16**(6), 913 (2005)
67. D. Routkevitch, T. Bigioni, M. Moskovits, J.M. Xu, Electrochemical fabrication of CdS nanowire arrays in porous anodic aluminum oxide templates. *J. Phys. Chem.* **100**(33), 14037–14047 (1996)
68. C. Liu, J.A. Zapien, Y. Yao, X. Meng, C.S. Lee, S. Fan, Y. Lifshitz, S.T. Lee, High-density, ordered ultraviolet light-emitting ZnO nanowire arrays. *Adv. Mater.* **15**(10), 838–841 (2003)
69. B.R. Martin, D.J. Dermody, B.D. Reiss, M. Fang, L.A. Lyon, M.J. Natan, T.E. Mallouk, Orthogonal self-assembly on colloidal gold-platinum nanorods. *Adv. Mater.* **11**(12), 1021–1025 (1999)
70. S.R. Nicewarner-Pena, R.G. Freeman, B.D. Reiss, L. He, D.J. Peña, I.D. Walton, R. Cromer, C.D. Keating, M.J. Natan, Submicrometer metallic barcodes. *Science* **294**(5540), 137–141 (2001)
71. C. Li, X. Sun, N. Wong, C. Lee, S. Lee, B.K. Teo, Ultrafine and uniform silicon nanowires grown with zeolites. *Chem. Phys. Lett.* **365**(1), 22–26 (2002)
72. B.K. Teo, C. Li, X. Sun, N. Wong, S. Lee, Silicon-silica nanowires, nanotubes, and biaxial nanowires: inside, outside, and side-by-side growth of silicon versus silica on zeolite. *Inorg. Chem.* **42**(21), 6723–6728 (2003)
73. C. Schönenberger, B. Van der Zande, L. Fokkink, M. Henny, C. Schmid, M. Krüger, A. Bachtold, R. Huber, H. Birk, U. Staufer, Template synthesis of nanowires in porous polycarbonate membranes: electrochemistry and morphology. *J. Phys. Chem. B* **101**(28), 5497–5505 (1997)
74. M. Tian, J. Wang, J. Kurtz, T.E. Mallouk, M. Chan, Electrochemical growth of single-crystal metal nanowires via a two-dimensional nucleation and growth mechanism. *Nano Lett.* **3**(7), 919–923 (2003)
75. C.R. Martin, Nanomaterials: a membrane-based synthetic approach. *Science* **266**(5193), 1961–1966 (1994)
76. L. Qin, S. Park, L. Huang, C.A. Mirkin, On-wire lithography. *Science* **309**(5731), 113–115 (2005)
77. S. Liu, J.B.-H. Tok, Z. Bao, Nanowire lithography: fabricating controllable electrode gaps using Au-Ag-Au nanowires. *Nano Lett.* **5**(6), 1071–1076 (2005)
78. H. Ringsdorf, B. Schlarb, J. Venzmer, Molecular architecture and function of polymeric oriented systems: models for the study of organization, surface recognition, and dynamics of biomembranes. *Angew. Chem. Int. Ed.* **27**(1), 113–158 (1988)
79. Y.-Y. Yu, S.-S. Chang, C.-L. Lee, C.C. Wang, Gold nanorods: electrochemical synthesis and optical properties. *J. Phys. Chem. B* **101**(34), 6661–6664 (1997)
80. S. Kwan, F. Kim, J. Akana, P. Yang, Synthesis and assembly of BaWO<sub>4</sub> nanorods. *Chem. Commun.* **5**, 447–448 (2001)
81. Y. Li, X. Li, Z.X. Deng, B. Zhou, S. Fan, J. Wang, X. Sun, From surfactant-inorganic mesostructures to tungsten nanowires. *Angew. Chem.* **114**(2), 343–345 (2002)
82. W. Han, S. Fan, Q. Li, Y. Hu, Synthesis of gallium nitride nanorods through a carbon nanotube-confined reaction. *Science* **277**(5330), 1287–1289 (1997)
83. Y. Zhang, H. Dai, Formation of metal nanowires on suspended single-walled carbon nanotubes. *Appl. Phys. Lett.* **77**(19), 3015–3017 (2000)

84. R. He, M. Law, R. Fan, F. Kim, P. Yang, Functional bimorph composite nanotapes. *Nano Lett.* **2**(10), 1109–1112 (2002)
85. C. Mao, D.J. Solis, B.D. Reiss, S.T. Kottmann, R.Y. Sweeney, A. Hayhurst, G. Georgiou, B. Iverson, A.M. Belcher, Virus-based toolkit for the directed synthesis of magnetic and semiconducting nanowires. *Science* **303**(5655), 213–217 (2004)
86. K.T. Nam, D.-W. Kim, P.J. Yoo, C.-Y. Chiang, N. Meethong, P.T. Hammond, Y.-M. Chiang, A.M. Belcher, Virus-enabled synthesis and assembly of nanowires for lithium ion battery electrodes. *Science* **312**(5775), 885–888 (2006)
87. Y.J. Lee, H. Yi, W.-J. Kim, K. Kang, D.S. Yun, M.S. Strano, G. Ceder, A.M. Belcher, Fabricating genetically engineered high-power lithium-ion batteries using multiple virus genes. *Science* **324**(5930), 1051–1055 (2009)
88. W.C. Lee, K. Kim, J. Park, J. Koo, H.Y. Jeong, H. Lee, D.A. Weitz, A. Zettl, S. Takeuchi, Graphene-templated directional growth of an inorganic nanowire. *Nat. Nanotechnol.* **10**, 423–428 (2015)
89. H. Dai, E.W. Wong, Y.Z. Lu, S. Fan, C.M. Lieber, Synthesis and characterization of carbide nanorods. *Nature* **375**(6534), 769–772 (1995)
90. B. Gates, Y. Wu, Y. Yin, P. Yang, Y. Xia, Single-crystalline nanowires of Ag<sub>2</sub>Se can be synthesized by templating against nanowires of trigonal Se. *J. Am. Chem. Soc.* **123**(46), 11500–11501 (2001)
91. N.A. Melosh, A. Boukai, F. Diana, B. Gerardot, A. Badolato, P.M. Petroff, J.R. Heath, Ultrahigh-density nanowire lattices and circuits. *Science* **300**(5616), 112–115 (2003)
92. H. Yu, J. Li, R.A. Loomis, P.C. Gibbons, L.-W. Wang, W.E. Buhro, Cadmium selenide quantum wires and the transition from 3D to 2D confinement. *J. Am. Chem. Soc.* **125**(52), 16168–16169 (2003)
93. M. Kuno, An overview of solution-based semiconductor nanowires: synthesis and optical studies. *Phys. Chem. Chem. Phys.* **10**(5), 620–639 (2008)
94. J. Ye, L. Qi, Solution-phase synthesis of one-dimensional semiconductor nanostructures. *J. Mater. Sci. Technol.* **24**(4), 529 (2008)
95. T.J. Trentler, K.M. Hickman, S.C. Goel, A.M. Viano, P.C. Gibbons, W.E. Buhro, Solution-liquid-solid growth of crystalline III-V semiconductors: an analogy to vapor-liquid-solid growth. *Science* **270**(5243), 1791–1794 (1995)
96. F. Wang, A. Dong, J. Sun, R. Tang, H. Yu, W.E. Buhro, Solution-liquid-solid growth of semiconductor nanowires. *Inorg. Chem.* **45**(19), 7511–7521 (2006)
97. J. Chun, J. Lee, Various synthetic methods for one-dimensional semiconductor nanowires/nanorods and their applications in photovoltaic devices. *Eur. J. Inorg. Chem.* **2010**(27), 4251–4263 (2010)
98. H. Yu, W.E. Buhro, Solution-liquid-solid growth of soluble GaAs nanowires. *Adv. Mater.* **15**(5), 416–419 (2003)
99. H. Yu, J. Li, R.A. Loomis, L.-W. Wang, W.E. Buhro, Two-versus three-dimensional quantum confinement in indium phosphide wires and dots. *Nat. Mater.* **2**(8), 517–520 (2003)
100. D.D. Fanfair, B.A. Korgel, Bismuth nanocrystal-seeded III-V semiconductor nanowire synthesis. *Cryst. Growth Des.* **5**(5), 1971–1976 (2005)
101. J.W. Grebinski, K.L. Hull, J. Zhang, T.H. Kosel, M. Kuno, Solution-based straight and branched CdSe nanowires. *Chem. Mat.* **16**(25), 5260–5272 (2004)
102. P.S. Shah, T. Hanrath, K.P. Johnston, B.A. Korgel, Nanocrystal and nanowire synthesis and dispersibility in supercritical fluids. *J. Phys. Chem. B* **108**(28), 9574–9587 (2004)
103. J.D. Holmes, K.P. Johnston, R.C. Doty, B.A. Korgel, Control of thickness and orientation of solution-grown silicon nanowires. *Science* **287**(5457), 1471–1473 (2000)
104. T. Hanrath, B.A. Korgel, Nucleation and growth of germanium nanowires seeded by organic monolayer-coated gold nanocrystals. *J. Am. Chem. Soc.* **124**(7), 1424–1429 (2002)
105. T. Hanrath, B.A. Korgel, Supercritical fluid-liquid-solid (SFLS) synthesis of Si and Ge nanowires seeded by colloidal metal nanocrystals. *Adv. Mater.* **15**(5), 437–440 (2003)



106. X. Lu, T. Hanrath, K.P. Johnston, B.A. Korgel, Growth of single crystal silicon nanowires in supercritical solution from tethered gold particles on a silicon substrate. *Nano Lett.* **3**(1), 93–99 (2003)
107. G. Zou, H. Li, Y. Zhang, K. Xiong, Y. Qian, Solvothermal/hydrothermal route to semiconductor nanowires. *Nanotechnology* **17**(11), S313 (2006)
108. W. Shi, S. Song, H. Zhang, Hydrothermal synthetic strategies of inorganic semiconducting nanostructures. *Chem. Soc. Rev.* **42**(13), 5714–5743 (2013)
109. D. Xu, Z. Liu, J. Liang, Y. Qian, Solvothermal synthesis of CdS nanowires in a mixed solvent of ethylenediamine and dodecanethiol. *J. Phys. Chem. B* **109**(30), 14344–14349 (2005)
110. X. Wang, Y. Li, Selected-control hydrothermal synthesis of  $\alpha$ - and  $\beta$ -MnO<sub>2</sub> single crystal nanowires. *J. Am. Chem. Soc.* **124**(12), 2880–2881 (2002)
111. B. Liu, E.S. Aydil, Growth of oriented single-crystalline rutile TiO<sub>2</sub> nanorods on transparent conducting substrates for dye-sensitized solar cells. *J. Am. Chem. Soc.* **131**(11), 3985–3990 (2009)
112. Z. Wang, Transmission electron microscopy of shape-controlled nanocrystals and their assemblies. *J. Phys. Chem. B* **104**(6), 1153–1175 (2000)
113. B. Wiley, Y. Sun, J. Chen, H. Cang, Z.-Y. Li, X. Li, Y. Xia, Shape-controlled synthesis of silver and gold nanostructures. *MRS Bull.* **30**(05), 356–361 (2005)
114. Y. Sun, Y. Yin, B.T. Mayers, T. Herricks, Y. Xia, Uniform silver nanowires synthesis by reducing AgNO<sub>3</sub> with ethylene glycol in the presence of seeds and poly (vinyl pyrrolidone). *Chem. Mat.* **14**(11), 4736–4745 (2002)
115. A. Gole, C.J. Murphy, Seed-mediated synthesis of gold nanorods: role of the size and nature of the seed. *Chem. Mat.* **16**(19), 3633–3640 (2004)
116. A.-Q. Zhang, H.-J. Li, D.-J. Qian, M. Chen, Kinetically-controlled template-free synthesis of hollow silica micro-/nanostructures with unusual morphologies. *Nanotechnology* **25**(13), 135608 (2014)

# Chapter 3

## Structure-Controlled Synthesis

**Abstract** Advances in nanoscience and nanotechnology critically depend on the development of nanostructures whose properties are controlled during synthesis. The ability to control and modulate the composition, doping, crystal structure and morphology of semiconductor NWs allows researchers to explore applications of NWs for investigating fundamental scientific questions through developing new technologies. The chapter expands significantly upon the basic methods introduced in the previous chapter for NW synthesis by focusing on controlled growth of a host of NWs with modulated morphologies and structures, including axial and radial heterostructures, kinked, branched, and/or modulated doped structures, where the increased complexity in the NWs can enable unique functional properties.

### 3.1 Introduction

The capability of creating new nanomaterials and assemblies, with tunable composition and structure on many length scales, offers a driving force towards the scientific breakthroughs that enable revolutionary advances and future technologies. In this regard, one-dimensional (1D) semiconductor NWs serve as one of the most powerful platforms available today in nanoscience, given that it is now possible to rationally design and synthetically realize these structures [1]. These capabilities, unique among different NWs, allow for creating systems or building blocks with predictable physical properties and enable testing fundamental limits of performance. With these characteristics and capabilities, it is also possible to assemble hybrid or multi-component functional architectures using these diverse NW building blocks, leading to rational exploration of possible applications. In this chapter, we summarize the synthesis of five distinct NW structural classes: homogeneous NWs, axial modulated NW structures, radial/coaxial modulated NW structures, branched/tree-like NWs, and kinked NW structures.

## 3.2 Homogeneous Nanowires

Previously in Chap. 2, we have described different synthetic methods to generate homogeneous NWs. In this section, we will discuss diameter-, length-, and doping-controlled synthesis of NWs in more detail.

Central to the nanocluster catalyzed VLS approach to NW growth is the idea that the size of the metal catalysts determine NW diameter, and thus NWs with a narrow size distribution should be obtained from approximately monodisperse nanocluster catalysts. This important idea has been verified through the demonstration of diameter-controlled growth of GaP [2], InP [3], and Si NWs [4] from nearly monodisperse Au nanocluster catalysts. Significantly, the widths of the NW diameter distributions observed in these studies were essentially the same as those of the starting Au nanoclusters, thus demonstrating that NW diameter can be controlled predictably by the nanocluster catalyst.

Pushing the limits of nanocluster catalyst size-controlled growth, Wu et al. [5] described in 2004 the controlled growth of single-crystal SiNWs with diameters approaching molecular dimensions ( $\sim 3$  nm), exhibiting the smallest diameter SiNWs obtained via VLS process. The cross-sectional high-resolution TEM (HRTEM) images of a representative 3.6-nm SiNW with a  $\langle 110 \rangle$  growth axis revealed that the NW had a hexagonal cross section with well-developed facets (Fig. 3.1a–d). Analysis of the lattice-resolved image showed that these facets corresponded to the low-free-energy (111) and (100) planes, consistent with the equilibrium shape (Fig. 3.1d).

Factors affecting the length limits have also been explored in several studies [6–8]. Ultra-long (up to several millimeters) NWs with controlled electronic and/or optical properties could be beneficial for device integration by facilitating the interconnection of individual NWs and NW arrays. Several techniques such as the high-temperature thermal evaporation of silicon monoxide [6] and silicon powders [7] have previously been reported for obtaining millimeter-long SiNWs. However, this goal was still challenging for the nanocluster catalyzed VLS-growth method, as most of the growth rates reported were predominantly in the order of 1–2  $\mu\text{m}$  per minute [9–11]. In the case of SiNWs, the growth rate is strongly temperature-dependent [11, 12], suggesting that the kinetics of thermal decomposition of  $\text{SiH}_4$  into atomic Si species could be the rate-determining step and much more important than gas-phase mass transport. Thus, accelerating the decomposition step can significantly enhance the overall growth rate. Due to the lower activation energy for cleavage of Si–Si versus Si–H bonds, disilane ( $\text{Si}_2\text{H}_6$ ) was selected as the Si gas precursor for a higher catalytic decomposition rate [8]. Notably, the average SiNW growth rate using  $\text{Si}_2\text{H}_6$  at 400 °C was 31  $\mu\text{m}/\text{min}$ , while the growth rate determined for  $\text{SiH}_4$  reactant under similar growth conditions was 130 times lower. Thus, the growth rate of SiNWs can be enhanced by almost 2 orders of magnitude, leading to ultra-high aspect ratio SiNWs, with tens of nanometers in diameter and  $\sim 2$  mm in length (Fig. 3.1e–g).

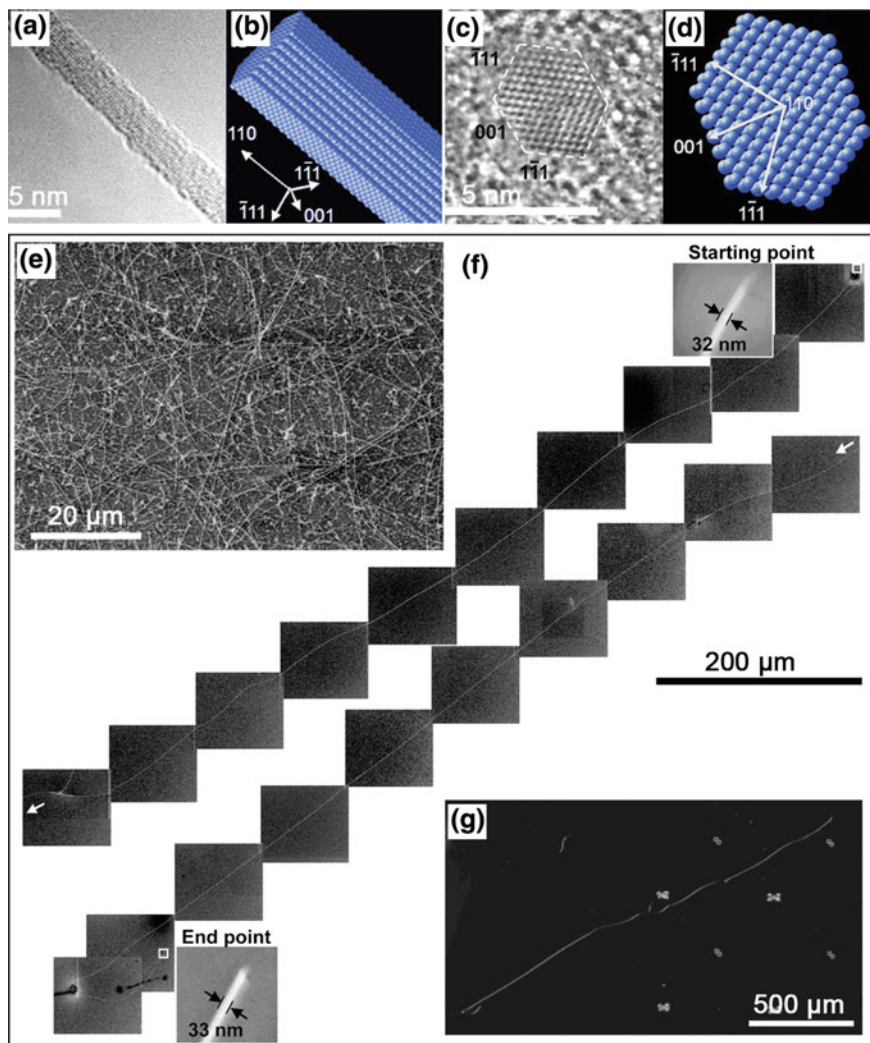


**Fig. 3.1** **a** TEM images of 3.6-nm SiNWs grown along the  $\langle 110 \rangle$  direction, **c** HRTEM cross-sectional image, and equilibrium shapes for the **b** NW and the **d** NW cross sections predicted by Wulff construction. Reproduced from [5]. Copyright 2004 American Chemical Society. **e** SEM image of as-grown ultra-long SiNWs. **f** A series of 20 SEM images of a 2.3 mm long SiNW transferred onto a  $\text{SiO}_2/\text{Si}$  substrate. Insets are SEM images of the starting and end segments of this NW. **g** Dark-field optical image of the same wire. Reproduced from [8]. Copyright 2008 American Chemical Society

In addition to diameter, morphology and length control, doping of NWs is crucial for tuning their physical and chemical properties. In one of the first demonstrations of controlled doping, Cui et al. [13] in 2000 reported LCG-based VLS method to introduce controllably either boron or phosphorus dopants during the vapor phase growth of SiNWs. However, the observed electron mobility values were much lower than expected for  $n$ -type silicon. Later, substantial efforts focused on studies of hole-doped ( $p$ -type) SiNWs, while electron-doped ( $n$ -type) received relatively less attention, although the intrinsic electron mobility in bulk silicon is substantially larger than the intrinsic hole mobility. In 2004, Zheng et al. [10] reported the first example of controlled growth and phosphorus doping of SiNWs, and the fabrication of high-performance  $n$ -type field effect transistors (FETs) from these nanomaterials.

### 3.3 Axial Modulated Structures

Modulated nanostructures in which the composition and/or doping are varied on the nanometer scale represent important targets of synthesis, since they can enable new and unique function and potential for integration in functional nanosystems. In this section, we will describe the synthesis of longitudinal NW heterostructures, including semiconductor superlattices, metal-semiconductor junctions, modulation-doped NWs, as well as NWs with ultra-short morphology features. Several reviews focused on semiconductor NW heterostructures have appeared [14, 15].

#### 3.3.1 Early Work

Silicon whiskers with modulated doping concentration were made in the pioneering studies of Wagner for the purposes of elucidating the VLS growth mechanism in 1970 [16]. In 1992, Haraguchi et al. [17] made substantial progress on the growth of GaAs whiskers, including the fabrication of  $p$ - $n$  junctions within whiskers. They employed gold catalyst particles in a reduced-pressure metal-organic chemical vapor deposition (MOCVD) reactor with trimethylgallium ( $\text{Ga}(\text{CH}_3)_3$ ) and arsine ( $\text{AsH}_3$ ) as precursors to produce cone-shaped nanostructures of micron lengths and ca. 100 nm average diameters. Later, Hu et al. [18] reported two approaches to prepare metal-semiconductor junctions between carbon nanotubes (CNTs) and SiNWs using either a common Fe-based nanocluster catalyst to grow CNTs from the ends of SiNWs or growth of SiNWs from gold clusters electrodeposited onto the CNT free ends.

### 3.3.2 *Semiconductor Heterojunctions*

In 2002, a significant step in the controlled synthesis of NW heterostructures was demonstrated by three groups almost simultaneously, with the growth of NW superlattices in a number of systems [19]. Wu et al. [20] combined thermal CVD using  $\text{SiCl}_4$  with the laser ablation of a solid germanium target to produce Si/SiGe NWs. During the growth process, when the laser was turned on, Ge vapor was generated and both Ge and Si species were deposited into the alloy droplets. The SiGe alloy then precipitated from the solid/liquid interface. By periodically turning the laser on and off, Si/SiGe superlattices were created on every individual NW in a block-by-block fashion. In addition, Björk et al. [21–23] used nanocluster catalysts and MBE techniques to prepare modulated InAs/InP NW structures with periods ranging from 100 to just several nanometers. Significantly, their lattice-resolved TEM images suggested that the interfaces were atomically perfect.

Using a nanocluster catalyzed CVD method, Gudiksen et al. [24] successfully synthesized GaAs/GaP, *n*-Si/*p*-Si, and *n*-InP/*p*-InP axial NW heterostructures and superlattices. As shown in Fig. 3.2a, to create a single junction within the NW, the addition of the first reactant was stopped during growth, and then a second reactant was introduced for the remainder of the synthesis; repeated modulation of the reactants during growth produces NW superlattices. In principle, this approach can be successfully implemented if a nanocluster catalyst suitable for growth of the different superlattice components under similar conditions is used. Figure 3.2b shows a TEM image of a typical GaAs/GaP junction region. Local elemental mapping of the heterojunction by energy dispersive X-ray spectroscopy (EDS) was carried out to probe composition variations across the heterostructure junction (Fig. 3.2c–f). The elemental mapping shows that Ga is uniformly distributed along the length of the NW, while P (Fig. 3.2e) and As (Fig. 3.2f) appear to be localized in the GaP and GaAs portions of the NW heterostructure, respectively. However, quantitative analysis of the P and As composition variations (Fig. 3.2g) show that the junction is not atomically abrupt, but has a transition segment between GaP and GaAs phases over a length scale of 15–20 nm. This length scale is consistent with the expectation that the  $\sim 20$  nm Au catalyst must re-alloy with GaP after initial GaAs growth. By repeating the modulation process, NW superlattices are produced, in which the number of periods and repeat spacing are readily varied during growth. In this work, a 21-layer GaAs/GaP superlattice was demonstrated, with arbitrary repeat spacing and the segment lengths controlled by the number of pulses delivered to each target.

### 3.3.3 *Metal-Semiconductor Heterostructures*

Besides semiconductor heterostructures, metal-semiconductor axial heterostructures and superlattices have also been demonstrated using various methods [25–27]. For

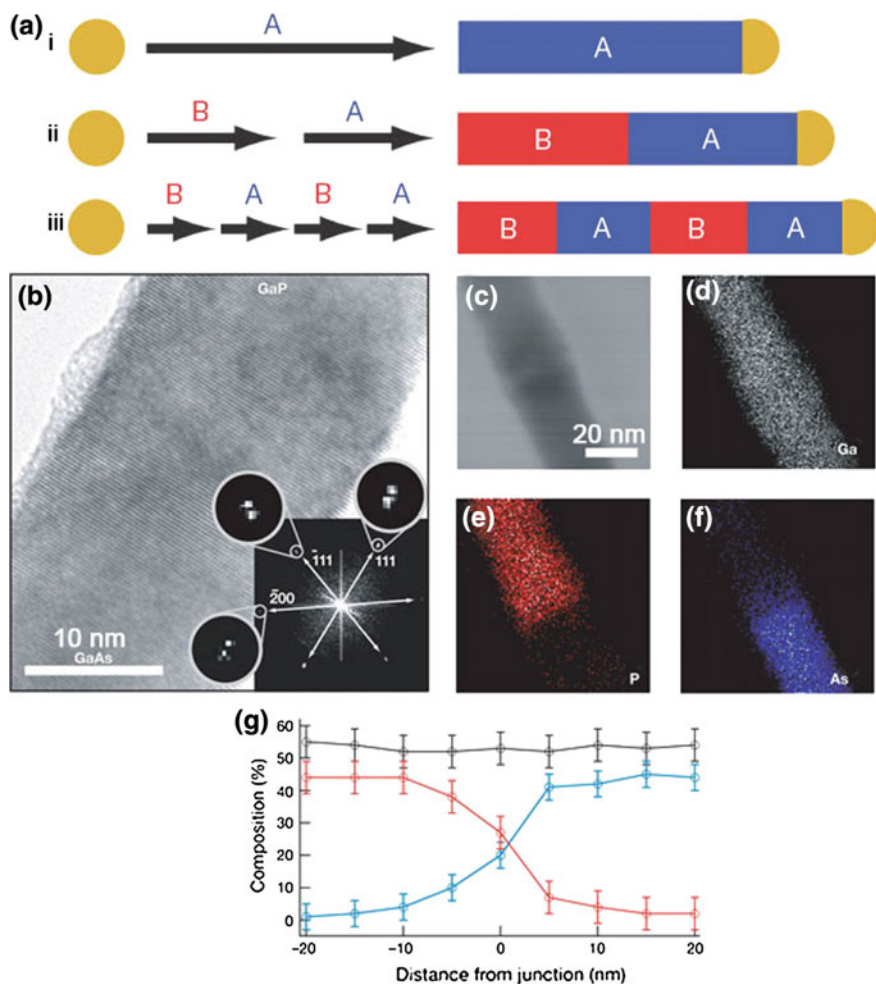


**Fig. 3.2** **a** Synthesis of NW superlattices: *i* A nanocluster catalyst nucleates and directs one-dimensional semiconductor NW growth with the catalyst remaining at the terminus of the NW; *ii* upon completion of the first growth step, a different material can be grown from the end of the NW; *iii* repetition of steps *i* and *ii* leads to a compositional superlattice within a single NW. **b, c** HRTEM of a GaAs/GaP junction. **d–f** Elemental mapping of the Ga (shown grey), P (red) and As (blue) content of the junction shown in **c**. **g** Line profiles of the composition through the junction region. Ga black, P red and As blue. Reproduced from [24]. Copyright 2002 Nature Publishing Group

example, Pena et al. [25] directly synthesized Au/CdSe/Au and Ni/CdSe/Ni segmented NWs by the template method through sequential deposition of materials in polycarbonate membranes, using commercially available plating solutions for Au and Ni segments and acid solution of CdSO<sub>4</sub> and SeO<sub>2</sub> for deposition of the semiconducting CdSe segments.

In contrast to direct synthesis, Wu et al. [26] reported that NiSi, a metal, could be obtained from Si via solid phase reaction with Ni. As a result, metallic NiSi NWs were produced by first evaporating Ni on SiNWs, followed by heating the sample above the NiSi transition temperature (Fig. 3.3a). A dark-field optical image of a NiSi/Si NW patterned in this way, using 1  $\mu\text{m}$  wide nickel regions on a 2  $\mu\text{m}$  pitch (Fig. 3.3b), exhibited periodic variations in contrast extending over the full length of the 65- $\mu\text{m}$ -long NW. Analysis of the image showed that the average lengths of the Si and NiSi regions were both 1  $\mu\text{m}$ , in good agreement with the width and pitch of nickel metal deposited on the NW during fabrication. TEM images of similar NiSi/SiNW heterostructures (Fig. 3.3c) showed a similar periodic contrast variation that was consistent with NiSi (dark) and Si (light) materials within the heterostructure. Detailed examination of NiSi/Si heterostructure by HRTEM (Fig. 3.3d) showed that the transformation yielded an atomically abrupt interfaces. The single crystalline nature of the NiSi/Si structures contrasts the polycrystalline structures obtained by templated-based electrodeposition, and moreover, represents ideal atomically-resolved structures for investigating fundamental electrical transport questions.

In subsequent work, Lin et al. [27] extended this work with the formation of PtSi/Si/PtSi NW heterostructures (Fig. 3.3e–g). The SiNW device with platinum contacts was fabricated on Si/Si<sub>3</sub>N<sub>4</sub> substrate using e-beam lithography and e-beam evaporation (Fig. 3.3e). Then, the device was annealed at high temperature to allow platinum to diffuse into the SiNW and form partially (Fig. 3.3f) or fully silicidized PtSi NW (Fig. 3.3g). The phenomenon was attributed to the fact that many platinum atoms were dissolved into silicon through the contacts between SiNWs and Pt pads so that supersaturation was reached. Hence, nucleation and growth of platinum silicide occurred from both platinum pads.

### 3.3.4 p-n Homojunctions

A general scheme for realizing dopant modulation in the frame of metal nanocluster catalyzed NW synthesis involves varying the dopant reactant concentration in the vapor phase during growth. In this approach, it is essential to avoid radial overcoating during growth (Fig. 3.4a), since this can eliminate the desired electronic modulation in NW properties. To meet the desired synthetic goals, Yang et al. [28] carried out growth in H<sub>2</sub>, which suppressed the decomposition of silane, and slowed the growth rate by uncatalyzed processes on the SiNW body. In addition, a local substrate heater was adopted to reduce reactant heating and possible homogeneous decomposition prior to delivery to the substrate and nanocluster catalyst. TEM studies of modulation-doped  $n^+n-n^+$  SiNWs (Fig. 3.4b), where  $n^+$  and  $n$  represent the heavily and lightly doped  $n$ -type regions, respectively, showed that the NWs prepared in this way had uniform diameters for lengths of >10  $\mu\text{m}$ . The diameters of the opposite ends of a representative  $n^+n-n^+$  SiNW were 17.4 and 17.1 nm, respectively. The 0.3-nm variation was on the order of a single atomic layer and



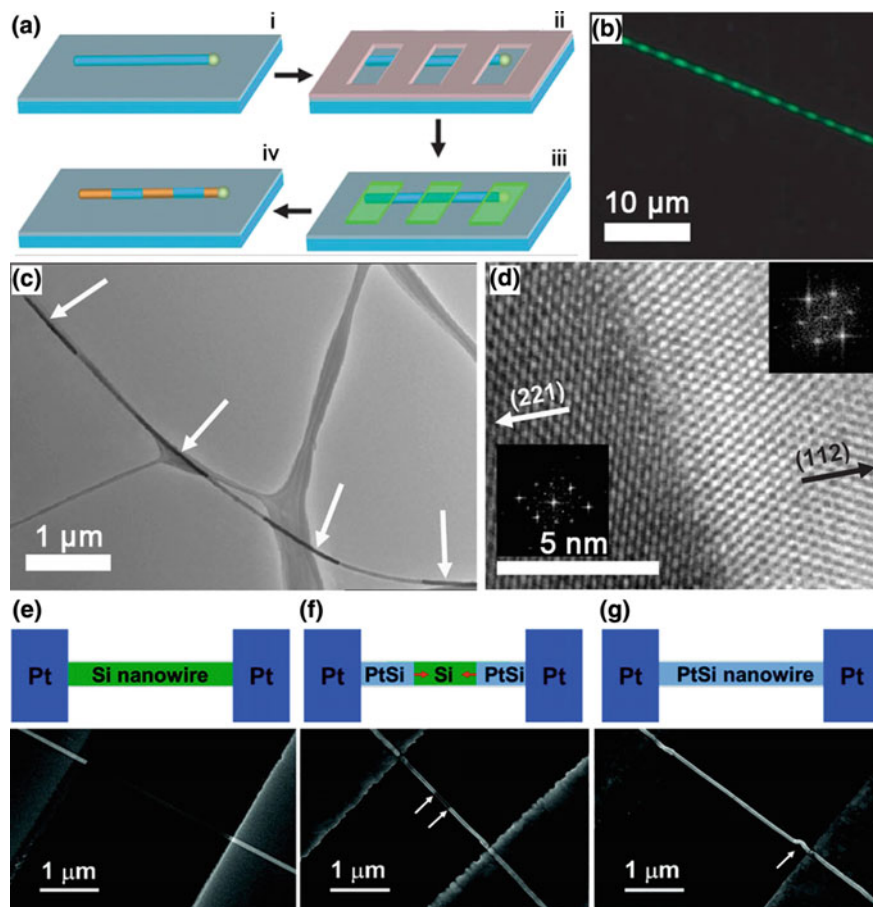


**Fig. 3.3** **a** Fabrication of NiSi/SiNW heterostructures and superlattices: *i* SiNWs (blue) dispersed on a substrate are *ii* coated with photoresist (grey) and lithographically patterned, *iii* selectively coated with Ni and *iv* annealed to form NiSi NWs. **b** Dark field optical image of a single NiSi/SiNW heterostructure. The *bright green* segments correspond to silicon and the *dark* segments to NiSi. **c** TEM image of a NiSi/SiNW heterostructure. The *bright* segments of the NW correspond to silicon and the *dark* segments correspond to NiSi. **d** HRTEM image of the junction between NiSi and Si showing an atomically abrupt interface. Reproduced from [26]. Copyright 2004 Nature Publishing Group. **e–g** Schematic illustrations and corresponding SEM images depicting growth of a PtSi/Si/PtSi nanoheterostructure and PtSi NWs. **e** SiNW device with two Pt contact pads before reaction. **f** PtSi/Si/PtSi heterostructure obtained through partial silicidation of the SiNW. **g** PtSi NW after complete silicidation. Reproduced from [27]. Copyright 2008 American Chemical Society

showed that radial overcoating was effectively eliminated during growth of these modulation-doped structures. Representative scanning gate microscopy (SGM) data taken on modulation doped  $n^+-(n-n^+)_N$  SiNWs with  $N = 3, 6$  and  $8$  were shown in Fig. 3.4c–e. The pitch spacings in these dopant modulated structures, defined as the

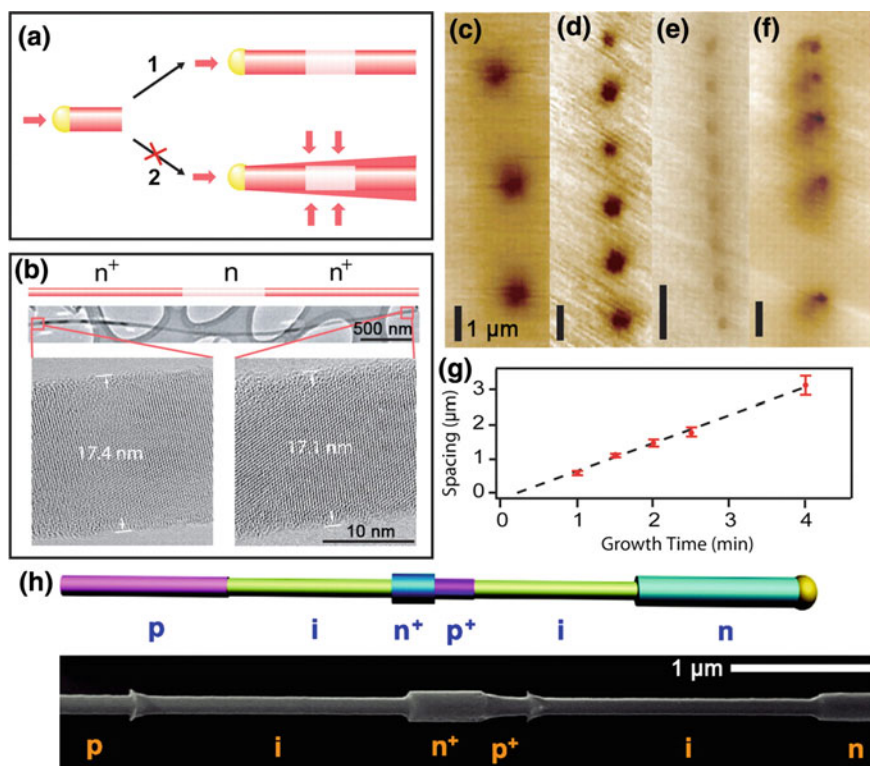


**Fig. 3.4** **a** Schematic of the synthesis of modulation doped SiNW. Au colloid (yellow) catalyses growth of a heavily doped region (red) and lightly doped region (pink) NW superstructures. 1 Pure axial growth, resulting in dopant modulated NW super structure. 2 Axial and radial growth, resulting in a layer of homogenous overcoating (red) and a tapered NW structure. **b** Schematic and TEM images of a representative  $n^+n^-n^+$  modulation doped SiNW. **c-f** SGM images of  $n^+-(n-n^+)_N$  NWs. **g** Repeat spacing versus growth time under fixed growth conditions. Reproduced from [28]. Copyright 2005 the American Association for the Advancement of Science. **h** Schematic and SEM image of a selectively etched tandem  $p-i-n^+-p^+-i-n$  SiNW. Reproduced from [29]. Copyright 2008 American Chemical Society

separation between two nearest  $n$  regions, were readily controlled by growth time, with the average values of 3.2  $\mu\text{m}$  (Fig. 3.4c), 1.6  $\mu\text{m}$  (Fig. 3.4d) and 0.8  $\mu\text{m}$  (Fig. 3.4e), and could even be varied within a single NW (Fig. 3.4f). Detailed studies revealed that the pitch spacing was directly proportional to growth time (Fig. 3.4g).

In another study, the experimental realization of axial modulation-doped  $p-i-n$  and tandem  $p-i-n^+-p^+-i-n$  SiNWs was reported [29] (Fig. 3.4h). The heavily doped  $n^+$  and  $p^+$  regions were readily identifiable because of their positions in the tandem device, reduced degree of post growth wet chemical etching, and expected lengths

( $\sim 0.5 \mu\text{m}$ ). These results confirm that the synthetic approach can yield the desired tandem junction sequence and allow precise control over the length of the doped regions.

### 3.3.5 Ultrashort Morphology Features

The formation of ultrashort NW structures could allow for superior and unconventional device performance. Cohen-Karni et al. [30] reported a new synthetic method that combines gold-nanocluster catalyzed VLS and VSS NW growth modes to produce synthetically encoded NW devices with ultra-sharp ( $<5 \text{ nm}$ )  $n$ -type highly doped ( $n^{++}$ ) to lightly doped ( $n$ ) transitions along the NW growth direction. The abrupt  $n$ -Si/ $n^{++}$ -Si junctions were made possible due to slow growth rates of the VSS mechanism, which were at least 10-100 times lower than for VLS grown NWs.

Later, Christesen et al. [31] reported a bottom-up method to break the conventional “wire” symmetry and synthetically encode a high-resolution array of arbitrary shapes, including nanorods, sinusoids, bowties, tapers, nanogaps, and gratings, along the NW growth axis. Rapid modulation of phosphorus doping combined with selective wet-chemical etching enabled morphological features as small as 10 nm to be patterned over wires more than 50  $\mu\text{m}$  in length. In their experiments, SiNWs were grown by a VLS mechanism in a home-built, hot-wall CVD system using Au nanoparticles as catalysts,  $\text{SiH}_4$  as the source of Si, and  $\text{H}_2$  as the carrier gas. As illustrated in Fig. 3.5a, an additional flow of phosphine ( $\text{PH}_3$ ) was rapidly modulated during growth to encode varying levels of P, an  $n$ -type substitution dopant with high solubility in Si. The etching rate of doped Si with aqueous KOH solution was decreased with higher dopant concentration. NWs with six intrinsic segments encoded along the axis for increasingly short time scales were obtained (Fig. 3.5b). The authors also used other complex doping profiles to encode the range of morphological features shown in SEM images in Fig. 3.5c. These structures included periodic (images 1–4) or nonperiodic (image 5) gratings, nanogaps with gap sizes as small as 10 nm (images 6–7), suspended nanorods (image 8), and sinusoidal profiles (images 9–10).

## 3.4 Radial/Coaxial Modulated Structures

During VLS growth of semiconductor NWs, two compositionally-distinct material surfaces are exposed to the vapor: that of the metal-semiconductor liquid nanocluster catalyst and that of the solid semiconductor (Fig. 3.6a). If vapor decomposition/adsorption continues exclusively at the surface of the metal-semiconductor catalyst, crystalline growth of the new semiconductor will continue, inducing axial growth (Fig. 3.6b). On the other hand, if the new

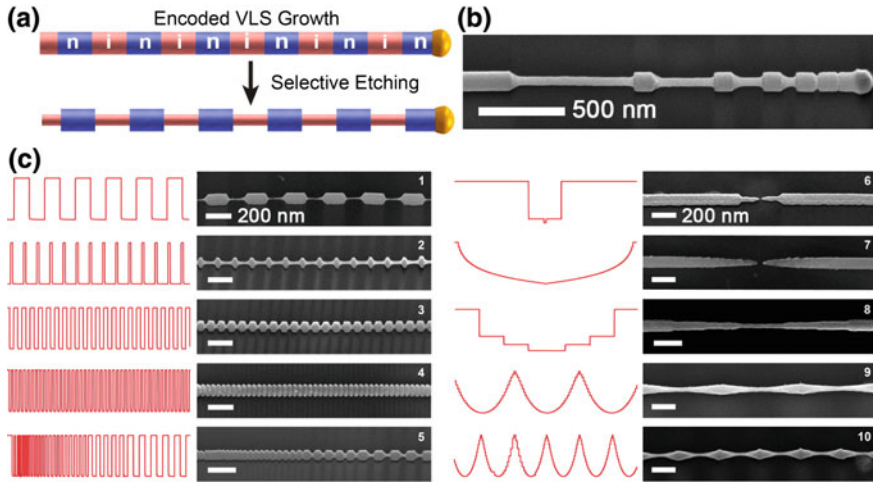


**Fig. 3.5** **a** Schematic illustration of NW with heavily doped *n*-type (*n*) and undoped intrinsic (*i*) segments. **b** SEM image of a NW grating encoded (from *left to right*) with sequential intrinsic segments for 200, 100, 50, 25, 10, and 5 s. **c** SEM images and phosphine flow profiles for the synthesis of SiNWs with complex morphology. The measured phosphine flow profile used to encode the morphology of each segment is depicted in *red* to the *left* of each SEM image. Reproduced from [31]. Copyright 2013 American Chemical Society

vapor/reactant does not decompose/adsorb exclusively at the catalyst surface, but at the surface of the semiconductor NW, a shell of material will grow on the original NW surface (Fig. 3.6c). Subsequent introduction of different reactants and/or dopants can then be used to produce multiple shell structures of nearly arbitrary composition (Fig. 3.6d), although the epitaxial growth of these shells requires consideration of the lattice structures [32]. The interfacial kinetics, controlled by varying the pressure, flow rate, temperature, reactant species and background gases, is therefore necessary to control the dominant growth mode. In the previous section, we have discussed the formation of axial NW superlattices, which can be induced by repeated changing of reactants in a regime favoring axial growth. In this section, core-multi-shelled radial structures formed by changing reactants in a radial-growth regime will be introduced.

### 3.4.1 Semiconductor Radial Structures

One of the first reports of core/shell NW heterostructures was reported by Lauhon et al. [32] by using a nanocluster catalyzed CVD approach to grow NW core/shell homo- and heterostructures from Si and Ge, with different dopant concentration and types including *i*-Si/*p*-Si, Si/Ge and Ge/Si core-shell NWs. TEM images of the *i*-Si/*p*-Si product showed a uniform core-shell structure consisting of a crystalline Si

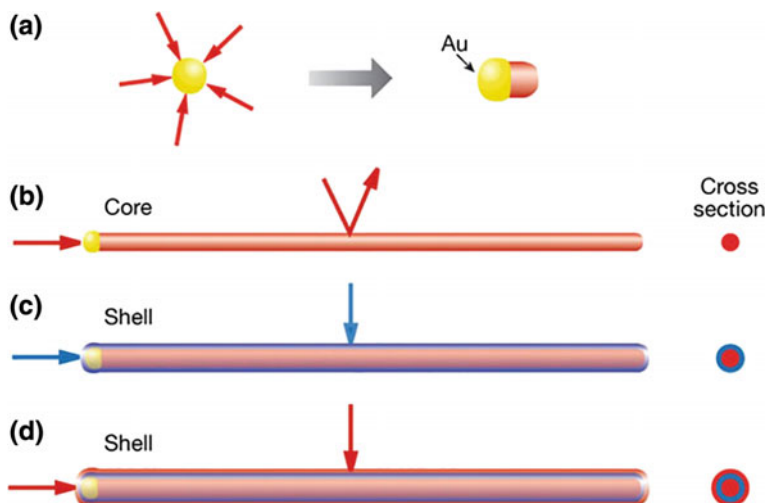


**Fig. 3.6** **a** Gaseous reactants (*red*) catalytically decompose on the surface of a gold nanocluster leading to nucleation and directed NW growth. **b** One-dimensional growth is maintained as reactant decomposition on the gold catalyst is strongly preferred. **c** Synthetic conditions are altered to induce homogeneous reactant decomposition on the NW surface, leading to a thin, uniform shell (*blue*). **d** Multiple shells are grown by repeated modulation of reactants. Reproduced from [32]. Copyright 2002 Nature Publishing Group

core and an amorphous Si shell (Fig. 3.7a). In contrast, TEM images of the *i*-Si/SiO<sub>x</sub>/*p*-Si core/shell/shell structures showed a smooth and abrupt interface between the crystalline core and amorphous shell (Fig. 3.7b, c). These results demonstrated that the thin oxide layer disrupted homoepitaxial growth. Further TEM studies showed that oxidation inhibited crystallization of the shell under annealing conditions. The authors also explored the synthesis of Si/Ge core/multishell NW structures. Figure 3.7d shows the bright-field TEM images and elemental mapping of a core/shell structure that is consistent with Ge-core (dark) and Si-shell (light) structure. High-resolution TEM images and cross-sectional elemental mapping of both Si/Ge and Ge/Si core-shell NWs are displayed in Fig. 3.7e, f. Later, Qian et al. demonstrated the synthesis of core/multishell NWs with an *n*-GaN core, In<sub>x</sub>Ga<sub>1-x</sub>N/GaN/*p*-AlGaN/*p*-GaN shells [33] and highly uniform (InGaN/GaN)<sub>*n*</sub> quantum wells [34]. In the latter case, cross-sectional STEM images of three distinct multi-quantum-well (MQW) NWs (Fig. 3.7g–i) showed structures with resolvable 3, 13, and 26 periods, quantum-well thicknesses of about 2.4, 3.0 and 1.5 nm and average GaN barrier thicknesses of about 40, 10 and 1 nm, respectively.

In 2013, Kempa et al. [35] demonstrated regioselective NW shell synthesis in studies of Ge and Si growth on faceted SiNW surfaces. Generally, the structures were realized by breaking the rotational symmetry of conventional radial shell growth (Fig. 3.7j, k). To explore more complex and opto-electronically active

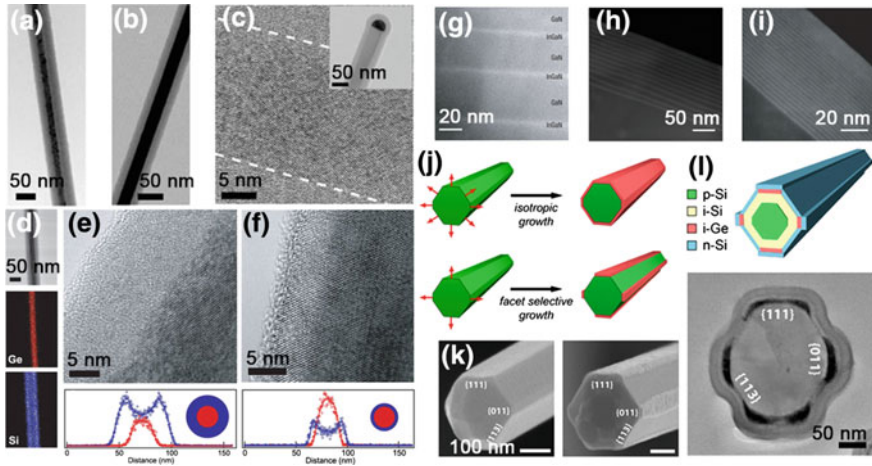


**Fig. 3.7** **a** TEM image of an unannealed intrinsic silicon core and *p*-type silicon shell NW. **b, c** TEM images of an *i*-Si/SiO<sub>2</sub>/*p*-Si NW. **d** Bright-field image and scanning TEM elemental maps of Ge (*red*) and Si (*blue*) concentrations of an unannealed Ge/Si core-shell NW. **e, f** HRTEM image and elemental mapping cross-section of an unannealed (**e**) and an annealed (**f**) Ge/Si core-shell NWs. Reproduced from [32]. Copyright 2002 Nature Publishing Group. **g–i** Dark-field cross-sectional STEM images MQW NW structures. Reproduced from [34]. Copyright 2008 Nature Publishing Group. **j** Schematics depicting isotropic versus anisotropic growth of Ge (*red*) on a faceted Si template (*green*). **k** SEM of a faceted Si template (*left*) and of a nanostructure (*right*) after selective deposition of Ge (*lighter contrast*) on Si. **l** Schematic and bright-field TEM image of the cross section of a complex nanostructure with Ge regions selectively embedded within a *p*-*n* junction. Reproduced from [35]. Copyright 2013 American Chemical Society

nanostructures, the authors encapsulated nanoscale Ge regions within a Si *p*-*n* interface. The targeted architecture included a faceted template with *p*-type and intrinsic Si shells, facet selectively grown Ge, and finally a conformal shell of *n*-type Si (Fig. 3.7l). Bright-field TEM image of the nanostructure cross sections verified that Ge was selectively embedded within the nanostructure while preserving the radial Si *p*-*n* junction. Later, the same group [36] demonstrated facet-selective growth of CdS on SiNWs. The crystalline CdS is grown epitaxially on the {111} and {110} surface facets of the SiNWs but the {113} facets remain bare. Further analysis of CdS on SiNWs grown at higher deposition rates to yield a conformal shell reveals a thin oxide layer on the Si{113} facet. This observation and control experiments suggest that facet-selective growth is enabled by the preferential formation of an oxide, which prevents subsequent shell growth on the Si{113} NW facets.

The Plateau–Rayleigh instability was first proposed in the mid-1800s to describe how a column of water breaks apart into droplets to lower its surface tension. This instability was later generalized to account for the constant volume rearrangement of various one-dimensional liquid and solid materials. The Lieber group [37] reported a growth phenomenon that is unique to one-dimensional materials and

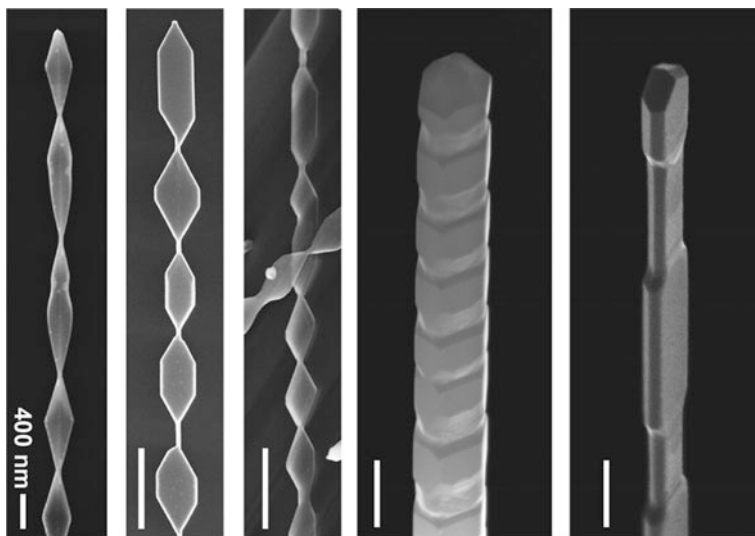


**Fig. 3.8** SEM images of Si periodic shells deposited on SiNW cores achieved by Plateau–Rayleigh growth. Reproduced from [37]. Copyright 2015 Nature Publishing Group

exploited the underlying physics of the Plateau–Rayleigh instability. This phenomenon can be used to grow periodic shells on one-dimensional substrates. Specifically, the authors showed that for certain conditions, depositing Si onto uniform-diameter Si cores, Ge onto Ge cores and Ge onto Si cores can generate diameter-modulated core–shell NWs. Rational control of deposition conditions enables tuning of distinct morphological features, including diameter-modulation periodicity and amplitude and cross sectional anisotropy. The results suggested that surface energy reductions drive the formation of periodic shells, and that variation in kinetic terms and crystal facet energetics provide the means for tunability (Fig. 3.8).

### 3.4.2 Coaxial Modulated Structures

In addition to semiconductor radial structures, coaxial modulated NW structures have also been demonstrated [38–40]. For example, Tian et al. [39] reported the realization of *p-i-n* coaxial SiNWs (Fig. 3.9a). In this work, SiNW *p*-cores were first synthesized by the nanocluster catalyzed VLS method. Si shells were then deposited at a higher temperature and lower pressure than for *p*-core growth (Fig. 3.9a, right panel) to inhibit axial elongation of the SiNW core during the shell deposition, where phosphine was used as the *n*-type dopant in the outer shell. SEM images of a typical *p-i-n* SiNW (Fig. 3.9b) show the single crystalline NW core expected for SiNWs obtained by the VLS method and polycrystalline shells with a

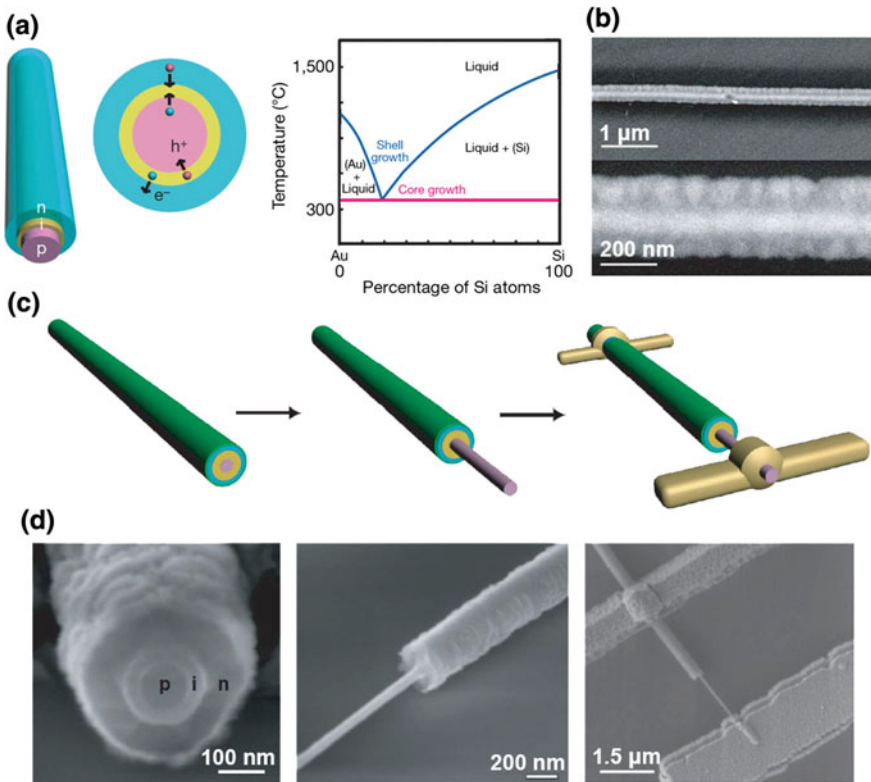


**Fig. 3.9** **a** Illustrations of the core/shell SiNW structure. The phase diagram of Au–Si alloy on the right panel illustrates that the core is grown by means of the VLS mechanism, whereas the shells are deposited at higher temperature and lower pressure to inhibit further NW axial elongation. **b** SEM images of the *p-i-n* coaxial SiNW. **c**, **d** Schematics and corresponding SEM images of selective etching to expose the *p*-core and deposition of metal contacts on the *p*-core and *n*-shell. Reproduced from [39]. Copyright 2007 Nature Publishing Group

grain size on the order of 30–80 nm. To characterize electrical transport through the *p-i-n* coaxial SiNWs, the authors fabricated metal contacts selectively to the inner *p*-core and outer *n*-shell (Fig. 3.9c, d), where NWs were etched selectively using KOH solution to expose the *p*-core in a lithographically defined region, enabling the deposition of metal contacts in a following lithography step.

### 3.5 Branched/Tree-Like Structures

There have recently been substantial interests in production of branched/tree-like NW structures. The higher degree of complexity in such structures increases the potential for NW applications by increasing the number of connection points and



providing a means for parallel connectivity and interconnection of functional elements. In this section, we introduce various methodologies and mechanisms developed for the synthesis of branched structures, ranging from sequential catalyst-assisted growth, solution growth on existing NWs, phase transition induced branching, one-step self-catalytic growth and screw dislocation driven growth. The growth of these branched NWs have been reviewed [41].

### 3.5.1 *Sequential Catalyst-Assisted Growth*

Similar to the VLS growth of 1D semiconductor NWs, growth of branched or even hyperbranched NWs can be carried out in a controlled manner by introducing new nanocluster catalysts onto the primary NW surfaces. As a result, many efforts to grow these complex structures have been focused on the sequential catalyst-assisted method [42–46]. Typically, the process of synthesizing hyperbranched NWs involves sequential steps, as shown in Fig. 3.10a [42]: First, a NW backbone of specific diameter and composition is prepared by nanocluster-mediated VLS growth. Second, nanocluster catalysts of defined diameter are deposited on the backbone, and then the first-order branches are grown by the VLS process. Third, the branch growth steps can be repeated one or more times to yield higher order or hyperbranched NW structures. This method allows good control of the density of branches by adjusting the amount of Au particles deposited on the primary NW trunks, and length of the branches by the growth time. Figure 3.10b–e show representative SEM images of branched SiNW structures prepared by using increasing concentrations of gold nanoclusters during the deposition process. Furthermore, this approach can be extended to produce more complex NW architectures by a three-step growth procedure, in which 40, 20, and 10 nm gold nanoclusters were used to catalyze the VLS growth of the SiNWs comprising the backbone, first generation, and second generation branches, respectively (Fig. 3.10f). Simultaneously, the Samuelson group [43] also fabricated ordered arrays of GaP nanotrees (Fig. 3.10g) using a similar method. Au aerosol particles were deposited onto the primary vertically-aligned GaP NW stems for the subsequent VLS growth of GaP branches.

Compared with the above homobranched NWs, there had been much less reports on heteroepitaxial growth of branches based on sequential catalyst-assisted method. The heterobranched growth is more challenging, as the solubility of dissimilar materials in the same metal catalyst are generally different, which requires different growth temperature and partial pressure. In addition, possible crystal phase change and lattice mismatching are also need to be considered and resolved. The reported successful growths include CdS nanobranched on ZnS backbone NWs [47, 48], GaAs, GaP and Ge nanobranched on SiNWs [49], and CdSe branches on ZnSe NWs based on a sequential growth [50]. For example, Jiang et al. [49] reported the

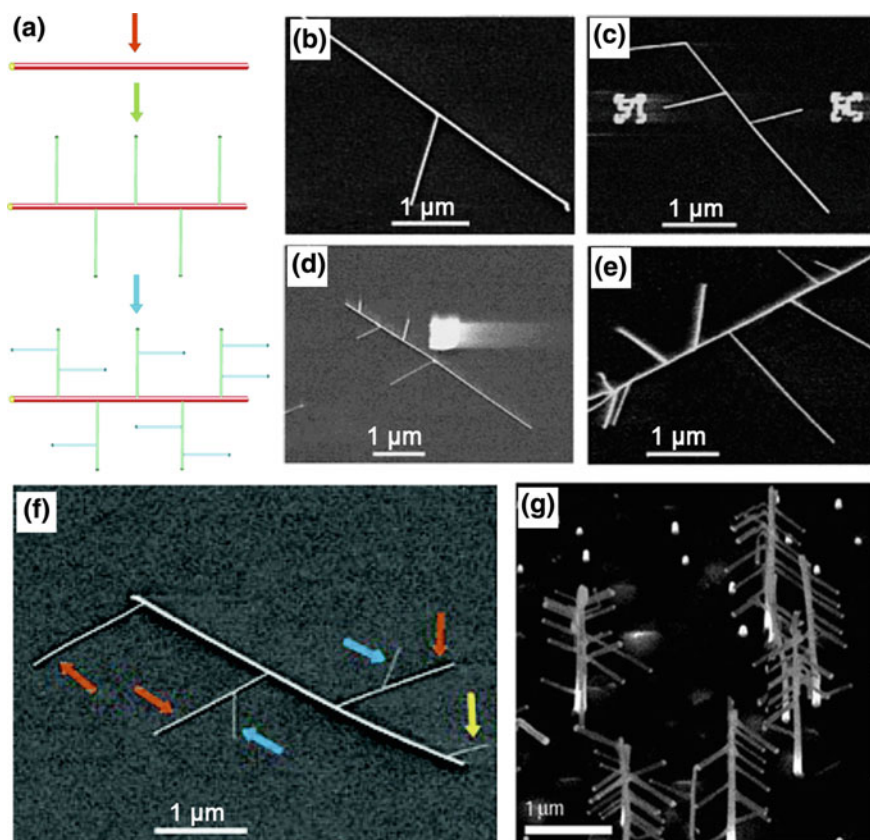


**Fig. 3.10** **a** Schematic illustrating the multistep syntheses of branched and hyperbranched NW structures. **b–e** Branched SiNW structures prepared following deposition of gold nanoclusters prepared from **b** 1:20, **c** 1:8, **d** 1:3, and **e** 1:1 diluted stock solutions and subsequent growth. **f** SEM image of a hyperbranched SiNW structure. The first-generation and second-generation branches are indicated by *orange* and *blue* arrows, respectively. *Yellow* arrow indicates a 10 nm SiNW (from second generation growth) grown from the backbone. Reproduced from [42]. Copyright 2004 American Chemical Society. **g** Ordered array of GaP nanotrees. Reproduced from [43]. Copyright 2004 Nature Publishing Group (Color figure online)

rational synthesis of branched NW structures, including group IV, III–V, and II–VI, with metal branches selectively grown on core or core-shell NW backbones. The composition, morphology and doping of core (core/shell) NWs and branched NWs were well controlled during the synthesis.

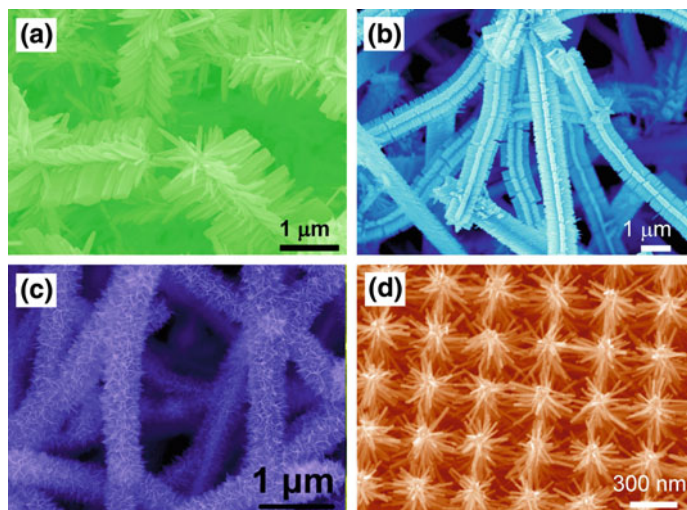


**Fig. 3.11** Branched NWs with different material combinations prepared by solution growth on preformed NW backbones: **a** SnO<sub>2</sub>/ZnO. Reproduced from [51]. Copyright 2009 American Chemical Society. **b** SnO<sub>2</sub>/Fe<sub>2</sub>O<sub>3</sub>. Reproduced from [52]. Copyright 2011 John Wiley and Sons. **c** SnO<sub>2</sub>/MnO<sub>2</sub>. Reproduced from [53]. Copyright 2011 John Wiley and Sons. **d** Si/ZnO. Reproduced from [54]. Copyright 2010 American Chemical Society

### 3.5.2 Solution Growth on Existing Nanowires

Solution methods, including hydrothermal, solvothermal, chemical bath deposition and electrodeposition, can be applied to produce hierarchically branched NWs using pre-formed NWs as the growth substrate. Various types of 3D branched metal oxide NW heterostructures have been realized by combining VLS growth for the backbone NWs with the subsequent solution growth of branches [51–53]. VLS-grown SnO<sub>2</sub> NWs are very stable and are ideal candidates for the backbones of SnO<sub>2</sub>/ZnO, SnO<sub>2</sub>/Fe<sub>2</sub>O<sub>3</sub> and SnO<sub>2</sub>/MnO<sub>2</sub> branched NWs (Fig. 3.11a–c). Further, this method has also been extended to fabricate Si/ZnO forest-like arrays by hydrothermal growth of ZnO nanorods on lithographic-prepared Si nanopillars [54] (Fig. 3.11d).

### 3.5.3 Phase Transition Induced Branching

The Alivisatos group [55–58] introduced a phase transition induced branching method, through which branched NWs can be fabricated without the addition of branching catalyst. The concept underlying their work rests on controlling the relative stability and growth of two different crystal phases. Generally, these

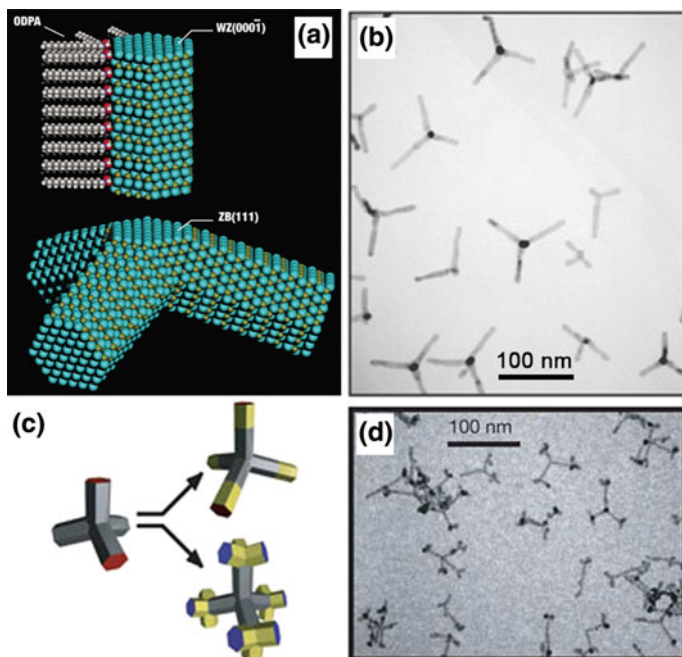


**Fig. 3.12** **a** Proposed model of a CdTe tetrapod. **b** TEM images of the CdTe tetrapods. Reproduced from [56]. Copyright 2003 Nature Publishing Group. **c**, **d** Branched tetrapods resulted from nucleation of CdTe zinc blende branch points on the end of each arm. Reproduced from [57]. Copyright 2004 Nature Publishing Group

materials are limited to those that can crystallize in either wurtzite (WZ) or zinc blende (ZB) close-pack crystal structure or even mixed polytype under specific conditions. In CdTe [56] and other tetrahedrally bonded compound semiconductors, cubic and hexagonal crystal phases are often sufficiently close in energy such that both can be accessed by simply varying the reaction conditions. Following initial nucleation of cubic nanocrystallites, it was shown that four hexagonal arms can be selectively grown in high yield from the tetrahedral cubic nuclei by using organic surfactants to inhibit growth at the sides of the arms but not at their ends, thereby resulting in selective elongation. Figure 3.12a, b display the model of a CdTe tetrapod and TEM image of such crystallographic phase change-induced CdTe nanotetrapod. In a later report, the authors demonstrated that branched and linear junctions can be created not just at nucleation, but at any point during the growth of heterostructures [57]. As a proof of concept, they obtained branched NWs with CdSe in the first and CdTe in the second generation (Fig. 3.12c, d).

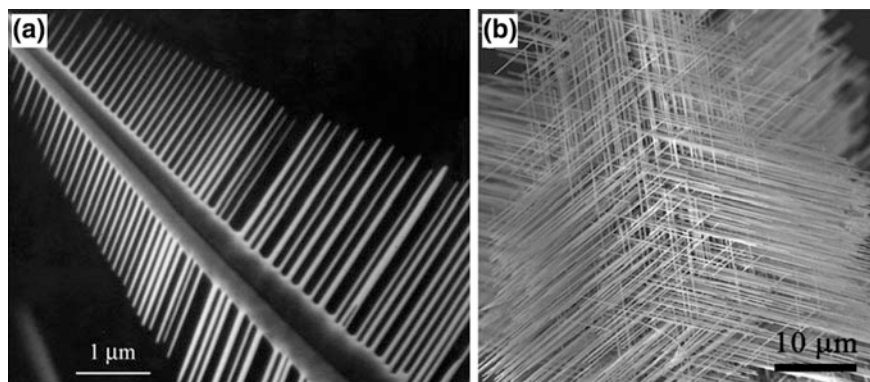


**Fig. 3.13** **a** SEM image of comb structures made of ZnO NWs. Reproduced from [59]. Copyright 2003 American Chemical Society. **b** SEM image PbTe branched NWs. Reproduced from [60]. Copyright 2007 John Wiley and Sons

### 3.5.4 One-Step Self-catalytic Growth

In contrast to the sequential multi-step nanocluster catalyst deposition and growth, self-catalyzed growth allows preparation of 3D branched and even hyperbranched NWs in a single step [59–62]. Wurtzite crystals like ZnO and ZnS often exhibit a branched nanostructure. For example, Yan et al. [59] used the chemical vapor transport (CVT) method to fabricate highly ordered 1D microscale ZnO arrays that resembled comb structures (Fig. 3.13a). The individual NWs had uniform diameters ranging from 10 to 300 nm, and were evenly spaced on a stem with a regular periodicity of 0.1–2  $\mu\text{m}$ . In another report, the same group [60] demonstrated CVT synthesis of arrays of PbS, PbSe, and PbTe NWs. As shown in Fig. 3.13b, the NW arrays were consisted of a central cube with NWs grown perpendicularly from each of the six faces.

### 3.5.5 Screw Dislocation Driven Growth

It has been suggested that the screw component of an axial dislocation can provide the self-perpetuating steps necessary to enable one-dimensional crystal growth without a nanocluster metal catalyst used in the VLS growth of NWs. In 2008, two groups reported NWs with rotating tree morphology made of PbS [63] and PbSe [64], respectively. In the former case, the authors observed pine tree-like NWs of PbS (Fig. 3.14) through CVD reactions [63]. These trees had trunks that are up to hundreds of micrometers in length and branches typically tens of micrometers long.

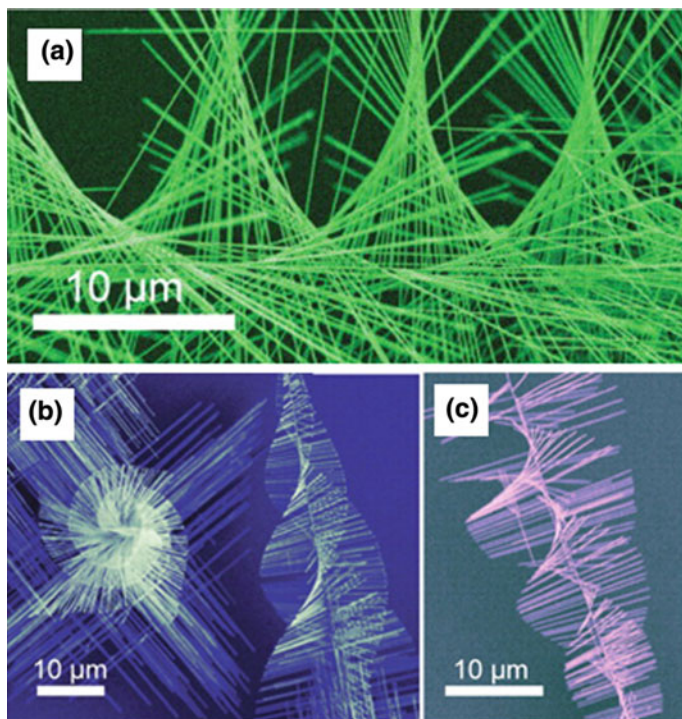


**Fig. 3.14** High-magnification views of trees highlighting the twisting (Eshelby twist) of the central trunk and helical rotating branches. Reproduced from [63]. Copyright 2008 the American Association for the Advancement of Science

Individual wires grew consistently along the  $\langle 100 \rangle$  crystallographic directions and their diameters ranged from 40 to 350 nm. Closer examination of these nanostructures revealed that each tree had four sets of epitaxial branches that were perpendicular to the trunk, and rotated around the trunk in a helical staircase fashion.

All dislocations create strain (and hence stress) within an otherwise perfect crystalline lattice. Using elasticity theory, it was shown that in a finite cylindrical rod containing an axial screw dislocation at the center, the stress field created by the dislocation exerts a torque at the free ends of the rod, resulting in a twist of the rod along the axial direction [63, 64]. The authors also carried out detailed examination of the formation mechanisms and kinetics of spontaneous NW and nanotube growth driven by screw dislocations [65, 66].

### 3.6 Kinked Structures

In this section, we will introduce methods to fabricate kinked NWs, which have unique 2 and 3D topologies defined by the kinks. Two basic classes of growth methods will be discussed, including the undersaturation/supersaturation-induced and confinement-guided kinking methods.

#### 3.6.1 Undersaturation/Supersaturation-Induced Kinking

The Lieber group [67] developed a “nanotectonic” approach that provides iterative control over the nucleation and growth of NWs, and used it to grow kinked or zigzag NWs, in which the straight sections (secondary building unit, SBU) were separated by triangular joints (Fig. 3.15a). The SBU formation involves three main steps during nanocluster catalyzed growth (Fig. 3.15b): (1) axial growth of one-dimensional NW arm segments, (2) purging of gaseous reactants to suspend NW elongation, and (3) re-supersaturation and nucleation of NW growth following

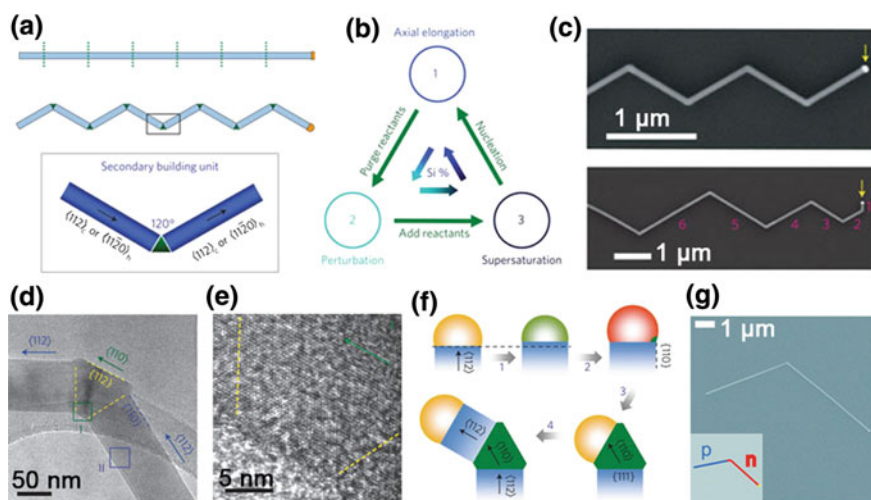


**Fig. 3.15** **a** Schematic of a coherently kinked NW and the SBU, which contains two arms (*blue*) and one joint (*green*). **b** Cycle for the introduction of an SBU by stepwise synthesis. **c** SEM image of a kinked 2D SiNWs with equal (*upper panel*) and decreasing (*lower panel*) arm segment lengths. **d** TEM image of a single kink. **e** Lattice-resolved TEM images from regions *I* and *II* in (**d**). **f** Schematic illustrating the key stages of kink formation. *Arrows 1–4* denote purge, re-introduction of reactant, joint growth and subsequent arm growth, respectively. Reproduced from [67]. Copyright 2009 Nature Publishing Group. **g** Representative SEM image of a kinked *p-n* SiNW with 120° tip angle. Inset: Schematic of a kinked *p-n* NW with 120° tip angle. The *blue* and *red* lines designate the *p*-doped arms and *n*-doped arms, respectively. Reproduced from [68]. Copyright 2012 American Chemical Society

re-introduction of reactants. As illustrated for the case of silicon, the concentration of silicon-reactant dissolved in the nanocluster catalyst drops during purging and then reaches a maximum upon supersaturation. Repeating this cycle allows linking a number of SBUs, thus generating a two-dimensional chain structure (Fig. 3.15c). TEM images of a single kink further illustrate key SBU features (Fig. 3.15d, e). The above studies suggest that the kink formation can be qualitatively explained by the proposed stepwise model (Fig. 3.15f). In step 1, the reactant concentration drops in the supersaturated catalyst during the purge, and if the concentration is reduced sufficiently, elongation will cease. When reactant is re-introduced in step 2, the catalyst becomes supersaturated again and undergoes heterogeneous nucleation and growth. In step 3, growth proceeds with preservation of the most stable facets, implying that the heterogeneous nucleation should occur preferentially at the active edges of the three-phase boundary. In step 4, the kink is completed with a transition to another direction, thus completing a single SBU with coherent arm growth directions. Using a similar method, the same group [68] designed nanoscale axial  $p$ - $n$  junctions that were synthetically introduced at the joints of kinked SiNWs (Fig. 3.15g).

Furthermore, the stereo configuration, such as *cis*- or *trans*-, has been demonstrated for the controlled kink growth. For example, two or three *cis*-linked kinked units can yield angles of  $60^\circ$  or  $0^\circ$ , respectively [69] (Fig. 3.16a, top and middle).

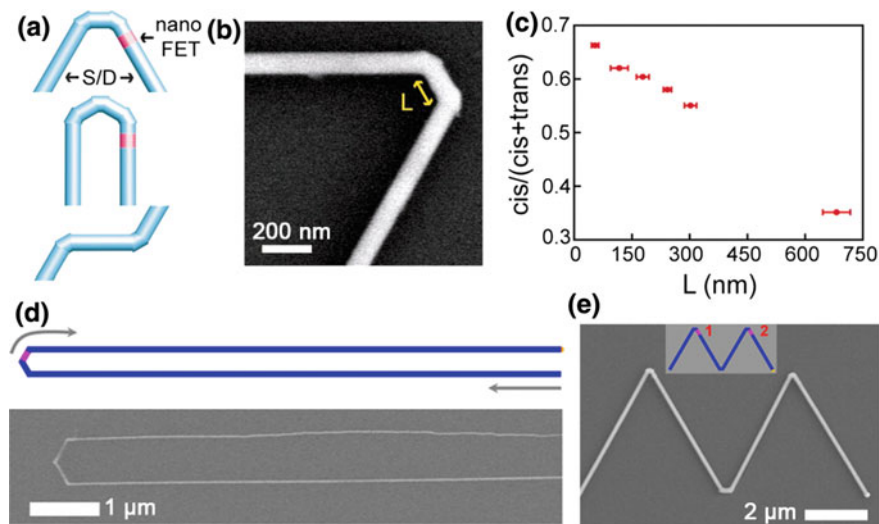


**Fig. 3.16** **a** Schematics of  $60^\circ$  (top) and  $0^\circ$  (middle) multiply kinked NWs and *cis* (top) and *trans* (bottom) configurations in NW structures. **b** SEM image of a doubly kinked NW with a *cis* configuration. **c**  $\text{cis}/(\text{cis} + \text{trans})$  versus  $L$  plot. Reproduced from [69]. Copyright 2010 the American Association for the Advancement of Science. **d** Schematic and SEM image of a U-shaped KNW with tip constructed from three  $120^\circ$  *cis*-linked kinks. **e** Schematic and SEM image of a W-shaped kinked NW. Reproduced from [70]. Copyright 2013 American Chemical Society



A representative SEM image of an 80-nm diameter, doubly kinked SiNW with an intervening segment length ( $L$ ) of  $\sim 160$  nm between kink units (Fig. 3.16b) shows well-defined *cis*-linkage and an overall  $60^\circ$  tip angle. To investigate the ability of this method to synthesize this *cis*-linkage of kink structural units reproducibly, the authors analyzed the plot of  $cis/(cis + trans)$ , as  $L$  was varied from  $\sim 700$  to 50 nm (Fig. 3.16c), showing that the *cis*-conformation becomes dominant as  $L$  decreases. In a follow-up report, Xu et al. [70] presented zero-degree kinked NW structures with U-shaped structures (Fig. 3.16d), as well as parallel kinked NWs with W-shaped structures (Fig. 3.16e).

### 3.6.2 Confinement-Guided Kinking

Pevzner et al. [71] demonstrated a confinement-guided NW growth method that allows unlimited control over geometry and location on a growth substrate. Following the VLS mechanism, semiconductor NWs down to a pitch lower than 50 nm of different compositions in a wide variety of two-dimensional shapes, such as any kinked (different turning angles), sinusoidal, linear, and spiral shapes, were demonstrated.

A schematic description of their method is shown in Fig. 3.17a. First, open trenches of a desired shape, size, number, density, orientation, and location are patterned by electron-beam lithography direct writing on a resist film on a Si wafer with a 600 nm thermal  $\text{SiO}_2$  layer (i and ii). Trenches are then defined in the  $\text{SiO}_2$  layer by chemical dry etching using RIE (iii). Second, titanium adhesion and gold layers of controlled thickness were deposited, where the latter functions as both the sacrificial material defining the enclosed channels and the catalyst for the following VLS-growth of Si, Ge and additional semiconductor NWs (iv). Subsequently, the resist film is lifted-off to reveal the gold lines on the substrate (v). Third, the openings of the tunnels are defined by photolithography (vi). Afterwards, a  $\text{SiO}_2$  capping layer is deposited over the substrate by PECVD (vii). Finally, after the remaining resist is lifted-off (viii), the gold buried under the  $\text{SiO}_2$  capping layer is controllably removed by wet etching with gold etchant to form the shape-controlled nanotunnels (ix). In order to retain a relatively short gold section at the end of the nanotunnels, which will sequentially serve as VLS catalysts for the NWs growth, the etching process is stopped by immersion of the substrate in deionized water. In the next process, Si or Ge NW growth is carried out in a hot-wall or cold-wall CVD reactor via the VLS process (x). Finally, the removal of  $\text{SiO}_2$  capping layer is done by chemical dry etching using RIE (xi). SEM images of synthesized NWs with a wide variety of 2D shapes are shown in Fig. 3.17b. These shapes include kinked Si and Ge NW structures with different turning angles of between  $80$  and  $120^\circ$  (i–iv), sinusoidal NWs (v–vii) with different periods and even more complex shapes like spirals (viii). The gold catalyst can be observed at the tip of the growing NWs (iii, v, viii), indicating that the growth proceeds via the VLS catalytic process throughout the entire synthesis.

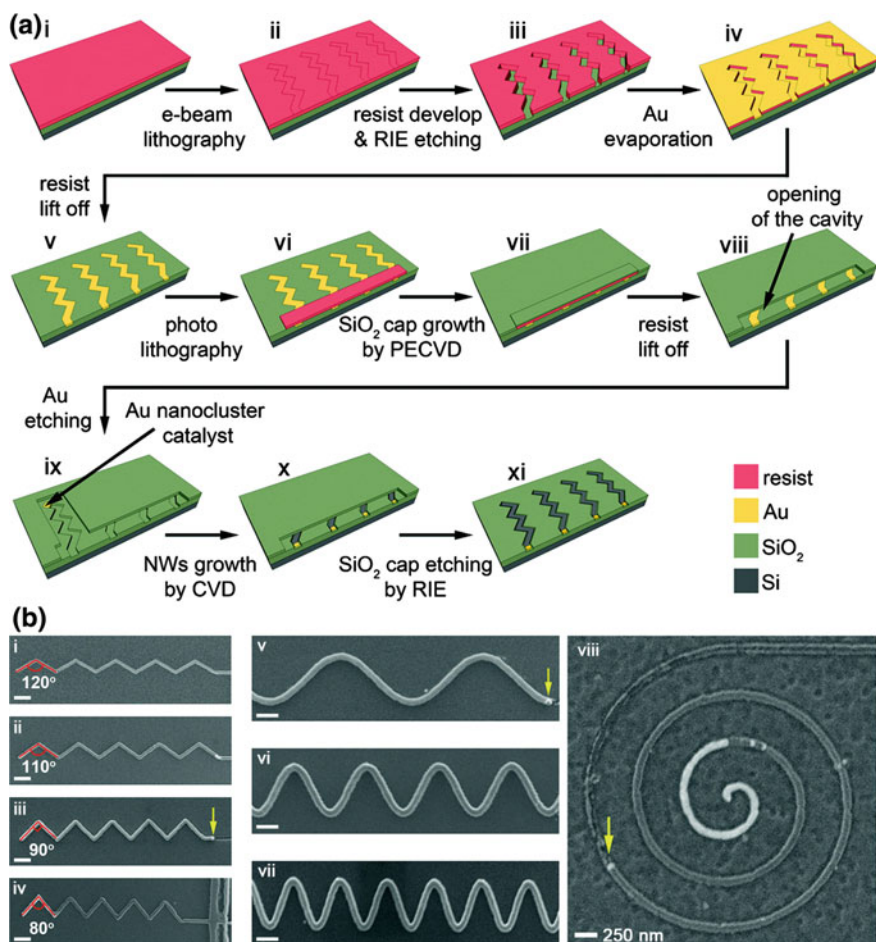


**Fig. 3.17** **a** Schematic illustration of the shape-guided growth method. **b** SEM images of synthesized NWs with a wide variety of 2D shapes. *i-iv* Multiply kinked two-dimensional SiNWs with different turning angles from 120 to 80°. *v-vii* Sinusoidal shape two-dimensional SiNWs with different periods. *viii* SEM image of a two-dimensional spiral shape SiNW. The *yellow arrows* in *iii, v, viii* highlight the position of the nanocluster catalyst. Reproduced from [71]. Copyright 2012 American Chemical Society (Color figure online)

### 3.7 Future Directions and Challenges

The bottom-up paradigm of NW growth by the nanocluster catalyzed VLS method provides the unique opportunity for realizing rational control of physical dimensions and morphology, chemical composition, electronic structure and doping, which are the central elements that determine predictable device functions. The examples described in this chapter illustrate broadly how it is possible to achieve

increasing control over key parameters of the basic NW building blocks from homogeneous doped materials to increasingly complex axial, radial and branched heterostructures, as well as simultaneous axial and radial modulated, and topologically-defined structures.

Overall, the capability to design and synthesize diverse NW building blocks has enabled and will continue to drive the exploration of physical limits of nanostructures, investigating a broad range of scientific problems, discovering and/or uncovering new concepts, and ultimately driving technologies of the future. Nonetheless, in order to use these NW as building blocks to construct complex architectures and systems with novel functions, the capability of patterning NW assemblies into arrays over multiple length scales can be critical, and will be addressed in the next chapter.

## References

1. C.M. Lieber, Semiconductor nanowires: a platform for nanoscience and nanotechnology. *MRS Bull.* **36**(12), 1052–1063 (2011)
2. M.S. Gudiksen, C.M. Lieber, Diameter-selective synthesis of semiconductor nanowires. *J. Am. Chem. Soc.* **122**(36), 8801–8802 (2000)
3. M.S. Gudiksen, J. Wang, C.M. Lieber, Synthetic control of the diameter and length of single crystal semiconductor nanowires. *J. Phys. Chem. B* **105**(19), 4062–4064 (2001)
4. Y. Cui, L.J. Lauhon, M.S. Gudiksen, J. Wang, C.M. Lieber, Diameter-controlled synthesis of single-crystal silicon nanowires. *Appl. Phys. Lett.* **78**(15), 2214–2216 (2001)
5. Y. Wu, Y. Cui, L. Huynh, C.J. Barrelet, D.C. Bell, C.M. Lieber, Controlled growth and structures of molecular-scale silicon nanowires. *Nano Lett.* **4**(3), 433–436 (2004)
6. W. Shi, H. Peng, Y. Zheng, N. Wang, N. Shang, Z. Pan, C. Lee, S. Lee, Synthesis of large areas of highly oriented, very long silicon nanowires. *Adv. Mater.* **12**(18), 1343–1345 (2000)
7. Y. Shi, Q. Hu, H. Araki, H. Suzuki, H. Gao, W. Yang, T. Noda, Long Si nanowires with millimeter-scale length by modified thermal evaporation from Si powder. *Appl. Phys. A* **80**(8), 1733–1736 (2005)
8. W.I. Park, G. Zheng, X. Jiang, B. Tian, C.M. Lieber, Controlled synthesis of millimeter-long silicon nanowires with uniform electronic properties. *Nano Lett.* **8**(9), 3004–3009 (2008)
9. F. Patolsky, G. Zheng, C.M. Lieber, Fabrication of silicon nanowire devices for ultrasensitive, label-free, real-time detection of biological and chemical species. *Nat. Protoc.* **1**(4), 1711–1724 (2006)
10. G. Zheng, W. Lu, S. Jin, C.M. Lieber, Synthesis and fabrication of high-performance n-type silicon nanowire transistors. *Adv. Mater.* **16**(21), 1890–1893 (2004)
11. J. Kikkawa, Y. Ohno, S. Takeda, Growth rate of silicon nanowires. *Appl. Phys. Lett.* **86**(12), 123109 (2005)
12. M. Masi, C. Cavallotti; S. Carrà, Gas phase and surface kinetics of silicon chemical vapor deposition from silane and chlorosilanes, in *Silicon-Based Materials and Devices*, ed. by M. Tomozawa, H. Nalwa (Academic Press, San Diego, 2001)
13. Y. Cui, X. Duan, J. Hu, C.M. Lieber, Doping and electrical transport in silicon nanowires. *J. Phys. Chem. B* **104**(22), 5213–5216 (2000)
14. L. Lauhon, M.S. Gudiksen, C.M. Lieber, Semiconductor nanowire heterostructures. *Phil. Trans. R. Soc. Lond. A* **2004**(362), 1247–1260 (1819)
15. R. Agarwal, Heterointerfaces in semiconductor nanowires. *Small* **4**(11), 1872–1893 (2008)

16. R.S. Wagner, Growth of whiskers by vapor-phase reactions, in *Whisker technology*, ed. by A.P. Levitt (Wiley, New York, 1970), pp. 15–119
17. K. Haraguchi, T. Katsuyama, K. Hiruma, K. Ogawa, GaAs p-n junction formed in quantum wire crystals. *Appl. Phys. Lett.* **60**(6), 745–747 (1992)
18. J. Hu, M. Ouyang, P. Yang, C.M. Lieber, Controlled growth and electrical properties of heterojunctions of carbon nanotubes and silicon nanowires. *Nature* **399**(6731), 48–51 (1999)
19. C.M. Lieber, Nanowire superlattices. *Nano Lett.* **2**(2), 81–82 (2002)
20. Y. Wu, R. Fan, P. Yang, Block-by-block growth of single-crystalline Si/SiGe superlattice nanowires. *Nano Lett.* **2**(2), 83–86 (2002)
21. M. Björk, B. Ohlsson, T. Sass, A. Persson, C. Thelander, M. Magnusson, K. Deppert, L. Wallenberg, L. Samuelson, One-dimensional steeplechase for electrons realized. *Nano Lett.* **2**(2), 87–89 (2002)
22. M. Björk, B. Ohlsson, T. Sass, A. Persson, C. Thelander, M. Magnusson, K. Deppert, L. Wallenberg, L. Samuelson, One-dimensional heterostructures in semiconductor nanowhiskers. *Appl. Phys. Lett.* **80**(6), 1058–1060 (2002)
23. M.T. Björk, C. Thelander, A.E. Hansen, L.E. Jensen, M.W. Larsson, L.R. Wallenberg, L. Samuelson, Few-electron quantum dots in nanowires. *Nano Lett.* **4**(9), 1621–1625 (2004)
24. M.S. Gudiksen, L.J. Lauhon, J. Wang, D.C. Smith, C.M. Lieber, Growth of nanowire superlattice structures for nanoscale photonics and electronics. *Nature* **415**(6872), 617–620 (2002)
25. D.J. Pena, J.K. Mbindyo, A.J. Carado, T.E. Mallouk, C.D. Keating, B. Razavi, T.S. Mayer, Template growth of photoconductive metal-CdSe-metal nanowires. *J. Phys. Chem. B* **106**(30), 7458–7462 (2002)
26. Y. Wu, J. Xiang, C. Yang, W. Lu, C.M. Lieber, Single-crystal metallic nanowires and metal/semiconductor nanowire heterostructures. *Nature* **430**(6995), 61–65 (2004)
27. Y.-C. Lin, K.-C. Lu, W.-W. Wu, J. Bai, L.J. Chen, K. Tu, Y. Huang, Single crystalline PtSi nanowires, PtSi/Si/PtSi nanowire heterostructures, and nanodevices. *Nano Lett.* **8**(3), 913–918 (2008)
28. C. Yang, Z. Zhong, C.M. Lieber, Encoding electronic properties by synthesis of axial modulation-doped silicon nanowires. *Science* **310**(5752), 1304–1307 (2005)
29. T.J. Kempa, B. Tian, D.R. Kim, J. Hu, X. Zheng, C.M. Lieber, Single and tandem axial p-i-n nanowire photovoltaic devices. *Nano Lett.* **8**(10), 3456–3460 (2008)
30. T. Cohen-Karni, D. Casanova, J.F. Cahoon, Q. Qing, D.C. Bell, C.M. Lieber, Synthetically encoded ultrashort-channel nanowire transistors for fast, pointlike cellular signal detection. *Nano Lett.* **12**(5), 2639–2644 (2012)
31. J.D. Christesen, C.W. Pinion, E.M. Grumstrup, J.M. Papanikolas, J.F. Cahoon, Synthetically encoding 10 nm morphology in silicon nanowires. *Nano Lett.* **13**(12), 6281–6286 (2013)
32. L.J. Lauhon, M.S. Gudiksen, D. Wang, C.M. Lieber, Epitaxial core-shell and core-multishell nanowire heterostructures. *Nature* **420**(6911), 57–61 (2002)
33. F. Qian, S. Gradečak, Y. Li, C.-Y. Wen, C.M. Lieber, Core/multishell nanowire heterostructures as multicolor, high-efficiency light-emitting diodes. *Nano Lett.* **5**(11), 2287–2291 (2005)
34. F. Qian, Y. Li, S. Gradečak, H.-G. Park, Y. Dong, Y. Ding, Z.L. Wang, C.M. Lieber, Multi-quantum-well nanowire heterostructures for wavelength-controlled lasers. *Nat. Mater.* **7**(9), 701–706 (2008)
35. T.J. Kempa, S.-K. Kim, R.W. Day, H.-G. Park, D.G. Nocera, C.M. Lieber, Facet-selective growth on nanowires yields multi-component nanostructures and photonic devices. *J. Am. Chem. Soc.* **135**(49), 18354–18357 (2013)
36. M.N. Mankin, R.W. Day, R. Gao, Y.-S. No, S.-K. Kim, A.A. McClelland, D.C. Bell, H.-G. Park, C.M. Lieber, Facet-selective epitaxy of compound semiconductors on faceted silicon nanowires. *Nano Lett.* **15**(7), 4776–4782 (2015)
37. R.W. Day, M.N. Mankin, R. Gao, Y.-S. No, S.-K. Kim, D.C. Bell, H.-G. Park, C.M. Lieber, Plateau-Rayleigh crystal growth of periodic shells on one-dimensional substrates. *Nat. Nanotechnol.* **10**(4), 345–352 (2015)

38. A.B. Greytak, L.J. Lauhon, M.S. Gudiksen, C.M. Lieber, Growth and transport properties of complementary germanium nanowire field-effect transistors. *Appl. Phys. Lett.* **84**(21), 4176–4178 (2004)
39. B. Tian, X. Zheng, T.J. Kempa, Y. Fang, N. Yu, G. Yu, J. Huang, C.M. Lieber, Coaxial silicon nanowires as solar cells and nanoelectronic power sources. *Nature* **449**(7164), 885–889 (2007)
40. D.C. Dillen, K. Kim, E.-S. Liu, E. Tutuc, Radial modulation doping in core-shell nanowires. *Nat. Nanotechnol.* **9**(2), 116–120 (2014)
41. C. Cheng, H.J. Fan, Branched nanowires: synthesis and energy applications. *Nano Today* **7**(4), 327–343 (2012)
42. D. Wang, F. Qian, C. Yang, Z. Zhong, C.M. Lieber, Rational growth of branched and hyperbranched nanowire structures. *Nano Lett.* **4**(5), 871–874 (2004)
43. K.A. Dick, K. Deppert, M.W. Larsson, T. Mårtensson, W. Seifert, L.R. Wallenberg, L. Samuelson, Synthesis of branched ‘nanotrees’ by controlled seeding of multiple branching events. *Nat. Mater.* **3**(6), 380–384 (2004)
44. Q. Wan, J. Huang, Z. Xie, T. Wang, E.N. Dattoli, W. Lu, Branched SnO<sub>2</sub> nanowires on metallic nanowire backbones for ethanol sensors application. *Appl. Phys. Lett.* **92**(10), 102101 (2008)
45. Q. Wan, E.N. Dattoli, W.Y. Fung, W. Guo, Y. Chen, X. Pan, W. Lu, High-performance transparent conducting oxide nanowires. *Nano Lett.* **6**(12), 2909–2915 (2006)
46. K.A. Dick, K. Deppert, L.S. Karlsson, M.W. Larsson, W. Seifert, L. Wallenberg, L. Samuelson, Directed growth of branched nanowire structures. *MRS Bull.* **32**(02), 127–133 (2007)
47. Y. Jung, D.-K. Ko, R. Agarwal, Synthesis and structural characterization of single-crystalline branched nanowire heterostructures. *Nano Lett.* **7**(2), 264–268 (2007)
48. W. Zhou, A. Pan, Y. Li, G. Dai, Q. Wan, Q. Zhang, B. Zou, Controllable fabrication of high-quality 6-fold symmetry-branched CdS nanostructures with ZnS nanowires as templates. *J. Phys. Chem. C* **112**(25), 9253–9260 (2008)
49. X. Jiang, B. Tian, J. Xiang, F. Qian, G. Zheng, H. Wang, L. Mai, C.M. Lieber, Rational growth of branched nanowire heterostructures with synthetically encoded properties and function. *Proc. Natl. Acad. Sci. USA* **108**(30), 12212–12216 (2011)
50. A. Dong, R. Tang, W.E. Buhro, Solution-based growth and structural characterization of homo- and heterobranched semiconductor nanowires. *J. Am. Chem. Soc.* **129**(40), 12254–12262 (2007)
51. C. Cheng, B. Liu, H. Yang, W. Zhou, L. Sun, R. Chen, S.F. Yu, J. Zhang, H. Gong, H. Sun, Hierarchical assembly of ZnO nanostructures on SnO<sub>2</sub> backbone nanowires: low-temperature hydrothermal preparation and optical properties. *ACS Nano* **3**(10), 3069–3076 (2009)
52. W. Zhou, C. Cheng, J. Liu, Y.Y. Tay, J. Jiang, X. Jia, J. Zhang, H. Gong, H.H. Hng, T. Yu, Epitaxial growth of branched  $\alpha$ -Fe<sub>2</sub>O<sub>3</sub>/SnO<sub>2</sub> nano-heterostructures with improved lithium-ion battery performance. *Adv. Funct. Mater.* **21**(13), 2439–2445 (2011)
53. J. Liu, J. Jiang, C. Cheng, H. Li, J. Zhang, H. Gong, H.J. Fan, Co<sub>3</sub>O<sub>4</sub> nanowire@ MnO<sub>2</sub> ultrathin nanosheet core/shell arrays: a new class of high-performance pseudocapacitive materials. *Adv. Mater.* **23**(18), 2076–2081 (2011)
54. C. Cheng, B. Yan, S.M. Wong, X. Li, W. Zhou, T. Yu, Z. Shen, H. Yu, H.J. Fan, Fabrication and SERS performance of silver-nanoparticle-decorated Si/ZnO nanotrees in ordered arrays. *ACS Appl. Mater. Interfaces* **2**(7), 1824–1828 (2010)
55. L. Manna, E.C. Scher, A.P. Alivisatos, Synthesis of soluble and processable rod-, arrow-, teardrop-, and tetrapod-shaped CdSe nanocrystals. *J. Am. Chem. Soc.* **122**(51), 12700–12706 (2000)
56. L. Manna, D.J. Milliron, A. Meisel, E.C. Scher, A.P. Alivisatos, Controlled growth of tetrapod-branched inorganic nanocrystals. *Nat. Mater.* **2**(6), 382–385 (2003)
57. D.J. Milliron, S.M. Hughes, Y. Cui, L. Manna, J. Li, L.-W. Wang, A.P. Alivisatos, Colloidal nanocrystal heterostructures with linear and branched topology. *Nature* **430**(6996), 190–195 (2004)

58. D. Wang, C.M. Lieber, Inorganic materials: nanocrystals branch out. *Nat. Mater.* **2**(6), 355–356 (2003)
59. H. Yan, R. He, J. Johnson, M. Law, R.J. Saykally, P. Yang, Dendritic nanowire ultraviolet laser array. *J. Am. Chem. Soc.* **125**(16), 4728–4729 (2003)
60. M. Fardy, A.I. Hochbaum, J. Goldberger, M.M. Zhang, P. Yang, Synthesis and thermoelectrical characterization of lead chalcogenide nanowires. *Adv. Mater.* **19**(19), 3047–3051 (2007)
61. M.J. Bierman, Y.A. Lau, S. Jin, Hyperbranched PbS and PbSe nanowires and the effect of hydrogen gas on their synthesis. *Nano Lett.* **7**(9), 2907–2912 (2007)
62. R. Liu, Z.-A. Li, C. Zhang, X. Wang, M.A. Kamran, M. Farle, B. Zou, Single-step synthesis of monolithic comb-like CdS nanostructures with tunable waveguide properties. *Nano Lett.* **13**(6), 2997–3001 (2013)
63. M.J. Bierman, Y.A. Lau, A.V. Kvit, A.L. Schmitt, S. Jin, Dislocation-driven nanowire growth and Eshelby twist. *Science* **320**(5879), 1060–1063 (2008)
64. J. Zhu, H. Peng, A. Marshall, D. Barnett, W. Nix, Y. Cui, Formation of chiral branched nanowires by the Eshelby twist. *Nat. Nanotechnol.* **3**(8), 477–481 (2008)
65. S.A. Morin, M.J. Bierman, J. Tong, S. Jin, Mechanism and kinetics of spontaneous nanotube growth driven by screw dislocations. *Science* **328**(5977), 476–480 (2010)
66. S. Jin, M.J. Bierman, S.A. Morin, A new twist on nanowire formation: screw-dislocation-driven growth of nanowires and nanotubes. *J. Phys. Chem. Lett.* **1**(9), 1472–1480 (2010)
67. B. Tian, P. Xie, T.J. Kempa, D.C. Bell, C.M. Lieber, Single-crystalline kinked semiconductor nanowire superstructures. *Nat. Nanotechnol.* **4**(12), 824–829 (2009)
68. Z. Jiang, Q. Qing, P. Xie, R. Gao, C.M. Lieber, Kinked p–n junction nanowire probes for high spatial resolution sensing and intracellular recording. *Nano Lett.* **12**(3), 1711–1716 (2012)
69. B. Tian, T. Cohen-Karni, Q. Qing, X. Duan, P. Xie, C.M. Lieber, Three-dimensional, flexible nanoscale field-effect transistors as localized bioprobes. *Science* **329**(5993), 830–834 (2010)
70. L. Xu, Z. Jiang, Q. Qing, L. Mai, Q. Zhang, C.M. Lieber, Design and synthesis of diverse functional kinked nanowire structures for nanoelectronic bioprobes. *Nano Lett.* **13**(2), 746–751 (2013)
71. A. Pevzner, Y. Engel, R. Elnathan, A. Tsukernik, Z. Barkay, F. Patolsky, Confinement-guided shaping of semiconductor nanowires and nanoribbons: “writing with nanowires”. *Nano Lett.* **12**(1), 7–12 (2012)

# Chapter 4

## Hierarchical Organization in Two and Three Dimensions

**Abstract** The rationally designed and synthesized semiconductor NWs offer as a platform material with the potential to realize unprecedented structural and functional complexity as building blocks. To utilize these building blocks for nanoscale devices through integrated systems, for example in electronics and photonics, requires controlled and scalable assembly of NWs on either rigid or flexible substrates. In this chapter, we will summarize recent advances in large-scale NW assembly and hierarchical organization with two general approaches. First, organization of pre-grown NWs onto target substrates in one or more independent steps, where distinct NW building blocks can be used in each assembly step, and second, the direct growth of aligned NWs on substrates will be discussed.

### 4.1 Introduction

In previous chapters, the rational design and controlled synthesis of complex NWs has been discussed. To exploit these unique building blocks for the development of NW-based device arrays and hierarchical architectures, which are important for exploring fundamental questions and practical applications in areas ranging from electronics and photonics to energy utilization and the life sciences. In the past, a number of assembly methods have been developed for hierarchical organization of individual NWs. In general, these NW assembly strategies can be placed into two classes, including (1) methods based on transferring pre-grown NWs onto target substrates in one or more distinct steps and (2) direct growth of aligned NWs at spatially-defined positions on substrates.

As discussed in the two previous chapters, NWs by the bottom-up approaches, such as nanocluster catalyzed VLS solution growth methods, often have random alignment and orientation, and thus are not directly used for fabricating arrays of devices or ultimately functional nanosystems. Below, we first will focus on the post-growth assembly methods, including flow-assisted alignment, the Langmuir–Blodgett technique, blown bubble methods, chemical binding and electrostatic interactions, interface-induced assembly, electric/magnetic field-assisted alignment,

poly(dimethylsiloxane) (PDMS) transfer, contact/roll printing techniques, nanocombing, as well as other assembly methods. Several comprehensive reviews regarding post-growth alignment of NWs can be found in [1–6]. In addition, we will introduce methods for direct growth of aligned NW arrays, including epitaxial growth from nanocluster catalyst arrays patterned by photolithography, EBL, nanosphere lithography (NSL), porous alumina deposition and nanoimprint lithography, as well as substrate-step-directed growth.

## 4.2 Post-growth Assembly

### 4.2.1 Fluidic Method

Liquid flow can be used for assembly because NWs will align along the flow direction to minimize the shear force. In order to avoid turbulent flow, which would produce uncontrolled fluid flow and corresponding shear force directions, micrometer-sized channels can be applied to yield well-defined laminar flows [7, 8]. Messer et al. [9] reported a flow-assisted alignment approach incorporated with the microfluidic technique for patterning  $[\text{Mo}_3\text{Se}_3]_\infty$  NWs. Microfluidic channel networks are formed between a PDMS micromold and a silicon or glass substrate. A droplet of NW solution is placed at the open end of the microchannels, filling the channels within minutes via capillary action. Upon evaporation of the solvent and PDMS removal, the NWs form bundles and align along the corners of the microchannels [4].

This work by Messer et al. suggested a unique potential for using liquid flows to align NWs, although it was not capable of producing individual aligned NWs nor was it able to tailor the periodicity of NWs, as the NW suspension passed through the microchannels only one time and then evaporated. To address these substantial challenges and exploit the power of fluid flows, Huang et al. [10] designed a flow-assisted assembly technique that combined fluidic alignment with surface-patterning, whereby the separation and spatial location of individual NWs were readily controlled. In this method, NWs or CNTs were aligned by passing a suspension of NWs through microfluidic channel structures formed between a PDMS mold and a flat substrate, pre-functionalized for enhancing the interaction with NWs (Fig. 4.1a). The alignment of the NWs was found to extend up to millimeter length scales, and was tuned by the size of the fluidic channels used. The flow rate was used to control the degree of alignment, and the average NW density increased systematically with the flow duration. Significantly, using a layer-by-layer sequential deposition process, the fluidic flow assembly approach was also shown to be capable of organizing NWs into more complex crossed structures, which are important for building up dense nanodevice arrays (Fig. 4.1b). The formation of crossed structures requires that the nanostructure-substrate interaction is sufficiently strong, so that sequential flow steps do not affect



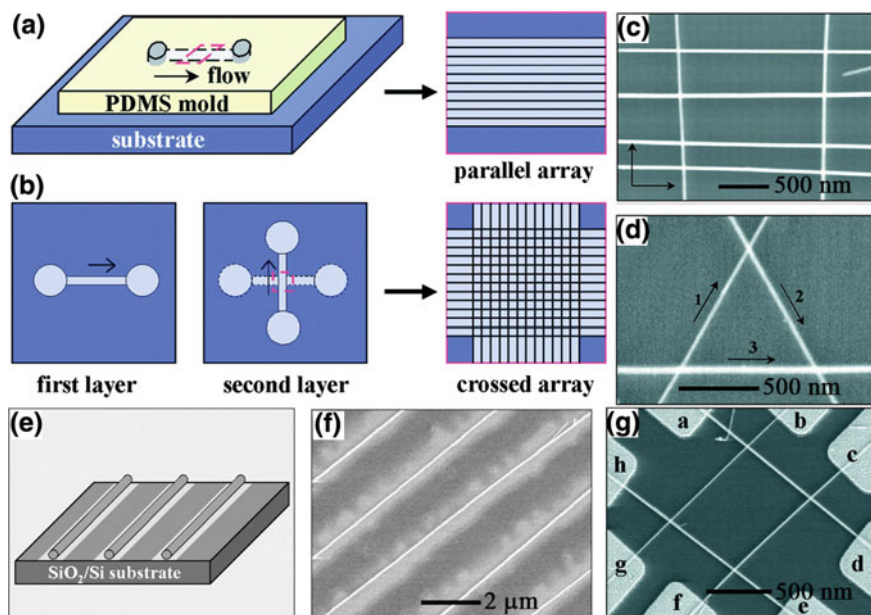


**Fig. 4.1** **a** Schematic of parallel NW arrays obtained by passing a NW solution through a channel on a substrate. **b, c** Schematic (**b**) and SEM image (**c**) of crossed NW matrix obtained by orthogonally changing the flow direction in a sequential flow alignment process. Flow directions in (**c**) are highlighted by *arrows*. **d** An equilateral triangle of NWs obtained in a three-step assembly process, with  $60^\circ$  angles between flow directions, which are indicated by *numbered arrows*. **e, f** Schematic (**e**) and SEM image (**f**) of regular NW arrays obtained by flowing NW solution over a chemically patterned surface. The *light gray* areas correspond to either  $\text{NH}_2$ -terminated surfaces, whereas the *dark gray* areas correspond to either methyl-terminated surfaces. **g** Crossed NW device arrays obtained with fluidic flow assembly. Reproduced from [10]. Copyright 2001 the American Association for the Advancement of Science (Color figure online)

preceding ones. This condition was readily achieved in these studies by modifying the substrate surface with proper functional chemical groups [10]. For example, alternating the flow in orthogonal directions in a two-step assembly process yielded crossbar structures (Fig. 4.1c), while equilateral triangles were assembled in a three-layer deposition sequence using  $60^\circ$  angles between the three flow directions (Fig. 4.1d). The capability to control NW assembly in sequential steps as shown in these studies is especially important since distinct NWs can be used in each step to combine materials and structures in this bottom-up approach that would otherwise be difficult to achieve by purely top-down fabrication.

To enable further control of spatial location and periodicity of assembled NW arrays, complementary chemical interactions between chemically patterned substrates and NWs have been explored (Fig. 4.1e). Specifically,  $\text{NH}_2$ -terminated and methyl-terminated surfaces were first lithographically patterned on substrates, with  $\text{NH}_2$ -terminated regions being selective to the oxide surface of SiNWs. Following

flow alignment, regular parallel NW arrays with lateral periods the same as those of the surface patterns were produced (Fig. 4.1f). Thus, the combination of flow-assisted alignment with conventional lithography patterning can yield integrated device structures as shown in Fig. 4.1g [11].

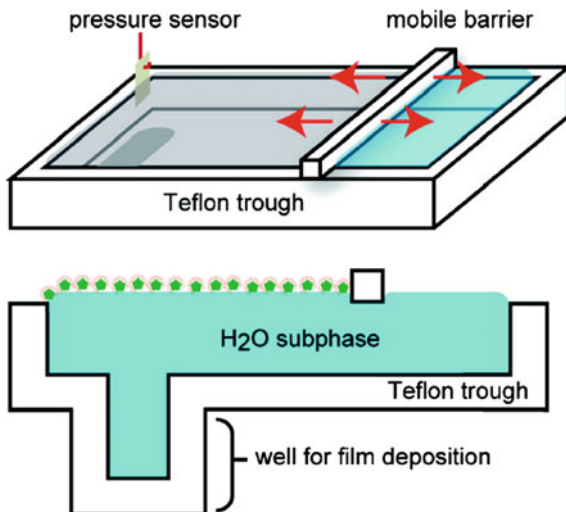
Yan et al. [12] reported a template-guided fluidic assembly based on oriented polymer nanofibers. In their experiments, CdS NWs dispersed in solution were selectively deposited and aligned at the central space of parallel micro/nano-channels formed by the well-oriented nanofibers, as a result of evaporation-induced flow and capillarity. Later, a new technique combining fluid flow with stirring-assisted assembly was reported and applied in the alignment of Ag NWs [13]. In contrast to the fluid flow alignment in microfluidic channels, the stirred flow has no strict requirements on the morphology and shape of the substrate. However, this method does not provide a high degree of control over the spacing and orientation of individual NWs [6]. The Mirkin group [14] reported the large-area alignment of multi-segmented NWs in nanoscale trenches. Briefly, the solution containing NWs was dropped onto a PDMS stamp with trenches, during the drying process, the droplet edge spontaneously shrank due to solvent evaporation and moved over the trench area, and the NWs were aligned into the trenches by nanoscale capillary forces.

Gas flows have also been used to guide the alignment of silica NWs during VLS growth [15]. To achieve better controlled growth, a sandwich-like configuration was employed; that is, a separate Si wafer was placed on top of the first Si wafer coated with Au film, served as the growth substrate. Other growth conditions are comparable to the commonly used nanocluster catalyzed VLS growth in CVD [16]. The sandwich-like structure functions as a microreactor for guiding the gas flow. Unlike randomly entangled NWs on the uncovered substrate under common CVD growth conditions, ordered NW arrays were grown along the flow of gaseous species by confining the gas flow.

### **4.2.2 Langmuir-Blodgett Method**

The Langmuir-Blodgett (LB) technique [17] is another method that has been used to align and assemble NWs (Fig. 4.2). The LB process is carried out in a water-filled trough equipped with a mobile barrier and a pressure sensor. In brief, NWs are dispersed in a volatile solvent that is immiscible in water, and the solution is then spread onto the water surface, forming a film of randomly oriented NWs at the water-air interface. The mobile barrier is then used to laterally compress the monolayer at a controlled speed, resulting in axially-aligned NWs [18, 19]. The LB approach is attractive since (i) axially-aligned monolayers can be formed over relatively large areas, (ii) these monolayers can be easily transferred to substrates, and (iii) the axial alignment and transfer processes can be repeated to yield multiple layers of the same or distinct materials [20]. The first demonstration of LB technique-assisted NW alignment was reported by the Yang group [21–23], where

**Fig. 4.2** Schematic of a water-filled LB trough from the top (*upper*) and side views (*lower*). Surfactant-coated NWs at the surface of the H<sub>2</sub>O subphase are highlighted in the side view by *filled green circles with yellow outer shell*. Reproduced from [19]. Copyright 2008 American Chemical Society (Color figure online)



NWs were rendered hydrophobic by surface functionalization of surfactant before the LB experiments. While this work showed the potential for axial alignment, it did not demonstrate control of spacing and other properties critical to integrated and interconnected arrays.

An important development of the LB alignment was reported by Whang et al. [24], who demonstrated the LB method for hierarchically organizing NW building blocks *en masse* into integrated large-scale arrays tiled over areas up to 20 cm<sup>2</sup> in area (Fig. 4.3a–c). In this work, the average spacing between NWs was controlled by reducing the area of the Langmuir monolayer, for example, by slow dissolution of surfactant into the water sub-phase. The layer of aligned NWs was then transferred in a single step to a planar substrate to yield parallel NWs covering entire substrate surfaces. Significantly, this process could be repeated in a second step with the substrate orientation rotated 90-degrees to assemble crossed NWs over the entire surface. In addition, photolithography was used to define a pattern over the entire substrate, and the NWs outside the patterned area were then removed by gentle sonication. Regular 10 μm × 10 μm square arrays with a 25 μm array pitch of both parallel and crossed NWs were achieved over large areas (Fig. 4.3d, e).

An important, albeit expected, limitation of the above reports was the absence of end-to-end registry in the transferred NWs. To overcome this issue, Acharya et al. [25] used NW coalescence to yield large-scale NW alignment with remarkable end-to-end and side-by-side registries using the LB technique. ZnSe wires capped with octadecylamine molecules were dispersed on the surface of a LB trough. Ordered superstructured islands randomly oriented in azimuth were observed in local units, each consisting of equally spaced, parallel NWs arranged in rows. After uniaxial compression, the NWs' long axes were aligned parallel to the barrier irreversibly, exhibiting tight end-to-end registry along with side-by-side registry. Park et al. [26] extended the LB method and introduced a gluing LB technique using a

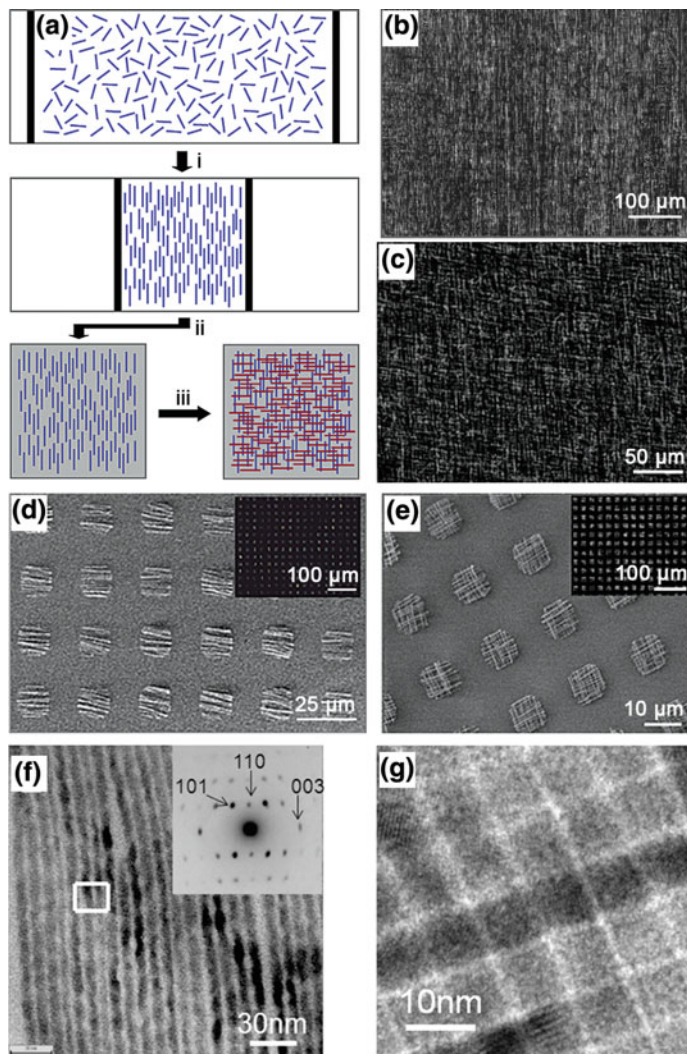


**Fig. 4.3** **a** NWs in a monolayer of surfactant at the air-water interface are *i* compressed on a LB trough to a specified pitch; *ii* The aligned NWs are transferred to the surface of a substrate to make a uniform parallel array; *iii* Crossed NW structures are formed by uniform transfer of a second layer of NWs perpendicular to the first layer. **b**, **c** Parallel and crossed NWs. **d** Image of patterned  $10\ \mu\text{m} \times 10\ \mu\text{m}$  parallel NW arrays. **e** Image of patterned crossed NW arrays. Reproduced from [24]. Copyright 2003 American Chemical Society. **f**, **g** TEM image of parallel and crossed Te NW assembly. Reproduced from [27]. Copyright 2010 American Chemical Society

lithographically patterned PDMS stamp. According to the orientation of the PDMS line patterns relative to the air-water interface, aligned orientation of  $\text{V}_2\text{O}_5$  NWs, either parallel or perpendicular to the patterns, were obtained and attributed to the moving direction of the water menisci formed between the PDMS stamp and water.

Although the LB technique has been a versatile and general tool for assembly of 1D nanosized materials, one limitation inherent in this fabrication method is that the surface of nanomaterials must be functionalized with hydrophobic ligands, restricting their subsequent application. In 2010, Liu et al. [27] showed that assemblies of hydrophilic flexible Te NWs were produced by the LB technique without any extra hydrophobic pretreatment or functionalization. Before adding to the water–air interface, hydrophilic Te NWs were first dissolved in N,N-dimethylformamide (DMF) and then added to a mixture of DMF and chloroform. After the evaporation of the mixed solvent, ordered islands consisting of parallel NWs were observed randomly oriented at the air/water interface. Due to the existence of the interfacial tension, NWs shrank to form close-packed arrays that could be compressed to yield large scale orientationally-ordered structures (Fig. 4.3f, g). This strategy was also extended to assemble other ultrathin 1D nanostructures, such as Ag<sub>2</sub>Te NWs and Pt nanotubes.

Bottom-up assembled NWs can also be exploited as masks for patterning lines with nanometer to micrometer scale pitches hierarchically over large areas [28]. The approach is illustrated in Fig. 4.4a: (i) surfactant-stabilized core-shell NWs are compressed on a LB trough to produce aligned NWs with a controlled pitch; (ii) the aligned NW arrays are horizontally transferred onto hydrophobic substrates; (iii) selective anisotropic etching is used to remove the oxide shell of core-shell NWs; (iv) metals are deposited using the aligned NWs as shadow masks to create arrays of nanoscale wires; (v) the NW masks are removed by isotropic wet etching and sonication to expose the etched or deposited parallel line features. The resulting sample shows well-defined metal lines with an average pitch of 90 nm and line width of 40 nm (Fig. 4.4b).

Previously reports of NW and NT FETs had used serial EBL to define interconnects, and thus precluded studies of large systems. To overcome this problem, Jin et al. [29] developed a new strategy that enabled parallel and scalable integration of NW devices over large areas without the need to register individual NW-electrode interconnects. This approach used LB method to organize NWs with controlled alignment and spacing over large areas, and subsequent photolithography to define interconnects in a statistical manner. As the LB method has a defined average value of pitch size but varies on the local scale, this approach allows for the large-scale assembly and parallel interconnection with electrode arrays. Therefore, a high yield of metal electrode-to-NW contacts was achieved simply by setting the average NW separation comparable to the electrode width (Fig. 4.4c). This approach includes the following steps (Fig. 4.4d): (i) a uniform parallel layer of aligned NWs with a controlled average spacing is deposited onto a substrate surface from NWs uniaxially aligned at the air-water interface on a LB trough; (ii) photolithography is used to remove extra NWs from regions outside of the designed device area; (iii) electrode arrays are fabricated by photolithography patterning. The method was demonstrated with the fabrication of large-scale NW-FET arrays repeated over the entire substrate (Fig. 4.4e).

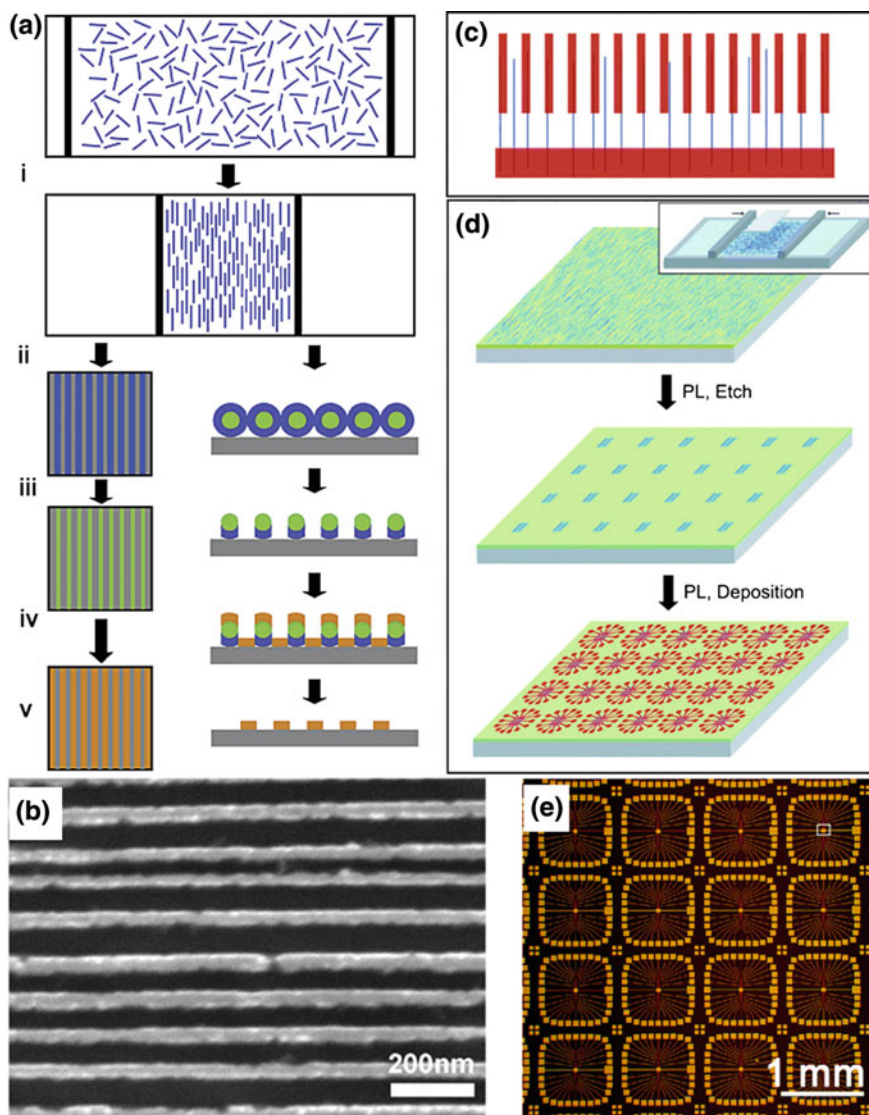


**Fig. 4.4** *a* *i* Alignment of NWs on the water surface of a LB trough. *ii* Transfer of aligned NWs onto substrates. The top (*left*) and the cross-sectional (*right*) view show the core-shell NWs compressed to close-packed structure. *iii* Selective anisotropic etching of the oxide shell of core-shell NWs. *iv* Deposition of metal or other materials. *v* Removal of the NW mask to yield parallel lines over the entire substrate surface. **b** SEM image of 15 nm thick Cr metal lines following removal of the NW mask. Reproduced from [28]. Copyright 2003 American Chemical Society. **c** Central electrode region of an array of interconnected NWs (*blue lines*) obtained without the registration of individual electrodes. **d** Schematic illustrating key steps of the interconnection approach, including the deposition of aligned NWs, hierarchical patterning to produce fixed size and pitch parallel NW arrays, and the deposition of a repeating metal electrode array using photolithography. **e** Optical micrograph of integrated metal electrode arrays deposited on top of patterned parallel NW arrays defined by photolithography. Reproduced from [29]. Copyright 2004 American Chemical Society

### 4.2.3 Blown Bubble Method

Blown film extrusion is a well-developed process for the manufacture of plastic films in large quantities, which involves extruding a molten polymer and inflating it to obtain a balloon. In 2007, Yu et al. [30, 31] adapted the basic ideas underlying this commercial film production method to develop the blown bubble film (BBF) approach for making large-area thin films containing well-organized 1D nanostructures. The method involves: (i) the preparation of a homogeneous solution containing dispersed nanostructures, analogous to the polymer melt used in industry; (ii) expansion of a bubble from the nanomaterial solution at a controlled direction and speed, and (iii) transfer of the bubble to a substrate to yield well-defined nanomaterial-incorporated thin films (Fig. 4.5a). The alignment of nanomaterials in bubble films was attributed to the shear stress present in the polymeric fluid during the bubble expansion process. Controlled bubble initiation, expansion, and transfer were done using a 50-mm-diameter circular die with a gas

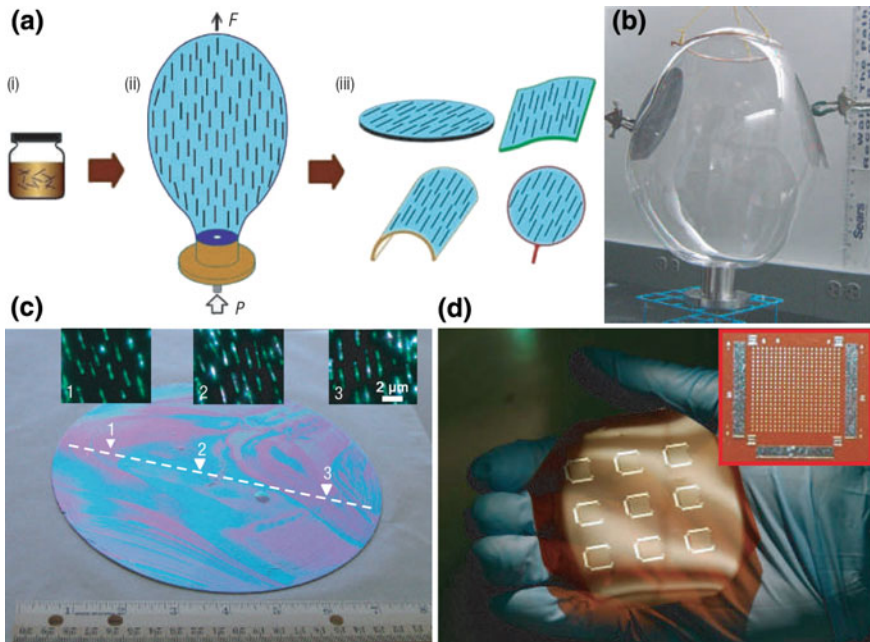


**Fig. 4.5** **a** Schematic illustration of BBF approach. Nanomaterials (e.g. nanotubes, NWs, nanobelts, and nanoparticles) are dispersed in a polymer solution, a volume of solution is expanded as a bubble using a die, and then BBFs are transferred to substrates, including crystalline wafers, plastic sheets, curved surfaces, and open frames. **b** Snapshots of the final stage of bubble expansion and coating of BBF on two wafers. **c** Image of an SWNT-BBF transferred to a 200-mm Si wafer. **d** Photograph of a plastic substrate containing nine SiNW-FETs device arrays. The device arrays were prepared by transfer of the SiNW-BBF to the plastic. *Inset* is the optical image of one device array. Reproduced from [30]. Copyright 2007 Nature Publishing Group

inlet at the bottom and an outlet at the top surface. The nanomaterial-polymer solution was deposited on the die surface and blown into a bubble by flowing gas (Fig. 4.5b). The upward bubble expansion was stabilized and controlled by a motor-driven ring. Bubbles were expanded in an elongated spherical shape (along the vertical axis). Sample substrates, such as silicon wafers, were fixed close to the central region of the elongated bubble during the transfer process. A representative image of a single-walled carbon nanotube (SWCNT)-BBF transferred to a 200-mm wafer (Fig. 4.5c) showed that the film was remarkably uniform across the whole substrate. To illustrate the potential of NW-BBFs to be used as integrated electronics, a  $3 \times 3$  repeating transistor array was fabricated (Fig. 4.5d), where each of the nine elements of the overall array was consisted of 400 independently addressable multi-NW transistors in a  $20 \times 20$  array.

#### 4.2.4 Chemical Interactions for Assembly

Hydrogen bonding, van der Waals interactions and electrostatic interactions between NW surfaces and chemically patterned substrates can be utilized to selectively deposit, assemble and align NWs. For example, Myung et al. [32] reported a “surface-programmed assembly” method for high-precision assembly of  $V_2O_5$  NWs on solid substrates. In this case, the authors utilized positively charged surface molecular patterns to align millions of NWs, and neutral surface regions where they wanted to avoid absorption of NWs. Figure 4.6a shows the schematic

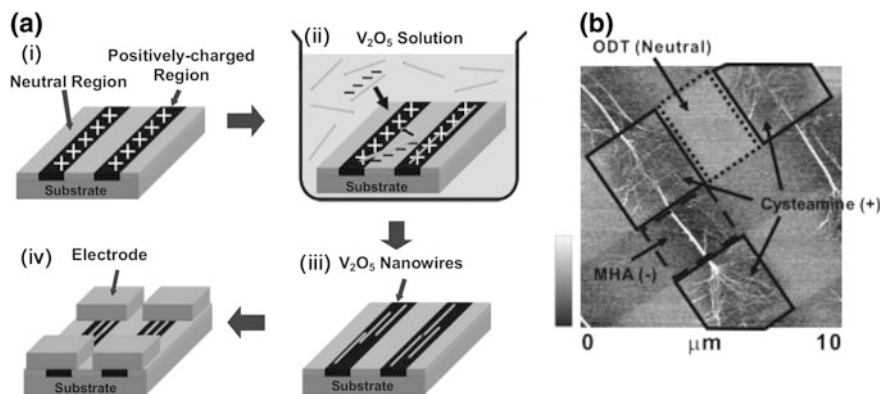


**Fig. 4.6** a Schematic diagram depicting “surface-programmed assembly” of  $V_2O_5$  NWs on solid substrates. *i* Patterning a self-assembled monolayer with positively charged and neutral terminal groups; *ii* assembly and alignment of NWs directed by surface molecular patterns; *iii* rinsing with de-ionized water leaves aligned NW patterns; *iv* additional micro-fabrication process to fabricate electrodes. b AFM topography image of  $V_2O_5$  NWs assembled onto SAM patterns comprised of ODT (neutral), MHA (negatively charged), and cysteamine (positively charged). Reproduced from [32]. Copyright 2005 John Wiley and Sons

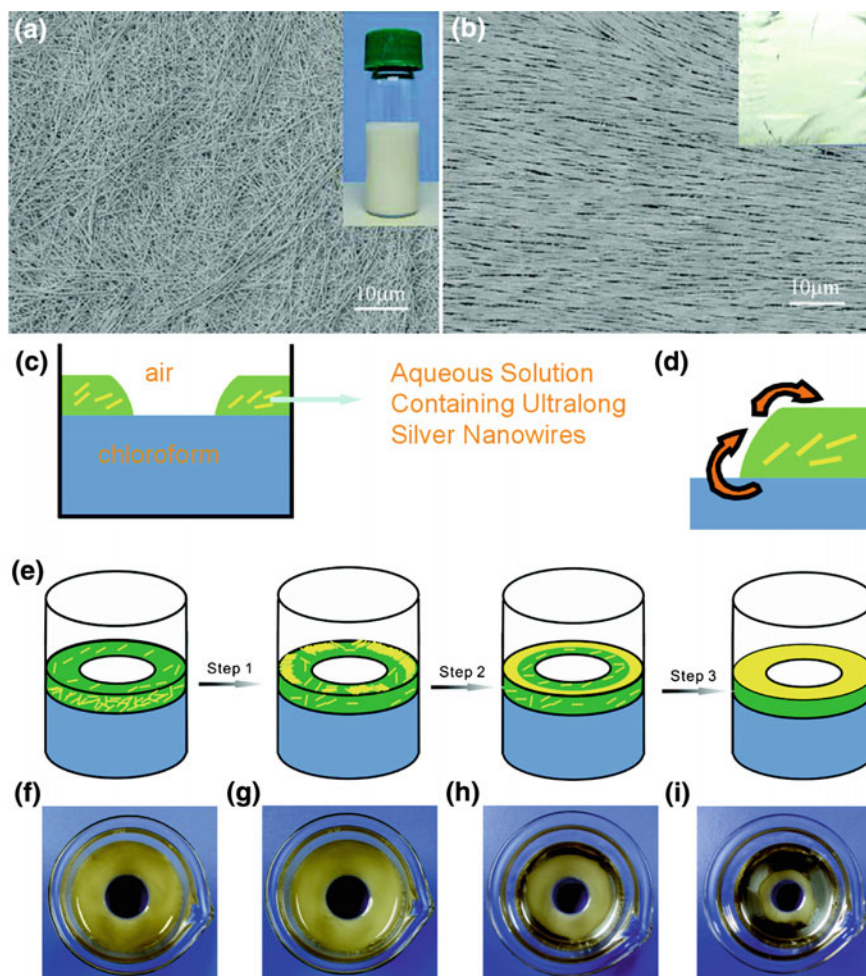


diagram of this approach: (i) self-assembled monolayers (SAMs) of molecules are patterned on substrates with positively-charged regions and neutral regions; (ii) the patterned substrates are dip into the solution of negatively-charged  $V_2O_5$  NWs and (iii) rinsed with deionized water to remove weakly bound NWs; (iv) the NW arrays are fabricated into integrated devices by deposition of electrodes using conventional lithography methods. Figure 4.6b shows the typical absorption behavior of  $V_2O_5$  NWs onto SAM patterns comprised of positively charged cysteamine, negatively charged mercaptohexadecanoic acid (MHA) and neutral 1-octadecanethiol (ODT). A large number of NWs were absorbed on cysteamine regions, while no NW were observed on ODT regions, indicating selective adhesion in the positively charged cysteamine regions. In a subsequent report, the authors studied two complementary methods for assembly of ZnO NWs [33]. In the solution-phase method, ZnO NWs were assembled and aligned selectively onto negatively charged surface patterns in solution. A substrate bias voltage and capillary forces were used to further enhance the adsorption rate and degree of alignment of ZnO NWs, respectively. In the direct-transfer method, a NW film grown on a solid substrate was placed in close proximity to a molecule-patterned substrate, and ultrasonic vibration was applied to transfer directly and align the NWs onto the patterned substrate. Lee et al. [34] used inert surface molecular patterns to direct the adsorption and alignment of NWs on bare surfaces to form device structures without the use of linker molecules. Applying bias voltages to the substrates could further enhance the density of absorbed NWs.

Segmented metal NWs, such as Au/Ni [35], Au/Ni/Au [36], Au/Pd/Au [37] NWs have also been assembled on various solid substrates, including Si,  $SiO_2$ , glass, Au and Al. For example, Lee et al. [37] used DNA hybridization to achieve a highly specific and selective assembly of Au/Pd/Au NWs on pre-patterned Au electrodes. In this method, two complementary single-stranded DNAs modified with thiol tags were adsorbed onto Au electrodes and Au segments of the NWs, enabling the NWs to be assembled across electrodes.

### 4.2.5 Assembly at Interfaces

Interfaces offer a significant opportunity for the organization of nanoscale building block films, based on interfacial ordering effects [3], and served as an important part of the LB assembly described above [21–29]. Building upon these ideas, Shi et al. [38] introduced a three-phase interfacial assembly approach to produce free-standing ordered Ag NW thin films. Figure 4.7a, b show SEM images of disordered and ordered Ag NWs after assembly, respectively. The formation of Ag NW arrays through this three-phase/two-interface approach is illustrated by Fig. 4.7c–e. Figure 4.7f–i shows the corresponding optical photographs of the steps shown in Fig. 4.7e. The three-phases of oil-water-air were formed by dropping aqueous solution of Ag NWs onto the surface of chloroform. Initially, the Ag NWs transferred from the water-oil interface to the water-air interface through the



**Fig. 4.7** **a** SEM image of the disordered Ag NWs. **b** SEM image of the assembly NWs. The insets of **(a)** and **(b)** are optical photographs of Ag NWs dispersed in distilled water and the assembled NWs transferred to a silicon wafer. **c** Cross section of the three-phase interface. **d** Schematic illustration of the movement of the Ag NWs in the first step with the evaporation of the oil phase. **e** Schematic representation of the stages of film formation of the Ag NWs at the three-phase interface. **f–i** Corresponding experimental optical photographs of the steps shown in **(e)**. Reproduced from [38]. Copyright 2010 John Wiley and Sons

oil-water-air interface line, due to the chloroform evaporation. Then, the Ag NWs at the water-air interface self-assembled, initially at the contact line of the beaker wall and the water phase, denoted as the water-air-substrate interface. Finally, the film of the Ag NWs at the water-air-substrate interface grew into a continuous, well-aligned NW film. Later, Liu et al. [39] reported a water-oil interface assembly strategy to fabricate large-area self-assembled nanofilms composed of various

building blocks at room temperature, including nanoparticles, nanocubes, NWs, and nanosheets.

## 4.2.6 Electric/Magnetic Field-Based Methods

### 4.2.6.1 Assembly Using Dielectrophoresis Or Electric Fields

Electric field (E-field)-assisted assembly, including dielectrophoretic (DEP) assembly of NWs suspended in a dielectric medium between two electrodes, offers another promising approach to align NWs, attributed to their highly anisotropic structures and large polarizability [40]. Duan et al. [41] exploited the efficacy of quasi-static electric fields to align and position individual NWs into parallel and crossed arrays (Fig. 4.8a, b). This E-field assembly of NWs between arrays of electrodes (Fig. 4.8c) showed that individual wires could be positioned to bridge pairs of diametrically opposed electrodes and form parallel arrays. In addition, by changing the field direction in sequential steps, layer-by-layer alignment of crossed NW junctions was demonstrated (Fig. 4.8d).

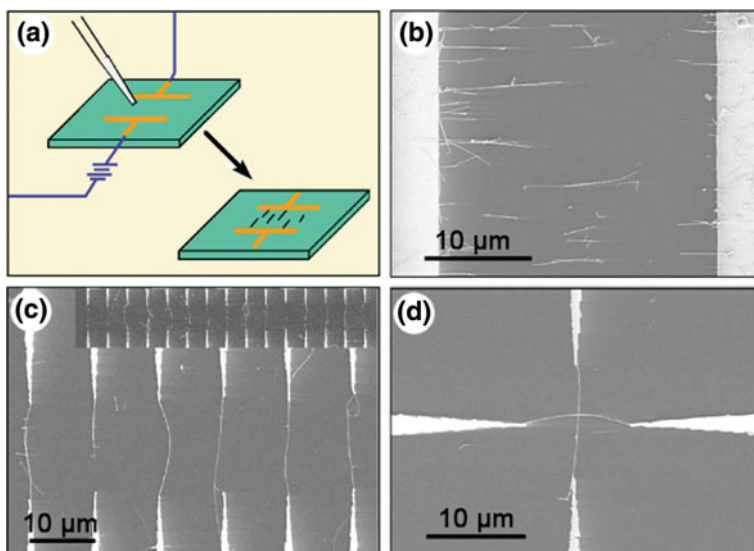


**Fig. 4.8** **a** Schematic view of E-field alignment. **b** Parallel array of NWs aligned between two parallel electrodes. **c** Spatially positioned parallel array of NWs obtained following E-field assembly. The *top inset* shows 15 pairs of parallel electrodes with individual NWs bridging each diametrically opposed electrode pair. **d** Crossed NW junction obtained using layer-by-layer alignment with the E-field applied in orthogonal directions in the two assembly steps. Reproduced from [41]. Copyright 2001 Nature Publishing Group

Significantly, high-yield single-NW integration over centimeter-scale chip areas was achieved via dielectrophoresis combined with fluidic assembly, which introduced additional molecular and capillary forces [42]. This work relied on a precise balance of forces to trap single NWs between electrode pairs, while avoiding trapping two or more NWs (which results in a self-limiting behavior). A colloidal suspension of NWs in a solution of isopropanol and water was directed through a channel over the array of electrode pairs, across each of which a relatively high-frequency voltage was applied. As the NWs flowed past the electrodes in the solution, the dielectrophoretic forces pulled NWs towards the electrodes. Furthermore, electrostatic forces caused the NWs to repel each other and to be attracted to the array surface. By ensuring uniform flow across the electrodes and by fine-tuning flow speed, and the amplitude and frequency of the applied electric field, highly-uniform large-scale assembly of NWs could be obtained [43]. Centimeter-scale high-yield integration of silicon and rhodium NW resonator arrays (over 2000 single-NW resonators) was also demonstrated via a refined electric field-assisted assembly technique with three combined forces, electric-field, capillary and NW lift-off [44].

#### 4.2.6.2 Assembly Using Magnetic Fields

Magnetic fields can also be used to direct the alignment of magnetic NWs suspended within a solution, although demonstrations have been limited to the assembly of NWs composed of ferromagnetic and superparamagnetic materials. Tanase et al. [45] reported the use of magnetic fields to assemble Ni NWs. In viscous solvents, magnetic fields were used to orient the NWs, while in mobile solvents, the NWs formed chains in a head-to-tail configuration when a small magnetic field was applied. Besides parallel NW arrays, hierarchical structures such as cross-junction and T-junction NW networks were also achieved via a sequential changes in the magnetic-field direction [46]. In another study, a low external magnetic field combined with a local dipolar magnetic field allowed assembly of magnetic Ni NWs on Co nanomagnet arrays (the local field) with a  $\sim 100\%$  trapping efficiency [47]. It should be noted that nonmagnetic NWs capped with magnetic ends could also be assembled using a magnetic field, including multi-segmented Ni/Au/Ni, Ni/Bi/Ni [48], Ni/ZnO [49], and Au/polypyrrole/Ni/Au [50] NWs.

#### 4.2.7 PDMS Transfer Method

Printing techniques with elastomeric stamps can be used to transfer NW arrays to a variety of substrates, while retaining good order and orientation. For example, the Rogers group [51] reported using PDMS to transfer top-down fabricated GaAs NW arrays to poly(ethyleneterephthalate) (PET) coated with a thin layer of cured

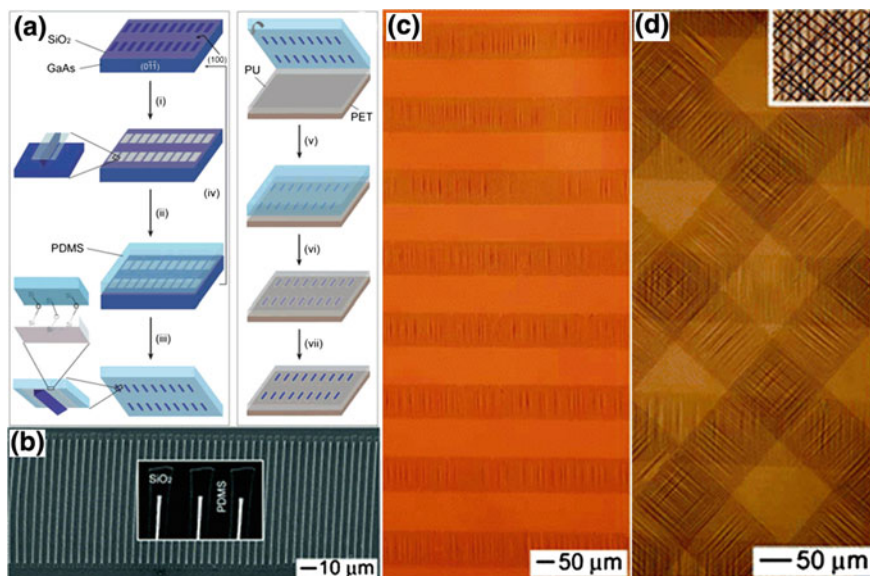


**Fig. 4.9** **a** Schematic illustration of the process of generating and transfer printing GaAs wire arrays onto plastic substrates. **b** SEM image of a GaAs wire array bonded to PDMS via the SiO<sub>2</sub> stripes. **c**, **d** Optical micrographs of GaAs wire arrays on PU/PET sheets with (c) single and (d) triple layers of NWs. Reproduced from [51]. Copyright 2004 American Chemical Society

polyurethane (PU). The whole process is shown schematically in Fig. 4.9a and involves the following key steps: (i) anisotropic chemical etching of a GaAs wafer using a SiO<sub>2</sub> stripe mask produces GaAs NW arrays; (ii) contact between PDMS and SiO<sub>2</sub> leads to the formation of siloxane (Si-O-Si) bonds via a condensation reaction; (iii) peeling the PDMS stamp from the GaAs substrate lifts off the wires; (iv) polishing the remaining GaAs wafer enables a new cycle of wire fabrication and lift-off; (v) contact between a PDMS stamp (with GaAs wires) and liquid film of PU cast on the PET sheet caused the PU to flow and conform to the wires; (vi) curing PU with UV light bonds the wires to the PU and the PU to the PET, and then peeling off the PDMS stamp left the wires embedded in PU; (vii) buffered oxide etching removes the SiO<sub>2</sub> mask. Figure 4.9b–d show images of GaAs wire arrays printed on PDMS and PU/PET substrates. The SEM image taken from GaAs wire arrays bonded to a flat PDMS stamp via the SiO<sub>2</sub> mask layer indicates that the order of wires was preserved (Fig. 4.9b). Optical image collected from a PU/PET substrate with embedded GaAs wires indicate that large-area of wire arrays could be routinely printed on the PU/PET substrate using PDMS transfer approach (Fig. 4.9c). PU/PET substrates with up to three layers of GaAs wire arrays were obtained by repeating the printing process (Fig. 4.9d). Later, the same group [52] used the transferred GaAs arrays to produce metal-semiconductor field-effect transistors. In another report, they used PDMS stamps to transfer different semiconductor nanomaterials, such as CNTs and NWs of GaN, Si, GaAs, onto rigid or

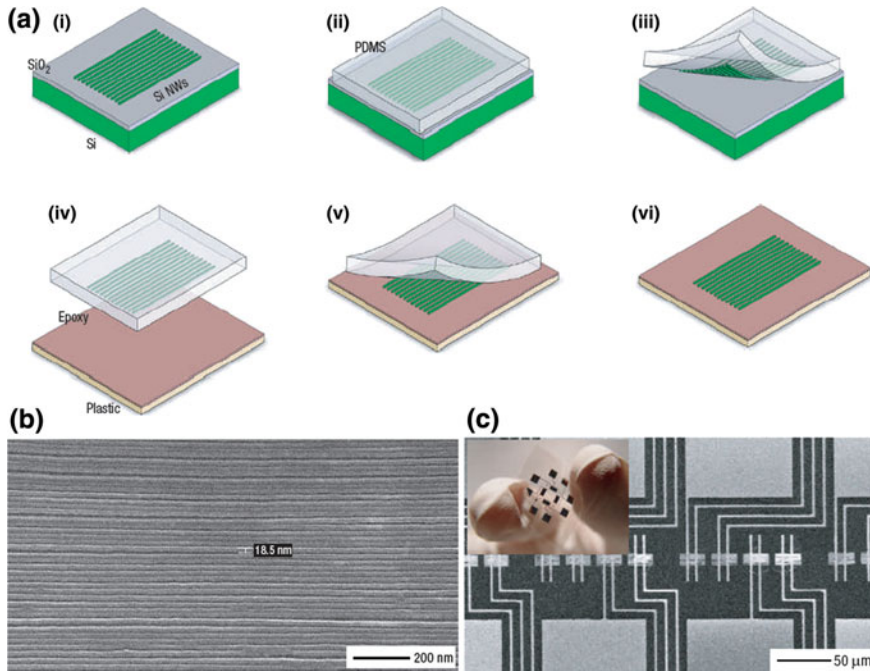


**Fig. 4.10** **a** Illustration of the steps for transfer printing NWs onto plastic substrates. **b** SEM image of the NWs transferred on plastic. **c** An array of NW sensors. Reproduced from [57]. Copyright 2007 Nature Publishing Group

flexible substrates to produce heterogeneously integrated electronic systems [53], similar to work demonstrated previously with small numbers of NW devices [41, 54–56]. As a result, arrays of FETs, thin-film transistors, *n*-channel unipolar inverters were fabricated.

McAlpine et al. [57] demonstrated PDMS transfer of hundreds of pre-aligned SiNWs onto a PET substrate to yield highly ordered films for low-power sensor chips. The process shown in Fig. 4.10a comprised the following steps: (i) SiNWs were fabricated from a standard silicon-on-insulator wafer; (ii) a piece of PDMS was brought into conformal contact with the wafer and (iii) then quickly peeled back to delaminate the ordered NW arrays; (iv) a PET substrate pre-coated with indium tin oxide (ITO) was spin-cast with a 2- $\mu$ m SU-8 resist; (v) the PDMS was conformally contacted with the substrate; (vi) peeling back the PDMS left behind the NWs on plastic. SEM images of the plastic substrate following PDMS transfer revealed that the highly aligned structure of the SiNWs similar to that defined during the initial fabrication (Fig. 4.10b). Subsequently, sensor arrays from the NW-on-plastic films were fabricated (Fig. 4.10c). Later, Lee et al. [58] also reported transfer methods for fabricating NW devices, which broadened the transferred substances to the entire NW devices, and demonstrated that this device level transfer could be carried out not only with PDMS but also using tapes.

### 4.2.8 Printing

NWs prepared by nanocluster catalyzed VLS typically grow vertically from the growth substrate surface, although can have a wide-range of orientational order. For planar growth substrates, Javey et al. [59] developed a contact printing method to prepare patterned NWs transferred directly from a NW growth substrate to a second device substrate. As illustrated in Fig. 4.11a, a NW growth substrate was placed on top of a photolithographically patterned device substrate, and with a gentle applied force the growth substrate was translated in a specific orientation over the device substrate (relative to the pattern) several millimeters. Finally, the growth substrate was removed. Devices and circuits were then fabricated on the printed arrays of NWs using conventional top-down lithography and metallization processes. To build a 3D structure, the NW printing and device fabrication steps were iterated multiple times, along with the deposition of an intervening insulating  $\text{SiO}_2$  buffer layer between adjacent NW layers (Fig. 4.11b). It has also been reported that surface chemical modification of the receiver device substrate can dramatically improve the density of the printed NWs [60]. A structure consisting of 10 layers of Ge/Si multi-NW-FETs was assembled and fabricated on a Si substrate (Fig. 4.11c) [59]. To further demonstrate the versatility of the contact printing process, Takahashi et al. [61] reported a patterned printing of NWs by using fluorinated

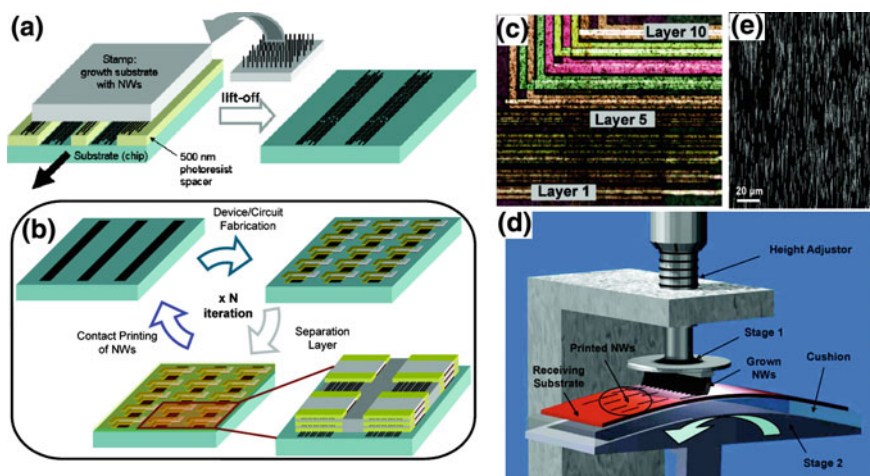


**Fig. 4.11** **a, b** Overview of 3D NW circuit integration. **a** Contact printing of NWs from growth substrate to pre-patterned substrate. **b** Three-dimensional NW circuit is fabricated by the iteration of the contact printing, device fabrication, and separation layer deposition steps. **c** Optical microscope image of 10 layers of Ge/Si NW-FETs. Each device is offset in  $x$  and  $y$  to facilitate imaging. Reproduced from [59]. Copyright 2007 American Chemical Society. **d** Experimental setup for transferring vertically grown ZnO NWs to a flexible substrate to make horizontally aligned ZnO NW arrays with crystallographic alignment. **e** SEM image of the as-transferred horizontal ZnO NWs. Reproduced from [62]. Copyright 2010 American Chemical Society

self-assembled monolayers (SAMs) as the resist layer. By projecting a light pattern on the surface of the SAM resist in an oxygen-rich environment, sticky and non-sticky regions on the surface were directly defined in a single-step process, which enabled the highly specific and patterned transfer of NWs by the printing process, without the need for a subsequent lift-off step.

Recently, Zhu et al. [62] developed a related printing method to transfer vertically aligned NWs onto a receiving substrate to form horizontally aligned arrays. The major components of the transfer setup included two stages (Fig. 4.11d). Stage 1 had a flat surface that faced downward and held the vertically aligned NWs; and stage 2 had a curved surface and held the receiving substrate. The as-transferred NWs are presented in Fig. 4.11e.

In addition, cylindrical growth substrates have been used for differential roll printing (DRP) of NWs have also been demonstrated [63–65]. As shown in Fig. 4.12a, b, the DRP approach was based on the growth of NWs on a cylindrical substrate (roller) via the nanocluster catalyzed VLS process, and the directional aligned transfer of the as-grown NWs from the donor cylinder to a receiver

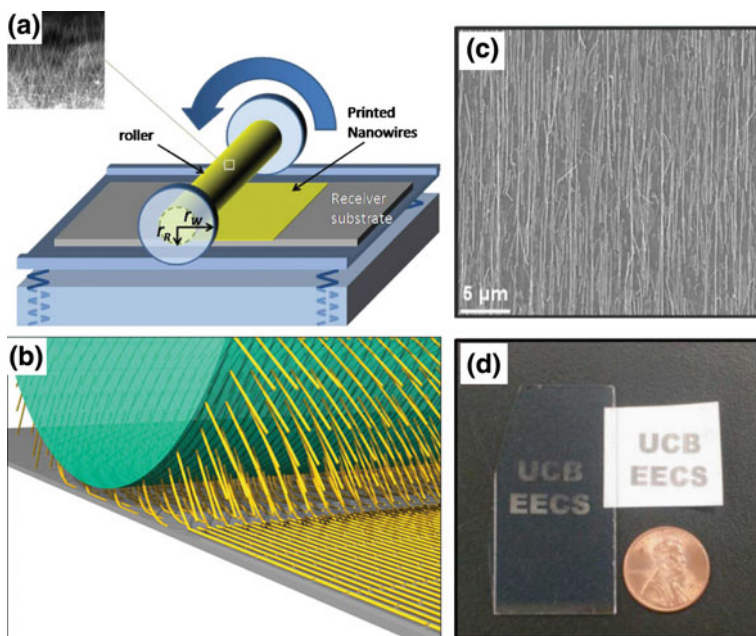


**Fig. 4.12** **a, b** Schematics of NW contact printing involving cylindrical growth (donor) substrates. The SEM images in the insets of **(a)** show that the grown GeNWs are randomly oriented on the growth substrate. The NWs are then aligned and transferred to the receiver substrate by application of a directional shear force, resulting in the printing of NW parallel arrays on the receiver substrate. Images are not to scale. Reproduced from [64]. Copyright 2009 John Wiley and Sons. **c** SEM images of GeNWs printed on a Si/SiO<sub>2</sub> substrate. **d** Large area and aligned arrays of GeNWs printed on glass and photography paper. Reproduced from [63]. Copyright 2007 AIP Publishing LLC



substrate by rolling [63]. This approach minimizes the contact area between the donor and receiver substrates, since the cylindrical donor substrate rolls over the receiver substrate with only a small tangent contact area consisting of fresh NWs at any given time. This is highly beneficial for printing large areas that would otherwise require large planar growth substrates and long contact-sliding distances. In addition, the roller can be repetitively used for the NW growth, which is important for a low-cost roll-to-roll processes. SEM images of the roller printed GeNWs on a Si/SiO<sub>2</sub> substrate show the patterned assembly of well aligned and dense parallel arrays. The DRP process is compatible with a wide range of rigid and flexible substrates, including Si, glass, polymer, and paper (Fig. 4.12d). Similarly, the rolling and transfer printing technologies have been combined to transfer vertically aligned NWs for the fabrication of NW-FETs [65].

### 4.2.9 Nanocombing-Based Assembly

Many assembly methods, even mechanical printing, exhibit alignment limitations due to the fact that forces used to anchor and align NWs coexist in the same substrate (printing) regions; that is, the anchoring force necessary for attachment of NWs to the device substrate can oppose the aligning force and result in less effective orientation control. Hence, improvements in the alignment of NWs during assembly may be achieved by separating the anchoring location of NWs from the aligning region, an approach termed nanocombing [66] in analogy to combing/straightening of hair anchored to the scalp.

There are several essential features of the nanocombing process (Fig. 4.13a). First, anchoring regions with strong NW interactions and aligning regions with weaker NW interactions are lithographically patterned on the target substrate. Second, the NW growth substrate is brought into contact with the target substrate and transferred in the desired direction with a defined applied force and speed. During contact and translation, the protruding NW end first sticks to the anchoring surface. The remaining portion is then pulled over the combing surface, where the aligning force, which is diametrically opposed to the anchoring force, is maximized due to the weak interaction with the combing surface. SEM images of the silicon NW arrays obtained from nanocombing onto a substrate with an array of anchoring regions are displayed in Fig. 4.13b–d. Quantitative analysis of alignment determined from analysis of more than 1600 NWs from arrays over the substrate chip (Fig. 4.13e) showed that  $\sim 98.6\%$  of the combed NWs were aligned to within  $\pm 1^\circ$  of the combing direction. The authors also explored the potential of extending nanocombing to laterally deterministic assembly by defining the x-coordinates of NWs during nanocombing. An SEM image of the devices produced in this manner (Fig. 4.13f) demonstrated a high yield (70 %) of single-NW devices, with the remainder being double-NW (20 %) and open contacts (10 %). This lateral position control, at the single-NW level, can greatly facilitate the efficient hybrid fabrication strategy that combines post-growth assembly by nanocombing with top-down

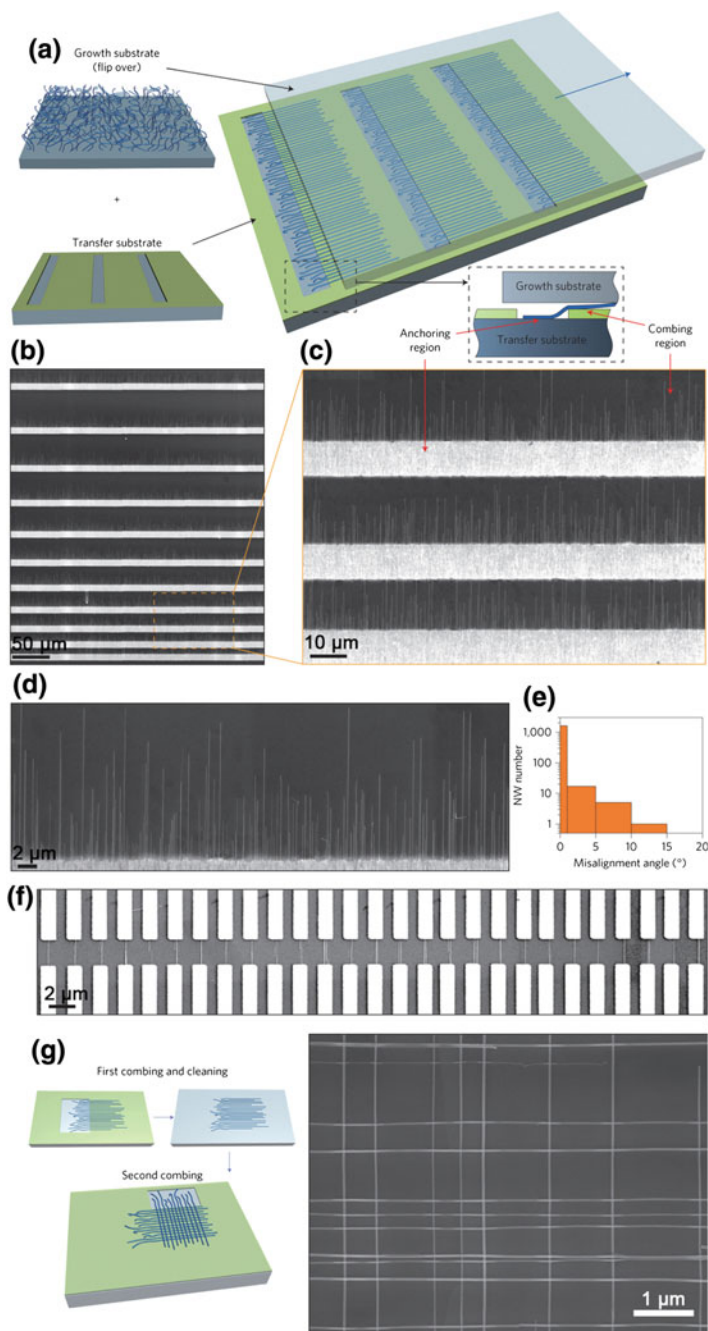


**Fig. 4.13** **a** Schematics of the nanocombing process. **b–d** SEM images of SiNWs on the combing (resist) surface at different magnifications. **e** Angle distribution of the combed NWs obtained from analysis of NW arrays combed over a  $3 \text{ mm} \times 11 \text{ mm}$  chip. **f** SEM image of a periodic SiNW device array made from the combing method. **g** *Left* schematics of the two consecutive combing steps used to define a crossed NW array. *Right* SEM image of a SiNW crossbar array. Reproduced from [66]. Copyright 2013 Nature Publishing Group

processing. The well-defined registration of one edge of the NW arrays produced by nanocombing can also be used to carry out multistep assembly of orthogonal NW crossbar arrays as illustrated in Fig. 4.13g.

## 4.2.10 Other Assembly Methods

### 4.2.10.1 Knocking-Down

The method termed “knocking-down” is based on controlled in-place planarization of vertical NW elements, and was demonstrated with the formation of large-scale ordered NW arrays [6, 67, 68]. The controlled planarization of the NWs was achieved by the use of a roller device. Compared with the contact-printing method, NWs in this method are directly grown on the final device substrate, which is advantageous over transferring the NWs from a “donor” to a device substrate.

### 4.2.10.2 Strain-Release

Strain-release based assembly can align inorganic NWs on stretchable substrates [69]. In this method, a PDMS substrate was pre-stretched to a desired level of strain, and SiNWs on a growth substrate were roughly aligned perpendicular to the stretching direction on the PDMS by contact printing, and then strain in the PDMS was released. Because the initial contact printing of NWs onto the PDMS was less controlled than in the work by Javey et al. [59] described above, the initial alignment rate was only 25 % (skew angle within  $\pm 5^\circ$ ). After releasing the strain, the inter-NW spacing and skew angles between neighboring NWs were reduced, resulting in an alignment rate increase to 53 %. Subsequently, the first (released) PDMS sheet with NWs was then brought into contact with a second pre-strained PDMS substrate to transfer NWs a second time. Releasing the strain of the second PDMS substrate further increased the NW alignment to 88 %. These transfer/release steps can be repeated multiple times as needed to increase the NW alignment and density.

### 4.2.10.3 Assemblies Induced By External Nanostructures

The interaction between NWs and other materials can promote NW alignment. Li et al. [70] studied the co-assembly of graphene oxide (GO) nanosheets and  $\text{Na}_{0.44}\text{MnO}_2$  NWs. With the addition of GO nanosheets to the NW aqueous suspension, concentration enrichment and orientation alignment of NWs at the air-water interface were observed. The mechanism for these observations was proposed to involve hydrogen bonding and ion-dipole interactions, where GO nanosheets adsorbed on the NW surfaces and altered the surface properties. As a

result, the GO-adsorbed NWs became surface active and were enriched at the air-water interface. In addition, the strong van der Waals and hydrophobic interactions that occur between the side chains of oleylamine-coated Au NWs and the sidewalls of CNTs could induce self-assembly of Au NWs along the axes of CNTs [71].

## 4.3 Patterned Growth

### 4.3.1 *Epitaxial Growth from Patterned Nanocluster Catalysts*

The realization of patterned arrays of metal nanocluster catalysts for VLS growth of semiconductor NWs provides an important approach for growth-based organization of NWs [72]. A number of patterning and templating methods have been used to prepare ordered metal nanocluster catalyst arrays on substrate surfaces, including photolithography or EBL, NSL, porous alumina templates, as well as nanoimprint lithography. These methods are distinguished by the effort required and their capability of patterning over large areas, as discussed below.

#### 4.3.1.1 Photolithography Or Electron-Beam Lithography

Photolithography is a standard method to generate patterned arrays, although often with the limited resolution. Phase-shift photolithography can improve the patterning resolution, and was used by Greyson et al. [73]. to define Au nanocluster arrays for the growth of ZnO NWs. In this case, masks containing lines with variable spacing were used twice with rotated orientations, for exposures of positive-tone photoresist. The resulting pattern was transferred by isotropic wet etching into a rather thick gold film, resulting in ordered arrays of Au nano-squares. Kayes et al. [74] deposited Au or Cu catalysts inside of the photolithographically-defined holes etched in the top SiO<sub>2</sub> layer on substrate, followed by the VLS growth of arrays of vertically oriented Si wires (Fig. 4.14a, b). The pattern fidelity depended critically on the presence of the SiO<sub>2</sub> layer, which prevented migration of the metal catalysts on the surface during annealing and in the early stages of NW growth.

A conventional tool for sub-100 nm patterning is EBL, and has been used extensively to prepare Au nanodot arrays for nanocluster catalyzed VLS growth of NWs. For example, Ng et al. [75]. grew patterned ZnO NWs through vapor transport and deposition. Under optimized growth conditions, a single long wire was obtained at each gold site protruding from a group of short rods. Applying the same technique, InP [76] and InAs [77, 78] NW arrays were also fabricated (Fig. 4.14c, d). The advantage of EBL is the exquisite control obtained for the

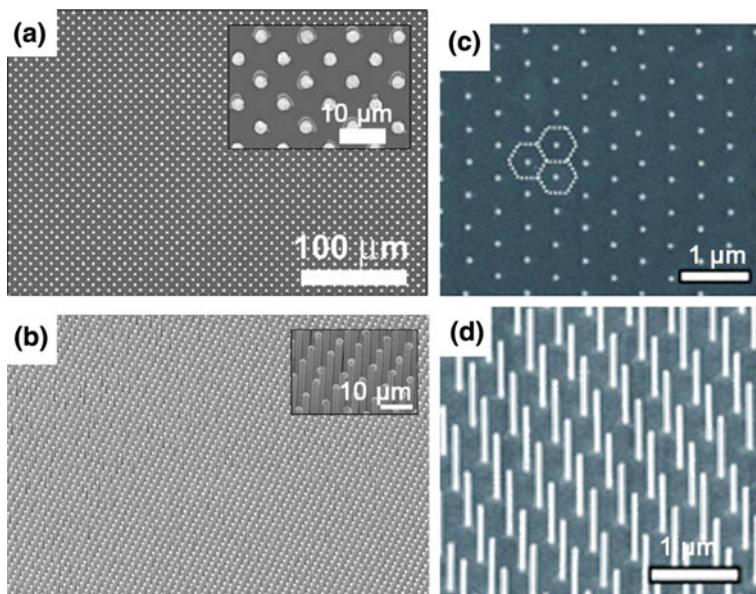


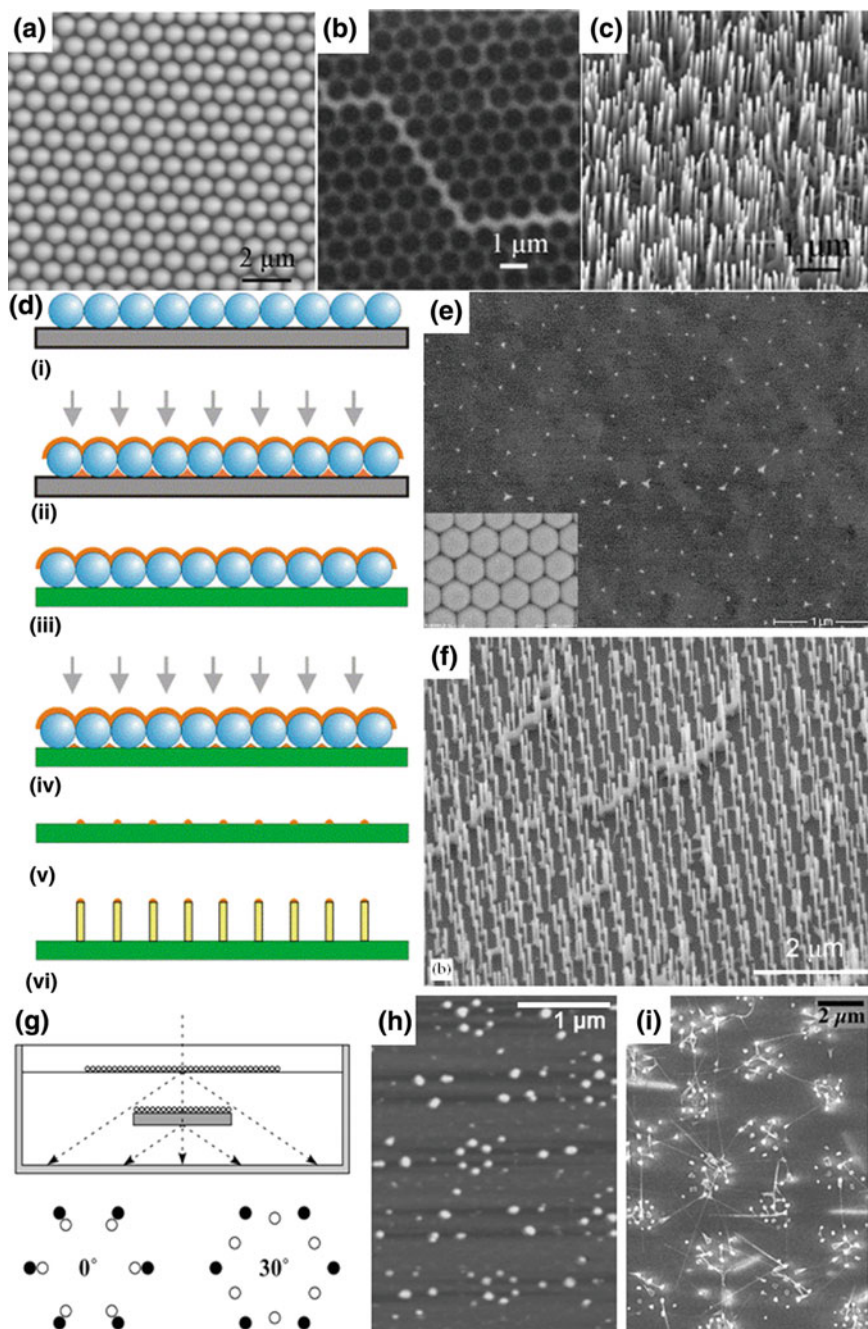
**Fig. 4.14** **a** Au arrays deposited inside of the holes in the etched  $\text{SiO}_2$  layer. *Inset* shows the effect of annealing on Au catalysts, demonstrating the importance of the buffer oxide to preventing migration of the catalyst particles. **b** Au-catalyzed Si wire array over a large ( $>1 \text{ cm}^2$ ) area. Reproduced from [74]. Copyright 2007 AIP Publishing LLC. **c, d** Au particles defined by EBL and subsequently grown InAs NWs, respectively. Reproduced from [77]. Copyright 2004 American Chemical Society

separation of wire sites, while a major drawback is low throughput due to serial (vs. parallel) writing, which can limit applications to large-area patterning.

#### 4.3.1.2 Nanosphere Lithography

Self-assembly of submicron to micron diameter monodispersed spheres into monolayers with a hexagonal close-packed structures is the basis of NSL [79]. Typical materials used for the spheres are polystyrene (PS) and silica, which are commercially available with diameters ranging from some 10 nm to a few micrometers. Using these close-packed sphere monolayers as the mask, the deposited metal islands (i.e., catalyst dots for NW growth) are expected to be triangular, the shadow projection of the mask opening, which is about one fifth of the size of the sphere diameter [80–85]. However, depositing metal nanoparticles within the 1–20 nm size range can be challenging due to the difficulty of self-assembly of small nanospheres into well ordered 2D arrays [86].

As an example, the Wang group [81] prepared self-assembled monolayers of ca. 900 nm PS spheres on a single-crystal  $\text{Al}_2\text{O}_3$  substrate (Fig. 4.15a). Au was



◀ **Fig. 4.15** **a** Self-assembled monolayer of PS spheres, **b** Au particles sputtered onto the PS mask with a honeycomb-like hexagonal pattern and **c** CVD grown ZnO NW arrays. Reproduced from [81]. Copyright 2004 American Chemical Society. **d** Schematics of the NSL process. **e** Au nanodot arrays. *Inset* shows the mask on GaN: monolayer of Au coated hexagonally packed PS nanospheres. **f** ZnO NW arrays obtained using a monolayer of PS spheres as the template. Reproduced from [80]. Copyright 2006 Elsevier. **g** Arrangement of the immersed first monolayer and the floating second monolayer with the schematic diffraction spots from the relative angles of 0° and 30°. **h** AFM image of Ni nanoclusters deposited on a double-layer PS mask with an alignment angle of 10°. **i** SEM image of ZnO NWs grown on Ni nanoclusters with an alignment angle of 7°. Reproduced from [84]. Copyright 2004 American Chemical Society

sputtered onto the PS mask, forming a honeycomb-like hexagonal pattern (Fig. 4.15b), which was subsequently used as the catalysts to grow perpendicular arrays of ZnO NWs with the same pattern (Fig. 4.15c). In this case, the opening/spacing between PS spheres determined the final arrangement and size of the NWs. In addition to the selection of the sphere size, PS spheres can be further tailored through annealing-induced deformation to reduce the opening size [87] or plasma etching to enlarge the spacing [88].

One limitation of the original NSL method is that the spheres can only be assembled on hydrophilic surfaces. In 2006, Fan et al. [80] employed a modified NSL technique for the growth of ZnO NWs on hydrophobic GaN layers using a mask transfer technique. The whole fabrication process is illustrated schematically in Fig. 4.15d: (i) ca. 500 nm PS spheres were spin-coated onto a glass substrate and self-assembled into a monolayer; (ii) a Au film was deposited on the nanospheres, forming a continuous coating of Au on the upper surface of the assembled PS spheres; (iii) the glass substrate coated with Au-coated nanospheres was immersed into water to separate the sphere layers from the substrate, and the resulting membranes were transferred onto the surface of GaN substrates by immersing the latter into the solution and lifting up the substrate together with the gold-coated PS membrane. This first gold layer ensures the connection of PS spheres during transfer and narrows the holes between the spheres; (iv) a second gold layer was thermally evaporated through the membrane mask; (v) the masks were removed, exposing the arrays of gold nanodots on the substrate surface; (vi) synthesis of 63 nm ZnO NWs was carried out via vapor transport with a nanocluster catalyzed VLS mechanism. Figure 4.15e and f show the deposited Au nanodots and ZnO NW arrays.

In the above works [80, 81], the metal clusters deposited by NSL possess a quasi-triangular shape and hexagonal pattern. To overcome this restriction, Ryczynski et al. [84], employed double layer PS self-assembled films and adjusted the relative alignment between these two layers to obtain different patterns in the metal cluster and subsequent NW arrays. Specifically, the first PS mask layer was assembled on a transparent sapphire substrate and a laser pointer was used to determine the mask orientation by the diffraction patterns on the bottom of the preparation dish. Then, a second PS mask was prepared on the water surface and rotated to a desired angle, and then fixed on top of the first PS layer (Fig. 4.15g). After Ni deposition, the double-layer mask results in a triangular array of nearly

spherical particles (Fig. 4.15h), depending on the relative alignment angle between the two PS layers. ZnO NWs in Fig. 4.15i exhibit a good correlation with arrays of Ni clusters.

#### 4.3.1.3 Gold Deposition Masks Based on Porous Alumina

The applications of AAO membranes, with pore diameters in the sub-micrometer range, have been used as masks for Au deposition and subsequent nanocluster catalyzed VLS growth of NWs. For example, Wu et al. [89] and Chik et al. [90] used this method for MBE growth of GaAs NWs on a GaAs (111)B substrates and growth of ZnO NWs on a GaN substrates, respectively. Later, Fan et al. [91] improved this method by using gold nanotube membranes (GNMs), which were formed on AAO templates, as a reduced diameter deposition mask to produce smaller Au nanodot arrays. First, GNMs comprising hexagonally arranged nanotubes were electrochemically fabricated by replicating the master structure of porous AAO. Subsequently, gold nanodot arrays are produced by thermal evaporation of gold using the GNMs as shadow masks. Finally, ZnO NWs were grown on GaN(0001)/Si(111) layers directed by the catalytic gold nanodots.

#### 4.3.1.4 Nanoimprint Lithography

Nanoimprint lithography (NIL) is another important technique for producing nanoscale patterns, as it is capable of producing structures comparable to or even smaller than those of EBL, but at lower cost and with greater efficiency [92, 93]. NIL generally consists of two steps: imprinting and pattern-transfer (Fig. 4.16a). In the imprinting step, a mold with nanostructures on its surface is used to deform a thin resist film or an active material deposited on a substrate. In the pattern-transfer step, an anisotropic etching process such as reactive ion etching (RIE) is used to remove the residual resist in the compressed area, transferring the thickness-contrast pattern created by the imprint into the entire resist. NIL can be used to pattern metal-catalyst dots for subsequent growth of NW arrays [94–96]. As an example, Hochbaum et al. [94] achieved the confinement of vertical SiNW growth in selected regions by patterned colloid deposition on the substrate. The schematic in Fig. 4.16b highlights several key points as follows: (i) a PMDS stamp is made using a photoresist master of 2  $\mu\text{m}$  lines with 2  $\mu\text{m}$  separations, and the pattern was transferred to the substrate; (ii) the stamp is “inked” with poly-*L*-lysine solution; (iii) the polymer pattern is transferred to a Si wafer by placing the stamp on the substrate and heating at 70 °C for 5 min; (iv) the patterned substrate is immersed in a solution containing 50 nm Au nanoparticles, such that Au only adheres to the patterned polyelectrolyte; (v) NWs are synthesized on the substrates by standard nanocluster catalyzed VLS method. Subsequent images of the growth substrate (Fig. 4.16c) showed that growth was strictly confined to the regions where poly-*L*-lysine was patterned.



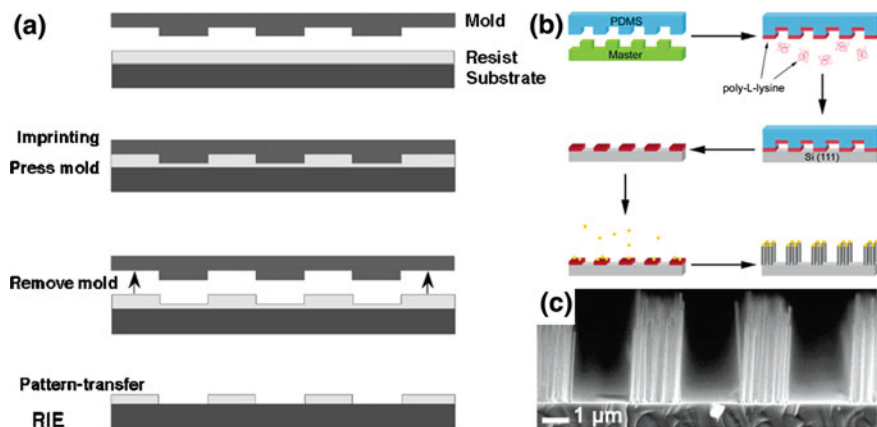


**Fig. 4.16** **a** Schematic illustration of the NIL process. Reproduced from [93]. Copyright 2001 Cambridge University Press. **b** Schematic of PDMS patterning of Au colloids. **c** Cross-sectional SEM image of PDMS patterned SiNW growth. Reproduced from [94]. Copyright 2005 American Chemical Society

### 4.3.2 Substrate-Step-Directed Growth

Although the post-growth assembly methods described previously yield relatively well-aligned arrays on a variety of surfaces on a wafer-scale size, their alignments are subject to thermal and dynamic fluctuations. The assembled NWs are usually not much longer than 10 μm and there is often limited control over their crystallographic orientation, although these challenges were overcome in nanocombing where NWs with up to millimeter lengths have been aligned to within less than a degree variation of designed directions [66]. Another interesting solution to these challenges demonstrated by the Joselevich group [97–100] involves nanocluster catalyzed VLS growth of up to millimeter-long, horizontal NWs orientations aligned with natural step edges found on sapphire substrates.

In one demonstration, the growth directions, crystallographic orientation, and faceting of GaN NWs varied with each surface orientation, as determined by their epitaxial relationship with the substrate, as well as by a graphoepitaxial effect that guided their growth along surface steps and grooves. Guided growth of horizontally aligned NWs (Fig. 4.17a, right) can overcome the limitations of post-growth assembly by combining synthesis and assembly in a single step, although it does limit versatility possible with multi-step bottom-up assembly. Three general modes of guided VLS growth of horizontal NWs were postulated, depending on the substrate morphology (Fig. 4.17b, c). First, epitaxial growth along specific lattice directions, driven by minimization of interfacial energy and strain; second, graphoepitaxial growth along L-shaped nanosteps spontaneously formed upon annealing a miscut substrate, driven by maximization of the interface area between the substrate and the NW or catalyst; and third, graphoepitaxial growth along V-shaped nanogrooves

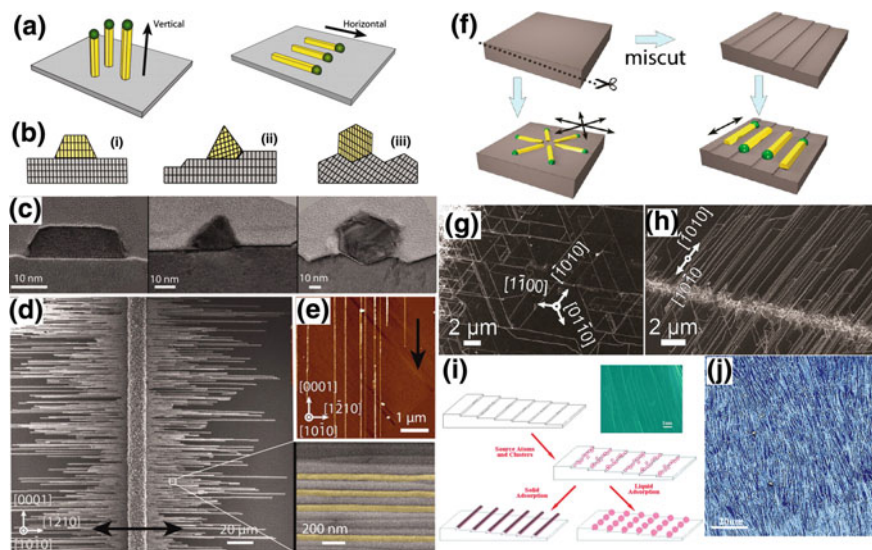


**Fig. 4.17** **a** Schematic view of guided VLS growth (*right*) versus conventional VLS growth (*left*). **b** Three postulated modes of guided VLS growth. **c** Experimental realization of (**b**) for GaN NWs on different planes of sapphire (cross-sectional TEM images). **d** Perfectly aligned GaN NWs grown on annealed plane sapphire. **e** AFM image of unidirectional GaN NWs grown on nonannealed M-plane sapphire. Reproduced from [97]. Copyright 2011 the American Association for the Advancement of Science. **f** Graphoepitaxial effect on the guided growth of horizontal ZnO NWs on (0001) SiC. **g, h** Patterned growth of GaN NWs from a catalyst island on (0001) plane of SiC. Reproduced from [99]. Copyright 2013 American Chemical Society. **i** An illustration of the assembly mechanism of the horizontal NW alignment and nanocluster alignment. **j** SEM image of the horizontal alignment of  $\text{Al}_4\text{C}_3$  NWs. Reproduced from [101]. Copyright 2013 Royal Society of Chemistry

spontaneously formed upon annealing an unstable low-index surface, driven similarly to the second growth mode. Growth from catalyst stripes on atomically flat plane sapphire yielded horizontally aligned GaN NWs longer than 1 mm. The improved alignment was attributed to the graphoepitaxial effect (Fig. 4.17d, e). Later, the authors demonstrated the guided growth of horizontal GaN NWs on both singular (i.e., perfectly cut along a low-index crystallographic plane) and vicinal (i.e., cut with a slight tilt with respect to a low-index crystallographic plane) SiC substrates [99] (Fig. 4.17f–h). The GaN NWs grown on flat (0001) SiC substrates were guided by lattice planes, resulting in a triangular network of NWs (Fig. 4.17g), while the NWs grown on vicinal SiC substrates grew only in two directions parallel to the surface atomic steps (Fig. 4.17h). In addition, it was demonstrated the guided growth for the parallel production of hundreds of independently addressable single-NW field-effect transistors, without the need for post-growth assembly [100].

Due to the requirement of lattice matching between NWs and substrates, the aforementioned approach developed by the Joselevich group could only be applied to limited materials. Later, Sun et al. [101] achieved step-edge induced ordered

growth suitable for non-epitaxial materials using highly-oriented pyrolytic graphite. The single crystal graphite was mechanically exfoliated into thin layers, producing regular step edges as defects. Using Al sheets and  $C_{60}$  powder as sources in a furnace heated to 1310 °C,  $Al_4C_3$  clusters nucleated preferentially at the step-edges to achieve minimized free energy and assembled into a NW, as illustrated in Fig. 4.17i, j. One major limitation of this method is the NWs are polycrystalline, due to the formation of many crystal seeds in a single NW.

## 4.4 Future Directions and Challenges

The rational design and synthesis of semiconductor NWs offer the potential to realize unprecedented structural and functional complexity in building blocks. However, to utilize these building blocks for nanoscale devices through integrated systems, requires controlled and scalable assembly of NWs on either rigid or flexible substrates, where precise control of NW density, orientation, spacing and placement is realized.

In this chapter, we have summarized recent advances in large-scale NW assembly and hierarchical organization with two general approaches. First, organization of pre-grown NWs onto target substrates in one or more independent steps, where distinct NW building blocks can be used in each assembly step, and second, the direct growth of aligned NWs on substrates were discussed. In the first area focused on post-growth assembly methods, we discussed a variety of methods, including flow-assisted alignment, the Langmuir–Blodgett technique, blown bubble methods, chemical binding and electrostatic interactions for assembly, interface-induced assembly, electric/magnetic field-assisted alignment, PDMS based transfer, contact and roll-based printing techniques, and nanocombing. In the second major section, we also introduced methods for direct growth of aligned NW arrays, including epitaxial growth from nanocluster catalyst arrays patterned by different lithography methods and substrate-step-directed growth. Advantages as well as limitations of different methods have been discussed, while at the same time we have highlighted key achievements in organizing individual NWs into large-scale assemblies that have shown substantial potential to realize semiconductor NW-based functional device arrays and nanosystems relevant to many areas of science and technology. These latter applications and their functional properties will be described in subsequent chapters.

## References

1. Y.-Z. Long, M. Yu, B. Sun, C.-Z. Gu, Z. Fan, Recent advances in large-scale assembly of semiconducting inorganic nanowires and nanofibers for electronics, sensors and photovoltaics. *Chem. Soc. Rev.* **41**(12), 4560–4580 (2012)

2. X. Liu, Y.-Z. Long, L. Liao, X. Duan, Z. Fan, Large-scale integration of semiconductor nanowires for high-performance flexible electronics. *ACS Nano* **6**(3), 1888–1900 (2012)
3. J.-W. Liu, H.-W. Liang, S.-H. Yu, Macroscopic-scale assembled nanowire thin films and their functionalities. *Chem. Rev.* **112**(8), 4770–4799 (2012)
4. B. Su, Y. Wu, L. Jiang, The art of aligning one-dimensional (1D) nanostructures. *Chem. Soc. Rev.* **41**(23), 7832–7856 (2012)
5. M.C. Wang, B.D. Gates, Directed assembly of nanowires. *Mater. Today* **12**(5), 34–43 (2009)
6. M. Kwiat, S. Cohen, A. Pevzner, F. Patolsky, Large-scale ordered 1D-nanomaterials arrays: assembly or not? *Nano Today* **8**, 677–694 (2013)
7. H.A. Stone, A.D. Stroock, A. Ajdari, Engineering flows in small devices: microfluidics toward a lab-on-a-chip. *Annu. Rev. Fluid Mech.* **36**, 381–411 (2004)
8. G.M. Whitesides, The origins and the future of microfluidics. *Nature* **442**(7101), 368–373 (2006)
9. B. Messer, J.H. Song, P. Yang, Microchannel networks for nanowire patterning. *J. Am. Chem. Soc.* **122**(41), 10232–10233 (2000)
10. Y. Huang, X. Duan, Q. Wei, C.M. Lieber, Directed assembly of one-dimensional nanostructures into functional networks. *Science* **291**(5504), 630–633 (2001)
11. Y. Huang, C.M. Lieber, Integrated nanoscale electronics and optoelectronics: exploring nanoscale science and technology through semiconductor nanowires. *Pure Appl. Chem.* **76**(12), 2051–2068 (2004)
12. S. Yan, L. Lu, H. Meng, N. Huang, Z. Xiao, Scalable alignment and transfer of nanowires based on oriented polymer nanofibers. *Nanotechnology* **21**(9), 095303 (2010)
13. W.-Z. Li, W. Wei, J.-Y. Chen, J.-X. He, S.-N. Xue, J. Zhang, X. Liu, X. Li, Y. Fu, Y.-H. Jiao, Stirring-assisted assembly of nanowires at liquid–solid interfaces. *Nanotechnology* **24**(10), 105302 (2013)
14. X. Zhou, Y. Zhou, J.C. Ku, C. Zhang, C.A. Mirkin, Capillary force-driven, large-area alignment of multi-segmented nanowires. *ACS Nano* **8**(2), 1511–1516 (2014)
15. C. Yan, T. Zhang, P.S. Lee, Flow assisted synthesis of highly ordered silica nanowire arrays. *Appl. Phys. A* **94**(4), 763–766 (2009)
16. F. Patolsky, G. Zheng, C.M. Lieber, Fabrication of silicon nanowire devices for ultrasensitive, label-free, real-time detection of biological and chemical species. *Nat. Protoc.* **1**(4), 1711–1724 (2006)
17. G. Roberts, *Langmuir-Blodgett Films* (Springer Science & Business Media, New York, 1990)
18. P. Yang, F. Kim, Langmuir-Blodgett assembly of one-dimensional nanostructures. *ChemPhysChem* **3**(6), 503–506 (2002)
19. A.R. Tao, J. Huang, P. Yang, Langmuir-Blodgett assembly of nanocrystals and nanowires. *Acc. Chem. Res.* **41**(12), 1662–1673 (2008)
20. D. Whang, S. Jin, C.M. Lieber, Large-scale hierarchical organization of nanowires for functional nanosystems. *Jpn. J. Appl. Phys.* **43**(7S), 4465 (2004)
21. F. Kim, S. Kwan, J. Akana, P. Yang, Langmuir-Blodgett nanorod assembly. *J. Am. Chem. Soc.* **123**(18), 4360–4361 (2001)
22. S. Kwan, F. Kim, J. Akana, P. Yang, Synthesis and assembly of BaWO<sub>4</sub> nanorods. *Chem. Commun.* **5**, 447–448 (2001)
23. A. Tao, F. Kim, C. Hess, J. Goldberger, R. He, Y. Sun, Y. Xia, P. Yang, Langmuir-Blodgett silver nanowire monolayers for molecular sensing using surface-enhanced Raman spectroscopy. *Nano Lett.* **3**(9), 1229–1233 (2003)
24. D. Whang, S. Jin, Y. Wu, C.M. Lieber, Large-scale hierarchical organization of nanowire arrays for integrated nanosystems. *Nano Lett.* **3**(9), 1255–1259 (2003)
25. S. Acharya, A.B. Panda, N. Belman, S. Efrima, Y. Golan, A semiconductor-nanowire assembly of ultrahigh junction density by the Langmuir-Blodgett technique. *Adv. Mater.* **18**(2), 210–213 (2006)

26. J. Park, G. Shin, J.S. Ha, Controlling orientation of  $V_2O_5$  nanowires within micropatterns via microcontact printing combined with the gluing Langmuir-Blodgett technique. *Nanotechnology* **19**(39), 395303 (2008)
27. J.-W. Liu, J.-H. Zhu, C.-L. Zhang, H.-W. Liang, S.-H. Yu, Mesostuctured assemblies of ultrathin superlong tellurium nanowires and their photoconductivity. *J. Am. Chem. Soc.* **132** (26), 8945–8952 (2010)
28. D. Whang, S. Jin, C.M. Lieber, Nanolithography using hierarchically assembled nanowire masks. *Nano Lett.* **3**(7), 951–954 (2003)
29. S. Jin, D. Whang, M.C. McAlpine, R.S. Friedman, Y. Wu, C.M. Lieber, Scalable interconnection and integration of nanowire devices without registration. *Nano Lett.* **4**(5), 915–919 (2004)
30. G. Yu, A. Cao, C.M. Lieber, Large-area blown bubble films of aligned nanowires and carbon nanotubes. *Nat. Nanotechnol.* **2**(6), 372–377 (2007)
31. G. Yu, X. Li, C.M. Lieber, A. Cao, Nanomaterial-incorporated blown bubble films for large-area, aligned nanostructures. *J. Mater. Chem.* **18**(7), 728–734 (2008)
32. S. Myung, M. Lee, G.T. Kim, J.S. Ha, S. Hong, Large-scale “surface-programmed assembly” of pristine vanadium oxide nanowire-based devices. *Adv. Mater.* **17**(19), 2361–2364 (2005)
33. J. Kang, S. Myung, B. Kim, D. Oh, G.T. Kim, S. Hong, Massive assembly of ZnO nanowire-based integrated devices. *Nanotechnology* **19**(9), 095303 (2008)
34. M. Lee, J. Im, B. Lee, S. Myung, J. Kang, L. Huang, Y.-K. Kwon, S. Hong, Linker-free directed assembly of high-performance integrated devices based on nanotubes and nanowires. *Nat. Nanotechnol.* **1**(1), 66–71 (2006)
35. A.K. Salem, J. Chao, K.W. Leong, P.C. Searson, Receptor-mediated self-assembly of multi-component magnetic nanowires. *Adv. Mater.* **16**(3), 268–271 (2004)
36. M. Chen, P.C. Searson, The dynamics of nanowire self-assembly. *Adv. Mater.* **17**(22), 2765–2768 (2005)
37. J. Lee, A.A. Wang, Y. Rheem, B. Yoo, A. Mulchandani, W. Chen, N.V. Myung, DNA assisted assembly of multisegmented nanowires. *Electroanalysis* **19**(22), 2287–2293 (2007)
38. H.-Y. Shi, B. Hu, X.-C. Yu, R.-L. Zhao, X.-F. Ren, S.-L. Liu, J.-W. Liu, M. Feng, A.-W. Xu, S.-H. Yu, Ordering of disordered nanowires: spontaneous formation of highly aligned, ultralong Ag nanowire films at oil–water–air interface. *Adv. Funct. Mater.* **20**(6), 958–964 (2010)
39. J.-W. Liu, S.-Y. Zhang, H. Qi, W.-C. Wen, S.-H. Yu, A general strategy for self-assembly of nanosized building blocks on liquid/liquid interfaces. *Small* **8**(15), 2412–2420 (2012)
40. P.A. Smith, C.D. Nordquist, T.N. Jackson, T.S. Mayer, B.R. Martin, J. Mbindyo, T.E. Mallouk, Electric-field assisted assembly and alignment of metallic nanowires. *Appl. Phys. Lett.* **77**(9), 1399–1401 (2000)
41. X. Duan, Y. Huang, Y. Cui, J. Wang, C.M. Lieber, Indium phosphide nanowires as building blocks for nanoscale electronic and optoelectronic devices. *Nature* **409**(6816), 66–69 (2001)
42. E.M. Freer, O. Grachev, X. Duan, S. Martin, D.P. Stumbo, High-yield self-limiting single-nanowire assembly with dielectrophoresis. *Nat. Nanotechnol.* **5**(7), 525–530 (2010)
43. B.D. Gates, Self-assembly: nanowires find their place. *Nat. Nanotechnol.* **5**(7), 484–485 (2010)
44. M. Li, R.B. Bhiladvala, T.J. Morrow, J.A. Sioss, K.-K. Lew, J.M. Redwing, C.D. Keating, T. S. Mayer, Bottom-up assembly of large-area nanowire resonator arrays. *Nat. Nanotechnol.* **3** (2), 88–92 (2008)
45. M. Tanase, L.A. Bauer, A. Hultgren, D.M. Silevitch, L. Sun, D.H. Reich, P.C. Searson, G. J. Meyer, Magnetic alignment of fluorescent nanowires. *Nano Lett.* **1**(3), 155–158 (2001)
46. C.M. Hangarter, Y. Rheem, B. Yoo, E.-H. Yang, N.V. Myung, Hierarchical magnetic assembly of nanowires. *Nanotechnology* **18**(20), 205305 (2007)
47. M. Liu, J. Lagdani, H. Imrane, C. Pettiford, J. Lou, S. Yoon, V.G. Harris, C. Vittoria, N.X. Sun, Self-assembled magnetic nanowire arrays. *Appl. Phys. Lett.* **90**(10), 103105 (2007)
48. C.M. Hangarter, N.V. Myung, Magnetic alignment of nanowires. *Chem. Mat.* **17**(6), 1320–1324 (2005)

49. S.-W. Lee, M.-C. Jeong, J.-M. Myoung, G.-S. Chae, I.-J. Chung, Magnetic alignment of ZnO nanowires for optoelectronic device applications. *Appl. Phys. Lett.* **90**(13), 133115 (2007)
50. M.A. Bangar, C.M. Hangarter, B. Yoo, Y. Rheem, W. Chen, A. Mulchandani, N.V. Myung, Magnetically assembled multisegmented nanowires and their applications. *Electroanal.* **21** (1), 61–67 (2009)
51. Y. Sun, J.A. Rogers, Fabricating semiconductor nano/microwires and transfer printing ordered arrays of them onto plastic substrates. *Nano Lett.* **4**(10), 1953–1959 (2004)
52. Y. Sun, S. Kim, I. Adesida, J.A. Rogers, Bendable GaAs metal-semiconductor field-effect transistors formed with printed GaAs wire arrays on plastic substrates. *Appl. Phys. Lett.* **87** (8), 083501 (2005)
53. J.-H. Ahn, H.-S. Kim, K.J. Lee, S. Jeon, S.J. Kang, Y. Sun, R.G. Nuzzo, J.A. Rogers, Heterogeneous three-dimensional electronics by use of printed semiconductor nanomaterials. *Science* **314**(5806), 1754–1757 (2006)
54. Y. Huang, X. Duan, Y. Cui, L.J. Lauhon, K.-H. Kim, C.M. Lieber, Logic gates and computation from assembled nanowire building blocks. *Science* **294**(5545), 1313–1317 (2001)
55. Y. Cui, C.M. Lieber, Functional nanoscale electronic devices assembled using silicon nanowire building blocks. *Science* **291**(5505), 851–853 (2001)
56. Y. Huang, X. Duan, Y. Cui, C.M. Lieber, Gallium nitride nanowire nanodevices. *Nano Lett.* **2**(2), 101–104 (2002)
57. M.C. McAlpine, H. Ahmad, D. Wang, J.R. Heath, Highly ordered nanowire arrays on plastic substrates for ultrasensitive flexible chemical sensors. *Nat. Mater.* **6**(5), 379–384 (2007)
58. C.H. Lee, D.R. Kim, X. Zheng, Fabricating nanowire devices on diverse substrates by simple transfer-printing methods. *Proc. Natl. Acad. Sci. U.S.A.* **107**(22), 9950–9955 (2010)
59. A. Javey, S. Nam, R.S. Friedman, H. Yan, C.M. Lieber, Layer-by-layer assembly of nanowires for three-dimensional, multifunctional electronics. *Nano Lett.* **7**(3), 773–777 (2007)
60. Z. Fan, J.C. Ho, Z.A. Jacobson, R. Yerushalmi, R.L. Alley, H. Razavi, A. Javey, Wafer-scale assembly of highly ordered semiconductor nanowire arrays by contact printing. *Nano Lett.* **8** (1), 20–25 (2008)
61. T. Takahashi, K. Takei, J.C. Ho, Y.-L. Chueh, Z. Fan, A. Javey, Monolayer resist for patterned contact printing of aligned nanowire arrays. *J. Am. Chem. Soc.* **131**(6), 2102–2103 (2009)
62. G. Zhu, R. Yang, S. Wang, Z.L. Wang, Flexible high-output nanogenerator based on lateral ZnO nanowire array. *Nano Lett.* **10**(8), 3151–3155 (2010)
63. R. Yerushalmi, Z.A. Jacobson, J.C. Ho, Z. Fan, A. Javey, Large scale, highly ordered assembly of nanowire parallel arrays by differential roll printing. *Appl. Phys. Lett.* **91**(20), 203104 (2007)
64. Z. Fan, J.C. Ho, T. Takahashi, R. Yerushalmi, K. Takei, A.C. Ford, Y.L. Chueh, A. Javey, Toward the development of printable nanowire electronics and sensors. *Adv. Mater.* **21**(37), 3730–3743 (2009)
65. Y.-K. Chang, F.C.-N. Hong, The fabrication of ZnO nanowire field-effect transistors by roll-transfer printing. *Nanotechnology* **20**(19), 195302 (2009)
66. J. Yao, H. Yan, C.M. Lieber, A nanoscale combing technique for the large-scale assembly of highly aligned nanowires. *Nat. Nanotechnol.* **8**(5), 329–335 (2013)
67. A. Pevzner, Y. Engel, R. Elnathan, T. Ducobni, M. Ben-Ishai, K. Reddy, N. Shpaisman, A. Tsukernik, M. Oksman, F. Patolsky, Knocking down highly-ordered large-scale nanowire arrays. *Nano Lett.* **10**(4), 1202–1208 (2010)
68. H. Song, M.H. Lee, Combing non-epitaxially grown nanowires for large-area electronic devices. *Nanotechnology* **24**(28), 285302 (2013)
69. F. Xu, J.W. Durham III, B.J. Wiley, Y. Zhu, Strain-release assembly of nanowires on stretchable substrates. *ACS Nano* **5**(2), 1556–1563 (2011)
70. Y. Li, Y. Wu, Coassembly of graphene oxide and nanowires for large-area nanowire alignment. *J. Am. Chem. Soc.* **131**(16), 5851–5857 (2009)

71. W. Yang, L. Qu, R. Zheng, Z. Liu, K.R. Ratinac, L. Shen, D. Yu, L. Yang, C. J. Barrow, S., P. Ringer, Self-assembly of gold nanowires along carbon nanotubes for ultrahigh-aspect-ratio hybrids. *Chem. Mat.* **23**(11), 2760–2765 (2011)
72. H.J. Fan, P. Werner, M. Zacharias, Semiconductor nanowires: from self-organization to patterned growth. *Small* **2**(6), 700–717 (2006)
73. E.C. Greyson, Y. Babayan, T.W. Odom, Directed growth of ordered arrays of small-diameter ZnO nanowires. *Adv. Mater.* **16**(15), 1348–1352 (2004)
74. B.M. Kayes, M.A. Filler, M.C. Putnam, M.D. Kelzenberg, N.S. Lewis, H.A. Atwater, Growth of vertically aligned Si wire arrays over large areas ( $>1\text{ cm}^2$ ) with Au and Cu catalysts. *Appl. Phys. Lett.* **91**(10), 103110 (2007)
75. H.T. Ng, J. Han, T. Yamada, P. Nguyen, Y.P. Chen, M. Meyyappan, Single crystal nanowire vertical surround-gate field-effect transistor. *Nano Lett.* **4**(7), 1247–1252 (2004)
76. T. Mårtensson, M. Borgström, W. Seifert, B. Ohlsson, L. Samuelson, Fabrication of individually seeded nanowire arrays by vapour-liquid-solid growth. *Nanotechnology* **14**(12), 1255 (2003)
77. L.E. Jensen, M.T. Björk, S. Jeppesen, A.I. Persson, B.J. Ohlsson, L. Samuelson, Role of surface diffusion in chemical beam epitaxy of InAs nanowires. *Nano Lett.* **4**(10), 1961–1964 (2004)
78. A. Persson, L. Fröberg, L. Samuelson, H. Linke, The fabrication of dense and uniform InAs nanowire arrays. *Nanotechnology* **20**(22), 225304 (2009)
79. A. Kosiorek, W. Kandulski, P. Chudzinski, K. Kempa, M. Giersig, Shadow nanosphere lithography: simulation and experiment. *Nano Lett.* **4**(7), 1359–1363 (2004)
80. H.J. Fan, B. Fuhrmann, R. Scholz, F. Syrowatka, A. Dadgar, A. Krost, M. Zacharias, Well-ordered ZnO nanowire arrays on GaN substrate fabricated via nanosphere lithography. *J. Cryst. Growth* **287**(1), 34–38 (2006)
81. X. Wang, C.J. Summers, Z.L. Wang, Large-scale hexagonal-patterned growth of aligned ZnO nanorods for nano-optoelectronics and nanosensor arrays. *Nano Lett.* **4**(3), 423–426 (2004)
82. B. Fuhrmann, H.S. Leipner, H.-R. Hoeche, L. Schubert, P. Werner, U. Gösele, Ordered arrays of silicon nanowires produced by nanosphere lithography and molecular beam epitaxy. *Nano Lett.* **5**(12), 2524–2527 (2005)
83. D. Liu, Y. Xiang, Q. Liao, J. Zhang, X. Wu, Z. Zhang, L. Liu, W. Ma, J. Shen, W. Zhou, A simple route to scalable fabrication of perfectly ordered ZnO nanorod arrays. *Nanotechnology* **18**(40), 405303 (2007)
84. J. Rybczynski, D. Banerjee, A. Kosiorek, M. Giersig, Z. Ren, Formation of super arrays of periodic nanoparticles and aligned ZnO nanorods-simulation and experiments. *Nano Lett.* **4**(10), 2037–2040 (2004)
85. L. Li, T.Y. Zhai, H.B. Zeng, X.S. Fang, Y. Bando, D. Golberg, Polystyrene sphere-assisted one-dimensional nanostructure arrays: synthesis and applications. *J. Mater. Chem.* **21**(1), 40–56 (2011)
86. Y. Song, Controlled fabrication of noble metal nanomaterials via nanosphere lithography and their optical properties. In ed. by B. Cui, *Recent Advances in Nanofabrication Techniques and Applications*, InTech: Croatia (2011)
87. A. Kosiorek, W. Kandulski, H. Glaczynska, M. Giersig, Fabrication of nanoscale rings, dots, and rods by combining shadow nanosphere lithography and annealed polystyrene nanosphere masks. *Small* **1**(4), 439–444 (2005)
88. A. Valsesia, T. Mezzani, F. Bretagnol, P. Colpo, G. Ceccone, F. Rossi, Plasma assisted production of chemical nano-patterns by nano-sphere lithography: application to bio-interfaces. *J. Phys. D Appl. Phys.* **40**(8), 2341 (2007)
89. Z. Wu, X. Mei, D. Kim, M. Blumin, H. Ruda, Growth of Au-catalyzed ordered GaAs nanowire arrays by molecular-beam epitaxy. *Appl. Phys. Lett.* **81**(27), 5177–5179 (2002)
90. H. Chik, J. Liang, S. Cloutier, N. Kouklin, J. Xu, Periodic array of uniform ZnO nanorods by second-order self-assembly. *Appl. Phys. Lett.* **84**(17), 3376–3378 (2004)

91. H.J. Fan, W. Lee, R. Scholz, A. Dadgar, A. Krost, K. Nielsch, M. Zacharias, Arrays of vertically aligned and hexagonally arranged ZnO nanowires: a new template-directed approach. *Nanotechnology* **16**(6), 913 (2005)
92. S.Y. Chou, P.R. Krauss, P.J. Renstrom, Imprint lithography with 25-nanometer resolution. *Science* **272**(5258), 85–87 (1996)
93. S.Y. Chou, Nanoimprint lithography and lithographically induced self-assembly. *MRS Bull.* **26**(7), 512–517 (2001)
94. A.I. Hochbaum, R. Fan, R. He, P. Yang, Controlled growth of Si nanowire arrays for device integration. *Nano Lett.* **5**(3), 457–460 (2005)
95. T. Mårtensson, P. Carlberg, M. Borgström, L. Montelius, W. Seifert, L. Samuelson, Nanowire arrays defined by nanoimprint lithography. *Nano Lett.* **4**(4), 699–702 (2004)
96. B. Nikoobakht, C.A. Michaels, S.J. Stranick, M.D. Vaudin, Horizontal growth and in situ assembly of oriented zinc oxide nanowires. *Appl. Phys. Lett.* **85**(15), 3244–3246 (2004)
97. D. Tsvion, M. Schwartzman, R. Popovitz-Biro, P. von Huth, E. Joselevich, Guided growth of millimeter-long horizontal nanowires with controlled orientations. *Science* **333**(6045), 1003–1007 (2011)
98. D. Tsvion, M. Schwartzman, R. Popovitz-Biro, E. Joselevich, Guided growth of horizontal ZnO nanowires with controlled orientations on flat and faceted sapphire surfaces. *ACS Nano* **6**(7), 6433–6445 (2012)
99. D. Tsvion, E. Joselevich, Guided growth of epitaxially coherent GaN nanowires on SiC. *Nano Lett.* **13**(11), 5491–5496 (2013)
100. M. Schwartzman, D. Tsvion, D. Mahalu, O. Raslin, E. Joselevich, Self-integration of nanowires into circuits via guided growth. *Proc. Natl. Acad. Sci. U.S.A.* **110**(38), 15195–15200 (2013)
101. Y. Sun, H. Cui, C. Wang, Step-edge induced ordered growth: targeting to assemble super long horizontal nanowire alignment in large-scale. *Phys. Chem. Chem. Phys.* **15**(28), 11808–11813 (2013)



# Chapter 5

## Nanoelectronics, Circuits and Nanoprocessors

**Abstract** As electronic device features have been pushed into the deep sub-100-nm regime, conventional scaling strategies in the semiconductor industry have faced technological and economic challenges. Electronics obtained through the bottom-up approach of molecular-level control of material composition and structure may lead to devices and fabrication strategies as well as new architectures not readily accessible or even possible within the context of the top-down driven industry and manufacturing infrastructure. This chapter presents a summary of recent advances in basic nanoelectronics devices, simple circuits and nanoprocessors assembled by semiconductor NWs.

### 5.1 Introduction and Historical Perspective

In 1965, Gordon Moore, the cofounder of the Intel Corporation, predicted that the number of on-chip transistors doubles approximately every two years, known as the “Moore’s law” [1]. Over the past four decades, sustained advances in integrated circuit technologies for memory and processors have followed this prediction, thereby leading to computers with ever more powerful processing capabilities, ever increasing nonvolatile memory capacity and a host of consumer electronics. But as device features continue to be pushed deep in the sub-100-nm regime, continuation of the scaling predictions of Moore’s law faces substantial fundamental, technological and economic challenges [2–4]. For example, device size fluctuations may result in a large spread in device characteristics at the nanoscale, affecting key parameters such as the threshold voltage and On/Off currents [3, 4]. In addition, the increasing costs associated with lithography equipment and operating facilities needed for conventional manufacturing might also create a huge economic barrier to continued increases in the capabilities of conventional processor and memory chips [3, 4].

Given these recognized challenges, researchers have intensively explored bottom-up and hybrid bottom-up/top-down paradigms in search of alternative approaches to continued scaling of electronic devices [5–9]. In this regard, one of

the most prominent classes of bottom-up nanostructure materials investigated has been NWs. Semiconductor NWs are especially attractive building blocks for electronic devices because they can be synthesized with precisely controlled size, composition, doping and heterostructures [5, 9–12]. In addition and as described in the previous chapter, NWs can be aligned into highly ordered geometries, which is a characteristic central to the construction of integrated circuits. To date, NWs have been used to build nanoelectronic devices, such as FETs and  $p$ - $n$  diodes, circuit units, including simple logic gates, ring oscillators, multiplexers/demultiplexers, and addressable nonvolatile memories, and even nanoprocessors [5–9, 13–15]. This chapter introduces unique features and opportunities of the bottom-up paradigm for nanoelectronics, assesses how it might merge with today’s top-down industry, and discusses the challenges that need to be met to take this area of science towards commercial applications.

## 5.2 Basic Nanoelectronic Devices

### 5.2.1 Field-Effect Transistors

The FET is the most fundamental building block of high-density integrated circuits. In a standard planar FET (Fig. 5.1a), the semiconductor substrate (e.g.,  $p$ -Si) is connected to the gate (G), the source (S) and the drain (D) electrodes. The source and drain regions, through which current is injected and collected, respectively, have an opposite doping (e.g.,  $n$ -type) to the substrate. The gate electrode is capacitively coupled to the semiconductor channel by an insulating oxide layer. If no gate voltage ( $V_g$ ) is applied (the “Off” state), the FET is equivalent to two

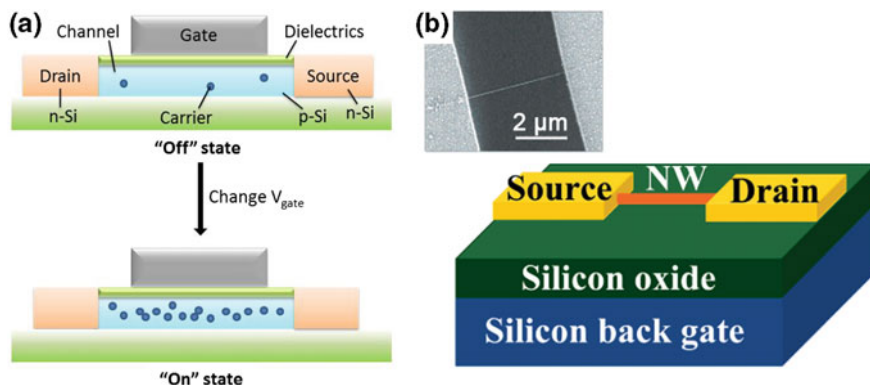


**Fig. 5.1** a A typical planar FET. The semiconductor substrate (e.g.,  $p$ -Si) is connected to gate (G), source (S) and drain (D) electrodes, and can be switches between the “Off” and “On” states by applying the  $V_g$ . b Schematic and SEM image of a NW-FET. Reproduced from [16]. Copyright 2002 American Chemical Society

$p$ - $n$  junctions connected back-to-back with almost no current flow. In the “On” state, when  $V_g$  exceeds a threshold voltage, charge carriers (e.g., holes for  $p$ -Si and electrons for  $n$ -Si) are induced at the semiconductor-oxide interface, and the potential barrier of the channel drops, resulting in a significant current flow. Therefore, the conductance of the semiconductor channel between the source and drain regions can be switched from Off to On and modulated in the On state by the potential at the gate electrode.

Similar to its planar counterpart, the basic electronic properties of a semiconductor NW can be characterized using electrical transport studies in a FET (NW-FET) configuration [16] (Fig. 5.1b). For example, NWs can be deposited on the surface of a silicon wafer covered with an oxidized layer (Si/SiO<sub>2</sub>), in which the underlying conducting silicon can serve as a global back gate. The naturally grown oxide layer on SiNWs can be used as the gate oxide. Source and drain electrodes are defined by lithography followed by evaporation of metal contacts. The electrostatic potential of the NWs is tuned by  $V_g$ , which modulates the carrier concentration and conductance of the NW. Comprehensive reviews focused on NW-FETs can be consulted for further details [8, 17].

### 5.2.1.1 Homogeneous Nanowire-Based Devices

In the case of NWs with homogeneous structure and composition, SiNWs have most extensively been studied due to control of key NW properties, such as size and doping, necessary for well-defined physical measurements. Other materials, such as Ge [18–20], GaN [21, 22], InAs [23, 24] and metal oxides [25–30], have also been investigated as NW-FETs. Research on NWs began to accelerate in 1998, when a laser-ablation method was introduced to fabricate SiNWs [31]. The ability to prepare NWs with diameters <20 nm made it possible for the first time to produce devices that could approach a 1D limit desirable for high-performance FETs. Initial efforts led to demonstration of NW-FETs and basic devices configured using crossed NW geometry, including  $p$ - $n$  diodes and bi-polar transistors [32–35]. However, the electrical properties of NWs in these initial studies were far from optimal, due to the large sample-to-sample variation and relatively low carrier mobility.

The development of CVD-based NW growth has led to much better control over the doping level and electrical properties of SiNWs, and correspondingly, the realization of high-performance  $p$ - and  $n$ -channel SiNW-FETs [36–39]. However, the use of metal (S and D) contacts suggests that such NW-FETs are Schottky barrier devices, in contrast to conventional metal-oxide-semiconductor field-effect transistors (MOSFETs) having degenerately doped semiconductor source/drain contacts. As a result, the device performance is to a large degree affected by the contact properties. Generally, annealing can lead to the formation of effectively ohmic contacts and dramatically increase the On current and the apparent field-effect mobility. For example, in an early study on boron-doped SiNWs, it was found that thermal annealing of source-drain contacts and passivation of oxide defects by chemical modification were able to increase the average transconductance from 45 to

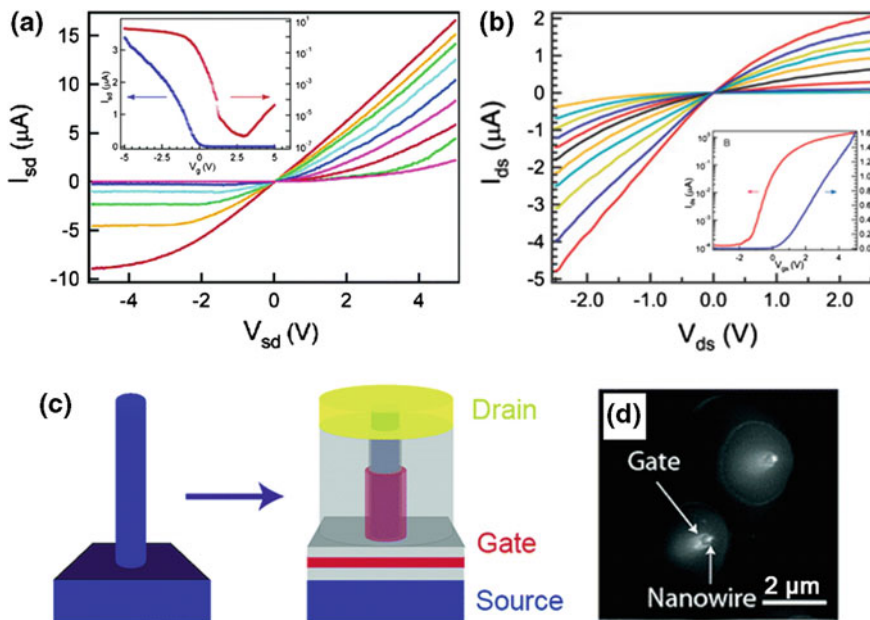


**Fig. 5.2** **a, b** Transistor characteristics of *p*- and *n*-type NWs. *Insets* show transfer characteristics of the back-gated devices. Reproduced from [38, 39]. Copyright 2004 American Chemical Society and John Wiley and Sons. **c, d** Schematic and SEM image of vertically integrated NW-FET device fabricated from vertical SiNWs. Reproduced from [45]. Copyright 2006 American Chemical Society

800 nS and average mobility from 30 to 560  $\text{cm}^2/\text{V s}$ , with peak values of 2000 nS and 1350  $\text{cm}^2/\text{V s}$ , respectively [36]. Later, Jin et al. [39] combined Langmuir-Blodgett (LB) assembly and photolithography techniques to achieve parallel fabrication of *p*-type SiNW devices. From the electrical characterization of randomly chosen NW devices within large arrays (Fig. 5.2a), both linear source-drain current ( $I_{sd}$ ) versus source-drain voltage ( $V_{sd}$ ) curves and saturation at larger negative voltages were obtained, as expected for *p*-type FETs. Furthermore, Zheng et al. [38], demonstrated the first example of controlled growth of *n*-type SiNWs with tunable phosphorus doping, and fabrication of high-performance *n*-type SiNW-FETs. The  $I_{ds}$ - $V_{ds}$  curves recorded with gate voltage ( $V_{gs}$ ) from  $-5$  to  $5$  V are linear from small values of  $V_{ds}$  and saturated at  $V_{ds} \sim 2$  V, and showed increases (decreases) in conductance as  $V_{gs}$  became more positive (negative), as expected for an *n*-channel FET (Fig. 5.2b). Ohmic-like contacts with lower source contact resistance ( $R_s$ ) were obtained with heavily-doped NWs, while the nonohmic contacts with higher  $R_s$  were observed for lightly-doped NWs, where the dopant concentration dependent  $R_s$  limits the measured transconductance.

Koo et al. [40], also reported the fabrication of dual-gated SiNW-FETs, having both a top metal gate and a backside substrate gate. A conducting channel of either

accumulated holes or inversion electrons was generated by the back gate, which also controls the shape of Schottky barrier between the channel and the source/drain electrodes. The top gate was then used to control ambipolar conduction (either hole or electron conduction occurs depending on the gate bias) in these SiNW-FETs. Enhanced channel conductance modulation could be achieved with these dual-gated SiNW devices.

Typically, SiNW transistors have been fabricated in a horizontal or planar architecture with either top and/or back gates [34, 35, 37], and dense arrays of these horizontal NW-FETs integrated for circuits have been realized by assembly [39, 41–44]. In situ growth of vertically aligned NWs can eliminate assembly costs of NW-based device fabrication, and yield vertically aligned NW-FETs with a gate-all-around structure (Fig. 5.2c, d) that improves gate coupling efficiency and thereby can reduce short-channel effects [45, 46]. However, realization of individually-addressable vertical NW-FETs in dense arrays is challenging due to routing of addressable gate and drain metal lines.

Compared to SiNW-FETs, GeNW devices are expected to have higher electron and hole mobilities, as well as smaller contact effects, since the smaller Ge band gap can yield a lower Schottky barrier at the metal/NW interface. For example, studies of *p*-type GeNW devices with palladium (Pd) S/D contacts yielded a hole mobility of  $600 \text{ cm}^2/\text{V s}$  [18]. Notably,  $\text{Si}_{1-x}\text{Ge}_x$  alloy NWs are also interesting as materials for FET channels, because their band gap can be tuned by controlling the composition of the alloy [47]. Nonetheless, adding Ge to yield  $\text{Si}_{1-x}\text{Ge}_x$  alloy NWs did not lead to an increase in the mobility as expected [48, 49], where Ge-O and related surface traps were postulated to reduce the mobility.

### 5.2.1.2 Axial Heterostructures

The homogeneous NW-FETs described above using metal S/D contacts yield Schottky barriers at the metal/NW interface. Metal silicides, which exhibit low resistivity, compatibility with conventional silicon manufacturing, have the ability to form ohmic contacts to both *p*- and *n*-type silicon. Motivated by these advantages, Wu et al. [50] fabricated NiSi/Si/NiSi NW heterostructures with atomically sharp metal-semiconductor interfaces, with the source/drain contacts defined by the metallic NiSi NW regions.

In addition, Lind et al. [51] fabricated an *n*-type InAs/InAsP heterostructure NW-FET (Fig. 5.3a) and compared it with a homogeneous InAs FET (Fig. 5.3b). The design made use of a heterostructure barrier between the source and drain region, which increased the gate control of drain current, because the heterojunction energy barrier is independent of any applied source-drain bias. For the same device geometry, introduction of the heterostructures led to an improvement of the maximum On current, the On/Off ratio, the subthreshold swing and the transconductance. As an example, the Off current was readily suppressed in the heterostructure device, and a large increase in the maximum On/Off current ratio was clearly obtained, approaching  $3 \times 10^4$  between  $V_{\text{gs}} = 2$  and  $-6$  V, compared to an On/Off

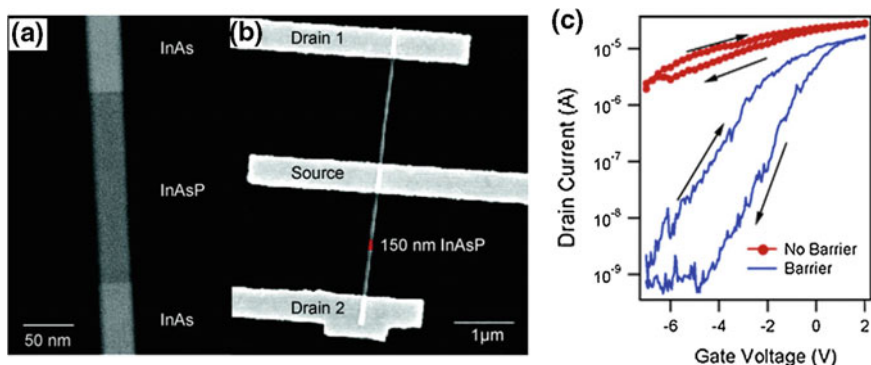


**Fig. 5.3** **a** STEM image of the barrier region, showing the interfaces between InAs and InAsP. **b** SEM image of a NW device ready for measurement. The three terminals allow for independent measurement of a transistor with and without a barrier. **c** Logarithmic plot of  $I_{ds}-V_{gs}$ . A large increase in the maximum current On/Off ratio as well as reduced subthreshold swing is obtained. Reproduced from [51]. Copyright 2006 American Chemical Society

ratio of 7.5 for similar gate values for the pure InAs transistor (Fig. 5.3c). Furthermore,  $n^+-p^-n^+$  SiNWs were used to fabricate stable and reproducible top-gate and wrap-around-gate MOSFETs that were operated by electron inversion of the  $p^-$  body segment and had significantly higher On current and On/Off current ratios than uniformly  $p^-$ -doped NW-FETs [52].

### 5.2.1.3 Radial Heterostructures

An important NW heterostructure is the Ge/Si core/shell system, which typically consists of a 3–5 nm Si shell epitaxially grown on top of a GeNW core. The large valence band offset between Ge and Si results in the Fermi level being pinned within the Si bandgap and below the Ge valence band edge (Fig. 5.4a) [53, 54]. This band line-up results in a negative Schottky barrier to the Ge channel, which favors injection of holes to the Ge core from the contacts. As a result, a hole gas is formed and confined inside the intrinsic (dopant-free) Ge core, thus eliminating dopant scattering [55, 56]. For example, in 2006, Xiang et al. [56] fabricated and characterized the performance of Ge/Si NW-FETs with  $ZrO_2$  high- $\kappa$  dielectric and gate-all-around geometry. The devices fabricated in this manner behaved like  $p$ -type depletion mode FETs and exhibited peak transconductance values,  $g_m$ , of 26  $\mu S$  and a maximum drain currents,  $I_{d(max)}$ , of 35  $\mu A$ , substantially outperforming other single semiconductor NW-based FETs. In addition, the estimated hole mobility of  $730 \text{ cm}^2 \text{ V}^{-1} \text{ s}^{-1}$  was more than 1 order of magnitude larger than state-of-the-art MOSFET and more than twice that of Ge and strained Si/Ge heterostructures PMOS devices (Fig. 5.4b). Later, scaling of Ge/Si NW-FETs was further demonstrated in studies of devices with channel length down to 40 nm [57]. Metallic  $NiSi_xGe_y$  NW electrical contacts were used to define sub-100-nm Ge/Si channels by controlled

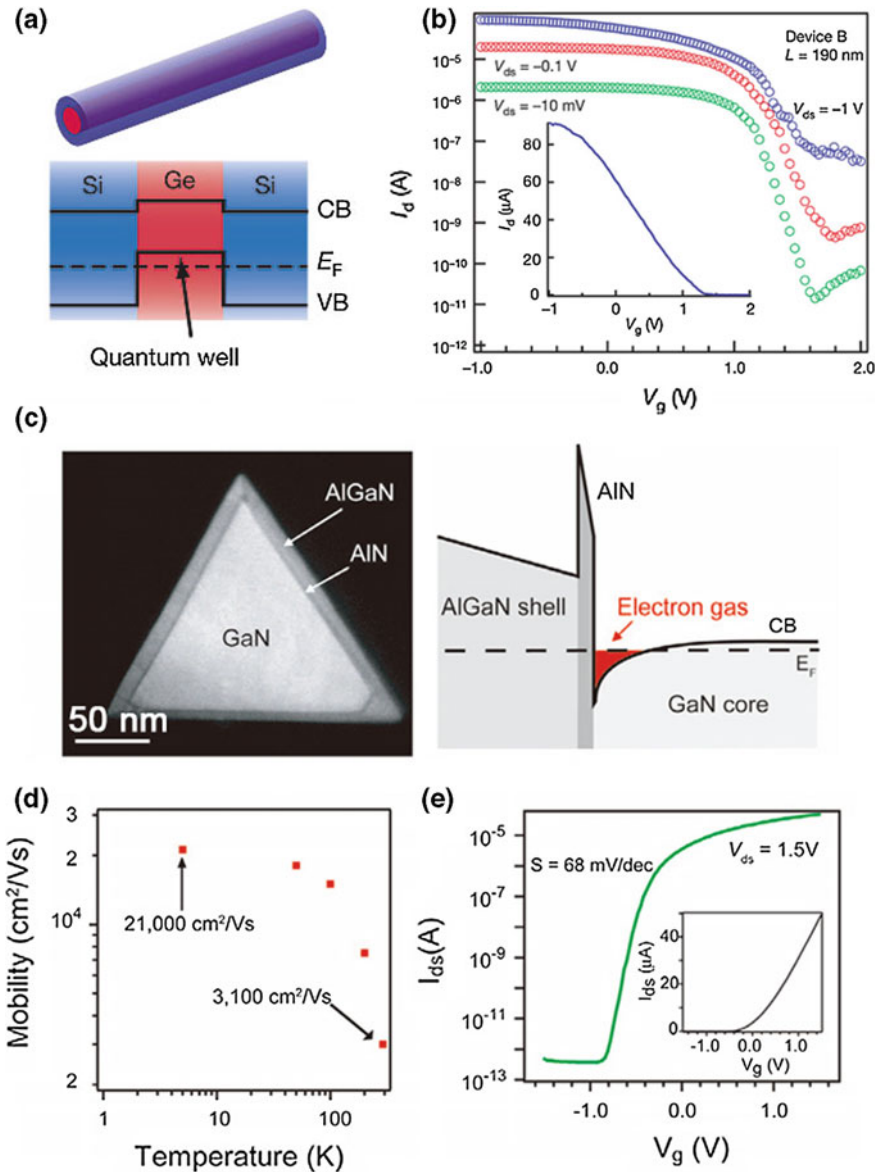


**Fig. 5.4** **a** Upper Schematic of a Ge/Si core/shell NW. Lower Cross-sectional diagram showing the formation of hole-gas in the Ge quantum well confined by the epitaxial Si shell, where CB is the conduction band and VB is the valence band. The dashed line indicates the Fermi level,  $E_F$ . **b**  $I_d$ - $V_g$  data for Ge/Si core/shell NW-FETs. Reproduced from [56]. Copyright 2006 Nature Publishing Group. **c** Left Cross-sectional TEM image of a GaN/AIN/AlGaN radial NW heterostructure. Right Band diagram of a dopant-free GaN/AIN/AlGaN NW. **d** Plot of the intrinsic electron mobility of a GaN/AIN/ $\text{Al}_{0.25}\text{Ga}_{0.75}\text{N}$  NW-FET as a function of temperature. **e**  $I_{ds}$ - $V_g$  curve recorded on a top-gated GaN/AIN/ $\text{Al}_{0.25}\text{Ga}_{0.75}\text{N}$  NW-FET (channel length 1  $\mu\text{m}$ , 6 nm  $\text{ZrO}_2$  dielectric); inset shows the linear scale plot of the same data. Reproduced from [59]. Copyright 2006 American Chemical Society

solid-state conversion of Ge/Si NW. The nanoscale metallic contacts were shown to overcome deleterious short-channel effects in lithographically defined sub-100 nm channels. Electrical transport data acquired on 70- and 40-nm channel length Ge/Si NW-FETs yielded scaled transconductances values of 5.3 and 6.2 mS/ $\mu\text{m}$  and scaled On currents of 1.8 and 2.1 mA/ $\mu\text{m}$ , respectively, which exceeded significantly the best reported values for planar  $p$ -Si MOSFETs. In addition, analysis of the intrinsic switching delay showed that terahertz intrinsic operation speed was possible when channel length was reduced to 70 nm and that an intrinsic delay of 0.5 ps was achievable in their 40-nm device. Comparison of the experimental data with simulations suggested that these sub-100-nm Ge/Si NW-FETs with integrated high- $\kappa$  gate dielectric operated very near the ballistic limit, which might further contribute to ultrafast nanoelectronics. Later, Dillen et al. [58], demonstrated radial modulation doping in coherently strained Ge-Si<sub>x</sub>Ge<sub>1-x</sub> core-shell NWs. Radial modulation doping was achieved by incorporating a B-doped layer during epitaxial shell growth, resulting in an enhancement in peak hole mobility. In addition, a decoupling of electron transport in the core and shell regions was also observed, due to the higher carrier mobility in the core versus the shell.

Analogous to the 1-D hole gas formed in the Ge/Si core/shell NWs, 1-D electron gases and high-performance  $n$ -channel NW-FETs have been demonstrated in NW radial heterostructures by exploring the conduction band offset in selected materials. For example, studies of undoped GaN/AlN/AlGaN radial NW heterostructures (Fig. 5.4c) suggested the formation of an electron gas inside the GaN core due to strong spontaneous piezoelectric polarization [59]. The precisely controlled 2-nm AlN interlayer was grown to provide a large conduction band discontinuity for better confinement of electrons and to reduce alloy scattering from the AlGaN outer shell. Electrical transport measurements carried out on GaN/AlN/AlGaN yielded an intrinsic electron mobility of 3100 and 21,000 cm<sup>2</sup>/V s at room temperature and 5 K, respectively (Fig. 5.4d). FETs fabricated with ZrO<sub>2</sub> dielectrics and metal top gates showed excellent gate coupling with near ideal subthreshold slopes of 68 mV/dec (Fig. 5.4e), an On/Off current ratio of 10<sup>7</sup>, and scaled On current and transconductance values of 500 mA/mm and 420 mS/mm, demonstrating the excellent interfacial properties and electrostatic control.

In 2007, the rational design and synthesis of InAs/InP core/shell NW heterostructures with quantum-confined high mobility electron channels was also reported [60]. InP is an attractive shell material because the conduction band offset of  $\sim 0.52$  eV provides an excellent confinement potential for electrons, and the type-I quantum well structure also confines holes that may be thermally generated or resulted from impact ionization in the channel. Room-temperature electrical measurements on InAs/InP NW-FETs showed significant improvement in the On current and transconductance compared to InAs NW-FETs fabricated in parallel. For example, the transconductance values showed an approximately five-fold increase for InAs/InP (2.2  $\mu\text{S}$ ) versus InAs (0.45  $\mu\text{S}$ ). The 11500 cm<sup>2</sup>/V s room-temperature electron mobility in these InAs/InP NW heterostructure further substantiated the promise of the radial core/shell approach for creating unique nanoscale building blocks. In addition, NW-FET devices configured with integral high dielectric



constant gate oxide and top-gate structure yielded scaled On current values up to 3.2 mA/ $\mu\text{m}$ . In two recent reports, Tomioka et al. [61] and Dey et al. [62] further demonstrated a surrounding-gate NW-FETs using InGaAs/InP/InAlAs/InGaAs core-multishell NWs and radial tunnel FETs in GaSb/InAs(Sb) NWs, respectively, thereby further extending the toolbox of NW building blocks for nanodevices.

#### 5.2.1.4 Crossed Nanowire Structures

One of the first demonstrations of crossed NW structure was reported by the Heath group [63], where two SiNWs were assembled to fabricate a four-terminal device. The resistivity through the crossed-wire junction was measured to be similar to the resistivity of individual wires forming the crossed device, indicating little or no tunneling barrier at the junction of the two wires. The Lieber group [35] developed nanoscale FETs in the crossed NW configuration, with one NW acting as the active conducting channel and the other crossed NW as the gate electrode. Significantly, three critical FET device metrics were naturally defined at the nanometer scale in the assembled crossed NW-FETs: (1) a nanoscale channel width determined by the diameter of the active NW; (2) a nanoscale channel length defined by the crossed gate NW diameter; and (3) a nanoscale gate dielectric thickness determined by the NW surface oxide. These distinct nanoscale device metrics led to greatly improved device characteristics such as high gain, high speed, and low power dissipation. For example, the conductance modulation of an NW-FET was much more significant with the NW gate ( $>10^5$ ) than that with a global back gate ( $<10$ ). The local NW gate enabled independently addressable FET arrays and thus highly integrated nanocircuits. Moreover, 3D multifunctional electronics were fabricated based on vertically stacked layers of multi-NW-FETs [42, 64, 65].

#### 5.2.1.5 Junctionless Nanowire Transistors

In modern transistors, the current flow is modulated by a gate electrode, relying on junctions between the channel and source/drain contacts (Fig. 5.5a). However, these junctions are becoming increasingly difficult to manufacture as transistor sizes are reduced in the pursuit of performance. To this point, Colinge et al. [66, 67] reported the fabrication of fully CMOS-capable long-channel (1  $\mu\text{m}$ ) junctionless transistors, in which the current flows through the bulk of the channel, rather than just along its surface. Figure 5.5b depicts the operation principle for a junctionless *n*-type accumulation device. In the On state, the whole NW body behaves as a conducting channel and the application of a voltage at the drain contact results in an On current that depends on the NW's geometry, mobility and doping. When the gate voltage is decreased, the transistor body is gradually depleted, until eventually the transistor is turned off. The devices have near-ideal subthreshold slope, extremely low leakage currents, and less degradation of mobility with gate voltage and temperature than classical transistors. Recently, Konar et al. [68] reported studies on

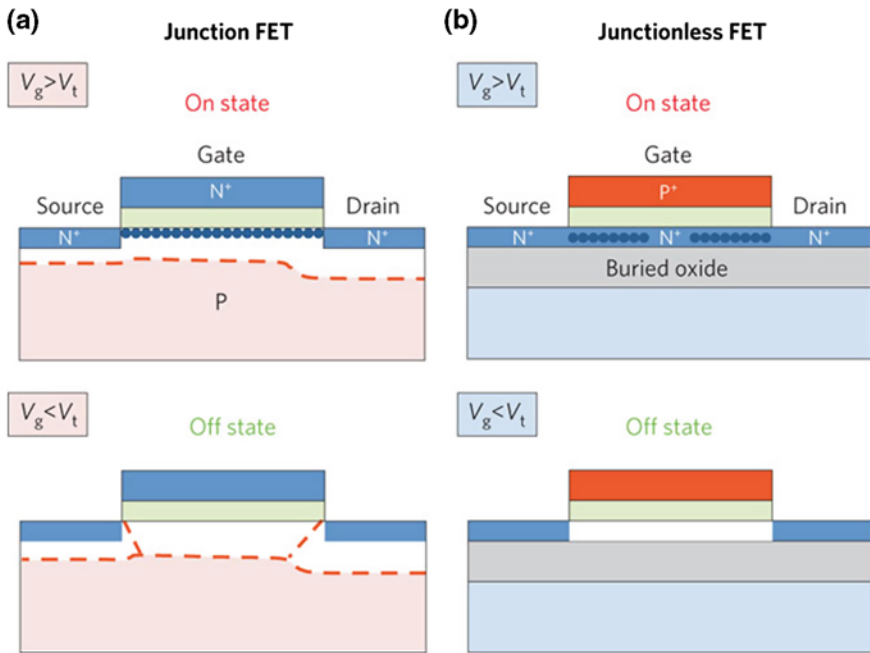


**Fig. 5.5** Cross sections and operation principles for an  $n$ -type junction FET and a junctionless FET. **a** A junction FET is turned on in the inversion condition, when a channel of minority carriers is formed just under the gate, and junction barriers to their flow are reduced. The horizontal red line shows the bottom of the depletion region, and the slanted red lines indicate the limits of the depletion region controlled by the gate. **b** The On state of a junctionless FET is obtained in ‘flat band’ conditions, with majority carriers travelling through a highly doped film. The device turns off when the gate-controlled depletion extends over the whole film. Blue and red colours depict electron and hole doping respectively, with a darker color indicating heavier doping. The white regions correspond to the depletion regions, and the green color represents the gate oxide. Reproduced from [67]. Copyright 2010 Nature Publishing Group

high-mobility junctionless gate-all-around NW-FET with carrier mobility reaching  $2000 \text{ cm}^2/\text{V s}$  at room temperature. At low temperatures, measurement shows an activated transport in NW-FETs due to donors present in the bulk as well as at the nanowire-high- $k$  interface. At room temperature, the carrier transport is limited by the interplay of remote Coulomb scattering and acoustic phonon scattering.

## 5.2.2 $p$ - $n$ Diodes

A  $p$ - $n$  diode is a type of semiconductor device based on the  $p$ - $n$  junction, which is the interface between  $p$ -type and  $n$ -type semiconductor materials. The diode has many important characteristics, including current rectification; that is, it conducts current in the dark only from  $p$  to  $n$  for modest operating voltages.

### 5.2.2.1 Crossed-wire $p$ - $n$ Junctions

One direct way to make  $p$ - $n$  diodes using  $p$ - and  $n$ -type semiconductor NWs is to assemble two doped NWs in a crossed NW configuration [21, 33–35]. For example, the Lieber group [33] reported the construction of crossed InP (a direct band gap semiconductor) NW  $p$ - $n$  junctions that exhibited rectifying behavior and light-emitting properties. Significantly, electroluminescence (EL) was readily observed from these nanoscale  $p$ - $n$  junctions under a forward bias (Fig. 5.6a). A photoluminescence (PL) image of a crossed NW junction (inset in Fig. 5.6a) showed a crossed wire-like structures, and comparison of the EL and PL images showed that the position of the EL maximum corresponded to the crossing point in the PL image, demonstrating that the light originated from the NW  $p$ - $n$  junction. The  $I$ - $V$  characteristics of the junction (Fig. 5.6b inset) showed clear rectification with a sharp current onset at  $\sim 1.5$  V. The EL intensity increased rapidly with bias voltage, and resembled the  $I$ - $V$  behavior.

### 5.2.2.2 Axial Nanowire $p$ - $n$ Diodes

Another configuration of NW  $p$ - $n$  diodes involves the formation of axial junctions by modulating  $p$ - and  $n$ -type dopants sequentially during axial elongation growth phase of NWs. The first axial  $p$ - $n$  diode was demonstrated in 1992, where the junction was formed in a cross-sectional area of GaAs wires with a diameter of  $\sim 100$  nm [69]. Later, Gudiksen et al. [70] reported the growth of NW superlattice structures, and fabricated  $p$ - $n$  junctions within individual silicon NWs by Au nanocluster-catalyzed CVD and dopant modulation. These NW  $p$ - $n$  junctions were characterized at the single NW level by a variety of electrical measurements (Fig. 5.7). Current ( $I$ ) versus voltage ( $V_{sd}$ ) measurements showed rectifying behavior consistent with the presence of an intra-NW  $p$ - $n$  junction (Fig. 5.7a). An

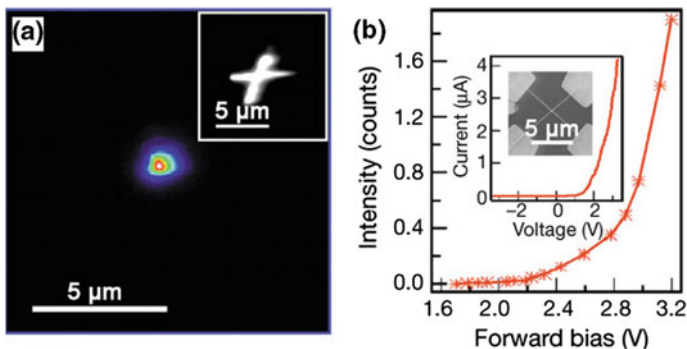


**Fig. 5.6** **a** EL image of the light emitted from a forward-biased NW  $p$ - $n$  junction. *Inset* PL image of the junction. **b** EL intensity versus voltage. *Inset*,  $I$ - $V$  characteristics; inset in this inset, FESEM image of the junction. Reproduced from [33]. Copyright 2001 Nature Publishing Group

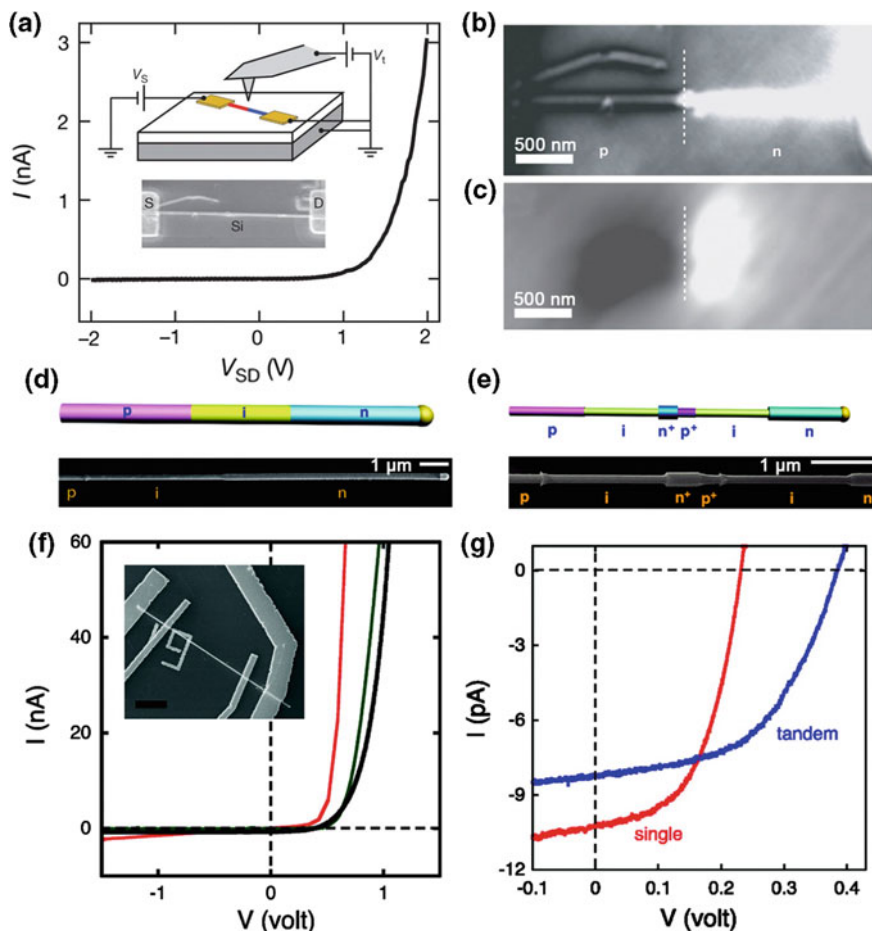


**Fig. 5.7** **a** Insets A diagram illustrating single-NW electrical characterization by transport and probe microscopy, and a SEM image of the SiNW device with source (S) and drain (D) electrodes indicated. **Main panel**  $I$  versus  $V_{sd}$  for the SiNW  $p$ - $n$  junction. **b** EFM phase image of the NW diode under reverse bias. **c** SGM image showing the source-drain current as the tip is scanned across the device. Reproduced from [70]. Copyright 2002 Nature Publishing Group. **d, e** Scheme and structural characterization of axial modulation-doped  $p$ - $i$ - $n$  (**d**) and tandem  $p$ - $i$ - $n^+$ - $p^+$ - $i$ - $n$  (**e**) SiNWs. **f** Dark  $I$ - $V$  characteristics of  $p$ - $i$ - $n$  SiNWs with different  $i$ -region lengths; red, green, and black curves correspond to  $i$ -segment lengths of 0, 2, and 4  $\mu\text{m}$ , respectively. **g**  $I$ - $V$  responses recorded on  $p$ - $i$  (2  $\mu\text{m}$ )- $n$  (red) and  $p$ - $i$ - $n^+$ - $p^+$ - $i$ - $n$ ,  $i = 2 \mu\text{m}$  (blue) SiNW devices under AM 1.5G illumination. Reproduced from [71]. Copyright 2008 American Chemical Society (Color figure online)

electrostatic force microscopy (EFM) image of the  $p$ - $n$  junction in reverse bias showed that the entire voltage drop occurred at the  $p$ - $n$  junction (Fig. 5.7b). In addition, scanned gate microscopy (SGM) image recorded with the NW device in forward bias and the scanned tip-gate positive (Fig. 5.7c) showed enhanced conduction to the right of the junction, indicating an  $n$ -type region, and reduced

conduction to the left of the junction, indicating depletion of a  $p$ -type region. In 2008, Kempa et al. [71] reported the synthesis of axial modulation-doped  $p$ - $i$ - $n$  and tandem  $p$ - $i$ - $n^+$ - $p^+$ - $i$ - $n$  SiNWs as photovoltaic elements, where axial modulation was achieved by switching dopant precursor gases at different times during elongation of the NW. Selective etching using KOH solution showed a clear delineation of the individual regions of the diode structure (Fig. 5.7d, e).  $I$ - $V$  measurements in Fig. 5.7f also show well-defined reverse bias current rectification and a current onset in forward bias at ca. 0.6 V. Comparison of  $I$ - $V$  data of  $p$ - $i$ - $n$  and tandem  $p$ - $i$ - $n^+$ - $p^+$ - $i$ - $n$  SiNWs under AM 1.5G illumination demonstrated a substantial increase in open circuit voltage for the tandem SiNW photovoltaic device (Fig. 5.7g).

In the case of GeNWs, the dominant mechanism for phosphorous and boron atom incorporation is through the NW surface versus the NW bulk. Thus, the  $p$ - $n$  junctions within GeNWs cannot be achieved simply by dopant modulation. To circumvent this constraint, Tutuc et al. [72] designed a novel device structure:  $n$ -type and undoped segments were subsequently fabricated, followed by uniform coating of  $p$ -type shell. The resulting GeNWs exhibited device characteristics similar to that expected for an axial  $p$ - $n$  junctions. In another report, Hoffmann et al. [73] utilized ion implantation, a standard doping technique in top-down semiconductor manufacturing, to achieve axial  $p$ - $n$  profiles post NW growth. This method offered advantages by allowing for precise control over the total dose of dopants, depth profile, and also worked well for high/degenerative doping levels of  $10^{20}$ – $10^{21}$   $\text{cm}^{-3}$ . A limitation of implantation is that high-temperature annealing is typically required to make the dopants electrically-active. In addition, both  $p$ - $n$  homojunctions and heterojunctions have synthetically integrated into branched NWs, including  $p$ -Si/ $n$ -GaAs backbone/branch heterostructures [74], and kinked NWs with axial  $p$ - $n$  junctions introduced at the kink joints [75].








## 5.3 Simple Circuits

### 5.3.1 Logic Gates

Logic gates are the elementary building blocks of digital integrated circuits, primarily implemented using diodes or transistors acting as electronic switches [76]. There are seven basic logic gates: AND, OR, NOT, NAND, NOR, XOR, and XNOR. Most logic gates, except the NOT gate, have an input of two binary values, and output one of the two binary conditions true (1) or false (0), represented by high and low voltage levels, respectively. The symbols and truth tables of all basic logic gates are shown in Table 5.1 [76].

1. The AND gate acts in the way as the logical “and” operator. The output is 1 only if both inputs are 1. Otherwise, the output is 0.
2. The OR gate behaves as the logical “or”. The output is 1 if one or both the inputs to the gate are 1. If both inputs are 0, then the output is 0.

**Table 5.1** Symbols and truth tables of seven basic logic gates [76]

Gate type	Symbol	Truth table															
AND		<table border="1"> <thead> <tr> <th>Input 1</th> <th>Input 2</th> <th>Output</th> </tr> </thead> <tbody> <tr> <td>0</td> <td>0</td> <td>0</td> </tr> <tr> <td>0</td> <td>1</td> <td>0</td> </tr> <tr> <td>1</td> <td>0</td> <td>0</td> </tr> <tr> <td>1</td> <td>1</td> <td>1</td> </tr> </tbody> </table>	Input 1	Input 2	Output	0	0	0	0	1	0	1	0	0	1	1	1
Input 1	Input 2	Output															
0	0	0															
0	1	0															
1	0	0															
1	1	1															
OR		<table border="1"> <thead> <tr> <th>Input 1</th> <th>Input 2</th> <th>Output</th> </tr> </thead> <tbody> <tr> <td>0</td> <td>0</td> <td>0</td> </tr> <tr> <td>0</td> <td>1</td> <td>1</td> </tr> <tr> <td>1</td> <td>0</td> <td>1</td> </tr> <tr> <td>1</td> <td>1</td> <td>1</td> </tr> </tbody> </table>	Input 1	Input 2	Output	0	0	0	0	1	1	1	0	1	1	1	1
Input 1	Input 2	Output															
0	0	0															
0	1	1															
1	0	1															
1	1	1															
NOT		<table border="1"> <thead> <tr> <th>Input</th> <th>Output</th> </tr> </thead> <tbody> <tr> <td>0</td> <td>1</td> </tr> <tr> <td>1</td> <td>0</td> </tr> </tbody> </table>	Input	Output	0	1	1	0									
Input	Output																
0	1																
1	0																
NAND		<table border="1"> <thead> <tr> <th>Input 1</th> <th>Input 2</th> <th>Output</th> </tr> </thead> <tbody> <tr> <td>0</td> <td>0</td> <td>1</td> </tr> <tr> <td>0</td> <td>1</td> <td>1</td> </tr> <tr> <td>1</td> <td>0</td> <td>1</td> </tr> <tr> <td>1</td> <td>1</td> <td>0</td> </tr> </tbody> </table>	Input 1	Input 2	Output	0	0	1	0	1	1	1	0	1	1	1	0
Input 1	Input 2	Output															
0	0	1															
0	1	1															
1	0	1															
1	1	0															
NOR		<table border="1"> <thead> <tr> <th>Input 1</th> <th>Input 2</th> <th>Output</th> </tr> </thead> <tbody> <tr> <td>0</td> <td>0</td> <td>1</td> </tr> <tr> <td>0</td> <td>1</td> <td>0</td> </tr> <tr> <td>1</td> <td>0</td> <td>0</td> </tr> <tr> <td>1</td> <td>1</td> <td>0</td> </tr> </tbody> </table>	Input 1	Input 2	Output	0	0	1	0	1	0	1	0	0	1	1	0
Input 1	Input 2	Output															
0	0	1															
0	1	0															
1	0	0															
1	1	0															
XOR		<table border="1"> <thead> <tr> <th>Input 1</th> <th>Input 2</th> <th>Output</th> </tr> </thead> <tbody> <tr> <td>0</td> <td>0</td> <td>0</td> </tr> <tr> <td>0</td> <td>1</td> <td>1</td> </tr> <tr> <td>1</td> <td>0</td> <td>1</td> </tr> <tr> <td>1</td> <td>1</td> <td>0</td> </tr> </tbody> </table>	Input 1	Input 2	Output	0	0	0	0	1	1	1	0	1	1	1	0
Input 1	Input 2	Output															
0	0	0															
0	1	1															
1	0	1															
1	1	0															
XNOR		<table border="1"> <thead> <tr> <th>Input 1</th> <th>Input 2</th> <th>Output</th> </tr> </thead> <tbody> <tr> <td>0</td> <td>0</td> <td>1</td> </tr> <tr> <td>0</td> <td>1</td> <td>0</td> </tr> <tr> <td>1</td> <td>0</td> <td>0</td> </tr> <tr> <td>1</td> <td>1</td> <td>1</td> </tr> </tbody> </table>	Input 1	Input 2	Output	0	0	1	0	1	0	1	0	0	1	1	1
Input 1	Input 2	Output															
0	0	1															
0	1	0															
1	0	0															
1	1	1															

3. The NOT gate, also known as an inverter, implements logical negation, it has only one input value. If the input is 1, the output is 0. On the other hand, when the input becomes 0, the output becomes 1.
4. The NAND gate equals to an AND gate followed by a NOT gate. The output is 0 if both inputs are 1. Otherwise, the output is 1.
5. The NOR gate equals to an OR gate followed by a NOT gate. Its output is 1 if both inputs are 0. Otherwise, the output is 0.
6. The XOR gate acts in the way as the logical “either/or”. The output is 1 when either one of the inputs are 1. The output becomes 0 if both inputs are 0 or if both inputs are 1. In another word, the output is 1 if two input values are different, but 0 if the inputs are the same.
7. The XNOR gate equals to a XOR gate followed by a NOT gate. Its output is 1 if the inputs are the same, and 0 if the inputs are different.

In this section, we will describe how crossed NW  $p$ - $n$  junctions and crossed NW-FET arrays can be assembled to yield different logic gate structures, and be used to implement basic computation [34, 35, 37, 43, 77–80]. The first work demonstrating the capability of  $p$ -Si/ $n$ -GaN NWs to build logic gates was reported by Huang et al. [35]. First, an OR gate was realized by using a  $2(p)$  by  $1(n)$  crossed  $p$ - $n$  junction array with the two  $p$ -SiNWs as inputs and the  $n$ -GaN NW as the output (Fig. 5.8a). In this device, the output was low (logic 0) when both input voltages were low (0 V), and the output was high (logic 1) when either or both of the input voltages were high (5 V) (Fig. 5.8b), where a high input corresponded to a forward bias of the corresponding  $p$ - $n$  junction. The output-input ( $V_o$ - $V_i$ ) voltage response (Fig. 5.8b, inset) showed that  $V_o$  increased linearly with  $V_i$  when one input was set low (0 V). The  $V_o$ - $V_i$  data also showed a nearly constant high output when the second input was set high (5 V). The experimental truth table for the 1 by 2 crossed NW device (Fig. 5.8c) demonstrated that this NW device behaved as an OR gate.

In addition, AND gates were fabricated from  $1(p$ -Si) by  $3(n$ -GaN) multiple junction arrays (Fig. 5.8d). In this structure, the  $p$ -SiNW was biased at 5 V, two of the GaN NWs were used as inputs and the third was used a gate with a constant voltage to create a resistor by depleting a portion of the  $p$ -SiNW. The logic 0 was observed from this device when either one or both of the inputs were low (Fig. 5.8e), because  $V_i = 0$  corresponded to a forward-biased, low-resistance  $p$ - $n$  junction that pulled down the output (logic “0”). The logic 1 was observed only when both inputs were high, because this condition corresponded to reverse-biased  $p$ - $n$  diodes with resistances much larger than that of the constant resistor; that is, there was a small voltage drop across the constant resistor and a high voltage was achieved at the output. The  $V_o$ - $V_i$  data (Fig. 5.8e, inset) showed constant low  $V_o$  when the other input was low, and nearly linear behavior when the other input was set at high. The truth table for the NW device (Fig. 5.8f) demonstrated that this device functioned as an AND gate.

Moreover, a logic NOR gate was assembled by using a  $1(p$ -Si) by  $3(n$ -GaN) crossed NW-FET array (Fig. 5.8g). The NOR gate was configured with 2.5 V applied to one crossed NW-FET to create a constant resistance of  $\sim 100$  M $\Omega$ , and

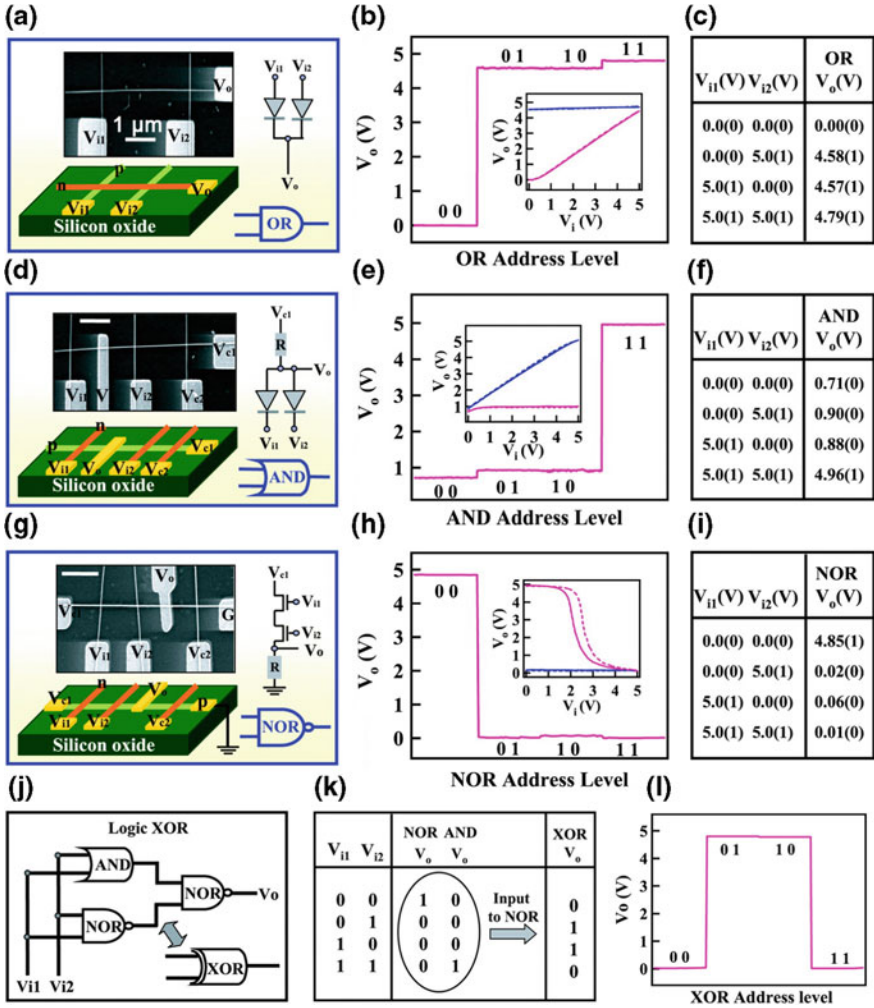


**Fig. 5.8** a Schematics of logic OR gate. *(Insets)* An example SEM image of the assembled OR gate and symbolic electronic circuit. **b** The output voltage versus logic address level inputs. *(Inset)* The  $V_o$ - $V_i$  relation. The *solid* and *dashed red (blue)* lines show  $V_o$ - $V_{i1}$  and  $V_o$ - $V_{i2}$  when the other input is 0 (1). **c** The experimental truth table for the OR gate. **d** Schematic of logic AND gate. *(Insets)* A typical SEM image of the assembled AND gate and symbolic electronic circuit. **e** The output voltage versus logic address level inputs. *(Inset)* The  $V_o$ - $V_i$ , where the *solid* and *dashed red (blue)* lines correspond to  $V_o$ - $V_{i1}$  and  $V_o$ - $V_{i2}$  when the other input is 0 (1). **f** The experimental truth table for the AND gate. **g** Schematic of logic NOR gate. *(Insets)* An example SEM image of the assembled NOR gate and symbolic electronic circuit. **h** The output voltage versus logic address level inputs. *(Inset)* The  $V_o$ - $V_i$  relation, where the *solid* and *dashed red (blue)* lines correspond to  $V_o$ - $V_{i1}$  and  $V_o$ - $V_{i2}$  when the other input is 0 (1). **i** The measured truth table for the NOR gate. **j** Schematic of logic XOR gate. **k** Truth table for logic XOR gate. **l** The output voltage versus logic address level inputs for the XOR gate. Reproduced from [35]. Copyright 2001 the American Association for the Advancement of Science



the *p*-SiNW channel was biased at 5 V. The two remaining *n*-GaN NW inputs act as gates for two crossed NW-FETs in series. In this way, the output depended on the resistance ratio of the two crossed NW-FETs and the constant resistor. The logic 0 was observed when either one or both of the inputs was high (Fig. 5.8h). The transistors were off and had resistances much higher than that of the constant resistor, and thus most of the voltage dropped across the transistors. A logic 1 state was only achieved when both of the transistors were On and both inputs were low. The  $V_o$ - $V_i$  relation (Fig. 5.8h, inset) showed constant low  $V_o$  when the other input was high, and a nonlinear response with large change in  $V_o$  when the other input was set low. The truth table for this NW device (Fig. 5.8i) demonstrated that the device behaved as a logic NOR gate. Furthermore, multiple-input logic NOR gates could function as NOT gates (simple inverters) by eliminating one of the inputs.

Lastly, the authors interconnected multiple AND and NOR gates to implement basic computation in the form of an XOR gate (Fig. 5.8j), which was configured by

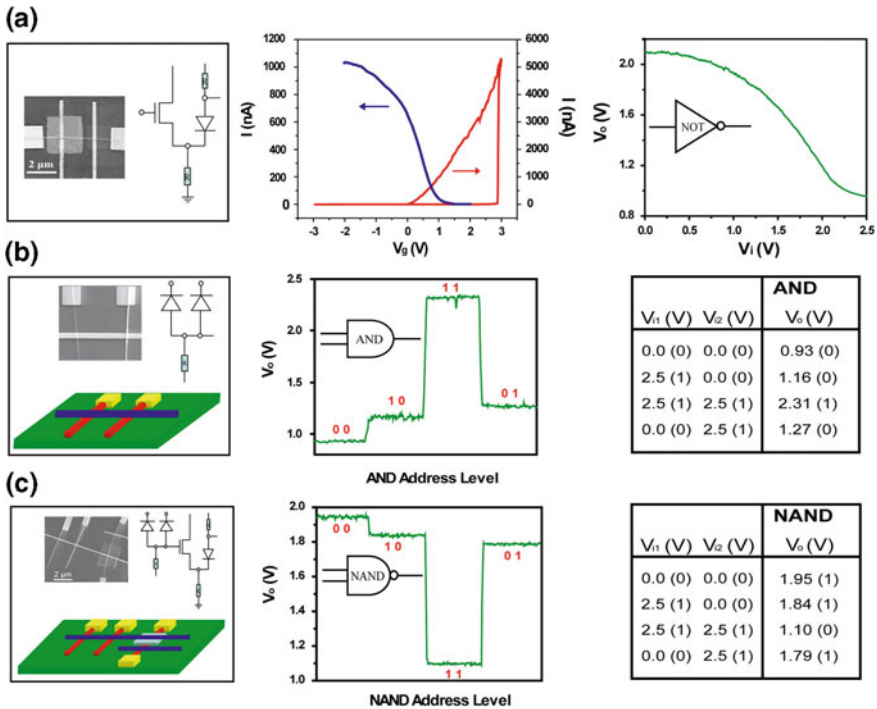


**Fig. 5.9** Logic gate structures based on core/shell Si  $\times$  Ag crossbar NW system. **a** (left) SEM image of assembled inverter structure and symbolic electronic circuit. (middle) *I*-*V* curves of both crosspoints showing that both diode switch (red curve) and FET (blue) functions can be achieved using a single SiNW crossing two metal NWs. (right) Output-input relation curve ( $V_o$ - $V_i$ ). **b, c** (left) Schematic and SEM images for assembled logic AND and NAND gates and their symbolic electronic circuits. (middle) Output voltage versus four possible logic address level inputs. (right) Experimental truth table for AND and NAND gates. Reproduced from [43]. Copyright 2010 De Gruyter

using the output from AND and NOR gates as the input to a second NOR gate. The truth table for the proposed logic XOR was summarized in Fig. 5.8k. Importantly, the experimental  $V_o$ - $V_i$  data for the XOR device (Fig. 5.8l) showed that the output was logic state 0 or low when the inputs were both low or both high, and logic state 1 or high when one input was low and the other was high.

In another report, Yu et al. [43]. used assembled Si/metal NW crossbar arrays to design and realize both diode and FET-based logic, including the inverter, AND and NAND logic structures (Fig. 5.9). For example, an inverter structure was realized by using a 1 Si/amorphous-Si (a-Si) NW  $\times$  2 Ag NW crossbar array with one Ag NW working as top-gate metal, and the other as contact electrode for the diode switch junction. Representative  $I$ - $V$  curves measured on both crossed junctions showed that two cross-points could function as FET (blue curve) and diode switch elements (red curve). Further, by the input voltage  $V_i$ -biased on top-gate Ag NW and giving a constant  $V_{sd}$  ( $\sim 2$  V), the output voltage measured from the diode electrode Ag NW can be tuned from the “high” state when the input voltage was set to low, to the “low” state when the input voltage was set to high (Fig. 5.9a). A logic AND gate was also assembled from a 2 Si/a-SiNWs  $\times$  1 Ag NW array (Fig. 5.9b), and a logic NAND gate was assembled by using a 3 Si/a-SiNWs  $\times$  2 Ag NW array (Fig. 5.9c). The controlled and predictable assembly of these logic gate structures enabled the organization of virtually any logic circuit.

### 5.3.2 Ring Oscillators

A ring oscillator is composed of a chain of an odd number of NOT gates (inverters), where the last output of the chain is the logical NOT of the first input, thus allowing for oscillation in the “ring”. In previous reports, NW-FET arrays have been utilized to develop ring oscillator circuits [65, 81–83]. For example, the Lieber group [81] fabricated NW ring oscillators consisting three inverters on glass substrates. The devices showed a maximal oscillation frequency of 11.7 MHz, corresponding to a stage delay of 14 ns. Significantly, all devices measured on glass have oscillation frequencies at or above 10 MHz. Later, the same group [65] also fabricated two-layered, three-stage vertically interconnected CMOS ring oscillators. An optical micrograph and circuit schematic (Fig. 5.10a) highlight the three CMOS inverters serially connected in a closed, positive feedback loop, with each inverter consisting of a layer-1 InAs NW  $n$ -FET and a layer-2 Ge/Si NW  $p$ -FETs, which were vertically interconnected. Measurement of the output signal with a high impedance probe demonstrated stable, self-sustained oscillations with a maximum frequency of 108 MHz for  $V_{DD} = 8$  V, as shown in Fig. 5.10b. This oscillation frequency corresponded to a propagation delay of 1.54 ns per stage.

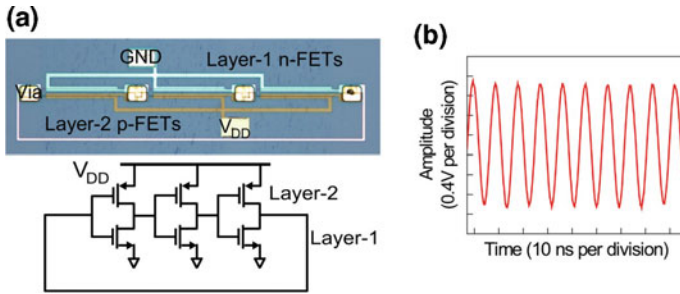


**Fig. 5.10** **a** Optical micrograph and circuit diagram of two-layer, vertically interconnected three-stage CMOS ring oscillator. **b** Amplitude versus time response recorded at via position by using a high-impedance probe. Reproduced from [65]. Copyright 2009 the National Academy of Sciences of the United States of America

### 5.3.3 Demultiplexers

Addressing large numbers of NWs inside a crossbar array requires demultiplexers (demuxes) that allow a relatively small number of control wires to access the large number of NWs selectively inside the memory array. In an ideal demux,  $n$  pairs of microscale control wires can be used to select  $2^n$  NWs; that is, 10 pairs of control wires can specifically address each of the  $2^{10} = 1024$  NWs, serving as the columns (or rows) of a 1 Mbit crossbar memory. By using a pair of demuxes serving respectively as row and column selectors, all  $2^{2n}$  cross-points inside the NW-FET array can be selectively addressed by  $2n$  pairs of control wires. This type of addressing has been experimentally realized by several groups using NW arrays [84–87].

In 2003, Zhong et al. [84] reported the first NW-based demuxes using molecular-level modification of crossed NW-FET arrays, where selective chemical modification of cross points in the arrays enabled NW inputs to turn specific FET array elements On and Off. The basic structure of the device was a regular crossed NW-FET array that consisted of  $n$ -input ( $I_1, I_2, \dots, I_n$ ) and  $m$ -output ( $O_1, O_2, \dots, O_m$ ) NWs, where outputs were the active channels of FETs and the inputs functioned as gate electrodes that turned these output lines On and Off. In this report, the cross points were differentiated by the chemical modification, such that inputs only affected selected output cross-points in the array. Before modification, the depletion mode device exhibited a threshold voltage of  $\sim 5$  V, which shifted to  $\sim 1.5$  V after modification. In the simplest scenario in which one output NW was turned On or Off by a single input, differentiation of diagonal elements of a square array (Fig. 5.11a) produced a code, where  $I_1, I_2, \dots, I_n$  addressed  $O_1, O_2, \dots, O_m$ , respectively. This concept was generalized to enable a small number of input NWs to address a larger number of output NWs, if two or more inputs were used to turn On or Off a given output. Similarly, a small number of lithographically defined wires could address a much denser array of NWs (Fig. 5.11b). This idea was tested

first in a 2 by 2 crossed NW-FET array (Fig. 5.11c). Conductance versus applied NW input gate voltage data (Fig. 5.11d) showed that, before modification, each of the four crossed NW-FET elements remained “on” for voltages greater than 2 V. After specific modification of the  $I_1/O_1$  and  $I_2/O_2$  elements, these devices were turned off with a gate voltage of  $\sim 1$  V. Hence, when  $I_1$  was set to 1 V and  $I_2$  was set to 0 V, only  $O_2$  was active, with an output of 2 V, and  $O_1$  was Off with an output of 0 V (Fig. 5.11e). In a larger 4 by 4 array (Fig. 5.11f), all of the 16 crossed NW-FET elements remained “on” for voltages greater than 3 V before surface modification. However, after specific modification of the four diagonal  $I_n/O_n$  elements, these FETs were selectively turned off by their respective inputs. Hence, by variation of the NW input voltages (Fig. 5.11g), it was possible to address selectively each of the four output lines, as required for multiplexing and demultiplexing signals.

Multi-input binary tree demuxes exhibit  $2[\log_2(N)]$  scaling, where  $N$  is the number of output NWs and  $2[\log_2(N)]$  is the number of the demultiplexing wires used to address the output lines, although extra NWs are necessary to compensate for randomness in organization and defects such as broken or nonconducting NWs, and thereby yield an effective large scale demux circuit [88]. This scheme requires modulation-doped NWs to address dense nanoscale arrays and threshold voltage modulation. Hence, the address coding is obtained at the different cross-points between gate wires and the NW channel, which may be either heavily or lightly doped. This idea was implemented experimentally by the Lieber group [85]. Furthermore, the Heath group [86] described a demux structure that used  $2[\log_2(N)] + R$  microwires to address  $N$  NWs, where  $R$  (for redundant address lines) was zero or a small integer. Their work did not require control over the axial doping profile of the underlying NWs but took advantage of top-down lithography to define the address code of gated versus non-gated FETs. This device concept shown in Fig. 5.11h, i with 32 NWs addressed with five pairs of (drawn) large wires. The binary tree pattern extends above and below the NW array. The green regions correspond to areas in which a voltage applied to the top (metal) wires can gate NWs as FETs nodes. For example, the binary address “1 0 1 0 1” in Fig. 5.11i indicates that the resistance of NWs that pass under a voltage-gated (red) region is increased. Only a single wire (colored red across the entire structure) remains in the high-conducting state and is addressed.

### 5.3.4 Nonvolatile Memory

Along with the advancement of semiconductor logic technology, the demand for memory devices with high-density, high-speed, and low power consumption has remained particularly high. One key property that distinguishes different classes of memory devices is the volatility [89]. In devices where stored information is volatile, such as dynamic random access memory (DRAM), information is lost when the power is turned off; however, access speed is generally very high and thus

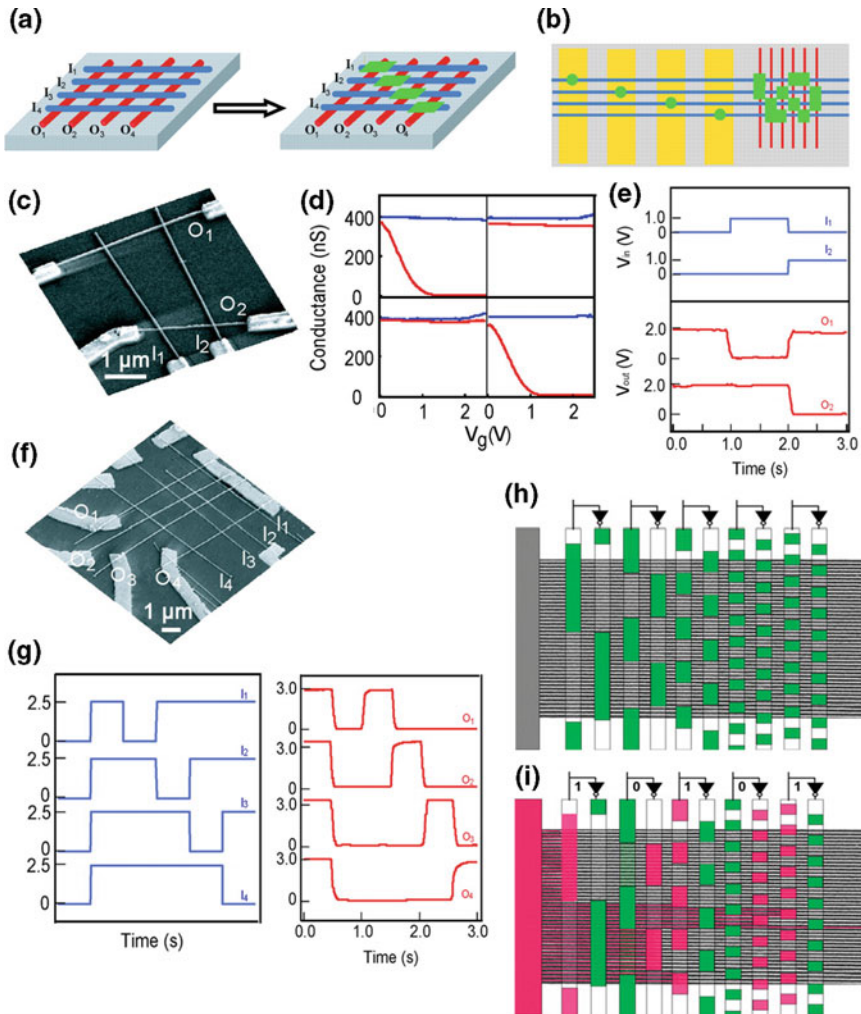


**Fig. 5.11** **a** A 4 by 4 crossed NW-FET array with  $I_1$  to  $I_4$  as inputs and  $O_1$  to  $O_4$  as outputs. The four diagonal cross points were chemically modified (*green rectangles*). This produced a 1-hot code in which  $I_n$  turns  $O_n$  On or Off. **b** Bridging between microscale metal wires (*yellow*) and denser nanoscale NWs is achieved with a 2-hot code (*green rectangles*), whereby two inputs (*blue NWs*) are required to address each output (*red NWs*). **c** An SEM image of a 2 by 2 crossed NW-FET demux. **d** Conductance versus gate voltage for each cross point for the NW-FET array in (**c**) before (*blue*) and after (*red*) chemical modification. Starting clockwise from the top left quadrant, data are from junctions  $I_1/O_1$ ,  $I_2/O_1$ ,  $I_2/O_2$ , and  $I_1/O_2$ , respectively. **e** Real-time monitoring of the gate voltage inputs (*blue*) and signal outputs (*red*) for the 2 by 2 demux. **f** An SEM image of a 4 by 4 crossed NW-FET demux. The four diagonal cross points were chemically modified. **g** Real-time monitoring of the gate voltage inputs (*blue*) and signal outputs (*red*) for the 4 by 4 demux. Reproduced from [84]. Copyright 2003 the American Association for the Advancement of Science. **h, i** The decoder concept, drawn over an electron micrograph of 32 silicon NWs. Reproduced from [86]. Copyright 2005 the American Association for the Advancement of Science

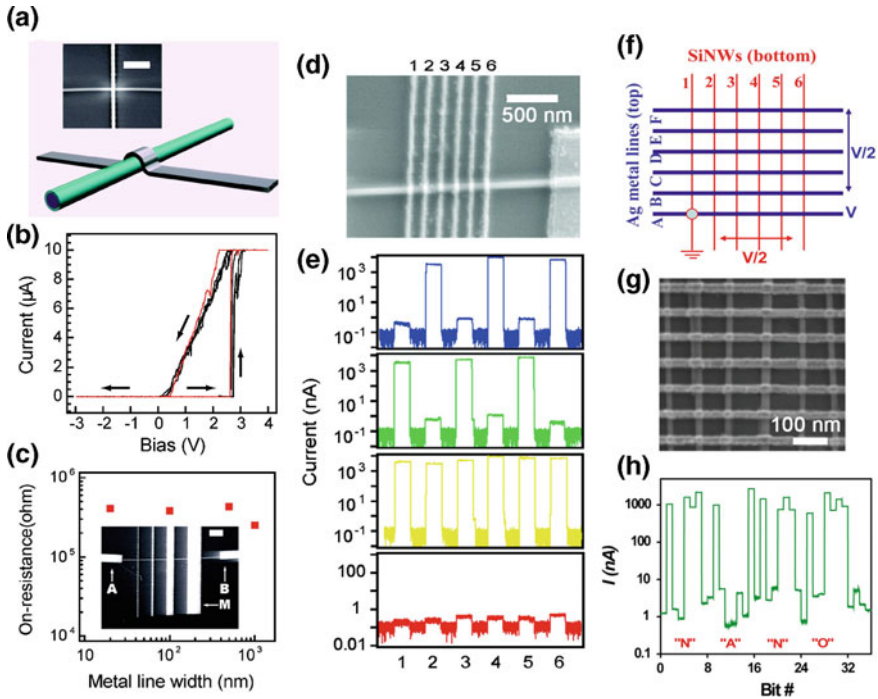


**Fig. 5.12** **a** Si/a-Si  $\times$  metal NW crossbar switch structure. **b**  $I$ - $V$  sweep curves showing basic switching behavior of crossbar NW element. **c** Current read at 1.5 V for devices fabricated with different metal line widths (1  $\mu\text{m}$  and 500, 200, and 30 nm) on a single core/shell NW. **d**, **e** SEM image of a  $1 \times 6$  array composed of one Si/a-SiNW crossing six Ag lines and corresponding states of crosspoints 1–6 read at 2 V: *blue* = 010101, *green* = 101010, *yellow* = 111111, *red* = 000000. Reproduced from [95]. Copyright 2008 American Chemical Society. **f**, **g** Schematic and SEM image of a  $6 \times 6$  NW crossbar memory structure and Write/Read modes for the memory array. **h** The use of 36-bit crossbar memory to store the word “NANO” (ASCII II) is demonstrated with read current values plotted on a log scale. Reproduced from [43]. Copyright 2010 De Gruyter

used to store information dynamically for a processor [90]. On the other hand nonvolatile RAM devices (NVRAM) can maintain stored information even when the power is turned off, but generally have much slower writing speeds compared to DRAM [89]. Nevertheless, nonvolatile devices have been central to the focus of work in nanoscience because of the opportunity to enable new computing architectures [7, 91]. In terms of basic storage mechanisms, NW-based nonvolatile memory devices can be divided into four categories [91–93].

1. Resistive memory devices generally refer to 2-terminal devices in which stable 2-state resistance values are produced in response to an applied bias voltage that turns the device On or Off [89, 94]. The most widely characterized resistive switching behavior arises from the formation of a conducting filament within an insulating or high-resistance layer that separates cross point between two much

more conducting NWs [15, 95]. The resulting switching behavior has been attributed to the formation and rupture of this conducting filament [96].

2. Flash memory is a 3-terminal transistor-based device in which charge can be stored on a “floating gate” that is isolated from the conducting channel, or a dielectric layer, and thereby change the On/Off state of the transistor [89, 97]. The charge is stored or removed by applying relatively large voltages to an external gate electrode. The programmed On/Off states of a flash memory device can be determined by measuring the drain current of the transistor.
3. Ferroelectric memory devices are 3-terminal devices utilizing the polarization states of a ferroelectric material to store information [89, 98]. Ferroelectric materials can be polarized in an external field and then remain polarized after the external field is removed. The polarization can simply be reversed by applying a field of opposite polarity. Most ferroelectric memory NW devices [99–102] are transistor-based, where the ferroelectric material directly gates the NW, and its polarization state can change the gate potential, similar to the mechanism of flash memory.
4. Phase-change memory is another type of 2-terminal device in which the resistance change of two memory states is based on a reversible crystalline to amorphous phase transition [103]. The phase change material is in the crystalline, low-resistance form after fabrication, and can be converted into the amorphous phase with high resistance by applying a short, large electrical current pulse. A longer smaller current pulse is applied to anneal the amorphous region and restore the crystalline phase. The resistance of a device is measured by using a small current/voltage that does not disturb the amorphous or crystalline states.

#### 5.3.4.1 Resistive Memory

The NW-based crossbar structure represents a powerful and scalable architecture for memory and logic devices in that key device features can be defined during the synthesis of NW building blocks and their subsequent assembly. In the context of memory, each cross-point represents a bit where information can be stored and addressed, as demonstrated by the Lieber group [15, 43, 95, 104]. For example, Dong et al. [95] reported the cross-point hysteretic resistance switches based on core/shell SiNW-metal NW crossbars. In this work, the core of the NW heterostructure consisted of doped crystalline Si and functions as one electrode contact, the amorphous shell (a-Si) function as the information storage medium, and a crossed silver metal NW serves as the second electrode contact (Fig. 5.12a). Room-temperature electrical measurements on single Si/a-Si  $\times$  Ag NW devices demonstrated the following key features: bi-stable switching between high (Off) and low (On) resistance states with well-defined switching threshold voltages (representative  $I$ - $V$  data shown in Fig. 5.12b), On/Off ratios  $>10^4$ , and current rectification in the On state. Furthermore, systematic studies of Si/a-Si  $\times$  Ag NW

devices showed that: (i) the bit size was at least as small as  $20 \times 20$  nm (Fig. 5.12c), (ii) the writing time was  $<100$  ns, (iii) the retention time was  $>2$  weeks, (iv) devices were switched  $>10^4$  times without degradation in performance. In addition, the scalability of the Si/a-Si  $\times$  Ag NW device structure was investigated in 1D ( $1 \times 6$ ) arrays (Fig. 5.12d). Transport measurements (Fig. 5.12e) further demonstrated its ability to write/erase the six crosspoint switches to an arbitrary state (e.g., 000000, 111111, 101010, 010101), and then read out the state of six switches without crosstalk between elements during writing, reading, or erasing.

Later, the same group [43] assembled nonvolatile memory switches into larger arrays. The point addressability and storage capability of memory array were tested on a  $6 \times 6$  (36 bit) crossbar NW array confirming uniform memory characteristics achieved with Si/a-Si  $\times$  Ag NW-based crossbar system [43] (Fig. 5.12f, g). Strings of 1s and 0s corresponding to standard ASCII alphanumeric symbols were stored into the array, and subsequently read out. Figure 5.12h presents the results of such write/read testing. An operational memory was demonstrated by successfully writing and reading out the word “NANO” (e.g., an “N” character (ASCII 78), represented as the 8-bit number “01001110”). The bit current read-out from the array was plotted in log scale to show the readily differentiated levels of the “On” and “Off” states of all bits within the crossbar circuit, with the 1/0 current ratio in the order of  $10^2$ . The findings demonstrate that excellent memory characteristics can be achieved with this Si/a-Si  $\times$  Ag NW-based crossbar system.

Similar resistive-switching results were also observed in NiO [105, 106],  $\text{Co}_3\text{O}_4$  [107], ZnO [108], MgO/NiO [109] and Ni/NiO core-shell NWs [110, 111], where the oxide shell served as the active layer, as well as Pt [112], Si [113], where a molecular monolayer acted as the data storage agent.

### 5.3.4.2 Flash Memory

Flash memory devices are based on transistors in which an electrically-isolated or floating gate electrode can store charge and thereby change the On/Off state of the transistor. As mentioned above, flash or floating gate FET memory devices are typically 3-terminal in design with the control gate used to inject/remove charge from the floating gate or a dielectric layer in programming or writing operations. By measuring the drain current, the programmed On or Off states of the memory devices can be determined in a read operation. NW-based flash memory devices have been fabricated based on NW-FETs [13, 14, 42, 114–116]. For example, intrinsic GeNWs with a Ge core covered by a thick Ge oxide shell were utilized to achieve flash memory devices [115]. The Ge oxide shell played a key role as the insulating tunneling dielectric, which was thick enough to prevent stored surface charges from leaking out. The Lieber group [13, 14] incorporated programmable NW-FETs in a top-gated geometry using *p*-Ge/Si core/shell NWs as the semiconductor channel. A trilayer  $\text{Al}_2\text{O}_3$ - $\text{ZrO}_2$ - $\text{Al}_2\text{O}_3$  dielectric structure was implemented for charge trapping. Further details of these two works including



incorporation of multi-bits flash memory along a single NW as well as addressable 2D arrays will be discussed below in section D.

Flash memory does, however, have disadvantage of relatively slow writing/erasing speed. To address this issue, the Samuelson group [117] demonstrated an alternative memory concept, in which a storage island was connected to a NW containing a stack of nine InAs quantum dots, each separated by thin InP tunnel barriers. As the barrier region was sliced up into thinner segments with a conducting material in between, electron transport occurred via a fast tunneling process through the thin barriers. The memory operated for temperatures up to around 150 K and had write times down to at least 15 ns.

### 5.3.4.3 Ferroelectric Memory

In ferroelectric memory, the polarization states of a ferroelectric material are used to store information by changing conductance of a NW-FET. There are several reports of NW-based ferroelectric memory devices [99–102]. For example, Liao et al. [100] reported the fabrication of ZnO NW memory devices using a ferroelectric Pb ( $\text{Zr}_{0.3}\text{Ti}_{0.7}$ ) $\text{O}_3$  (PZT) film as the gate dielectric and charge storage medium. When a negative  $V_g$  pulse was applied between the NW channel and the Pt gate (i.e., writing), the polarizations of the ferroelectric film were aligned downward. After the gate voltage pulse was removed, the remnant polarization of the ferroelectric functioned as a nonvolatile gate in analogy to the flash memory devices described above. The ability to reverse the polarization state by the writing voltage applied to the Pt gate electrodes produces nonvolatile Off or “0” and On or “1” states. Compared to flash memory, ferroelectric memory is quite difficult to scale down due to the deterioration of the ferroelectric materials at small dimensions [118]. In addition, a decay in polarization is often observed after the ferroelectric film experiences repeated cycles of polarization change, and thus a lower reliability [119]. On the other hand, the charge injection/removal of flash memory is relatively slow compared to the polarization change, which yields a faster writing time in the latter [120].

### 5.3.4.4 Phase-Change Memory

The bottom-up approach may also lead to improved performance of memory devices based on conventional structures, or serve as a well-controlled platform for studying the memory mechanisms. One such example is the crystalline NW-based phase-change memory (PCM). PCM has sparked considerable interest as a potential next-generation nonvolatile solid-state memory technology, and has been shown to possess many of the necessary attributes, including high resistance contrast, the potential for multilevel storage, and better endurance and writing speeds than flash memory [121]. Chalcogenide-based (Ge-Sb-Te alloys) PCMs, in which data is “recorded” by switching the material into either an amorphous or crystalline state, are promising for data storage [122–127].

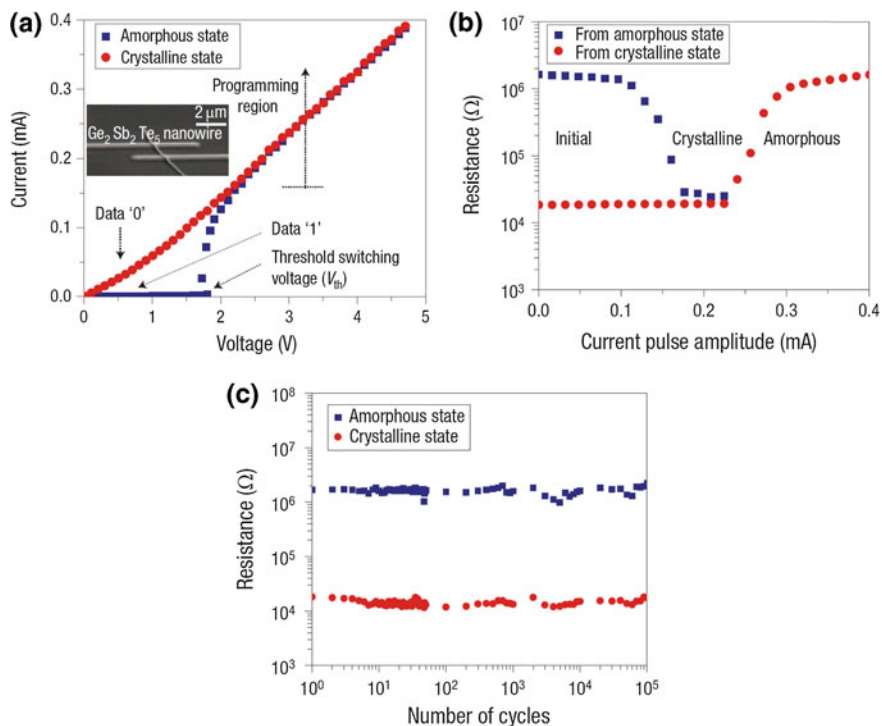


**Fig. 5.13** **a**  $I$ - $V$  characteristics of a 60-nm NW device (*inset* SEM image) in amorphous and crystalline states. **b** Resistance change as a function of writing pulses with different current amplitudes obtained for initially amorphous and crystalline phases. **c** Endurance-cycling test for the NW memory device. Reproduced from [126]. Copyright 2007 Nature Publishing Group

As an example, Lee et al. [126] explored the effects of size scaling the key memory characteristic of  $\text{Ge}_2\text{Sb}_2\text{Te}_5$  NWs. To demonstrate memory switching behavior, the  $I$ - $V$  characteristics of a  $\text{Ge}_2\text{Sb}_2\text{Te}_5$  NWs were measured (Fig. 5.13a). The as-synthesized crystalline NWs showed linear  $I$ - $V$  characteristics with low resistance state characteristic of the crystalline phase. Upon the application of a current pulse, which caused the NW to transition to an amorphous state,  $I$ - $V$  curves initially displayed higher resistance, and subsequently switched to its original low resistive state at a threshold voltage of 1.8 V. Detailed phase-change behavior of the same NW device was studied by measuring the programming characteristics of reversible crystalline-amorphous switching, for which resistance ( $R$ ) change was obtained as a function of writing/erasing current ( $I$ ) pulse amplitude (Fig. 5.13b). The operation of the device was maintained without failure for up to  $>10^5$  cycles performed with alternating write/read/erase/read pulses (Fig. 5.13c). A unique aspect of this work has been to readily study the size dependence of these properties simply by using different diameter NWs [126].

## 5.4 Nanoprocessors

A nanoprocessor constructed from intrinsically nanometer-scale building blocks is an essential component for controlling memory, nanosensors and other functions proposed for nanosystems assembled from the bottom up. As mentioned in previous sections, simple logic gates with individually assembled semiconductor NWs have been realized, but with only 16 devices or fewer and a single function for each circuit. This section first introduces the structure of a logic tile consisting of two interconnected arrays with functional configurable nonvolatile FET nodes, based on two reports of the Lieber group [13, 14]. Then, the use of programmable and scalable logic tiles for configuring nanoprocessors, including the construction of arithmetic and sequential logic circuits, is described. Last, long-standing goal of assembling nanocomputers is introduced and demonstrated with the realization of a all NW finite-state machines.

### 5.4.1 Logic Tiles

The programmable NW-FETs was incorporated a top-gated geometry using *p*-Ge/Si core/shell NWs as the semiconductor channel. A trilayer  $\text{Al}_2\text{O}_3\text{-ZrO}_2\text{-Al}_2\text{O}_3$  dielectric structure was implemented for charge trapping. The multi-input programmable NW-FET integrated circuits were fabricated using two coupled NW elements (Fig. 5.14a, left), where the first element, NW1, had four independently configurable input gates, G1-G4, and the second element, NW2, had a single input gate connected to the output of NW1. In this demonstration, the first and third gate nodes of NW1 and the gate node of NW2 were set to the active (transistor) state (Fig. 5.14a, green dots), and the other gate nodes were set to the inactive (resistor) state. With source voltages applied to NW1 and NW2, input G1 was switched between 0 and 1 V while G2-G4 were held at 0 V (Fig. 5.14a, top right). Notably, simultaneous measurements of the output voltage from NW1,  $V_{\text{IG}}$ , and NW2,  $V_{\text{out}}$ , with the 0- and 1-V G1 input variations (Fig. 5.14a, lower right), showed that  $V_{\text{IG}}$  was switched between high (2.2-V) and low (0.2-V) levels and  $V_{\text{out}}$  was toggled between low (0.6-V) and high (3.0-V) levels. These result showed that the programmable NW-FET functioned as a transistor switch and multiple switches were coupled together by feeding the output of one FET into the input gate of another.

Subsequently, a unit logic tile was designed and constructed (Fig. 5.14b). This new logic tile consists of two programmable, nonvolatile NW transistor arrays (PNNTAs). Metal electrodes were used to gate NWs in the block-1 PNNTA (Fig. 5.14b, upper left), and the output of the NWs was connected by metal electrodes to static load devices. By programming selected NW gate nodes to the active transistor state, NOR logic gates were mapped into block 1. The outputs of this NOR logic circuit were passed over and used as gate inputs to the block-2 PNNTA (Fig. 5.14b, lower right), which is also programmed with NOR logic gates. In this

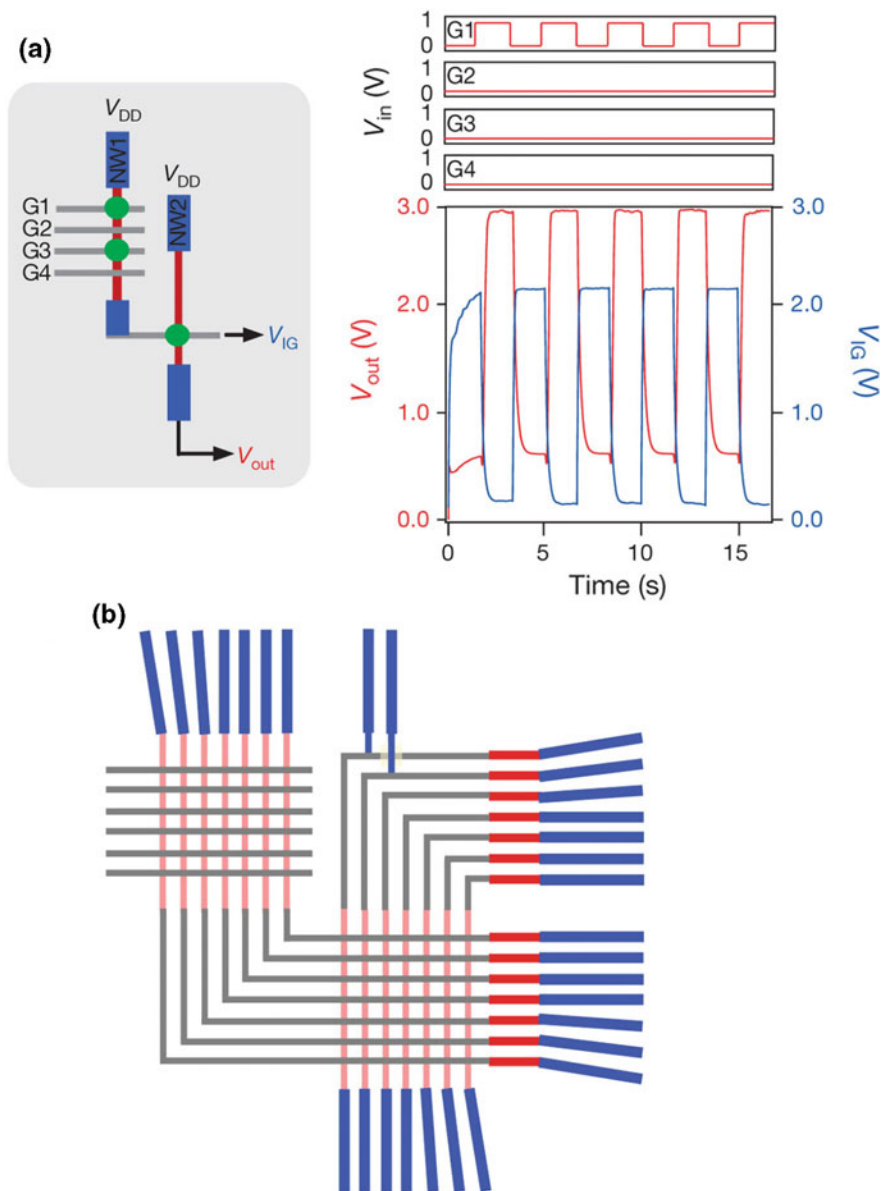


**Fig. 5.14** **a** Characterization of a NW-NW, coupled multigate device. *Left* schematic of the device. *Green dots* indicate the gate nodes that were programmed as an active state. *Top right* input signals to G1-G4. *Bottom right* output signals from NW1 ( $V_{IG}$ , blue) and NW2 ( $V_{out}$ , red). **b** Design of the unit logic tile for integrated nanoprocessors containing two PNNTAs, block 1 (*upper left*) and block 2 (*lower right*), comprising charge-trapping NWs (pink) and metal gate electrodes (grey). The PNNTAs are connected to two sets of load devices (red). Lithographic-scale electrodes (blue) are integrated for input and output. Reproduced from [13]. Copyright 2011 Nature Publishing Group

way, the outputs of the logic circuits in block 1 were used to drive the circuit in block 2, thus making it possible to form two-level networks of NOR logic gates in the unit tile, which is capable of representing arbitrary Boolean functions [13].

### 5.4.2 Arithmetic Logic

An arithmetic logic unit, such as an adder or a subtractor, is a digital circuit that performs integer arithmetic and logical operations [128]. A full adder performs the

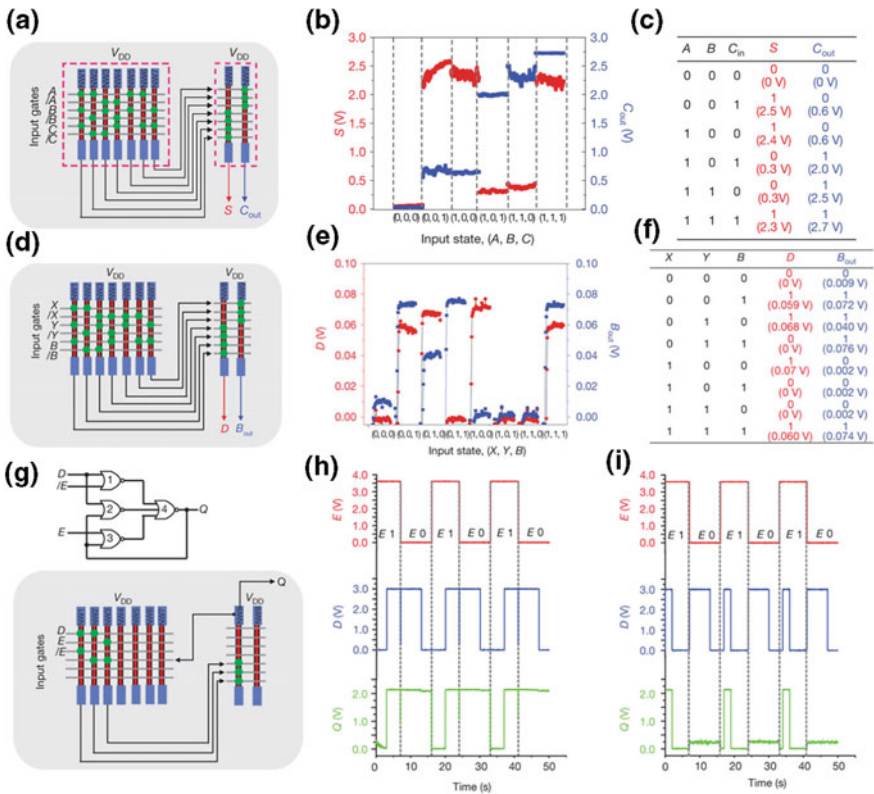


**Fig. 5.15** **a** Circuit design implementing a one-bit full adder. *A*, *B* and *C* denote the complementary inputs of *A*, *B* and *C*, respectively. **b** Output voltage levels for *S* (red) and *C<sub>out</sub>* (blue) for six typical input states. **c** Truth table of full-adder logic for the six input states in **(b)**. The measured output voltages are shown in brackets. **d** Schematic of a circuit implementing a full subtractor. **e** Output of *D* (red) and *B<sub>out</sub>* (blue) of the full subtractor implemented with the same PNNTA structure shown in **(a)** with eight input states. **f** Truth table of the full subtractor with measured output voltages shown in brackets. **g** Schematics of logic (upper) and circuit design (lower) of a D latch implemented with the same PNNTA tile used in **(a)** and **(d)**. **h**, **i** Output, *Q*, waveforms (green) at two sets of clock (*E*, red) and data (*D*, blue) inputs. Reproduced from [13]. Copyright 2011 Nature Publishing Group

addition of binary numbers and accounts for values carried in and out, while a full subtractor performs subtraction. In the work of Yan et al. [13], the two-block PNNTA tile was programmed to function as a full adder. Figure 5.15a illustrates the configuration of the one-bit full-adder logic circuit, comprising two blocks with the output of block 1 (Fig. 5.15a, left-hand box) fed into block 2 (Fig. 5.15a, right-hand box) as input through external wiring. The programmed active node pattern (Fig. 5.15a, green dots) determines the circuit function, and in this case the outputs  $S$  and  $C_{\text{out}}$  represented the sum and carry-out of the summation of inputs  $A + B + C$ , respectively, with  $S = A \oplus B \oplus C$  and  $C_{\text{out}} = A \cdot B + A \cdot C + B \cdot C$ . The symbols “ $\oplus$ ”, “ $\cdot$ ” and “ $+$ ” represented logical XOR, AND and OR, respectively. As the input levels of  $A$ ,  $B$  and  $C$  were swept from logic state 0 (0 V) to logic state 1 (3.5 V), the outputs  $S$  and  $C_{\text{out}}$  switched from logic 0 (both 0 V) to logic 1 (2.0 and 2.7 V, respectively). Further tests showed that the output of  $S$  and  $C_{\text{out}}$  for six typical input combinations (Fig. 5.15b) all had similar output ranges: 0–0.6 V for logic state 0 and 2.0–2.7 V for logic state 1. The expected and experimental results for a full adder were summarized in a truth table (Fig. 5.15c), which showed good consistency for this fundamental logic unit.

In addition, the authors also reprogrammed the same tile to function as a full subtractor (Fig. 5.15d). The two outputs of the reprogrammed circuit,  $D$  and  $B_{\text{out}}$ , represent the difference and borrow, respectively, of the subtraction of inputs  $X - Y - B$ , with  $D = X \oplus Y \oplus B$  and  $B_{\text{out}} = B \cdot \overline{(X \oplus Y)} + \bar{X} \cdot Y$ , where  $\bar{X}$  represents the logical negation (complementary input) of  $X$ . Measurements of  $D$  and  $B_{\text{out}}$  for different  $X - Y - B$  input combinations (Fig. 5.15e) showed that the output voltage levels for logic state 0 (0–0.01 V) and logic state 1 (0.04–0.08 V) were well separated and represented robust states. Moreover, the truth table summarizing the expected and experimental results for the full subtractor (Fig. 5.15f) showed full and correct logic for this processing unit [13].

### 5.4.3 Sequential Logic

In sequential logic circuits (e.g., flip-flops and latches), the output not only depends on the current inputs, but also on the history of the input. In other words, sequential logic has memory [129]. A flip-flop is the basic storage element in sequential logic, whose state can be changed from one to another by an external pulse. It is clocked, or edge-sensitive. That is, the output of a flip-flop only changes at the rising or falling edge of the clock signal (repetitive pulses), so that the logic outputs shift at regular intervals. For latches, however, their outputs changes immediately when the inputs change [129]. For example, the D latch can capture the logical level at high clock input, the output,  $Q$ , will follow the input,  $D$ . When the clock signal becomes logic 0, the last high state will be trapped in the device. On the other hand, the D flip-flop (DFF) is known as a “delay” flip-flop, it captures the value of the input at the edges of the clock cycle, and later produces the output,  $Q$ . At other times, the output does not change. The DFF delays the input by one clock cycle.

To explore the capability to also carry out critical sequential logic, the NW tile was also programmed to demonstrate a D latch (Fig. 5.15g) [13]. The D-latch circuit is composed of four NOR gates with a positive-feedback connection between the output,  $Q$ , and inputs to NOR gates 2 and 3 (Fig. 5.15g, upper panel). As a consequence,  $Q$  equals input data,  $D$ , when clock,  $E$ , is in logic state 1 but retains its previous value when  $E$  is switched into logic state 0. The NOR gates were implemented in the tile using NW1-NW3 in block 1 and NW8 in block 2 (Fig. 5.15g, lower panel), and formed the positive feedback by connecting the output to an input gate in block 1. Measurement of  $Q$  as a function of repetitive  $E$  and  $D$  pulses (Fig. 5.15h) showed that  $Q$  followed  $D$  when  $E$  was switched to logic 1 (3.6 V) at time points 16 and 33 s, but retained as its previous value when  $E$  was switched to logic 0 (0 V) at 7, 24 and 41 s, as expected for a D latch. The robustness of this sequential logic circuit was tested further by inputting a more complex data waveform (Fig. 5.15i), where measurements of  $Q$  demonstrated sharp logic operation by following  $D$  with high fidelity in the time intervals 16-24 and 33-41 s. Moreover, the voltage range of output,  $Q$  (0–2.2 V), closely matched that of input data,  $D$ , and clock,  $E$  [13].

#### 5.4.4 Basic Nanocomputer

A finite-state machine (FSM) is a representation for a nanocomputer in that it is a fundamental model for clocked, programmable logic circuits and integrates key arithmetic and memory logic elements [130]. In general, a FSM can change from one state to another in response to external stimuli, and it is characterized by all the possible states and the triggering signals for each transition. A basic state transition diagram for the 2-bit four-state FSM investigated in the work of Yao et al. [14] (Fig. 5.16a) highlighted the four binary representations “00”, “01”, “10” and “11”, and the transition from one state to another triggered by a binary input signal, “0” or “1”. To realize the nanoFSM, the authors used three NW tiles that are interconnected and programmed for distinct logic functions (Fig. 5.16b). Following fabrication, the common tiles or modules were differentiated by programming, with tile-1 programmed to perform arithmetic operations and tile-2 and tile-3 programmed to function as the register elements for the first and second digits of the state, respectively.

The operation of the FSM circuit was programmed with  $A_1A_0$ ,  $C_{in}$ , and CLK representing the 2-bit state, control input, and clock signal, respectively. In this architecture, tile-1 was configured as a half adder that computed the summation of  $A_1A_0 + C_{in}$ . Its output  $A'_1A'_0$  was the new state, where  $A'_0 = A_0 \oplus C_{in}$ ,  $A'_1 = A_1 \oplus (A_0 \cdot C_{in})$ , and “ $\oplus$ ” and “ $\cdot$ ” represented XOR and AND logic, respectively. The computed  $A'_0$  and  $A'_1$  values were input to tile-2 and tile-3, configured as D flip-flops (DFFs). The DFFs registered the new state on the rising edge of the

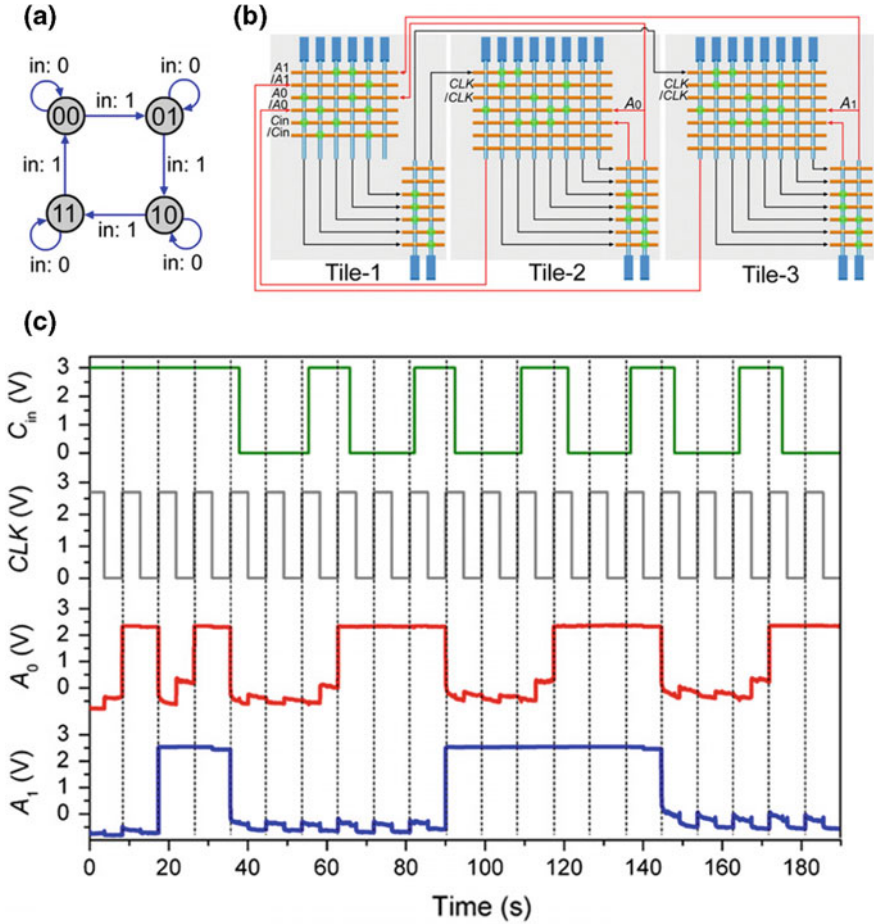


**Fig. 5.16** **a** Logic diagram of the FSM. **b** Schematic of the three-tile circuit of the nanoFSM. **c** The logic flow of the output state  $A_1$  and  $A_0$  with respect to the control input  $C_{in}$  and clock signal CLK as indicated in (b). Reproduced from [14]. Copyright 2014 the National Academy of Sciences of the United States of America

synchronized CLK, and then this registered state was instantly fed back as input to the half adder to compute the next-level state.

The logic flow of the nanoFSM for a variety of  $C_{in}$  and CLK sequences was investigated by continuously recording  $A_0$  and  $A_1$ . First, for a constant control input  $C_{in} = 1$  (Fig. 5.16c), the state  $A_1A_0$  underwent a complete logic circle from  $00 \rightarrow 01 \rightarrow 10 \rightarrow 11 \rightarrow 00$ , with each transition triggered by the CLK rising edge. The capability to fully control and lock the state by varying  $C_{in}$  is displayed for  $t = 38\text{--}190$  s. For example, for  $C_{in} = 0$  ( $t = 38\text{--}55$  s), the state  $A_1A_0 = 00$  was locked and not triggered to the next level at the two consecutive rising edges of CLK ( $t = \sim 45, 54$  s). As the control input was changed to  $C_{in} = 1$ , the state was unlocked and



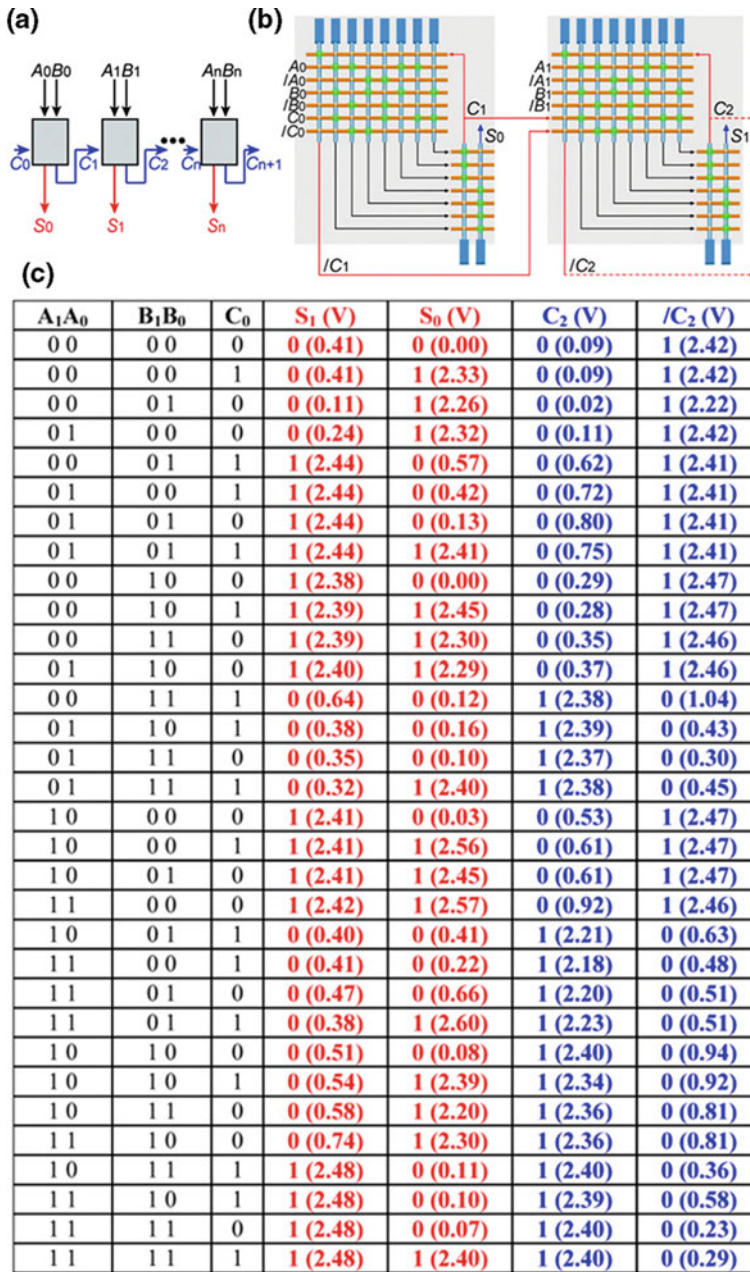


**Fig. 5.17** **a** Schematic of an n-bit full adder constructed from serial 1-bit full adders. **b** The two-tile circuit design for the 2-bit full adder. **c** Experimental truth table for the 2-bit full adder. The table consists of 32 sets of input combinations ( $A_1A_0, B_1B_0, C_0$ ) with the corresponding outputs  $S_1, S_0, C_2$ , and  $/C_2$ . The voltage output values are shown in brackets. The input values for 1 and 0 are 2.3 and 0 V, respectively. Reproduced from [14]. Copyright 2014 the National Academy of Sciences of the United States of America

moved to  $A_1A_0 = 01$  at the rising edge of CLK ( $t = \sim 63$  s). This high fidelity in the control was shown for all of the other states of 01, 10, and 11, which were locked when  $C_{in} = 0$  and continued in the logic loop when  $C_{in} = 1$  ( $t = 66\text{--}190$  s).

In addition, a multibit full adder can be realized by serial interconnection of 1-bit full adders (Fig. 5.17a). To investigate the feasibility of extending the number of cascaded tiles, the authors reprogrammed the circuit to a 2-bit full adder. In this cascaded two-tile circuit (Fig. 5.17b), each 1-bit full adder computed the sum  $S_i = A_i \oplus B_i \oplus C_i$  carry-out  $C_{i+1} = A_i \cdot B_i + A_i \cdot C_i + B_i \cdot C_i$  ( $i = 1, 2$ ; “+” denotes OR logic), with the computed  $C_{i+1}$  and complementary/ $C_{i+1}$  serving as the input to the higher-bit adder. Overall, the 2-bit full adder computed the summation of  $A_1A_0 + B_1B_0 + C_0$ , with  $S_0$  and  $S_1$  the first and second digits of the sum and  $C_2$  the carry-out. Significantly, examination of the values for the complete 32-element truth table (Fig. 5.17c) demonstrated that the complete logic outputs for  $S_0$ ,  $S_1$ ,  $C_2$ , and  $\bar{C}_2$  were correct, and that their average logic 1 output voltages  $2.43 \pm 0.03$ ,  $2.39 \pm 0.12$ ,  $2.34 \pm 0.08$ , and  $2.43 \pm 0.06$  V, respectively, were well-matched relative to the common logic input 1 value, 2.3 V. These results strongly validated the feasibility of implementing >2-bit full adder to improved performances by cascading a larger number of tiles [14].

## 5.5 Future Directions and Challenges

NW-based nanoelectronic devices provide a robust approach to build integrated circuits in the deep sub-100-nm regime from the bottom up. They have been utilized to process, transmit and store information by taking advantage of the unique properties of nanoscale NW building blocks. These exquisite examples of a variety of NW-based nanoelectronics have well demonstrated the potential of utilizing the bottom-up synthesis paradigm and assembly for developing the next-generation electronic devices and integrated circuits. Nonetheless, in order to realize the complexity and functional level of current electronic industry that has been developed over the past half a century, several challenges need to be addressed. First, the uniformity of the synthesized NWs, including morphology, structure and doping level, needs to be further improved, as the variations on the obtained NW products can be detrimental to the resulting electronics, although defect tolerant architectures could be used to overcome in part these variations. Second and perhaps most challenging is the need to develop efficient and very large-scale assembly and organization of individual NW elements, including in 3D architectures. These challenges will require substantial effort focused on fundamental scientific issues related to controlling synthesis and assembly closer and closer to the atomic scale. Looking to the future, the bottom-up approach will open many unique opportunities for nanoelectronics, including the development of 3D multifunctional nanoelectronics, the realization of general-purpose nanoprocessors, and the ultimate seamless integration of electronics with biological systems, which will be discussed further in later chapters.

## References

1. G.E. Moore, Craming more components onto integrated circuits. *Electronics* **38**(8), 114–117 (1965)
2. M. Waldrop, The chips are down for Moore's law. *Nature* **530**(7589), 144–147 (2016)
3. D.J. Frank, R.H. Dennard, E. Nowak, P.M. Solomon, Y. Taur, H.-S.P. Wong, Device scaling limits of Si MOSFETs and their application dependencies. *Proc. IEEE* **89**(3), 259–288 (2001)
4. K. Likharev, J. Greer, A. Korkin, J. Labanowski, Nano and giga challenges in microelectronics, in *Nano and Giga Challenges in Microelectronics*, ed. by J. Greer, A. Korkin, J. Labanowski (Elsevier, Amsterdam, 2003), pp. 27–68
5. C.M. Lieber, Nanoscale science and technology: building a big future from small things. *MRS Bull.* **28**(07), 486–491 (2003)
6. W. Lu, C.M. Lieber, Semiconductor nanowires. *J. Phys. D Appl. Phys.* **39**(21), R387–R406 (2006)
7. W. Lu, C.M. Lieber, Nanoelectronics from the bottom up. *Nat. Mater.* **6**(11), 841–850 (2007)
8. W. Lu, P. Xie, C.M. Lieber, Nanowire transistor performance limits and applications. *IEEE T. Electron. Dev.* **55**(11), 2859–2876 (2008)
9. C.M. Lieber, Semiconductor nanowires: a platform for nanoscience and nanotechnology. *MRS Bull.* **36**(12), 1052–1063 (2011)
10. V. Schmidt, J.V. Wittemann, S. Senz, U. Gösele, Silicon nanowires: a review on aspects of their growth and their electrical properties. *Adv. Mater.* **21**(25–26), 2681–2702 (2009)
11. R.G. Hobbs, N. Petkov, J.D. Holmes, Semiconductor nanowire fabrication by bottom-up and top-down paradigms. *Chem. Mat.* **24**(11), 1975–1991 (2012)
12. C.M. Lieber, Z.L. Wang, Functional nanowires. *MRS Bull.* **32**(02), 99–108 (2007)
13. H. Yan, H.S. Choe, S. Nam, Y. Hu, S. Das, J.F. Klemic, J.C. Ellenbogen, C.M. Lieber, Programmable nanowire circuits for nanoprocessors. *Nature* **470**(7333), 240–244 (2011)
14. J. Yao, H. Yan, S. Das, J.F. Klemic, J.C. Ellenbogen, C.M. Lieber, Nanowire nanocomputer as a finite-state machine. *Proc. Natl. Acad. Sci. U.S.A.* **111**(7), 2431–2435 (2014)
15. W. Shim, J. Yao, C.M. Lieber, Programmable resistive-switch nanowire transistor logic circuits. *Nano Lett.* **14**(9), 5430–5436 (2014)
16. Y. Huang, X. Duan, Y. Cui, C.M. Lieber, Gallium nitride nanowire nanodevices. *Nano Lett.* **2**(2), 101–104 (2002)
17. X. Duan, Nanowire thin-film transistors: a new avenue to high-performance macroelectronics. *IEEE T. Electron. Dev.* **55**(11), 3056–3062 (2008)
18. D. Wang, Q. Wang, A. Javey, R. Tu, H. Dai, H. Kim, P.C. McIntyre, T. Krishnamohan, K.C. Saraswat, Germanium nanowire field-effect transistors with SiO<sub>2</sub> and high- $\kappa$  HfO<sub>2</sub> gate dielectrics. *Appl. Phys. Lett.* **83**(12), 2432–2434 (2003)
19. A.B. Greytak, L.J. Lauhon, M.S. Gudixsen, C.M. Lieber, Growth and transport properties of complementary germanium nanowire field-effect transistors. *Appl. Phys. Lett.* **84**(21), 4176–4178 (2004)
20. L. Zhang, R. Tu, H. Dai, Parallel core-shell metal-dielectric-semiconductor germanium nanowires for high-current surround-gate field-effect transistors. *Nano Lett.* **6**(12), 2785–2789 (2006)
21. Z. Zhong, F. Qian, D. Wang, C.M. Lieber, Synthesis of p-type gallium nitride nanowires for electronic and photonic nanodevices. *Nano Lett.* **3**(3), 343–346 (2003)
22. H.-Y. Cha, H. Wu, M. Chandrashekhara, Y. Choi, S. Chae, G. Koley, M. Spencer, Fabrication and characterization of pre-aligned gallium nitride nanowire field-effect transistors. *Nanotechnology* **17**(5), 1264 (2006)
23. S.A. Dayeh, D.P. Aplin, X. Zhou, P.K. Yu, E.T. Yu, D. Wang, High electron mobility InAs nanowire field-effect transistors. *Small* **3**(2), 326–332 (2007)
24. T. Bryllert, L.-E. Wernersson, L. Froberg, L. Samuelson, Vertical high-mobility wrap-gated InAs nanowire transistor. *IEEE Electr. Device L.* **27**(5), 323–325 (2006)

25. M.S. Arnold, P. Avouris, Z.W. Pan, Z.L. Wang, Field-effect transistors based on single semiconducting oxide nanobelts. *J. Phys. Chem. B* **107**(3), 659–663 (2003)
26. H.T. Ng, J. Han, T. Yamada, P. Nguyen, Y.P. Chen, M. Meyyappan, Single crystal nanowire vertical surround-gate field-effect transistor. *Nano Lett.* **4**(7), 1247–1252 (2004)
27. J. Goldberger, D.J. Sirbuly, M. Law, P. Yang, ZnO nanowire transistors. *J. Phys. Chem. B* **109**(1), 9–14 (2005)
28. E.N. Dattoli, Q. Wan, W. Guo, Y. Chen, X. Pan, W. Lu, Fully transparent thin-film transistor devices based on SnO<sub>2</sub> nanowires. *Nano Lett.* **7**(8), 2463–2469 (2007)
29. Q. Wan, E. Dattoli, W. Lu, Doping-dependent electrical characteristics of SnO<sub>2</sub> nanowires. *Small* **4**(4), 451–454 (2008)
30. Z.L. Wang, Piezopotential gated nanowire devices: piezotronics and piezo-phototronics. *Nano Today* **5**(6), 540–552 (2010)
31. A.M. Morales, C.M. Lieber, A laser ablation method for the synthesis of crystalline semiconductor nanowires. *Science* **279**(5348), 208–211 (1998)
32. Y. Cui, X. Duan, J. Hu, C.M. Lieber, Doping and electrical transport in silicon nanowires. *J. Phys. Chem. B* **104**(22), 5213–5216 (2000)
33. X. Duan, Y. Huang, Y. Cui, J. Wang, C.M. Lieber, Indium phosphide nanowires as building blocks for nanoscale electronic and optoelectronic devices. *Nature* **409**(6816), 66–69 (2001)
34. Y. Cui, C.M. Lieber, Functional nanoscale electronic devices assembled using silicon nanowire building blocks. *Science* **291**(5505), 851–853 (2001)
35. Y. Huang, X. Duan, Y. Cui, L.J. Lauhon, K.-H. Kim, C.M. Lieber, Logic gates and computation from assembled nanowire building blocks. *Science* **294**(5545), 1313–1317 (2001)
36. Y. Cui, Z. Zhong, D. Wang, W.U. Wang, C.M. Lieber, High performance silicon nanowire field effect transistors. *Nano Lett.* **3**(2), 149–152 (2003)
37. X. Duan, C. Niu, V. Sahi, J. Chen, J.W. Parce, S. Empedocles, J.L. Goldman, High-performance thin-film transistors using semiconductor nanowires and nanoribbons. *Nature* **425**(6955), 274–278 (2003)
38. G. Zheng, W. Lu, S. Jin, C.M. Lieber, Synthesis and fabrication of high-performance n-type silicon nanowire transistors. *Adv. Mater.* **16**(21), 1890–1893 (2004)
39. S. Jin, D. Whang, M.C. McAlpine, R.S. Friedman, Y. Wu, C.M. Lieber, Scalable interconnection and integration of nanowire devices without registration. *Nano Lett.* **4**(5), 915–919 (2004)
40. S.-M. Koo, Q. Li, M.D. Edelstein, C.A. Richter, E.M. Vogel, Enhanced channel modulation in dual-gated silicon nanowire transistors. *Nano Lett.* **5**(12), 2519–2523 (2005)
41. D. Whang, S. Jin, Y. Wu, C.M. Lieber, Large-scale hierarchical organization of nanowire arrays for integrated nanosystems. *Nano Lett.* **3**(9), 1255–1259 (2003)
42. A. Javey, S. Nam, R.S. Friedman, H. Yan, C.M. Lieber, Layer-by-layer assembly of nanowires for three-dimensional, multifunctional electronics. *Nano Lett.* **7**(3), 773–777 (2007)
43. G. Yu, C.M. Lieber, Assembly and integration of semiconductor nanowires for functional nanosystems. *Pure Appl. Chem.* **82**(12), 2295–2314 (2010)
44. J. Yao, H. Yan, C.M. Lieber, A nanoscale combing technique for the large-scale assembly of highly aligned nanowires. *Nat. Nanotechnol.* **8**(5), 329–335 (2013)
45. J. Goldberger, A.I. Hochbaum, R. Fan, P. Yang, Silicon vertically integrated nanowire field effect transistors. *Nano Lett.* **6**(5), 973–977 (2006)
46. B. Yang, K. Buddharaju, S. Teo, N. Singh, G. Lo, D. Kwong, Vertical silicon-nanowire formation and gate-all-around MOSFET. *IEEE Electr. Device L.* **29**(7), 791–794 (2008)
47. J.-E. Yang, C.-B. Jin, C.-J. Kim, M.-H. Jo, Band-gap modulation in single-crystalline Si<sub>1-x</sub>Ge<sub>x</sub> nanowires. *Nano Lett.* **6**(12), 2679–2684 (2006)
48. H.-K. Seong, E.-K. Jeon, M.-H. Kim, H. Oh, J.-O. Lee, J.-J. Kim, H.-J. Choi, Interface charge induced p-type characteristics of aligned Si<sub>1-x</sub>Ge<sub>x</sub> nanowires. *Nano Lett.* **8**(11), 3656–3661 (2008)

49. M. Amato, M. Palumbo, R. Rurali, S. Ossicini, Silicon-germanium nanowires: chemistry and physics in play, from basic principles to advanced applications. *Chem. Rev.* **114**(2), 1371–1412 (2014)
50. Y. Wu, J. Xiang, C. Yang, W. Lu, C.M. Lieber, Single-crystal metallic nanowires and metal/semiconductor nanowire heterostructures. *Nature* **430**(6995), 61–65 (2004)
51. E. Lind, A.I. Persson, L. Samuelson, L.-E. Wernersson, Improved subthreshold slope in an InAs nanowire heterostructure field-effect transistor. *Nano Lett.* **6**(9), 1842–1846 (2006)
52. T.-T. Ho, Y. Wang, S. Eichfeld, K.-K. Lew, B. Liu, S.E. Mohny, J.M. Redwing, T.S. Mayer, In situ axially doped n-channel silicon nanowire field-effect transistors. *Nano Lett.* **8**(12), 4359–4364 (2008)
53. F. Schäffler, High-mobility Si and Ge structures. *Semicond. Sci. Tech.* **12**(12), 1515–1549 (1997)
54. C.G. Van de Walle, R.M. Martin, Theoretical calculations of heterojunction discontinuities in the Si/Ge system. *Phys. Rev. B* **34**(8), 5621 (1986)
55. W. Lu, J. Xiang, B.P. Timko, Y. Wu, C.M. Lieber, One-dimensional hole gas in germanium/silicon nanowire heterostructures. *Proc. Natl. Acad. Sci. U.S.A.* **102**(29), 10046–10051 (2005)
56. J. Xiang, W. Lu, Y. Hu, Y. Wu, H. Yan, C.M. Lieber, Ge/Si nanowire heterostructures as high-performance field-effect transistors. *Nature* **441**(7092), 489–493 (2006)
57. Y. Hu, J. Xiang, G. Liang, H. Yan, C.M. Lieber, Sub-100 nanometer channel length Ge/Si nanowire transistors with potential for 2 THz switching speed. *Nano Lett.* **8**(3), 925–930 (2008)
58. D.C. Dillen, K. Kim, E.-S. Liu, E. Tutuc, Radial modulation doping in core-shell nanowires. *Nat. Nanotechnol.* **9**, 116–120 (2014)
59. Y. Li, J. Xiang, F. Qian, S. Gradecak, Y. Wu, H. Yan, D.A. Blom, C.M. Lieber, Dopant-free GaN/AlN/AlGaIn radial nanowire heterostructures as high electron mobility transistors. *Nano Lett.* **6**(7), 1468–1473 (2006)
60. X. Jiang, Q. Xiong, S. Nam, F. Qian, Y. Li, C.M. Lieber, InAs/InP radial nanowire heterostructures as high electron mobility devices. *Nano Lett.* **7**(10), 3214–3218 (2007)
61. K. Tomioka, M. Yoshimura, T. Fukui, A III-V nanowire channel on silicon for high-performance vertical transistors. *Nature* **488**(7410), 189–192 (2012)
62. A.W. Dey, J. Svensson, M. Ek, E. Lind, C. Thelander, L.-E. Wernersson, Combining axial and radial nanowire heterostructures: Radial Esaki diodes and tunnel field-effect transistors. *Nano Lett.* **13**(12), 5919–5924 (2013)
63. J.-Y. Yu, S.-W. Chung, J.R. Heath, Silicon nanowires: preparation, device fabrication, and transport properties. *J. Phys. Chem. B* **104**(50), 11864–11870 (2000)
64. J.-H. Ahn, H.-S. Kim, K.J. Lee, S. Jeon, S.J. Kang, Y. Sun, R.G. Nuzzo, J.A. Rogers, Heterogeneous three-dimensional electronics by use of printed semiconductor nanomaterials. *Science* **314**(5806), 1754–1757 (2006)
65. S. Nam, X. Jiang, Q. Xiong, D. Ham, C.M. Lieber, Vertically integrated, three-dimensional nanowire complementary metal-oxide-semiconductor circuits. *Proc. Natl. Acad. Sci. U.S.A.* **106**(50), 21035–21038 (2009)
66. J.-P. Colinge, C.-W. Lee, A. Afzaljian, N.D. Akhavan, R. Yan, I. Ferain, P. Razavi, B. O’Neill, A. Blake, M. White, Nanowire transistors without junctions. *Nat. Nanotechnol.* **5**(3), 225–229 (2010)
67. A.M. Ionescu, Electronic devices: nanowire transistors made easy. *Nat. Nanotechnol.* **5**(3), 178–179 (2010)
68. A. Konar, J. Mathew, K. Nayak, M. Bajaj, R.K. Pandey, S. Dhara, K. Murali, M.M. Deshmukh, Carrier transport in high mobility InAs nanowire junctionless transistors. *Nano Lett.* **15**(3), 1684–1690 (2015)
69. K. Haraguchi, T. Katsuyama, K. Hiruma, K. Ogawa, GaAs p-n junction formed in quantum wire crystals. *Appl. Phys. Lett.* **60**(6), 745–747 (1992)

70. M.S. Gudiksen, L.J. Lauhon, J. Wang, D.C. Smith, C.M. Lieber, Growth of nanowire superlattice structures for nanoscale photonics and electronics. *Nature* **415**(6872), 617–620 (2002)
71. T.J. Kempa, B. Tian, D.R. Kim, J. Hu, X. Zheng, C.M. Lieber, Single and tandem axial p-i-n nanowire photovoltaic devices. *Nano Lett.* **8**(10), 3456–3460 (2008)
72. E. Tutuc, J. Appenzeller, M.C. Reuter, S. Guha, Realization of a linear germanium nanowire p-n junction. *Nano Lett.* **6**(9), 2070–2074 (2006)
73. S. Hoffmann, J. Bauer, C. Ronning, T. Stelzner, J. Michler, C. Ballif, V. Sivakov, S. Christiansen, Axial p-n junctions realized in silicon nanowires by ion implantation. *Nano Lett.* **9**(4), 1341–1344 (2009)
74. X. Jiang, B. Tian, J. Xiang, F. Qian, G. Zheng, H. Wang, L. Mai, C.M. Lieber, Rational growth of branched nanowire heterostructures with synthetically encoded properties and function. *Proc. Natl. Acad. Sci. U.S.A.* **108**(30), 12212–12216 (2011)
75. Z. Jiang, Q. Qing, P. Xie, R. Gao, C.M. Lieber, Kinked p-n junction nanowire probes for high spatial resolution sensing and intracellular recording. *Nano Lett.* **12**(3), 1711–1716 (2012)
76. C.H. Roth, L.L. Kinney, *Fundamentals of logic design*, 7th edn. (Cengage Learning, Stamford, Connecticut, 2014)
77. W.I. Park, J.S. Kim, G.C. Yi, H.J. Lee, ZnO nanorod logic circuits. *Adv. Mater.* **17**(11), 1393–1397 (2005)
78. R.-M. Ma, L. Dai, H.-B. Huo, W.-J. Xu, G. Qin, High-performance logic circuits constructed on single CdS nanowires. *Nano Lett.* **7**(11), 3300–3304 (2007)
79. W. Wu, Y. Wei, Z.L. Wang, Strain-gated piezotronic logic nanodevices. *Adv. Mater.* **22**(42), 4711–4715 (2010)
80. S.R. Raza, P. JináJeon, Long single ZnO nanowire for logic and memory circuits: NOT, NAND, NOR gate, and SRAM. *Nanoscale* **5**(10), 4181–4185 (2013)
81. R.S. Friedman, M.C. McAlpine, D.S. Ricketts, D. Ham, C.M. Lieber, High-speed integrated nanowire circuits. *Nature* **434**(7037), 1085 (2005)
82. D. Kim, J. Ahn, H. Kim, K.J. Lee, T. Kim, C. Yu, R.G. Nuzzo, J.A. Rogers, Complementary logic gates and ring oscillators on plastic substrates by use of printed ribbons of single-crystalline silicon. *IEEE Electr. Device L.* **29**(1), 73 (2008)
83. R.-G. Huang, D. Tham, D. Wang, J.R. Heath, High performance ring oscillators from 10-nm wide silicon nanowire field-effect transistors. *Nano Res.* **4**(10), 1005–1012 (2011)
84. Z. Zhong, D. Wang, Y. Cui, M.W. Bockrath, C.M. Lieber, Nanowire crossbar arrays as address decoders for integrated nanosystems. *Science* **302**(5649), 1377–1379 (2003)
85. C. Yang, Z. Zhong, C.M. Lieber, Encoding electronic properties by synthesis of axial modulation-doped silicon nanowires. *Science* **310**(5752), 1304–1307 (2005)
86. R. Beckman, E. Johnston-Halperin, Y. Luo, J.E. Green, J.R. Heath, Bridging dimensions: demultiplexing ultrahigh-density nanowire circuits. *Science* **310**(5747), 465–468 (2005)
87. M. Schwartzman, D. Tsvion, D. Mahalu, O. Raslin, E. Joselevich, Self-integration of nanowires into circuits via guided growth. *Proc. Natl. Acad. Sci. U.S.A.* **110**(38), 15195–15200 (2013)
88. A. DeHon, P. Lincoln, J.E. Savage, Stochastic assembly of sublithographic nanoscale interfaces. *IEEE T. Nanotechnol.* **2**(3), 165–174 (2003)
89. W.D. Brown, J.E. Brewer, *Nonvolatile Semiconductor Memory Technology* (IEEE, New York, 1998)
90. B. Keeth, R.J. Baker, B. Johnson, F. Lin, *DRAM Circuit Design: Fundamental and High-Speed Topics* (Wiley, Hoboken, New Jersey, 2008)
91. J.-S. Lee, Progress in non-volatile memory devices based on nanostructured materials and nanofabrication. *J. Mater. Chem.* **21**(37), 14097–14112 (2011)
92. O. Hayden, R. Agarwal, W. Lu, Semiconductor nanowire devices. *Nano Today* **3**(5), 12–22 (2008)
93. D. Ielmini, C. Cagli, F. Nardi, Y. Zhang, Nanowire-based resistive switching memories: devices, operation and scaling. *J. Phys. D Appl. Phys.* **46**(7), 074006 (2013)

94. L. Chua, Resistance switching memories are memristors. *Appl. Phys. A* **102**(4), 765–783 (2011)
95. Y. Dong, G. Yu, M.C. McAlpine, W. Lu, C.M. Lieber, Si/a-Si core/shell nanowires as nonvolatile crossbar switches. *Nano Lett.* **8**(2), 386–391 (2008)
96. R. Waser, M. Aono, Nanoionics-based resistive switching memories. *Nat. Mater.* **6**(11), 833–840 (2007)
97. P. Cappelletti, C. Golla, P. Olivo, E. Zanoni, *Flash Memory* (Kluwer Academic Publishers, New York, 1999)
98. H. Ishiwara, M. Okuyama, Y. Arimoto, *Ferroelectric Random Access Memories: Fundamentals and Applications* (Springer, New York, 2004)
99. B. Lei, C. Li, D. Zhang, Q. Zhou, K. Shung, C. Zhou, Nanowire transistors with ferroelectric gate dielectrics: enhanced performance and memory effects. *Appl. Phys. Lett.* **84**(22), 4553–4555 (2004)
100. L. Liao, H. Fan, B. Yan, Z. Zhang, L. Chen, B. Li, G. Xing, Z. Shen, T. Wu, X. Sun, Ferroelectric transistors with nanowire channel: toward nonvolatile memory applications. *ACS Nano* **3**(3), 700–706 (2009)
101. J.I. Sohn, S.S. Choi, S.M. Morris, J.S. Bendall, H.J. Coles, W.-K. Hong, G. Jo, T. Lee, M.E. Welland, Novel nonvolatile memory with multibit storage based on a ZnO nanowire transistor. *Nano Lett.* **10**(11), 4316–4320 (2010)
102. Y.T. Lee, P.J. Jeon, K.H. Lee, R. Ha, H.J. Choi, S. Im, Ferroelectric nonvolatile nanowire memory circuit using a single ZnO nanowire and copolymer top layer. *Adv. Mater.* **24**(22), 3020–3025 (2012)
103. H.P. Wong, S. Raoux, S. Kim, J. Liang, J.P. Reifenberg, B. Rajendran, M. Asheghi, K.E. Goodson, Phase change memory. *Proc. IEEE* **98**(12), 2201–2227 (2010)
104. X. Duan, Y. Huang, C.M. Lieber, Nonvolatile memory and programmable logic from molecule-gated nanowires. *Nano Lett.* **2**(5), 487–490 (2002)
105. S.I. Kim, J.H. Lee, Y.W. Chang, S.S. Hwang, K.-H. Yoo, Reversible resistive switching behaviors in NiO nanowires. *Appl. Phys. Lett.* **93**(3), 033503 (2008)
106. K. Oka, T. Yanagida, K. Nagashima, T. Kawai, J.-S. Kim, B.H. Park, Resistive-switching memory effects of NiO nanowire/metal junctions. *J. Am. Chem. Soc.* **132**(19), 6634–6635 (2010)
107. K. Nagashima, T. Yanagida, K. Oka, M. Taniguchi, T. Kawai, J.-S. Kim, B.H. Park, Resistive switching multistate nonvolatile memory effects in a single cobalt oxide nanowire. *Nano Lett.* **10**(4), 1359–1363 (2010)
108. Y.-D. Chiang, W.-Y. Chang, C.-Y. Ho, C.-Y. Chen, C.-H. Ho, S.-J. Lin, T.-B. Wu, H. He, Single-ZnO-nanowire memory. *IEEE T. Electron. Dev.* **58**(6), 1735–1740 (2011)
109. K. Oka, T. Yanagida, K. Nagashima, H. Tanaka, T. Kawai, Nonvolatile bipolar resistive memory switching in single crystalline NiO heterostructured nanowires. *J. Am. Chem. Soc.* **131**(10), 3434–3435 (2009)
110. L. He, Z.-M. Liao, H.-C. Wu, X.-X. Tian, D.-S. Xu, G.L. Cross, G.S. Duesberg, I. Shvets, D.-P. Yu, Memory and threshold resistance switching in Ni/NiO core–shell nanowires. *Nano Lett.* **11**(11), 4601–4606 (2011)
111. C. Cagli, F. Nardi, B. Harteneck, Z. Tan, Y. Zhang, D. Ielmini, Resistive-switching crossbar memory based on Ni–NiO core-shell nanowires. *Small* **7**(20), 2899–2905 (2011)
112. Y. Chen, G.-Y. Jung, D.A. Ohlberg, X. Li, D.R. Stewart, J.O. Jeppesen, K.A. Nielsen, J.F. Stoddart, R.S. Williams, Nanoscale molecular-switch crossbar circuits. *Nanotechnology* **14**(4), 462 (2003)
113. J.E. Green, J.W. Choi, A. Boukai, Y. Bunimovich, E. Johnston-Halperin, E. DeIonno, Y. Luo, B.A. Sheriff, K. Xu, Y.S. Shin, A 160-kilobit molecular electronic memory patterned at 1011 bits per square centimetre. *Nature* **445**(7126), 414–417 (2007)
114. Y. Sun, H. Yu, N. Singh, N. Shen, G. Lo, D. Kwong, Multibit programmable flash memory realized on vertical Si nanowire channel. *IEEE Electr. Device L.* **31**(5), 390–392 (2010)

115. W.-H. Chen, C.-H. Liu, Q.-L. Li, Q.-J. Sun, J. Liu, X. Gao, X. Sun, S.-D. Wang, Intrinsic Ge nanowire nonvolatile memory based on a simple core-shell structure. *Nanotechnology* **25**(7), 075201 (2014)
116. X. Zhu, Q. Li, D.E. Ioannou, D. Gu, J.E. Bonevich, H. Baumgart, J.S. Suehle, C.A. Richter, Fabrication, characterization and simulation of high performance Si nanowire-based non-volatile memory cells. *Nanotechnology* **22**(25), 254020 (2011)
117. H.A. Nilsson, C. Thelander, L.E. Fröberg, J.B. Wagner, L. Samuelson, Nanowire-based multiple quantum dot memory. *Appl. Phys. Lett.* **89**(16), 163101 (2006)
118. T. Shaw, S. Trolier-McKinstry, P. McIntyre, The properties of ferroelectric films at small dimensions. *Annu. Rev. Mater. Sci.* **30**(1), 263–298 (2000)
119. A. Chung, J. Deen, J.-S. Lee, M. Meyyappan, Nanoscale memory devices. *Nanotechnology* **21**(41), 412001 (2010)
120. Y. Kato, Y. Kaneko, H. Tanaka, K. Kaibara, S. Koyama, K. Isogai, T. Yamada, Y. Shimada, Overview and future challenge of ferroelectric random access memory technologies. *Jpn. J. Appl. Phys.* **46**(4S), 2157 (2007)
121. M. Wuttig, N. Yamada, Phase-change materials for rewriteable data storage. *Nat. Mater.* **6** (11), 824–832 (2007)
122. Y. Jung, S.-H. Lee, D.-K. Ko, R. Agarwal, Synthesis and characterization of Ge<sub>2</sub>Sb<sub>2</sub>Te<sub>5</sub> nanowires with memory switching effect. *J. Am. Chem. Soc.* **128**(43), 14026–14027 (2006)
123. S.-H. Lee, D.-K. Ko, Y. Jung, R. Agarwal, Size-dependent phase transition memory switching behavior and low writing currents in GeTe nanowires. *Appl. Phys. Lett.* **89**(22), 223116 (2006)
124. D. Yu, J. Wu, Q. Gu, H. Park, Germanium telluride nanowires and nanohelices with memory-switching behavior. *J. Am. Chem. Soc.* **128**(25), 8148–8149 (2006)
125. S. Meister, H. Peng, K. McIlwrath, K. Jarausch, X.F. Zhang, Y. Cui, Synthesis and characterization of phase-change nanowires. *Nano Lett.* **6**(7), 1514–1517 (2006)
126. S.-H. Lee, Y. Jung, R. Agarwal, Highly scalable non-volatile and ultra-low-power phase-change nanowire memory. *Nat. Nanotechnol.* **2**(10), 626–630 (2007)
127. Y. Jung, C.-Y. Yang, S.-H. Lee, R. Agarwal, Phase-change Ge-Sb nanowires: synthesis, memory switching, and phase-instability. *Nano Lett.* **9**(5), 2103–2108 (2009)
128. M. Lu, *Arithmetic and Logic in Computer Systems* (Wiley, Hoboken, New Jersey, 2005)
129. J.J. Sparkes, *Transistor Switching and Sequential Circuits* (Pergamon Press, Oxford, 1969)
130. H. Kaeslin, *Digital Integrated Circuit Design: From VLSI Architectures to CMOS Fabrication* (Cambridge University Press, New York, 2008)



# Chapter 6

## Nanophotonics

**Abstract** Single crystalline semiconductor NWs have been extensively investigated as building blocks for ultra-small and entirely new electronic and photonic devices, due to their unique electronic and optical properties. The sub-wavelength diameters of NW structures and tunable energy band gaps provide a host of advantages for investigating generation, detection, amplification and modulation of light. Photonic platforms using NW building blocks also offers the promise of integrated functionalities at dimensions compatible with top-down fabricated electronics. With rational design and synthesis of the NW structures, the capability of controlling and manipulating these structures on surface to form single devices and networks is a crucial step for realizing these chemically synthesized NWs into photonic circuitry. In this chapter we will review progress made in the area of NW photonic devices, including waveguides, light-emitting diodes, lasers, and photodetectors.

### 6.1 Introduction

The field of photonics in essence focuses on the control of photons in free space or in matter [1]. Manipulation of photons in semiconductor bulk crystals and thin films has culminated in breakthroughs such as light-emitting diodes (LEDs) and lasers [2]. With the shrinking of devices to smaller length scales in the microelectronics industry, the continuing success of photonic technologies also relies on the discovery of new optical materials, integration strategies and the miniaturization of optoelectronic devices for better performance, lower cost and lower power consumption. Although state-of-the-art lithography technologies are capable of fabricating nanostructured features and functionalities [3], chemically grown NWs still possess unique advantages, including single-crystalline, diameter and morphology controlled structures with near atomically smooth surfaces, as well as the potential for hetero-integration with electronics and other materials via bottom-up assembly [4–7]. NW photonics is a particularly exciting frontier due to the ability to precisely control NW composition and hence the resulting bandgap, which cannot be

accomplished with CNTs, and using a combination of nanolithography tools, it is possible to assemble photonic circuits with designed functions [8–13]. NWs synthesized from direct bandgap semiconductors have shown tremendous promise for assembling subwavelength nanophotonic devices for the generation, waveguiding, and detection of light at the nanoscale [10]. Nanophotonic devices such as optically-pumped and electrically-driven NW lasers, waveguides, light emitting diodes (LEDs), photodetectors, have been successfully demonstrated [8, 9, 11–13]. In addition to miniaturization of devices, NW-based photonic systems can provide many interesting and novel device concepts in comparison to planar technology. The potential for co-assembling nanoscale light sources and detectors, fabricated from a variety of different materials, opens up unique opportunities for integrated photonic systems as well as the integration of nanophotonic systems with silicon micro- and nano-electronics [14]. In this chapter, we will discuss the optical properties, including photoluminescence and nonlinear responses, of semiconductor NWs, and review the significant progress made in the field of semiconductor NW photonic devices. Other comprehensive reviews of NW photonics can be found in [8, 12, 13].

## 6.2 Optical Phenomena

### 6.2.1 *Photoluminescence from Nanowire Structures*

Photoluminescence (PL) is a light emission process in which a substance absorbs and then re-radiates photons. PL data collected from individual direct-bandgap NWs can reveal a wealth of information, both in terms of characterization of the materials and optical properties, such as band-edge emission, trap states, radiative efficiency, carrier and photon confinement [8, 10]. In this section, we briefly introduce PL from homogeneous NWs and NW heterostructures.

#### 6.2.1.1 Homogeneous Nanowires

The optical properties of homogeneous NWs, including GaAs [15–17], InP [18, 19], GaN [20], ZnO [21], ZnS [22], ZnSe [23], CdS [24], CdSe [25], Si [26], have been extensively studied by steady state and transient PL spectroscopy. The results from these studies show that individual growth methods and conditions can strongly affect NW optical properties in terms of emission intensity, spectral width and peak position, and the presence of long wavelength components from impurity states that emit radiatively. High quality NWs synthesized under controlled conditions at high temperatures typically emit brightly with a spectral peak near the band edge. The width of the PL spectra at room temperature reveal critical information about the quality of the NWs with narrower widths ( $\sim 20\text{--}30$  nm)

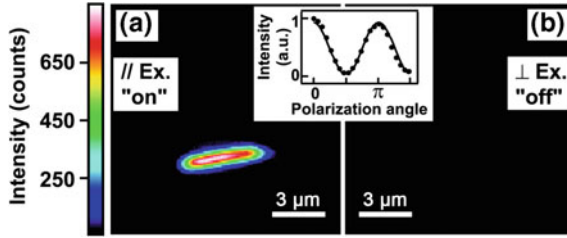


**Fig. 6.1** **a** PL image of a single 20-nm InP NW with the exciting laser polarized along the wire axis. **b** PL image of the same NW as in **(a)** under perpendicular excitation. *Inset*, variation of overall PL intensity as a function of excitation polarization angle with respect to the NW axis. Reproduced from [18]. Copyright 2001 the American Association for the Advancement of Science

corresponding to high optical quality of NWs. The narrower widths can be attributed to lower defect density within and at the passivated surfaces of the NWs [8].

Optical absorption and emission from NWs have been found to be predominantly polarized along the long axis of the wires [18, 27]. The observed polarization anisotropy can be explained from a purely classical perspective as arising from the anisotropic geometry of the NWs—where the NW diameter is much smaller than the wavelength of light but the length is much larger—and also due to the large dielectric mismatch between a free standing NW and its surrounding environment [18]. PL images of single InP NWs recorded at room temperature with the polarization of the exciting laser both parallel (Fig. 6.1a) and perpendicular (Fig. 6.1b) to the NW showed a large polarization anisotropy with the observed PL turning from “on” to “off” as the excitation polarization was rotated from parallel to perpendicular. Integration of the emission as a function of excitation angle showed that the intensity exhibited the expected periodic dependence on angle (Fig. 6.1, inset).

### 6.2.1.2 Axial Heterostructures

PL measurements provide a unique means to verify quantum confinement of charge carriers in NW heterostructures. PL studies have been carried out for several II–VI and III–V direct-gap systems, including ZnSe–CdSe [28], ZnO–ZnMgO [29], InAs–GaAs [30], InAs–InP [31] and AlGaIn–GaIn [32]. Park et al. [29] observed a clear blue-shift in the PL peak energy of ZnO–ZnMgO nanorod heterostructures with decreasing ZnO well width, demonstrating quantum confinement in the axial direction. Panev et al. [30] observed sharp exciton emission from InAs quantum dots inside GaAs NW hosts. The peak energies emitted by the InAs dots were substantially blue shifted from bulk InAs, indicating that substantial alloying with the GaAs NW occurred. Accordingly, the effects of possible confinement potentials on the peak energy could not be determined. Poole et al. [31] synthesized InP–InAs–InP NWs on InP substrates without catalyst. During PL excitation at low power densities, a single well-defined peak is observed at 921 meV. At higher power densities, excited state peaks are observed at energy spacings consistent with

the quantum confinement of excitons within the estimated well widths. More recently, Holmes et al. [32] demonstrated triggered single photon emission at room temperature from a site-controlled III–nitride quantum dot embedded in a NW. The photon statistics are found to be insensitive to temperature, in contrast to other QD-based triggered single photon emitters which exhibit a pronounced degradation at elevated temperatures. Arrays of such single photon emitters were proposed for room-temperature quantum information processing applications such as on-chip quantum communication [32].

### 6.2.1.3 Radial Heterostructures

Confinement and quantum confinement effects in radial NW heterostructures have also been verified by PL spectra [33–35]. In 2004, Qian et al. [33] obtained PL spectra from  $n$ -GaN/InGaN/ $p$ -GaN core/shell/shell (CSS) structures, exhibiting a dominant emission peak at 448 nm. This wavelength is consistent with band-edge emission from an InGaN structure of composition  $\text{In}_{0.18}\text{Ga}_{0.82}\text{N}$ . The InGaN emission is approximately 20 times stronger than the small GaN band-edge emission peak also present in the PL spectrum, which shows that the much smaller volume InGaN shell in the CSS structures provides an efficient region for radiative recombination. In 2008, the same group [34] reported the growth of highly uniform  $(\text{InGaN}/\text{GaN})_n$  multi-quantum-well (MQW) core/shell NW heterostructures, with  $n = 3, 13$  and  $26$  and each InGaN well thicknesses of 1–3 nm (Fig. 6.2a). PL spectra from individual 26-MQW NWs containing different indium compositions are displayed in Fig. 6.2b, c. It can be seen that the InGaN emission peak red-shifts from 382 to 440 and then to 484 nm (Fig. 6.2c) with increasing indium composition. The peak broadening with In% is consistent with InGaN planar structures. Later, the synthesis of AlN/GaN MQW NW structures has also been demonstrated. The observed blue-shifted emission of PL spectra was attributed to the quantum confinement in the GaN layers [35].

## 6.2.2 Nonlinear Processes

In linear optics, the dielectric polarization  $P$  depends linearly to the electric field,  $E$ , of the light,  $P = \varepsilon_0 \chi^{(1)} E$ , where  $\chi^{(1)}$  is the first order susceptibility tensor and  $\varepsilon_0$  is the vacuum permittivity. While this consideration is sufficient at low incident field strengths, when the field strength increases it is possible for higher order terms to be important. In general,  $P$  can be expressed as a series expansion in powers of  $E$  as:

$$P = P^{(1)} + P^{(2)} + P^{(3)} + \dots = \varepsilon_0 \left[ \chi^{(1)} E + \chi^{(2)} E^2 + \chi^{(3)} E^3 + \dots \right]$$

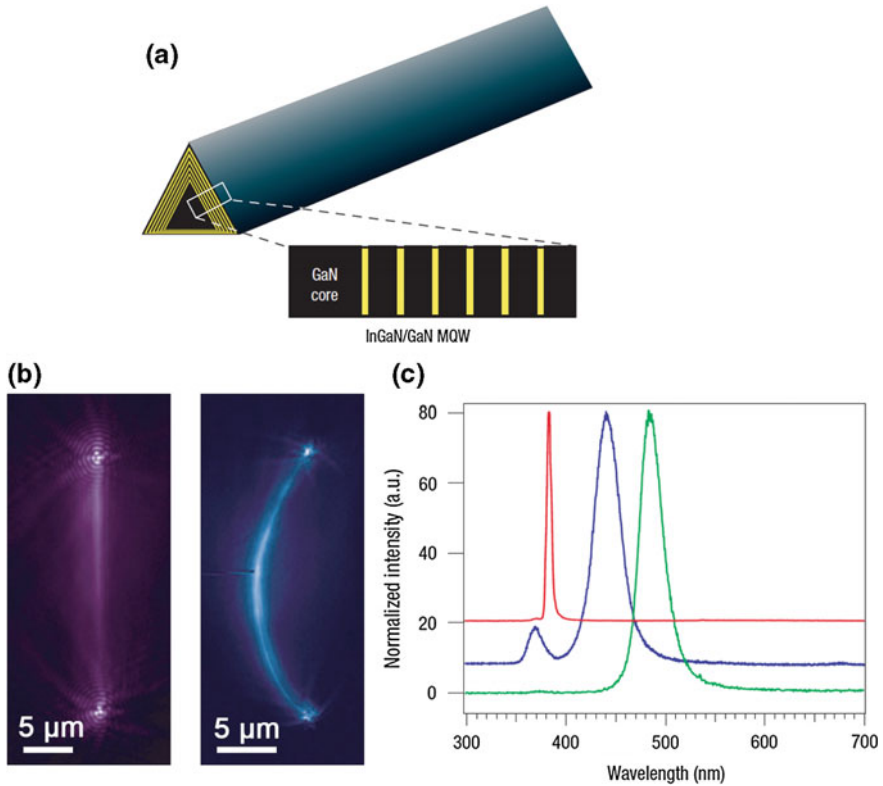


**Fig. 6.2** **a** Schematic diagram of an MQW NW. The InGaN layer is indicated in *yellow color*. **b** PL images (*false color*) recorded from GaN/In<sub>0.05</sub>Ga<sub>0.95</sub>N (*left*) and GaN/In<sub>0.23</sub>Ga<sub>0.77</sub>N (*right*) MQW NW structures. **c** PL spectra collected from three representative 26MQW NW structures with increasing In composition. Reproduced from [34]. Copyright 2008 Nature Publishing Group

where  $\chi^{(2)}$  and  $\chi^{(3)}$  are the second- and third-order nonlinear optical susceptibilities [36, 37]. Nonlinear optical (NLO) processes are often referred to as “N wave mixing” where N is the number of photons involved (including the emitted one). Many nanostructures exhibit strong intrinsic NLO signals under tight focusing conditions. Combining NLO signals with scanning microscopy has generated an array of label-free imaging modalities for material and biological studies [38, 39]. Unlike linear optical microscopy, NLO microscopy offers inherent 3D spatial resolution, relatively large optical penetration into tissues with near infrared (NIR) excitation, and reduced photo-damage due to reduced optical interaction with endogenous molecules [38, 39]. This section introduces different NLO processes in semiconductor NWs (Fig. 6.3), including second harmonic generation (SHG), third-harmonic generation (THG), four-wave mixing (FWM), and stimulated Raman scattering (SRS), with an emphasis on SHG.

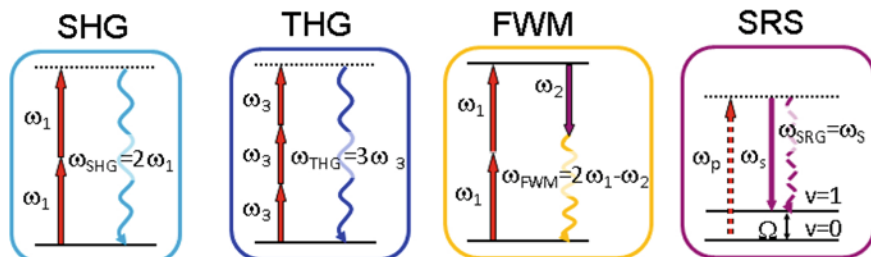


**Fig. 6.3** Energy diagrams of NLO modalities. *Solid lines* represent electronic and vibrational states of molecules, *dashed lines* are virtual states. The *straight arrows* are excitation beams, the *wavy arrows* are output signal beams. The *gray arrows* represent relaxation in electronically excited states.  $\omega_1$  and  $\omega_2$  are excitation beams.  $\Omega$  is the frequency of vibrational transition between vibrational ground state and vibrationally excited state. Reproduced from [38]. Copyright 2011 John Wiley and Sons

### 6.2.2.1 Second Harmonic Generation

SHG is a second-order NLO process in which two incident photons ( $\omega_1$ ) are converted to one scattered photon ( $2\omega_1$ ) with energy equal to the sum of the excitation photons. Since all even-order nonlinear susceptibilities  $\chi^{(n)}$  vanish in centrosymmetric media, SHG cannot occur in materials with inversion symmetry, such as bulk Si [36, 37]. As the excitation beam and SHG have different wavelength in the same material, if no specific measures are taken, there will be a phase mismatch, where the phase difference  $\Delta\varphi$  after propagating a distance  $z$  will be  $\Delta\varphi = (k_{2\omega} - 2k_{\omega})z$ , where  $k_{2\omega}$  and  $k_{\omega}$  are wave vectors at frequencies  $2\omega_1$  and  $\omega_1$ . The efficient generation of SHG requires phase matching,  $\Delta\varphi = 0$ , over the whole length of the material,  $L$ , otherwise SHG waves will interfere destructively, resulting in decreased intensity [36, 37]. If  $\Delta\varphi$  is very small, SHG waves can add constructively over a coherence length  $L_c = \lambda/2(n_{2\omega} - n_{\omega})$ , where  $\lambda$  is the excitation wavelength, and  $n_{2\omega}$  and  $n_{\omega}$  are refractive indices corresponding to the excitation and SHG wavelengths. The most commonly used crystals for nonlinear optics are birefringent (e.g. LiNbO<sub>3</sub>), in which the phase matching condition can be achieved by propagating the beams at different frequencies as ordinary or extraordinary rays [36, 37]. It is important to note that the wave vectors of pump and SHG are always nonparallel, i.e., phase matching is not formally possible in 1D in bulk materials.

Although the generation of SHG requires non-centrosymmetric structures, the broken symmetry at the surface of NWs and the mismatch of dielectric constants at the interface of NWs and the environment can cause SHG even in materials with a high symmetry crystal lattice [40]. In addition, NWs with diameters much smaller than the incident wavelengths can act as subwavelength waveguides that radially confine optical modes, with increased  $L_c$  and therefore a longer effective length over which 1D nonlinear process takes place [41]. Furthermore, the intensity of the optical electric field inside illuminated NWs can depend dramatically on the NW

orientation relative to the excitation light polarization, with the maximum relative amplitude at the electric-field polarization oriented along the NWs [40].

Many types of NWs have been reported to be able to emit SHG signals [41–48]. As an example, Nakayama et al. [44] reported the development of continuously tunable coherent visible light source from individual  $\text{KNbO}_3$  NWs, which exhibited efficient SHG and acted as frequency converters, allowing for the local synthesis of a wide range of colors via sum and difference frequency generation. As shown in Fig. 6.4a, single  $\text{KNbO}_3$  NWs were optically trapped using an infrared optical tweezer with the trap wavelength at 1064 nm. A diffraction-limited spot is observed by an electron-multiplying charge-coupled device (CCD) at the distal end of the wire, revealing optical waveguiding away from the site of photon conversion and

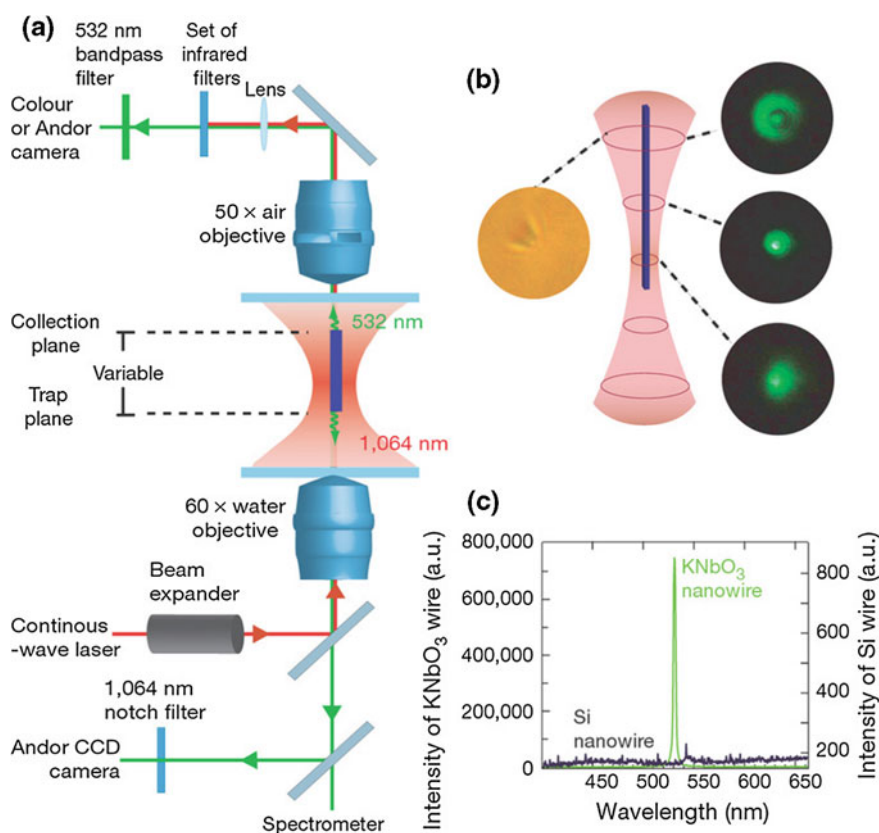


**Fig. 6.4** **a** Detailed set-up for the single-beam optical trapping instrument. **b** Bright field (*left*) and SHG (*right*) images of the trapped  $\text{KNbO}_3$  NW. Waveguiding of the SHG signal (*green*) leads to diffraction rings at the distal (*top*) end of the NW which acts as a subwavelength aperture. **c** Observed spectra for  $\text{KNbO}_3$  and SiNWs. Strong SHG signal is collected from the trapped  $\text{KNbO}_3$  NW (*green, left axis*), while no signal was observed from SiNWs (*black, right axis*). Reproduced from [44]. Copyright 2007 Nature Publishing Group

emission from the aperture defined by the NW cross-section (Fig. 6.4b). Spectral analysis reveals that the light is green with a wavelength of  $531 \pm 1.8$  nm (Fig. 6.4c), matching well with the expected SHG signal given a trapping/pump wavelength of 1,064 nm, this SHG might originate from both the bulk and the surface of the NW. In another report [46], SHG was experimentally observed from periodic arrays of vertical GaP nanopillars. Polarization of the measured light was used to distinguish between the bulk and surface SHG signals. For larger diameters (250 nm), it is mainly the bulk nonlinearity which contributes to the SHG, the polarization of SHG is predominantly orthogonal to that of the pump; while for smaller diameters (150 nm), the surface contribution becomes significant, the polarization of the SHG signal is predominantly parallel to the pump.

### 6.2.2.2 Third-Harmonic Generation and Four-Wave Mixing

THG and FWM are third-order NLO processes and are not limited to non-centrosymmetric structures [36, 37]. THG requires three photons ( $\omega_1$ ) in order to generate one photon at the tripled frequency ( $3\omega_1$ ) [49–51], while for FWM, three incident laser fields with frequencies of  $\omega_1, \omega_2, \omega_3$  interact with the material's  $\chi^{(3)}$  to generate a signal field at a frequency of  $\omega_4$  [50, 52–54]. Similar to SHG, the generation of THG and FWM also requires phase matching. As an example, Jung et al. [50] observed strong emission of THG signal from SiNWs of 40 nm diameters (Fig. 6.5a). The THG emission spectra recorded from individual NWs in the 400–680 nm region display a peak at 428 nm, in agreement with the emission wavelength of THG, 430 nm, produced by a 1290-nm excitation. The THG intensity exhibits a periodic dependence on the angle  $\theta$ : the signal intensity arising from the perpendicular polarization is much smaller than that from parallel polarization. In addition, THG intensity of the SiNWs remains consistent over the time (Fig. 6.5b). The authors [50] also observed a very strong FWM response along the long axis of SiNWs (Fig. 6.5c), with the peak positioned at 645 nm, in agreement with the emission wavelengths of FWM generated by collinearly combined pump field (790 nm) and Stokes field (1018 nm). The FWM signal from these nanomaterials is brighter than the nonresonant FWM contribution from the biological material itself, which enables identification of SiNW probes in live cells and tissues. As a proof of concept, the authors monitored blood circulation of PEGylated SiNWs in live animals and mapped the distribution of SiNWs in organs after systemic clearance (Fig. 6.5d, e).

### 6.2.2.3 Stimulated Raman Scattering

In spontaneous Raman scattering, a pump laser at a frequency  $\omega_p$  illuminates the sample, and the sample emits photons at the Stokes and anti-Stokes frequencies,  $\omega_s$  and  $\omega_{as}$ , due to inelastic scattering. However, if one additional laser with frequency  $\omega_s$  (Stokes beam) coincide with  $\omega_p$  on the sample, the Raman signal with  $\omega_s$



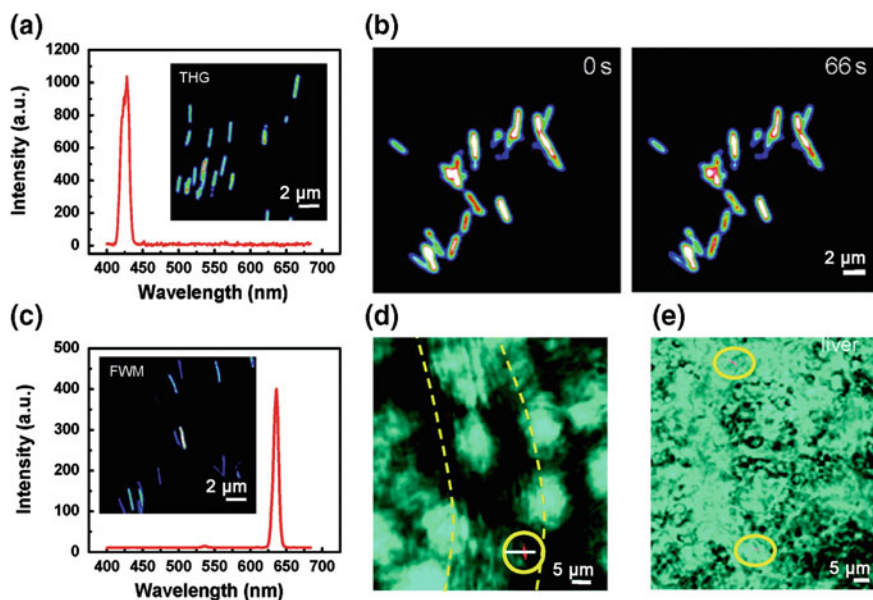


**Fig. 6.5** **a** THG image and spectrum from SiNWs, excited by a 1290 nm laser. **b** THG images of SiNWs acquired at different scanning time. **c** FWM image and spectrum from SiNWs. **d** FWM imaging of PEGylated SiNWs (*red*) flowing in a blood vessel (outlined by *dashed yellow line*) in the earlobe of a living mouse. **e** FWM imaging of SiNWs (*red*) in liver after systemic clearance in a mouse. Reproduced from [50]. Copyright 2009 American Chemical Society

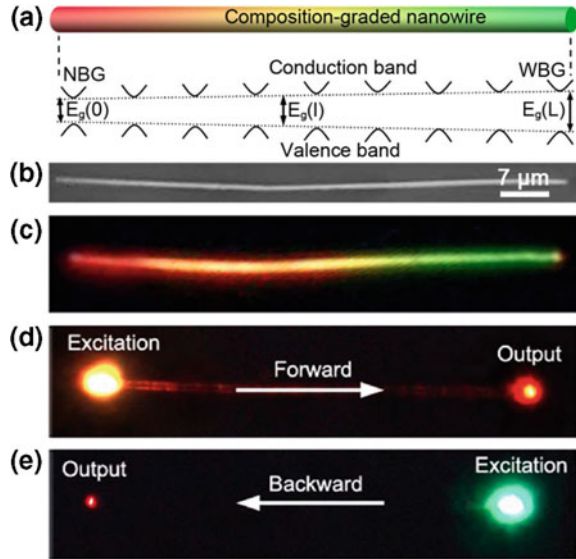
frequency is largely amplified, therefore this process is called SRS. The intensity of spontaneous Raman is proportional to pump power, but smaller by many orders of magnitude, while the intensity of SRS depends nonlinearly on incident intensity, and can be comparable to the pump intensity [55, 56]. When the length of the NW becomes comparable to wavelength of light, the NW behaves similar to a cavity, so that inelastic photons may form standing waves confined by the NW cavity. As a result, SRS becomes possible. For example, Wu et al. [57] measured the integrated Raman–Stokes intensity of transverse optical (TO) phonon band versus laser power for a series of GaP NWs with length between 200 nm and 3.3 μm. It was found that as the NW length decreases, the nonlinear effect becomes dominant. For NWs longer than  $\sim 2$  μm, the Raman intensity is approximately a linear function of laser power up to 1 mW, a characteristic of spontaneous (linear) Raman scattering. For powers over 1 mW, laser-induced heating is shown. For NWs shorter than 1.1 μm, Raman scattering exhibits spontaneous characteristics ( $I_{TO} \propto P$ ) at lower laser power; however, above a threshold power ( $P_T$ ), a strong nonlinear behavior  $I_{TO} \propto P^n$  is observed, where the exponent  $n$  grows rapidly as the length decreases to a value  $\sim 4.3$  for the shortest segment of 270 nm. Another interesting observation is that  $P_T$  decreases as the length decreases. Further studies of these interesting results are certainly warranted and could open unique research and application opportunities.

## 6.3 Photonic Devices

### 6.3.1 Nanowire Waveguides

In order to assemble light-based devices into highly-integrated photonic circuits, an important step is to develop NW waveguides that can transport light over relatively large distances from one part of a chip to another, and provide flexible interconnection patterns needed to carry out complex tasks. In this section, we describe NW waveguides with bends/twists. In 2003, Tong et al. [58] used a flame-heated fiber drawing method to fabricate long free-standing silica NWs with diameters down to 50 nm and lengths up to tens of millimeters. The NWs did not break when being bent/twisted, indicating their excellent flexibility and mechanical properties. Light was launched into these NWs by optical evanescent coupling. The NWs allowed single-mode operation, and had an optical loss of less than  $0.1 \text{ dB mm}^{-1}$ . Barrelet et al. [59] carried out quantitative studies of CdS NW structures showing that light propagation takes place with only ca. 1 dB loss or less per abrupt bend, after accounting for loss in the straight portion of the NW. In addition, light can be guided and coupled efficiently through the sharp bends or turns, defined by crossed NWs and end-to-end assembled NWs. In 2004, Yang and coworkers [60] used  $\text{SnO}_2$  nanoribbons as subwavelength waveguides for light with energies less than  $\text{SnO}_2$  bandgap. Freestanding nanoribbons were repeatedly and elastically curved into loops with radii as small as  $5 \mu\text{m}$ . On appropriately chosen surfaces, single nanoribbons were easily fashioned into a variety of shapes with the help of NW-substrate forces to prevent elastic recoil. Depending on ribbon cross-sectional area and the density of scattering centers, these nanoribbons demonstrated efficient waveguiding with losses from 1–8 dB/mm at a wavelength of 450–550 nm. Furthermore, because of their remarkable mechanical flexibility, the  $\text{SnO}_2$  nanoribbons could be linked to other lasing NWs [61] (e.g. GaN and ZnO) and plasmonic NWs [62]. Notably, Sirbuly et al. [61] simultaneously guided the output of two (or more) nanolasers by coupling multiple ZnO and GaN wires to the same ribbon, establishing the possibility of performing all-NW nonlinear wave mixing within single nanocavities. In 2008, Park et al. [63] presented an optically or electrically driven photonic structure that used CdS NWs as photon sources to inject light into  $\text{Si}_3\text{N}_4$  photonic-crystal waveguides. The photonic crystal was used to either guide or filter out different colors of light. In this work, the authors synthesized CdS/CdSe core/shell NWs consisting of two semiconductor materials, in which a CdS core emits green light and the CdSe shell emits red. By defining two photonic-crystal waveguides at either end, two different colors of light were sent in opposite directions. Later, Xu et al. [64] reported the design and realization of asymmetric light propagation in single  $\text{CdS}_x\text{Se}_{1-x}$  alloy NWs with a composition gradient along the length the NWs, as schematically shown in Fig. 6.6a. The bandgap of these NWs can be tuned from 2.4 eV at one end to 1.7 eV at the other end. Illumination of the entire NW showed that the PL color varied continuously from green to red along its length (Fig. 6.6b, c). In contrast to homogeneous NW

**Fig. 6.6** **a** Schematic diagrams of a composition-graded NW and its corresponding bandgap structure. **b** SEM image of an examined composition-graded NW. **c** Real-color PL photograph of the NW under the illumination of a diffused 405-nm semiconductor laser. **d, e** Real-color PL photographs with local excitation at one of its ends. Reproduced from [64]. Copyright 2012 Nature Publishing Group



waveguides, light propagation along one axial direction of such composition-graded NWs is different to the propagation along the reverse direction, leading to asymmetric light propagation (Fig. 6.6d, e).

### 6.3.2 Nanoscale Light-Emitting Diodes

LED is a two-lead semiconductor light source that resembles a basic  $p$ - $n$  junction diode, except that an LED also emits light [65]. In response to the passage of an electric current, electrons are able to recombine with holes within the device, releasing energy in the form of photons. The process is termed as electroluminescence (EL). In this section, we summarize recent advances in NW LED assembly, including crossed NW structures, axial and radial heterostructures, and branched NWs.

#### 6.3.2.1 Crossed Nanowire Structures

Previously, we discussed the formation of NW  $p$ - $n$  diodes by crossing a  $p$ - and a  $n$ -type NWs. In direct band gap semiconductors, the  $p$ - $n$  diode also forms the basis for the critical optoelectronics devices, such as LEDs [14, 66, 67]. As an example, Huang et al. [14] fabricated nanoLEDs with colors spanning from the ultraviolet to near-infrared region of the electromagnetic spectrum. Single- and multicolor nanoLED devices and arrays are made with colors specified in a predictable way by

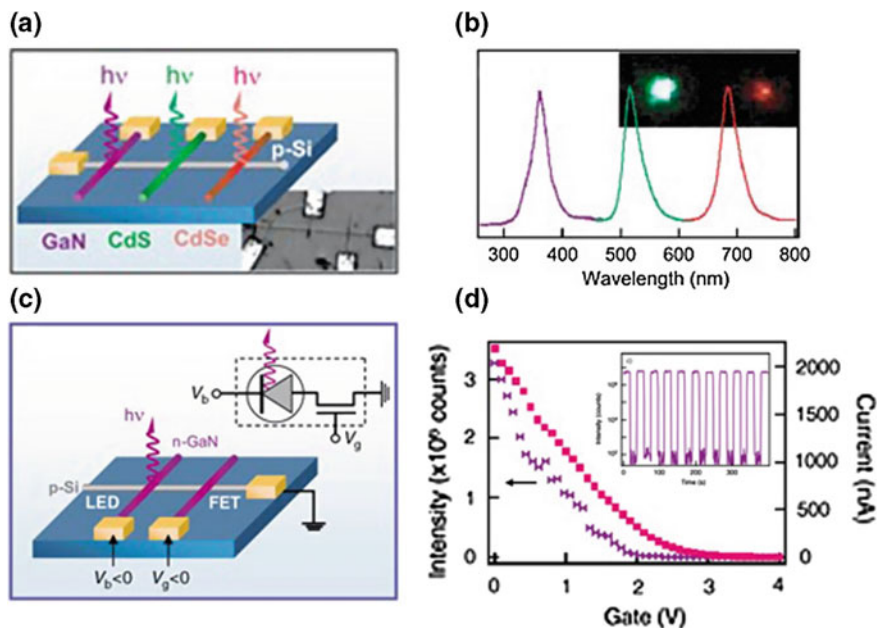


**Fig. 6.7** **a** Schematic and corresponding SEM image of a tricolor nanoLED array. **b** Normalized EL spectra and color images from the three elements. **c** Schematic of an integrated crossed NW-FET and LED. **d** Plots of current and emission intensity of the nanoLED as a function of voltage applied to the NW gate at a fixed bias of  $-6$  V. (*inset*) EL intensity versus time relation a voltage applied to NW gate is switched between 0 and  $+4$  V for fixed bias of  $-6$  V. Reproduced from [14]. Copyright 2005 John Wiley and Sons

the bandgaps of the III–V and II–VI NW building blocks. As shown in Fig. 6.7a, nanoLEDs with non-emissive SiNW hole-injectors are used to assemble multicolor arrays, in which  $n$ -type GaN, CdS, and CdSe NWs cross a single  $p$ -type SiNW. Normalized emission spectra recorded from the array demonstrates three spatially and spectrally distinct peaks with maxima at 365, 510, and 690 nm (Fig. 6.7b) consistent with band-edge emission from GaN, CdS, and CdSe, respectively. Color images of EL from the array show the green and red emission from  $p$ -Si/ $n$ -CdS and  $p$ -Si/ $n$ -CdSe crosses, respectively (inset, Fig. 6.7b). In addition, optoelectronic circuits consisting of integrated crossed NW LED and FET elements have been assembled (Fig. 6.7c). Specifically, one GaN NW forms a  $p$ - $n$  diode with the SiNW, and a second GaN NW functions as a local gate, as described in the previous chapter. Measurements of current and emission intensity versus gate voltage showed that (i) the current decreased rapidly with increasing voltage as expected for a depletion mode FET, and (ii) the intensity of emitted light also decreased with increasing gate voltage. When the gate voltage was increased from 0 to  $+3$  V, the current was reduced from ca. 2200 nA to an off state, where the supply voltage is  $-6$  V (Fig. 6.7d). The ability to use the nanoscale FET to switch reversibly the nanoLED on and off has also been demonstrated (inset, Fig. 6.7d).

### 6.3.2.2 Axial Heterostructures

One of the first demonstrations of axial  $p$ - $n$  junctions was made in vertical GaAs cone-like nanostructures grown epitaxially on GaAs(111)B substrates [68]. These structures also exhibited light emission by current injection at 77 K and room temperature. Later, the Lieber group [69] reported the synthesis of  $n$ -InP/ $p$ -InP modulation doped NWs and their applications as nanoscale LEDs. In a forward bias, individual InP NW devices exhibit light emission from  $p$ - $n$  junctions, both highly polarized and blue-shifted due to the 1D structure and radial quantum confinement, respectively. Kim et al. [70] demonstrated the realization of the high-brightness and high-efficiency LEDs using dislocation-free InGaN/GaN MQW NW arrays. A blue-shift of EL occurs, directly with increasing current, which is attributed to screening of the built-in internal polarization field in the quantum wells by the injected carriers. Subsequently, Ra et al. [71] reported the controlled synthesis of InGaN/GaN MQW uniaxial ( $c$ -plane) and coaxial ( $m$ -plane) NW heterostructures. The  $c$ -plane and  $m$ -plane oriented MQW single NWs are utilized for the parallel assembly fabrication of the LEDs via a focused ion beam. The electrical properties of  $m$ -plane NWs exhibit superior characteristics than that of  $c$ -plane NWs, owing to the absence of piezoelectric polarization fields. Therefore, high-quality  $m$ -plane coaxial NWs can be utilized for the realization of high-brightness LEDs.

### 6.3.2.3 Radial Heterostructures

The radial NW concept also offers substantial opportunities for NW LEDs since the required  $n$ - and  $p$ -type active materials can be incorporated as the core and shell, enabling carrier injection or collection over a much larger area than those in crossed NW devices and axial NW heterostructures [33, 72, 73]. The Lieber group [33, 72] first demonstrated a general strategy for realizing these photonic nanostructures through the synthesis of well-defined doped III-nitride-based core-multishell (CMS) NW heterostructures (Fig. 6.8a). In these materials, a  $n$ -type GaN core and  $p$ -type GaN outer shell served as electron and hole injection layers, an  $\text{In}_x\text{Ga}_{1-x}\text{N}$  shell provided a tunable band gap quantum well for efficient radiative recombination of injected carriers, and an AlGaIn shell was incorporated to enhance confinement of both carriers and photons in the InGaIn active layer. Current versus voltage characteristics of CMS NW devices with separate contacts to the  $n$ -type core and  $p$ -type outer shell show the expected  $p$ - $n$  diode current rectification (Fig. 6.8b). In a forward bias, the devices yield strong light emission with the LED color dependent on the indium composition in the CMS NW heterostructure that is defined during synthesis (Fig. 6.8c). Significantly, LED spectra collected from CMS NW devices with intentionally increasing indium composition demonstrate a systematic redshift of emission from 367 to 577 nm, covering the short wavelength region of the visible spectrum (Fig. 6.8d).

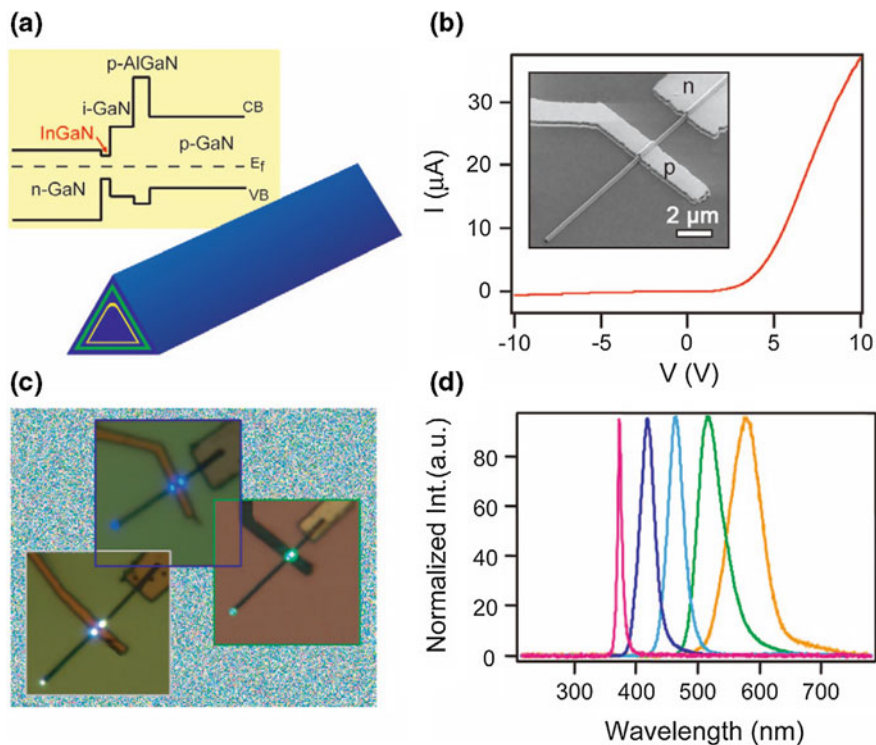


**Fig. 6.8** **a** Schematic and corresponding band diagram for an  $n$ -GaN/InGaN/GaN/ $p$ -AlGaN/ $p$ -GaN CMS NW. The InGaN and AlGaN shells are highlighted with yellow and green colors, respectively. **b**  $I$ - $V$  data recorded from a typical CMS NW device with contacts to the  $n$ -core and  $p$ -shell. **c** Electroluminescence (EL) images of three forward-biased CMS NW LEDs with  $\sim 15$ , 30, and 35 % In, showing blue, greenish-blue, and greenish-yellow emission, respectively. **d** Normalized EL spectra recorded from five multicolor CMS NW LEDs with 1, 10, 20, 25, and 35 % In (left to right), respectively. Reproduced from [72]. Copyright 2005 American Chemical Society

### 6.3.3 Optically-Pumped Nanowire Lasers

Semiconductor NWs with high optical gain offer promising solutions for lasers with small footprints and low power consumption. In this section, we introduce the principles of optically-pumped semiconductor NW lasers, followed by experimental demonstrations categorized by their output wavelengths within UV, visible, and near-IR spectral ranges, as well as multicolor emissions. For a comprehensive review of semiconductor NWs lasers, readers can refer to [11].

### 6.3.3.1 Principles of Optically-Pumped Nanowire Lasers

The word laser is an acronym for light amplification by stimulated emission of radiation. A laser is a device that is able to generate light via optical amplification based on the stimulated emission of electromagnetic radiation. Generally, three basic elements are necessary for a laser: an active gain medium that provides optical gain by stimulated emission, a pumping process to excite the electrons into higher energy levels to realize population inversion (i.e., the density of excited states is larger than that of the ground states), and an optical resonant cavity that confines the photons to create positive optical feedback [74]. In a stimulated emission, the probability of emission of a photon of a given frequency is enhanced by the presence of another photon of the same frequency. Therefore, stimulated emission induced by population inversion leads to an increase in the number of photons to produce a coherent beam. The realization of a semiconductor NW laser is similar to that of a bulk semiconductor lasers [11, 75]. The NWs can serve as both the gain medium, which is optically excited, and flat end facets can act as partially reflecting mirrors, which provide optical feedback as a Fabry-Perot cavity [76].

### 6.3.3.2 UV Lasers

Among semiconductor NW materials for lasing in the UV spectral range, ZnO and GaN have attracted the greatest research interest [77]. In this section, we introduce several experimental demonstrations of ZnO and GaN NW lasers. ZnO NWs have a bandgap of 3.37 eV, and a high exciton binding energy ( $\sim 60$  meV) that ensures efficient exciton emission above room temperature, making it an ideal candidate for UV lasing. The first NW laser was reported by the Yang group in 2001, where the room-temperature laser emission of ZnO NWs (with diameters varying from 20 to 150 nm and lengths up to 10  $\mu\text{m}$ ) was demonstrated [78]. Upon optical excitation, surface-emitting lasing was observed at 385 nm, with an emission line width less than 0.3 nm. Later, they also reported the first observation of single ZnO NWs acting as both optical waveguides and lasers, depending on the quality factor of the NW cavity [79]. In 2003, comb-like ZnO NW structures, with individual ZnO NWs (whose diameters range from 10 to 300 nm) evenly spaced on a stem with a regular periodicity of 0.1–2  $\mu\text{m}$ , were constructed to be highly ordered NW ultraviolet laser arrays, in which each individual ZnO NW serves as a Fabry-Perot optical cavity [80]. Subsequently, Johnson et al. [81] utilized time-resolved second-harmonic generation (TRSHG) and transient PL spectroscopy to probe excited carriers immediately following band-gap excitation in single ZnO NW and nanoribbon lasers. They demonstrated transient PL consisting of a pump-independent slow component (free-exciton decay, 75–100 ps) and a significantly faster decay component that was correlated with stimulated emission (exciton-exciton lasing,  $\sim 10$  ps). Zhang et al. [82] measured the absolute light emission intensity, and both the external and internal quantum efficiency of ZnO NW nanolasers at room temperature. The external differential quantum efficiency reaches 60 % for lasing ZnO

NWs of 7.5  $\mu\text{m}$  in length, compared to a value of approximately 10 % for PL. The absolute light emission intensity for individual NWs was found to be in the vicinity of 0.1 mW. By measuring the dependence of external differential quantum efficiency on the cavity length, the internal quantum efficiency was estimated to be about 85 %. Later, the influence of annealing on stimulated emission in ZnO nanorods was reported by Kwok et al. [83]. The lowest lasing threshold and defect emission as well as the longest spontaneous emission decay times were obtained for nanorods annealed in oxygen flow, which indicates that interstitial oxygen is not the dominant defect in hydrothermally grown nanorods. In 2008, Zimmerler et al. [84] presented direct evidence of the transition from amplified spontaneous emission (ASE) to lasing in optically pumped ZnO NWs at room temperature. The optical power evolves from a superlinear region (characteristic of ASE) to a quasi-linear region (characteristic of laser oscillation) as the pump power exceeds threshold, concomitant with a transition to directional emission along the NW axis and the emergence of Fabry–Perot cavity modes around a wavelength of  $\sim 385$  nm, the intensity of which exceeds the spontaneous emission background by orders of magnitude. In a later work, Gargas et al. [85] used pulsed laser spectroscopy and UV-confocal microscopy to characterize single vertical NW lasers. As shown in Fig. 6.9a, the PL spectra (vertically offset) are collected at pump energy densities of 383, 536, 980, 1378, 1454, and 1760  $\mu\text{J}/\text{cm}^2$ . The threshold in the 390 nm lasing spectra is estimated to be 400  $\mu\text{J}/\text{cm}^2$ . A 3D mapping of the PL emission intensity from a single vertical NW on a sapphire substrate is shown in Fig. 6.9b. The X and Y-axes denote spatial position, whereas the Z-axis represents the PL emission intensity collected at a set planar position.

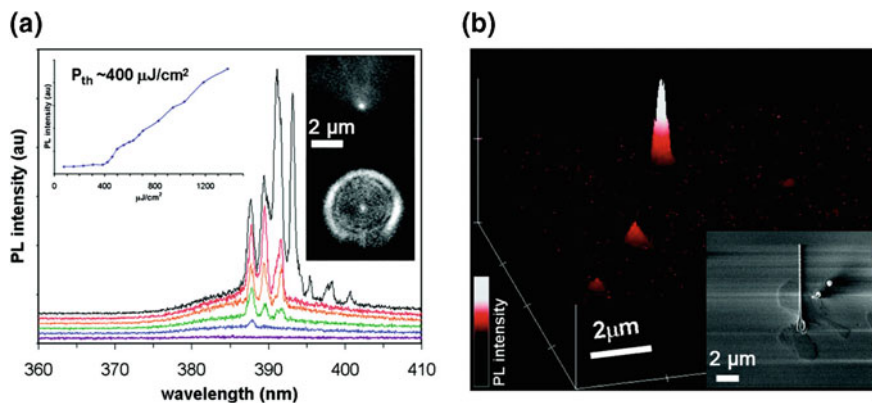


**Fig. 6.9** **a** Diagram of a ZnO vertical NW cavity and its corresponding PL images collected along the NW. Lasing spectra of a single ZnO vertical NW cavity. *Left inset* power dependence graph showing lasing threshold at roughly 400  $\mu\text{J}/\text{cm}^2$ . *Right inset* dark-field images of a ZnO NW under white light illumination (*top*) and lasing induced by 266 nm pulsed excitation (*bottom*). **b** 3D confocal PL image of a ZnO vertical NW cavity. *Inset* SEM image of a ZnO vertical NW. Reproduced from [85]. Copyright 2009 American Chemical Society



The Wang group used the time-resolved PL to study three types of lasing mechanisms (i.e., exciton-exciton interaction, bipolaronic exciton condensation, and plasma) in pure, lightly doped, and heavily doped ZnO NWs [86]. Specifically, they demonstrated that the dopant concentration may significantly change the exciton-phonon coupling and the binding energy of excitons. Moreover, it may also affect the formation of bound excitons and exciton dissociation processes. Thus, all three types of lasing mechanisms can exist in ZnO NW lasers.

The UV-blue lasing behavior in single GaN NW was first observed in 2002 by Johnson et al. [87]. Lasing oscillation around 378 nm was observed in a 300 nm diameter and 40  $\mu\text{m}$  long GaN NW, with evident axial Fabry–Perot cavity modes. Gradečak et al. [88] also studied GaN NWs with triangular cross sections, dislocation-free structures, and uniform diameters, which together contributed to excellent cavity properties, thus reducing the excitation power density (22  $\text{kW}/\text{cm}^2$ ) required for stimulated emission. Combining bottom-up and top-down approaches, Park et al. [89] constructed a GaN NW emitter with a fabricated  $\text{Si}_3\text{N}_4$  stadium microresonator. The PL from the GaN NW was coupled and confined in the  $\text{Si}_3\text{N}_4$  stadium microcavity. Using ultrafast optical pump-probe spectroscopy, Upadhyaya et al. [90] studied the influence of defect states on carrier dynamics in GaN NWs by probing carrier relaxation through the states responsible for yellow luminescence, an undesirable effect that plagues many GaN-based photonic devices [91, 92]. Lower growth temperature tends to allow more impurity sites in the NWs, which may trap photo-excited carriers and thus increase the lasing thresholds. Furthermore, excitation density-dependent measurements reveal a decrease in carrier lifetimes with increasing pump power. In 2014, Zhang et al. [93] demonstrated the first strong room temperature ultraviolet surface plasmon (SP) polariton laser with an extremely low threshold ( $\sim 3.5 \text{ MW cm}^{-2}$ ). The authors found that a closed-contact planar semiconductor–insulator–metal interface greatly lessens the scattering loss, and efficiently promotes the exciton–SP energy transfer thus furnishes adequate optical gain to compensate the loss.

In addition to linear NW cavities, a ring-type cavity was formed by manipulating a GaN NW into a closed loop, and optically connecting both ends via evanescent coupling (Fig. 6.10a–c), which shows markedly different lasing and spontaneous emission properties compared to its linear counterpart. As shown in Fig. 6.10d, the laser-mode emission for the ring structure is substantially red-shifted relative to that for a linear cavity of similar length. This effect originates from enhanced coupling efficiencies for longer wavelengths across the overlapping junction, due to an increase of the electric field penetration depth with increasing wavelength [94].

### 6.3.3.3 Visible Lasers

CdS (2.42 eV) and CdSe NWs have been the most actively studied materials for lasing in the visible regime [11]. Detailed temperature-dependent optically-pumped studies of single CdS NW lasers reveal that a highly efficient exciton-exciton scattering phenomena was responsible for lasing from 4.2 to 70 K, when the lasing

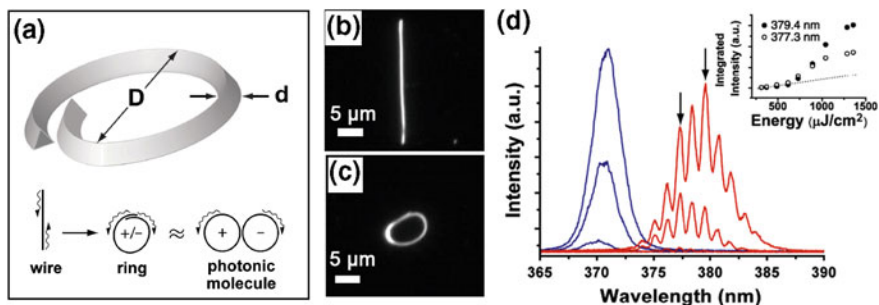


**Fig. 6.10** **a** Schematic of ring and waveguiding analogy to coupled photonic molecule. **b, c** Dark-field images of a linear NW cavity and a ring-type NW cavity. **d** Comparison of lasing emission from ring and cavity geometries. *Inset* integrated area under ring modes, indicated by arrows. Reproduced from [94]. Copyright 2006 American Physical Society

mechanism shifts to an exciton-optic phonon scattering mechanism at higher temperatures [95]. In a later report [96], electric field modulation of visible NW laser consisting of single CdS NW was achieved using integrated, microfabricated electrodes. Modulation of laser emission intensity was achieved with no detectable change in the laser wavelength. The devices can also be operated below the lasing threshold to modulate the intensity of light propagating within the NW waveguide. As shown in Fig. 6.11a, electro-optic modulator (EOM) devices with a parallel-plate structure are used to apply a uniform electric field over a length  $L$  of the NW. Figure 6.11b shows the modulation of the output spectrum of a representative CdS NW EOM with modulation length ( $L$ ) of 6  $\mu\text{m}$  and  $\text{SiO}_2$  dielectric thicknesses of 50 nm. The 489 nm lasing peak can be modulated by 40 % at 45 V, which is more than two times the modulation of the emission around 515 nm, while maintaining no detectable change in the laser wavelength (Fig. 6.11c). In 2011, Liu et al. [97] presented exciton-related optical studies of CdS nanobelts. The PL spectrum at 10 K shows rich spectral features identified by means of temperature-dependent spectral evolution. The strong excitonic emission in the samples enables the observation of random lasing action at room temperature. Geburt et al. [98] investigated the synthesis of various CdS nanostructures (bands, wires, irregular structures) and further investigated the lasing properties and necessary length-diameter relations for lasing of individual CdS NWs. Furthermore, CdSe NWs, with a bandgap of 1.74 eV, have also been used to realize red-color (around 710 nm wavelength) lasing [99, 100].

### 6.3.3.4 Near-IR Lasers

NW laser emission and waveguides with near-infrared (NIR) wavelengths are of interest given their potential suitability for applications in optical communications [11]. However, it has been challenging to obtain NIR NW lasers because a large

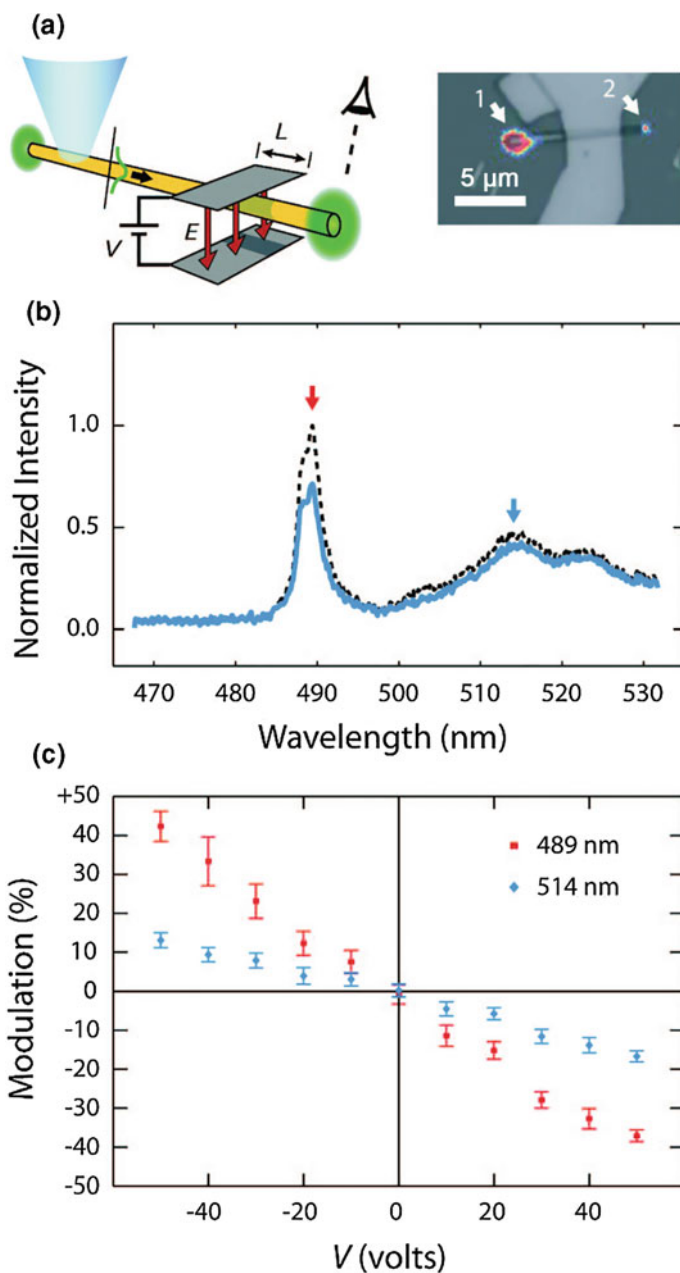


**Fig. 6.11** **a** Diagram indicating the excitation site, region of field modulation, and observed NW end. At right, superimposed PL image (recorded below laser threshold) and white-light optical micrograph of a representative CdS NW EOM-laser device. Numerals 1 and 2 indicate excitation site and observed NW end, respectively. **b** Emission spectra of a CdS NW laser showing effect of a 30 V signal. **c** Modulation versus  $V$  at the two indicated wavelengths for the EOM-laser in **(b)**. Reproduced from [96]. Copyright 2005 AIP Publishing LLC

fraction of the optical modes exist outside of the NWs for reasonable diameters, which increases propagation losses, and there is relatively poor reflectivity at the end facets. In 2006, Chin et al. [101] reported the first NIR NW lasing using subwavelength GaSb wires with a cross-sectional dimension of 700–1500 nm and lengths of 10–70  $\mu\text{m}$  dispersed on a sapphire substrate. The measured lasing emission centered around 1553 nm. In the subsequent studies, the Fukui group also investigated GaAs, InP, and GaAs/GaAsP NIR NW lasers [102–104]. As an example, GaAs (1.424 eV) is an important NIR lasing material; however, a high density of surface states leads to strong decay of its emission quantum yield, making it difficult to realize GaAs NW lasers. In 2007, Hua et al. [102] investigated Fabry-Perot cavity effects in a single GaAs NW (320 nm in diameter, 4.5  $\mu\text{m}$  in length), although the cavity losses were too large for lasing. After effectively passivating the surface states of a GaAs NW (290 nm in diameter, 2.8  $\mu\text{m}$  in length) by a 50 nm GaAsP coating layer, the authors fabricated a high-quality optically active single GaAs/GaAsP coaxial core-shell NW, and realized 817 nm lasing under laser pulse excitation [104].

### 6.3.3.5 Wavelength-Tunable Lasers

In the previous sections, NW lasers for several homogeneous binary semiconductors have been discussed, where the lasing wavelengths correspond approximately to the fundamental bandgap energies of the respective homogeneous NW materials. The distinct NW bandgaps led to lasing over a relatively wide range of discrete wavelengths but did not enable continuous tuning in emission color. To address this issue, several research groups studied wavelength-tunable lasing in alloy systems. In 2005, Liu et al. [105] reported the first wavelength-controlled semiconductor NW lasers using ternary alloy  $\text{Zn}_x\text{Cd}_{1-x}\text{S}$  nanoribbons, which allows systematic variation of the bandgap of  $\text{Zn}_x\text{Cd}_{1-x}\text{S}$  from 2.42 eV for CdS to 3.7 eV for ZnS, and showed that it was possible to sustain lasing emission continuously in two spectral regions, 485–515 and 340–390 nm, by controlling the composition  $x$  close to CdS ( $0.25 \geq x \geq 0$ ) and ZnS ( $0.75 \geq x \geq 0$ ), respectively. Following this work, the synthesis of single crystal ternary  $\text{CdS}_x\text{Se}_{1-x}$  nanobelts and the observation of their color-tunable PL emission from green ( $\sim 500$  nm) to the near-infrared ( $\sim 700$  nm) was also demonstrated [106–110]. For example, by controlling local substrate temperature in a CVD system, Pan et al. [109] achieved spatial composition grading covering the complete composition range of ternary alloy CdSSe NWs on a single substrate of 1.2 cm in length. Figure 6.12a and b show real-color photographs of a quartz substrate with the as-grown NWs under regular room lighting (a) and under a 266 nm UV laser illumination (b), respectively. Figure 6.12c presents five SEM images taken from selected spots along the sample length, as indicated by the white spots in Fig. 6.12b. The as-grown sample shows the color change gradually from light-yellow (similar to CdS) to dark

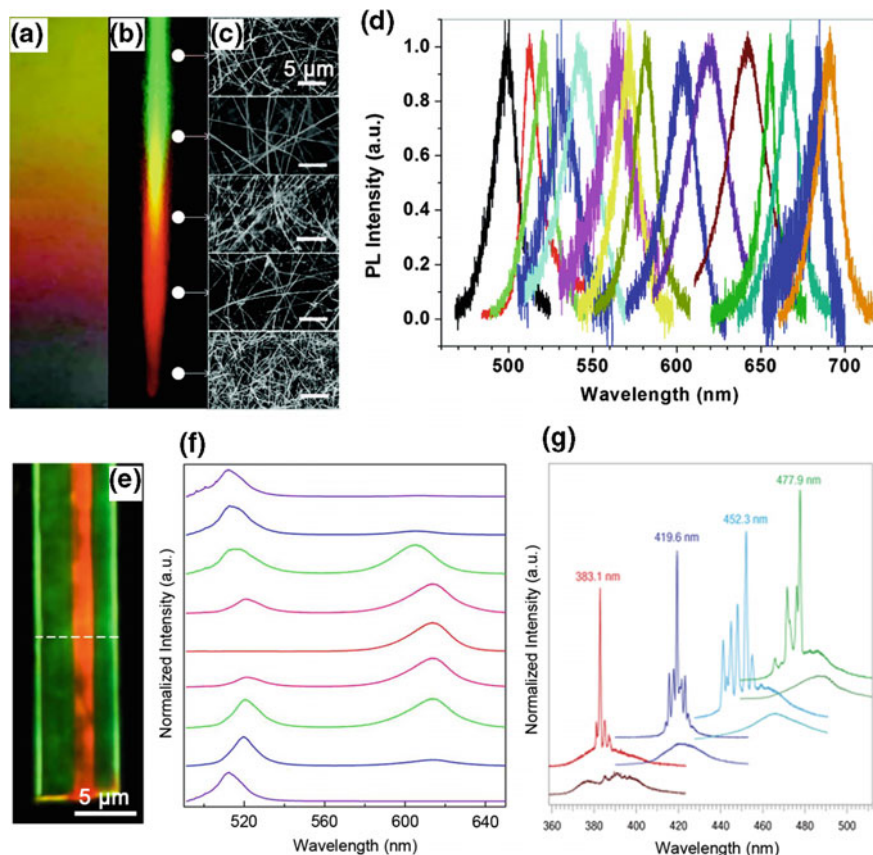


**Fig. 6.12** **a, b** The real-color photographs of a quartz substrate with the as-grown spatially composition-graded CdSSe NWs under room lighting **(a)** and under UV laser illumination **(b)** (266 nm). Size of the substrate:  $0.3 \times 1.2$  cm. **c** The SEM images taken at the white spots in panel **b**. **d** PL spectra collected at different locations along the substrate length. Reproduced from [109]. Copyright 2009 American Chemical Society. **e** A real-color photograph of a representative nanoribbon lateral heterostructure illuminated with a 405-nm laser. **f** PL spectra collected along the dashed line in **(e)**. Reproduced from [113]. Copyright 2012 American Chemical Society. **g** PL spectra collected from four representative 26MQW NW structures with increasing In composition pumped at  $\sim 250$  and  $\sim 700$   $\text{kW cm}^{-2}$ , respectively. Reproduced from [34]. Copyright 2008 Nature Publishing Group

(similar to CdSe) along the sample length direction, while the PL spectra exhibits the color change from green (consistent to the PL color of CdS) to red (consistent to the PL color of CdSe) along the same direction. These results indicate the formation of composition graded CdSSe alloys on a single substrate. Zapien et al. [111] and Luan et al. [112] have also shown that II–VI nanoribbons ( $\text{CdS}_x\text{Se}_{1-x}$  and  $\text{Zn}_y\text{Cd}_{1-y}\text{S}$ ) are capable of room-temperature lasing over the NIR to UV spectral

range with  $\text{CdS}_x\text{Se}_{1-x}$  nanoribbons lasing from NIR (710 nm) to green (510 nm) as  $x$  changes from 0 to 1, and  $\text{Zn}_y\text{Cd}_{1-y}\text{S}$  nanoribbons lasing from green (510 nm) to UV (340 nm) as  $Y$  varies from 0 to 1. In addition, Xu et al. [113] reported the growth of new  $\text{CdS}_x\text{Se}_{1-x}$ -CdS nanoribbon lateral heterostructures, with composition-tunable alloy  $\text{CdS}_x\text{Se}_{1-x}$  at the center and epitaxial CdS at the lateral sides. Under laser excitation, the emission of these ribbons indicates sandwich-like structures along the width direction, with characteristic red emission in the center and green emission at both edges (Fig. 6.12e, f). The spacing of the lasing wavelength of these nanoribbon lasers can be continuously tuned by controlling the composition and bandgap of the central  $\text{CdS}_x\text{Se}_{1-x}$  in the ribbons.

In previous examples of NW lasers, the NWs functioned as both the gain medium and optical cavity. However, Qian et al. [34] showed that decoupling the gain medium and cavity can offer advantages over homogeneous NW structures for designed laser wavelength output in parallel with independent optimization of the cavity. For example, they designed multi-quantum-well (MQW) NW structures composed of a GaN NW core, which functions as the primary part of the optical cavity, and epitaxial InGaN/GaN MQW shells, which serve as the composition-tunable gain medium. Optical excitation of individual MQW NW structures yield lasing with emission engineered from 365 to 494 nm through modulation of quantum well composition (Fig. 6.12g).

Recently, organic-inorganic perovskite material was introduced as a new system for NW lasers. Zhu et al. [114] studied room-temperature and wavelength-tunable lasing from single-crystal lead halide perovskite NWs with very low lasing thresholds ( $220 \text{ nJ cm}^{-2}$ ) and high quality factors ( $Q \sim 3600$ ). The lasing threshold corresponds to a charge carrier density as low as  $1.5 \times 10^{16} \text{ cm}^{-3}$ . Kinetic analysis based on time-resolved fluorescence revealed little charge carrier trapping in these single-crystal NWs and yielded estimated lasing quantum yields approaching 100 %.

### 6.3.3.6 Single-Mode Lasers

Semiconductor NW lasers usually exhibit multimode behaviors (i.e., emitting at multiple frequencies simultaneously) corresponding to the longitudinal modes of the NW Fabry–Perot cavities. In order to control the laser to oscillate at a single frequency, Xiao et al. [115] introduced an approach of coupling NW cavities by folding NWs into loop mirrors (LMs). According to the Vernier effect, when two sets of Fabry–Perot modes interact coherently with each other, only the modes that share the same frequencies will be observed in the lasing spectra. By having a single NW forming a small loop at one end, single frequency lasing with high suppression ratio (against the neighboring modes) around a wavelength of 738 nm was demonstrated in CdS NWs (Fig. 6.13). This form of wave coupling is highly sensitive to geometric parameters such as inter-NW distances, lengths of the coupled segments, and perimeters of the NW loops. Shortly after, the same group [116]

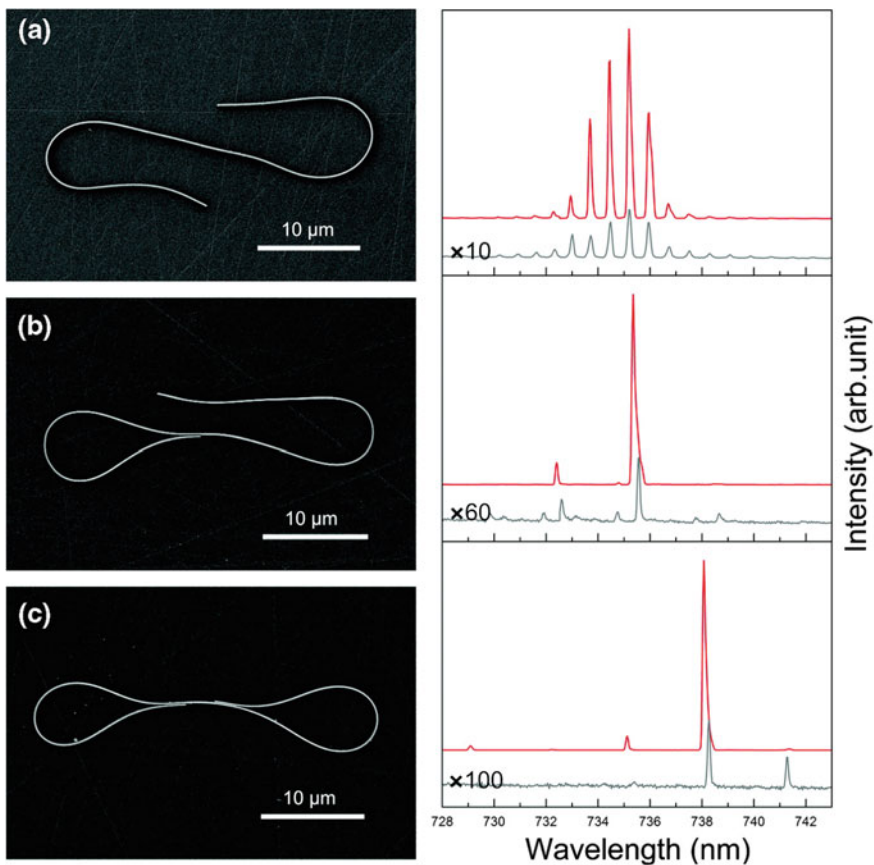


**Fig. 6.13** SEM images and lasing spectra of single-NW structures **a** without LM, **b** with one LM, and **c** with double LMs. The *top lines* represent lasing spectra obtained at pump fluence well above the threshold, while the *bottom lines* represent the spectra obtained near the threshold. Reproduced from [115]. Copyright 2011 American Chemical Society

proposed another approach to enable single-mode lasing in coupled CdSe NW cavities, this is, coupling two CdSe NWs to form an X-structure coupled cavity for mode selection. Xu et al. [117] placed GaN NWs with different lengths side-by-side in contact to form a coupled cavity through nanoprobe manipulation. An alternative approach to achieve single-mode lasing is to construct two Fabry-Perot cavities that are axially coupled through an air gap [118]. The precisely defined smooth end-faces and inter-cavity gap widths (as narrow as 30 nm) on GaN NWs provide strong coupling between different cavities while maintaining low diffraction loss of the NWs. Single-wavelength lasing can be observed from the coupled cavity, and each component NW emits laser at multiple wavelengths when they are separated.

### 6.3.4 Electrically-Pumped Nanowire Lasers

Despite the excitement generated from the first demonstration of optically pumped NW lasers, it has been critical to achieve electrical injection NW lasers in terms of most technological applications. The first demonstration of electrically-pumped NW lasers was reported in 2003 [119]. To enable electrical injection of carriers in a NW optical cavity, *n*-CdS NWs were assembled on heavily doped *p*-Si substrates and contacts to CdS were fabricated by lithographic techniques (the *p*-Si substrate functioned as the second electrode), as shown schematically in Fig. 6.14a. A thin layer of Al<sub>2</sub>O<sub>3</sub> is deposited in between the top and bottom contacts to force the current through the *p*-Si/*n*-CdS diode formed at the NW-substrate junction. The device under a low forward bias, produces EL with a broad featureless spectrum from the exposed NW end (Fig. 6.14b, c). Upon increasing the forward bias voltage or injection current, the electroluminescence spectrum quickly collapses into single mode lasing line at 493 nm with instrument resolution limited line-width of 0.7 nm, clearly demonstrating the possibility of electrically pumped lasing in NW optical cavities. In several other subsequent reports, ZnO NWs have been proved to be efficient electrically-pumped ultraviolet lasers [120–123]. For example, Chu et al. [121] demonstrated electrically pumped Fabry–Perot type waveguide lasing from laser diodes that consisted of Sb-doped *p*-type ZnO NWs and *n*-type ZnO thin films. By coating a MgO layer, which serves as electron blocking, hole supplying and surface passivation layer, electrically pumped near-ultraviolet lasing has been achieved in a metal/insulator/semiconductor (MIS) laser diode based on ZnO/MgO core/shell NWs [122]. Recently, the Mi group [124] reported the fabrication and performance of electrically driven lasers based on AlGaN core-shell NWs.

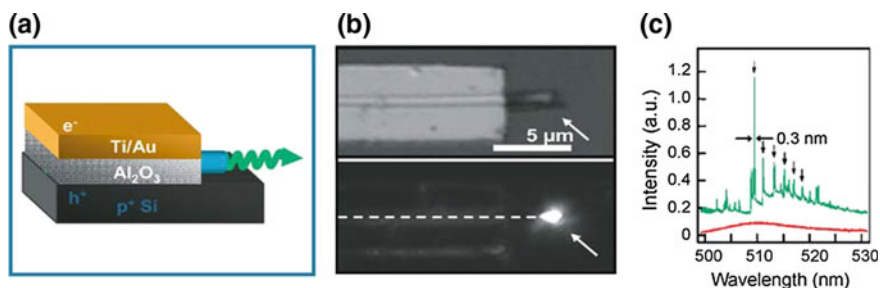


**Fig. 6.14** **a** Schematic showing the NW electrical injection laser device structure. In this structure, electrons and holes can be injected into the CdS NW along the whole length from the top metal layer and the bottom *p*-Si layer, respectively. **b** *Top panel* shows an optical image of a laser device and the *arrow* highlights the exposed CdS NW end. *Bottom panel* shows an electroluminescence image recorded from this device. The *dashed line* highlights the NW position. **c** Electroluminescence spectra obtained from the NW end with injection currents of 120 μA (*red*, below lasing threshold) and 210 μA (*green*). The *black arrows* highlight F–P cavity modes with an average spacing of 1.83 nm. The *green* spectrum is shifted upwards by 0.15 intensity units for clarity. Reproduced from [119]. Copyright 2003 Nature Publishing Group (Color figure online)



These lasers emit across the entire ultraviolet AII band (320–340 nm) and work at a low temperature of 6 K. Because of the diffusion-driven compositions within the NWs, electrons and holes recombine more efficiently than usual.

### 6.3.5 Photodetectors

Photodetectors can sense incident photons, and are critical to many areas of science and technology [125]. Homogeneous NW photoconductors are the simplest configuration of NW-based photodetectors [18, 126]. The unique properties of individual NWs, such as light polarization sensitivity, light absorption enhancement, and internal photoconductive gain, can be exploited for the realization of efficient devices such as optical switches and interconnects, near-field imaging, and high-resolution detectors. Apart from NW photoconductors, other one-dimensional photodetector structures based on semiconducting or superconducting NWs are being actively investigated for efficient conversion of optical to electrical signals. In this section, we present NW photodetector concepts demonstrated in previous literature, including photodiodes, phototransistors, and detectors based on superconducting NWs. Several comprehensive reviews about NW photodetectors can be found in [127].

#### 6.3.5.1 Photodiodes

Photodetection has been realized in diodes consisting of homo- and heterogeneous semiconductor NW junctions, either formed within single NWs during growth or as crossed NW configurations [128–132]. In the case of the *n*-CdS/*p*-Si crossed avalanche photodiode, a photocurrent increase ( $I_{\text{PC}}/I_{\text{dark}}$ ) of  $\sim 10,000$  times higher than in individual *n*-CdS or *p*-SiNW photoconductors has been observed, due to avalanche multiplication at the *p*-*n* crossed NW junction, with multiplication factors as high as  $M = 7 \times 10^4$ . It has been demonstrated that the NW avalanche photodiodes (APDs) have ultrahigh sensitivity with detection limits of less than 100 photons, and subwavelength spatial resolution of at least 250 nm [131]. Later, the same group [132] obtained similar sensitivity in the case of the axial *p*-*i*-*n* SiNW avalanche photodiodes, with multiplication factors in excess of ca. 30. Interestingly, electron- and hole-initiated avalanche gains are separately measured by localized photoexcitation of the *p*-type and *n*-type regions, yielding multiplication factors of ca. 100 and 20, respectively. Furthermore, metal-semiconductor junctions (i.e., Schottky junctions) [133–135] can also be used as photodiodes, where the electrons excited in the metal and the electron–hole pairs generated in the semiconductor can both contribute to the photocurrent. As an example, Gu et al. [134] reported the application of a near-field scanning optical microscope (NSOM) to map the local photocurrent in individual CdS NWs configured as metal-semiconductor-metal (MSM) photodetectors. The NW MSM photodetectors

exhibited photocurrents  $\sim 10^5$  larger than the dark current under uniform monochromatic illumination. Under local illumination, the photoresponse was localized to the near-contact regions.

### 6.3.5.2 Phototransistors

A phototransistor is a bipolar or unipolar transistor where light can reach the base, creating optically generated carriers. Upon illumination, the base-collector junction can be modulated, resulting in an amplified current, which can lead to much greater photosensitivity. In 2002, Fujiwara et al. [136] demonstrated the detection of single electrons and single holes in SiNW transistors using an electron-hole system. Photogenerated carriers were stored in a quantum dot electrically formed in a SiNW by a front gate. The stored charges affected the current of the complementary carriers that flow along the bottom of the SiNW. A linear photoresponse of single-charge generation was observed. Later, the Park group [133, 137] reported both Si and Ge NW-FETs as polarization-sensitive, high-resolution light detectors in the visible range.

### 6.3.5.3 Superconductor Nanowire Photodetectors

Another photodetector concept that makes use of the unique geometrical properties of NWs is that of superconducting NW photodetectors, which are able to perform single-photon counting with exceptional sensitivity and time resolution at near-infrared wavelengths. Demonstrations of this concept have focused on NbN NWs with typical dimensions of  $\sim 5$  nm thickness and 50–200 nm width [138–143]. The working principle of superconducting NW detectors is described as follows [144]: the NW is maintained well below its superconducting critical temperature,  $T_c$ , and direct current biased just below its critical current. The absorption of a photon with energy higher than the superconducting energy gap creates a local nonequilibrium perturbation with a large number of excited hot electrons, which increases the average electron temperature above  $T_c$  and results in the formation of a hotspot—a local nonsuperconducting region. The local current density in the sidewalks increases beyond the critical current density and forms a resistive barrier across the width of the NW. The sudden increase in resistance from zero to a finite value generates a measurable output voltage pulse across the NW.

## 6.4 Future Directions and Challenges

Chemically synthesized NWs have witnessed a substantial interest in the past decade for building up photonic devices, and have been demonstrated for a host of photonic building blocks that exhibit sub-wavelength optical functionalities, such as

light emission, lasing, waveguiding and nonlinear optical mixing. Nonetheless, enormous challenges still remain to realize arrays of devices and circuits from these unique NW materials.

First, it is still challenging to achieve the accurate control of NW growth, including geometric perfection, size dispersion, and shape control, which are critical for developing high quality photonic devices due to, for example, changes in light confinements in these subwavelength structures. Second, although the 1D nanosized feature of NWs is appealing for high optical quality, these NWs have a significant external surface area, which potentially introduces a high density of surface-trap states that reduce desired radiative quantum yields (i.e., emission efficiency). Thus, proper passivation of those surface states should be considered to optimize the NW-based solid-state lighting. Third, compared to monolithic structures defined by lithography the efficiency of light coupling between adjacent NWs has been low. A potential approach to improve this coupling efficiency will be to grow branched NW structures with clean and crystalline interfaces. Fourth, quantitative and critical comparisons between NW photonic structures and conventional thin-film technologies, in terms of efficiency, fabrication cost and stability, is still lacking. Such benchmarking is important to evaluate whether this new class of nanostructures is a viable candidate for future generation of photonic technologies as commonly proposed, or perhaps, a new direction not yet envisioned where the unique properties can be better exploited. We suggest this avenue of thought and investigation, for example taking advantage of unique size and assembly capabilities to make very nontraditional free standing and three-dimensional structures, may yield the most impact in the future perhaps at the interface between nanophotonics, nanoelectronics and biology.

## References

1. A. Yariv, P. Yeh, *Photonics: Optical Electronics in Modern Communications (The Oxford Series in Electrical and Computer Engineering)* (Oxford University Press Inc., New York, 2006)
2. M.J. Deen, P.K. Basu, *Silicon Photonics: Fundamentals and Devices* (Wiley, Chichester, 2012)
3. R.G. Hobbs, N. Petkov, J.D. Holmes, Semiconductor nanowire fabrication by bottom-up and top-down paradigms. *Chem. Mat.* **24**(11), 1975–1991 (2012)
4. C.M. Lieber, Nanoscale science and technology: building a big future from small things. *MRS Bull.* **28**(07), 486–491 (2003)
5. C.M. Lieber, Z.L. Wang, Functional nanowires. *MRS Bull.* **32**(02), 99–108 (2007)
6. C.M. Lieber, Semiconductor nanowires: a platform for nanoscience and nanotechnology. *MRS Bull.* **36**(12), 1052–1063 (2011)
7. Y.-Z. Long, M. Yu, B. Sun, C.-Z. Gu, Z. Fan, Recent advances in large-scale assembly of semiconducting inorganic nanowires and nanofibers for electronics, sensors and photovoltaics. *Chem. Soc. Rev.* **41**(12), 4560–4580 (2012)
8. R. Agarwal, C.M. Lieber, Semiconductor nanowires: optics and optoelectronics. *Appl. Phys. A* **85**(3), 209–215 (2006)

9. Y. Li, F. Qian, J. Xiang, C.M. Lieber, Nanowire electronic and optoelectronic devices. *Mater. Today* **9**(10), 18–27 (2006)
10. D.J. Sirbully, M. Law, H. Yan, P. Yang, Semiconductor nanowires for subwavelength photonics integration. *J. Phys. Chem. B* **109**(32), 15190–15213 (2005)
11. Y. Ma, X. Guo, X. Wu, L. Dai, L. Tong, Semiconductor nanowire lasers. *Adv. Opt. Photonics* **5**(3), 216–273 (2013)
12. P.J. Pauzauskie, P. Yang, Nanowire photonics. *Mater. Today* **9**(10), 36–45 (2006)
13. R. Yan, D. Gargas, P. Yang, Nanowire photonics. *Nat. Photonics* **3**(10), 569–576 (2009)
14. Y. Huang, X. Duan, C.M. Lieber, Nanowires for integrated multicolor nanophotonics. *Small* **1**(1), 142–147 (2005)
15. K. Hiruma, M. Yazawa, T. Katsuyama, K. Ogawa, K. Haraguchi, M. Koguchi, H. Kakibayashi, Growth and optical properties of nanometer-scale GaAs and InAs whiskers. *J. Appl. Phys.* **77**(2), 447–462 (1995)
16. Y. Nagamune, H. Watabe, F. Sogawa, Y. Arakawa, One-dimensional exciton diffusion in GaAs quantum wires. *Appl. Phys. Lett.* **67**(11), 1535–1537 (1995)
17. X. Duan, J. Wang, C.M. Lieber, Synthesis and optical properties of gallium arsenide nanowires. *Appl. Phys. Lett.* **76**(9), 1116–1118 (2000)
18. J. Wang, M.S. Gudiksen, X. Duan, Y. Cui, C.M. Lieber, Highly polarized photoluminescence and photodetection from single indium phosphide nanowires. *Science* **293**(5534), 1455–1457 (2001)
19. M.S. Gudiksen, J. Wang, C.M. Lieber, Size-dependent photoluminescence from single indium phosphide nanowires. *J. Phys. Chem. B* **106**(16), 4036–4039 (2002)
20. H.W. Seo, S.Y. Bae, J. Park, H. Yang, K.S. Park, S. Kim, Strained gallium nitride nanowires. *J. Chem. Phys.* **116**(21), 9492–9499 (2002)
21. P. Yang, H. Yan, S. Mao, R. Russo, J. Johnson, R. Saykally, N. Morris, J. Pham, R. He, H.-J. Choi, Controlled growth of ZnO nanowires and their optical properties. *Adv. Funct. Mater.* **12**(5), 323 (2002)
22. Q. Xiong, G. Chen, J. Acord, X. Liu, J. Zengel, H. Gutierrez, J. Redwing, L. Lew Yan Voon, B. Lassen, P. Eklund, Optical properties of rectangular cross-sectional ZnS nanowires. *Nano Lett.* **4**(9), 1663–1668 (2004)
23. B. Xiang, H. Zhang, G. Li, F. Yang, F. Su, R. Wang, J. Xu, G. Lu, X. Sun, Q. Zhao, Green-light-emitting ZnSe nanowires fabricated via vapor phase growth. *Appl. Phys. Lett.* **82**(19), 3330–3332 (2003)
24. P.V. Radovanovic, C.J. Barrelet, S. Gradecak, F. Qian, C.M. Lieber, General synthesis of manganese-doped II–VI and III–V semiconductor nanowires. *Nano Lett.* **5**(7), 1407–1411 (2005)
25. C. Ma, Y. Ding, D. Moore, X. Wang, Z.L. Wang, Single-crystal CdSe nanosaws. *J. Am. Chem. Soc.* **126**(3), 708–709 (2004)
26. S. Bhattacharya, D. Banerjee, K. Adu, S. Samui, S. Bhattacharyya, Confinement in silicon nanowires: optical properties. *Appl. Phys. Lett.* **85**(11), 2008–2010 (2004)
27. D. van Dam, D.R. Abujetas, R. Paniagua-Dominguez, J.A. Sánchez-Gil, E.P. Bakkers, J. Haverkort, J. Gómez-Rivas, Directional and polarized emission from nanowire arrays. *Nano Lett.* **15**(7), 4557–4563 (2015)
28. R. Solanki, J. Huo, J. Freeouf, B. Miner, Atomic layer deposition of ZnSe/CdSe superlattice nanowires. *Appl. Phys. Lett.* **81**(20), 3864–3866 (2002)
29. W.I. Park, G.C. Yi, M. Kim, S.J. Pennycook, Quantum confinement observed in ZnO/ZnMgO nanorod heterostructures. *Adv. Mater.* **15**(6), 526–529 (2003)
30. N. Panev, A.I. Persson, N. Sköld, L. Samuelson, Sharp exciton emission from single InAs quantum dots in GaAs nanowires. *Appl. Phys. Lett.* **83**(11), 2238–2240 (2003)
31. P. Poole, J. Lefebvre, J. Fraser, Spatially controlled, nanoparticle-free growth of InP nanowires. *Appl. Phys. Lett.* **83**(10), 2055–2057 (2003)
32. M.J. Holmes, K. Choi, S. Kako, M. Arita, Y. Arakawa, Room-temperature triggered single photon emission from a III-nitride site-controlled nanowire quantum dot. *Nano Lett.* **14**(2), 982–986 (2014)

33. F. Qian, Y. Li, S. Gradečak, D. Wang, C.J. Barrelet, C.M. Lieber, Gallium nitride-based nanowire radial heterostructures for nanophotonics. *Nano Lett.* **4**(10), 1975–1979 (2004)
34. F. Qian, Y. Li, S. Gradečak, H.-G. Park, Y. Dong, Y. Ding, Z.L. Wang, C.M. Lieber, Multi-quantum-well nanowire heterostructures for wavelength-controlled lasers. *Nat. Mater.* **7**(9), 701–706 (2008)
35. F. Qian, M. Brewster, S.K. Lim, Y. Ling, C. Greene, O. Laboutin, J.W. Johnson, S. Gradečak, Y. Cao, Y. Li, Controlled synthesis of AlN/GaN multiple quantum well nanowire structures and their optical properties. *Nano Lett.* **12**(6), 3344–3350 (2012)
36. Y.-R. Shen, *Principles of Nonlinear Optics* (Wiley, New York, 1984)
37. R.W. Boyd, *Nonlinear Optics*, 2nd edn. (Academic Press, San Diego, 2003)
38. S. Yue, M.N. Slipchenko, J.X. Cheng, Multimodal nonlinear optical microscopy. *Laser Photonics Rev.* **5**(4), 496–512 (2011)
39. L. Tong, J.-X. Cheng, Label-free imaging through nonlinear optical signals. *Mater. Today* **14**(6), 264–273 (2011)
40. R. Cisek, V. Barzda, H.E. Ruda, A. Shik, Nonlinear optical properties of semiconductor nanowires. *IEEE J. Sel. Top. Quant.* **17**(4), 915–921 (2011)
41. C.J. Barrelet, H.-S. Ee, S.-H. Kwon, H.-G. Park, Nonlinear mixing in nanowire subwavelength waveguides. *Nano Lett.* **11**(7), 3022–3025 (2011)
42. J.C. Johnson, H. Yan, R.D. Schaller, P.B. Petersen, P. Yang, R.J. Saykally, Near-field imaging of nonlinear optical mixing in single zinc oxide nanowires. *Nano Lett.* **2**(4), 279–283 (2002)
43. J. Long, B. Simpkins, D. Rowenhorst, P. Pehrsson, Far-field imaging of optical second-harmonic generation in single GaN nanowires. *Nano Lett.* **7**(3), 831–836 (2007)
44. Y. Nakayama, P.J. Pauzauskie, A. Radenovic, R.M. Onorato, R.J. Saykally, J. Liphardt, P. Yang, Tunable nanowire nonlinear optical probe. *Nature* **447**(7148), 1098–1101 (2007)
45. F. Wang, P.J. Reece, S. Paiman, Q. Gao, H.H. Tan, C. Jagadish, Nonlinear optical processes in optically trapped InP nanowires. *Nano Lett.* **11**(10), 4149–4153 (2011)
46. R. Sanatinia, M. Swillo, S. Anand, Surface second-harmonic generation from vertical GaP nanopillars. *Nano Lett.* **12**(2), 820–826 (2012)
47. X. Liu, Q. Zhang, W.K. Chong, J.N. Yip, X. Wen, Z. Li, F. Wei, G. Yu, Q. Xiong, T.C. Sum, Cooperative enhancement of second-harmonic generation from a single CdS nanobelt-hybrid plasmonic structure. *ACS Nano* **9**(5), 5018–5026 (2015)
48. R. Sanatinia, S. Anand, M. Swillo, Modal engineering of second-harmonic generation in single GaP nanopillars. *Nano Lett.* **14**(9), 5376–5381 (2014)
49. O. Schwartz, D. Oron, Background-free third harmonic imaging of gold nanorods. *Nano Lett.* **9**(12), 4093–4097 (2009)
50. Y. Jung, L. Tong, A. Tanaudomongkon, J.-X. Cheng, C. Yang, In vitro and in vivo nonlinear optical imaging of silicon nanowires. *Nano Lett.* **9**(6), 2440–2444 (2009)
51. J. Jang, S. Park, N. Frazer, J. Ketterson, S. Lee, B. Roy, J. Cho, Strong P-band emission and third harmonic generation from ZnO nanorods. *Solid State Commun.* **152**(14), 1241–1243 (2012)
52. Y. Jung, H. Chen, L. Tong, J.-X. Cheng, Imaging gold nanorods by plasmon-resonance-enhanced four wave mixing. *J. Phys. Chem. C* **113**(7), 2657–2663 (2009)
53. E. Poutrina, C. Ciraci, D.J. Gauthier, D.R. Smith, Enhancing four-wave-mixing processes by nanowire arrays coupled to a gold film. *Opt. Express* **20**(10), 11005–11013 (2012)
54. Y. Wang, C.-Y. Lin, A. Nikolaenko, V. Raghunathan, E.O. Potma, Four-wave mixing microscopy of nanostructures. *Adv. Opt. Photonics* **3**(1), 1–52 (2011)
55. R.W. Hellwarth, Theory of stimulated Raman scattering. *Phys. Rev.* **130**(5), 1850 (1963)
56. M.F.S. Ferreira, Stimulated Raman scattering. In *Nonlinear Effects in Optical Fibers* (Wiley, New Jersey, 2011), pp. 245–272
57. J. Wu, A.K. Gupta, H.R. Gutierrez, P.C. Eklund, Cavity-enhanced stimulated Raman scattering from short GaP nanowires. *Nano Lett.* **9**(9), 3252–3257 (2009)

58. L. Tong, R.R. Gattass, J.B. Ashcom, S. He, J. Lou, M. Shen, I. Maxwell, E. Mazur, Subwavelength-diameter silica wires for low-loss optical wave guiding. *Nature* **426**(6968), 816–819 (2003)
59. C.J. Barrelet, A.B. Greytak, C.M. Lieber, Nanowire photonic circuit elements. *Nano Lett.* **4** (10), 1981–1985 (2004)
60. M. Law, D.J. Sirbuly, J.C. Johnson, J. Goldberger, R.J. Saykally, P. Yang, Nanoribbon waveguides for subwavelength photonics integration. *Science* **305**(5688), 1269–1273 (2004)
61. D.J. Sirbuly, M. Law, P. Pauzauskie, H. Yan, A.V. Maslov, K. Knutsen, C.-Z. Ning, R. J. Saykally, P. Yang, Optical routing and sensing with nanowire assemblies. *Proc. Natl. Acad. Sci. U.S.A.* **102**(22), 7800–7805 (2005)
62. R. Yan, P. Pauzauskie, J. Huang, P. Yang, Direct photonic–plasmonic coupling and routing in single nanowires. *Proc. Natl. Acad. Sci. U.S.A.* **106**(50), 21045–21050 (2009)
63. H.-G. Park, C.J. Barrelet, Y. Wu, B. Tian, F. Qian, C.M. Lieber, A wavelength-selective photonic-crystal waveguide coupled to a nanowire light source. *Nat. Photonics* **2**(10), 622–626 (2008)
64. J. Xu, X. Zhuang, P. Guo, W. Huang, W. Hu, Q. Zhang, Q. Wan, X. Zhu, Z. Yang, L. Tong, Asymmetric light propagation in composition-graded semiconductor nanowires. *Sci. Rep.* **2**, 820 (2012)
65. E.F. Schubert, J. Cho, J.K. Kim, Light-emitting diodes. In *Kirk-Othmer Encyclopedia of Chemical Technology* (Wiley, Hoboken, NJ, 2015)
66. X. Duan, Y. Huang, Y. Cui, J. Wang, C.M. Lieber, Indium phosphide nanowires as building blocks for nanoscale electronic and optoelectronic devices. *Nature* **409**(6816), 66–69 (2001)
67. Z. Zhong, F. Qian, D. Wang, C.M. Lieber, Synthesis of p-type gallium nitride nanowires for electronic and photonic nanodevices. *Nano Lett.* **3**(3), 343–346 (2003)
68. K. Haraguchi, T. Katsuyama, K. Hiruma, K. Ogawa, GaAs p-n junction formed in quantum wire crystals. *Appl. Phys. Lett.* **60**(6), 745–747 (1992)
69. M.S. Gudiksen, L.J. Lauhon, J. Wang, D.C. Smith, C.M. Lieber, Growth of nanowire superlattice structures for nanoscale photonics and electronics. *Nature* **415**(6872), 617–620 (2002)
70. H.-M. Kim, Y.-H. Cho, H. Lee, S.I. Kim, S.R. Ryu, D.Y. Kim, T.W. Kang, K.S. Chung, High-brightness light emitting diodes using dislocation-free indium gallium nitride/gallium nitride multiquantum-well nanorod arrays. *Nano Lett.* **4**(6), 1059–1062 (2004)
71. Y.-H. Ra, R. Navamathavan, H.-I. Yoo, C.-R. Lee, Single Nanowire Light-Emitting Diodes Using Uniaxial and Coaxial InGaN/GaN Multiple Quantum Wells Synthesized by Metalorganic Chemical Vapor Deposition. *Nano Lett.* **14**, 1537–1545 (2014)
72. F. Qian, S. Gradecak, Y. Li, C.-Y. Wen, C.M. Lieber, Core/multishell nanowire heterostructures as multicolor, high-efficiency light-emitting diodes. *Nano Lett.* **5**(11), 2287–2291 (2005)
73. Y.-H. Ra, R. Navamathavan, J.-H. Park, C.-R. Lee, Coaxial In<sub>x</sub>Ga<sub>1-x</sub>N/GaN multiple quantum well nanowire arrays on Si(111) substrate for high-performance light-emitting diodes. *Nano Lett.* **13**(8), 3506–3516 (2013)
74. O. Svelto, D.C. Hanna, *Principles of Lasers*, 5th edn. (Springer, New York, 2010)
75. M.A. Zimmler, F. Capasso, S. Müller, C. Ronning, Optically pumped nanowire lasers: invited review. *Semicond. Sci. Tech.* **25**(2), 024001 (2010)
76. R.M. Ma, R.F. Oulton, V.J. Sorger, X. Zhang, Plasmon lasers: coherent light source at molecular scales. *Laser Photonics Rev.* **7**(1), 1–21 (2013)
77. D. Vanmaekelbergh, L.K. van Vugt, ZnO nanowire lasers. *Nanoscale* **3**(7), 2783–2800 (2011)
78. M.H. Huang, S. Mao, H. Feick, H. Yan, Y. Wu, H. Kind, E. Weber, R. Russo, P. Yang, Room-temperature ultraviolet nanowire nanolasers. *Science* **292**(5523), 1897–1899 (2001)
79. J.C. Johnson, H. Yan, R.D. Schaller, L.H. Haber, R.J. Saykally, P. Yang, Single nanowire lasers. *J. Phys. Chem. B* **105**(46), 11387–11390 (2001)
80. H. Yan, R. He, J. Johnson, M. Law, R.J. Saykally, P. Yang, Dendritic nanowire ultraviolet laser array. *J. Am. Chem. Soc.* **125**(16), 4728–4729 (2003)

81. J.C. Johnson, K.P. Knutsen, H. Yan, M. Law, Y. Zhang, P. Yang, R.J. Saykally, Ultrafast carrier dynamics in single ZnO nanowire and nanoribbon lasers. *Nano Lett.* **4**(2), 197–204 (2004)
82. Y. Zhang, R.E. Russo, S.S. Mao, Quantum efficiency of ZnO nanowire nanolasers. *Appl. Phys. Lett.* **87**(4), 043106–043106–3 (2005)
83. W. Kwok, A.B. Djurišić, Y.H. Leung, D. Li, K. Tam, D. Phillips, W. Chan, Influence of annealing on stimulated emission in ZnO nanorods. *Appl. Phys. Lett.* **89**(18), 183112 (2006)
84. M.A. Zimmler, J. Bao, F. Capasso, S. Müller, C. Ronning, Laser action in nanowires: observation of the transition from amplified spontaneous emission to laser oscillation. *Appl. Phys. Lett.* **93**(5), 051101 (2008)
85. D.J. Gargas, M.E. Toimil-Molares, P. Yang, Imaging single ZnO vertical nanowire laser cavities using UV-laser scanning confocal microscopy. *J. Am. Chem. Soc.* **131**(6), 2125–2127 (2009)
86. B. Zou, R. Liu, F. Wang, A. Pan, L. Cao, Z.L. Wang, Lasing mechanism of ZnO nanowires/nanobelts at room temperature. *J. Phys. Chem. B* **110**(26), 12865–12873 (2006)
87. J.C. Johnson, H.-J. Choi, K.P. Knutsen, R.D. Schaller, P. Yang, R.J. Saykally, Single gallium nitride nanowire lasers. *Nat. Mater.* **1**(2), 106–110 (2002)
88. S. Gradečak, F. Qian, Y. Li, H.-G. Park, C.M. Lieber, GaN nanowire lasers with low lasing thresholds. *Appl. Phys. Lett.* **87**(17), 173111 (2005)
89. H.-G. Park, F. Qian, C.J. Barrelet, Y. Li, Microstadium single-nanowire laser. *Appl. Phys. Lett.* **91**(25), 251115–251115-3 (2007)
90. P.C. Upadhyaya, Q. Li, G.T. Wang, A.J. Fischer, A.J. Taylor, R.P. Prasankumar, The influence of defect states on non-equilibrium carrier dynamics in GaN nanowires. *Semicond. Sci. Tech.* **25**(2), 024017 (2010)
91. A. Armstrong, Q. Li, K.H.A. Bogart, Y. Lin, G.T. Wang, A.A. Talin, Deep level optical spectroscopy of GaN nanorods. *J. Appl. Phys.* **106**(5), 053712 (2009)
92. A. Armstrong, G. Wang, A. Talin, Depletion-mode photoconductivity study of deep levels in GaN nanowires. *J. Electron. Mater.* **38**(4), 484–489 (2009)
93. Q. Zhang, G. Li, X. Liu, F. Qian, Y. Li, T.C. Sum, C.M. Lieber, Q. Xiong, A room temperature low-threshold ultraviolet plasmonic nanolaser. *Nat. Commun.* **5**, 4953 (2014)
94. P.J. Pauzauskie, D.J. Sirbully, P. Yang, Semiconductor nanowire ring resonator laser. *Phys. Rev. Lett.* **96**(14), 143903 (2006)
95. R. Agarwal, C.J. Barrelet, C.M. Lieber, Lasing in single cadmium sulfide nanowire optical cavities. *Nano Lett.* **5**(5), 917–920 (2005)
96. A.B. Greytak, C.J. Barrelet, Y. Li, C.M. Lieber, Semiconductor nanowire laser and nanowire waveguide electro-optic modulators. *Appl. Phys. Lett.* **87**(15), 151103 (2005)
97. B. Liu, R. Chen, X. Xu, D. Li, Y. Zhao, Z. Shen, Q. Xiong, H. Sun, Exciton-related photoluminescence and lasing in CdS nanobelts. *J. Phys. Chem. C* **115**(26), 12826–12830 (2011)
98. S. Geburt, A. Thielmann, R. Röder, C. Borschel, A. McDonnell, M. Kozlik, J. Kühnel, K.A. Sunter, F. Capasso, C. Ronning, Low threshold room-temperature lasing of CdS nanowires. *Nanotechnology* **23**(36), 365204 (2012)
99. A. Pan, R. Liu, Q. Zhang, Q. Wan, P. He, M. Zacharias, B. Zou, Fabrication and red-color lasing of individual highly uniform single-crystal CdSe nanobelts. *J. Phys. Chem. C* **111**(38), 14253–14256 (2007)
100. Y. Ye, Y. Ma, S. Yue, L. Dai, H. Meng, Z. Li, L. Tong, G. Qin, Lasing of CdSe/SiO<sub>2</sub> nanocables synthesized by the facile chemical vapor deposition method. *Nanoscale* **3**(8), 3072–3075 (2011)
101. A. Chin, S. Vaddiraju, A. Maslov, C. Ning, M. Sunkara, M. Meyyappan, Near-infrared semiconductor subwavelength-wire lasers. *Appl. Phys. Lett.* **88**(16), 163115 (2006)
102. B. Hua, J. Motohisa, Y. Ding, S. Hara, T. Fukui, Characterization of Fabry-Perot microcavity modes in GaAs nanowires fabricated by selective-area metal organic vapor phase epitaxy. *Appl. Phys. Lett.* **91**(13), 131112 (2007)

103. Y. Ding, J. Motohisa, B. Hua, S. Hara, T. Fukui, Observation of microcavity modes and waveguides in InP nanowires fabricated by selective-area metalorganic vapor-phase epitaxy. *Nano Lett.* **7**(12), 3598–3602 (2007)
104. B. Hua, J. Motohisa, Y. Kobayashi, S. Hara, T. Fukui, Single GaAs/GaAsP coaxial core-shell nanowire lasers. *Nano Lett.* **9**(1), 112–116 (2009)
105. Y. Liu, J.A. Zapien, Y. Shan, C.Y. Geng, C.S. Lee, S.T. Lee, Wavelength-controlled lasing in  $Zn_xCd_{1-x}S$  single-crystal nanoribbons. *Adv. Mater.* **17**(11), 1372–1377 (2005)
106. A. Pan, H. Yang, R. Liu, R. Yu, B. Zou, Z. Wang, Color-tunable photoluminescence of alloyed  $CdS_xSe_{1-x}$  nanobelts. *J. Am. Chem. Soc.* **127**(45), 15692–15693 (2005)
107. A. Pan, R. Liu, F. Wang, S. Xie, B. Zou, M. Zacharias, Z.L. Wang, High-QUALITY ALLOYED  $CdS_xSe_{1-x}$  whiskers as waveguides with tunable stimulated emission. *J. Phys. Chem. B* **110**(45), 22313–22317 (2006)
108. Y. Liu, J. Zapien, Y. Shan, H. Tang, C. Lee, S. Lee, Wavelength-tunable lasing in single-crystal  $CdS_{1-x}Se_x$  nanoribbons. *Nanotechnology* **18**(36), 365606 (2007)
109. A. Pan, W. Zhou, E.S. Leong, R. Liu, A.H. Chin, B. Zou, C. Ning, Continuous alloy-composition spatial grading and superbroad wavelength-tunable nanowire lasers on a single chip. *Nano Lett.* **9**(2), 784–788 (2009)
110. F. Gu, Z. Yang, H. Yu, J. Xu, P. Wang, L. Tong, A. Pan, Spatial bandgap engineering along single alloy nanowires. *J. Am. Chem. Soc.* **133**(7), 2037–2039 (2011)
111. J. Zapien, Y. Liu, Y. Shan, H. Tang, C. Lee, S. Lee, Continuous near-infrared-to-ultraviolet lasing from II-VI nanoribbons. *Appl. Phys. Lett.* **90**(21), 213114 (2007)
112. C. Luan, Y. Liu, Y. Jiang, J. Jie, I. Bello, S. Lee, J. Zapien, Composition tuning of room-temperature nanolasers. *Vacuum* **86**(6), 737–741 (2012)
113. J. Xu, L. Ma, P. Guo, X. Zhuang, X. Zhu, W. Hu, X. Duan, A. Pan, Room-temperature dual-wavelength lasing from single-nanoribbon lateral heterostructures. *J. Am. Chem. Soc.* **134**(30), 12394–12397 (2012)
114. H. Zhu, Y. Fu, F. Meng, X. Wu, Z. Gong, Q. Ding, M.V. Gustafsson, M.T. Trinh, S. Jin, X. Zhu, Lead halide perovskite nanowire lasers with low lasing thresholds and high quality factors. *Nat. Mater.* **14**(6), 636–642 (2015)
115. Y. Xiao, C. Meng, P. Wang, Y. Ye, H. Yu, S. Wang, F. Gu, L. Dai, L. Tong, Single-nanowire single-mode laser. *Nano Lett.* **11**(3), 1122–1126 (2011)
116. Y. Xiao, C. Meng, X. Wu, L. Tong, Single mode lasing in coupled nanowires. *Appl. Phys. Lett.* **99**(2), 023109 (2011)
117. H. Xu, J.B. Wright, T.-S. Luk, J.J. Figiel, K. Cross, L.F. Lester, G. Balakrishnan, G.T. Wang, I. Brener, Q. Li, Single-mode lasing of GaN nanowire-pairs. *Appl. Phys. Lett.* **101**(11), 113106 (2012)
118. H. Gao, A. Fu, S.C. Andrews, P. Yang, Cleaved-coupled nanowire lasers. *Proc. Natl. Acad. Sci. U.S.A.* **110**(3), 865–869 (2013)
119. X. Duan, Y. Huang, R. Agarwal, C.M. Lieber, Single-nanowire electrically driven lasers. *Nature* **421**(6920), 241–245 (2003)
120. X. Ma, J. Pan, P. Chen, D. Li, H. Zhang, Y. Yang, D. Yang, Room temperature electrically pumped ultraviolet random lasing from ZnO nanorod arrays on Si. *Opt. Express* **17**(16), 14426–14433 (2009)
121. S. Chu, G. Wang, W. Zhou, Y. Lin, L. Chernyak, J. Zhao, J. Kong, L. Li, J. Ren, J. Liu, Electrically pumped waveguide lasing from ZnO nanowires. *Nat. Nanotechnol.* **6**(8), 506–510 (2011)
122. C. Liu, H. Xu, J. Ma, X. Li, X. Zhang, Y. Liu, R. Mu, Electrically pumped near-ultraviolet lasing from ZnO/MgO core/shell nanowires. *Appl. Phys. Lett.* **99**(6), 063115 (2011)
123. X.-Y. Liu, C.-X. Shan, S.-P. Wang, Z.-Z. Zhang, D.-Z. Shen, Electrically pumped random lasers fabricated from ZnO nanowire arrays. *Nanoscale* **4**(9), 2843–2846 (2012)
124. K. Li, X. Liu, Q. Wang, S. Zhao, Z. Mi, Ultralow-threshold electrically injected AlGaIn nanowire ultraviolet lasers on Si operating at low temperature. *Nat. Nanotechnol.* **10**(2), 140–144 (2015)



125. F. Omnes, Introduction to semiconductor photodetectors. In *Optoelectronic Sensors* (ISTE, Arlington, VA, 2010), pp. 1–14
126. H. Kind, H. Yan, B. Messer, M. Law, P. Yang, Nanowire Ultraviolet Photodetectors and Optical Switches. *Adv. Mater.* **14**(2), 158–160 (2002)
127. C. Soci, A. Zhang, X.-Y. Bao, H. Kim, Y. Lo, D. Wang, Nanowire photodetectors. *J. Nanosci. Nanotechnol.* **10**(3), 1430–1449 (2010)
128. M. Son, S. Im, Y. Park, C. Park, T. Kang, K.-H. Yoo, Ultraviolet photodetector based on single GaN nanorod p–n junctions. *Mater. Sci. Eng., C* **26**(5), 886–888 (2006)
129. H. Pettersson, J. Trägårdh, A.I. Persson, L. Landin, D. Hessman, L. Samuelson, Infrared photodetectors in heterostructure nanowires. *Nano Lett.* **6**(2), 229–232 (2006)
130. Z. Guo, D. Zhao, Y. Liu, D. Shen, J. Zhang, B. Li, Visible and ultraviolet light alternative photodetector based on ZnO nanowire/n-Si heterojunction. *Appl. Phys. Lett.* **93**(16), 163501–163501-3 (2008)
131. O. Hayden, R. Agarwal, C.M. Lieber, Nanoscale avalanche photodiodes for highly sensitive and spatially resolved photon detection. *Nat. Mater.* **5**(5), 352–356 (2006)
132. C. Yang, C.J. Barrelet, F. Capasso, C.M. Lieber, Single p-type/intrinsic/n-type silicon nanowires as nanoscale avalanche photodetectors. *Nano Lett.* **6**(12), 2929–2934 (2006)
133. Y. Ahn, J. Dunning, J. Park, Scanning photocurrent imaging and electronic band studies in silicon nanowire field effect transistors. *Nano Lett.* **5**(7), 1367–1370 (2005)
134. Y. Gu, E.-S. Kwak, J. Lensch, J. Allen, T.W. Odom, L.J. Lauhon, Near-field scanning photocurrent microscopy of a nanowire photodetector. *Appl. Phys. Lett.* **87**(4), 043111 (2005)
135. G. Cheng, X. Wu, B. Liu, B. Li, X. Zhang, Z. Du, ZnO nanowire Schottky barrier ultraviolet photodetector with high sensitivity and fast recovery speed. *Appl. Phys. Lett.* **99**(20), 203105 (2011)
136. A. Fujiwara, K. Yamazaki, Y. Takahashi, Detection of single charges and their generation-recombination dynamics in Si nanowires at room temperature. *Appl. Phys. Lett.* **80**(24), 4567–4569 (2002)
137. Y. Ahn, J. Park, Efficient visible light detection using individual germanium nanowire field effect transistors. *Appl. Phys. Lett.* **91**(16), 162102 (2007)
138. J.K. Yang, E. Dauler, A. Ferri, A. Pearlman, A. Verevkin, G. Gol'tsman, B. Voronov, R. Sobolewski, W.E. Keicher, K.K. Berggren, Fabrication development for nanowire GHz-counting-rate single-photon detectors. *IEEE T. Appl. Supercon.* **15**(2), 626–630 (2005)
139. K.M. Rosfjord, J.K. Yang, E.A. Dauler, A.J. Kerman, V. Anant, B.M. Voronov, G.N. Gol'Tsman, K.K. Berggren, Nanowire single-photon detector with an integrated optical cavity and anti-reflection coating. *Opt. Express* **14**(2), 527–534 (2006)
140. F. Marsili, D. Bitauld, A. Fiore, A. Gaggero, F. Mattioli, R. Leoni, M. Benkahoul, F. Lévy, High efficiency NbN nanowire superconducting single photon detectors fabricated on MgO substrates from a low temperature process. *Opt. Express* **16**(5), 3191–3196 (2008)
141. S. Miki, M. Fujiwara, M. Sasaki, B. Baek, A.J. Miller, R.H. Hadfield, S.W. Nam, Z. Wang, Large sensitive-area NbN nanowire superconducting single-photon detectors fabricated on single-crystal MgO substrates. *Appl. Phys. Lett.* **92**(6), 061116 (2008)
142. F. Marsili, F. Najafi, E. Dauler, F. Bellei, X. Hu, M. Csete, R.J. Molnar, K.K. Berggren, Single-photon detectors based on ultranarrow superconducting nanowires. *Nano Lett.* **11**(5), 2048–2053 (2011)
143. S. Ferrari, O. Kahl, V. Kovalyuk, G.N. Goltsman, A. Korneev, W.H. Pernice, Waveguide-integrated single- and multi-photon detection at telecom wavelengths using superconducting nanowires. *Appl. Phys. Lett.* **106**(15), 151101 (2015)
144. C.M. Natarajan, M.G. Tanner, R.H. Hadfield, Superconducting nanowire single-photon detectors: physics and applications. *Supercond. Sci. Technol.* **25**(6), 063001 (2012)

# Chapter 7

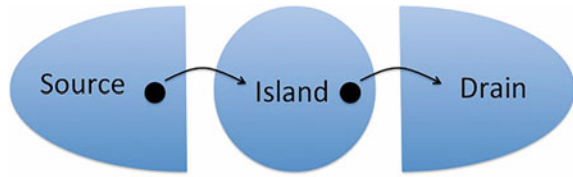
## Quantum Devices

**Abstract** The NW structure is highly anisotropic with radial dimensions confined by the diameters to  $<100$  nm and axial lengths  $>1000$  nm, although the axial device dimension can be confined during synthesis, for example by modulation doping, or by device fabrication. When the confined dimensions of the NWs become comparable to the electron wavelength, the fundamental quantum properties of charge carriers dominate the charge transport and new device properties become possible. In this chapter, we introduce studies over the past decade where quantum properties are critical to the observed behavior, including quantum dot systems in semiconductor NWs, hybrid superconductor-semiconductor NW devices, and NW topological insulators.

### 7.1 Introduction

The continuous miniaturization of electronic devices has naturally led to the research addressing the device size scales needed to achieve fundamentally new properties. Here, “new properties” refers to quantum phenomena that can only be detected in meso- or nanoscale systems [1–10]. For example, consider the basic case of charge transport between two electrodes through an intermediary small island that is weakly coupled to the two electrodes (Fig. 7.1) [1, 2]. Assume the number of electrons on this island is  $N$ , when a voltage is applied between the two electrodes, electrons can travel from the source, via the island, to the drain, with the current dependent on a number of established factors [1, 2]. In this tunneling regime, the energy to add (or remove) a single electron is given by the charging energy,  $E_C = e^2/C$ , where  $e$  is fundamental charge of an electron and  $C$  denotes the capacitance of the island. If  $E_C$  is  $<$  the thermal energy,  $k_B T$ , the current will increase continuously to yield an effectively conventional current–voltage response; however, when  $E_C > k_B T$ , discrete step-wise increases in current can be observed. This interesting single-charge tunneling regime can be accessed by reducing the size and hence capacitance of the island, and by carrying out measurements at ultralow temperature to decrease the thermal energy [1, 2]. Single charge tunneling

**Fig. 7.1** Single charge tunneling between the source and drain electrodes through an intermediate “island”



effects were predicted by Likharev et al. [11, 12] and controllably demonstrated in 1987 [13] for aluminum island or quantum dot (QD) structures, where the QD size was varied during device fabrication.

Similar structures have been widely studied in 2D electron gases (2DEGs) prepared for example from GaAs/AlGaAs heterostructures [14, 15], where lithographically defined electrodes patterned on the intrinsic upper semiconductor layers can be used to define the central QD islands and tune the coupling between the islands and source/drain electrodes. More complex coupled QD systems, such as double QDs appear to be especially interesting due to the possibility to control the entanglement of electron spins by tuning the exchange coupling between the dots [16, 17]. In this case, NWs may serve as an ideal platform for defining QDs, because the cylindrical geometry of NWs not only provides lateral confinement, but also makes it natural to envision linear arrays of coupled QDs along the length of a NW [8]. Up to now, QDs have been realized within NWs in various material systems, and it has been shown that control of the number of electrons down to the last one is possible [18–24]. In addition, NWs have been used to explore applications in quantum information technology where double dots as quantum gates or even serial arrays of dots along a wire are needed [25–31]. In Sect. 7.2, we introduce four configurations of QD systems in NWs, basic electronic properties of QDs, single QD and coupled QDs in NWs, as well as the effective  $g$ -factor ( $g^*$ ) and spin-orbit interaction properties.

When a normal state metal or semiconductor is connected to a superconductor (S), superconductivity can be induced in the metal or semiconductor. This phenomenon, known as the superconducting proximity effect [32], becomes more interesting when the normal state conductor consists of a nanoscale semiconductor with a reduced dimensionality whose electronic states can be tuned by means of electric or magnetic fields. This hybrid combination of superconductors and low-dimensional semiconductors offers a versatile ground for novel device concepts [9]. Such concepts, which form an emerging domain between superconducting electronics and spintronics, rest on rich and largely unexplored physics that involves both superconductivity and spin-related effects [33]. In Sect. 7.3, we will focus on Josephson junctions in which two superconducting electrodes are connected to a single NW [34–37], and the observation of Majorana fermions in NWs with superconducting electrodes [33, 38–42].

In addition, topological insulators (TIs) display unique properties that are distinct from insulators and metals, with the bulk being insulating and the topologically-protected surface states being metallic [43]. The direct manipulation

of these edge/surface states has been difficult in macroscale objects because the contributions from bulk carriers [44]. In Sect. 7.4, we review TIs with well-defined nanoscale morphology, which has larger surface-to-volume ratios than bulk materials and is ideal for interference-type experiments for surface states.

## 7.2 Quantum Dot Systems in Semiconductor Nanowires

In semiconductor NW devices, the low-temperature quantum transport of carriers will depend on several factors, including (i) the coupling of electrodes to the NW and (ii) diameter and length with respect to carrier Bohr radii and temperature. When the contacts are close to transparent and the NW diameters are sufficiently small, then it is possible to observe quantized conductance through discrete 1D sub-bands (assuming temperature is less than the level spacing) with the conductance increasing by  $\sim 2e^2/h$  for each additional sub-band [45, 46]. In the more general case where the electrodes are weakly coupled, the NW behaves as an elongated QD with the size defined by the electrode separation and NW diameter, or alternatively, in modulated NWs by the synthetically-imposed barriers along the NW axial direction [8]. In this section, several aspects of QD systems in both homogeneous and heterogeneous NWs will be introduced, including several configurations of NW-based QD systems, basic electronic properties of QDs, single and coupled QDs in NWs, as well as  $g^*$  and spin-orbit interaction properties. A comprehensive review of QD systems in semiconductor NWs can be found in [8].

### 7.2.1 Configurations of Quantum Dot Systems in Nanowires

In previous reports, four different methods have been employed to define QD systems in NWs, based on how junctions (along the NW axial direction) are formed. They include QDs defined by the metallic electrodes, QD segments in NWs, QDs defined by patterned gates, and etched constrictions in NWs [8]. The first method involves the deposition of metallic contact electrodes to form tunneling barriers between the NW and the electrodes, where the QD size is determined by the separation of electrodes, due to a sharp potential profile defined by the contact [18–20, 47]. For example, Fig. 7.2a shows SEM image of InP NW-based QD with two EBL fabricated Ti/Al electrodes. The distance between the electrodes varied between 0.2 and 2  $\mu\text{m}$ . In this experiment, a degenerately-doped Si was used as an electrostatic gate to tune the number of electrons in the QD [18]. The second QD configuration is defined during NW growth. For example, in the works of the Samuelson group [21–23, 48], NW-based QDs have been fabricated by the growth of double barriers of InP (arrows, Fig. 7.2b) in InAs NWs. Control of the lengths of the InAs and InP sections has been achieved down to a few nm, with the spacing between barriers ranging from 8 nm to more than 100 nm. The diameter and length

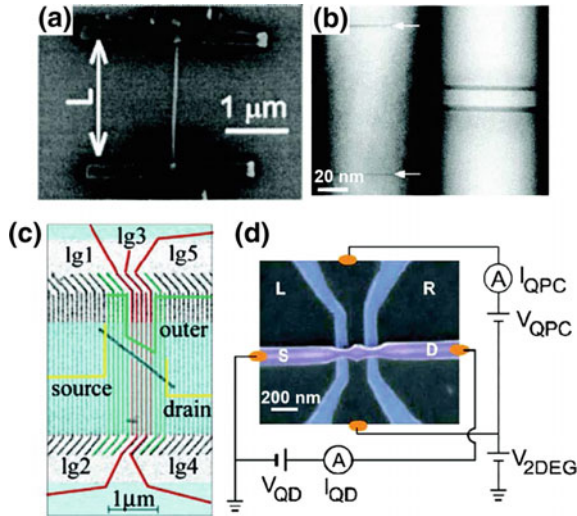


**Fig. 7.2** **a** SEM image of the InP NW QD formed between two electrodes spaced  $2\ \mu\text{m}$  apart. Reproduced from [18]. Copyright 2003 AIP Publishing LLC. **b** Dark field scanning TEM images of few nm wide InP (*dark*) barriers in InAs NWs. Reproduced from [22]. Copyright 2004 American Chemical Society. **c** SEM of grid of five electrodes lg1–lg5 buried underneath SiN layer, with the InAs NW and source/drain electrodes deposited on top. Reproduced from [49]. Copyright 2005 American Chemical Society. **d** SEM of and two etched constrictions in the InAs NW (*purple*) forming tunnelling barriers to the central InAs QD. Reproduced from [53]. Copyright 2008 American Physical Society

of the InAs section between the InP barriers control the transverse and axial confinement energies, respectively. Long sections of InAs on either side of the QD acted as highly conductive source and drain leads.

The third scheme involves lithographic patterning of closely spaced metallic gates on the top of (or below) NWs, where variations in the applied gate voltages can be used to define the size carriers in the a QD for a homogeneous NW [25, 49–52]. Figure 7.2c shows SEM image of a InAs NW deposited on top of an array of EBL-defined gold gate electrodes. The metallic gate electrodes are electrically isolated from the conducting channel of the NW by a thin layer of SiN dielectric film to prevent current flow. These electrostatic gates are biased to deplete or enhance the carrier concentration in the NW, and to produce an electrostatic potential landscape for confinement of electrons or holes at different positions along the length of the NW [49]. The fourth approach uses post-fabrication processing, such as wet chemical etching, to modify a small region of the NW structure and thus define a NW-based QD [53]. Figure 7.2d shows a InAs NW with double-barrier constrictions defined by wet etching, yielding a central QD connected to the NW arms.

### 7.2.2 Basic Electronic Properties of Quantum Dots

As described above, single electron devices differ from classical devices in the sense that the discreteness of electrons and the electrochemical potential changes associated with adding or removing a single electron have to be considered. Single electron devices consist of an “island”, a region containing localized carriers isolated by tunnel junctions with barriers to carrier tunneling [1, 2]. For example, a single-electron transistor (SET) is a device in which electrons tunnel one at a time through a small island connected to two leads via tunnel junctions [10]. When tunneling barriers are present such that the number of electrons on the island is a well-defined number, an additional electron can be transferred to the island only if there is sufficient energy to overcome the increase in electrochemical potential associated with adding the electron number. In a classical picture, the change in electrochemical potential is due to the change in Coulomb energy when an electron is added (or subtracted). If quantum confinement is strong, the electrochemical potential also includes contributions from the discrete single particle energy states. A signature of QDs is the Coulomb blockade (CB) effect [1, 2]: current only flows through a QD when the incoming electrons have enough energy to overcome the Coulomb repulsion (i.e., the charging energy) due to the electrons that are already on the dot. The energy barrier caused by Coulomb repulsion can be lowered with the aid of a gate voltage or a sufficiently large source–drain bias voltage. When the current through the dot is plotted as pseudo 3D color or gray scale versus gate voltage on one axis and the source–drain bias voltage on another axis, the CB manifests itself as a series of diamonds inside which current cannot flow, separated by regions of voltage space in which current flows. To observe this phenomena the measurement temperature must be sufficiently low that the thermal energy is much smaller than the charging energy [1, 3].

Correlation between charge and spin filling in the QDs energy levels is relevant for applications such as spin qubits, where control of the spin degree freedom is essential [54]. A key parameter related to spin state is the effective g-factor,  $g^*$ , which can be determined from level splitting for different spin states as a function of magnetic field. Consider a free electron with spin  $s$  and orbital angular momentum  $l$ , and associated magnetic moment,  $\mu_s$  and  $\mu_l$ , calculated from the following equations:

$$\mu_l = -\frac{e}{2m_0}l$$

$$\mu_s = -g_s\frac{e}{2m_0}s$$

where  $g_s$  is known as the g-factor. Classically it should be 1, but is 2 according to Dirac’s relativistic quantum theory. The above equations indicate that the spin angular momentum is twice as effective in producing a magnetic moment. For charge and spin carriers in semiconductors, the g-factor is renormalized from the

bare value 2 by band structure effects and is referred to as the effective g-factor ( $g^*$ ), in analogy with the effective mass ( $m^*$ ) [54].

Spin can also be indirectly manipulated by electric fields via the spin-orbit interaction, which denotes the interaction between  $\mu_s$  and  $\mu_l$  [54]. For an electron spinning around nucleus, an internal magnetic field,  $B_l$ , is generated on its orbit. The shift in energy due to spin-orbit interaction, named magnetic potential energy,  $V_{l,s}$ , is thus defined by:

$$V_{l,s} = -\mu_s \cdot B_l$$

Besides the internal magnetic field, the external electric fields coupled with electron spin can also change the magnetic field [55]. In QDs at a low temperature, strong spin-orbit interaction will make electrons more susceptible to spin-flip processes when experiencing fluctuations in environmental electric fields but may also enable effective manipulation of spin via electric fields [5, 8, 54, 56].

### 7.2.3 Single Quantum Dots in Nanowires

In 2003, Kouwenhoven and coworkers [18] reported the SET behavior in InP NW devices. The electron density in the wires is changed with a back gate. Transport measurements were measured down to 0.35 K, where single-electron tunneling and quantum effects play a dominant role, and show CB behavior with single-electron charging energies of  $\sim 1$  meV. However, the Coulomb peaks had irregularly distributed sizes, and their  $V_g$  spacings varied considerably, suggesting the formation of more than one electronic island along the NW length. The Samuelson group [21–23] fabricated SETs using heterostructure NW growth, by introducing InP barriers into InAs NWs. These devices showed ideal SET characteristics at low temperatures, where the blockage of the current between the isolated InAs island varied periodically as a function of the gate voltage. By changing the length of the InAs island, the authors designed devices ranging from SETs to few-electron QDs. In the latter case, electrons could be added one by one to the dots from 0 to  $\sim 50$  electrons. While the charging energy was found to be almost constant for each addition, analyses of the results provided quantized energy level or shell structure resulting from spin and orbital degeneracies. Magnetic-field dependent measurements also yielded the Zeeman splitting in these InAs QDs, and analyses of this data showed that the values of the  $g^*$  of the first few electrons entering the dot depended on the dot size. Specifically, compared with the bulk value of 14.7, the authors reported that larger dots had bulk-like values of  $\sim 13$ , and that  $|g^*|$  decreased to 2.3 for the smallest dots.

Later, Zhong et al. [19] fabricated single crystal *p*-type SiNWs SETs, and observed single QD behavior with the two tunnel barriers formed by the patterned *S/D* contacts, as evident in Fig. 7.3a, b. In Fig. 7.3a,  $I$ - $V_g$  data recorded with a 0.5 mV  $V_{sd}$  at 4.2 K is plotted for a device with source–drain separation of 400 nm.

The  $I-V_g$  curves exhibit regular oscillations over a broad range of  $V_g$ , in which the current peaks are separated by regions of zero conductance with an average peak-to-peak separation of  $0.015 \pm 0.001$  V. The position and heights of the peaks are reproducible on repeated  $V_g$  scans in these devices. In addition, differential conductance ( $\partial I/\partial V_{sd}$ ) versus  $V_{sd}$  and  $V_g$  (Fig. 7.3b) exhibit 33 CB diamonds, where transport is “blocked” for values of  $V_{sd}-V_g$  in the light-colored regions. The regular closed diamond structure provides strong evidence for transport through a single quantum structure. Figure 7.3c shows  $\partial I/\partial V_{sd}-V_{sd}-V_g$  at higher resolution for a 3 nm diameter SiNW device with a 100 nm source-drain separation. The data exhibit well-defined peaks in  $\partial I/\partial V_{sd}$  that appear as lines running parallel to the edges of the CB diamonds and consistent with discrete single particle quantum levels extending across the SiNW. Temperature dependent  $I-V_g$  measurements (Fig. 7.3d) indicate that peak current decreases rapidly as the temperature is increased from 1.5 to 10 K and is approximately constant above 30 K, consistent with coherent tunneling through a discrete SiNW quantum level at low temperature and classical single-electron effects at higher temperature [1]. Cui et al. [24] employed the SET approach to investigate transport in single nanoscale branch points in CdTe tetrapods. The authors found that carriers can delocalize across the branches or localize and hop between arms depending on the coupling strength. In addition, a new SET operation scheme enabled by the multiple branched arms of a tetrapod was demonstrated: one arm can be used as a sensitive gate to control the electrical transport through the whole system (Fig. 7.3e).

Compared with the Schottky contacts normally formed at the NW/electrode interface of single-component NWs, transparent Ohmic contacts to the NW channel can be achieved in band-structure engineered heterostructure NWs. For example, in the Ge/Si core/shell NW heterostructure [20], the Fermi level, pinned inside the Si bandgap, may lie below the Ge valence band due to the large band offset between Ge and Si (Fig. 7.4a). This band line-up results in Ohmic contacts to the Ge channel. Furthermore, since holes can be injected electrically from the contacts due to the energy band line-up, a hole gas can be formed in the Ge NW core even when both the core and shell are undoped. In this case, the NW can be considered as a 1D hole-gas system and works as a depletion type device. The Ge/Si core/shell NWs thus possess two key advantages compared with single component NWs: (i) transparent contacts from metal electrodes to the conduction channel can be readily obtained and (ii) dopant scattering can be eliminated. For the Ge/Si NW devices fabricated without annealing, carriers need to tunnel through the non-conducting Si layer, resulting in a barrier in transport data recorded at low temperatures, and the devices behave as SETs with CB oscillations (Fig. 7.4b). Such observed SET behavior is similar to that in single-component semiconductor NW devices, where a Schottky barrier always forms at the contact because the Fermi level lies inside the semiconductor band gap. In contrast, annealing the Ge/Si NW devices produces reproducible transparent contacts to the hole gas even at low temperatures (Fig. 7.4c). Due to strong radial confinement of the holes in the Ge channel, discrete 1D sub-bands are formed and can be probed by transport measurements.



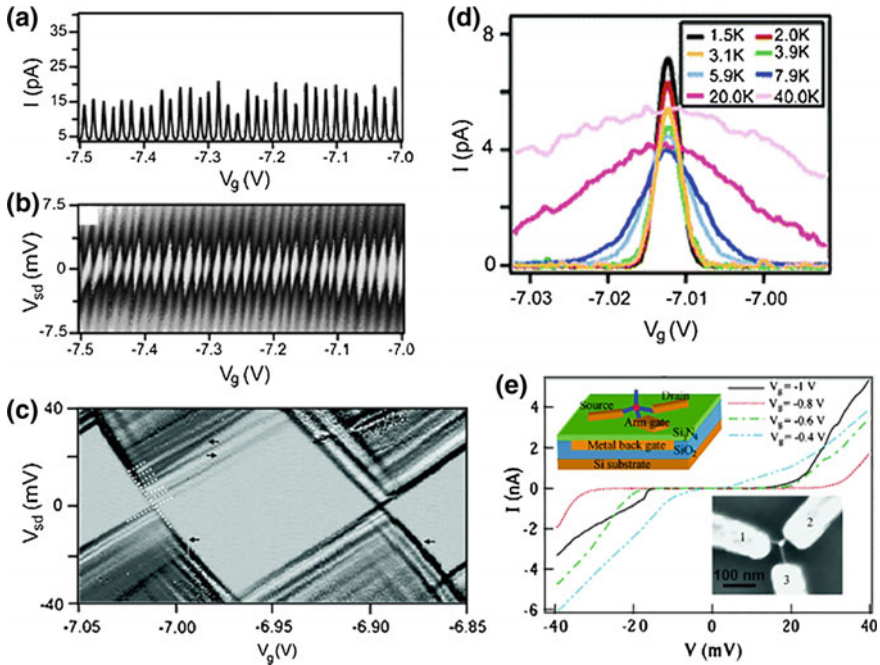


**Fig. 7.3** **a** CB oscillations observed at 4.2 K with  $V_{sd} = 0.5$  mV. **b** Gray scale plot of  $(\partial I/\partial V_{sd})$  versus  $V_{sd}$  and  $V_g$  recorded at 4.2 K; the light (*dark*) regions correspond to low (*high*) values of  $\partial I/\partial V_{sd}$ . **c**  $\partial I/\partial V_{sd}-V_{sd}-V_g$  data recorded at 1.5 K. *Dark lines* (peaks in  $\partial I/\partial V_{sd}$ ) running parallel to the edges of the *diamonds* correspond to individual excited states. **d** Temperature-dependent  $I-V_g$  curves recorded at increasing temperature. Reproduced from [19]. Copyright 2005 American Chemical Society. **e** Scheme of tetrapod SET and  $I-V$ . Reproduced from [24]. Copyright 2005 American Chemical Society

Low-temperature electrical transport studies have shown distinct conductance plateaus corresponding to transport through the first four subbands in the Ge/Si NW (Fig. 7.4d), where the subband spacings (Fig. 7.4e),  $\Delta E_{1,2} = 25$  mV and  $\Delta E_{2,3} = 30$  mV, are in good agreement with calculations. Notably, the conductance exhibits little temperature dependence, consistent with the calculation of reduced backscattering in this 1D system, suggesting that transport is ballistic even at room temperature.

### 7.2.4 Coupled Quantum Dots in Nanowires

In 2005, the Lieber group [26] reported controlling the size and separation of modulation-doped regions during synthesis to define QD structures in  $n^+-n-n^+$  modulation-doped SiNWs (Fig. 7.5a). In these structures, Fermi level offset due to variations in dopant concentration produces potential barriers confining the QD,

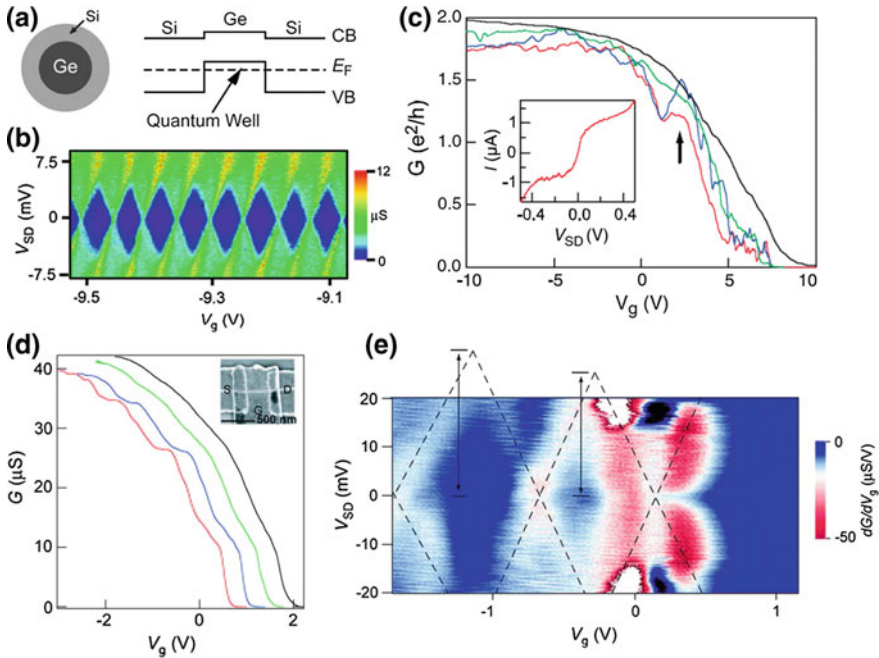


**Fig. 7.4** **a** Schematics of a cross-section through the Ge/Si core/shell structure and the band diagram for a Si/Ge/Si heterostructure. **b** Coulomb diamonds in  $G-V_{SD}-V_g$  plot for a 10-nm core diameter Ge/Si NW. **c**  $G-V_g$  data recorded for a device measured at different temperatures: *black*, *green*, *blue* and *red* correspond to 300, 50, 10 and 4.7 K, respectively. *Inset*  $I-V_{SD}$  curve recorded at  $V_g = 10$  V. **d**  $G-V_g$  recorded at different temperatures on a 400 nm long top-gated device; the *red*, *blue*, *green*, and *black* curves correspond to temperatures of 5, 10, 50, and 100 K, respectively. **e** Transconductance  $dG/dV_g$  as a function of  $V_{SD}$  and  $V_g$ . The *vertical arrows* highlight values of subband spacings  $\Delta E_{1,2}$  and  $\Delta E_{2,3}$ , respectively. Reproduced from [20]. Copyright 2005 the National Academy of Sciences of the United States of America

where the lightly doped  $n$ -type regions define barriers for a variable length QD,  $n_{QD}^+$ . The single-period diamond (Fig. 7.5b, c) showed that transport occurs through a single QD structure. The potential of this approach for encoding coupled quantum structures was also explored in structures of the form  $n^+-n_1-n_{QD}^+-n_2-n_{QD}^+-n_1-n^+$ , where  $n_1$  are fixed-width tunnel barriers that weakly couple the structure to source and drain electrodes, and  $n_2$  is a variable-width barrier that couples the two QDs (Fig. 7.5d, left panel). The  $I-V_g$  data recorded from representative NW devices with three different  $n_2$  barrier widths coupling the QDs (Fig. 7.5d, right panel) demonstrated several key points. First, the device with the largest barrier exhibited a single Coulomb oscillation period with capacitance consistent with the size of each individual QD determined from scanning gate microscopy (SGM) measurements. This result showed qualitatively that the two QDs were weakly coupled, and moreover, had sizes that are similar. Second, the data from the device with an intermediate-width  $n_2$  barrier exhibited a splitting of each of the Coulomb

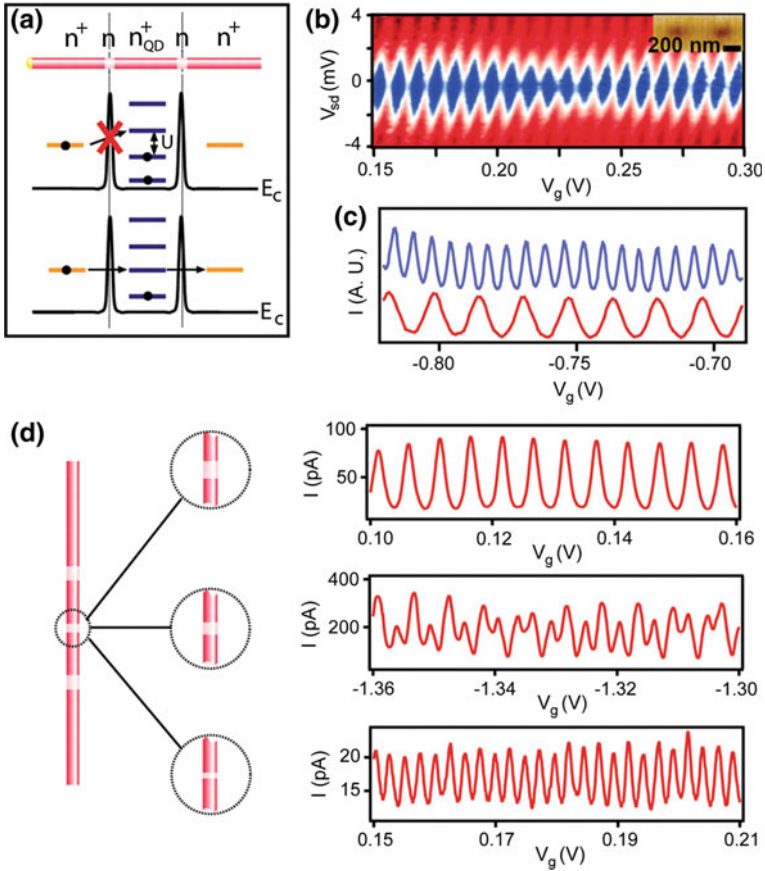


**Fig. 7.5** **a** Schematic of  $n^+$  QD structure confined by two  $n$ -type barriers within a modulation-doped NW. The conduction band ( $E_c$ ) offset of the  $n^+$  and  $n$  sections induce tunneling barriers with CB phenomenon. **b** Plot of  $\partial I / \partial V_{sd}$  versus  $V_{sd}$  and  $V_g$  recorded at 1.5 K on a  $n^+ - n - n^+$  device. *Inset* SGM image of the same device. **c**  $I - V_g$  data taken at 1.5 K on two devices with different  $n^+$  section length. **d** Coupled double-QD structure with variable width  $n_2$  section between the two QDs. (*Right*)  $I - V_g$  data recorded at 1.5 K on three devices with different  $n_2$  sections. Reproduced from [26]. Copyright 2005 the American Association for the Advancement of Science

oscillation peaks into doublets, which is the signature of enhanced tunneling conductance between the QDs. Last, as the barrier width is reduced further, a single Coulomb oscillation period is again observed, although the capacitance was consistent with an effective QD size twice that of the individual  $n^+$  regions; that is, the structures are fully delocalized.

In related studies, few-electron double QDs were fabricated in InAs/InP heterostructured NWs with three InP barriers separating two QDs from each other [27]. When the global back-gate voltage is changed, the chemical potentials on both

QDs are simultaneously tuned and the larger QD fills up with electrons faster than the smaller QD, because the larger QD has a smaller charging energy and energy level spacing. The authors also found a clear magic number structure of 2, 6, 10, 12, ..., and the extracted charging and quantization energies were similar to those observed in single QDs in InAs/InP heterostructure NWs. In addition, Pfund et al. observed spin pairing and Pauli spin blockade in states with odd total electron occupation [28] and studied the spin relaxation time [29, 30]. Recently, Rossella et al. [31] showed that the quantum-confined Stark effect allows two QDs only 5 nm apart to be independently addressed without the requirement for aligned nanometer-sized local gating. The InAs/InP NW double QDs display an experimentally detectable spin blockade up to 10 K, a relatively high temperature compared to the typical temperature used to observe spin operations in double QDs.

Though many experiments of NW-based qubits have focused on QDs made from III–V semiconductors, the coherence of electron spins in these materials is limited by hyperfine interactions with the non-zero nuclear spins. To overcome this problem, Hu et al. [25] synthesized Ge/Si core/shell NWs, in which the most abundant nuclei have spin zero thus minimizing spin-decoherence through the hyperfine interaction, for quantum device studies. Tuning the barrier height between the QDs formed in Ge/Si core/shell NW with gate voltage, provided a controlled means to achieve coherent overlap of the charge and spin states in neighboring dots (Fig. 7.6a). In addition, an integrated charge sensor was developed to reach quasi-depletion QD regime where direct electrical measurement may not be able to measure the transport due to the instrument detection limit. Significantly, the charge states in the dots and the coupling between them were detected in situ using the integrated charge sensor in the form of a third QD configured in another Ge/Si NW located more than 1  $\mu\text{m}$  away. Clear charge signals were detected by the NW-based QD detector even after direct transport measurements would no longer be carried out in the coupled dots. The signals in this experiment shown in Fig. 7.6b, c clearly illustrate the near-ideal performance of the double QDs defined in the NWs and the excellent sensitivity of the charge sensing setup. The demonstration of coupled QDs and integrated sensing devices in turn has paved the way for future studies on quantum computing schemes using 1D systems like NWs. In particular, compared to commonly used III–V systems, the Ge/Si NW system offers potential for longer spin coherence time due to the suppression of hyperfine interactions and, thus, a clear advantage for quantum devices based on a linear 1D architecture.

### 7.2.5 *g*-Factor and Spin-Orbit Interaction

The effective  $g$ -factor,  $g^*$ , discussed earlier, is an important parameter for spin manipulation. One reason why NW QDs are interesting is that in low-dimensional semiconductor heterostructures  $g^*$  depends critically on the system size and the dimensionality as a result of the spin-orbit interaction. The discrete energy spectrum

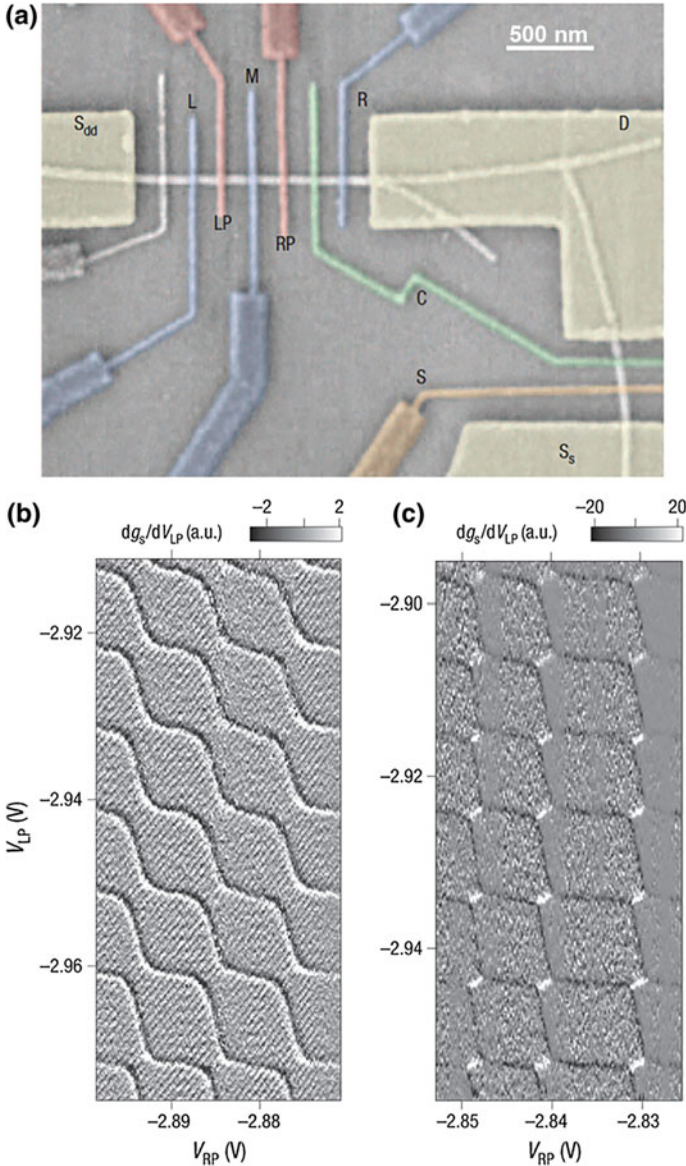


**Fig. 7.6** **a** SEM image of Ge/Si NW double dot device. The double dot is formed with gates L, M and R, shown in *blue*, and the plunger gates LP and RP (*red*) tune the energy levels of each dot. On an adjacent NW, the charge sensor is a contact-defined single dot capacitively coupled to the double dot with the coupler C (*green*). The sensor is biased to the side of a CB peak using gate S (*orange*). The gate shown in grey was not used. S<sub>dd</sub>, S<sub>s</sub> and D label the double dot source, sensor source and shared drain contacts, respectively. **b**, **c** Differentiated sensor conductance  $dg_s/dV_{LP}$  measured with the double dot weakly coupled to the leads for strong (**b**) and weak (**c**) interdot coupling. Reproduced from [25]. Copyright 2007 Nature Publishing Group

of a quantized system can quench the orbital angular momentum, pushing the electron  $g^*$  towards 2 (as for free electrons), even when bulk materials having negative  $g^*$  [57]. In addition, factors such as strain, geometry and confinement energy can also modify the  $g^*$ . For example and as discussed above, reducing the size of InAs NW QDs led to a reduction of  $|g^*|$  to 2.3, compared with the bulk value of 14.7. The possibility of defining multiple QDs in a NW, each with a different  $g^*$ , suggests the possibility of individually addressable spin qubits. In addition, Nilsson et al. [58] reported magneto-transport measurements on InSb NW QDs, showing that the quantum levels of the InSb QDs have giant  $g^*$ , with absolute values up to  $\sim 70$ , the largest value ever reported for semiconductor QDs. They also observed that these  $g^*$  values are quantum level dependent and can differ strongly between different quantum levels. The presence of giant  $g^*$  values indicates considerable contributions from orbital motion of electrons was preserved in the measured InSb NW QDs, while the level-to-level fluctuations arise from spin-orbit coupling. An  $g^* \approx 2$  was also measured in QDs formed by electrostatically gating Ge/Si core/shell NWs [52], where bulk values for Ge and Si are 1.563 and 1.998, respectively [59].

For quantum electronic applications such as quantum computing based on qubits, accurate control over the electron number, precise control of the spin state and control of the coupling between spins in neighboring QDs are all required. Furthermore, the spin-orbit interaction is of crucial importance since coupling of the spin to orbital degrees of freedom determines spin relaxation and decoherence rates, which in turn determines the decoherence time of spin-based qubits. It is thus of fundamental interest to determine experimentally the spin-orbit length scale,  $\lambda_{SO}$ . Fasth et al. [60] demonstrated few-electron QDs in InAs NWs, and used these tunable QDs to show how effective size, coupling, and electron number could be controlled by external voltages. Because of a large  $|g^*|$  of  $8 \pm 1$ , the transition from a singlet  $S$  to a triplet  $T^+$  ground state with increasing magnetic field was dominated by the Zeeman energy rather than by orbital effects. They also found that the spin-orbit coupling mixes the  $T^+$  and  $S$  states and thus induces an avoided crossing with magnitude  $\Delta_{SO} = 0.25 \pm 0.05$  meV, from which  $\lambda_{SO} \approx 127$  nm was calculated.

In 2009, Zwanenburg et al. [61] reported measurements on a SiNW QD that allows for complete understanding of the spin states of the first four holes. First, the hole number was controlled down to one. Detailed measurements at perpendicular magnetic fields reveal the Zeeman splitting of a single hole in Si. Additionally, magneto-spectroscopy of the first four holes allowed determination of the successive spins that were added to an empty state and revealed a spin filling with alternating spin-down and spin-up holes. Kouwenhoven and co-workers [62] exploited the unique material properties of an InAs NW to rapidly control the quantum state of a single electron spin using only electric fields. Beyond just flipping the spin orientation of a single electron, the authors tailored the precise timing of electric-field pulses to extend the spin coherence time (during which the information encoded in the quantum state of the spin is preserved), allowing for the conversion of an electronic qubit into a photon, which can serve as a flying qubit for

long-distance quantum communication. Hu et al. [63] demonstrated pulsed gate control and charge-sensing spin readout of hole spins confined in a Ge/Si core/shell NW device (Fig. 7.7). They developed singlet-triplet spin qubits in a double QD and observed Pauli spin blockade. With fast gating, the authors measured  $T_1$  spin relaxation times of up to 0.6 ms in coupled QDs at zero magnetic field (Fig. 7.8). The observed increase in relaxation time with decreasing magnetic field was consistent with a spin-orbit mechanism that is usually masked by hyperfine contributions. Later, Pribiag et al. [64] showed that gate-tunable hole QDs can be formed in InSb NWs and used these devices to demonstrate Pauli spin blockade and electrical control of single hole spins. The devices were fully tunable between hole

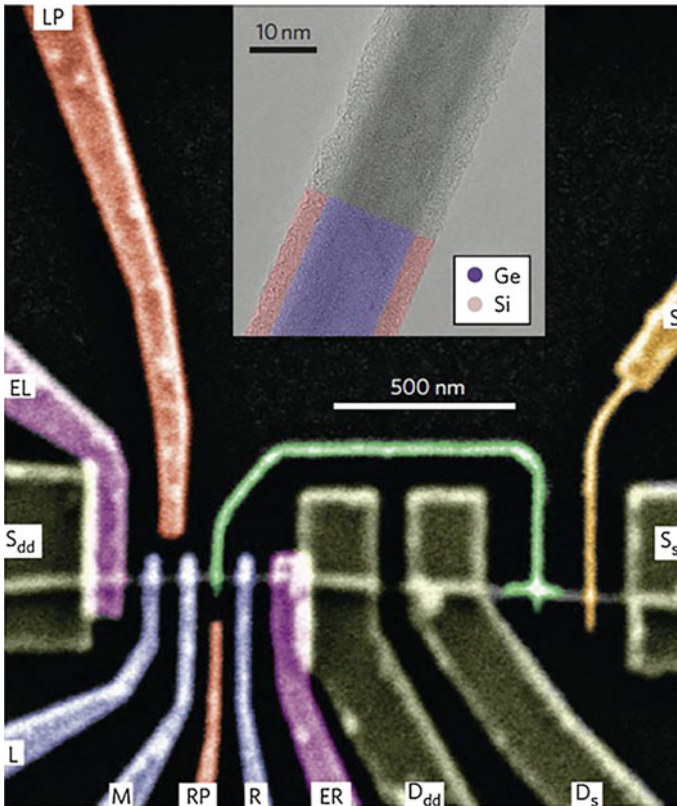


**Fig. 7.7** Spin qubit device based on a Ge/Si heterostructure NW. SEM of a Ge/Si NW contacted by four contacts ( $S_{dd}$ ,  $D_{dd}$ ,  $S_s$ ,  $D_s$ , grey) and covered by a  $\text{HfO}_2$  gate dielectric layer. Top gates L, M and R (blue) induce a double QD on the left device. Plunger gates LP and RP (orange) change the chemical potential of each dot independently, and side gates EL and ER (purple) improve electrical contact to the NW. A single QD on the right half of the NW (isolated by chemical etching between  $D_{dd}$  and  $D_s$ ) is capacitively coupled to a floating gate (green) and a tuning gate (yellow), and senses the charge state of the double dot. Inset TEM image of a typical NW with a single-crystal germanium core and an epitaxial silicon shell. Reproduced from [63]. Copyright 2012 Nature Publishing Group

and electron QDs, allowing the hyperfine interaction strengths,  $g^*$  and spin blockade anisotropies to be compared directly in the two regimes. In a more recent work, Higginbotham et al. [65] measured relaxation and dephasing of hole spins in a gate-defined Ge/Si NW double QD and observed inhomogeneous dephasing times 20 times longer than in III–V semiconductors, suggesting that the strong coupling regime may be accessible for the application in quantum information processing.

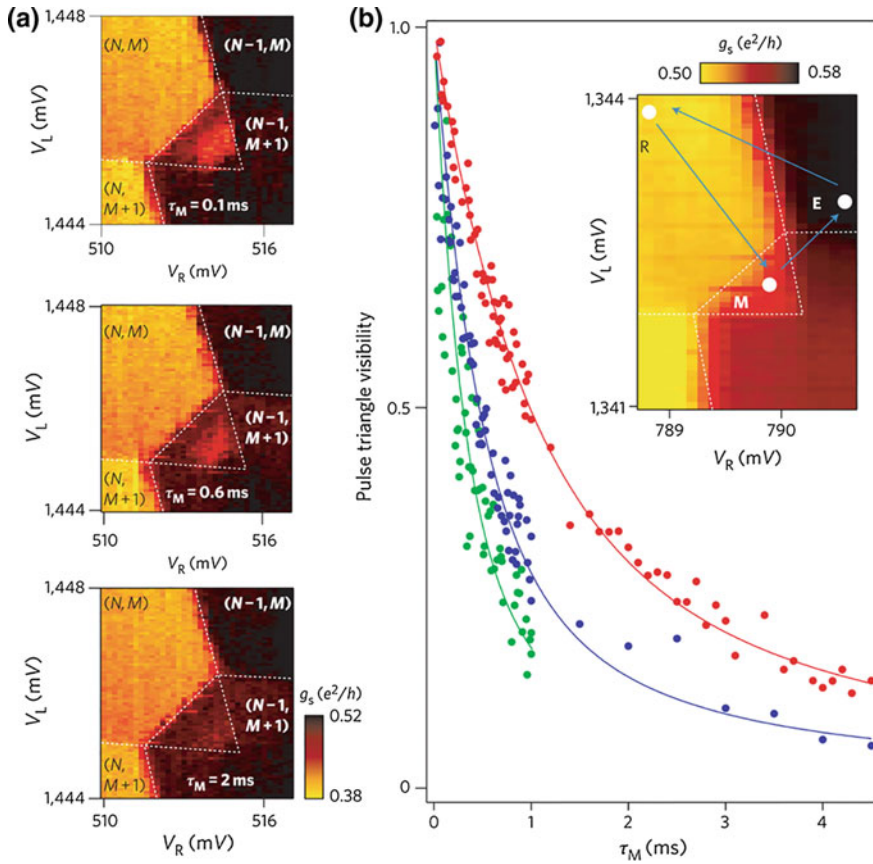


**Fig. 7.8** Pulsed gate measurements of spin relaxation times. **a** Sensor conductance  $g_s$  near a spin-blocked charge transition between the left and right dot. Spin-to-charge conversion results in pulse triangles that fade away with increasing measurement time  $\tau_M$ . **b** Visibility  $I(\tau_M)$  measured at the center of the pulse triangle versus  $\tau_M$  at different magnetic fields. The fitting curves (*solid lines*) give  $T_1 = 0.6, 0.3$  and  $0.2$  ms at  $B = 0$  (*red*),  $0.1$  (*blue*) and  $1$  T (*green*), respectively. Reproduced from [63]. Copyright 2012 Nature Publishing Group



## 7.3 Hybrid Superconductor-Semiconductor Devices

### 7.3.1 Josephson Junctions

Electrons in the superconducting state of conventional superconductors exist as Cooper pairs. When two superconductors are weakly connected, for example, in a superconductor/normal metal/superconductor (S/N/S) structure, a dissipationless supercurrent can flow through the junction as a result of the Josephson effect [66]. In essence, this effect can be observed when the junction thickness is less than the phase coherence length of the Cooper pairs. In this section, the discussion will be limited to NW-based devices. For more information on hybrid superconductor–nanostructure devices, readers are referred to [9].

Initially, Kouwenhoven and co-workers demonstrated supercurrents in *n*-type InAs NWs [34], and studied supercurrents coupled with CB phenomena in QDs [35]. The relatively large diameters and small mean free paths in these NWs suggested, however, that carrier transport was in a bulk diffusive regime. In 2006, the Lieber group [36] presented studies of proximity-induced superconductivity in undoped Ge/Si core/shell NW heterostructures contacted by superconducting aluminum leads (Fig. 7.9a, b). In measurements taken above the superconducting temperature of 1.6 K, where the aluminum behaves as a normal metal, quantization of the energy states manifested itself as steps in the conductance plotted as a function of applied gate voltage (Fig. 7.9c). The effects of this quantization persisted when the device was cooled below 1.6 K superconducting transition temperature, but also new features were observed. Specifically, the maximum or critical supercurrent of the Josephson junction did not increase continuously with the gate voltage, but in steps (Fig. 7.9d). The precise correlation between the steps in the normal state conductance and the supercurrent is in almost perfect agreement with the predictions of mesoscopic transport theory [67]. Besides the supercurrent branch, the high-quality devices allow the observation of additional peaks due to coherent backscattering or Andreev reflections of electron/hole pairs at the semiconductor/superconductor interface. Here, multiple Andreev reflection peaks up to order 25 were observed (Fig. 7.9e), suggesting carriers can move freely through the devices up to 25 times without being backscattered inside the channel and once again demonstrating the near-perfect nature of the Ge/Si NW.

In 2008, Doh et al. [37] investigated the competition between the CB effect, Andreev reflection, and quantum interference, in InAs and InP NWs connected to aluminum based superconducting electrodes. Three limiting cases were compared depending on the tunnel coupling strength and the characteristic Coulomb interaction energy. For weak coupling and large charging energies, negative differential conductance is observed. For intermediate coupling and charging energy smaller than the superconducting gap, the current-voltage characteristic is dominated by Andreev reflection and CB produces an effect only near zero bias. For almost ideal contact transparencies and negligible charging energies, universal conductance

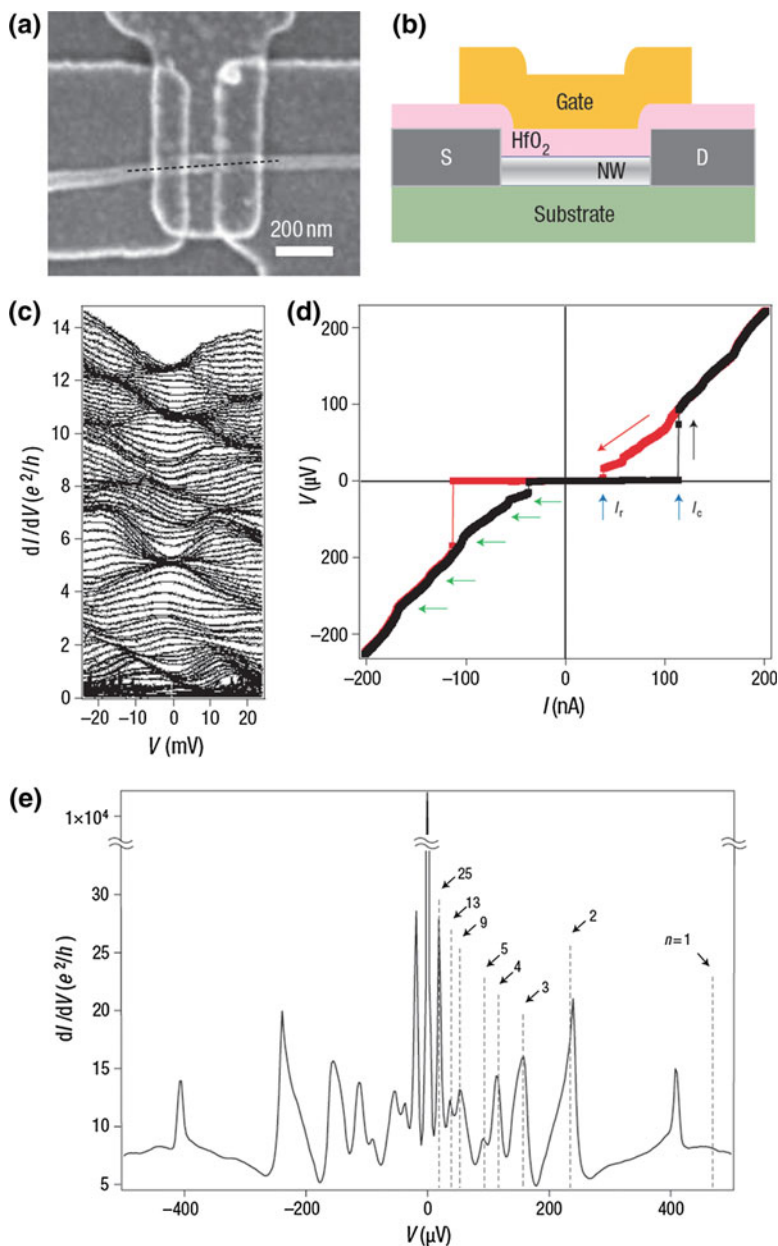


**Fig. 7.9** **a** SEM image of a representative top-gated device. **b** Cross-sectional schematic of the device showing the Al *S/D* contact electrodes, HfO<sub>2</sub> dielectric and Cr/Au top gate. **c, d** Transport characteristics of Ge/Si NW above **(c)** and below **(d)** the superconducting transition temperature. Black and red curves in **(d)** correspond to different current sweeping directions as indicated by arrows. **e** Multiple Andreev reflections in the Ge/Si NW device. Reproduced from [36]. Copyright 2006 Nature Publishing Group

fluctuations were observed with amplitudes enhanced due to Andreev reflection at the contacts.

### 7.3.2 Majorana Fermions

Quantum mechanics and special relativity were merged into a single theory when Dirac presented his equation in 1929 [68], with a solution predicting an electron and an antielectron partner, the positron. In 1937, Majorana discovered a purely real-valued solution to the Dirac equation, and thus hypothesized the existence of Majorana fermions (MFs) [69]. Research interest in condensed-matter physics has been focused on the “Majorana zero modes”, that is, emergent MFs occurring at exactly zero energy that have a remarkable property of being their own antiparticles. Any ordinary fermion can be thought of as being composed of two MFs. An interesting situation arises when a single MF can be spatially separated from its partner and independently probed. Particularly interesting for the realization of qubits in quantum computing are pairs of localized MFs separated from each other by a superconducting region in a topological phase [69]. Recently, signatures consistent with the existence of MFs in NWs coupled to conventional superconductors have been reported [70].

The starting point is a NW made of semiconducting material with a large spin-orbit interaction. In the presence of a magnetic field  $B$  along the axis of the NW (i.e., a Zeeman field), a gap is opened at the crossing between the two spin-orbit bands. The next ingredient is to connect the semiconducting NW to an ordinary s-wave superconductor. The proximity of the superconductor induces pairing in the NW between electron states of opposite momentum and opposite spins. Near the ends of the wire, the electron density is reduced to zero, and MFs arise as zero-energy (i.e., midgap) bound states—one at each end of the wire. Tunneling spectroscopy from a normal conductor into the end of the wire should reveal a state at zero energy. In the work of the Kouwenhoven group [38], electrical measurements were reported on InSb NWs contacted with one normal (Au) and one superconducting (NbTiN) electrode. The dependence of the differential tunneling conductance on the bias voltage for different values of the magnetic field is shown in Fig. 7.10a. Note that a zero-bias peak (ZBP) emerges when the applied magnetic field exceeds about 100 mT. The ZBP is robust to further increases of the magnetic field until about 400 mT, above which the single peak appears to split into a two-peak structure. These observations are consistent with the MF interpretation of the tunneling conductance. In addition, an important consistency check on the MF interpretation of the ZBP is the requirement that the peak must disappear if the angle between the applied magnetic field and the direction of the effective spin-orbit field vanishes. The angle dependence of the ZBP (Fig. 7.10b, c) was found to be consistent with the Majorana scenario, thus strengthening the identification of the observed ZBP with the presence of a MF bound state. These observations, in particular the emergence of a ZBP at finite magnetic field, have been subsequently

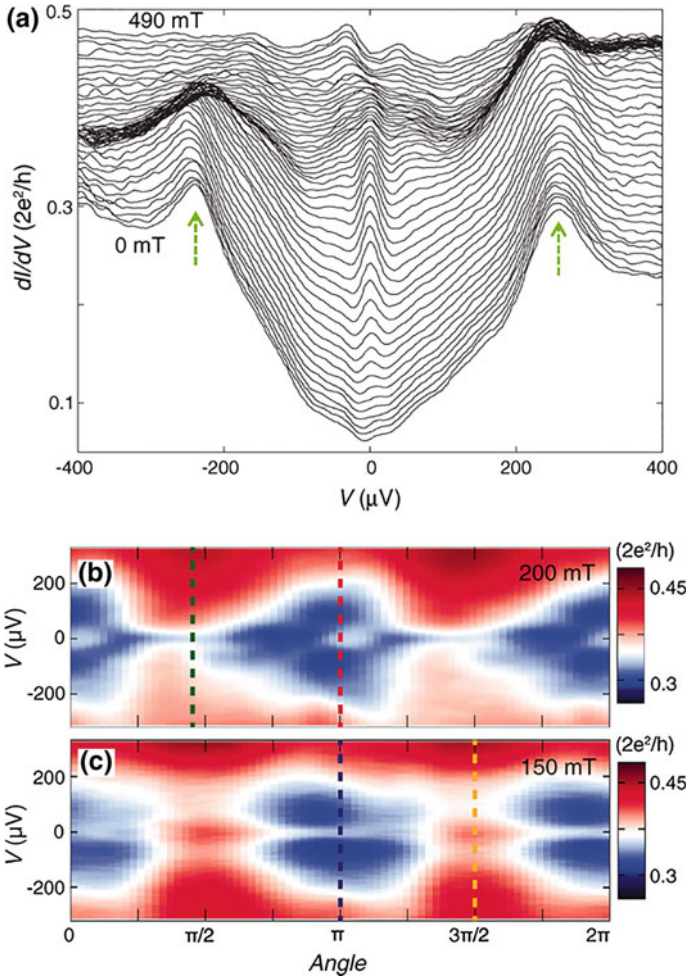


**Fig. 7.10** **a**  $dI/dV$  versus  $V$  at 70 mK taken at different  $B$  fields (traces are offset for clarity). **b, c** Dependence of  $dI/dV$  on the magnetic field orientation. **b** Rotation in the plane of the substrate for a magnetic field  $|B| = 200$  mT. The ZBP vanishes when  $B$  is perpendicular to the wire. **c** Rotation in the plane perpendicular to the spin-orbit field for  $|B| = 150$  mT. The ZBP is present for all angles. Reproduced from [38]. Copyright 2012 the American Association for the Advancement of Science

confirmed by other groups [39–41]. In addition, Rokhinson et al. [42] reported the observation of the fractional a.c. Josephson effect in a hybrid semiconductor–superconductor InSb/Nb NW junction. The observation suggests the presence of the quantized voltage steps twice as high as the value expected for conventional superconductor junctions, which would be consistent with the presence of MFs. In 2014, Lee et al. [33] reported a direct measurement of the Zeeman effect on the

Andreev levels (elementary subgap excitations) of a QD strongly coupled to a superconductor with a large critical magnetic field. It was shown that a spin-split Andreev level crossing the Fermi energy results in a quantum phase transition to a spin-polarized state, which implied a change in the fermionic parity of the system. This crossing manifests itself as a zero-bias conductance anomaly at finite magnetic field with properties that resemble those expected for Majorana modes in a topological superconductor. For a comprehensive review of MFs in semiconductor NWs, please refer to [70].

## 7.4 Topological Insulators

TIs [43] are different from both insulators and metals since the bulk material exhibits a finite electronic bandgap, and can be referred to as an insulator, but the surface states are gapless and metallic. In these surface states, the spin and momentum states are coupled, resulted in suppression of backscattering due to the protection of the coupled spin states. As a result, low-dissipation, metallic states exist in such materials up to room temperature in ambient conditions. The exotic electronic nature of the TI surface states has been the focus of intense interest as it allows studies of several fundamental physical phenomena inaccessible in ordinary materials. However, transport experiments have been hampered by insufficient control over the bulk. In particular, unintentional and uncontrolled doping has often yielded residual conductance that masks that of the topological surface states of interest [44].

In 2010, Peng et al. [71] showed transport evidence of topological surface states through periodic quantum interference effects in layered single-crystalline  $\text{Bi}_2\text{Se}_3$  nanoribbons. The unique advantage that TI nanostructures offer is their well-defined nanoscale morphology, which has larger surface-to-volume ratios than bulk materials and is ideal for interference-type experiments to probe the TI surface states. One such interference is Aharonov–Bohm (AB) oscillations, which refer to periodic oscillations in conductance arising from constructively and destructively interfering electrons travelling in a well-defined path in the presence of magnetic flux. The magnetic fields thread through the cross-section of the well-defined path (Fig. 7.11a). Pronounced periodic AB oscillations in the magnetoresistance clearly demonstrate the coherent propagation of 2D electrons around the perimeter of the nanoribbon surface, as expected from the topological nature of the surface states (Fig. 7.11b, c). The phase of the AB oscillations observed in these nanoribbons indicated that the TI surface electrons were in the diffusive regime [72]. In the same year, the Cui group also reported several synthetic methods, including VLS growth [73] and AFM tip exfoliation [74], of topological insulator NWs and nanoribbons. Later, Xiu et al. [75] reported the modulation of surface states of TIs by using a gate voltage to control quantum oscillations in  $\text{Bi}_2\text{Te}_3$  nanoribbons. Readers can refer to [76, 77] for comprehensive reviews and perspectives of TI nanostructures.

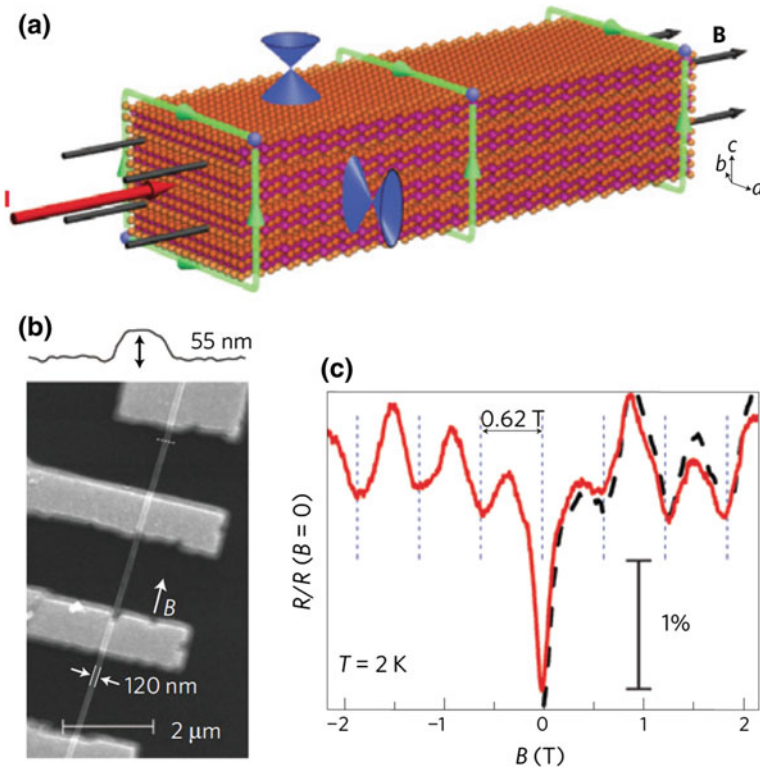


**Fig. 7.11** **a** Schematic diagram of the surface electrons travelling on the surface of the Bi<sub>2</sub>Se<sub>3</sub> nanoribbon, indicated by the green paths, while the magnetic field (*black arrows*) threads through the nanoribbon. **b** SEM image of the Bi<sub>2</sub>Se<sub>3</sub> nanoribbon device with four Ti/Au contacts. **c** Normalized magnetoresistance as a function of the parallel magnetic field at 2 K. The periodic oscillations observed in the resistance trace are AB oscillations. Reproduced from [71]. Copyright 2010 Nature Publishing Group

## 7.5 Future Directions and Challenges

NWs with diameters comparable to the electron wavelength can readily exhibit fundamental quantum properties of charge transport that are relevant to basic understanding of quantum devices and potential directions in quantum electronics. In this chapter, we reviewed a broad range of research on QD systems in semiconductor NWs, hybrid superconductor-semiconductor devices, and TIs. An important lesson provided by the recent developments is that, in real systems, key observable features are often determined by various details of the structure thus underscoring the critical importance of controlled NW synthesis discussed in earlier chapters. This feedback between synthesis and fundamental measurements has opened up broad research vistas that go far beyond uniform composition materials. Looking to future, there remain great opportunities in basic research, such as

exploring expanded concepts for quantum computers, where multiple quantum bits on different NWs are coherently coupled. For example, recent work has shown that floating gates may be used to couple different NWs together [78]. Random noise from the environment ultimately places limits on many types of quantum bit devices, although exciting advances defining Majorana modes in superconductor/NW devices [79] and topological insulator NWs offer well-defined strategies for overcoming such issues. More generally, the goal of quantum computing, while very challenging, will no doubt continue to spark new basic research on nanoscale structures at the interface between physics, materials science and electronic engineering and lead to potential applications well-beyond this current application goal.

## References

1. L. Kouwenhoven, C. Marcus, P. McEuen, S. Tarucha, R. Westervelt, N. Wingreen, Electron transport in quantum dots, in *Mesoscopic Electron Transport*, vol. 345, ed. by L. Sohn, L. Kouwenhoven, G. Schön (Springer, Netherlands, 1997), pp. 105–214
2. H. Grabert, M.H. Devoret, *Single Charge Tunneling: Coulomb Blockade Phenomena in Nanostructures* (Plenum Press, New York, 1992)
3. A. Tilke, F. Simmel, R. Blick, H. Lorenz, J. Kotthaus, Coulomb blockade in silicon nanostructures. *Prog. Quant. Electron.* **25**(3), 97–138 (2001)
4. L.P. Kouwenhoven, D. Austing, S. Tarucha, Few-electron quantum dots. *Rep. Prog. Phys.* **64**(6), 701 (2001)
5. R. Hanson, L. Kouwenhoven, J. Petta, S. Tarucha, L. Vandersypen, Spins in few-electron quantum dots. *Rev. Mod. Phys.* **79**(4), 1217 (2007)
6. M.J. Biercuk, S. Ilani, C.M. Marcus, P.L. McEuen, Electrical transport in single-wall carbon nanotubes, in *Carbon Nanotubes* (Springer, Berlin, 2007) pp. 455–493
7. S. Ilani, P.L. McEuen, Electron transport in carbon nanotubes. *Annu. Rev. Condens. Matter Phys.* **1**(1), 1–25 (2010)
8. J. Salfi, S. Roddaro, D. Ercolani, L. Sorba, I. Savelyev, M. Blumin, H. Ruda, F. Beltram, Electronic properties of quantum dot systems realized in semiconductor nanowires. *Semicond. Sci. Tech.* **25**(2), 024007 (2010)
9. S. De Franceschi, L. Kouwenhoven, C. Schönenberger, W. Wernsdorfer, Hybrid superconductor-quantum dot devices. *Nat. Nanotechnol.* **5**(10), 703–711 (2010)
10. E. Prati, Single electron effects in silicon quantum devices. *J. Nanopart. Res.* **15**(5), 1–10 (2013)
11. K. Likharev, A. Zorin, Theory of the Bloch-wave oscillations in small Josephson junctions. *J. Low Temp. Phys.* **59**(3–4), 347–382 (1985)
12. D. Averin, K. Likharev, Coulomb blockade of single-electron tunneling, and coherent oscillations in small tunnel junctions. *J. Low Temp. Phys.* **62**(3–4), 345–373 (1986)
13. T. Fulton, G. Dolan, Observation of single-electron charging effects in small tunnel junctions. *Phys. Rev. Lett.* **59**(1), 109–112 (1987)
14. B. Van Wees, H. Van Houten, C. Beenakker, J.G. Williamson, L. Kouwenhoven, D. Van der Marel, C. Foxon, Quantized conductance of point contacts in a two-dimensional electron gas. *Phys. Rev. Lett.* **60**(9), 848 (1988)
15. C. Beenakker, H. van Houten, Quantum transport in semiconductor nanostructures. *Solid State Phys.* **44**(1), 1–228 (1991)

16. G. Burkard, D. Loss, D.P. DiVincenzo, Coupled quantum dots as quantum gates. *Phys. Rev. B* **59**(3), 2070 (1999)
17. D. Loss, D.P. DiVincenzo, Quantum computation with quantum dots. *Phys. Rev. A* **57**(1), 120 (1998)
18. S. De Franceschi, J. Van Dam, E. Bakkers, L. Feiner, L. Gurevich, L.P. Kouwenhoven, Single-electron tunneling in InP nanowires. *Appl. Phys. Lett.* **83**(2), 344–346 (2003)
19. Z. Zhong, Y. Fang, W. Lu, C.M. Lieber, Coherent single charge transport in molecular-scale silicon nanowires. *Nano Lett.* **5**(6), 1143–1146 (2005)
20. W. Lu, J. Xiang, B.P. Timko, Y. Wu, C.M. Lieber, One-dimensional hole gas in germanium/silicon nanowire heterostructures. *Proc. Natl. Acad. Sci. USA* **102**(29), 10046–10051 (2005)
21. C. Thelander, T. Mårtensson, M. Björk, B. Ohlsson, M. Larsson, L. Wallenberg, L. Samuelson, Single-electron transistors in heterostructure nanowires. *Appl. Phys. Lett.* **83**(10), 2052–2054 (2003)
22. M.T. Björk, C. Thelander, A.E. Hansen, L.E. Jensen, M.W. Larsson, L.R. Wallenberg, L. Samuelson, Few-electron quantum dots in nanowires. *Nano Lett.* **4**(9), 1621–1625 (2004)
23. M. Björk, A. Fuhrer, A. Hansen, M. Larsson, L. Fröberg, L. Samuelson, Tunable effective  $g$  factor in InAs nanowire quantum dots. *Phys. Rev. B* **72**(20), 201307 (2005)
24. Y. Cui, U. Banin, M.T. Björk, A.P. Alivisatos, Electrical transport through a single nanoscale semiconductor branch point. *Nano Lett.* **5**(7), 1519–1523 (2005)
25. Y. Hu, H.O. Churchill, D.J. Reilly, J. Xiang, C.M. Lieber, C.M. Marcus, A Ge/Si heterostructure nanowire-based double quantum dot with integrated charge sensor. *Nat. Nanotechnol.* **2**(10), 622–625 (2007)
26. C. Yang, Z. Zhong, C.M. Lieber, Encoding electronic properties by synthesis of axial modulation-doped silicon nanowires. *Science* **310**(5752), 1304–1307 (2005)
27. A. Fuhrer, L.E. Fröberg, J.N. Pedersen, M.W. Larsson, A. Wacker, M.-E. Pistol, L. Samuelson, Few electron double quantum dots in InAs/InP nanowire heterostructures. *Nano Lett.* **7**(2), 243–246 (2007)
28. A. Pfund, I. Shorubalko, K. Ensslin, R. Leturcq, Suppression of spin relaxation in an InAs nanowire double quantum dot. *Phys. Rev. Lett.* **99**(3), 036801 (2007)
29. A. Pfund, I. Shorubalko, R. Leturcq, K. Ensslin, Pauli spin-blockade in an InAs nanowire double quantum dot. *Physica E* **40**(5), 1279–1281 (2008)
30. A. Pfund, I. Shorubalko, K. Ensslin, R. Leturcq, Dynamics of coupled spins in quantum dots with strong spin-orbit interaction. *Phys. Rev. B* **79**(12), 121306 (2009)
31. F. Rossella, A. Bertoni, D. Ercolani, M. Rontani, L. Sorba, F. Beltram, S. Roddaro, Nanoscale spin rectifiers controlled by the Stark effect. *Nat. Nanotechnol.* **9**, 997–1001 (2014)
32. A.I. Buzdin, Proximity effects in superconductor-ferromagnet heterostructures. *Rev. Mod. Phys.* **77**(3), 935 (2005)
33. E.J. Lee, X. Jiang, M. Houzet, R. Aguado, C.M. Lieber, S. De Franceschi, Spin-resolved Andreev levels and parity crossings in hybrid superconductor-semiconductor nanostructures. *Nat. Nanotechnol.* **9**, 79–84 (2014)
34. Y.-J. Doh, J.A. van Dam, A.L. Roest, E.P. Bakkers, L.P. Kouwenhoven, S. De Franceschi, Tunable supercurrent through semiconductor nanowires. *Science* **309**(5732), 272–275 (2005)
35. J.A.V. Dam, Y.V. Nazarov, E.P. Bakkers, S. De Franceschi, L.P. Kouwenhoven, Supercurrent reversal in quantum dots. *Nature* **442**(7103), 667–670 (2006)
36. J. Xiang, A. Vidan, M. Tinkham, R.M. Westervelt, C.M. Lieber, Ge/Si nanowire mesoscopic Josephson junctions. *Nat. Nanotechnol.* **1**(3), 208–213 (2006)
37. Y.-J. Doh, S.D. Franceschi, E.P. Bakkers, L.P. Kouwenhoven, Andreev reflection versus Coulomb blockade in hybrid semiconductor nanowire devices. *Nano Lett.* **8**(12), 4098–4102 (2008)
38. V. Mourik, K. Zuo, S. Frolov, S. Plissard, E. Bakkers, L. Kouwenhoven, Signatures of Majorana fermions in hybrid superconductor-semiconductor nanowire devices. *Science* **336**(6084), 1003–1007 (2012)



39. M. Deng, C. Yu, G. Huang, M. Larsson, P. Caroff, H. Xu, Anomalous zero-bias conductance peak in a Nb–InSb nanowire–Nb hybrid device. *Nano Lett.* **12**(12), 6414–6419 (2012)
40. A. Das, Y. Ronen, Y. Most, Y. Oreg, M. Heiblum, H. Shtrikman, Zero-bias peaks and splitting in an Al–InAs nanowire topological superconductor as a signature of Majorana fermions. *Nat. Phys.* **8**(12), 887–895 (2012)
41. A. Finck, D. Van Harlingen, P. Mohseni, K. Jung, X. Li, Anomalous modulation of a zero-bias peak in a hybrid nanowire–superconductor device. *Phys. Rev. Lett.* **110**(12), 126406 (2013)
42. L.P. Rokhinson, X. Liu, J.K. Furdyna, The fractional ac Josephson effect in a semiconductor–superconductor nanowire as a signature of Majorana particles. *Nat. Phys.* **8**(11), 795–799 (2012)
43. B.A. Bernevig, T.L. Hughes, *Topological Insulators and Topological Superconductors* (Princeton University Press, Princeton, 2013)
44. T. Ihn, Topological insulators: oscillations in the ribbons. *Nat. Mater.* **9**(3), 187–188 (2010)
45. S. Cronenwett, H. Lynch, D. Goldhaber-Gordon, L. Kouwenhoven, C. Marcus, K. Hirose, N. Wingreen, V. Umansky, Low-temperature fate of the 0.7 structure in a point contact: a Kondo-like correlated state in an open system. *Phys. Rev. Lett.* **88**(22), 226805 (2002)
46. A. Kristensen, H. Bruus, A.E. Hansen, J. Jensen, P. Lindelof, C. Marckmann, J. Nygård, C. Sørensen, F. Beuscher, A. Forchel, Bias and temperature dependence of the 0.7 conductance anomaly in quantum point contacts. *Phys. Rev. B* **62**(16), 10950 (2000)
47. T.S. Jespersen, M. Aagesen, C. Sørensen, P.E. Lindelof, J. Nygård, Kondo physics in tunable semiconductor nanowire quantum dots. *Phys. Rev. B* **74**(23), 233304 (2006)
48. C. Thelander, H.A. Nilsson, L.E. Jensen, L. Samuelson, Nanowire single-electron memory. *Nano Lett.* **5**(4), 635–638 (2005)
49. C. Fasth, A. Fuhrer, M.T. Björk, L. Samuelson, Tunable double quantum dots in InAs nanowires defined by local gate electrodes. *Nano Lett.* **5**(7), 1487–1490 (2005)
50. A. Pfund, I. Shorubalko, R. Leturcq, K. Ensslin, Top-gate defined double quantum dots in InAs nanowires. *Appl. Phys. Lett.* **89**(25), 252106 (2006)
51. I. Shorubalko, A. Pfund, R. Leturcq, M. Borgström, F. Gramm, E. Müller, E. Gini, K. Ensslin, Tunable few-electron quantum dots in InAs nanowires. *Nanotechnology* **18**(4), 044014 (2007)
52. S. Roddaro, A. Fuhrer, P. Brusheim, C. Fasth, H. Xu, L. Samuelson, J. Xiang, C. Lieber, Spin states of holes in Ge/Si nanowire quantum dots. *Phys. Rev. Lett.* **101**(18), 186802 (2008)
53. S. Gustavsson, I. Shorubalko, R. Leturcq, T. Ihn, K. Ensslin, S. Schön, Detecting terahertz current fluctuations in a quantum point contact using a nanowire quantum dot. *Phys. Rev. B* **78**(3), 035324 (2008)
54. D.D. Awschalom, D. Loss, N. Samarth, *Semiconductor Spintronics and Quantum Computation* (Springer, Berlin, Heidelberg, 2013)
55. K. Nowack, F. Koppens, Y.V. Nazarov, L. Vandersypen, Coherent control of a single electron spin with electric fields. *Science* **318**(5855), 1430–1433 (2007)
56. C. Kloeffel, D. Loss, Prospects for spin-based quantum computing in quantum dots. *Annu. Rev. Condens. Matter Phys.* **4**, 51–81 (2013)
57. C.E. Pryor, M.E. Flatté, Landé g factors and orbital momentum quenching in semiconductor quantum dots. *Phys. Rev. Lett.* **96**(2), 026804 (2006)
58. H.A. Nilsson, P. Caroff, C. Thelander, M. Larsson, J.B. Wagner, L.-E. Wernersson, L. Samuelson, H. Xu, Giant, level-dependent g factors in InSb nanowire quantum dots. *Nano Lett.* **9**(9), 3151–3156 (2009)
59. R. Vrijen, E. Yablonovitch, K. Wang, H.W. Jiang, A. Balandin, V. Roychowdhury, T. Mor, D. DiVincenzo, Electron-spin-resonance transistors for quantum computing in silicon-germanium heterostructures. *Phys. Rev. A* **62**(1), 012306 (2000)
60. C. Fasth, A. Fuhrer, L. Samuelson, V.N. Golovach, D. Loss, Direct measurement of the spin-orbit interaction in a two-electron InAs nanowire quantum dot. *Phys. Rev. Lett.* **98**(26), 266801 (2007)
61. F.A. Zwanenburg, C.E. van Rijmenam, Y. Fang, C.M. Lieber, L.P. Kouwenhoven, Spin states of the first four holes in a silicon nanowire quantum dot. *Nano Lett.* **9**(3), 1071–1079 (2009)

62. S. Nadj-Perge, S. Frolov, E. Bakkers, L.P. Kouwenhoven, Spin-orbit qubit in a semiconductor nanowire. *Nature* **468**(7327), 1084–1087 (2010)
63. Y. Hu, F. Kuemmeth, C.M. Lieber, C.M. Marcus, Hole spin relaxation in Ge-Si core-shell nanowire qubits. *Nat. Nanotechnol.* **7**(1), 47–50 (2012)
64. V. Pribiag, S. Nadj-Perge, S. Frolov, J. van den Berg, I. van Weperen, S. Plissard, E. Bakkers, L. Kouwenhoven, Electrical control of single hole spins in nanowire quantum dots. *Nat. Nanotechnol.* **8**(3), 170–174 (2013)
65. A.P. Higginbotham, T.W. Larsen, J. Yao, H. Yan, C.M. Lieber, C.M. Marcus, F. Kuemmeth, Hole spin coherence in a Ge/Si heterostructure nanowire. *Nano Lett.* **14**(6), 3582–3586 (2014)
66. Weiss, U., *Quantum dissipative systems*. World Scientific: Singapore, 1999; Vol. 10
67. C. Beenakker, H. Van Houten, Josephson current through a superconducting quantum point contact shorter than the coherence length. *Phys. Rev. Lett.* **66**(23), 3056 (1991)
68. P.A. Dirac, Quantum mechanics of many-electron systems. *Proc. R. Soc. Lond. Ser. A* **123** (792), 714–733 (1929)
69. J. Alicea, New directions in the pursuit of Majorana fermions in solid state systems. *Rep. Prog. Phys.* **75**(7), 076501 (2012)
70. T.D. Stanescu, S. Tewari, Majorana fermions in semiconductor nanowires: fundamentals, modeling, and experiment. *J. Phys. Condens. Matter* **25**(23), 233201 (2013)
71. H. Peng, K. Lai, D. Kong, S. Meister, Y. Chen, X.-L. Qi, S.-C. Zhang, Z.-X. Shen, Y. Cui, Aharonov-Bohm interference in topological insulator nanoribbons. *Nat. Mater.* **9**(3), 225–229 (2010)
72. J.H. Bardarson, P. Brouwer, J. Moore, Aharonov-Bohm oscillations in disordered topological insulator nanowires. *Phys. Rev. Lett.* **105**(15), 156803 (2010)
73. D. Kong, J.C. Randel, H. Peng, J.J. Cha, S. Meister, K. Lai, Y. Chen, Z.-X. Shen, H.C. Manoharan, Y. Cui, Topological insulator nanowires and nanoribbons. *Nano Lett.* **10**(1), 329–333 (2010)
74. S.S. Hong, W. Kundhikanjana, J.J. Cha, K. Lai, D. Kong, S. Meister, M.A. Kelly, Z.-X. Shen, Y. Cui, Ultrathin topological insulator  $\text{Bi}_2\text{Se}_3$  nanoribbons exfoliated by atomic force microscopy. *Nano Lett.* **10**(8), 3118–3122 (2010)
75. F. Xiu, L. He, Y. Wang, L. Cheng, L.-T. Chang, M. Lang, G. Huang, X. Kou, Y. Zhou, X. Jiang, Manipulating surface states in topological insulator nanoribbons. *Nat. Nanotechnol.* **6** (4), 216–221 (2011)
76. J.J. Cha, K.J. Koski, Y. Cui, Topological insulator nanostructures. *Phys. Status Solidi RRL* **7** (1–2), 15–25 (2013)
77. D. Kong, Y. Cui, Opportunities in chemistry and materials science for topological insulators and their nanostructures. *Nat. Chem.* **3**(11), 845–849 (2011)
78. L. Trifunovic, O. Dial, M. Trif, J.R. Wootton, R. Abebe, A. Yacoby, D. Loss, Long-distance spin-spin coupling via floating gates. *Phys. Rev. X* **2**(1), 011006 (2012)
79. S. Albrecht, A. Higginbotham, M. Madsen, F. Kuemmeth, T. Jespersen, J. Nygård, P. Krogstrup, C. Marcus, Exponential protection of zero modes in Majorana islands. *Nature* **531**(7593), 206–209 (2016)

# Chapter 8

## Nanowire-Enabled Energy Storage

**Abstract** A variety of energy storage systems are currently being explored and in some cases commercialized to meet the needs for both small and large-scale energy storage/usage. Among these systems, rechargeable batteries have been extensively investigated in the research community in efforts to make breakthroughs beyond existing commercial lithium ion systems and thereby provide enhancements to capacity, power density and other metrics that would be beneficial to ubiquitous consumer electronic devices through electric automobiles. In this chapter, the advantages of NW structures for efficient energy storage will be illustrated and discussed, including their high surface area, efficient charge transport and capability to sustain large volume expansion/contraction during charge/discharge cycles. In particular, we will introduce and discuss representative works focused on lithium ion batteries, electrochemical capacitors, and sodium ion batteries. Finally, prospects and challenges for implementing NWs for practical energy storage solutions will be briefly discussed.

### 8.1 Introduction

A significant challenge of this century centers on energy, and in particular, how can clean and renewable energy be efficiently produced as well as stored for efficient reuse and/or distribution [1–5]. In the case of energy storage, the performance, for example of batteries, depends intimately on the properties of anode and cathode materials. Innovative nanomaterials chemistry lies at the heart of advances that have already been made in improving rechargeable lithium–ion batteries (LIBs) [6, 7]. Further breakthroughs in materials can further fuel improvements of existing storage systems and also hold the key to new generations of energy storage devices. In this regard, nanostructured materials have attracted great interest in recent years because of the unusual mechanical and electrical properties endowed by confining the dimensions of such materials, and because the combination of bulk and high surface area properties can further enhance overall behavior. For example, battery electrode materials that in bulk form would degrade or fail due to large volume

changes during charge/discharge cycles can become viable in nanoscale morphologies, since the latter are capable of sustaining much greater strains before failure.

In this context, NWs are becoming increasingly important for electrochemical energy storage, and they represent unique candidates with several exciting advantages [8, 9]. First, the direct attachment and electrical contact of each NW to the metallic current collector provide efficient, 1D charge transport pathways, without the need of adding binders and conducting additives. Second, the void space between adjacent NWs and the high surface-to-volume ratios of NWs allow for fast penetration of electrolyte solution into deep portion of NWs, as well as rapid electrochemical reactions over the surface. Third, compared to flat electrode structures, the small diameters and the large curvatures of NWs are beneficial for accommodating more volume change, thus reducing mechanical failure of electrodes and maintaining the electronic pathways during many discharge-recharge cycles. In this chapter, we will introduce and discuss representative NW studies focused on lithium ion batteries (LIBs), electrochemical capacitors (ECs), and sodium ion batteries.

## 8.2 Lithium-Ion Batteries

Rechargeable LIBs are efficient, light-weight, and rechargeable power sources for a large variety of applications ranging from portable electronics to the development of electric automobiles, in which the electrodes are the central issue [10, 11]. A combination of a negative lithium intercalation material (anode) with another lithium intercalation material (cathode) having a more positive redox potential gives a Li-ion transfer cell [12]. An anode and a cathode are separated by an electrolyte, which is an electronic insulator but a Li-ion conductor. Upon charging, lithium ions are released by the cathode and intercalated at the anode. When the cell is discharged, lithium ions are extracted by the cathode from the anode. An ideal electrode should provide high gravimetric and volumetric capacity, high power density and long cycle life, as well as being environmentally benign and low cost [13]. One of the main challenges in the design of LIBs is to ensure that the electrodes maintain their integrity over many discharge-recharge cycles. Although promising electrode systems have been proposed, their lifespans are often limited by Li-alloying agglomeration or the growth of passivation layers, which prevent the fully reversible insertion of Li ions into the negative electrodes (anodes) [14]. 1D NWs, especially the self-supporting NW arrays grown directly on a current-collecting substrate offer several attractive features for LIB electrodes [15]. The open space between neighboring NWs allows for easy diffusion of electrolyte into the inner region of the electrode, resulting in reduced internal resistance and improved high-power performance. Each NW has its own contact with the current collector substrate, which can ensure that every NW participates in the electrochemical reaction. In addition, using NW arrays also saves the tedious process of mixing

active material with ancillary materials such as carbon black and polymer. Moreover, NWs share the same advantages as other nanostructured electrodes, such as nanoparticles, with high electrode-electrolyte contact area, fast Li-ion diffusion rate, and good strain accommodation.

## 8.2.1 Anodes

### 8.2.1.1 Si

Si has the highest gravimetric capacity (4200 mAh/g, lithiated to  $\text{Li}_{4.4}\text{Si}$ ) among all anode candidates other than Li metal [10]. The average discharge voltage of Si is low ( $\sim 0.4$  V), providing a high voltage difference against the cathode [16]. Nonetheless, the insertion and extraction of lithium ions from Si leads to a large volume change, up to  $\sim 400\%$  volume increase upon insertion, and this large volume change results in mechanical failure of electrodes and discontinuous charge transport during cycling (top, Fig. 8.1a). In addition, the large volume change also affects the formation of dense and stable solid-electrolyte inter-phase (SEI) layer over Si surface, which functions as an ionic conducting and electronic insulating passivation layer to prevent further side chemical reactions from occurring [13]. Thus, the Si-based anode usually suffers from substantially reduced stability and a large irreversible capacity decrease during charge/discharge cycles [17].

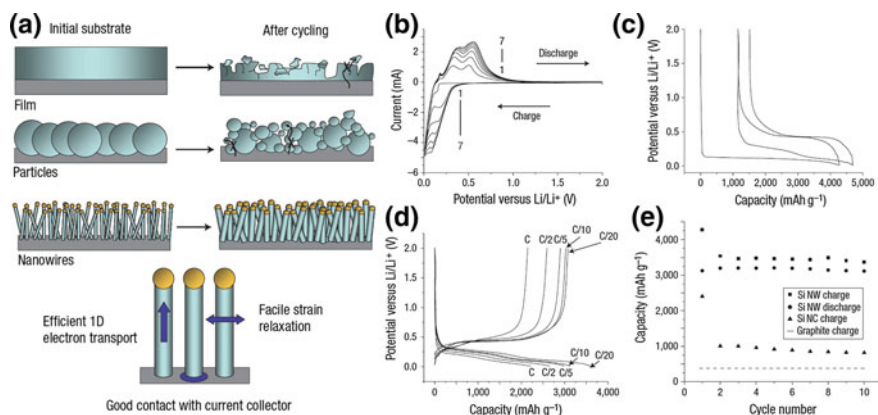


**Fig. 8.1** **a** Schematics of the morphological changes that occur in Si during electrochemical cycling, where Si films and particles tend to fail during cycling, while NWs grown directly on the current collector do not break-up into smaller particles. **b** Cyclic voltammograms for SiNWs from 2.0 to 0.01 V versus  $\text{Li}/\text{Li}^+$ . The first seven cycles are shown. **c** Voltage profiles for the first and second galvanostatic cycles of the SiNWs. The first charge achieved the theoretical capacity of  $4200 \text{ mAh g}^{-1}$  for  $\text{Li}_{4.4}\text{Si}$ . **d** The voltage profiles for the SiNWs cycled at different power rates. **e** Capacity versus cycle number for the SiNWs at the C/20 rate showing the charge (*squares*) and discharge capacity (*circles*). The charge data for Si nanocrystals (*triangles*) and the theoretical capacity for lithiated graphite (*dashed line*) are shown as a comparison to show the improvement when using SiNWs. Reproduced from [8]. Copyright 2008 Nature Publishing Group

A number of research efforts have addressed these challenges of Si anodes for LIBs by focusing on the rational design and fabrication of Si-based nanostructures [18–20]. In 2008, the Cui group [8] reported the first SiNW-based LIB anode, in which SiNWs were grown by the nanocluster-catalyzed VLS method on stainless steel substrates (Fig. 8.1a). LIB anodes made using these SiNW electrodes achieve nearly the theoretical discharge capacity of Si during the first cycle, and maintained a discharge capacity of  $\sim 3100$  mAh/g, about 75 % of the maximum, with little fading over 10 cycles (Fig. 8.1b–e). Structural characterization after the battery test showed an increase of SiNW diameter from 89 nm initially to 141 nm after lithiation, and importantly, demonstrated that the SiNWs remained connected with the current collectors versus breaking up into smaller particles. These latter results suggested that the nanoscale diameters provided superior mechanical properties and allowed the SiNWs to sustain the strains associated with large volume changes during charge/discharge cycles.

Similar to VLS-grown samples, SiNWs made by other approaches have been investigated as LIB anode materials. For example, Schulz et al. [21] reported using an electrospinning method with  $\text{Si}_6\text{H}_{12}$  as the Si precursor to synthesize Si nanofibers, while the LIB anodes made of these samples only achieve a reversible capacity  $\sim 400$  mAh/g after 30 cycles. On the other hand, SiNWs fabricated by the metal-assisted solution etching approach have exhibited characteristics similar to nanocluster-catalyzed VLS NWs, and thus are good candidates for LIB anodes. An added advantage of this latter etching-based approach to SiNWs is that it is possible to precisely control the crystal orientation and doping based on the starting Si-substrate [18, 22, 23]. The rougher surface of solution etched SiNWs also increases the surface area, which could be beneficial for the insertion/extraction of Li ions [18]. As a result, SiNWs obtained from the solution etching approach have demonstrated substantially improved capacity and cycling stability for the use of LIB anodes [24, 25].

SiNWs with core-shell designs provide additional structural advantages in optimizing the electrochemical performance for Si-based anodes. For example, a thin carbon shell could facilitate electrical contact and charge conduction. Huang et al. [26] reported synthesis of carbon-coated etched SiNW arrays by pyrolysis of a carbon aerogel. Compared to the pristine SiNWs, which exhibited capacity fading after 10 cycles, the carbon-coated SiNWs showed a high initial discharge capacity of 3344 mAh/g and retained a reversible capacity of 1326 mAh/g after 40 cycles. The continuous structure of most of these SiNWs is still maintained after the cycling test. Polymer has also been demonstrated for coating of SiNWs for improving the stability and capacity of the anodes [27]. In addition, a scalable supercritical fluid-liquid-solid method was reported to grow SiNWs [28], which were further coated with carbon by pyrolysis of sucrose on the SiNW surface. LIB anodes made of these carbon-coated SiNWs have retained a reversible capacity of 1500 mAh/g after 30 cycles.

In addition to Si/carbon core/shell designs, Cui and coworkers has demonstrated the utilization of crystalline/amorphous core/shell SiNWs for enhanced lithium ion storage capacity [29]. The crystalline Si core and amorphous Si shell are sequentially grown via the nanocluster-catalyzed VLS and shell deposition strategies described in earlier chapters. As the amorphous Si shell reacts with  $\text{Li}^+$  at a slightly higher potential than the crystalline Si core, this design of crystalline/amorphous core/shell SiNWs allows for selective lithiation of the amorphous Si shell. The crystalline Si core is not affected during the lithiation step and serves as a continuous structure for both electrical conduction and mechanical support, thus resulting in substantial improvement in power rate and cycling stability. Specifically, crystalline/amorphous core/shell SiNWs have demonstrated a reversible capacity of 1000 mAh/g over 100 cycles. TEM images revealed that the crystalline/amorphous core/shell SiNWs become completely amorphous when the anodes are discharged to 10 mV, while the crystalline Si core is maintained for discharge potentials above 150 mV. This structural characterization confirms that the enhanced stability is due to the existence of crystalline Si core after cycling.

This crystalline core/amorphous shell concept was further extended to the synthesis of carbon/Si core/shell NWs, in which amorphous Si layer is deposited on the surface of carbon nanofibers [30]. In this case, the carbon nanofiber core serves as an electrical conductor and stable mechanical support [31]. In addition, the carbon cores have much less volume change than that of Si, and thus the core structures are maintained at a much lower low discharge potential of  $\sim 10$  mV. A higher charge capacity of 2000 mAh/g was reported for carbon/Si core/shell NWs. In addition, other core/shell NW designs have been reported for amorphous Si on different core materials, including metal silicides [32], nitrides [33], and carbon nanotubes [34].

The shape and volume changes of crystalline SiNWs with different crystal orientations have been studied by in situ electron microscopy [35, 36]. SEM images showed that lithiation transforms the initially circular cross sections of NWs with  $\langle 100 \rangle$ ,  $\langle 110 \rangle$ , and  $\langle 111 \rangle$  axial orientations into expanded structures with cross sections having cross, ellipse, and hexagonal shapes, respectively [37] (Fig. 8.2a). These observations were explained in terms of a rapid lithium ion diffusion channel along the  $\langle 110 \rangle$  direction, which causes preferential volume expansion along this direction. It was also found that the  $\langle 111 \rangle$  and  $\langle 100 \rangle$  NWs shrink in height after partial lithiation, while  $\langle 110 \rangle$  NWs increase in height. This length contraction was attributed to a collapse of  $\{111\}$  planes early in the lithiation process. In another work [38], the anisotropic swelling of SiNWs during lithiation in either a conventional liquid cell or an all-solid electrochemical cell was characterized by TEM (Fig. 8.2b). In this latter work, the authors directly observed that the large volumetric expansion  $\langle 112 \rangle$  axis NWs occurs in a highly anisotropic fashion to yield intermediate dumbbell-shaped cross sections. These results give new insight into the Si volume change process and may help in designing better Si anodes.

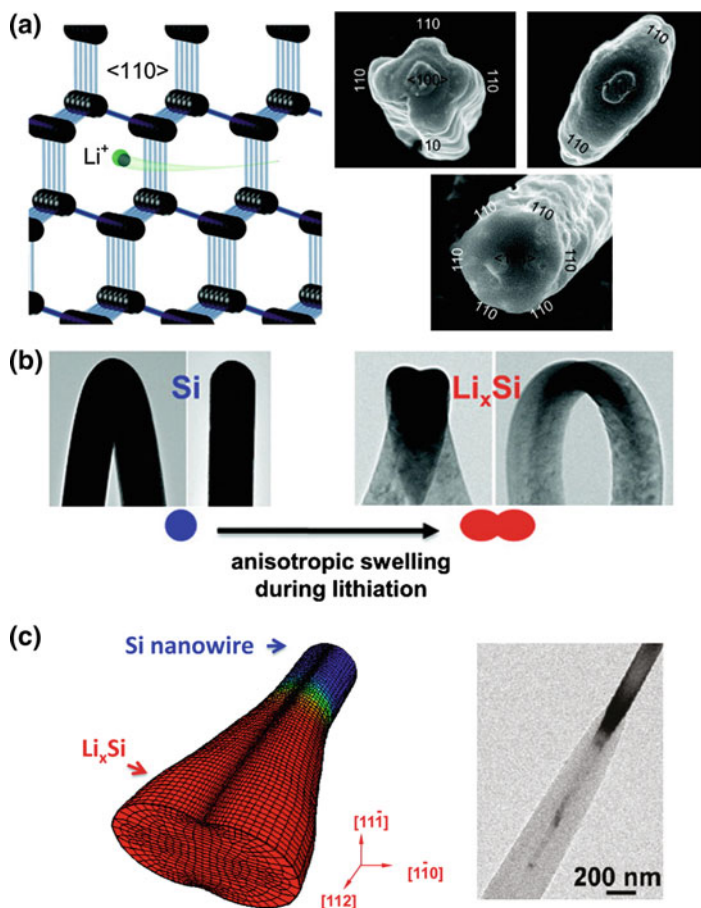


**Fig. 8.2** **a** Anisotropic lateral expansion of crystalline SiNWs with  $\langle 100 \rangle$ ,  $\langle 110 \rangle$  and  $\langle 111 \rangle$  axial orientations upon lithiation. Reproduced from [37]. Copyright 2011 American Chemical Society. **b** Dumbbell shape of a  $\langle 112 \rangle$  axis SiNW following lithiation contrasts the round cross section of the pristine SiNW. **c** 3D simulation (left) and TEM image (right) of a progressively lithiated NW (i.e., the Li flux is prescribed at the front end), showing the development of the dumbbell-shaped cross section along the longitudinal direction. Reproduced from [38]. Copyright 2011 American Chemical Society

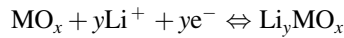
### 8.2.1.2 Metal Oxides

Metal oxides, especially in the form of nanomaterials, have been extensively investigated as potential anode materials for LIBs because these materials have diverse chemical and physical properties and most of them possess relatively high theoretical capacities between 500 and 1000 mAh/g compared to graphite (372 mAh/g) in commercial LIBs [39–42], although still much lower than the theoretical capacity of Si (4200 mAh/g) [10]. However, the use of metal oxides as LIB anodes still faces



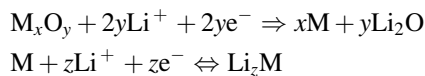
multiple challenges including: (i) similar to Si, most metal oxides exhibit substantial expansion and contraction during charging/discharging processes [43, 44]; and (ii) most abundant metal oxides are semiconductors with large band gaps and typically have poor electrical conductivity and ion transport kinetics as LIB electrodes [41, 45]. To address these issues, researchers have been focused on the design of electrode structures and the use of multi-functional hybrid materials [39–42]. Based on the overall mechanism, metal oxide-based LIB anodes can be divided into three categories: (i) intercalation/deintercalation of Li ions into and from layered metal oxides; (ii) alloying/dealloying to store/release Li ions; (iii) conversion between Li and  $\text{Li}_2\text{O}$  by reduction/oxidation of transition metal oxides [39–42]. Here we focus on well-studied  $\text{TiO}_2$ ,  $\text{SnO}_2$  and  $\text{Co}_3\text{O}_4$  NWs as examples for these three categories.

- (i) Several transition metal oxides with layered and open channel structures can store Li ions via the intercalation/deintercalation mechanism [39–42]. These materials can exhibit a range of theoretical capacities depending on the structure of the metal oxide and number of Li ions intercalated into layer or channel sites during intercalation. This mechanism can be written as [39]:



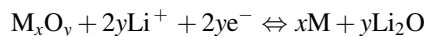
For example,  $\text{TiO}_2$ , is a potential candidate for use as LIB anodes due to its low cost and abundance in nature, and has various polymorphs such as anatase, rutile, and  $\text{TiO}_2(\text{B})$  (bronze). In 2005, the Bruce group [46] reported the intercalation of Li ions into  $\text{TiO}_2(\text{B})$  NWs.  $\text{TiO}_2(\text{B})$  NWs were synthesized by an ion-exchanging  $\text{K}^+$  for  $\text{H}^+$  in  $\text{K}_2\text{Ti}_4\text{O}_9$  to form a hydrated hydrogen titanate, which was transformed into  $\text{TiO}_2$  NWs by heating at 500 °C. The structure of  $\text{TiO}_2(\text{B})$  NWs is composed of corrugated sheets of edge- and corner-sharing  $\text{TiO}_2$  octahedra, with these sheets being linked together by bridging oxygen atoms to form a 3D network, with significant voids and continuous channels that are capable of rendering the material a host structure for intercalation. The reversible charge-storage capacity of 205 mAh/g was obtained without structural degradation or loss of NW morphology. In comparison, the capacity for bulk material is 240 mAh/g, with the composition  $\text{Li}_{0.71}\text{TiO}_2(\text{B})$ . The best result using other  $\text{TiO}_2(\text{B})$  nanostructures was observed for needle-shaped  $\text{TiO}_2(\text{B})$  nanoparticles with a reversible capacity of  $\sim 288$  mAh/g after 50 cycles [47].

- (ii) Metal oxide anodes that undergo an alloying/dealloying mechanism typically have higher capacities than intercalation/deintercalation, but necessarily as a result of high capacity suffer from significant volume change during cycling [22]. The basic mechanism can be written in two steps [39]:



Taking SnO<sub>2</sub> (theoretical capacity, 782 mAh/g) as an example, Park et al. [48] reported the preparation and electrochemical performance of SnO<sub>2</sub> NWs to determine their potential use as an anode material. The SnO<sub>2</sub> NWs were synthesized by thermal evaporation combined with a self-catalyzed growth procedure, where the authors used a high surface area powder to increase production at lower temperature. The SnO<sub>2</sub> NWs produced in this manner showed higher initial Coulombic efficiency and an improved capacity retention on cycling compared with those of SnO<sub>2</sub> powder and SnO<sub>2</sub> NWs produced by Au-assisted VLS growth. Kim et al. [49] reported the synthesis of SnO<sub>2</sub>-In<sub>2</sub>O<sub>3</sub> core-shell NW heterostructures via a thermal evaporation method. The electronic conductivity of the individual SnO<sub>2</sub>-In<sub>2</sub>O<sub>3</sub> core-shell NWs was 2 orders of magnitude higher than that of pure SnO<sub>2</sub> NWs, due to the formation of Sn-doped In<sub>2</sub>O<sub>3</sub> during the nucleation and growth of the In<sub>2</sub>O<sub>3</sub> shell nanostructures. Kim et al. [50] reported the synthesis of SnO<sub>2</sub> NWs using 1D mesoporous SiO<sub>2</sub> sacrificial templates that were subsequently dissolved in NaOH. These ultrasmall 6 nm diameter SnO<sub>2</sub> NWs with lengths >3 μm and surface area of 80 m<sup>2</sup>/g exhibited a capacity of 800 mAh/g, while the capacity was reduced to 250 mAh/g at a 10C rate (4000 mA/g). Liu et al. [51] reported the synthesis of SnO<sub>2</sub> nanorod arrays on large-area flexible metallic substrates (Fe-Co-Ni alloy and Ni foil) via a hydrothermal process. The electrochemical behavior was found to depend crucially on the structural parameters of the array. An array consisting of SnO<sub>2</sub> nanorods of average 60 nm in diameter and 670 nm in length delivered a reversible Li-capacity as high as 580 mAh/g after 100 cycles (0.1C) and showed less than 50 % reduction to 350 mAh/g at a higher rate of 5C rate. Structural disintegration and agglomeration were not observed for the SnO<sub>2</sub> nanorod arrays even after 50 cycles. In comparison, commercially available ca. 40 nm SnO<sub>2</sub> particles yield an initial capacity of 500 mAh/g, although this capacity dropped to 100 mAh/g after 50 cycles [52]. The best performance so far was observed for 3 nm SnO<sub>2</sub> nanoparticles, which exhibited an initial capacity of 740 mAh/g with negligible capacity fading [53].

- (iii) Li can be stored reversibly in transition metal oxides through a conversion reaction mechanism, where the transition metal experiences reduction/oxidation reactions [39–42]. Anodes based on these materials also exhibit relatively high capacities (500–1000 mAh/g).



For instance, the theoretical capacity of Co<sub>3</sub>O<sub>4</sub> is 890 mAh/g. In 2008, Li et al. [15] utilized a mild template-free, ammonia-evaporation-induced method for large-area growth of self-supported Co<sub>3</sub>O<sub>4</sub> NW arrays on different substrates, including Si wafers, glass slides, and Cu or Ti foils. Ti foil is an excellent substrate for this work, as it is resistive to the alkaline ammonia solution and oxidation, and it does not alloy with metallic Li at low voltage and thus serves as a good current collector. In addition, the NW arrays produced by their method had mesoporous

structures, which provided extra freedom for volumetric changes during lithiation. The NW arrays show a stable capacity of 700 mAh/g at 1C after 20 cycles, and can maintain the capacity around 50 % at a higher charging rate of 50C, substantially better than freestanding  $\text{Co}_3\text{O}_4$  NWs not grown on Ti foils. Later, Wu et al. [54] reported a two-step hydrothermal synthesis of a  $\text{Co}_3\text{O}_4/\alpha\text{-Fe}_2\text{O}_3$  branched NW heterostructures. The single-crystalline, primary  $\text{Co}_3\text{O}_4$  NW trunk arrays directly grown on Ti substrates allow for efficient electrical and ionic transport. The secondary  $\alpha\text{-Fe}_2\text{O}_3$  branches provide enhanced surface area and high theoretical  $\text{Li}^+$  storage capacity, and can also serve as volume spacers between neighboring  $\text{Co}_3\text{O}_4$  NW arrays to maintain electrolyte penetration as well as reduce the aggregation during  $\text{Li}^+$  intercalation. These  $\text{Co}_3\text{O}_4/\alpha\text{-Fe}_2\text{O}_3$  branched NW heterostructures yielded improved electrochemical energy storage performance with reversible capacity of  $\sim 980$  mAh/g after 60 cycles. In comparison, the best performance using other nanomaterials so far was observed in graphene-encapsulated  $\text{Co}_3\text{O}_4$  nanoparticles, exhibiting a reversible capacity of 1100 mAh/g in the first 10 cycles, and over 1000 mAh/g after 130 cycles [55].

## 8.2.2 Cathodes

Since the concept of a rechargeable lithium cell based on Li intercalation reactions was initiated in the early 1970s, numerous lithium intercalation cathode electrodes have been proposed to date [10]. Two categories of materials have been used for LIB cathodes [43, 56–58]. The first category include lithium transition metal oxides with layered anion close-packed lattice, where the transition metal ions occupy alternate layers and Li ions can be intercalated into the remaining layers. Commonly used materials include  $\text{LiCoO}_2$ ,  $\text{LiNiO}_2$  and  $\text{LiMn}_2\text{O}_4$ . One intrinsic advantage of this category of cathode is their higher energy density owing to their compact lattice structures. The second category includes layered materials with more open structures, such as  $\text{V}_2\text{O}_5$  and transition metal phosphates (e.g., the olivine  $\text{LiFePO}_4$ ). These materials provide the advantages of better safety and lower cost compared to the first category.

Currently,  $\text{LiCoO}_2$ ,  $\text{LiNiO}_2$  and  $\text{LiMn}_2\text{O}_4$  are used as commercial LIB cathode materials, among which  $\text{LiCoO}_2$  being the most popular candidate owing to the convenience and simplicity of preparation [10].  $\text{LiCoO}_2$  cathode materials are typically cycled with excellent stability between the fully lithiated discharge state  $\text{LiCoO}_2$  ( $\sim 3.0$  V vs.  $\text{Li}/\text{Li}^+$ ) and a roughly half-delithiated state  $\text{Li}_x\text{CoO}_2$  ( $x = 0.5\text{--}0.6$ , 4.2 V vs.  $\text{Li}/\text{Li}^+$ ), leading to a capacity of  $\sim 140$  mAh/g, while its theoretical capacity is 273 mAh/g [59]. In 2005, Jiao et al. [60] reported a hard template route to synthesize  $\text{LiCoO}_2$  NWs. Preliminary electrochemical tests using these  $\text{LiCoO}_2$  NW arrays as cathodes showed an initial discharge capacity of 80 mAh/g and a capacity retention of 40 mAh/g after 50 cycles, much less than that of commercial  $\text{LiCoO}_2$  cathodes [59]. Later, Xiao et al. [61] demonstrated the synthesis of cobalt precursor  $\text{Co}(\text{CO}_3)_{0.35}\text{Cl}_{0.2}(\text{OH})_{1.1}$  NW aggregates by a hydrothermal method, and

transformed these into  $\text{Co}_3\text{O}_4$  NWs at high temperature. Subsequent reaction with LiOH yielded  $\text{LiCoO}_2$  NWs. High-resolution TEM revealed that these  $\text{LiCoO}_2$  NWs were composed of nanoparticles, with most of the nanoparticles having exposed (010) planes. The as-prepared  $\text{LiCoO}_2$  NWs exhibited charge/discharge capacity stabilized at 100 mAh/g after 100 cycles. In comparison, the most recent report on flake-like  $\text{LiCoO}_2$  nanoparticles synthesized using  $\text{Co}(\text{OH})_2$  nanoflakes as sacrificial templates via a simple coprecipitation method showed a reversible discharge capacity up to 179 mAh/g [62].

The disadvantages of  $\text{LiCoO}_2$  as cathode material include its high cost and toxicity [43, 56–58]. As an alternative,  $\text{LiMn}_2\text{O}_4$  can be a lower cost, environmentally friendly, and highly abundant material for LIB cathodes. The theoretical charge storage capacity is 148 mAh/g [63], although it can be limited due to phase changes during cycling [64, 65]. The Cui group [66] reported the hydrothermal synthesis of single-crystalline  $\beta\text{-MnO}_2$  nanorods and their chemical conversion into free-standing single-crystalline  $\text{LiMn}_2\text{O}_4$  nanorods. The  $\text{LiMn}_2\text{O}_4$  nanorods had an average diameter of 130 nm and length of 1.2  $\mu\text{m}$ . Galvanostatic battery testing showed that  $\text{LiMn}_2\text{O}_4$  nanorods had a charge storage capacity of 100 mAh/g at a high current density of 148 mA/g (1C) with high reversibility and 85 % capacity retention after 100 cycles, while the capacity of commercially available powders was only 50 mAh/g at the same current density. Structural studies showed that the Li ions intercalated into the cubic phase of  $\text{LiMn}_2\text{O}_4$  with a small change of lattice parameter, followed by the coexistence of two nearly identical cubic phases in the potential range of 3.5–4.3 V. Similarly, they also reported ultrathin  $\text{LiMn}_2\text{O}_4$  NWs with cubic spinel structure synthesized by a solvothermal reaction. This approach produced  $\alpha\text{-MnO}_2$  NWs which were converted in a second step to  $\text{LiMn}_2\text{O}_4$  NWs with diameters less than 10 nm and lengths of several micrometers [67]. These small diameters NWs yielded 100 and 78 mAh/g at high charging rates of 60 and 150C, respectively [67]. Hosono et al. [68] synthesized single crystalline cubic spinel  $\text{LiMn}_2\text{O}_4$  NWs using  $\text{Na}_{0.44}\text{Mn}_2\text{O}_2$  NWs as a self-template. These self-templated NWs exhibited reversible capacities of 108, 102, and 88 mAh/g at fast charge/discharge rates of  $\sim 50$ , 100, and 200C, respectively. More recently, Wang et al. [69] reported an all NW based flexible LIB, using homologous  $\text{Mn}_2\text{O}_3$  and  $\text{LiMn}_2\text{O}_4$  NWs for anodes and cathodes, respectively. As shown in Fig. 8.3, the same precursors,  $\text{MnOOH}$  NWs, were transformed from hydrothermally grown  $\text{MnO}_2$  nanoflakes and directly attached on Ti foils via reaction with poly(vinyl pyrrolidone). The  $\text{Mn}_2\text{O}_3$  anode and  $\text{LiMn}_2\text{O}_4$  cathode were subsequently formed by thermal annealing and reaction with lithium salt, respectively. The  $\text{LiMn}_2\text{O}_4$  NW cathode showed a reversible capacity of 94.7 mAh/g at a charging rate of 1C and high capacity retention of  $\sim 96$  % after 100 cycles. Furthermore, the flexible  $\text{Mn}_2\text{O}_3/\text{LiMn}_2\text{O}_4$  full LIB exhibited an output voltage of  $>3$  V, a thickness of 0.3 mm, high flexibility, and a specific capacity of 99 mAh/g based on the total weight of the cathode material. It also exhibited good cycling stability with a capacity of  $\sim 80$  mAh/g after 40 charge/discharge cycles. Notably, a recent study reported the synthesis of nanoparticles with a new composition  $\text{Li}_4\text{Mn}_2\text{O}_5$ , prepared by direct mechanochemical synthesis at room temperature [70] yielded a discharge

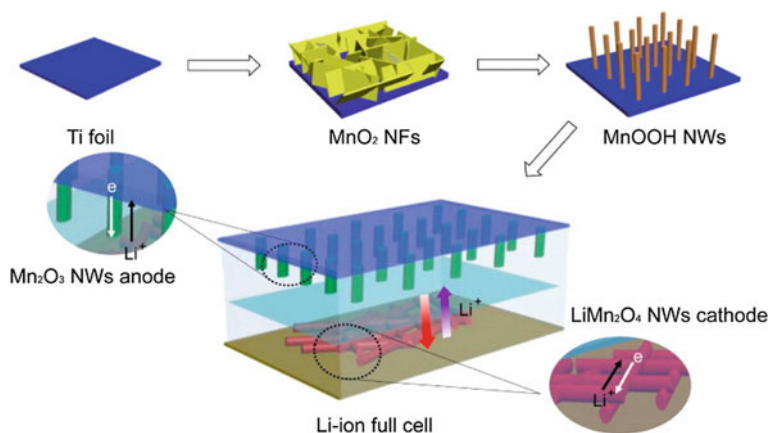
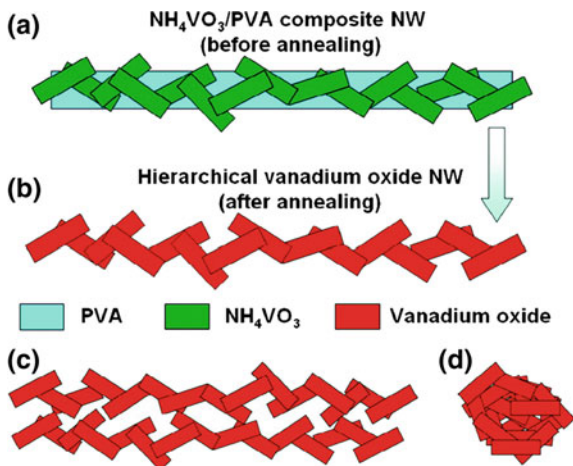


**Fig. 8.3** Schematic of the synthesis and fabrication of the  $\text{Mn}_2\text{O}_3/\text{LiMn}_2\text{O}_4$  LIB full cell. Reproduced from [69]. Copyright 2014 American Chemical Society

capacity of 355 mAh/g. This is the highest yet reported among known lithium manganese oxide electrode materials. Such a high capacity is in principle unexpected, as the oxidation state of Mn in  $\text{Li}_4\text{Mn}_2\text{O}_5$  is 3+. If one assumes that only the  $\text{Mn}^{3+}/\text{Mn}^{4+}$  redox couple is active, then two Li ions could be extracted, resulting in the formation of  $\text{Li}_2\text{Mn}_2\text{O}_5$  with a theoretical capacity of 245 mAh/g. According to the magnetic measurements, the authors proposed that the electrochemical activity is due to the  $\text{Mn}^{3+}/\text{Mn}^{4+}$ ,  $\text{O}^{2-}/\text{O}^-$ , as well as  $\text{Mn}^{4+}/\text{Mn}^{5+}$  redox couples. Future studies could help to illuminate better these interesting results.

For Li ion intercalation applications,  $\text{V}_2\text{O}_5$  offers advantages of low cost, natural abundance and straightforward synthesis [12]. Interestingly, different  $\text{Li}_x\text{V}_2\text{O}_5$  phases form after intercalation of Li ions, each with different theoretical capacities. The highest capacity  $\omega\text{-Li}_x\text{V}_2\text{O}_5$  phase yields  $\sim 440$  mAh/g for deep discharge, although all of the intercalated Li ions cannot be extracted from the host structure, indicating an irreversible transition [71]. In 2010, Mai et al. [72] reported the synthesis of ultralong hierarchical  $\text{V}_2\text{O}_5$  NWs with diameters of 100–200 nm and lengths up to several millimeters using electrospinning combined with annealing. As shown in Fig. 8.4, the hierarchical NWs were constructed from attached  $\text{V}_2\text{O}_5$  nanorods of diameter  $\sim 50$  nm and length of 100 nm. The initial and 50th discharge capacities of the ultralong hierarchical  $\text{V}_2\text{O}_5$  NW cathodes were 390 and 201 mAh/g when the LIB was cycled between 1.75 and 4.0 V, much higher than the self-aggregated short nanorods synthesized by a hydrothermal method. Chan et al. [73] used in situ TEM to study the chemical, structural, and electrical transformations of  $\text{V}_2\text{O}_5$  nanoribbons at the single nanostructure level. It was found that transformation of  $\text{V}_2\text{O}_5$  into the  $\text{Li}_3\text{V}_2\text{O}_5$  phase depends not only on the width but also the thickness of the nanoribbons. Transformation can take place within 10 s in thin nanoribbons, suggesting a  $\text{Li}^+$  diffusion constant that is 3 orders of magnitude faster than in bulk materials, resulting in a significant increase in battery

**Fig. 8.4** **a, b** Schematic illustration of formation of the ultralong hierarchical vanadium oxide NWs during annealing. **c** Side view of two ultralong hierarchical vanadium oxide NWs near each other. **d** Self-aggregation of short vanadium oxide nanorods. Reproduced from [72]. Copyright 2010 American Chemical Society



power density. Recently, it was reported that NWs/nanorods assembled into a 3D interconnected  $\text{V}_2\text{O}_5$  nano-network yielded improved electron/ion transport and enhanced structure stability [74]. The inner porous structure was proposed to promote ion diffusion and to buffer volume change during cycling. As a cathode, the interconnected  $\text{V}_2\text{O}_5$  nano-network exhibited little capacity fading after 1000 charge/discharge cycles at high current densities of 1.0 and 2.0 A/g.

Lithium metal phosphates are presently at the center of much interest as cathodes for LIBs, with a theoretical capacity of 170 mAh/g for the commonly investigated  $\text{LiFePO}_4$ . Lim et al. [75] used a hard template for the synthesis of  $\text{LiFePO}_4$  NWs. In this work, a 2D hexagonal Santa Barbara amorphous (SBA-15) silica template, containing parallel cylindrical pores arranged with a hexagonal  $P6mm$  symmetry, served to organize the wires into parallel bundles. After impregnation of the template with a solution consisting of  $\text{LiFePO}_4$  precursor, the silica template was removed and the resultant  $\text{LiFePO}_4$  NWs were subsequently annealed. Electrochemical cycling demonstrates the discharge capacity at a rate of 15C shows 137 mAh/g, corresponding to a capacity retention of 89 % compared with the capacity at a rate of 0.2C. This capacity value was less than that reported for hollow  $\text{LiFePO}_4$  nanoparticles, which was 153 mAh/g at 15C and had a 95 % capacity retention compared to that at 0.2C.

### 8.3 Electrochemical Capacitors

LIBs are attractive energy storage devices in terms of their overall energy density (Wh/kg), although the rate of discharge and charge, which is defined by the power density (kW/kg), can be too slow for some applications [10, 11]. High power density needs can in principle be met by ECs, also known as supercapacitors or

ultracapacitors [76, 77]. ECs are power devices that can be fully charged or discharged in seconds, and can yield high power densities of the order of 10 kW/kg for short times [78]. There are two classes of ECs depending on the charge storage mechanism [41, 77, 79–81]. The first class is electrical double layer capacitors (EDLCs), which operate by adsorbing/desorbing charged ions from an electrolyte onto high surface area electrodes forming a double layer structure. Carbon-based materials with high surface area are typically used for EDLCs. A second group of ECs, known as pseudo-capacitors or redox supercapacitors, use transition metal oxides or conducting polymers as electrode materials, with the charge storage depending on fast Faradaic redox reactions. Energy and power densities are two crucial parameters for evaluating the EC performance. The maximum energy,  $E$ , and power densities,  $P$ , of a EC can be obtained using the following equations [78]:

$$E = CV^2/2$$

$$P = V^2/4R$$

where  $C$  is the specific capacitance (SC) of the cell,  $V$  is the operating voltage, and  $R$  is the series resistance. Therefore, a good EC should possess a high SC, wide operating voltage, and minimum resistance. The advantages of nanomaterials in ECs include: (i) the large surface to volume ratio, which provides more ion adsorption or active sites for the formation of electrical double-layer and charge-transfer reactions; (ii) short diffusion and transport length scales for electrolyte ions within the nanostructures, which can facilitate transport of electrolyte ions; and (iii) can effectively buffer stress from volume change in redox EC electrodes during charge/discharge. In this section, we introduce several examples of transition metal oxide [82–86] NWs as electrode materials for pseudo-capacitors.

Among all transition metal oxides, RuO<sub>2</sub> has ultrahigh theoretical SC (~2000 F/g), excellent electrical conductivity, a wide potential window, long cycle life, and high chemical stability; all of these features have made it one of the most promising candidates for EC electrodes [87–89]. The highest SC value reported was for anodically-deposited amorphous RuO<sub>2</sub> thin films on stainless steel substrates, where a maximum SC of 1190 F/g in H<sub>2</sub>SO<sub>4</sub> electrolyte was reported [90]. In comparison, RuO<sub>2</sub> nanorod arrays grown on LiNbO<sub>3</sub>(100) substrates were reported by Ke et al. [91] to have a SC value of 569 F/g. The decreased SC for the crystalline nanorods versus amorphous films can be attributed to slower transport and diffusion of ions [80, 81]. The major drawbacks of RuO<sub>2</sub> are high cost and toxicity, which prevent it from being used in the commercial ECs. Alternative transition metal oxide materials include MnO<sub>2</sub>, NiO, Co<sub>3</sub>O<sub>4</sub>, and V<sub>2</sub>O<sub>5</sub>, as well as hybrid mixtures of two or more of these oxides [87–89]. However, these higher abundance and lower toxicity metal oxides have lower conductivity and theoretical SC than RuO<sub>2</sub> [87–89].

For example, Lu et al. [92] reported the synthesis of large-area manganese oxide (MnO<sub>2</sub>) nanorod arrays on F-doped SnO<sub>2</sub> (FTO) coated substrates. The free-standing MnO<sub>2</sub> nanorods of 70–100 nm in diameter and 1.5 μm in length were

grown on FTO substrates via anodic electrodeposition in dimethyl sulfoxide (DMSO) aqueous solution. While the theoretical SC is  $\sim 1100$  F/g [93], electrochemical measurements showed that the  $\text{MnO}_2$  nanorod electrodes exhibited SC as high as 660.7 F/g at a scan rate of 10 mV/s and 485.2 F/g at a current density of 3 A/g. Interestingly, during 1500 cycles at room temperature with a current density of 3 A/g, the  $\text{MnO}_2$  nanorod electrode SC increased more than 20 % of its initial value over the first 700 cycles, and then retained almost constant SC. This work represents arguably the best reported performance for  $\text{MnO}_2$  EC electrodes.

The electrical conductivity of many transition metal oxides is lower than  $\text{RuO}_2$ , and this limits their SC and power characteristics (due to high charge-transfer resistance). The design of hybrid materials containing different metal oxides, carbon structures, and conductive polymers is a potential route to enhance the electrical conductivity and charge-storage capability by introducing more defects and charge carriers. In addition, coating an ultrathin layer of metal oxide on the surface of a porous, high surface area material can shorten the electron transport distances and thus lead to good electrochemical performance. Xia et al. [94] presented a general two-step solution-based method for the fabrication of transition metal oxide core/shell nanostructure arrays on various conductive substrates. Demonstrated examples include  $\text{Co}_3\text{O}_4$  on ZnO NW cores and NiO nanoflake shells with a hierarchical and porous morphology (Fig. 8.5a, b). Supercapacitor electrodes based on the  $\text{Co}_3\text{O}_4/\text{NiO}$  core/shell NW arrays on a 3D macroporous Ni foam exhibited a high SC of 853 F/g and stable cycling performance up to 6000 cycles (Fig. 8.5c, d).

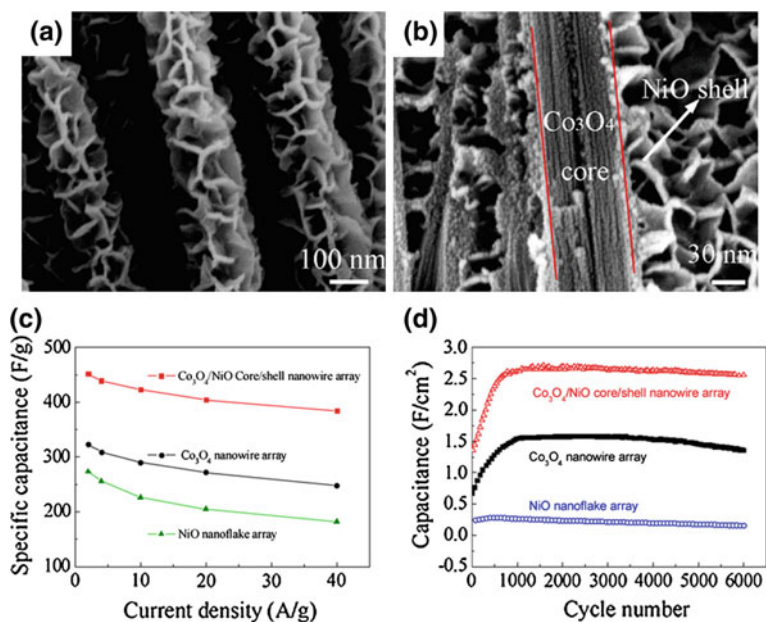


**Fig. 8.5** a, b  $\text{Co}_3\text{O}_4/\text{NiO}$  core/shell NW arrays showing the flake morphology of the NiO. c SC at different current densities. d Cycling performances at 2 A/g. Reproduced from [94]. Copyright 2012 American Chemical Society



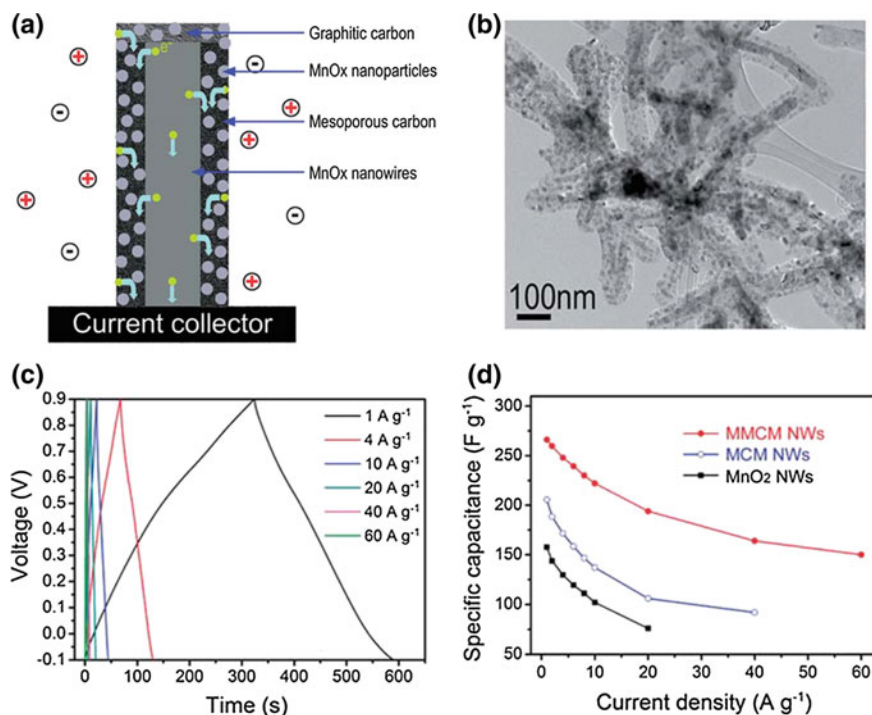


**Fig. 8.6** **a, b** Schematic and TEM image of the highly graphitic carbon-tipped MMCM hybrid NWs. **c** Charge-discharge curves at 1–60 A g<sup>-1</sup>. **d** SC as a function of different current densities of the MMCM hybrid NWs (red lines), the MCM hybrid NWs (blue lines) and the pristine MnO<sub>2</sub> NWs (black lines). Reproduced from [97]. Copyright 2011 Royal Society of Chemistry

These results can be compared to the theoretical SC for NiO of 2573 F/g [95]. In 2013, Lou and coworkers [96] developed a cost-effective and simple strategy to design and fabricate novel hierarchical NiCo<sub>2</sub>O<sub>4</sub>@MnO<sub>2</sub> core-shell heterostructured NW arrays on Ni foams for supercapacitor electrodes. These electrodes, which had slim mesoporous NiCo<sub>2</sub>O<sub>4</sub> NW cores and ultrathin MnO<sub>2</sub> nanoflake shells, achieved a SC value of >1200 F/g.

In addition to those aforementioned hybrid structures, more complex heterostructures have also been demonstrated. For example, Jiang et al. [97] reported the design and synthesis of a highly graphitic carbon-tipped MnO<sub>2</sub>/mesoporous carbon/MnO<sub>2</sub> (MMCM) hybrid NW, using a multi-step hydrothermal method combined with soft-template method for mesopore formation (Fig. 8.6a, b). The hybrid NW with optimal carbon content, when applied as an electrode, exhibited superior capacitive properties in 1 M Na<sub>2</sub>SO<sub>4</sub> aqueous solution, including high SC of 266 F/g (Fig. 8.6c), rate capability (56.4 % capacity retention at 60 A/g, Fig. 8.6d), and cycling stability without degradation after 1200 cycles. The energy densities achieved was as high as

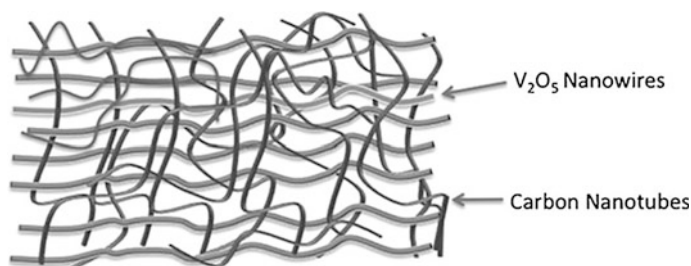


**Fig. 8.7** Schematic of method to form supercapacitor material based on interpenetrating networks of CNTs and  $V_2O_5$  NW. Reproduced from [99]. Copyright 2009 John Wiley and Sons

20.8 Wh/kg, at a power density of 30 kW/kg, indicating that the  $MnO_2$  in this hybrid nanomaterial was efficiently utilized with the assistance of the highly conductive graphitic carbon-tipped mesoporous carbon shell.

In addition to hybrid materials containing multiple metal oxides, carbon-based materials have also been extensively used to form hybrid structures with metal oxide NWs for enhancing their electrical conductivity [98]. The Lu group [99] demonstrated the synthesis of hierarchically porous nanocomposites of interpenetrating CNTs and  $V_2O_5$  NW networks (Fig. 8.7), with the SC values of 440 and 200 F/g achieved at current densities of 0.25 and 10 A/g, respectively. In comparison, Boukhalifa et al. [100] used ALD method to deposit ultrathin  $V_2O_5$  on the surfaces of CNTs that were assembled as a self-supporting paper. Flexible electrodes fabricated using this method were able to deliver remarkable SCs of up to 1550 F/g per active mass of the  $V_2O_5$  and 600 F/g per mass of the composite electrode at 1 A/g in 8 M LiCl. Conducting polymers can also be applied as the main electrical transport channels for nanocomposites with metal oxides. For instance, Zang et al. [101] demonstrated a one-step in situ co-precipitation approach to synthesize ultrafine  $MnO_2$ /polypyrrole (PPy) nanorod composite powders at room temperature. In this approach, pyrrole monomers worked as a reduction agent to reduce  $Mn^{7+}$  ions in  $KMnO_4$  solution to form  $Mn^{4+}$  ions in the form of  $\beta$ - $MnO_2$  crystal. At the same time the pyrrole monomers were subjected to an oxidative polymerization process to form conductive PPy. The SC of the  $\beta$ - $MnO_2$  NWs reached as 294 F/g. In another example, Zhou et al. [102] developed a supercapacitor electrode composed of well-aligned CoO NW arrays grown on 3D nickel foam with PPy uniformly immobilized onto or firmly anchored to each NW surface to boost the pseudocapacitive performance. This CoO NW/PPy hybrid electrode reached a SC of 2333 F/g, almost achieving the theoretical value of the hybrid, 2467 F/g.

## 8.4 Sodium-Ion Batteries

Na-ion batteries (NIBs), as an alternative to LIBs, have attracted extensive investigations, owing to abundant supply and widespread terrestrial reserves of sodium mineral salts [103]. Much progress on developing electrode materials for NIBs has been achieved [103]. Similar to LIB, a NIB consists of two Na intercalation materials as anode and cathode, and share the basic requirements for these electrodes. For instance, single-crystalline layered  $V_2O_5$  NWs were synthesized by a simple solvothermal method, and presented a large (001) interlayer spacing of 11.53 Å, which can accommodate Na ion intercalation [104]. When applied as cathode materials in NIBs,  $V_2O_5$  NWs exhibited a high capacity of 231.4 mAh/g at a current density of 80 mA/g. This capacity corresponds well to the theoretical capacity of 236 mAh/g to form  $Na_2V_2O_5$  [105] on Na-ion intercalation. Su et al. [106] demonstrated the synthesis of  $MnO_2$  nanorods with exposed tunnel structures by a hydrothermal method. The as-prepared  $MnO_2$  nanorods had exposed {111} crystal planes, which led to Na ion intercalation/deintercalation, were used as cathode materials for NIBs, with a high initial Na ion storage capacity of 350 mAh/g, and a discharge capacity of 192 mAh/g maintained after 100 cycles, still much lower than the theoretical capacity, 1232 mAh/g [107]. In another report [108], the  $Na_4Mn_9O_{18}$  NWs deliver a reversible capacity of 128 mAh/g at 0.1C with an initial capacity retention capability of 77 % after 1000 cycles at 0.5C.

Recently, Kim et al. [109] reported the electrochemical activity of anatase  $TiO_2$  nanorods as anode materials in NIB. The anatase  $TiO_2$  nanorods were synthesized by a hydrothermal method, and their surfaces were coated with carbon to improve the electric conductivity. In cell tests, anodes of bare and carbon-coated anatase  $TiO_2$  nanorods exhibit stable cycling performance and attained a capacity of about 172 and 193 mAh/g on the first charge, respectively, in the voltage range of 3–0 V. The carbon-coated anatase  $TiO_2$  delivered good capacity at high rates, 104 mAh/g at a 10C rate, 82 mAh/g at a 30C rate and 53 mAh/g at a 100C rate, while the theoretical capacity is 1348 mAh/g. In addition, Yuan et al. [110] realized a strategy for fabrication of flexible and porous CuO nanorod arrays by simply engraving commercial copper foils in situ, and the foils were then used directly as the anodes for a NIB. The efficacy of this concept was demonstrated by the high initial capacity of over 640 mAh/g, which is close to the theoretical capacity of 674 mAh/g, for a high charging rate of  $\sim 8C$  at room temperature.

## 8.5 Future Directions and Challenges

It is important to appreciate the advantages and disadvantages of nanomaterials for electrochemical energy storage, as well as how to control their synthesis and properties [111]. Although NW structures have enabled the potential to provide higher energy density than current energy storage systems, this research field is still

in the developmental stage and will require efforts to understand potentially novel electrochemical behavior in order to achieve practical applications. Specifically, there are challenges facing the development and utilization of NW materials in energy storage, and systematic and detailed studies are still required to promote the progress of this field. For example, further fundamental studies directed toward electrochemical reaction processes and mechanisms in different electrolyte systems (e.g. aprotic, aqueous, hybrid and solid electrolytes) are required to better understand the overall energy storage process. Such studies also will guide the development of novel NW cathode and anode materials, as well as electrolytes and separators.

The research field of NW materials for energy storage has a very bright future, due to the existence of a wide and distinct variety of compounds with various NW structures that have been studied, and will continue to be investigated with foci on discovering new and novel materials, as well as optimizing the performance of the already established ones. As a result, the materials chemistry and electrochemistry of these NW materials will be further enhanced and enriched in the future.

## References

1. Y. Demirel, *Energy: Production, Conversion, Storage, Conservation, and Coupling* (Springer, London, 2012)
2. R.H. Crabtree, *Energy Production and Storage: Inorganic Chemical Strategies for a Warming World* (John Wiley & Sons, Chichester, 2010)
3. R.-S. Liu, L. Zhang, X. Sun, H. Liu, J. Zhang, *Electrochemical Technologies for Energy Storage and Conversion* (John Wiley & Sons, Weinheim, 2012)
4. J.Z. Zhang, J. Li, Y. Li, Y. Zhao, *Hydrogen Generation, Storage, and Utilization* (Wiley, Hoboken, New Jersey, 2014)
5. X. Chen, C. Li, M. Grätzel, R. Kostecki, S.S. Mao, Nanomaterials for renewable energy production and storage. *Chem. Soc. Rev.* **41**(23), 7909–7937 (2012)
6. P.G. Bruce, B. Scrosati, J.M. Tarascon, Nanomaterials for rechargeable lithium batteries. *Angew. Chem. Int. Ed.* **47**(16), 2930–2946 (2008)
7. C.M. Hayner, X. Zhao, H.H. Kung, Materials for rechargeable lithium-ion batteries. *Annu. Rev. Chem. Biomol. Eng.* **3**, 445–471 (2012)
8. C.K. Chan, H. Peng, G. Liu, K. McIlwrath, X.F. Zhang, R.A. Huggins, Y. Cui, High-performance lithium battery anodes using silicon nanowires. *Nat. Nanotechnol.* **3**(1), 31–35 (2008)
9. L. Mai, X. Tian, X. Xu, L. Chang, L. Xu, Nanowire electrodes for electrochemical energy storage devices. *Chem. Rev.* **114**(23), 11828–11862 (2014)
10. K. Ozawa, *Lithium Ion Rechargeable Batteries: Materials, Technology, and New Applications* (John Wiley & Sons, Weinheim, 2012)
11. G.-A. Nazri, G. Pistoia, *Lithium Batteries: Science and Technology* (Springer, New York, 2008)
12. Y. Wang, G. Cao, Developments in nanostructured cathode materials for high-performance lithium-ion batteries. *Adv. Mater.* **20**(12), 2251–2269 (2008)
13. H. Wu, Y. Cui, Designing nanostructured Si anodes for high energy lithium ion batteries. *Nano Today* **7**(5), 414–429 (2012)

14. N.S. Choi, Z. Chen, S.A. Freunberger, X. Ji, Y.K. Sun, K. Amine, G. Yushin, L.F. Nazar, J. Cho, P.G. Bruce, Challenges facing lithium batteries and electrical double-layer capacitors. *Angew. Chem. Int. Ed.* **51**(40), 9994–10024 (2012)
15. Y. Li, B. Tan, Y. Wu, Mesoporous  $\text{Co}_3\text{O}_4$  nanowire arrays for lithium ion batteries with high capacity and rate capability. *Nano Lett.* **8**(1), 265–270 (2008)
16. R.A. Huggins, Lithium alloy negative electrodes. *J. Power Sour.* **81**, 13–19 (1999)
17. U. Kasavajjula, C. Wang, A.J. Appleby, Nano-and bulk-silicon-based insertion anodes for lithium-ion secondary cells. *J. Power Sour.* **163**(2), 1003–1039 (2007)
18. K.-Q. Peng, X. Wang, L. Li, Y. Hu, S.-T. Lee, Silicon nanowires for advanced energy conversion and storage. *Nano Today* **8**(1), 75–97 (2013)
19. X. Su, Q. Wu, J. Li, X. Xiao, A. Lott, W. Lu, B.W. Sheldon, J. Wu, Silicon-based nanomaterials for lithium-ion batteries: a review. *Adv. Energy Mater.* **4**(1), 1300882 (2014)
20. E. Peled, F. Patolsky, D. Golodnitsky, K. Freedman, G. Davidi, D. Schneier, Tissue-like silicon nanowires-based 3D anodes for high-capacity lithium ion batteries. *Nano Lett.* **15**(6), 3907–3916 (2015)
21. D.L. Schulz, J. Hoey, J. Smith, A. Elangovan, X. Wu, I. Akhatov, S. Payne, J. Moore, P. Boudjouk, L. Pederson,  $\text{Si}_6\text{H}_{12}$ /polymer inks for electrospinning a-Si nanowire lithium ion battery anodes. *Electrochem. Solid-State Lett.* **13**(10), A143–A145 (2010)
22. J.Y. Huang, L. Zhong, C.M. Wang, J.P. Sullivan, W. Xu, L.Q. Zhang, S.X. Mao, N.S. Hudak, X.H. Liu, A. Subramanian, In situ observation of the electrochemical lithiation of a single  $\text{SnO}_2$  nanowire electrode. *Science* **330**(6010), 1515–1520 (2010)
23. K. Peng, J. Jie, W. Zhang, S.-T. Lee, Silicon nanowires for rechargeable lithium-ion battery anodes. *Appl. Phys. Lett.* **93**(3), 033105 (2008)
24. K. Peng, M. Zhang, A. Lu, N.-B. Wong, R. Zhang, S.-T. Lee, Ordered silicon nanowire arrays via nanosphere lithography and metal-induced etching. *Appl. Phys. Lett.* **90**(16), 163123 (2007)
25. W. Xu, S.S.S. Vegunta, J.C. Flake, Surface-modified silicon nanowire anodes for lithium-ion batteries. *J. Power Sour.* **196**(20), 8583–8589 (2011)
26. R. Huang, X. Fan, W. Shen, J. Zhu, Carbon-coated silicon nanowire array films for high-performance lithium-ion battery anodes. *Appl. Phys. Lett.* **95**(13), 133119 (2009)
27. Y. Yao, N. Liu, M.T. McDowell, M. Pasta, Y. Cui, Improving the cycling stability of silicon nanowire anodes with conducting polymer coatings. *Energy Environ. Sci.* **5**(7), 7927–7930 (2012)
28. C.K. Chan, R.N. Patel, M.J. O’Connell, B.A. Korgel, Y. Cui, Solution-grown silicon nanowires for lithium-ion battery anodes. *ACS Nano* **4**(3), 1443–1450 (2010)
29. L.-F. Cui, R. Ruffo, C.K. Chan, H. Peng, Y. Cui, Crystalline-amorphous core-shell silicon nanowires for high capacity and high current battery electrodes. *Nano Lett.* **9**(1), 491–495 (2008)
30. C.K. Chan, R. Ruffo, S.S. Hong, Y. Cui, Surface chemistry and morphology of the solid electrolyte interphase on silicon nanowire lithium-ion battery anodes. *J. Power Sour.* **189**(2), 1132–1140 (2009)
31. L.-F. Cui, Y. Yang, C.-M. Hsu, Y. Cui, Carbon-silicon core-shell nanowires as high capacity electrode for lithium ion batteries. *Nano Lett.* **9**(9), 3370–3374 (2009)
32. J. Xie, X. Yang, S. Zhou, D. Wang, Comparing one-and two-dimensional heteronanostructures as silicon-based lithium ion battery anode materials. *ACS Nano* **5**(11), 9225–9231 (2011)
33. Y. Yao, K. Huo, L. Hu, N. Liu, J.J. Cha, M.T. McDowell, P.K. Chu, Y. Cui, Highly conductive, mechanically robust, and electrochemically inactive TiC/C nanofiber scaffold for high-performance silicon anode batteries. *ACS Nano* **5**(10), 8346–8351 (2011)
34. K. Evanoff, J. Khan, A.A. Balandin, A. Magasinski, W.J. Ready, T.F. Fuller, G. Yushin, Towards ultrathick battery electrodes: aligned carbon nanotube-enabled architecture. *Adv. Mater.* **24**(4), 533–537 (2012)

35. X.H. Liu, L.Q. Zhang, L. Zhong, Y. Liu, H. Zheng, J.W. Wang, J.-H. Cho, S.A. Dayeh, S.T. Picraux, J.P. Sullivan, Ultrafast electrochemical lithiation of individual Si nanowire anodes. *Nano Lett.* **11**(6), 2251–2258 (2011)
36. L. Luo, H. Yang, P. Yan, J.J. Travis, Y. Lee, N. Liu, D. Molina Piper, S.-H. Lee, P. Zhao, S. M. George, Surface-coating regulated lithiation kinetics and degradation in silicon nanowires for lithium ion battery. *ACS Nano* **9**(5), 5559–5566 (2015)
37. S.W. Lee, M.T. McDowell, J.W. Choi, Y. Cui, Anomalous shape changes of silicon nanopillars by electrochemical lithiation. *Nano Lett.* **11**(7), 3034–3039 (2011)
38. X.H. Liu, H. Zheng, L. Zhong, S. Huang, K. Karki, L.Q. Zhang, Y. Liu, A. Kushima, W.T. Liang, J.W. Wang, Anisotropic swelling and fracture of silicon nanowires during lithiation. *Nano Lett.* **11**(8), 3312–3318 (2011)
39. L. Ji, Z. Lin, M. Alcoutlabi, X. Zhang, Recent developments in nanostructured anode materials for rechargeable lithium-ion batteries. *Energy Environ. Sci.* **4**(8), 2682–2699 (2011)
40. H.B. Wu, J.S. Chen, H.H. Hng, X. Wen Lou, Nanostructured metal oxide-based materials as advanced anodes for lithium-ion batteries. *Nanoscale* **4**(8), 2526–2542 (2012)
41. J. Jiang, Y. Li, J. Liu, X. Huang, C. Yuan, X.W.D. Lou, Recent advances in metal oxide-based electrode architecture design for electrochemical energy storage. *Adv. Mater.* **24**(38), 5166–5180 (2012)
42. M. Reddy, G. Subba Rao, B. Chowdari, Metal oxides and oxyalts as anode materials for Li ion batteries. *Chem. Rev.* **113**(7), 5364–5457 (2013)
43. H. Li, Z. Wang, L. Chen, X. Huang, Research on advanced materials for Li-ion batteries. *Adv. Mater.* **21**(45), 4593–4607 (2009)
44. A.S. Arico, P. Bruce, B. Scrosati, J.-M. Tarascon, W. Van Schalkwijk, Nanostructured materials for advanced energy conversion and storage devices. *Nat. Mater.* **4**(5), 366–377 (2005)
45. N. Li, C.J. Patrissi, G. Che, C.R. Martin, Rate capabilities of nanostructured  $\text{LiMn}_2\text{O}_4$  electrodes in aqueous electrolyte. *J. Electrochem. Soc.* **147**(6), 2044–2049 (2000)
46. A.R. Armstrong, G. Armstrong, J. Canales, R. García, P.G. Bruce, Lithium-ion intercalation into  $\text{TiO}_2$ -B nanowires. *Adv. Mater.* **17**(7), 862–865 (2005)
47. M. Saito, Y. Murota, M. Takagi, M. Tajima, T. Asao, H. Inoue, A. Tasaka, M. Inaba, Improvement of the reversible capacity of  $\text{TiO}_2$  (B) high potential negative electrode. *J. Electrochem. Soc.* **159**(1), A49–A54 (2011)
48. M.S. Park, G.X. Wang, Y.M. Kang, D. Wexler, S.X. Dou, H.K. Liu, Preparation and electrochemical properties of  $\text{SnO}_2$  nanowires for application in lithium-ion batteries. *Angew. Chem.* **119**(5), 764–767 (2007)
49. D.-W. Kim, I.-S. Hwang, S.J. Kwon, H.-Y. Kang, K.-S. Park, Y.-J. Choi, K.-J. Choi, J.-G. Park, Highly conductive coaxial  $\text{SnO}_2$ - $\text{In}_2\text{O}_3$  heterostructured nanowires for Li ion battery electrodes. *Nano Lett.* **7**(10), 3041–3045 (2007)
50. H. Kim, J. Cho, Hard templating synthesis of mesoporous and nanowire  $\text{SnO}_2$  lithium battery anode materials. *J. Mater. Chem.* **18**(7), 771–775 (2008)
51. J. Liu, Y. Li, X. Huang, R. Ding, Y. Hu, J. Jiang, L. Liao, Direct growth of  $\text{SnO}_2$  nanorod array electrodes for lithium-ion batteries. *J. Mater. Chem.* **19**(13), 1859–1864 (2009)
52. I.A. Courtney, J. Dahn, Key factors controlling the reversibility of the reaction of lithium with  $\text{SnO}_2$  and  $\text{Sn}_2\text{BPO}$  6 glass. *J. Electrochem. Soc.* **144**(9), 2943–2948 (1997)
53. C. Kim, M. Noh, M. Choi, J. Cho, B. Park, Critical size of a nano  $\text{SnO}_2$  electrode for Li-secondary battery. *Chem. Mat.* **17**(12), 3297–3301 (2005)
54. H. Wu, M. Xu, Y. Wang, G. Zheng, Branched  $\text{Co}_3\text{O}_4/\text{Fe}_2\text{O}_3$  nanowires as high capacity lithium-ion battery anodes. *Nano Res.* **6**(3), 167–173 (2013)
55. S. Yang, X. Feng, S. Ivanovici, K. Müllen, Fabrication of graphene-encapsulated oxide nanoparticles: towards high-performance anode materials for lithium storage. *Angew. Chem. Int. Ed.* **49**(45), 8408–8411 (2010)
56. Y. Wang, G. Cao, Developments in nanostructured cathode materials for high-performance lithium-ion batteries. *Adv. Mater.* **20**(12), 2251–2269 (2008)

57. J.W. Fergus, Recent developments in cathode materials for lithium ion batteries. *J. Power Sour.* **195**(4), 939–954 (2010)
58. B.L. Ellis, K.T. Lee, L.F. Nazar, Positive electrode materials for Li-ion and Li-batteries†. *Chem. Mat.* **22**(3), 691–714 (2010)
59. T. Ohzuku, A. Ueda, Why transition metal (di) oxides are the most attractive materials for batteries. *Solid State Ion.* **69**(3), 201–211 (1994)
60. F. Jiao, K.M. Shaju, P.G. Bruce, Synthesis of nanowire and mesoporous low-temperature LiCoO<sub>2</sub> by a post-templating reaction. *Angew. Chem. Int. Ed.* **44**(40), 6550–6553 (2005)
61. X. Xiao, L. Yang, H. Zhao, Z. Hu, Y. Li, Facile synthesis of LiCoO<sub>2</sub> nanowires with high electrochemical performance. *Nano Res.* **5**(1), 27–32 (2012)
62. N. Wu, Y. Zhang, Y. Guo, S. Liu, H. Liu, H. Wu, Flake-like LiCoO<sub>2</sub> with exposed {010} facets as a stable cathode material for highly reversible lithium storage. *ACS Appl. Mater. Interfaces* (2016)
63. M. Thackeray, P. Johnson, L. De Picciotto, P. Bruce, J. Goodenough, Electrochemical extraction of lithium from LiMn<sub>2</sub>O<sub>4</sub>. *Mater. Res. Bull.* **19**(2), 179–187 (1984)
64. Q. Liu, D. Mao, C. Chang, F. Huang, Phase conversion and morphology evolution during hydrothermal preparation of orthorhombic LiMnO<sub>2</sub> nanorods for lithium ion battery application. *J. Power Sour.* **173**(1), 538–544 (2007)
65. M.M. Thackeray, Spinel electrodes for lithium batteries. *J. Am. Ceram. Soc.* **82**(12), 3347–3354 (1999)
66. D.K. Kim, P. Muralidharan, H.-W. Lee, R. Ruffo, Y. Yang, C.K. Chan, H. Peng, R.A. Huggins, Y. Cui, Spinel LiMn<sub>2</sub>O<sub>4</sub> nanorods as lithium ion battery cathodes. *Nano Lett.* **8** (11), 3948–3952 (2008)
67. H.-W. Lee, P. Muralidharan, R. Ruffo, C.M. Mari, Y. Cui, D.K. Kim, Ultrathin spinel LiMn<sub>2</sub>O<sub>4</sub> nanowires as high power cathode materials for Li-ion batteries. *Nano Lett.* **10**(10), 3852–3856 (2010)
68. E. Hosono, T. Kudo, I. Honma, H. Matsuda, H. Zhou, Synthesis of single crystalline spinel LiMn<sub>2</sub>O<sub>4</sub> nanowires for a lithium ion battery with high power density. *Nano Lett.* **9**(3), 1045–1051 (2009)
69. Y. Wang, Y. Wang, D. Jia, Z. Peng, Y. Xia, G. Zheng, All-nanowire based Li-ion full cells using homologous Mn<sub>2</sub>O<sub>3</sub> and LiMn<sub>2</sub>O<sub>4</sub>. *Nano Lett.* **14**(2), 1080–1084 (2014)
70. M. Freire, N. Kosova, C. Jordy, D. Chateigner, O. Lebedev, A. Maignan, V. Pralong, A new active Li-Mn-O compound for high energy density Li-ion batteries. *Nat. Mater.* 173–177 (2016)
71. C. Delmas, H. Cognac-Auradou, J. Cocciantelli, M. Menetrier, J. Doumerc, The Li<sub>x</sub>V<sub>2</sub>O<sub>5</sub> system: an overview of the structure modifications induced by the lithium intercalation. *Solid State Ion.* **69**(3–4), 257–264 (1994)
72. L. Mai, L. Xu, C. Han, X. Xu, Y. Luo, S. Zhao, Y. Zhao, Electrospun ultralong hierarchical vanadium oxide nanowires with high performance for lithium ion batteries. *Nano Lett.* **10** (11), 4750–4755 (2010)
73. C.K. Chan, H. Peng, R.D. Twisten, K. Jarausch, X.F. Zhang, Y. Cui, Fast, completely reversible Li insertion in vanadium pentoxide nanoribbons. *Nano Lett.* **7**(2), 490–495 (2007)
74. Q. An, Q. Wei, P. Zhang, J. Sheng, K.M. Hercule, F. Lv, Q. Wang, X. Wei, L. Mai, Three-dimensional interconnected vanadium pentoxide nanonetwork cathode for high-rate long-life lithium batteries. *Small* **11**(22), 2654–2660 (2015)
75. S. Lim, C.S. Yoon, J. Cho, Synthesis of nanowire and hollow LiFePO<sub>4</sub> cathodes for high-performance lithium batteries. *Chem. Mat.* **20**(14), 4560–4564 (2008)
76. J.R. Miller, P. Simon, Electrochemical capacitors for energy management. *Science* **321** (5889), 651–652 (2008)
77. P. Simon, Y. Gogotsi, Materials for electrochemical capacitors. *Nat. Mater.* **7**(11), 845–854 (2008)
78. B.E. Conway, *Electrochemical Supercapacitors: Scientific Fundamentals and Technological Applications* (Springer, New York, 1999)

79. Q. Zhang, E. Uchaker, S.L. Candelaria, G. Cao, Nanomaterials for energy conversion and storage. *Chem. Soc. Rev.* **42**(7), 3127–3171 (2013)
80. J. Yan, Q. Wang, T. Wei, Z. Fan, Recent advances in design and fabrication of electrochemical supercapacitors with high energy densities. *Adv. Energy Mater.* **4**(4) (2014)
81. G. Wang, L. Zhang, J. Zhang, A review of electrode materials for electrochemical supercapacitors. *Chem. Soc. Rev.* **41**(2), 797–828 (2012)
82. X. Wang, X. Wang, W. Huang, P. Sebastian, S. Gamboa, Sol-gel template synthesis of highly ordered MnO<sub>2</sub> nanowire arrays. *J. Power Sour.* **140**(1), 211–215 (2005)
83. C. Guan, J. Liu, C. Cheng, H. Li, X. Li, W. Zhou, H. Zhang, H.J. Fan, Hybrid structure of cobalt monoxide nanowire @ nickel hydroxidenitrate nanoflake aligned on nickel foam for high-rate supercapacitor. *Energy Environ. Sci.* **4**(11), 4496–4499 (2011)
84. X.-H. Xia, J.-P. Tu, Y.-J. Mai, X.-L. Wang, C.-D. Gu, X.-B. Zhao, Self-supported hydrothermal synthesized hollow Co<sub>3</sub>O<sub>4</sub> nanowire arrays with high supercapacitor capacitance. *J. Mater. Chem.* **21**(25), 9319–9325 (2011)
85. J. Bae, M.K. Song, Y.J. Park, J.M. Kim, M. Liu, Z.L. Wang, Fiber supercapacitors made of nanowire-fiber hybrid structures for wearable/flexible energy storage. *Angew. Chem. Int. Ed.* **50**(7), 1683–1687 (2011)
86. P. Yang, Y. Ding, Z. Lin, Z. Chen, Y. Li, P. Qiang, M. Ebrahimi, W. Mai, C.P. Wong, Z.L. Wang, Low-cost high-performance solid-state asymmetric supercapacitors based on MnO<sub>2</sub> nanowires and Fe<sub>2</sub>O<sub>3</sub> nanotubes. *Nano Lett.* **14**(2), 731–736 (2014)
87. J. Zhang, J. Jiang, H. Li, X. Zhao, A high-performance asymmetric supercapacitor fabricated with graphene-based electrodes. *Energy Environ. Sci.* **4**(10), 4009–4015 (2011)
88. H. Wang, Y. Liang, T. Mirfakhrai, Z. Chen, H.S. Casalongue, H. Dai, Advanced asymmetrical supercapacitors based on graphene hybrid materials. *Nano Res.* **4**(8), 729–736 (2011)
89. Z.S. Wu, D.W. Wang, W. Ren, J. Zhao, G. Zhou, F. Li, H.M. Cheng, Anchoring hydrous RuO<sub>2</sub> on graphene sheets for high-performance electrochemical capacitors. *Adv. Funct. Mater.* **20**(20), 3595–3602 (2010)
90. V. Patake, S. Pawar, V. Shinde, T. Gujar, C. Lokhande, The growth mechanism and supercapacitor study of anodically deposited amorphous ruthenium oxide films. *Curr. Appl. Phys.* **10**(1), 99–103 (2010)
91. Y.-F. Ke, D.-S. Tsai, Y.-S. Huang, Electrochemical capacitors of RuO<sub>2</sub> nanophase grown on LiNbO<sub>3</sub> (100) and sapphire (0001) substrates. *J. Mater. Chem.* **15**(21), 2122–2127 (2005)
92. X. Lu, D. Zheng, T. Zhai, Z. Liu, Y. Huang, S. Xie, Y. Tong, Facile synthesis of large-area manganese oxide nanorod arrays as a high-performance electrochemical supercapacitor. *Energy Environ. Sci.* **4**(8), 2915–2921 (2011)
93. W. Wei, X. Cui, W. Chen, D.G. Ivey, Manganese oxide-based materials as electrochemical supercapacitor electrodes. *Chem. Soc. Rev.* **40**(3), 1697–1721 (2011)
94. X. Xia, J. Tu, Y. Zhang, X. Wang, C. Gu, X.-B. Zhao, H.J. Fan, High-quality metal oxide core/shell nanowire arrays on conductive substrates for electrochemical energy storage. *ACS Nano* **6**(6), 5531–5538 (2012)
95. C. Chen, C. Chen, P. Huang, F. Duan, S. Zhao, P. Li, J. Fan, W. Song, Y. Qin, NiO/nanoporous graphene composites with excellent supercapacitive performance produced by atomic layer deposition. *Nanotechnology* **25**(50), 504001 (2014)
96. L. Yu, G. Zhang, C. Yuan, X.W.D. Lou, Hierarchical NiCo<sub>2</sub>O<sub>4</sub>@MnO<sub>2</sub> core-shell heterostructured nanowire arrays on Ni foam as high-performance supercapacitor electrodes. *Chem. Commun.* **49**(2), 137–139 (2013)
97. H. Jiang, L. Yang, C. Li, C. Yan, P.S. Lee, J. Ma, High-rate electrochemical capacitors from highly graphitic carbon-tipped manganese oxide/mesoporous carbon/manganese oxide hybrid nanowires. *Energy Environ. Sci.* **4**(5), 1813–1819 (2011)
98. P. Chen, H. Chen, J. Qiu, C. Zhou, Inkjet printing of single-walled carbon nanotube/RuO<sub>2</sub> nanowire supercapacitors on cloth fabrics and flexible substrates. *Nano Res.* **3**(8), 594–603 (2010)



99. Z. Chen, Y. Qin, D. Weng, Q. Xiao, Y. Peng, X. Wang, H. Li, F. Wei, Y. Lu, Design and synthesis of hierarchical nanowire composites for electrochemical energy storage. *Adv. Funct. Mater.* **19**(21), 3420–3426 (2009)
100. S. Boukhalifa, K. Evanoff, G. Yushin, Atomic layer deposition of vanadium oxide on carbon nanotubes for high-power supercapacitor electrodes. *Energy Environ. Sci.* **5**(5), 6872–6879 (2012)
101. J. Zang, X. Li, In situ synthesis of ultrafine  $\beta$ - $\text{MnO}_2$ /polypyrrole nanorod composites for high-performance supercapacitors. *J. Mater. Chem.* **21**(29), 10965–10969 (2011)
102. C. Zhou, Y. Zhang, Y. Li, J. Liu, Construction of high-capacitance 3D  $\text{CoO}$ @polypyrrole nanowire array electrode for aqueous asymmetric supercapacitor. *Nano Lett.* **13**(5), 2078–2085 (2013)
103. N. Yabuuchi, K. Kubota, M. Dahbi, S. Komaba, Research development on sodium-ion batteries. *Chem. Rev.* **114**(23), 11636–11682 (2014)
104. D. Su, G. Wang, Single-crystalline bilayered  $\text{V}_2\text{O}_5$  nanobelts for high-capacity sodium-ion batteries. *ACS Nano* **7**(12), 11218–11226 (2013)
105. S. Tepavcevic, H. Xiong, V.R. Stamenkovic, X. Zuo, M. Balasubramanian, V.B. Prakapenka, C.S. Johnson, T. Rajh, Nanostructured bilayered vanadium oxide electrodes for rechargeable sodium-ion batteries. *ACS Nano* **6**(1), 530–538 (2012)
106. D. Su, H.-J. Ahn, G. Wang,  $\beta$ - $\text{MnO}_2$  nanorods with exposed tunnel structures as high-performance cathode materials for sodium-ion batteries. *NPG Asia Mater.* **5**(11), e70 (2013)
107. L. Feng, Z. Xuan, H. Zhao, Y. Bai, J. Guo, C.-W. Su, X. Chen,  $\text{MnO}_2$  prepared by hydrothermal method and electrochemical performance as anode for lithium-ion battery. *Nanoscale Res. Lett.* **9**(1), 1–8 (2014)
108. Y. Cao, L. Xiao, W. Wang, D. Choi, Z. Nie, J. Yu, L.V. Saraf, Z. Yang, J. Liu, Reversible sodium ion insertion in single crystalline manganese oxide nanowires with long cycle life. *Adv. Mater.* **23**(28), 3155–3160 (2011)
109. K.-T. Kim, G. Ali, K.Y. Chung, C.S. Yoon, H. Yashiro, Y.-K. Sun, J. Lu, K. Amine, S.-T. Myung, Anatase titania nanorods as an intercalation anode material for rechargeable sodium batteries. *Nano Lett.* **14**(2), 416–422 (2014)
110. S. Yuan, X.L. Huang, D.L. Ma, H.G. Wang, F.Z. Meng, X.B. Zhang, Engraving copper foil to give large-scale binder-free porous  $\text{CuO}$  arrays for a high-performance sodium-ion battery anode. *Adv. Mater.* **26**, 2273–2279 (2014)
111. A.S. Aricò, P. Bruce, B. Scrosati, J.-M. Tarascon, W. Van Schalkwijk, Nanostructured materials for advanced energy conversion and storage devices. *Nat. Mater.* **4**(5), 366–377 (2005)

# Chapter 9

## Nanowire-Enabled Energy Conversion

**Abstract** Substantial recent scientific effort has been focused on the development of renewable energy sources, such as solar energy, in order to lower the carbon footprint for energy usage. Semiconductor NWs are attractive candidates for energy conversion materials since their composition, size and other factors that determine basic electronic and optical properties can be synthetically manipulated in complex ways. In this chapter, we discuss representative NW-based structures and devices for energy conversion, particularly focusing on photovoltaic, thermoelectric, and piezoelectric systems that have been used produce energy by converting light, heat, and mechanical sources.

### 9.1 Introduction

Renewable clean energy sources will become increasingly important in the coming decades due to decreasing availability of fossil fuel sources and problematic long-term consequences of fossil fuel usage associated with increases in CO<sub>2</sub> green-house gas emission [1]. There exist many potential renewable energy technologies in the form of solid-state devices [2], such as solar cells and photoelectrochemical (PEC) cells, which convert solar energy in the form of light to the more practical form of electricity or chemical fuels [3]. Since electricity is ubiquitously used to power machines and instruments, the practical end product of many energy conversion processes is electrical energy. Even in devices which produce other forms of energy, such as storable chemical fuels, the conversion process often requires, at least as an intermediate energy state, an electrical potential. The study of energy conversion in materials is a field full of opportunities for practical and socially significant applications [4].

Due to their tailorable compositions and structures, capability for efficient and wavelength-tunable photon absorption, and anisotropic charge transport properties, many semiconductor NW-based materials are promising candidates for energy conversion devices [4, 5]. To realize this potential, a fundamental understanding of the electrochemical properties and electron transfer characteristics of NW electrodes

and catalysts will be essential. The following sections will review advanced semiconductor NW devices that can enable photovoltaic, thermoelectric, and piezoelectric energy conversion.

## 9.2 Photovoltaics

Solar energy conversion is an attractive process for clean and renewable power [6–8]. For over two decades, commercial single- and multi-crystalline silicon solar panels have dominated the world market for photovoltaics (PVs) [9]. More recent developments in commercial PVs have centered on second generation solar cells based on thinner semiconductor absorber layers such as  $\text{CuIn}_x\text{Ga}_{1-x}\text{Se}_2$  (CIGS), CdTe, and amorphous silicon [6, 10]. Third generation solar cells, including tandem cells and down-converter cells, have demonstrated energy conversion efficiencies beyond the Shockley-Queisser limiting efficiency of 31 % for a single cell at 1-sun illumination, but at much higher cost [10–12]. Due to their excellent material quality and tunable band gaps, III–V compound semiconductors are normally key components of such high efficiency solar cells. Moreover, studies attempting to harness effects such as multiple exciton generation and hot carriers in quantum confined nanostructures have also created much interest [13]. These ideas suggest that fundamental studies of the synthesis and PV properties of nanoscale structures could serve as a rich area to search for high efficiency and low-cost solar cell solutions.

The basic solar cell is based on a  $p$ – $n$  junction photodiode to generate power (Fig. 9.1a) [7, 8]. The photogenerated electrons and holes are separated by the electric field in the junction region, which has a depletion width ( $W$ ). The first step in PV conversion process is light absorption. Photon energy absorption leads to excitation of electrons to various energy levels in the active material. To get efficient energy absorption, light has to be confined inside the active material. Light confinement is obtained in standard solar cells with various features, including

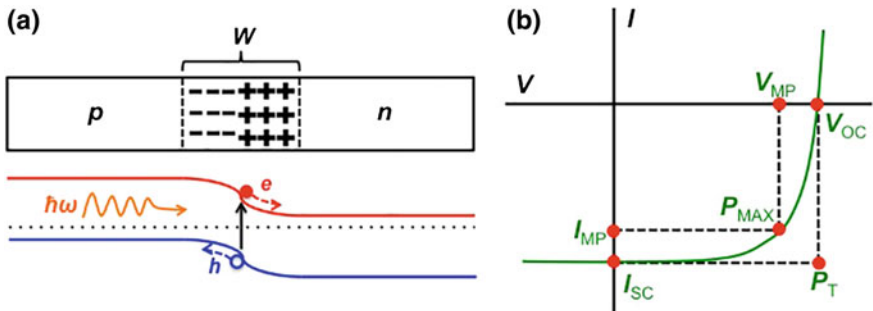


**Fig. 9.1** **a** Schematic of a  $p$ – $n$  junction showing depletion region ( $W$ ) and the corresponding energy-band diagram. Incident light  $h\omega$  creates an electron–hole ( $e$ – $h$ ) pair. **b** Typical photodiode  $I$ – $V$  characteristics under illumination

reflective layers on the back side, front and back surface texture to enhance optical coupling [14] and antireflective coating on the front side [15]. The second step is carrier separation and charge collection. Carriers generated in either the  $p$ - or  $n$ -type material within a minority charge carrier diffusion length of the depletion region can be collected at the junction and contribute to the total current.

As shown in Fig. 9.1b, the typical parameters relevant to solar cell characterization include [7, 8]: (i) short-circuit current  $I_{SC}$ , sometimes evaluated in the current density form  $J_{SC}$ , corresponds to the short circuit condition when the voltage equals 0. For an ideal cell,  $I_{SC}$  is the total current produced by photon excitation; (ii) open-circuit voltage  $V_{OC}$ , the voltage when no current passing through the cell; (iii) maximum power  $P_{MAX}$ , indicated by the dashed lines, that can be achieved by the solar cell, the voltage and current at  $P_{MAX}$  are denoted as  $V_{MP}$  and  $I_{MP}$ , respectively; (iv) the fill factor (FF), the ratio of  $P_{MAX}$  and the theoretical power  $P_T$ ; (v) efficiency  $\eta$ , the ratio of the power output and the solar power input. The maximum  $\eta$  is achieved at  $P_{MAX}$ . Solar cell are typically characterized under 1-sun, air mass 1.5-global illumination (AM 1.5 G) as a standard for comparison.

The use of single semiconductor NWs or NW arrays as PV elements presents several key advantages that could be leveraged to produce high-efficiency, robust, integrated PV power sources [4, 9, 16–19]. Using NW arrays instead of wafers or thin films provides opportunities to minimize losses in photon absorption and carrier separation and collection at a lower cost. The potential cost benefits come primarily from lowering the purity standard and the amount of semiconductor material needed to obtain high efficiencies; increasing the defect tolerance; and enabling new single-crystalline materials to be used without expensive, lattice-matched substrates. For single NW PV devices, the principle of bottom-up design allows the rational control of key nanomaterial parameters, which will determine PV performance, including chemical/dopant composition, diode junction structure, size, and morphology. Also, studies of PV properties at the single NW level will permit determination of the intrinsic limits, areas of improvement, and potential benefits of nano-enabled PV. As the most predominant products in the current PV market are Si-based modules (band gap  $\sim 1.1$  eV) [7, 8], here we use SiNW arrays as examples to discuss the enhancement of light absorption, both single SiNWs and SiNW arrays with radial  $p$ - $n$  junctions for enhanced carrier separation, and III-V compound materials for tunable band gaps.

### 9.2.1 Nanowire Arrays for Enhanced Light Absorption

Two major aspects for a solar cell design are the light absorption and charge separation/collection. Strong photon trapping and absorption are prerequisites for generating sufficient charge carriers and obtaining high photoconversion efficiency [20]. Absorption losses can be divided into two categories: reflection and transmission.

Reflection at an interface arises from a difference in refractive index between two media [21]. One common strategy to reduce reflection of a solar cell is to add anti-reflection coatings that have a refractive index intermediate between that of the semiconductor and that of air [22]. As NW arrays with air filled in the spacings can be regarded as an intermediate layer between air and the substrate, the anti-reflection design of NWs has been further optimized by fabricating NW arrays with gradual modulation of the effective refractive index [23] (Fig. 9.2a). With graded-refractive index layers, light experiences a gradual change of the refractive index instead of a sharp change, which substantially reduces light reflection over a

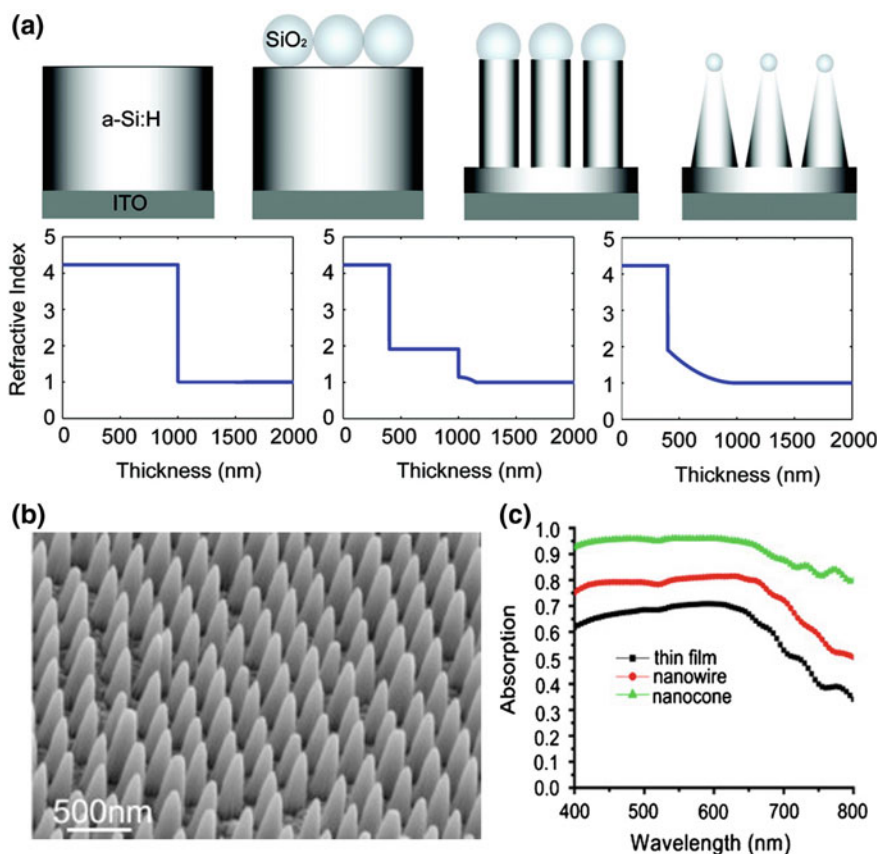


**Fig. 9.2** **a** Top (from left to right): Schematic illustration of an amorphous hydrogenated Si layer (a-Si:H) on ITO glass, a monolayer of SiO<sub>2</sub> nanoparticles on top of a Si layer, a uniform SiNW array, and a Si nanocone array. **Bottom** (from left to right): The effective refractive index profiles of the interfaces between air and the Si thin film, SiNW array, and Si nanocone array. **b** SEM image of amorphous Si:H nanocones prepared by nanosphere lithography. **c** Measured value of absorption on samples with Si:H thin film, uniform NW arrays, and nanocone arrays as the top layer over a large range of wavelengths at normal incidence. Reproduced from [23]. Copyright 2009 American Chemical Society

large range of wavelength and angles of incidence. For example, Huang et al. [24] reported a simple aperiodic array of tapered SiNWs (nanocones) with a sub-wavelength structure that can suppress the reflection of light at a range of wavelengths from the ultraviolet, through the visible part of the spectrum, to the THz region. Reflection is suppressed for a wide range of angles of incidence and for both *s*- and *p*-polarized light. The antireflection properties result from changes in the refractive index caused by variations in the height of the SiNWs. Later, Zhu et al. [23, 25] also reported tapered SiNW solar cells with an efficient broadband

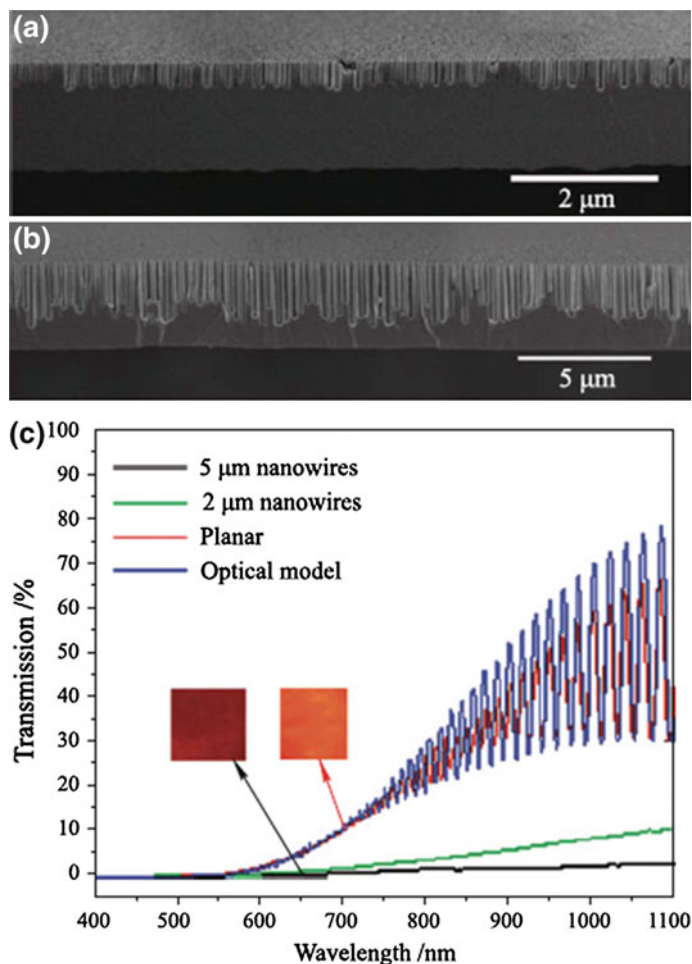


**Fig. 9.3** Optical measurements of SiNW arrays of various lengths. Cross-sectional SEM image of SiNW arrays with lengths of **a** 2 μm and **b** 5 μm. **c** Transmission spectra of planar and NW samples. NW samples exhibit significantly decreased transmission across a broad wavelength range due to increased light-trapping in the NW arrays. Reproduced from [27]. Copyright 2010 American Chemical Society

anti-reflection property. The SiNWs were fabricated by RIE with a SiO<sub>2</sub> nanosphere monolayer mask, followed by HF etching of the SiO<sub>2</sub> mask. As shown in Fig. 9.2b, c, for wavelength between 400 and 650 nm, the absorption of the tapered SiNW arrays is maintained above 93 %, which is much better than that of the uniform SiNW arrays (75 %) and amorphous Si thin films (64 %). Later, Lu et al. [26] reported the use of EBL and RIE to form periodically aligned SiNWs with a nano-conical-frustum shape. The top and bottom diameters of the conical SiNWs are 340 and 800 nm, respectively, and the array periodicity is 800 nm. For solar cells with only bare Si and with these ordered SiNWs arrays, they showed  $I_{sc}$  of 13.6 and 26.4 mA/cm<sup>2</sup>,  $V_{oc}$  of 0.54 and 0.59 V, FF of 0.71 and 0.69, and  $\eta$  of 5.2 and 10.8 %, respectively.

In addition to suppressing reflection, NW arrays are also very efficient at reducing transmission. This permits the use of significantly less material than bulk crystalline PV devices by reducing the overall thickness of the semiconductor absorber layer [3]. To quantify the light-trapping capability of the SiNW arrays, transmission measurements were performed through the free-standing Si-thin films on transparent SiO<sub>2</sub> support layers (Fig. 9.3a, b) [27]. These thin Si films were subsequently patterned and etched to form NWs, and the optical measurements performed on these films before and after NW fabrication show that the transmission over the entire spectral range from 600 to 1100 nm is reduced by factors of 2.9–7.8 and 12–29 for the 2 and 5  $\mu$ m NWs, respectively, compared to the planar sample (Fig. 9.3c). This demonstrates the ability of NW architectures to reduce the

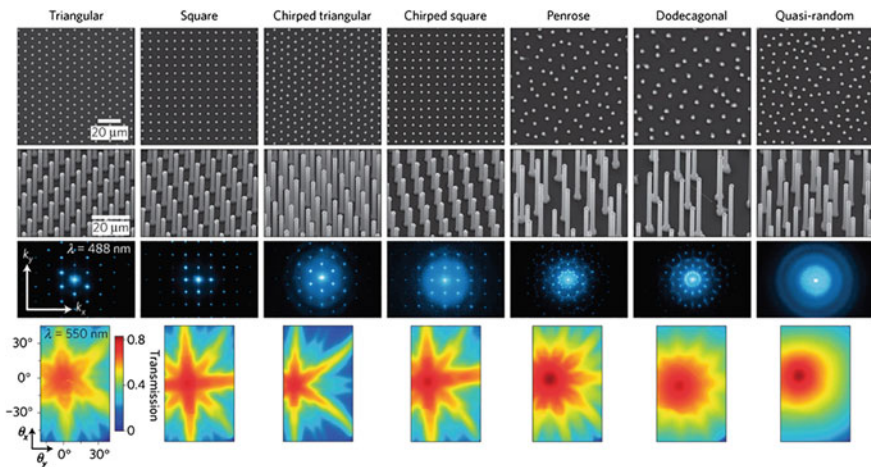


**Fig. 9.4** Representative composition and optical properties of each wire-array tiling pattern. The scale bars in the *left column* apply to all images across each row. *Top row* SEM images of as-grown wire arrays viewed from a *top-down* perspective. *Second row* SEM images viewed at a 20° angle. *Third row* transmitted diffraction patterns of polymer-embedded wire arrays on a quartz slide. *Bottom row* integrated transmission of each wire array as a function of the beam incidence angle. Reproduced from [28]. Copyright 2010 Nature Publishing Group

raw material requirements to fully absorb the solar spectrum, which could eventually lead to decreased PV manufacture cost.

Atwater and coworkers [28] studied the absorption of SiNW arrays independently from the optical effects of the growth substrate by embedding them in transparent PDMS. Numerous arrays of varying NW length, diameter, spacing and tiling patterns (including periodic, quasi-periodic and random motifs) were investigated (Fig. 9.4). It was shown that arrays having less than 5 % areal fraction of NWs could achieve up to 96 % peak absorption with up to 85 % absorption of day-integrated, above-band gap direct sunlight. The observed absorption enhancement and collection efficiency enable a cell geometry that not only uses 1/100th the material of traditional wafer-based devices, but also may offer increased PV efficiency owing to an effective optical concentration of up to 20 times.

### 9.2.2 Radial Junction Nanowires for Enhanced Carrier Separation

In addition to the superior light trapping and harvesting capabilities, NWs with radial core-shell  $p-n$  junctions can allow for light absorption and charge carrier separation/collection in two orthogonal directions [6, 9, 16]. The incident photons can be efficiently absorbed in the axial direction of NWs, typically several to tens of microns. After holes and electrons are generated, they can quickly diffuse across the  $p-n$  junctions in the radial direction, typically in the order of several to tens of nanometers, leading to effective charge separation and collection. NW arrays with excellent light absorption and high quality interfaces between their core-shell  $p-n$  junctions could then lead to high-efficiency photoconversion. Simulations of radial  $p-n$  junctions confirmed this core-shell NW design concept [29], and suggested that radial  $p-n$  junctions prepared from lower quality materials, which would lead to shorter carrier diffusion length, could still achieve efficient charge separation. For axial junction NWs, the  $p$ -type and  $n$ -type regions can be made arbitrarily short since their main purpose is to provide contact to the junction embedded within the NW. Therefore, the active device area can be kept very small so as to enhance integration. In this section, we introduce representative examples of radial  $p-n$  SiNWs synthesized via both bottom-up and top-down methods.

In 2007, Lieber and coworkers [30] reported the first example of solar cell based on single SiNWs with radial junctions. The SiNWs were synthesized by Au-nanoparticle catalyzed VLS growth and had a  $p-i-n$  coaxial structure (Fig. 9.5a, c). To fabricate the single NW PVs, the  $n$ -type and intrinsic Si shells on one end of SiNW were selectively etched to expose the  $p$ -Si core inside, and then separate contacts were made to the  $p$ -type core and outer  $n$ -type shell.  $I-V$  data shown in Fig. 9.5d yielded a  $V_{oc}$  of 0.26 V,  $I_{sc}$  of 0.503 nA ( $J_{sc}$  of 23.9 mA/cm<sup>2</sup>), and FF of 55.0 %, and a maximum photoconversion efficiency of 3.4 % (Fig. 9.5e). In comparison, the same group [31] reported the fabrication of tandem solar cells based on



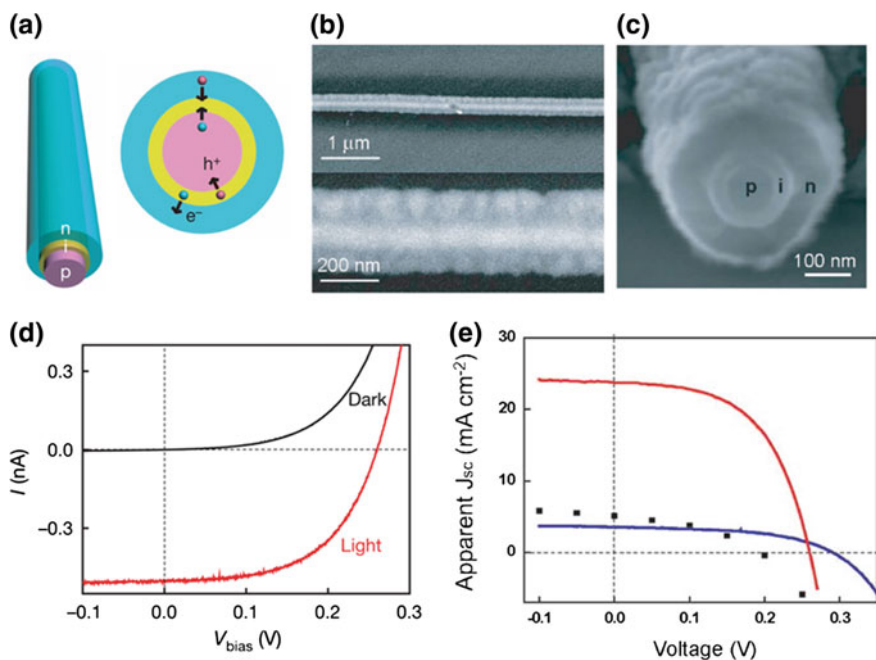


**Fig. 9.5** **a** Illustrations of the core/shell SiNW structure; its cross-sectional diagram shows that the photogenerated electrons ( $e^-$ ) and holes ( $h^+$ ) are swept into the  $n$ -shell and  $p$ -core, respectively, by the built-in electric field. **b** SEM images of the  $p$ - $i$ - $n$  coaxial SiNW at two different magnifications. **c** Cross-section SEM image of a coaxial SiNW after wet-chemical etching from the cleaved end. **d** Dark and light  $I$ - $V$  curves of a coaxial SiNW device. **e** Current density versus voltage for single SiNW coaxial  $p$ - $i$ - $n$  (red), axial  $p$ - $i$ - $n$  (blue) and Schottky junction (black squares) PV devices. Reproduced from [30]. Copyright 2007 Nature Publishing Group

SiNWs with axial doping variation of  $p$ - $i$ - $n^+$ - $p^+$ - $i$ - $n$ . The introduction of tandem structures increased the  $V_{oc}$  to 0.29 V, while the  $J_{sc}$  dropped to 3.5 mA/cm<sup>2</sup>, leading to a maximum efficiency of 0.5 %.

In addition to single NWs, Tsakalakos et al. [32] reported direct growth of SiNW arrays on stainless steel foils coated with Ta<sub>2</sub>N for all-inorganic solar cells in 2007. The diameter and length of these SiNWs were  $\sim 100$  and 16  $\mu\text{m}$ , respectively, and the SiNWs were  $p$ -type with a doping concentration of  $\sim 10^{18}$  cm<sup>-3</sup>. Following NW growth, the surface of these  $p$ -type SiNWs was covered with a  $\sim 40$  nm-thick, amorphous  $n$ -type Si shell by plasma-enhanced CVD to form  $p$ - $n$  junctions. Strong suppression of the light reflection was observed, although the measured efficiency was relatively low at  $\sim 0.1$  %. This low efficiency was attributed to the limitations in photogenerated carrier separation,  $p$ - $n$  junction quality, and electrical contacts. Kendrick et al. [33] prepared well-aligned radial  $p$ - $n$  junction SiNW array with an average NW diameter of 2.6  $\mu\text{m}$ , by Au-nanoparticle catalyzed VLS growth, and used an oxidation cleaning process to remove residual Au catalytic material from the NW tips. The measured  $V_{oc}$  and  $J_{sc}$

were 500 mV and 7.6 mA/cm<sup>2</sup>, with an improved efficiency of 2.3 % and a FF of 57 %, much higher than the randomly oriented SiNW arrays reported previously [32].

SiNWs prepared by the top-down methods, such as RIE or the metal-assisted solution etching, have also been employed for solar cell applications. For instance, the Yang group [27] reported the fabrication of SiNW-based solar cells by deep RIE etching of *n*-type Si wafer, using the self-assembled ~500-nm-diameter SiO<sub>2</sub> nanosphere monolayer as masks. The average lengths of the *n*-type SiNWs obtained in this way were about 5 μm, and the average distance between adjacent SiNWs in the array was ~500 nm, where the separation was determined by the size of the SiO<sub>2</sub> nanosphere mask. After removal of the SiO<sub>2</sub> nanospheres by HF etching, *p*-*n* junctions were formed by boron diffusion. Solar cell performance measured on a 0.67 cm × 0.67 cm SiNW array and AM 1.5G illumination showed  $V_{oc}$  of 525 mV,  $J_{sc}$  of 16.45 mA/cm<sup>2</sup>, FF of 55.9 %, and an efficiency of ~4.83 %. For solution-etched SiNW arrays, Li et al. [34] reported an efficiency of ~9.2 % for an array obtained with a size of ~1 × 1 cm<sup>2</sup>. Although this solution-based method is cost effective, the surface of the SiNWs prepared in this way is much rougher than VLS-grown SiNWs, and this roughness can limit the formation of high quality *p*-*n* junctions and good electrical contacts. In addition, rough surfaces may introduce a higher density of surface defects that substantially enhance carrier recombination and thus further limit solar cell performance.

In 2012, Kempa et al. [35] demonstrated the controlled synthesis of a series of polymorphic core/multi-shell NWs with highly crystalline, hexagonally-faceted shells, and well-defined coaxial *p/n* and *p/in* diode junctions. Designed 200–300 nm diameter *p/in* NW diodes exhibit  $V_{oc}$  and FF up to 0.5 V and 73 %, respectively. Single-NW wavelength-dependent photocurrent measurements reveal size-tunable optical resonances, external quantum efficiencies greater than unity, and current densities double those for Si films of comparable thickness. In addition, finite-difference-time-domain (FDTD) simulations for the measured NW structures agree quantitatively with the photocurrent measurements, and demonstrate that the optical resonances are due to Fabry–Perot and whispering-gallery cavity modes supported in the high-quality faceted nanostructures (Fig. 9.6). Synthetically optimized NW devices achieved current densities as high as 17 mA/cm<sup>2</sup> and power conversion efficiencies of 6 %.

In spite of these substantial research effort and progress, the performance of SiNW-based solar cells still remain lower than microscale Si wires [36]. This can be partially rationalized as the high surface-to-volume ratio of SiNWs can enhance photocarrier recombination and reduce  $V_{oc}$ , although  $J_{sc}$  of SiNWs can be improved by the relaxation of charge diffusion distance requirement and enhanced light absorption [28]. Yuan et al. [37] carried out a detailed study of SiNW electronic properties that aims at understanding what limits the performance of SiNWs, which demonstrated that the performance of SiNW solar cells is not a result of the NW morphology, but intrinsic to the growth chemistry. This work suggested more attention should be paid to the optimization of the synthesis of SiNWs in order to realize the full potential of this exciting material for energy conversion purposes.

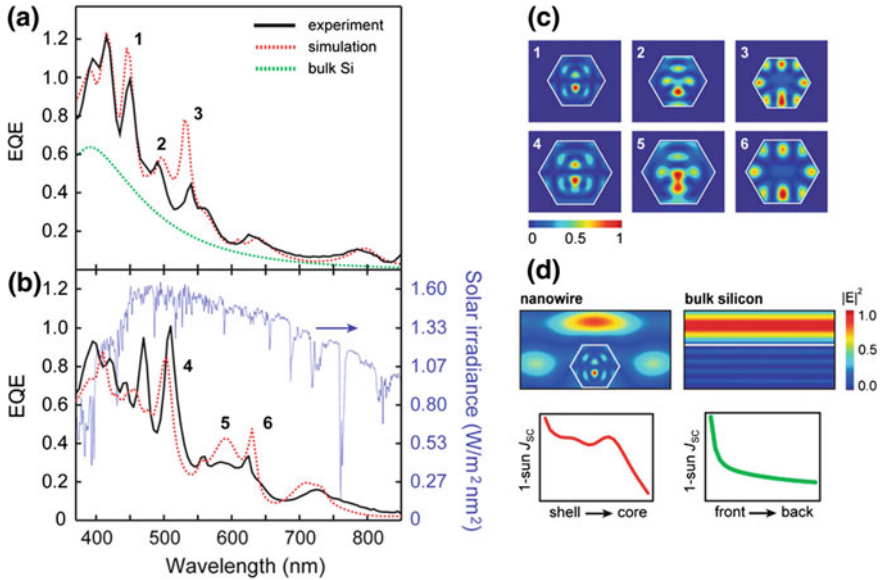


**Fig. 9.6** Enhanced and tunable absorption in NWs. **a** External quantum efficiency (EQE) as a function of wavelength for a *p/in* NW (black curve) and simulated EQE spectrum (dashed red curve). **b** EQE spectrum of a *p/pin* NW compared to the irradiance of the AM1.5G solar spectrum (dashed blue curve). **c** FDTD simulations of resonant mode spatial profiles for *p/in* (profiles 1–3) and *p/pin* (profiles 4–6) structures. Labeled profiles correspond to the EQE peaks labeled within (a) and (b). Resonant modes labeled 3 and 6 correspond to whispering-gallery type modes while all others correspond to Fabry-Perot resonances. **d** Plot of electric field intensity for plane wave ( $\lambda = 445$  nm) interacting with a NW (left) and bulk Si (right). Beneath are plots of total  $J_{SC}$  as a function of position inside the NW or bulk Si. Reproduced from [35]. Copyright 2012 the National Academy of Sciences of the United States of America

Oh et al. [38] reported that the Auger recombination is a more dominating charge recombination process than the surface recombination for solar cells made of SiNWs and Si nanopores. This Auger recombination, induced by excessive doping related to in-diffusion through the high surface area of these Si nanostructures, can be suppressed with light and shallow doping as well as the surface area control. By this means, an all-inorganic solar cell made of “black-silicon” has achieved 18.2 % efficiency under AM 1.5G illumination without additional antireflection coating.

### 9.2.3 Tuning Band Gaps of III–V Compounds

Group III–V compounds have also attracted considerable attention as potential full-solar-spectrum PV materials, since their band gaps can be tuned over a large range with different composition and doping [39, 40]. For instance, the band gap of  $\text{In}_x\text{Ga}_{1-x}\text{N}$  can in principle be tuned to span nearly the entire solar spectrum from

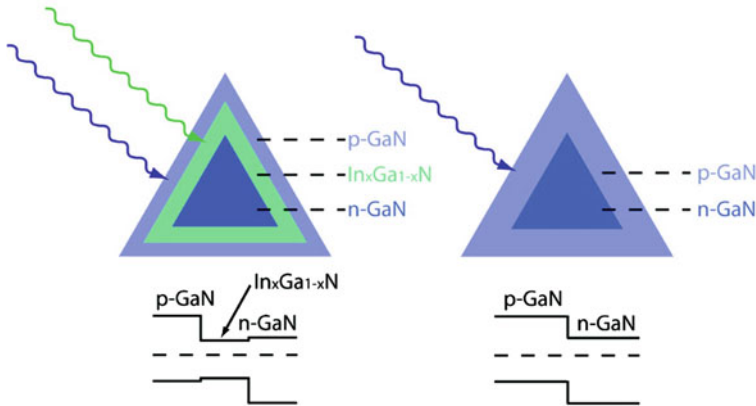


**Fig. 9.7** Cross-sectional view of  $p\text{-GaN}/i\text{-In}_x\text{Ga}_{1-x}\text{N}/n\text{-GaN}$  heterojunction (left) and  $p\text{-GaN}/n\text{-GaN}$  homojunction (right) NW structural motifs and their corresponding energy band diagrams. The wavy colored arrows in the cross-section view indicate light of different wavelengths that is absorbed by the NWs. The dashed lines in the band diagrams indicate the position of the Fermi level. Reproduced from [53]. Copyright 2009 American Chemical Society

0.7 to 3.4 eV [41, 42]. Previously, research focused on the growth of III-nitride thin films on lattice mismatched sapphire substrates had shown relatively high densities of threading dislocations, which degraded  $p\text{-}n$  diode device performance by increasing leakage current [43–45]. In contrast, the synthesis of III-nitride NWs can be virtually substrate-free, which prevents the formation of dislocations originating from lattice mismatch between NWs and the planar growth substrate [46–51]. Moreover, the effective relaxation of lateral strain in coaxial heterostructured NWs can allow for high-quality integration of materials with larger lattice mismatches than possible in traditional planar structures [52]. In 2009, the Lieber group [53] reported the first experimental realization of coaxial group III-nitride NW PV devices,  $n\text{-GaN}/i\text{-In}_x\text{Ga}_{1-x}\text{N}/p\text{-GaN}$ , where variation of indium mole fraction was used to control the active layer band gap and hence light absorption (Fig. 9.7). A key advantage of this core/shell/shell architecture is that the  $p/i/n$  interface extends along the entire length of the NW with carrier separation in the radial direction. In this geometry, photogenerated carriers can be collected from the  $p/i/n$  junction with high efficiency since diffusion lengths are relatively short. Hence, >85 % of the incident light with energy above the band gap, which can be tuned with the value of  $x$ , can be absorbed within the first 200 nm of material. Electroluminescence measurements demonstrate tunable emission from 556 to 371 nm and thus confirm band gap variations in the  $\text{In}_x\text{Ga}_{1-x}\text{N}$  active layer from 2.25 to 3.34 eV. AM 1.5G illumination yielded  $V_{oc}$  from 1.0 to 2.0 V and  $J_{sc}$  from 0.39 to 0.059  $\text{mA}/\text{cm}^2$  as the indium composition is decreased from 0.27 to 0, and a maximum efficiency of  $\sim 0.19\%$ .

### 9.3 Photoelectrochemical Conversion/Photocatalysis

Electricity and hydrogen produced through light energy-driven water splitting are two important forms of clean energy [54–58]. Water splitting is a thermodynamically uphill or endothermic process:  $\text{H}_2\text{O} \rightarrow \text{H}_2 + 1/2\text{O}_2$ , where  $\Delta G = 237.2 \text{ kJ/mol}$  and  $E^0 = 1.23 \text{ V}$  versus normal hydrogen electrode (NHE). This process can be carried out in a PEC cell, where the light energy is absorbed by the electrodes (cathode and anode) and converted into electrical energy as well as chemical energy stored in hydrogen (Fig. 9.8a). Since the first demonstration in 1972 reporting the PEC cells using  $\text{TiO}_2$ -based electrode [59], substantial research have been carried out focusing on the design and fabrication of the semiconductor electrodes [3, 4, 58, 60, 61].

NW arrays have been explored as potential PEC electrodes for several years [3, 4, 58]. A large variety of materials have been utilized as photocathodes and photoanodes, in which a reduction reaction and an oxidation reaction take place, respectively [62]. For anodes, semiconductors with low valence band edge are often investigated, due to their high oxidation potential. The current research has been focused on several materials, including  $\text{TiO}_2$  [63, 64],  $\text{ZnO}$  [65, 66],  $\text{WO}_3$  [67],  $\text{Fe}_2\text{O}_3$  [68, 69],  $\text{BiVO}_4$  [70],  $\text{Ta}_3\text{N}_5$  [71], and *n*-type Si [72]. Common photocathode candidates include III-V compounds such as GaN [73] and GaP [74, 75], *p*-type Si [76, 77] and combined core/shell structures [78]. In addition, catalysts for water splitting half-reactions, such as hydrogen evolution reaction (HER) [79–81] and oxygen evolution reaction (OER) [82–84], are often needed to enhance the reaction rate and efficiency. Here, we will focus on SiNWs as an example for description of the PEC-related works. Since the band gap of Si ( $\sim 1.1 \text{ eV}$ ) is smaller than that required for full water splitting, a redox couple such as alcohols,  $\text{Br}_2/\text{Br}^-$  or  $\text{I}_3/\text{I}^-$  is often used for sacrificial hole scavenging in the electrolyte solution without oxygen evolution [85] to yield an overall thermodynamically favorable reaction (Fig. 9.8b). For other PEC materials, readers are referred to several reviews [55–57, 62].

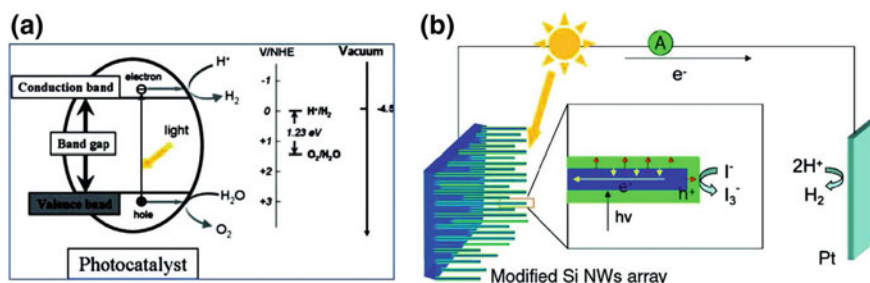


**Fig. 9.8** **a** Fundamental principle of semiconductor-based photocatalytic water splitting for hydrogen generation. Reproduced from [56]. Copyright 2010 American Chemical Society. **b** Schematic diagram of the hydrogen production PEC cell using SiNW arrays. Reproduced from [85]. Copyright 2012 IOP Publishing Ltd.

### 9.3.1 *Si Nanowire-Based Photoelectrochemical Water Splitting*

In 2007, Mallouk and coworkers [86] demonstrated one of the first PEC energy conversion devices based on VLS-synthesized *p*-type SiNWs. The  $V_{oc}$  of the SiNW photocathode,  $\sim 220$  mV, was substantially lower than the best result achieved for bulk Si sample (ca. 500 mV). Another challenge of this early work was that the SiNWs were produced as free-standing structures, limiting the potential for large-scale device fabrication. At the same time, Lewis and coworkers [87] reported VLS-grown vertically aligned microscale *n*-type Si wire arrays with high aspect ratios, where the growth was performed at high temperature, 1050 °C, using SiCl<sub>4</sub> diluted in H<sub>2</sub>. These  $\sim 1.5$   $\mu\text{m}$  diameter Si wires were epitaxially grown from a degenerately doped *n*-type Si(111) wafers, and yielded a slightly better  $V_{oc}$  of  $\sim 389$  mV and  $J_{sc} \sim 1.43$  mA/cm<sup>2</sup>; these values were higher than the control substrate without NWs where  $V_{oc}$  was  $\sim 232$  mV and  $J_{sc}$  was  $\sim 0.28$  mA/cm<sup>2</sup>. Later, Yuan et al. [72] developed a method for synthesis of vertically aligned SiNWs using a simple hot-wall CVD system and SiH<sub>4</sub> as the precursor. The  $J_{sc}$  and  $V_{oc}$  obtained from their work were 4.19 mA/cm<sup>2</sup> and 324 mV, respectively. In 2010, the Atwater and Lewis groups [76] reported the growth of *p*-type Si wires on *p*<sup>+</sup>-Si(111) substrates using Cu NPs as catalyst and SiCl<sub>4</sub>/BCl<sub>3</sub> as the precursors. By controlling the bulk impurities, surface defects and doping, NWs, with 100  $\mu\text{m}$  in length and 1.6  $\mu\text{m}$  in diameter were found to yield PEC efficiency of 2.6 %. These *p*-type SiNWs could also be transferred to flexible and transparent PDMS films, with a PEC performance similar to those attached to the Si wafer [88]. On the other hand, SiNWs arrays formed by metal-assisted solution etching offer an alternative means of obtaining large-scale substrates for PEC electrodes. In 2008, Peng et al. [89] demonstrated PEC conversion using *n*-type solution-etched SiNWs with a doping concentration of  $\sim 3.4\text{--}6.4 \times 10^{14}$ /cm<sup>3</sup>. The etched SiNW arrays have a relatively uniform length of  $\sim 15$   $\mu\text{m}$  but a 20–300 nm distribution in diameters. A modest  $J_{sc}$  of 1.36 mA/cm<sup>2</sup> was obtained with a Br<sub>2</sub>/Br<sup>-</sup> redox couple, while the photo-voltage,  $V_{oc} \sim 730$  mV, was substantially higher than other reports.

Recently, the mechanism of the water splitting on Si surfaces was further investigated in pure water under light illumination [90]. It was reported that hydrogen gas can indeed be produced from SiNWs when illuminated in water, but the reactions are not a real water-splitting process. Instead, the production of hydrogen gas on the SiNWs occurs through the cleavage of Si–H bonds and the formation of Si–OH bonds, resulting in the low probability of generating oxygen. On the other hand, these two types of surface dangling bonds both extract photoexcited electrons, whose competition greatly impacts carrier lifetime and reaction efficiency. Thus, surface chemistry represents another key area to address in order to achieve high efficiency in such Si-based photocatalytic systems.

In addition to pristine SiNWs, other materials have been explored to form hybrid structures with SiNWs to improve their PEC performance. Platinum nanoparticles (PtNPs) are one of the most frequently used materials due to superior catalytic

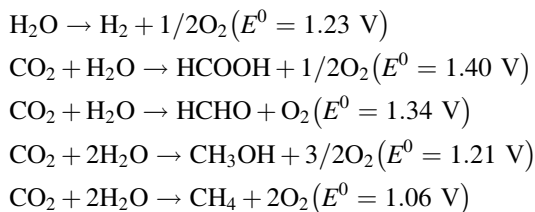
properties [58] of this precious metal. Deposition of 5–10 nm PtNPs on the sidewall surfaces of solution-etched *n*-type SiNW arrays was demonstrated by Peng et al. [91]. The resulting SiNW/PtNP hybrid yielded a photo-conversion efficiency of 8.14 %, which was the highest value reported at that time. The Si/PtNP junctions and the excellent catalytic activity of PtNPs for the electrode process were suggested to be responsible for enhancing the solar energy conversion efficiency. Carbon structures, such as CNTs and graphene, were also studied as hybrid structures with SiNWs [58]. Shu et al. [92] reported a hybrid solar cell composed of a heterojunction cell and a PEC cell. A thin film of double-walled CNTs forms a heterojunction with the SiNW array in the hybrid cell, and also functions as the transparent counter electrode of the PEC cell. This hybrid heterojunction solar cell and PEC cell shows an efficiency of 1.29 %, at an optimal SiNW density of 15 %. Furthermore, by transferring pre-formed CNT arrays on the top of the SiNW arrays to make the CNT/SiNW junctions, an efficiency up to 6 % was achieved [93].

Key challenges identified to SiNW-based PEC include addressing surface photo-oxidation and photo-corrosion of Si when it is in contact with the electrolyte [94] and reducing recombination losses. Carbon coating has been frequently applied to improve the stability of SiNWs. For example, SiNWs with covalently attached methyl groups demonstrate excellent stability even in the presence of water [94]. When using a room temperature ionic liquids as electrolyte solvent, negligible surface oxidation was observed on the SiNW surfaces, and an efficiency of 6.0 % was obtained from these methylated SiNW/PtNP photoelectrodes under AM 1.5G irradiation. Later, the same group [95] reported that coating SiNWs with an ultra-thin carbon film by CVD deposition to form a Si/C core/shell structure, followed by decoration with PtNPs. The environmentally friendly and chemically stable carbon film not only passivates the SiNW surface and protects them against photo-corrosion, but also reduces recombination losses that increase due to solution etching. The PtNPs can further improve the stability of SiNWs and lead to a significant increase in the efficiency owing to enhanced interfacial charge transfer. As a result, these SiNW/C/PtNP arrays display a high photoconversion efficiency up to 10.86 % and excellent performance stability in aqueous  $\text{Br}_2/\text{Br}^-$  solution.

### 9.3.2 Dual-Band Gap Artificial Photosynthesis

The concept of “artificial photosynthesis” has inspired substantial research interest for over three decades, in which abundant energy-poor molecules (such as water and carbon dioxide) are converted into energy-rich molecules (such as hydrogen and hydrocarbons), using sunlight as the energy source, mimicking the natural photosynthesis process occurring in plants [62, 96–99]. The carbon-fixing scheme in nature displays crucial design features for an engineered solar-to-fuel conversion system: spatial and directional arrangement of the light-harvesting components, charge separation and transport, and conversion of the stored potential to chemicals at catalytic sites in compartmentalized spaces [4].

The thermodynamic potential needed to drive the water splitting or carbon dioxide reduction is typically greater than 1 V [100]:



Hence, if only one light-absorber material is used, the voltage requirements limit the choice of materials to wide band gap semiconductors [100]. Inspired by biological photosynthesis with two light-absorbing centers that relay excited electrons in a nanoscopic space, a dual-band gap PEC system, known as “Z-scheme”, is expected to have higher theoretical energy conversion efficiency than a single band gap system [99, 101, 102].

A model “Z-scheme” system with two light-absorbing NW materials, Si and TiO<sub>2</sub>, were chosen to demonstrate the capability of an integrated nanostructure to use sunlight to split water (Fig. 9.9a, b) [103]. For such asymmetric NW heterostructures with the dual-band gap configuration, electron-hole pairs can be generated in the Si and TiO<sub>2</sub> using photons of different wavelengths, corresponding to their different band gaps. Because of the band-bending of the space-charge layer at the semiconductor/electrolyte interface [54], solar illumination leaves positively charged holes on the *n*-TiO<sub>2</sub> side (anode) and negatively charged electrons on the *p*-Si side (cathode), while the majority carriers recombine at the Si/TiO<sub>2</sub> interface. Charge transport of photogenerated electrons and holes within a single asymmetric Si/TiO<sub>2</sub> NW was measured as shown in Fig. 9.9c, f. Under UV illumination, a higher surface potential was observed on the *n*-TiO<sub>2</sub> side, relative to the potential of the *p*-Si side. This asymmetric NW heterostructure with a dual band gap configuration and simultaneously exposed anode and cathode surfaces represents an ideal platform for the development of technologies for the generation of solar fuels, although better photoanode materials, which can more efficiently absorb the solar spectrum, remain to be developed.

Subsequent studies [104] have further developed this system by demonstrating a fully integrated system of nanoscale photoelectrodes. This system consisted of arrays of *p*-SiNW backbones with highly branched *n*-TiO<sub>2</sub> NW protruding from a portion of the backbone NWs (Fig. 9.10). Similar to the photosynthetic system in a chloroplast, the artificial photosynthetic system comprises two semiconductor light absorbers with large surface area, an interfacial layer for charge transport, and spatially separated cocatalysts to facilitate the water reduction and oxidation. All of the individual components, including two NW photoelectrodes with large surface area, an ohmic contact, and two cocatalysts, were carefully positioned in order to maximize the energy conversion efficiency (Fig. 9.10). Under simulated sunlight, a 0.12 % solar-to-fuel conversion efficiency is achieved, which is comparable to that



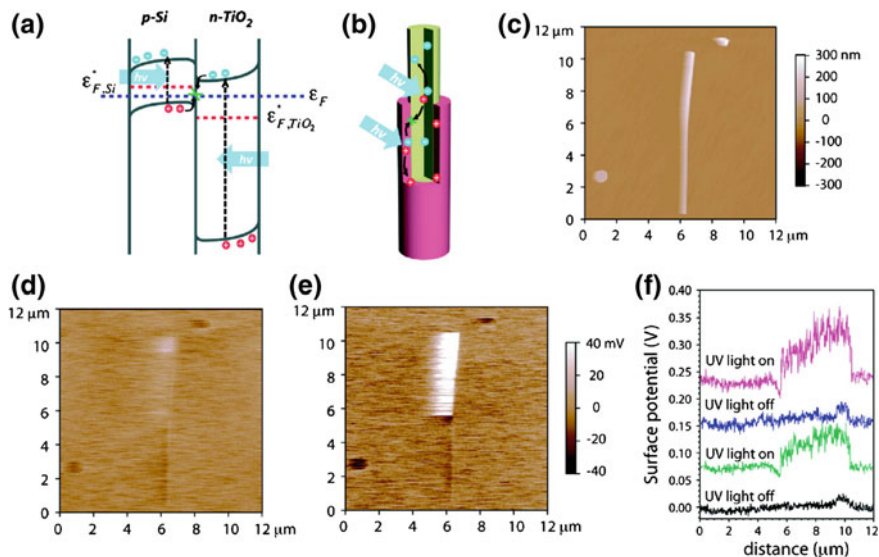


**Fig. 9.9** **a** Schematic energy diagram of charge separation for the Si/TiO<sub>2</sub> dual-band gap configuration. The Fermi level in dark (*dashed blue*) and quasi-Fermi levels under illumination (*dashed red*) are shown. **b** Schematic of the spatial charge distribution within an asymmetric NW under illumination according to **(a)**. **c** Topographical AFM image of the asymmetric NW and measured surface potential mapping of an asymmetric NW in the *dark* **d** and under 365 nm UV illumination with 4.5 mW/cm<sup>2</sup> intensity **e**. **f** Surface potential profiles along an asymmetric NW from Si (distance 0 μm) to Si/TiO<sub>2</sub>. The curves are offset for clarity. Reproduced from [103]. Copyright 2011 American Chemical Society

of natural photosynthesis [105]. The result demonstrates the possibility of integrating material components into a functional system that mimics the nanoscopic integration in chloroplasts. It also provides a conceptual blueprint of modular design that allows incorporation of newly discovered components for improved performance.

Recently, Liu et al. reported an artificial photosynthetic scheme that functions via a similar two-step process by developing a biocompatible light-capturing NW array that enables a direct interface with microbial systems [106]. In this system, a hybrid semiconductor NW—bacteria system can reduce CO<sub>2</sub> at neutral pH to a wide array of chemical targets, such as fuels, polymers, and complex pharmaceutical precursors, using only solar energy input (Fig. 9.11). The SiNW array harvests light energy to provide reducing equivalents to the anaerobic bacterium, *Sporomusa ovata*, for the PEC production of acetic acid under aerobic conditions (21 % O<sub>2</sub>) with low overpotential (<200 mV), high Faradaic efficiency (up to 90 %), and

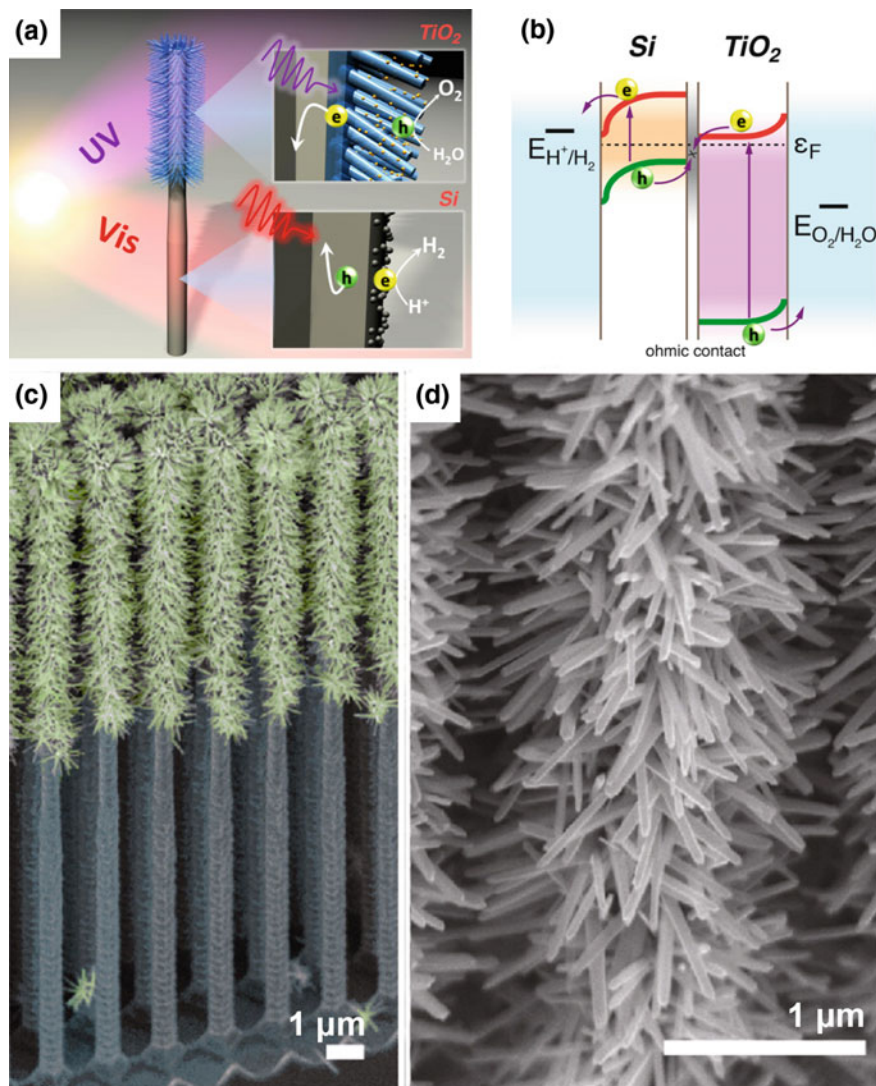


**Fig. 9.10** **a** Structural schematics of the nanotree heterostructure. TiO<sub>2</sub> NWs (blue) were grown on the upper half of a SiNW (gray), and the two semiconductors absorb different regions of the solar spectrum. Photoexcited electron—hole pairs are separated at the semiconductor-electrolyte interface to carry out water splitting with the help of cocatalysts (yellow and gray dots on the surface). **b** Energy band diagram of the nanotree heterostructure for solar-driven water splitting. **c, d** False-colored SEM image (c) and magnified SEM image (d) of the details of a nanotree heterostructure. Reproduced from [104]. Copyright 2013 American Chemical Society

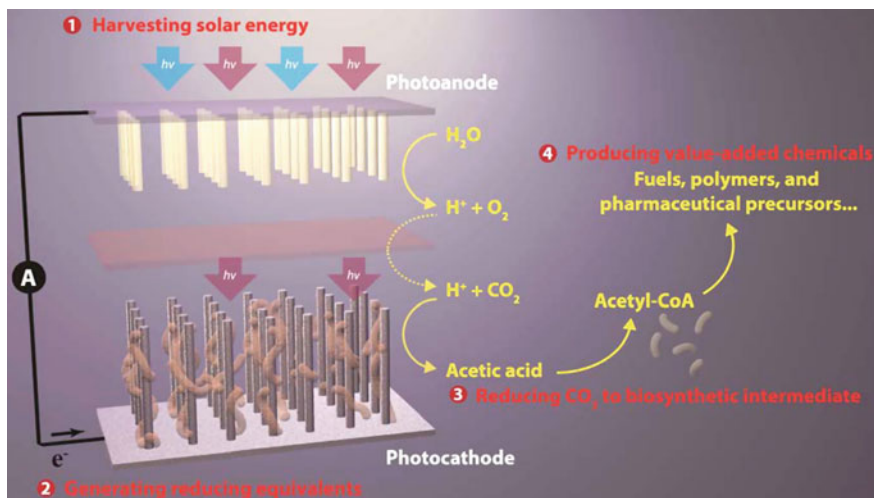


**Fig. 9.11** Schematic of a general artificial photosynthetic approach, it includes four general components: 1 harvesting solar energy, 2 generating reducing equivalents, 3 reducing  $\text{CO}_2$  to biosynthetic intermediates, and 4 producing value-added chemicals. Reproduced from [106]. Copyright 2015 American Chemical Society

long-term stability (up to 200 h). The resulting acetate ( $\sim 6$  g/L) can be activated by genetically engineered *Escherichia coli* and used as a building block for a variety of value-added chemicals, such as *n*-butanol, polyhydroxybutyrate polymer, and three different isoprenoid natural products. As such, interfacing biocompatible solid-state nanodevices with living systems provides a starting point for developing a programmable system of chemical synthesis entirely powered by sunlight.

## 9.4 Thermoelectrics

In addition to solar-related energy conversion, electricity generated from other energy sources, such as heat, can also contribute to the production of renewable energy [107]. When placed in a temperature gradient, thermoelectric materials generate an electrical potential that can be used to power an external load. Approximately 90 % of the world's power is generated by heat engines that use fossil fuel combustion as a heat source and typically operate at 30–40 % efficiency, such that roughly 15 TW of heat is lost to the environment [108]. Thermoelectric modules could potentially convert part of this low-grade waste heat to electricity. Their efficiency depends on the thermoelectric figure of merit,  $ZT$ , of their material components, which is defined as  $ZT = S^2 T / \rho k$ , where  $S$ ,  $\rho$ ,  $k$ , and  $T$  are the Seebeck coefficient, electrical resistivity, thermal conductivity, and absolute temperature, respectively [107]. Therefore, ideal thermoelectric materials should have a low  $k$ , to

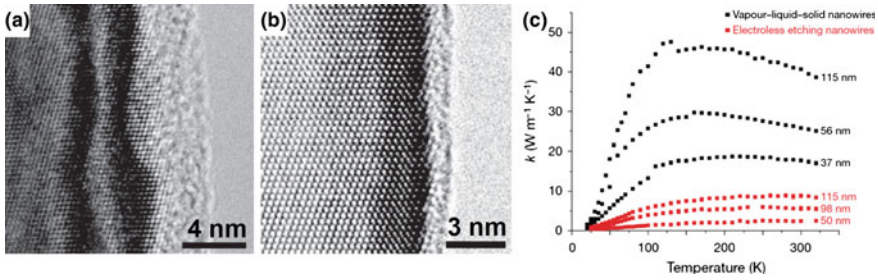


**Fig. 9.12** Rough SiNWs and their thermal conductivity. **a, b** TEM images of an EE NW and a VLS NW, respectively. **c** Temperature-dependent thermal conductivity of EE NWs and VLS NWs. Reproduced from [108]. Copyright 2008 Nature Publishing Group

maintain large temperature gradients, and a low  $\rho$ , to minimize Joule heating and maximize the available charge carriers contributing to the thermoelectric effect. Both electrons and lattice vibrations, called phonons, can conduct heat and thus contribute to  $k$ .  $S$  depends on the electronic band structure of the material near the Fermi level and varies with the change in carrier density per degree Kelvin [4, 107]. Over the past five decades, however, it has been challenging to increase  $ZT > 1$ , since the parameters of  $ZT$  are generally interdependent [109, 110]. Theoretical calculations have shown that the reduction of materials dimension can benefit for the  $ZT$  enhancement, as the electronic band structure tuned by quantum confinement effect in nanostructures should increase the power factor ( $S^2/\rho$ ) for quantum wire structure dramatically [111]. Bismuth compounds [112] (such as  $\text{Bi}_2\text{Te}_3$  and  $\text{Bi}_2\text{Se}_3$ ) and lead chalcogenides [113] (such as  $\text{PbSe}$ ) are among the most promising candidates for thermoelectric conversion close to room temperature, while the fabrication of these materials in nanostructures are not often easy to scale to practically useful dimensions [114–116].

Si, on the other hand, is the most abundant and widely used semiconductor, with a large industrial infrastructure for low-cost and high-yield processing. Bulk Si, however, has a high  $k \sim 150 \text{ W/mK}$  at room temperature, giving  $ZT < 0.01$  at 300 K [117]. In 2008, the Yang group [108] demonstrated the use of wafer-scale SiNWs synthesized by an aqueous electroless etching (EE) method for thermoelectric conversion. SiNWs synthesized by this method had diameters of  $\sim 50 \text{ nm}$  and rough surfaces (Fig. 9.12a, b), which led to substantial reduction of  $k$ . Figure 9.12c shows the measured  $k$  of both VLS and EE SiNWs. The  $k$  of both type of NWs is strongly diameter-dependent [118], which is attributed to boundary scattering of phonons. In the case of the EE NWs, the roughness at the NW surface behaves like secondary scattering boundary, and was proposed to contribute to higher rates of diffuse reflection or backscattering of phonons. Regardless of the details, measurements yielded a thermal conductivity  $\sim 1.6 \text{ W/mK}$ , approximately unchanged power factor  $S^2/\rho$ , and resulting  $ZT$  of 0.6 at room temperature. At the same time, the Heath group [119] also reported efficient thermoelectric performance from SiNWs with cross-sectional areas of only  $10 \times 20$  and  $20 \times 20 \text{ nm}^2$ . By

varying the NW size and impurity doping levels,  $ZT$  values representing an approximately 100-fold improvement over bulk Si were achieved over a broad temperature range, including  $ZT \sim 1$  at 200 K. Their measurements of  $S$ ,  $\rho$  and  $k$  indicated that the improved efficiency originates from phonon effects [117, 120]. In 2012, Lee et al. [121] employed a Si–Ge alloy NW structure to maximize the depletion of heat-carrying phonons. This resulted in a  $k$  of  $\sim 1.2$  W/mK, significantly lower than those of bulk SiGe,  $k \sim 7\text{--}8$  W/mK. The  $ZT$  measured for the SiGe alloy NW was 0.46 at 450 K and can theoretically reach 2.2 at 800 K. The authors suggested that the surface-boundary scattering is prominent when the NW diameter is over  $\sim 100$  nm, whereas alloying plays a more important role in suppressing phonon transport for smaller diameter NWs.

## 9.5 Piezoelectric Effects

The piezoelectric effect [122], which corresponds to the ability of a material to generate a voltage in response to an applied mechanical force, has also been explored as an alternative approach for energy conversion [123, 124]. This concept has been subsequently explored in a range of NW structures [125, 126], as first discussed for ZnO NWs as a nanogenerator in 2006 [127]. In this initial NW case, an AFM tip was scanned across a vertically grown ZnO NW, and a corresponding electric voltage/current was generated during NW deformation (Fig. 9.13). The working mechanism of the nanogenerator can be described as a transient flow of electrons driven by the piezopotential. When the nanogenerator is subject to a compressive stress, a piezopotential field is created along the NWs. As a result of the electrostatic force, inductive charges accumulate on the top and bottom electrodes. In other words, the strained NWs are analogous to polarized dipole moments in a plate capacitor filled by a dielectric material. Once the stress is released, the disappearance of the piezopotential leads to a back flow of the electrons through the external circuit. Later in 2008, a new design of nanogenerator was developed with a single ZnO NW bonded horizontally on a flexible substrate [128]. Cycled bending of the substrate produced an AC electric output from the NW. Since then, the power output has been directed along a rapidly ascending path [129]. Up to now, substantial progress has been made to integrate a large number of NWs together, aiming at collecting an electric current from all NWs simultaneously [130, 131]. For more recent development of the ZnO NW-based nanogenerators, readers can refer to several review articles [125, 126].

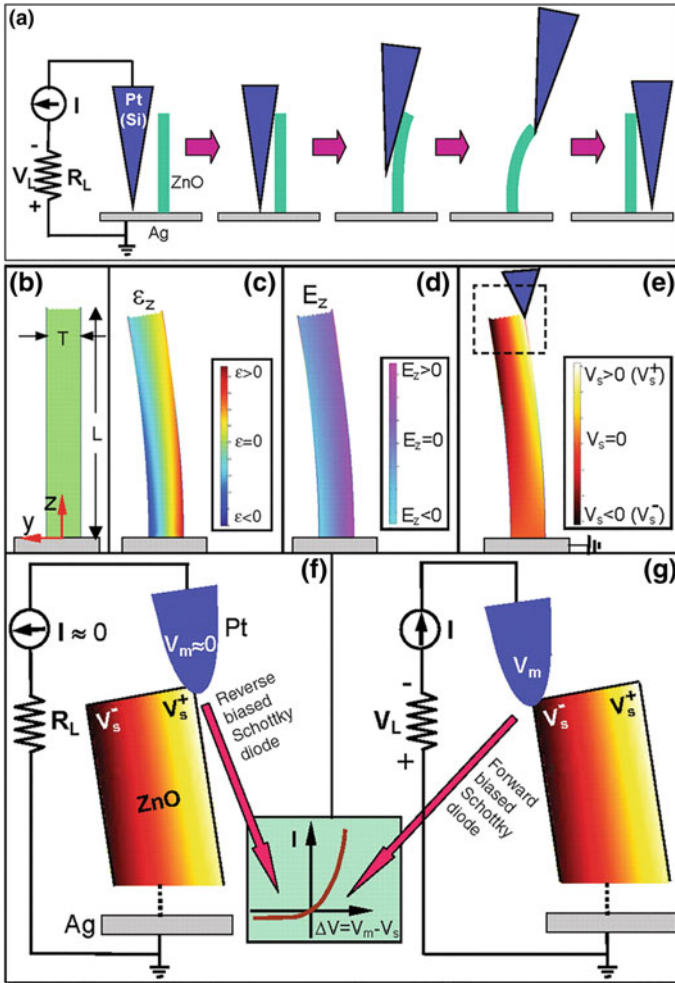


**Fig. 9.13** a Experimental setup and procedures for generating electricity by deforming a piezoelectric NW with a conductive AFM tip. b Schematic definition of a NW and the coordination system. c Longitudinal strain  $\epsilon_z$  distribution in the NW after being deflected by an AFM tip from the side. d The corresponding longitudinal piezoelectric-induced electric field  $E_z$  distribution in the NW. e Potential distribution in the NW as a result of the piezoelectric effect. f, g Contacts between the AFM tip and the semiconductor ZnO NW at two reversed local contact potentials (*positive* and *negative*), showing reverse- and forward-biased Schottky rectifying behavior, respectively. This oppositely biased Schottky barrier across the NW preserves the PZ charges and later produces the discharge output. Reproduced from [127]. Copyright 2006 American Association for the Advancement of Science

## 9.6 Future Directions and Challenges

Harvesting renewable energy from the environment provides a potentially endless source of energy, whether for increasing the efficiency of existing generation processes, charging batteries quasi-continuously, or enabling self-powered devices. Various environmental energy sources can be utilized in the conversion process, including solar, thermal and mechanical energy sources. A promising general strategy for developing efficient and durable systems for energy conversion outlined in this chapter involves the rational design, synthesis, and assembly of the inorganic/organic/hybrid nanostructures at multiple length scales. Semiconductor NWs, with their unique capability of bridging nanoscopic and macroscopic worlds, represent novel and efficient building blocks for implementing this general strategy, and correspondingly for tapping into these energy sources, as discussed in this chapter. One emerging and exciting direction is their application in solar-to-fuel conversion. The generation of fuels by the direct conversion of light energy to chemical bonds in a single device is an attractive goal, although no such systems yet have been demonstrated with the required efficiency and durability for economical commercialization. Future work focused on pushing the limits and control of electrical and thermal transport in NWs, as well as their efficient organization into larger scale arrays, will be crucial to the development of new energy conversion technologies that can benefit humankind.

## References

1. W. Bartok, A.F. Sarofim, *Fossil Fuel Combustion: A Source Book* (Wiley, New York, 1991)
2. T.B. Johansson, *Renewable Energy: Sources for Fuels and Electricity* (Island press, Washington, D.C., 1993)
3. N.P. Dasgupta, P. Yang, Semiconductor nanowires for photovoltaic and photoelectrochemical energy conversion. *Front. Phys.* **9**(3), 289–302 (2014)
4. A.I. Hochbaum, P. Yang, Semiconductor nanowires for energy conversion. *Chem. Rev.* **110** (1), 527–546 (2010)
5. N.P. Dasgupta, J. Sun, C. Liu, S. Brittman, S.C. Andrews, J. Lim, H. Gao, R. Yan, P. Yang, 25th anniversary article: semiconductor nanowires-synthesis, characterization, and applications. *Adv. Mater.* **26**(14), 2137–2184 (2014)
6. N.S. Lewis, Toward cost-effective solar energy use. *Science* **315**(5813), 798–801 (2007)
7. L.M. Fraas, L.D. Partain, *Solar Cells and Their Applications* (Wiley, Hoboken, 2010)
8. M.A. Green, *Solar cells: Operating Principles, Technology, and System Applications* (Prentice Hall, Englewood Cliffs, 1982)
9. T.J. Kempa, R.W. Day, S.-K. Kim, H.-G. Park, C.M. Lieber, Semiconductor nanowires: a platform for exploring limits and concepts for nano-enabled solar cells. *Energy Environ. Sci.* **6**(3), 719–733 (2013)
10. D. Ginley, M.A. Green, R. Collins, Solar energy conversion toward 1 terawatt. *MRS Bull.* **33** (04), 355–364 (2008)
11. F. Dimroth, S. Kurtz, High-efficiency multijunction solar cells. *MRS Bull.* **32**(03), 230–235 (2007)

12. A. Polman, H.A. Atwater, Photonic design principles for ultrahigh-efficiency photovoltaics. *Nat. Mater.* **11**(3), 174–177 (2012)
13. A. Luque, A. Martí, A.J. Nozik, Solar cells based on quantum dots: multiple exciton generation and intermediate bands. *MRS Bull.* **32**(03), 236–241 (2007)
14. D. Kray, M. Hermle, S.W. Glunz, Theory and experiments on the back side reflectance of silicon wafer solar cells. *Prog. Photovolt: Res. Appl.* **16**(1), 1–15 (2008)
15. M.H. Kang, K. Ryu, A. Upadhyaya, A. Rohatgi, Optimization of SiN AR coating for Si solar cells and modules through quantitative assessment of optical and efficiency loss mechanism. *Prog. Photovolt Res. Appl.* **19**(8), 983–990 (2011)
16. B. Tian, T.J. Kempa, C.M. Lieber, Single nanowire photovoltaics. *Chem. Soc. Rev.* **38**(1), 16–24 (2009)
17. E.C. Garnett, M.L. Brongersma, Y. Cui, M.D. McGehee, Nanowire solar cells. *Annu. Rev. Mater. Res.* **41**, 269–295 (2011)
18. S.T. Picraux, J. Yoo, I.H. Campbell, S.A. Dayeh, D.E. Perea, Semiconductor Nanowires for Solar Cells, in *Semiconductor Nanostructures for Optoelectronic Devices: Processing, Characterization and Applications*, ed. by G.-C. Yi (Springer, Berlin, 2012), pp. 297–328
19. P. Thony, Semiconductor nanowires for solar cells, in *Semiconductor Nanowires*, ed. by Q. Xiong (Elsevier, Cambridge, 2015), pp. 411–439
20. Z. Yu, A. Raman, S. Fan, Fundamental limit of nanophotonic light trapping in solar cells. *Proc. Natl. Acad. Sci. U.S.A.* **107**(41), 17491–17496 (2010)
21. E. Hecht, *Optics*. San Francisco (2002)
22. J. Zhao, M.A. Green, Optimized antireflection coatings for high-efficiency silicon solar cells. *IEEE T. Electron. Dev.* **38**(8), 1925–1934 (1991)
23. J. Zhu, Z. Yu, G.F. Burkhard, C.-M. Hsu, S.T. Connor, Y. Xu, Q. Wang, M. McGehee, S. Fan, Y. Cui, Optical absorption enhancement in amorphous silicon nanowire and nanocone arrays. *Nano Lett.* **9**(1), 279–282 (2009)
24. Y.-F. Huang, S. Chattopadhyay, Y.-J. Jen, C.-Y. Peng, T.-A. Liu, Y.-K. Hsu, C.-L. Pan, H.-C. Lo, C.-H. Hsu, Y.-H. Chang, Improved broadband and quasi-omnidirectional anti-reflection properties with biomimetic silicon nanostructures. *Nat. Nanotechnol.* **2**(12), 770–774 (2007)
25. J. Zhu, Z. Yu, S. Fan, Y. Cui, Nanostructured photon management for high performance solar cells. *Mater. Sci. Eng., R* **70**(3), 330–340 (2010)
26. Y. Lu, A. Lal, High-efficiency ordered silicon nano-conical-frustum array solar cells by self-powered parallel electron lithography. *Nano Lett.* **10**(11), 4651–4656 (2010)
27. E. Garnett, P. Yang, Light trapping in silicon nanowire solar cells. *Nano Lett.* **10**(3), 1082–1087 (2010)
28. M.D. Kelzenberg, S.W. Boettcher, J.A. Petykiewicz, D.B. Turner-Evans, M.C. Putnam, E.L. Warren, J.M. Spurgeon, R.M. Briggs, N.S. Lewis, H.A. Atwater, Enhanced absorption and carrier collection in Si wire arrays for photovoltaic applications. *Nat. Mater.* **9**(3), 239–244 (2010)
29. B.M. Kayes, H.A. Atwater, N.S. Lewis, Comparison of the device physics principles of planar and radial pn junction nanorod solar cells. *J. Appl. Phys.* **97**(11), 114302 (2005)
30. B. Tian, X. Zheng, T.J. Kempa, Y. Fang, N. Yu, G. Yu, J. Huang, C.M. Lieber, Coaxial silicon nanowires as solar cells and nanoelectronic power sources. *Nature* **449**(7164), 885–889 (2007)
31. T.J. Kempa, B. Tian, D.R. Kim, J. Hu, X. Zheng, C.M. Lieber, Single and tandem axial p-i-n nanowire photovoltaic devices. *Nano Lett.* **8**(10), 3456–3460 (2008)
32. L. Tsakalakos, J. Balch, J. Fronheiser, B. Korevaar, O. Sulima, J. Rand, Silicon nanowire solar cells. *Appl. Phys. Lett.* **91**(23), 233117 (2007)
33. C.E. Kendrick, H.P. Yoon, Y.A. Yuwen, G.D. Barber, H. Shen, T.E. Mallouk, E.C. Dickey, T.S. Mayer, J.M. Redwing, Radial junction silicon wire array solar cells fabricated by gold-catalyzed vapor-liquid-solid growth. *Appl. Phys. Lett.* **97**(14), 143108 (2010)



34. X. Li, J. Li, T. Chen, B.K. Tay, J. Wang, H. Yu, Periodically aligned Si nanopillar arrays as efficient antireflection layers for solar cell applications. *Nanoscale Res. Lett.* **5**(11), 1721–1726 (2010)
35. T.J. Kempa, J.F. Cahoon, S.-K. Kim, R.W. Day, D.C. Bell, H.-G. Park, C.M. Lieber, Coaxial multishell nanowires with high-quality electronic interfaces and tunable optical cavities for ultrathin photovoltaics. *Proc. Natl. Acad. Sci. U.S.A.* **109**(5), 1407–1412 (2012)
36. M.D. Kelzenberg, D.B. Turner-Evans, M.C. Putnam, S.W. Boettcher, R.M. Briggs, J.Y. Baek, N.S. Lewis, H.A. Atwater, High-performance Si microwire photovoltaics. *Energy Environ. Sci.* **4**(3), 866–871 (2011)
37. G. Yuan, K. Aruda, S. Zhou, A. Levine, J. Xie, D. Wang, Understanding the origin of the low performance of chemically grown silicon nanowires for solar energy conversion. *Angew. Chem. Int. Ed.* **50**(10), 2334–2338 (2011)
38. J. Oh, H.-C. Yuan, H.M. Branz, An 18.2 %-efficient black-silicon solar cell achieved through control of carrier recombination in nanostructures. *Nat. Nanotechnol.* **7**(11), 743–748 (2012)
39. M. Yao, N. Huang, S. Cong, C.-Y. Chi, M.A. Seyedi, Y.-T. Lin, Y. Cao, M.L. Povinelli, P. D. Dapkus, C. Zhou, GaAs nanowire array solar cells with axial p–i–n junctions. *Nano Lett.* **14**(6), 3293–3303 (2014)
40. M. Beeler, C. Lim, P. Hille, J. Bleuse, J. Schörmann, M. de la Mata, J. Arbiol, M. Eickhoff, E. Monroy, Long-lived excitons in GaN/AlN nanowire heterostructures. *Phys. Rev. B* **91**(20), 205440 (2015)
41. J. Wu, W. Walukiewicz, K. Yu, J. Ager Iii, E. Haller, H. Lu, W.J. Schaff, Y. Saito, Y. Nanishi, Unusual properties of the fundamental band gap of InN. *Appl. Phys. Lett.* **80**(21), 3967–3969 (2002)
42. J. Wu, W. Walukiewicz, K. Yu, W. Shan, J. AgerIii, E. Haller, H. Lu, W.J. Schaff, W. Metzger, S. Kurtz, Superior radiation resistance of  $\text{In}_{1-x}\text{Ga}_x\text{N}$  alloys: Full-solar-spectrum photovoltaic material system. *J. Appl. Phys.* **94**(10), 6477–6482 (2003)
43. O. Jani, I. Ferguson, C. Honsberg, S. Kurtz, Design and characterization of GaN/ InGaN solar cells. *Appl. Phys. Lett.* **91**(13), 132117 (2007)
44. C.J. Neufeld, N.G. Toledo, S.C. Cruz, M. Iza, S.P. DenBaars, U.K. Mishra, High quantum efficiency InGaN/GaN solar cells with 2.95 eV band gap. *Appl. Phys. Lett.* **93**(14), 3502 (2008)
45. P. Kozodoy, J. Ibbetson, H. Marchand, P. Fini, S. Keller, J. Speck, S. DenBaars, U. Mishra, Electrical characterization of GaN pn junctions with and without threading dislocations. *Appl. Phys. Lett.* **73**, 975 (1998)
46. F. Qian, Y. Li, S. Gradecak, D. Wang, C.J. Barrelet, C.M. Lieber, Gallium nitride-based nanowire radial heterostructures for nanophotonics. *Nano Lett.* **4**(10), 1975–1979 (2004)
47. F. Qian, S. Gradecak, Y. Li, C.-Y. Wen, C.M. Lieber, Core/multishell nanowire heterostructures as multicolor, high-efficiency light-emitting diodes. *Nano Lett.* **5**(11), 2287–2291 (2005)
48. S. Gradečak, F. Qian, Y. Li, H.-G. Park, C.M. Lieber, GaN nanowire lasers with low lasing thresholds. *Appl. Phys. Lett.* **87**(17), 173111 (2005)
49. F. Qian, Y. Li, S. Gradečak, H.-G. Park, Y. Dong, Y. Ding, Z.L. Wang, C.M. Lieber, Multi-quantum-well nanowire heterostructures for wavelength-controlled lasers. *Nat. Mater.* **7**(9), 701–706 (2008)
50. Y. Li, J. Xiang, F. Qian, S. Gradecak, Y. Wu, H. Yan, D.A. Blom, C.M. Lieber, Dopant-free GaN/AlN/AlGaIn radial nanowire heterostructures as high electron mobility transistors. *Nano Lett.* **6**(7), 1468–1473 (2006)
51. T. Kuykendall, P. Ulrich, S. Aloni, P. Yang, Complete composition tunability of InGaIn nanowires using a combinatorial approach. *Nat. Mater.* **6**(12), 951–956 (2007)
52. L.J. Lauhon, M.S. Gudiksen, D. Wang, C.M. Lieber, Epitaxial core–shell and core–multishell nanowire heterostructures. *Nature* **420**(6911), 57–61 (2002)
53. Y. Dong, B. Tian, T.J. Kempa, C.M. Lieber, Coaxial group III – nitride nanowire photovoltaics. *Nano Lett.* **9**(5), 2183–2187 (2009)
54. M. Grätzel, Photoelectrochemical cells. *Nature* **414**(6861), 338–344 (2001)

55. M.G. Walter, E.L. Warren, J.R. McKone, S.W. Boettcher, Q. Mi, E.A. Santori, N.S. Lewis, Solar water splitting cells. *Chem. Rev.* **110**(11), 6446–6473 (2010)
56. X. Chen, S. Shen, L. Guo, S.S. Mao, Semiconductor-based photocatalytic hydrogen generation. *Chem. Rev.* **110**(11), 6503–6570 (2010)
57. F.E. Osterloh, Inorganic nanostructures for photoelectrochemical and photocatalytic water splitting. *Chem. Soc. Rev.* **42**(6), 2294–2320 (2013)
58. Y. Wang, T. Wang, P. Da, M. Xu, H. Wu, G. Zheng, Silicon nanowires for biosensing, energy storage, and conversion. *Adv. Mater.* **25**(37), 5177–5195 (2013)
59. A. Fujishima, K. Honda, Electrochemical photolysis of water at a semiconductor electrode. *Nature* **238**, 37–38 (1972)
60. R.E. Blankenship, D.M. Tiede, J. Barber, G.W. Brudvig, G. Fleming, M. Ghirardi, M. Gunner, W. Junge, D.M. Kramer, A. Melis, Comparing photosynthetic and photovoltaic efficiencies and recognizing the potential for improvement. *Science* **332**(6031), 805–809 (2011)
61. Y. Tachibana, L. Vayssieres, J.R. Durrant, Artificial photosynthesis for solar water-splitting. *Nat. Photonics* **6**(8), 511–518 (2012)
62. C. Liu, N.P. Dasgupta, P. Yang, Semiconductor nanowires for artificial photosynthesis. *Chem. Mat.* **26**(1), 415–422 (2013)
63. I.S. Cho, Z. Chen, A.J. Forman, D.R. Kim, P.M. Rao, T.F. Jaramillo, X. Zheng, Branched TiO<sub>2</sub> nanorods for photoelectrochemical hydrogen production. *Nano Lett.* **11**(11), 4978–4984 (2011)
64. I.S. Cho, C.H. Lee, Y. Feng, M. Logar, P.M. Rao, L. Cai, D.R. Kim, R. Sinclair, X. Zheng, Codoping titanium dioxide nanowires with tungsten and carbon for enhanced photoelectrochemical performance. *Nat. Commun.* **4**, 1723 (2013)
65. H.M. Chen, C.K. Chen, Y.C. Chang, C.W. Tsai, R.S. Liu, S.F. Hu, W.S. Chang, K.H. Chen, Quantum dot monolayer sensitized zno nanowire-array photoelectrodes: true efficiency for water splitting. *Angew. Chem.* **122**(34), 6102–6105 (2010)
66. H.M. Chen, C.K. Chen, R.S. Liu, C.C. Wu, W.S. Chang, K.H. Chen, T.S. Chan, J.F. Lee, D.P. Tsai, A new approach to solar hydrogen production: a ZnO–ZnS solid solution nanowire array photoanode. *Adv. Energy Mater.* **1**(5), 742–747 (2011)
67. W. Li, P. Da, Y. Zhang, Y. Wang, X. Lin, X. Gong, G. Zheng, WO<sub>3</sub> nanoflakes for enhanced photoelectrochemical conversion. *ACS Nano* **8**(11), 11770–11777 (2014)
68. Y. Ling, G. Wang, D.A. Wheeler, J.Z. Zhang, Y. Li, Sn-doped hematite nanostructures for photoelectrochemical water splitting. *Nano Lett.* **11**(5), 2119–2125 (2011)
69. L. Li, Y. Yu, F. Meng, Y. Tan, R.J. Hamers, S. Jin, Facile solution synthesis of  $\alpha$ -Fe<sub>2</sub>O<sub>3</sub> nanowires and their conversion to  $\alpha$ -Fe<sub>2</sub>O<sub>3</sub> nanowires for photoelectrochemical application. *Nano Lett.* **12**(2), 724–731 (2012)
70. T.W. Kim, K.-S. Choi, Nanoporous BiVO<sub>4</sub> photoanodes with dual-layer oxygen evolution catalysts for solar water splitting. *Science* **343**(6174), 990–994 (2014)
71. M. Li, W. Luo, D. Cao, X. Zhao, Z. Li, T. Yu, Z. Zou, A Co-catalyst-loaded Ta<sub>3</sub>N<sub>5</sub> photoanode with a high solar photocurrent for water splitting upon facile removal of the surface layer. *Angew. Chem. Int. Ed.* **52**(42), 11016–11020 (2013)
72. G. Yuan, H. Zhao, X. Liu, Z.S. Hasanali, Y. Zou, A. Levine, D. Wang, Synthesis and photoelectrochemical study of vertically aligned silicon nanowire arrays. *Angew. Chem.* **121**(51), 9860–9864 (2009)
73. D. Wang, A. Pierre, M.G. Kibria, K. Cui, X. Han, K.H. Bevan, H. Guo, S. Paradis, A.-R. Hakima, Z. Mi, Wafer-level photocatalytic water splitting on GaN nanowire arrays grown by molecular beam epitaxy. *Nano Lett.* **11**(6), 2353–2357 (2011)
74. J. Sun, C. Liu, P. Yang, Surfactant-free, large-scale, solution–liquid–solid growth of gallium phosphide nanowires and their use for visible-light-driven hydrogen production from water reduction. *J. Am. Chem. Soc.* **133**(48), 19306–19309 (2011)
75. C. Liu, J. Sun, J. Tang, P. Yang, Zn-doped p-type gallium phosphide nanowire photocathodes from a surfactant-free solution synthesis. *Nano Lett.* **12**(10), 5407–5411 (2012)

76. S.W. Boettcher, J.M. Spurgeon, M.C. Putnam, E.L. Warren, D.B. Turner-Evans, M.D. Kelzenberg, J.R. Maiolo, H.A. Atwater, N.S. Lewis, Energy-conversion properties of vapor-liquid-solid-grown silicon wire-array photocathodes. *Science* **327**(5962), 185–187 (2010)
77. S.W. Boettcher, E.L. Warren, M.C. Putnam, E.A. Santori, D. Turner-Evans, M.D. Kelzenberg, M.G. Walter, J.R. McKone, B.S. Brunschwig, H.A. Atwater, Photoelectrochemical hydrogen evolution using Si microwire arrays. *J. Am. Chem. Soc.* **133**(5), 1216–1219 (2011)
78. A. Kargar, S.J. Kim, P. Allameh, C. Choi, N. Park, H. Jeong, Y. Pak, G.Y. Jung, X. Pan, D. Wang, p-Si/SnO<sub>2</sub>/Fe<sub>2</sub>O<sub>3</sub> core/shell/shell nanowire photocathodes for neutral pH water splitting. *Adv. Funct. Mater.* **25**(17), 2609–2615 (2015)
79. J. Tian, Q. Liu, N. Cheng, A.M. Asiri, X. Sun, Self-supported Cu<sub>3</sub>P nanowire arrays as an integrated high-performance three-dimensional cathode for generating hydrogen from water. *Angew. Chem. Int. Ed.* **53**(36), 9577–9581 (2014)
80. P. Jiang, Q. Liu, Y. Liang, J. Tian, A.M. Asiri, X. Sun, A cost-effective 3D hydrogen evolution cathode with high catalytic activity: FeP nanowire array as the active phase. *Angew. Chem. Int. Ed.* **53**(47), 12855–12859 (2014)
81. L. Liao, S. Wang, J. Xiao, X. Bian, Y. Zhang, M.D. Scanlon, X. Hu, Y. Tang, B. Liu, H.H. Girault, A nanoporous molybdenum carbide nanowire as an electrocatalyst for hydrogen evolution reaction. *Energy Environ. Sci.* **7**(1), 387–392 (2014)
82. T.Y. Ma, S. Dai, M. Jaroniec, S.Z. Qiao, Metal-organic framework derived hybrid Co<sub>3</sub>O<sub>4</sub>-carbon porous nanowire arrays as reversible oxygen evolution electrodes. *J. Am. Chem. Soc.* **136**(39), 13925–13931 (2014)
83. Y. Wang, T. Zhou, K. Jiang, P. Da, Z. Peng, J. Tang, B. Kong, W.B. Cai, Z. Yang, G. Zheng, Reduced mesoporous Co<sub>3</sub>O<sub>4</sub> nanowires as efficient water oxidation electrocatalysts and supercapacitor electrodes. *Adv. Energy Mater.* **4**(16), 1400696 (2014)
84. Z. Peng, D. Jia, A.M. Al-Enizi, A.A. Elzatahry, G. Zheng, From water oxidation to reduction: homologous Ni-Co based nanowires as complementary water splitting electrocatalysts. *Adv. Energy Mater.* **5**(9), 1402031 (2015)
85. Z. Liu, H. Wang, X.-M. Ou, C.-S. Lee, F. Li, X.-H. Zhang, A silicon/zinc 2, 9, 16, 23-tetraaminophthalocyanine coaxial core-shell nanowire array as an efficient solar hydrogen generation photocatalyst. *Nanotechnology* **23**(17), 175401 (2012)
86. A.P. Goodey, S.M. Eichfeld, K.-K. Lew, J.M. Redwing, T.E. Mallouk, Silicon nanowire array photoelectrochemical cells. *J. Am. Chem. Soc.* **129**(41), 12344–12345 (2007)
87. J.R. Maiolo, B.M. Kayes, M.A. Filler, M.C. Putnam, M.D. Kelzenberg, H.A. Atwater, N.S. Lewis, High aspect ratio silicon wire array photoelectrochemical cells. *J. Am. Chem. Soc.* **129**(41), 12346–12347 (2007)
88. J.M. Spurgeon, S.W. Boettcher, M.D. Kelzenberg, B.S. Brunschwig, H.A. Atwater, N.S. Lewis, Flexible, polymer-supported. Si Wire Array Photoelectrodes. *Adv. Mater.* **22**(30), 3277–3281 (2010)
89. K. Peng, X. Wang, S.-T. Lee, Silicon nanowire array photoelectrochemical solar cells. *Appl. Phys. Lett.* **92**(16), 163103 (2008)
90. D. Liu, L. Li, Y. Gao, C. Wang, J. Jiang, Y. Xiong, The nature of photocatalytic “water splitting” on silicon nanowires. *Angew. Chem. Int. Ed.* **54**(10), 2980–2985 (2015)
91. K.-Q. Peng, X. Wang, X.-L. Wu, S.-T. Lee, Platinum nanoparticle decorated silicon nanowires for efficient solar energy conversion. *Nano Lett.* **9**(11), 3704–3709 (2009)
92. Q. Shu, J. Wei, K. Wang, H. Zhu, Z. Li, Y. Jia, X. Gui, N. Guo, X. Li, C. Ma, Hybrid heterojunction and photoelectrochemistry solar cell based on silicon nanowires and double-walled carbon nanotubes. *Nano Lett.* **9**(12), 4338–4342 (2009)
93. Q. Shu, J. Wei, K. Wang, S. Song, N. Guo, Y. Jia, Z. Li, Y. Xu, A. Cao, H. Zhu, Efficient energy conversion of nanotube/nanowire-based solar cells. *Chem. Commun.* **46**(30), 5533–5535 (2010)

94. X. Shen, B. Sun, F. Yan, J. Zhao, F. Zhang, S. Wang, X. Zhu, S. Lee, High-performance photoelectrochemical cells from ionic liquid electrolyte in methyl-terminated silicon nanowire arrays. *ACS Nano* **4**(10), 5869–5876 (2010)
95. X. Wang, K.Q. Peng, X.J. Pan, X. Chen, Y. Yang, L. Li, X.M. Meng, W.J. Zhang, S.T. Lee, High-performance silicon nanowire array photoelectrochemical solar cells through surface passivation and modification. *Angew. Chem. Int. Ed.* **50**(42), 9861–9865 (2011)
96. A.J. Bard, M.A. Fox, Artificial photosynthesis: solar splitting of water to hydrogen and oxygen. *Acc. Chem. Res.* **28**(3), 141–145 (1995)
97. T.J. Meyer, Chemical approaches to artificial photosynthesis. *Acc. Chem. Res.* **22**(5), 163–170 (1989)
98. D. Gust, T.A. Moore, A.L. Moore, Solar fuels via artificial photosynthesis. *Acc. Chem. Res.* **42**(12), 1890–1898 (2009)
99. H.B. Gray, Powering the planet with solar fuel. *Nat. Chem.* **1**(1), 7 (2009)
100. J.R. Bolton, S.J. Strickler, J.S. Connolly, Limiting and realizable efficiencies of solar photolysis of water. *Nature* **316**, 495 (1985)
101. A. Kudo, Z-scheme photocatalyst systems for water splitting under visible light irradiation. *MRS Bull.* **36**(01), 32–38 (2011)
102. K. Maeda, Z-scheme water splitting using two different semiconductor photocatalysts. *ACS Catal.* **3**(7), 1486–1503 (2013)
103. C. Liu, Y.J. Hwang, H.E. Jeong, P. Yang, Light-induced charge transport within a single asymmetric nanowire. *Nano Lett.* **11**(9), 3755–3758 (2011)
104. C. Liu, J. Tang, H.M. Chen, B. Liu, P. Yang, A fully integrated nanosystem of semiconductor nanowires for direct solar water splitting. *Nano Lett.* **13**(6), 2989–2992 (2013)
105. J. Barber, Photosynthetic energy conversion: natural and artificial. *Chem. Soc. Rev.* **38**(1), 185–196 (2009)
106. C. Liu, J.J. Gallagher, K.K. Sakimoto, E.M. Nichols, C.J. Chang, M.C. Chang, P. Yang, Nanowire-bacteria hybrids for unassisted solar carbon dioxide fixation to value-added chemicals. *Nano Lett.* **15**(5), 3634–3639 (2015)
107. G.S. Nolas, J. Sharp, J. Goldsmid, *Thermoelectrics: Basic Principles and New Materials Developments* (Springer, New York, 2001)
108. A.I. Hochbaum, R. Chen, R.D. Delgado, W. Liang, E.C. Garnett, M. Najarian, A. Majumdar, P. Yang, Enhanced thermoelectric performance of rough silicon nanowires. *Nature* **451** (7175), 163–167 (2008)
109. R.R. Heikes, R.W. Ure, *Thermoelectricity: Science and Engineering* (Interscience Publishers, New York, 1961)
110. A. Majumdar, Thermoelectricity in semiconductor nanostructures. *Science* **303**(5659), 777–778 (2004)
111. Y.-M. Lin, M. Dresselhaus, Thermoelectric properties of superlattice nanowires. *Phys. Rev. B* **68**(7), 075304 (2003)
112. B. Hamdou, J. Kimling, A. Dorn, E. Pippel, R. Rostek, P. Woias, K. Nielsch, Thermoelectric characterization of bismuth telluride nanowires, synthesized via catalytic growth and post-annealing. *Adv. Mater.* **25**(2), 239–244 (2013)
113. W. Liang, O. Rabin, A.I. Hochbaum, M. Fardy, M. Zhang, P. Yang, Thermoelectric properties of p-type PbSe nanowires. *Nano Res.* **2**(5), 394–399 (2009)
114. K.F. Hsu, S. Loo, F. Guo, W. Chen, J.S. Dyck, C. Uher, T. Hogan, E.K. Polychroniadis, M.G. Kanatzidis, Cubic AgPbmSbTe<sub>2</sub> + m: Bulk thermoelectric materials with high figure of merit. *Science* **303**(5659), 818–821 (2004)
115. T. Harman, P. Taylor, M. Walsh, B. LaForge, Quantum dot superlattice thermoelectric materials and devices. *Science* **297**(5590), 2229–2232 (2002)
116. R. Venkatasubramanian, E. Siivola, T. Colpitts, O’quinn, B., thin-film thermoelectric devices with high room-temperature figures of merit. *Nature* **413**(6856), 597–602 (2001)
117. L. Weber, E. Gmelin, Transport properties of silicon. *Appl. Phys. A* **53**(2), 136–140 (1991)

118. D. Li, Y. Wu, P. Kim, L. Shi, P. Yang, A. Majumdar, Thermal conductivity of individual silicon nanowires. *Appl. Phys. Lett.* **83**(14), 2934–2936 (2003)
119. A.I. Boukai, Y. Bunimovich, J. Tahir-Kheli, J.-K. Yu, W.A. Goddard, J.R. Heath, Silicon nanowires as efficient thermoelectric materials. *Nature* **451**(7175), 168–171 (2008)
120. C. Herring, Theory of the thermoelectric power of semiconductors. *Phys. Rev.* **96**(5), 1163 (1954)
121. E.K. Lee, L. Yin, Y. Lee, J.W. Lee, S.J. Lee, J. Lee, S.N. Cha, D. Whang, G.S. Hwang, K. Hippalgaonkar, Large thermoelectric figure-of-merits from SiGe nanowires by simultaneously measuring electrical and thermal transport properties. *Nano Lett.* **12**(6), 2918–2923 (2012)
122. T. Ikeda, *Fundamentals of Piezoelectricity* (Oxford University Press, New York, 1996)
123. H.A. Sodano, D.J. Inman, G. Park, A review of power harvesting from vibration using piezoelectric materials. *Shock Vib. Dig.* **36**(3), 197–206 (2004)
124. T.T. Le, J. Han, A. Von Jouanne, K. Mayaram, T.S. Fiez, Piezoelectric micro-power generation interface circuits. *IEEE J. Solid-St. Circ.* **41**(6), 1411–1420 (2006)
125. Z.L. Wang, From nanogenerators to piezotronics—a decade-long study of ZnO nanostructures. *MRS Bull.* **37**(09), 814–827 (2012)
126. Z.L. Wang, G. Zhu, Y. Yang, S. Wang, C. Pan, Progress in nanogenerators for portable electronics. *Mater. Today* **15**(12), 532–543 (2012)
127. Z.L. Wang, J. Song, Piezoelectric nanogenerators based on zinc oxide nanowire arrays. *Science* **312**(5771), 242–246 (2006)
128. Y. Qin, X. Wang, Z.L. Wang, Microfibre–nanowire hybrid structure for energy scavenging. *Nature* **451**(7180), 809–813 (2008)
129. R. Yang, Y. Qin, L. Dai, Z.L. Wang, Power generation with laterally packaged piezoelectric fine wires. *Nat. Nanotechnol.* **4**(1), 34–39 (2009)
130. S. Xu, Y. Qin, C. Xu, Y. Wei, R. Yang, Z.L. Wang, Self-powered nanowire devices. *Nat. Nanotechnol.* **5**(5), 366–373 (2010)
131. C. Pan, L. Dong, G. Zhu, S. Niu, R. Yu, Q. Yang, Y. Liu, Z.L. Wang, High-resolution electroluminescent imaging of pressure distribution using a piezoelectric nanowire LED array. *Nat. Photonics* **7**(9), 752–758 (2013)

# Chapter 10

## Nanowire Field-Effect Transistor Sensors

**Abstract** Sensitive and quantitative analysis of proteins and other biochemical species are central to disease diagnosis, drug screening and proteomic studies. Research advances exploiting SiNWs configured as FETs for biomolecule analysis have emerged as one of the most promising and powerful platforms for label-free, real-time, and sensitive electrical detection of proteins as well as many other biological species. In this chapter, we first briefly introduce the fundamental principle for semiconductor NW-FET sensors. Representative examples of semiconductor NW sensors are then summarized for sensitive chemical and biomolecule detection, including proteins, nucleic acids, viruses and small molecules. In addition, this chapter discusses several electrical and surface functionalization methods for enhancing the sensitivity of semiconductor NW sensors.

### 10.1 Introduction

Fundamental biomedical research demands novel biosensors and assays that can fulfill the requirements of ultra-sensitivity and high-throughput [1, 2]. Many semiconducting nanomaterials, such as NWs, carbon nanotubes and graphene have been studied for the electronic sensing in an effort to address these needs. Among them, SiNWs possess unique structural and chemical characteristics, including diameters similar to proteins, high surface-to-volume ratios, chemically well-defined and tailorable silicon oxide surfaces, which have enabled them to be configured as high-performance FETs for label-free, real-time, sensitive detection of proteins and other biomolecules [3–5].

The electrical detection of biomolecules using a NW-FET can be understood as follows. The surface of a NW-FET is functionalized with biomolecule receptors, such as monoclonal antibodies or single-strand DNA (ssDNA) probes, which can selectively bind to biomolecule targets in solution. The binding of charged biomolecules, (the sign and number of charges depend on the isoelectric point of the biomolecules and the solution pH), leads to a variation of charge or electric potential at the NW surface, in a way similar to applying an external potential to gate electrode

in a conventional FET device. The charge carrier densities of the NW-FET is thus tuned and leads to an electrical conductivity change associated with the biomolecular binding events in real time. Since the NW diameters can be similar to biomolecules such as proteins and nucleic acids, these binding events can be sensitively detected by the NW-FETs. Furthermore, incorporation of a number of NW-FET elements in a single sensor chip where the NWs are functionalized with different surface receptors allows for multiplexed electrical detection in the same assay, enabling a unique and powerful platform for chemical/biological recognition [6].

In this chapter, we first briefly introduce the fundamental principles of the NW-FET sensor. Then, representative examples in which FET sensors are applied to detect chemical and biomolecule targets, including proteins, nucleic acids, viruses, and small molecules, are summarized. Furthermore, several methods for improving the sensitivity and/or capabilities of NW-FET sensors, including the use of branched NWs to enhance the capture efficiency of molecular analytes, operation of the FET in the subthreshold regime, increasing the analyte concentration by electrokinetic effects, and detection in physiological fluids, are briefly illustrated.

## 10.2 Fundamental Principles of Field-Effect Transistor Sensors

As previously discussed in Chap. 5, FETs are among the fundamental building blocks of today's high-density integrated circuits. In a standard planar metal-oxide semiconductor FET (Fig. 10.1a), the semiconductor substrate is connected to the gate (G), the source (S) and the drain (D) electrodes. If no gate voltage is applied (the "Off" state), the FET is equivalent to two back-to-back  $p$ - $n$  junctions with almost no current flows. In the "On" state, when the gate bias exceeds a threshold voltage, carriers (e.g., holes for  $p$ -Si and electrons for  $n$ -Si) are induced at the semiconductor-oxide interface, the potential barrier of the channel drops, resulting in a significant current flow. Therefore, the conductance of the semiconductor channel between the source and drain regions can be switched on and off by the potential at the gate electrode.

The use of planar FETs for ion-selective sensors was introduced several decades ago [7], while their opportunities as chemical and biological sensors have further been advanced in new and significant ways using NWs. Similar to planar FET, the conductance of a NW-FETs can be controlled by variations in the charge density or electric potential in the channel region. This response makes NW-FETs ideal candidates for chemical and biological sensing, as the change in electric field due to binding of a charged molecule to the NW surface, which is analogous to applying a voltage via a gate electrode, can readily change the device conductance. For example, a  $p$ -type SiNW functionalized with surface receptors that can specifically capture chemical/biomolecule targets will exhibit an increase in conductance when negatively charged molecules bind to the receptors. This increase in conductance is

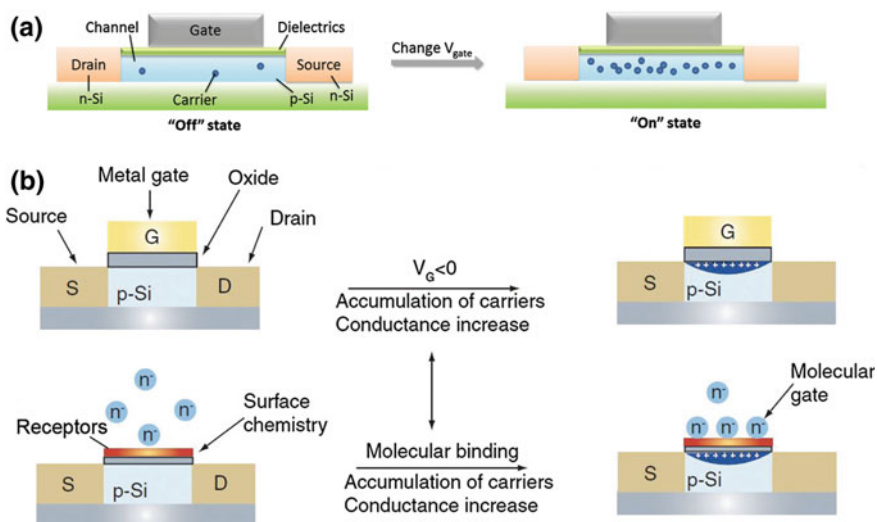


**Fig. 10.1** **a** A typical planar FET. The semiconductor substrate (e.g.,  $p$ -Si) is connected to gate ( $G$ ), source ( $S$ ) and drain ( $D$ ) electrodes, and can switch between the “off” and “on” states by applying the gate voltage. **b** Schematic comparison of (*top*) a standard FET device and (*bottom*) a SiNW-FET sensor. The NW surface is functionalized with a receptor layer to recognize target biomolecules in a solution, which are charged and provide a molecular gating effect on SiNWs. Reproduced from [76]. Copyright 2006 Future Medicine Ltd. (color figure online)

similar to applying a negative gate voltage and results from accumulation of charge carriers (holes) in the  $p$ -type FET (Fig. 10.1b). Conversely, binding positively charged molecules will deplete hole carriers and reduce the conductance. Hence, NW-FETs can enable real-time label-free direct electrical readout of biological events, including binding/unbinding, enzymatic reactions and electron transfer. These detection capabilities are ideal for developing a platform system for analyzing biological samples.

Semiconductor NWs composed of Si or other materials (e.g., ZnO, SnO<sub>2</sub> and In<sub>2</sub>O<sub>3</sub>) have been explored extensively as FET sensors [8–10]. Among these NW materials, the potential to achieve molecular-size diameters [11], high electron or hole mobility [12], and versatile surface functionalization of SiNWs [13], as well as the potential of interfacing with existing mature silicon industry processing, have made SiNWs one of the most widely studied for biomolecular sensing [3–5]. SiNW-FETs are transformed into nanosensors by surface functionalization with probe molecules that enable the specific recognition of chemical/biological molecule targets. Covalent binding to the native silicon oxide (SiO<sub>2</sub>) layer that naturally grows on SiNWs represents one of the most robust approaches for probe attachment and takes advantage of the wealth of knowledge available from studies focused on functionalization of glass (SiO<sub>2</sub>) slides [14]. A detailed surface functionalization process is described elsewhere [13]. The simplest and earliest established example of this approach is hydrogen-ion concentration detection or pH sensing [8]. In this case,



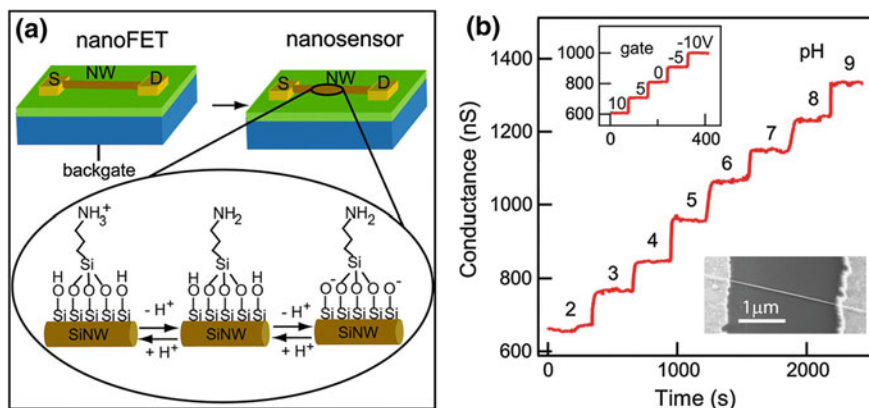


**Fig. 10.2** **a** Schematic of a functionalized NW device and the protonation/deprotonation process that changes the surface charge state. **b** Changes in NW conductance versus pH. Reproduced from [8]. Copyright 2001 the American Association for the Advancement of Science (color figure online)

the SiO<sub>2</sub> layer at a *p*-SiNW surface is modified with 3-aminopropyltriethoxysilane (APTES), which yields amino group (-NH<sub>2</sub>) termination on the NW surface (Fig. 10.2a). The amino groups and silanol groups (Si-OH) on the unreacted regions of the oxide layer undergo protonation and deprotonation as the hydrogen-ion concentration varies, thereby changing the surface charge and the NW conductance. The NW electrical conductance shows a stepwise, discrete and stable increase, in response to increasing pH from 2 to 9 (Fig. 10.2b). More recently, Noy and coworkers demonstrated SiNW-FETs modified with lipid bilayers with and without ligand-gated and voltage-gated ion channels to monitor the solution pH. For lipid bilayer containing ion channels, devices responded to changes in solution pH, and when the channels were blocked the device response was strongly diminished [15]. Sensing studies of several distinct classes of biological targets are discussed below.

## 10.3 Examples of Nanoelectronic Sensors

### 10.3.1 Protein Detection

The sensitive detection of proteins, especially those known as disease markers, offers substantial potential to benefit disease diagnosis and treatment. In 2001, pioneering work demonstrated real-time protein sensing with SiNW-FET device [8]. Specifically, SiNWs functionalized with biotin receptors were used to selectively detect streptavidin at concentrations down to 10 pM, substantially lower than other methods at the time. However, the strong binding affinity between biotin and streptavidin leads to effectively irreversible binding and precluded monitoring

unbinding and sequential measurements at different streptavidin concentrations. To overcome this limitation, several reversible surface modifications have been explored, including biotin–monoclonal antibiotin binding and calmodulin (CaM)-Ca<sup>2+</sup> interaction, to investigate quantitative concentration-dependent analyses [8]. In a more recent study [16], CaM–modified SiNWs are used to detect Ca<sup>2+</sup> and CaM–binding proteins through the association/dissociation interaction between glutathione and glutathione S–transferase. In addition, this basic approach has been used to demonstrate successful concentration-dependent detection of cardiac troponin T [17] (a biomarker for myocardial infarction), SARS virus nucleocapsid proteins [18], and bovine serum albumin [19] in recent literature and thus further validate the efficacy of NW-FETs as protein sensors.

In genomics and proteomics research, simultaneous detection of multiple proteins is believed to be especially important for diagnosing complex diseases such as cancers [20, 21]. Moreover, the availability of different biomarkers matched with different stages of diseases could allow for early detection and robust diagnosis. Early work on SiNW-FET devices [8], although powerful in detecting binding/unbinding of proteins, lacked the capability of selective multiplexed sensing. To address this issue, Zheng et al. [22] developed integrated NW sensor arrays, in which ~100 individually addressable NW-FETs were functionalized with several different receptors (Fig. 10.3a), and demonstrated several new sensing capabilities. Specifically, monoclonal antibodies for the cancer marker proteins prostate specific antigen (PSA) carcinoembryonic antigen (CEA) and mucin-1 were used to functionalize SiNW-FETs in the same device array (Fig. 10.3b). Upon addition of buffer solutions containing different concentrations of these cancer biomarkers,

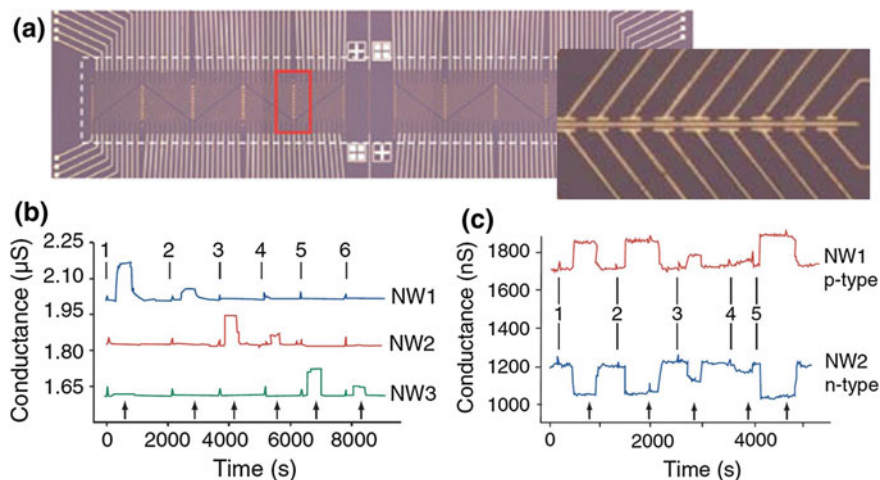


**Fig. 10.3** **a** Optical image of a NW array. **b** Sequential detection of PSA, CEA and mucin-1 solutions using three SiNW-FET sensors. **c** Complementary sensing of PSA using a *p*-type (NW1) and a *n*-type (NW2) SiNW-FET sensors in a same array. Reproduced from [22]. Copyright 2005 Nature Publishing Group

changes in electrical conductance of the corresponding NW-FETs were recorded with femtomolar sensitivity, which is several orders of magnitude better than possible with the standard enzyme-linked immunosorbent assay (ELISA) [22]. This work also introduced the new concept of incorporating both *p*-type and *n*-type NWs into the same device array (Fig. 10.3c). In so doing, the binding of a negatively charged biomarker such as PSA on the NW sensor surfaces led to an increase in conductance for *p*-SiNWs and a decrease for the *n*-SiNWs in the same sensor chip. These complementary, opposite electric signals can be used to distinguish false positive signals and enable real-time, highly sensitive and selective detection of multiplexed biomolecule targets. Similarly, Li et al. [9] reported the complementary sensing of PSA using *n*-type In<sub>2</sub>O<sub>3</sub> NWs and *p*-type carbon nanotubes. The enhanced electrical conductance for the NW sensors and the suppressed electrical signal for the carbon nanotube sensors upon the PSA addition are demonstrated with concentrations down to 5 ng/mL sensitivity at physiological buffer concentrations.

Later, an anisotropic wet-etch fabrication method was reported as an alternative ‘top-down’ NW device fabrication strategy for NW-FET sensors [23]. The sensitivity of these top-down fabricated SiNW devices were shown to have sub-100 fM sensitivity for biotin-streptavidin interaction, mouse immunoglobulin G (IgG), and mouse immunoglobulin A (IgA) detection.

### 10.3.2 Nucleic Acid Detection

In addition to detection of protein binding/unbinding, real-time detection of nucleic acids (e.g., DNAs and RNAs) has been successfully carried out using Si and GaN NW-FET devices [24–27]. The surface functionalization methods and detection schemes used in these studies were similar to those described above for protein sensing, where nucleic acid concentration is transduced following binding to a probe by changes in device conductance. A major difference between nucleic acid and protein detections exists in the fact that the high density of negative charges on the nucleic acid phosphate backbones requires high ionic strength buffers to screen the repulsion and allow for binding when DNA or RNA is used as the probe molecule. However, high ionic strength solutions have short Debye screening lengths (see Sect. 10.4.3), which can make difficult or preclude detection. A solution that overcomes this high ionic strength binding/screening issue involves using neutral charge peptide nucleic acids (PNAs) [28, 29], which exhibit excellent binding affinity with DNA at lower ionic strengths. Indeed, modification of SiNWs with PNA probe molecules was shown to exhibit time-dependent conductance changes associated with selective binding of complimentary target DNA at concentrations as low as 10 fM. Moreover, this work showed that a DNA SiNW-FET biosensor could be used to distinguish fully complementary (wild type) versus single-base mismatched (mutant) DNA targets associated with Cystic fibrosis [25]. Additional studies using SiNWs functionalized with PNA probes in which the DNA target binding domain distance was changed exhibited a reduction in sensitivity

with increasing distance between the hybridization site and the NW surface [30]. This observation is consistent with basic sensing mechanism since the ‘field effect’ is reduced for fixed charge as the separation from the SiNW surface increases.

An alternative approach for surface functionalization of SiNW surfaces for DNA detection involves electrostatic adsorption of the probes. For example, Bunimovich et al. [31] reported electrostatic adsorption of primary DNA probe strands onto an amine-terminated SiNW surfaces, where the  $\sim$ parallel orientation of the DNA probes along the NW surface reduces Debye screening effects and can thereby yield sensitive DNA detection.

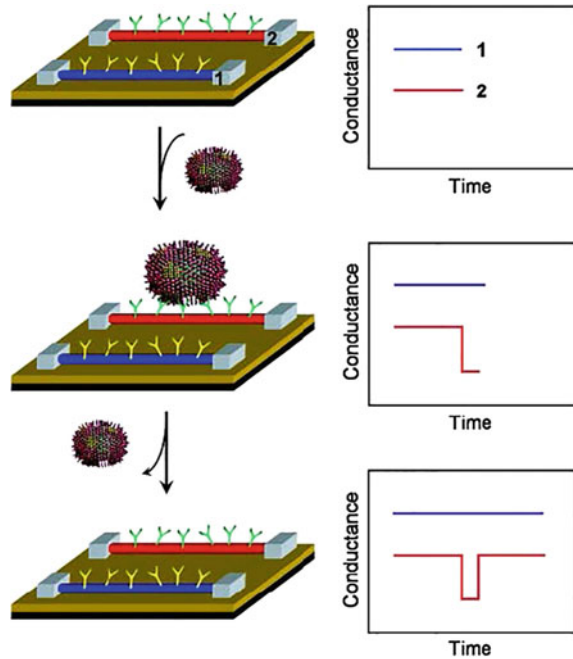
More recently, detection of other nucleic acid targets, such as microRNAs (miRNAs) have been carried out using PNA-modified SiNWs. Focus on microRNAs (miRNAs), which are a large class of short, noncoding RNA molecules that regulate animal and plant genomes, is intriguing because they have been proposed as biomarkers for cancer diagnosis [32]. PNA-functionalized SiNW devices have shown the capability to detect miRNAs down to a remarkable sensitivity of 1 fM [33], ca. one order of magnitude better than reported earlier for DNA detection [30]. This phenomenon can be attributed to the higher thermal stability and melting temperature of PNA–RNA complex than that of PNA–DNA complex. The technique enabled identification of fully complementary versus one-base mismatched miRNA sequences, as well as detection of miRNA in total RNA extracted from HeLa cells, and thus offers substantial potential as a new diagnostic tool.

### 10.3.3 Virus Detection

Viruses are a major cause of infectious diseases and remain the world’s leading cause of death [34]. Successful treatment of viral diseases often depends upon rapid and accurate identification of viruses at ultralow concentrations. The first demonstration of nanoFET based virus sensors involved the detection of influenza A virus using SiNW devices. By recording the electrical conductance changes upon binding/unbinding of virus particles to monoclonal antibody-modified SiNWs, the selective detection of influenza A at the single particle level was demonstrated [35]. The binding kinetics between different virus–receptor interactions were also electrically differentiated by SiNW-FETs (Fig. 10.4). In addition, simultaneous detection of influenza A and adenovirus using independent SiNW biosensors functionalized with distinct antibodies for these two types of viruses was demonstrated [35], and more recently, SiNW-FET based selective detection of influenza A viruses down to 29 viral particles per micro-liter was achieved for breath condensate samples [36]. These achievements represent important proof-of-concept steps towards powerful viral diagnostic devices.

Another example of virus detection was the diagnosis of Dengue, a arthropod-borne viral infection [37]. In this latter work, a specific nucleic acid fragment with 69 base pairs derived from Dengus serotype 2 virus genome

**Fig. 10.4** Schematic of virus binding/unbinding to a SiNW-FET and the corresponding time-dependent conductance change. Reproduced from [35]. Copyright 2004 the National Academy of Sciences of the United States of America



sequence was selected as the target DNA and amplified by the reverse transcription polymerase chain reaction (RT-PCR). The hybridization of the target DNA and PNA-functionalized SiNW-FET sensors increases the device resistance, leading to a sensitivity limit down to 10 fM.

### 10.3.4 Small Molecule Detection

Detection of small molecules that bind specifically to proteins is of vital importance to drug discovery and screening. One example of small molecule detection involves the identification of adenosine triphosphate (ATP) binding, and the small-molecule inhibition of ATP binding to the tyrosine kinase, Abl, which are proteins that mediate signal transduction in mammalian cells. Gleevec, which competitively inhibits ATP binding to Abl, has been used to monitor binding/unbinding behaviors of ATP. The gleevec concentration at fixed ATP concentration yields conductance decrease, which is consistent with reversible competitive inhibition of an agonist (ATP) with an antagonist (Gleevec) [38]. In a different direction, highly ordered flexible SiNW films, have been applied to detect  $\text{NO}_2$  with parts-per-billion (ppb) sensitivity [39]. Other small molecules, such as ammonia ( $\text{NH}_3$ ), acetic acid ( $\text{AcOH}$ ) [40] and 2,4,6-trinitrotoluene (TNT) [41], have also been successfully detected by surface-functionalized SiNW-FET sensors.

Despite numerous approaches developed for achieving highly sensitive detection of polar molecules, the detection of nonpolar volatile organic compounds (VOCs) still remains challenging, due to the weak adsorption of nonpolar VOCs on the surface of NWs and the lack of suitable nonpolar organic functionalities that can be attached to the SiNWs. To address this issue, silane monolayers with a low fraction of Si–O–Si bonds between the adjacent molecules were used to modify SiNW-FETs to enhance their sensitivity towards nonpolar VOCs [42]. In another work [43], it was demonstrated that multiple independent parameters of a specific molecularly modified SiNW-FET can provide high selectivity towards specific VOCs in both single-component and multi-component environments as well as estimating the constituent VOC concentrations.

## 10.4 Methods for Enhancing the Sensitivity of Nanowire Sensors

### 10.4.1 *3D Branched Nanowires for Enhanced Analyte Capture Efficiency*

3D branched NWs [44–49] in which secondary NW branches are grown in a radial direction from a primary NW backbone, provide a number of unique capabilities including a substantially-enhanced surface area compared to the backbone alone. By functionally encoding at well-defined branch junctions during synthesis, rationally designed and synthesized branched NWs can provide well-controlled variations in the composition of the NW backbone and branches, and thus allow for complex electronic and photonic nanodevices. Focusing on sensing, Jiang et al. [47] developed the general synthesis of branched, single-crystalline semiconductor NW heterostructures, including Si backbones with Au branches. The Au-branched NW devices were investigated as nanoelectronic sensors for biomolecular detection (Fig. 10.5). The Au branches, which can be modified in a highly-specific manner using thiol chemistry, can be considered as receptor-functionalized “antennae” for biomolecular analytes. The high surface area of the Au branches provides the potential for enhanced capture efficiency, and thereby can increase the overall device sensitivity. For example, a sensitivity of 80 pg/mL for PSA detection was obtained from mAb-modified *p*-Si/Au-branch NW-FET sensors, with high selectivity.

### 10.4.2 *Detection in the Subthreshold Regime*

The fundamental characteristics of NW-FET devices, such as the transconductance and noise, can have substantial effect on the ultimate detection sensitivity. Conventionally, nanoFET-based sensors are operated in the ‘ON’ state (above the

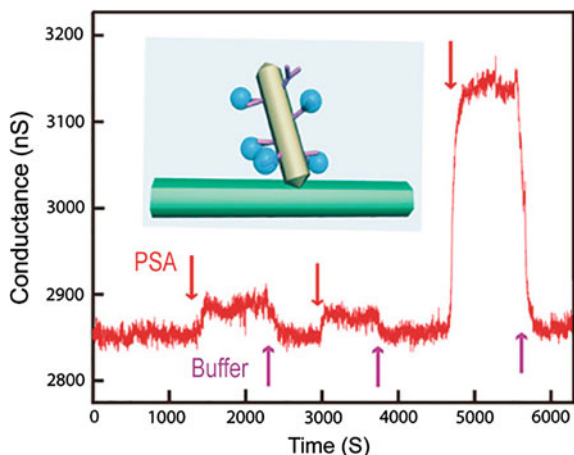


**Fig. 10.5** Conductance versus time curve recorded on a  $p$ -Si/Au branched NW sensor with alternate delivery of PSA (4 ng/mL, 80 pg/mL, 200 ng/mL) and pure buffer solutions. The *top and bottom arrows* mark the delivery of protein and buffer solutions into the sensing channel, respectively. Inset: schematic of Si/Au branched NW sensor. Reproduced from [47]. Copyright 2011 the National Academy of Sciences of the United States of America (color figure online)

threshold voltage), where the transconductance depends linearly on gate-voltage or surface potential. However, in the subthreshold regime it is well-known that the device conductance depends exponentially on gate-voltage [50], which could in principle lead to much higher analyte binding sensitivity. Indeed, Gao et al. [51] studied and compared the detection sensitivity of SiNW-FET sensors in the linear and subthreshold regimes (Fig. 10.6). In previous literature using SiNW-FET sensors [8], the conductance change ( $\Delta G$ ) or the resistance change ( $\Delta R$ ) of the sensor devices was used to quantify the concentration of the target molecules. However, an

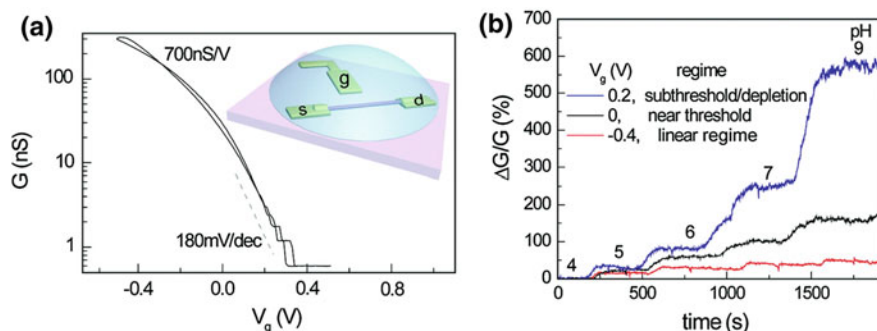


**Fig. 10.6** **a** Conductance,  $G$ , versus  $V_g$  for a  $p$ -type SiNW-FET. Inset: scheme for electrolyte gating. **b** Real time pH sensing. The device in the subthreshold regime shows much larger  $\Delta G/G$  change versus pH. Reproduced from [51]. Copyright 2010 American Chemical Society

absolute signal change, such as  $\Delta G$ , does not reflect the intrinsic device sensitivity, especially when working in the subthreshold regime where device conductance is very small. To better compare sensing in different device regimes Gao et al. used a dimensionless parameter,  $\Delta G/G$ , to characterize and compare device sensitivities. This principle is exemplified in both pH and protein sensing experiments, where the electrolyte gating is used to tune the operational mode of NW-FETs (Fig. 10.6b). These results showed that significant sensitivity enhancement could be achieved by optimization of the FET operating conditions and understanding the fundamental electrical gating property of NW-FETs. One caveat to the success of this work is that the device noise should be dominated by carrier-carrier scattering, such that the noise is also exponentially reduced in the subthreshold regime. If the noise is dominated by other scattering mechanisms, such as contact current injection and/or interface trapping/detrapping, then it may not be possible to exploit the exponential dependence of conductance on gate-voltage/surface potential in the subthreshold regime.

### 10.4.3 Reducing the Debye Screening Effect

Conventional FET sensors detect the concentration of the target species by their intrinsic charge. The charges of solution-based molecules, however, can be screened by dissolved counter ions in the solution. The Debye length, which is inversely proportional to the square root of the ionic strength of an electrolyte, represents the net or screened electrostatic effect of a charged species in ionic solution. A high ionic strength electrolyte solution leads to a short Debye length, and charges outside of the Debye length are electrically screened. For instance, the Debye length of  $1 \times$  PBS,  $\sim 0.7$  nm, can screen most protein antigen charges when they bind to an antibody modified FET surface. In order to reduce the charge screening effect of electrolyte solutions, the Debye length is typically increased by using dilute buffer solutions with low ion concentrations [18, 52].

Recently, several groups have reported approaches based on smaller receptors, such as aptamers [53] or antibody fragments [54] to reduce the distance between the FET surface and the receptor-bound biomolecule analyte. In one example [54], the sizes of antibody probes were reduced through common biochemical methods (Fig. 10.7), thereby improving the analyte detection capability. These studies are promising, although further studies are needed to determine how general detection is under the limit of physiological conditions (Debye length  $< 1$  nm) as the sizes of the aptamer and antibody fragment receptors are similar to or greater than this critical length scale. Zhong and co-workers [55] also reported a direct high-frequency measurement strategy for standard biological receptors, although those measurement requires significantly more complex device geometry, making difficult or precluding application to cellular and in vivo sensing.

Recently, Lieber and coworkers [56] developed a new and general strategy to overcome this challenge for NW-FET sensors that involves incorporating a biomolecule permeable polymer layer, such as polyethylene glycol (PEG), linked to



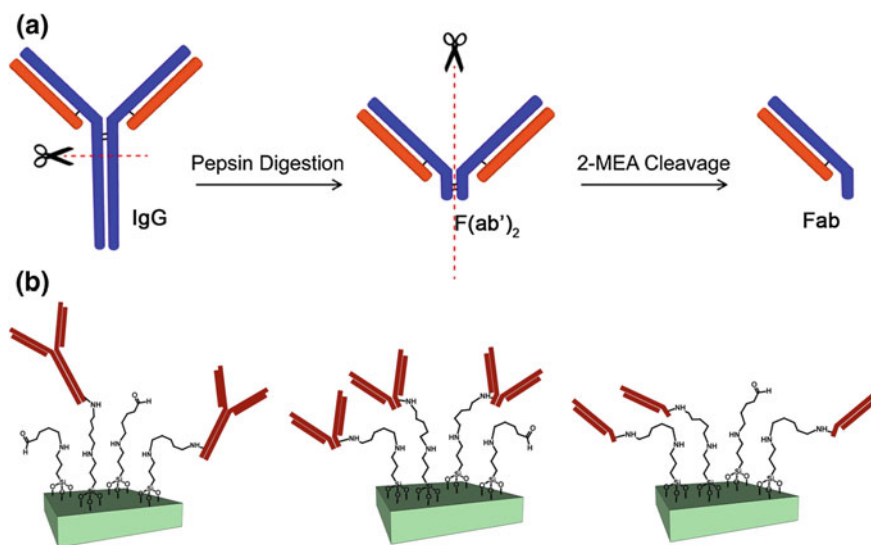


**Fig. 10.7** **a** Schematic for the generation of F(ab')<sub>2</sub>/Fab fragments from a whole IgG molecule. **b** Schematic for the immobilization of a full IgG, F(ab')<sub>2</sub> and Fab antibody-fragments which contain free amine groups onto the SiO<sub>2</sub> surface as receptor layers. Reproduced from [54]. Copyright 2012 American Chemical Society

the FET sensor, where the polymer increases the effective screening length near the NW-FET surface to allow for detection in high ionic strength solutions (Fig. 10.8a). Using PSA as a model system, they showed that PEG-coated SiNW-FETs can detect PSA in phosphate buffer concentrations up to 150 mM, with a detection

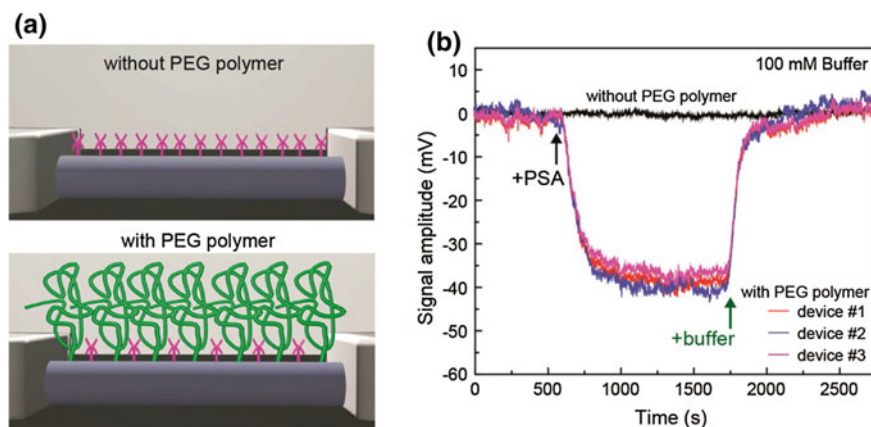


**Fig. 10.8** **a** Schematic illustration of a NW-FET device (*top*) without and (*bottom*) with a porous and biomolecule permeable PEG surface modification. **b** Comparison of signal response traces recorded from three SiNW-FET devices with and without PEG modification. Reproduced from [56]. Copyright 2015 American Chemical Society

sensitivity of  $\sim 10$  nM and linear response range up to 1000 nM. In contrast, similar FETs without PEG functionalization can only detect PSA in buffer salt concentrations lower than 10 mM (Fig. 10.8b). This work suggests a new and general device design strategy for the FET sensor applications in physiological environments, important for in vitro and in vivo biological sensing.

#### 10.4.4 *Electrokinetic Enhancement*

Concentration of analyte near a device surface by electrokinetic effects offers another approach for high-sensitivity protein detection [57]. In a nonuniform alternating current (AC) electric field, the dielectrophoresis (DEP) force can induce polarized particles to move in a directed manner leading to the formation of concentration enhancement and depletion regions in a microfluidic flow channel. Compared to the detection limit without AC excitation, NW sensors modified with monoclonal antibodies for PSA in an appropriate AC field exhibit close to a  $\sim 10^4$  fold increase in sensitivity; that is, the protein concentration at the sensor surface is increased by DEP. In addition, NW devices functionalized with other receptors for capturing cholera toxin subunit B were also demonstrated, suggesting the general applicability of this method for enhanced sensitivity detection [22, 57, 58]. It is important to recognize, however, the DEP enhancement, including frequency response, depends sensitively on solution ionic strength [58, 59].

#### 10.4.5 *Frequency Domain Measurement*

In addition to the conventional real time measurement device conductance to monitor sensing, frequency-dependent fluctuations in the NW-FET electric signal at equilibrium can convey additional information about the dynamics of the biomolecule-NW hybrid system through a coupling to carrier transport in the device to binding events. For example, binding and unbinding can affect the intrinsic device noise, and thus can be characterized through measurements of the frequency-dependent noise spectra (Fig. 10.9a) [60]. In a recent study, the noise spectra was used to analyze contributions from different noise sources [60]. The frequency domain spectrum of a fluctuating two-level system has the form of a Lorentzian function similar to that of a  $RC$  circuit (Fig. 10.9b and c). The  $1/f$  noise is well-known in conventional metal-oxide semiconductor FETs (MOSFETs), and arises from electron capture/emission from trap states [61, 62]. If biomolecule binding/unbinding contributes substantially to the noise, it can lead to a Lorentzian peak in addition to the  $1/f$  background. Specifically, a  $p$ -type SiNW-FET was first modified with PSA monoclonal antibodies, then solutions with different PSA concentrations and pure buffer were sequentially delivered to the NW sensor via a microfluidic channel. In conventional time-domain measurements (Fig. 10.9d), a

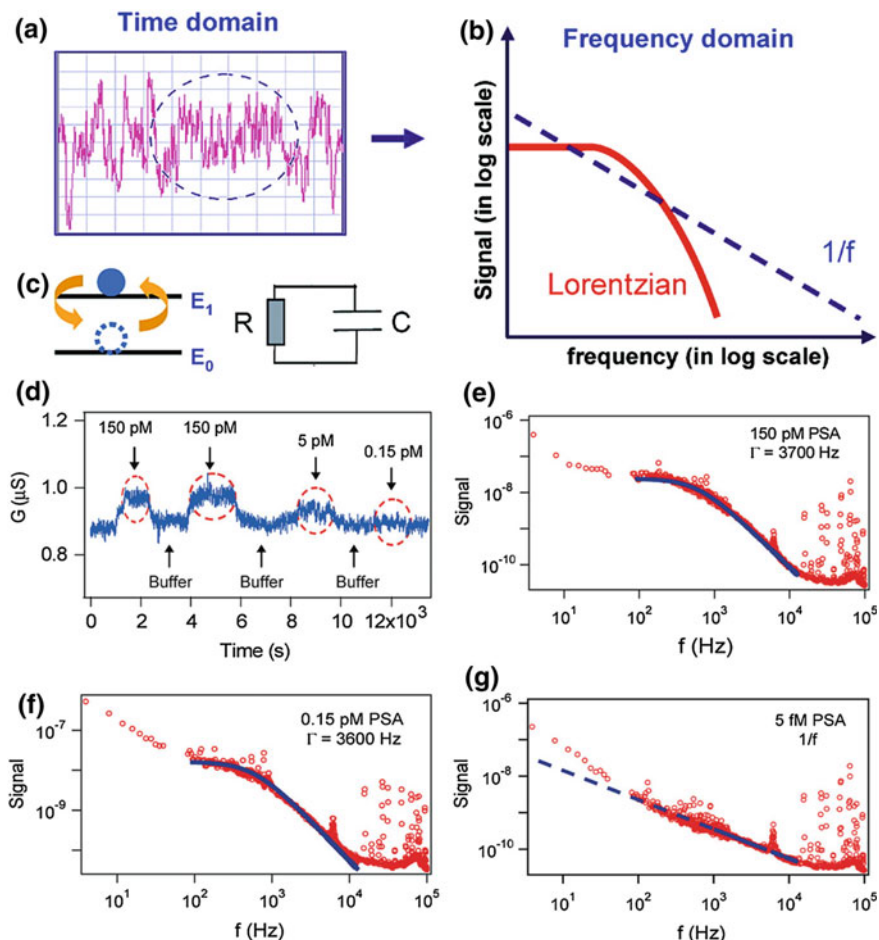


**Fig. 10.9** **a** Electrical noise in a time-domain measurement. **b** Lorentzian and  $1/f$  functions in the frequency domain. **c** Models of a two-level system (left) and a  $RC$  circuit (right). **d** Time domain conductance measurement of a  $p$ -type SiNW-FET sensor modified with PSA monoclonal antibodies, when different concentrations of PSA solutions were delivered to the sensor. **e–g** Power spectra recorded in solutions with different PSA concentrations, 150 (e) and 0.15 pM (f), show Lorentzian shape curves, while power spectrum recorded in 5 fM PSA solution shows a  $1/f$  frequency dependence (g). Reproduced from [60]. Copyright 2010 American Chemical Society

reliable PSA detection limit for this device was ca. 5 pM. However, the frequency domain noise spectra (Fig. 10.9e–g) from the same NW-FET device showed that the Lorentzian curve shape was still clearly observed at a PSA concentration as low as 0.15 pM, ca. 30 times better than that the same device measured in the time domain. The improved detection sensitivity was attributed to the separation of the Lorentzian characteristic frequency from the most dominant background of  $1/f$  noise, which becomes less important at high frequencies.

### 10.4.6 Nanowire–Nanopore Sensors

The integrated NW–nanopore FET sensor has the potential for single-molecule DNA sequencing at low cost and with high throughput [63]. The conventional nanopore DNA sequencing technique records ionic current from nanopores [64], while NW–nanopore sensors allow for direct sequencing of DNA molecules with fast translocation rates given the much higher bandwidth of NW-FETs.

Studies have shown that nanopores can be introduced adjacent to SiNW-FETs using the focused electron beam in a transmission electron microscopy (TEM) [63] (Fig. 10.10a). A sensor device can then be configured by attaching PDMS solution reservoir chambers above and below the silicon nitride membrane on which the SiNW-FET nanopore devices are fabricated. When the two chambers are filled with solutions of different ionic strength, FET signals corresponding to DNA translocation events can be reproducibly recorded (Fig. 10.10b and c). Notably, a 10–60 times higher signal was observed from the SiNW-FET than that of the corresponding ionic current change in these studies. This work demonstrates a new nanopore sequencing device concept with fast sequencing and large-scale integration properties.

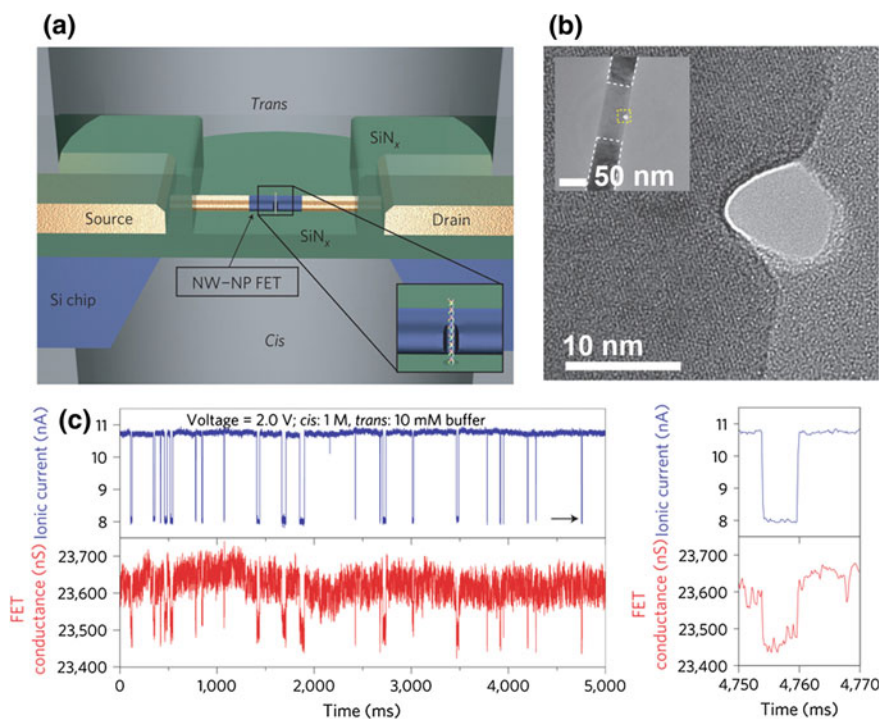


**Fig. 10.10** a, b Schematic and TEM image of a SiNW–nanopore sensor. c Recording of SiNW–nanopore FET conductance and ionic current during DNA translocation. Reproduced from [63]. Copyright 2012 Nature Publishing Group

### 10.4.7 *Double-Gate Nanowire Sensors*

In order to achieve higher sensitivity NW-FET sensors, extensive effort has been focused on advanced device designs prepared by top-down lithography [65, 66]. For example, several groups have fabricated and explored double-gate NW-FET biosensor, with two separated gates, G1 (primary) and G2 (secondary), straddling both sidewalls of the SiNW, to enhance device sensitivity [65, 66]. This work has shown that by applying the same voltage to G1 and G2, the threshold voltage ( $V_T$ ) in the double gate mode is very sensitive to a small change of  $V_{G2}$  (the G2 voltage). Therefore, compared to a single-gate FET sensor, the sensing window of the double-gated FET is significantly broadened, especially in the subthreshold regime described earlier.

### 10.4.8 *Detection of Biomolecules in Physiological Fluids*

Rapid and accurate molecular analysis in physiological fluids (i.e., blood or serum) is essential for disease diagnosis and management. NW-FET sensors have routinely demonstrated ultrasensitive, real-time, multiplexed detection biomolecular species, but also have limitations with respect to sensing in complex, physiological solutions as describe in Sect. 10.4.3. To reiterate, the primary limitation for FETs is related to Debye screening effect [67] in high ionic strength blood/serum samples.

To overcome the limitation of Debye length, researchers have developed several methods to detect analytes in blood/serum samples, including simply reducing the solution ionic strength. For example, the ion concentration can be reduced by diluting a blood sample with buffer solution [68]. Dilution will reduce analyte concentration and can affect ligand- and protein-protein interactions, and thereby reduce device sensitivity. A second approach involves desalting the serum samples before detection of biomarkers [22], which can maintain or even be used to increase analyte concentrations (after dissolution in buffer). Similar to off-chip desalting using rapid size-exclusion chromatography [22], a microfluidic purification chip (MPC) can be used to pre-isolate the target molecules and then release them into a pure buffer suitable for analysis using SiNW-FET arrays [69]. A fourth method adopts a steady-state measurement instead of a real-time recording [70]. Specifically, the resistance of the SiNW is measured in a low ionic strength buffer solution after antibody functionalization. Then, the SiNW sensor is incubated with undiluted serum and subsequently washed to remove unbound proteins, followed by the measurement of the second resistance value in the buffer solution. The concentration of the target molecules can be calculated according to the resistance change before and after antibody-antigen interaction. This method is independent of the ionic strength of the sample solution, thus circumventing the Debye screening in physiological fluids; however, it is subject to variations in device properties between steps since slow changes in background conductance are not

followed. Other reported methods include using smaller receptors, such as aptamers [53] or antibody fragments [54], and adding biomolecule permeable polymer layers to the FET sensor [56], as discussed in Sect. 10.4.3.

The long-term stability of the NW nanoelectronic devices in physiological studies has also been investigated [71]. Coated with a thin layer of  $\text{Al}_2\text{O}_3$ , SiNW-FETs yield long-term stability (>4 months) in physiological model solutions at 37 °C. Notably, coating with  $\text{Al}_2\text{O}_3/\text{HfO}_2$  layers has suggested that an even longer of stability of >1 year is possible for SiNW-FETs in physiological model solutions. These latter results suggest the potential of the SiNW-FETs for long-term chronic in vivo studies in animals and biomedical implants.

## 10.5 Future Directions and Challenges

Over the last decade, remarkable research progresses have been achieved on the design and implementation of semiconductor NW sensors. In this chapter, we have illustrated how the NW-based FET sensors modified with specific surface receptors represent a powerful chemical/biomolecule detection platform. The examples described here summarize several unique capabilities for direct, label-free, real-time, ultrasensitive and highly selective multiplexed detection of proteins, nucleic acids, viruses, and small molecules, and show clearly the potential of these materials and devices to significantly impact disease diagnosis, genetic screening, and drug discovery, as well as offering powerful new tools for research in many areas of disease diagnosis and life sciences.

Nonetheless, there are several areas of scientific study, which if addressed, could further push the limits of this technology for applications. First, one fundamental challenge to the ultrasensitive detection is to obtain well-defined receptor structures on nanodevice surfaces. In part, this reflects difficulties in characterizing receptor-device structure at the single nanodevice level and correlating such results with sensing results. One approach that could address this structural issue at the single device level would be by exploiting the substantial advances in cyro-EM [72, 73], which could yield high-resolution structural information of the organic/biologic/nanodevice interface. A second direction that could improve this critical device-receptor interface would be through exploration of highly-selective, self-limiting covalent chemistry that precisely defines distance and orientation of the receptors. Second, the real-time and multiplexed detection capabilities of nanoelectronic FET sensors for direct analyses of whole blood/serum detection could yield important advances in clinical monitoring and diagnostics. As discussed in Sects. 10.4.3 and 10.4.8, the most critical issue has been overcoming Debye screening in physiological solutions. The new strategy of modifying FET nanodevices with a permeable polymer layer to increase the effective screening length [56] is one promising strategy for achieving real-time detection, although further fundamental studies will be necessary to develop this and/or other approaches to the level of a technology. Third, almost all the nanoFET-based sensors are exclusively

surface-bound devices. For many applications, one of the most impactful directions could be the transformation from on-chip signaling to the in vivo monitoring as an implant. Recent advances in the development of NW-FET arrays embedded in engineered tissue patches [74], which could be implanted, and incorporation of sensors in injectable electronics [75], which is directly implanted in specific tissue, could enable the goal of direct in vivo monitoring.

In the next decade, continued efforts to achieve the capability in controlling the mechanisms of the NW sensor arrays will move beyond current technologies and take advantage of information emerging from genomics and proteomics to improve the diagnosis and treatment of cancer and other complex diseases. We believe that these advances can be developed in simple NW sensor devices that would represent a clear application of nanotechnology and, more importantly, a substantial benefit to the society.

## References

1. S. Vigneshvar, C. Sudhakumari, B. Senthilkumaran, H. Prakash, Recent advances in biosensor technology for potential applications—an overview. *Front. Bioeng. Biotechnol.* **4**, 11 (2016)
2. J. Li, N. Wu, *Biosensors Based on Nanomaterials and Nanodevices* (CRC Press, Boca Raton, 2013)
3. Y. Wang, T. Wang, P. Da, M. Xu, H. Wu, G. Zheng, Silicon nanowires for biosensing, energy storage, and conversion. *Adv. Mater.* **25**(37), 5177–5195 (2013)
4. A. Zhang, C.M. Lieber, Nano-bioelectronics. *Chem. Rev.* **116**(1), 215–257 (2016)
5. K.-I. Chen, B.-R. Li, Y.-T. Chen, Silicon nanowire field-effect transistor-based biosensors for biomedical diagnosis and cellular recording investigation. *Nano Today* **6**(2), 131–154 (2011)
6. F. Patolsky, B.P. Timko, G. Zheng, C.M. Lieber, Nanowire-based nanoelectronic devices in the life sciences. *MRS Bull.* **32**(02), 142–149 (2007)
7. J. Janata, Historical review. Twenty years of ion-selective field-effect transistors. *Analyst* **119** (11), 2275–2278 (1994)
8. Y. Cui, Q. Wei, H. Park, C.M. Lieber, Nanowire nanosensors for highly sensitive and selective detection of biological and chemical species. *Science* **293**(5533), 1289–1292 (2001)
9. C. Li, M. Curreli, H. Lin, B. Lei, F. Ishikawa, R. Datar, R.J. Cote, M.E. Thompson, C. Zhou, Complementary detection of prostate-specific antigen using  $\text{In}_2\text{O}_3$  nanowires and carbon nanotubes. *J. Am. Chem. Soc.* **127**(36), 12484–12485 (2005)
10. R. Yu, C. Pan, Z.L. Wang, High performance of ZnO nanowire protein sensors enhanced by the piezotronic effect. *Energy Environ. Sci.* **6**(2), 494–499 (2013)
11. Y. Wu, Y. Cui, L. Huynh, C.J. Barrelet, D.C. Bell, C.M. Lieber, Controlled growth and structures of molecular-scale silicon nanowires. *Nano Lett.* **4**(3), 433–436 (2004)
12. Y. Cui, Z. Zhong, D. Wang, W.U. Wang, C.M. Lieber, High performance silicon nanowire field effect transistors. *Nano Lett.* **3**(2), 149–152 (2003)
13. F. Patolsky, G. Zheng, C.M. Lieber, Fabrication of silicon nanowire devices for ultrasensitive, label-free, real-time detection of biological and chemical species. *Nat. Protoc.* **1**(4), 1711–1724 (2006)
14. G. MacBeath, S.L. Schreiber, Printing proteins as microarrays for high-throughput function determination. *Science* **289**(5485), 1760–1763 (2000)
15. N. Misra, J.A. Martinez, S.-C.J. Huang, Y. Wang, P. Stroeve, C.P. Grigoropoulos, A. Noy, Bioelectronic silicon nanowire devices using functional membrane proteins. *Proc. Natl. Acad. Sci. U.S.A.* **106**(33), 13780–13784 (2009)

16. T.-W. Lin, P.-J. Hsieh, C.-L. Lin, Y.-Y. Fang, J.-X. Yang, C.-C. Tsai, P.-L. Chiang, C.-Y. Pan, Y.-T. Chen, Label-free detection of protein-protein interactions using a calmodulin-modified nanowire transistor. *Proc. Natl. Acad. Sci. U.S.A.* **107**(3), 1047–1052 (2010)
17. J.H. Chua, R.-E. Chee, A. Agarwal, S.M. Wong, G.-J. Zhang, Label-free electrical detection of cardiac biomarker with complementary metal-oxide semiconductor-compatible silicon nanowire sensor arrays. *Anal. Chem.* **81**(15), 6266–6271 (2009)
18. F.N. Ishikawa, M. Curreli, H.-K. Chang, P.-C. Chen, R. Zhang, R.J. Cote, M.E. Thompson, C. Zhou, A calibration method for nanowire biosensors to suppress device-to-device variation. *ACS Nano* **3**(12), 3969–3976 (2009)
19. R. Tian, S. Regonda, J. Gao, Y. Liu, W. Hu, Ultrasensitive protein detection using lithographically defined Si multi-nanowire field effect transistors. *Lab Chip* **11**(11), 1952–1961 (2011)
20. P.R. Srinivas, B.S. Kramer, S. Srivastava, Trends in biomarker research for cancer detection. *Lancet Oncol.* **2**(11), 698–704 (2001)
21. J.D. Wulffkuhle, L.A. Liotta, E.F. Petricoin, Proteomic applications for the early detection of cancer. *Nat. Rev. Cancer* **3**(4), 267–275 (2003)
22. G. Zheng, F. Patolsky, Y. Cui, W.U. Wang, C.M. Lieber, Multiplexed electrical detection of cancer markers with nanowire sensor arrays. *Nat. Biotechnol.* **23**(10), 1294–1301 (2005)
23. E. Stern, J.F. Klemic, D.A. Routenberg, P.N. Wyrembak, D.B. Turner-Evans, A.D. Hamilton, D.A. LaVan, T.M. Fahmy, M.A. Reed, Label-free immunodetection with CMOS-compatible semiconducting nanowires. *Nature* **445**(7127), 519–522 (2007)
24. A. Ganguly, C.-P. Chen, Y.-T. Lai, C.-C. Kuo, C.-W. Hsu, K.-H. Chen, L.-C. Chen, Functionalized GaN nanowire-based electrode for direct label-free voltammetric detection of DNA hybridization. *J. Mater. Chem.* **19**(7), 928–933 (2009)
25. J.-I. Hahm, C.M. Lieber, Direct ultrasensitive electrical detection of DNA and DNA sequence variations using nanowire nanosensors. *Nano Lett.* **4**(1), 51–54 (2004)
26. Z. Li, Y. Chen, X. Li, T. Kamins, K. Nauka, R.S. Williams, Sequence-specific label-free DNA sensors based on silicon nanowires. *Nano Lett.* **4**(2), 245–247 (2004)
27. N. Lu, A. Gao, P. Dai, S. Song, C. Fan, Y. Wang, T. Li, CMOS-compatible silicon nanowire field-effect transistors for ultrasensitive and label-free microRNAs sensing. *Small* **10**(10), 2022–2028 (2014)
28. P.E. Nielsen, M. Egholm, R.H. Berg, O. Buchardt, Sequence-selective recognition of DNA by strand displacement with a thymine-substituted polyamide. *Science* **254**(5037), 1497–1500 (1991)
29. K.K. Jensen, H. Ørum, P.E. Nielsen, B. Nordén, Kinetics for hybridization of peptide nucleic acids (PNA) with DNA and RNA studied with the BIAcore technique. *Biochemistry* **36**(16), 5072–5077 (1997)
30. G.-J. Zhang, G. Zhang, J.H. Chua, R.-E. Chee, E.H. Wong, A. Agarwal, K.D. Buddharaju, N. Singh, Z. Gao, N. Balasubramanian, DNA sensing by silicon nanowire: charge layer distance dependence. *Nano Lett.* **8**(4), 1066–1070 (2008)
31. Y.L. Bunimovich, Y.S. Shin, W.-S. Yeo, M. Amori, G. Kwong, J.R. Heath, Quantitative real-time measurements of DNA hybridization with alkylated nonoxidized silicon nanowires in electrolyte solution. *J. Am. Chem. Soc.* **128**(50), 16323–16331 (2006)
32. K.A. Cissell, S. Shrestha, S.K. Deo, MicroRNA detection: challenges for the analytical chemist. *Anal. Chem.* **79**(13), 4754–4761 (2007)
33. G.-J. Zhang, J.H. Chua, R.-E. Chee, A. Agarwal, S.M. Wong, Label-free direct detection of MiRNAs with silicon nanowire biosensors. *Biosens. Bioelectron.* **24**(8), 2504–2508 (2009)
34. E.G. Strauss, J.H. Strauss, *Viruses and human disease* (Academic Press, San Diego, 2007)
35. F. Patolsky, G. Zheng, O. Hayden, M. Lakadamyali, X. Zhuang, C.M. Lieber, Electrical detection of single viruses. *Proc. Natl. Acad. Sci. U.S.A.* **101**(39), 14017–14022 (2004)
36. F. Shen, J. Wang, Z. Xu, Y. Wu, Q. Chen, X. Li, X. Jie, L. Li, M. Yao, X. Guo, Rapid flu diagnosis using silicon nanowire sensor. *Nano Lett.* **12**(7), 3722–3730 (2012)



37. G.-J. Zhang, L. Zhang, M.J. Huang, Z.H.H. Luo, G.K.I. Tay, E.-J.A. Lim, T.G. Kang, Y. Chen, Silicon nanowire biosensor for highly sensitive and rapid detection of Dengue virus. *Sens. Actuators B Chem.* **146**(1), 138–144 (2010)
38. W.U. Wang, C. Chen, K.-H. Lin, Y. Fang, C.M. Lieber, Label-free detection of small-molecule–protein interactions by using nanowire nanosensors. *Proc. Natl. Acad. Sci. U.S.A.* **102**(9), 3208–3212 (2005)
39. M.C. McAlpine, H. Ahmad, D. Wang, J.R. Heath, Highly ordered nanowire arrays on plastic substrates for ultrasensitive flexible chemical sensors. *Nat. Mater.* **6**(5), 379–384 (2007)
40. M.C. McAlpine, H.D. Agnew, R.D. Rohde, M. Blanco, H. Ahmad, A.D. Stuparu, W.A. Goddard Iii, J.R. Heath, Peptide–nanowire hybrid materials for selective sensing of small molecules. *J. Am. Chem. Soc.* **130**(29), 9583–9589 (2008)
41. Y. Engel, R. Elnathan, A. Pevzner, G. Davidi, E. Flaxer, F. Patolsky, Supersensitive detection of explosives by silicon nanowire arrays. *Angew. Chem. Int. Ed.* **49**(38), 6830–6835 (2010)
42. Y. Paska, T. Stelzner, S. Christiansen, H. Haick, Enhanced sensing of nonpolar volatile organic compounds by silicon nanowire field effect transistors. *ACS Nano* **5**(7), 5620–5626 (2011)
43. B. Wang, J.C. Cancilla, J.S. Torrecilla, H. Haick, Artificial sensing intelligence with silicon nanowires for ultrasensitive detection in the gas phase. *Nano Lett.* **14**(2), 933–938 (2014)
44. C. Cheng, H.J. Fan, Branched nanowires: synthesis and energy applications. *Nano Today* **7**(4), 327–343 (2012)
45. D. Wang, F. Qian, C. Yang, Z. Zhong, C.M. Lieber, Rational growth of branched and hyperbranched nanowire structures. *Nano Lett.* **4**(5), 871–874 (2004)
46. K.A. Dick, K. Deppert, M.W. Larsson, T. Märtensson, W. Seifert, L.R. Wallenberg, L. Samuelson, Synthesis of branched ‘nanotrees’ by controlled seeding of multiple branching events. *Nat. Mater.* **3**(6), 380–384 (2004)
47. X. Jiang, B. Tian, J. Xiang, F. Qian, G. Zheng, H. Wang, L. Mai, C.M. Lieber, Rational growth of branched nanowire heterostructures with synthetically encoded properties and function. *Proc. Natl. Acad. Sci. U.S.A.* **108**(30), 12212–12216 (2011)
48. L. Manna, D.J. Milliron, A. Meisel, E.C. Scher, A.P. Alivisatos, Controlled growth of tetrapod-branched inorganic nanocrystals. *Nat. Mater.* **2**(6), 382–385 (2003)
49. H. Yan, R. He, J. Johnson, M. Law, R.J. Saykally, P. Yang, Dendritic nanowire ultraviolet laser array. *J. Am. Chem. Soc.* **125**(16), 4728–4729 (2003)
50. S.M. Sze, K.K. Ng, *Physics of Semiconductor Devices*. (Wiley, 2006)
51. X.P. Gao, G. Zheng, C.M. Lieber, Subthreshold regime has the optimal sensitivity for nanowire FET biosensors. *Nano Lett.* **10**(2), 547–552 (2010)
52. E. Stern, R. Wagner, F.J. Sigworth, R. Breaker, T.M. Fahmy, M.A. Reed, Importance of the Debye screening length on nanowire field effect transistor sensors. *Nano Lett.* **7**(11), 3405–3409 (2007)
53. K. Maehashi, T. Katsura, K. Kerman, Y. Takamura, K. Matsumoto, E. Tamiya, Label-free protein biosensor based on aptamer-modified carbon nanotube field-effect transistors. *Anal. Chem.* **79**(2), 782–787 (2007)
54. R. Elnathan, M. Kwiat, A. Pevzner, Y. Engel, L. Burstein, A. Khatchourints, A. Lichtenstein, R. Kantsev, F. Patolsky, Biorecognition layer engineering: overcoming screening limitations of nanowire-based FET devices. *Nano Lett.* **12**(10), 5245–5254 (2012)
55. G.S. Kulkarni, Z. Zhong, Detection beyond the Debye screening length in a high-frequency nanoelectronic biosensor. *Nano Lett.* **12**(2), 719–723 (2012)
56. N. Gao, W. Zhou, X. Jiang, G. Hong, T.-M. Fu, C.M. Lieber, General strategy for biodetection in high ionic strength solutions using transistor-based nanoelectronic sensors. *Nano Lett.* **15**(3), 2143–2148 (2015)
57. J.R. Gong, Label-free attomolar detection of proteins using integrated nanoelectronic and electrokinetic devices. *Small* **6**(8), 967–973 (2010)
58. G. Zheng, *Semiconductor nanowire FET sensors: label-free, ultrasensitive, multiplexed biomolecule detection and biophysical studies* (Harvard University, Cambridge, 2006)

59. P.K. Wong, C.-Y. Chen, T.-H. Wang, C.-M. Ho, Electrokinetic bioprocessor for concentrating cells and molecules. *Anal. Chem.* **76**(23), 6908–6914 (2004)
60. G. Zheng, X.P. Gao, C.M. Lieber, Frequency domain detection of biomolecules using silicon nanowire biosensors. *Nano Lett.* **10**(8), 3179–3183 (2010)
61. M. Weissman,  $1/f$  noise and other slow, nonexponential kinetics in condensed matter. *Rev. Mod. Phys.* **60**(2), 537 (1988)
62. E. Simoen, C. Claeys, On the flicker noise in submicron silicon MOSFETs. *Solid State Electron.* **43**(5), 865–882 (1999)
63. P. Xie, Q. Xiong, Y. Fang, Q. Qing, C.M. Lieber, Local electrical potential detection of DNA by nanowire-nanopore sensors. *Nat. Nanotechnol.* **7**(2), 119–125 (2012)
64. D. Branton, D.W. Deamer, A. Marziali, H. Bayley, S.A. Benner, T. Butler, M. Di Ventra, S. Garaj, A. Hibbs, X. Huang, The potential and challenges of nanopore sequencing. *Nat. Biotechnol.* **26**(10), 1146–1153 (2008)
65. J.-H. Ahn, S.-J. Choi, J.-W. Han, T.J. Park, S.Y. Lee, Y.-K. Choi, Double-gate nanowire field effect transistor for a biosensor. *Nano Lett.* **10**(8), 2934–2938 (2010)
66. M.S. Parihar, A. Kranti, Enhanced sensitivity of double gate junctionless transistor architecture for biosensing applications. *Nanotechnology* **26**(14), 145201 (2015)
67. M.S. Makowski, A. Ivanisevic, Molecular analysis of blood with micro-/nanoscale field-effect-transistor biosensors. *Small* **7**(14), 1863–1875 (2011)
68. K.S. Kim, H.-S. Lee, J.-A. Yang, M.-H. Jo, S.K. Hahn, The fabrication, characterization and application of aptamer-functionalized Si-nanowire FET biosensors. *Nanotechnology* **20**(23), 235501 (2009)
69. E. Stern, A. Vacic, N.K. Rajan, J.M. Criscione, J. Park, B.R. Ilic, D.J. Mooney, M.A. Reed, T.M. Fahmy, Label-free biomarker detection from whole blood. *Nat. Nanotechnol.* **5**(2), 138–142 (2010)
70. G.-J. Zhang, K.T.C. Chai, H.Z.H. Luo, J.M. Huang, I.G.K. Tay, A.E.-J. Lim, M. Je, Multiplexed detection of cardiac biomarkers in serum with nanowire arrays using readout ASIC. *Biosens. Bioelectron.* **35**(1), 218–223 (2012)
71. W. Zhou, X. Dai, T.-M. Fu, C. Xie, J. Liu, C.M. Lieber, Long term stability of nanowire nanoelectronics in physiological environments. *Nano Lett.* **14**(3), 1614–1619 (2014)
72. W. Kühlbrandt, The resolution revolution. *Science* **343**(6178), 1443–1444 (2014)
73. Y. Cheng, Single-particle cryo-EM at crystallographic resolution. *Cell* **161**(3), 450–457 (2015)
74. B. Tian, J. Liu, T. Dvir, L. Jin, J.H. Tsui, Q. Qing, Z. Suo, R. Langer, D.S. Kohane, C.M. Lieber, Macroporous nanowire nanoelectronic scaffolds for synthetic tissues. *Nat. Mater.* **11**(11), 986–994 (2012)
75. J. Liu, T.-M. Fu, Z. Cheng, G. Hong, T. Zhou, L. Jin, M. Duvvuri, Z. Jiang, P. Kruskal, C. Xie, Syringe-injectable electronics. *Nat. Nanotechnol.* **10**, 629–636 (2015)
76. F. Patolsky, G. Zheng, C.M. Lieber, Nanowire sensors for medicine and the life sciences. *Nanomedicine* **1**, 55–65 (2006)

# Chapter 11

## Nanowire Interfaces to Cells and Tissue

**Abstract** The interface between nanosystems and biosystems is emerging as one of the broadest and most dynamic areas of science and technology, bringing together biology, chemistry, physics and many areas of engineering, biotechnology and medicine. The combination of these diverse areas of research promises to yield revolutionary advances in healthcare, medicine and the life science through, for example, the creation of new and powerful tools that enable direct, sensitive and rapid analysis of biological species and cellular activities. Research at the interface between nanomaterials and biology could yield breakthroughs in fundamental science and lead to revolutionary technologies. In this chapter, we will introduce studies focused on building the interface of NWs to cells and tissues, including extracellular and intracellular signal recording, synthetic cyborg tissues and in vivo recording.

### 11.1 Introduction

The field of nanomaterials has the potential to have a particularly high impact on medicine. It is thus appropriate to assess the current state and project the future role of nanotechnology within relevant areas of biomedical science and engineering. Interfacing with cells and tissues, for example, is an especially challenging problem that is unsolved by current technologies [1, 2]. There exist a wide range of health problems that can be treated by stimulation of the nervous system, including hearing loss, chronic pain, incontinence, obesity, and diabetes. Some of these problems, such as paralysis or retinal degeneration, are exceptionally hard to treat. At the same time, the set of medical devices and treatments available to a practitioner in this field for evaluating and treating disorders related to neural tissues is especially limited. This situation is caused in part by the poor accessibility of most of the nervous system and by insufficient development of methods to intercept and alter the transmission of neural signals [3]. This chapter introduces the studies of building the interface of NWs to cells and tissues, including imaging, drug delivery, extracellular and intracellular signal recording, synthetic cyborg tissues and in vivo recording.

## 11.2 Nanowire/Cell Interfaces and Electrophysiological Recording

Electrophysiology is an important approach to investigate and understand bio-electrical signals and activity in the body, including but not limited to, the brain, heart, and muscles [4]. For instance, neurons are the elementary processing units in the brain, and are organized and interconnected into complex networks. Information in neural networks is processed by the opening and closing of ion channels on the membrane, producing action potentials (APs) that propagate within cells and between interconnected cells. Electrophysiological recording and decoding of the functional connectivity in brain is central to basic neuroscience research.

In addition, a variety of imaging techniques have been developed for the purpose of brain mapping, such as magnetic resonance imaging (MRI) and positron emission tomography (PET) [5–7]. Although these noninvasive methods offer coarse views, they cannot be used to analyze neural networks. To this end, many optical methods have emerged for both recording and stimulating signal propagation in neural circuits [8–13]. However, optical approaches also have limitations, including difficulty of accessing deep brain activity and of obtaining simultaneously high spatial and temporal resolution. NW-based bioelectronics has the potential to allow multiplexed, long-term, and deep-brain detection of neural activity with high spatiotemporal resolution. More generally, nanotechnology offers a number of opportunities for brain science [1, 2, 14–17].

### 11.2.1 *Traditional Extracellular Electrophysiological Recording*

#### 11.2.1.1 Principles of Extracellular Recording

An active cellular process in electrogenic cells is accompanied by ionic current flows across the cell membrane, which change both the intracellular and extracellular potentials. A microelectrode positioned near to the outer membrane can in principle detect an extracellular potential change, and is termed extracellular recording. Two common recording paradigms are based on passive metallic microelectrodes and active transistor electrodes. In the former case, the extracellular potential induces an interfacial electric current owing to the electrochemical impedance, while for the latter, the extracellular potential acts as a gate modulating the transistor conductance. In both cases, the output signal is closely related to the interface between cell and device.

### 11.2.1.2 Passive Metallic Microelectrodes and Their Scaling Limits

In 1972, Thomas et al. [18] described a planar multielectrode array for use in recording from cultured cells. This technique is now referred to as a microelectrode arrays (MEAs) and has been widely applied to record neural activity [19]. In an MEA, each electrode is connected to a recording amplifier for signal processing and has the potential for recording single-unit spike activity from each electrode at the same time. This capability makes MEAs a useful tool for the investigation of fast network dynamics both *in vitro* [20–22] and *in vivo* [23, 24]. In addition to recording signals from cells, MEAs are also capable of stimulating them [25]. A limiting feature of conventional MEAs is the relatively large electrode sizes, 10–30  $\mu\text{m}$  diameters for recording (100–200  $\mu\text{m}$  for stimulation), similar to or larger than the size of neuron soma. Reduction of the size of metal electrodes could increase their spatial resolution, but also leads to an increase in impedance that results in larger thermal noise and smaller recording amplitudes [26, 27]. To overcome this impedance limitation, surface modification methods that increase the effective electrode surface area have been employed [28–31].

### 11.2.1.3 Active Transistor Electrodes

In 1991, Fromherz and coworkers reported coupling and extracellular recording from neuron cells using planar Si FETs [32], including mammalian cells [33]. As an alternative to metallic microelectrodes, electrolyte-oxide-silicon field-effect transistors (EOS-FETs) and their arrays can be fabricated by standard industrial CMOS technology, and have been actively investigated for a further improvement of signal detection capabilities in electrophysiological recording.

### 11.2.1.4 Extracellular Electrode/Cell Interfaces

The electrode/cell interface for passive and active electrodes plays a central role in extracellular recording since it affects the signal amplitude and shape as well as noise levels. A general goal for improving the electrode/cell interface involves decreasing their separation in order to increase the electrode/cell seal resistance [26]. When neurons are cultured on a recording device, a gap or cleft exists between the electrode and cell membrane [34–36], where this cleft determines the seal resistance. Methods to promote cell adhesion and reduce the cleft/increase seal resistance include surface modification, substrate modulation and electrode shape control. For example, self-assembled monolayer modified MEAs have been reported to significantly improve device performance [37–39]. Surface patterned MEAs have also been employed to immobilize cultured neurons to enhance coupling [40, 41]. In addition, studies of electrodes with 3D tips have been shown to promote cell membrane wrapping around the tips, thus resulting in improved seal resistances compared to flat and recessed electrodes [35, 42].

## 11.2.2 Nanowire Transistors for Extracellular Recording

### 11.2.2.1 Extracellular Recording from Cultured Neurons

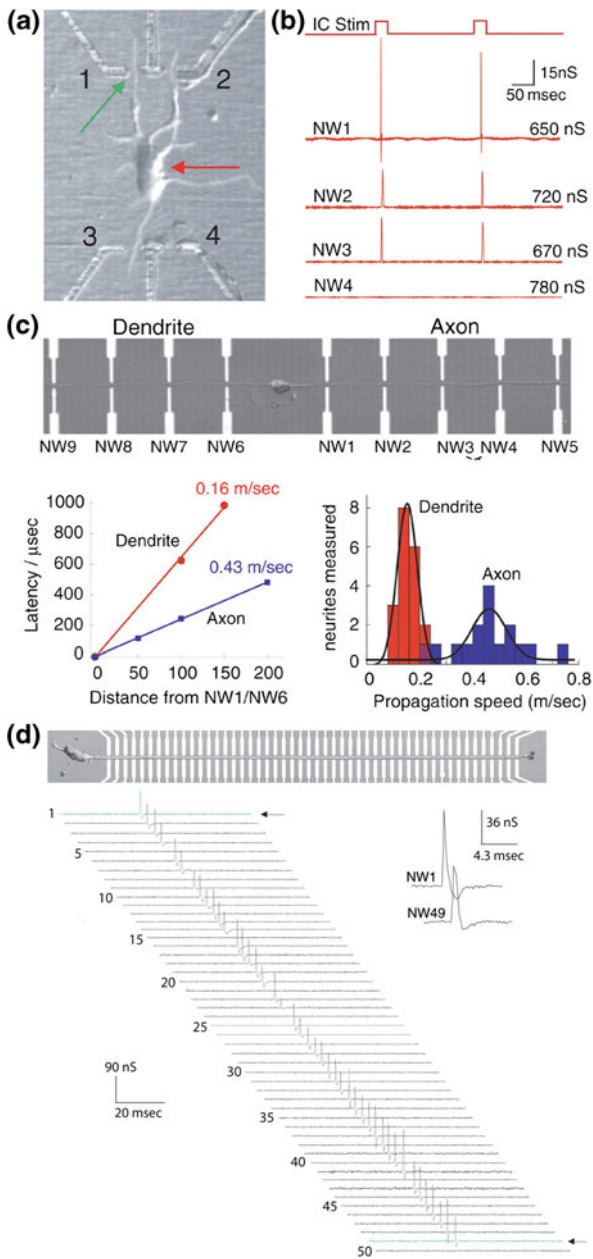
The Lieber group first applied SiNW-FETs for extracellular recording from cultured mammalian neurons in 2006 [43]. They adopted the bottom-up paradigm to fabricate the SiNW-FETs and passivated the arrays for cell-culture. For example, they showed that polylysine patterning could promote the patterned growth of neuronal projections (axons and dendrites) over arrays of four SiNW-FETs (Fig. 11.1a). At each point where the axon or dendrite crosses a NW device, a highly localized  $0.01\text{--}0.02\ \mu\text{m}^2$  synapse-like junction is formed, which allows for multisite recording with multiple SiNW-FET devices from single neurons in contrast to the typical one neuron per electrode achieved with MEA and planar FETs.

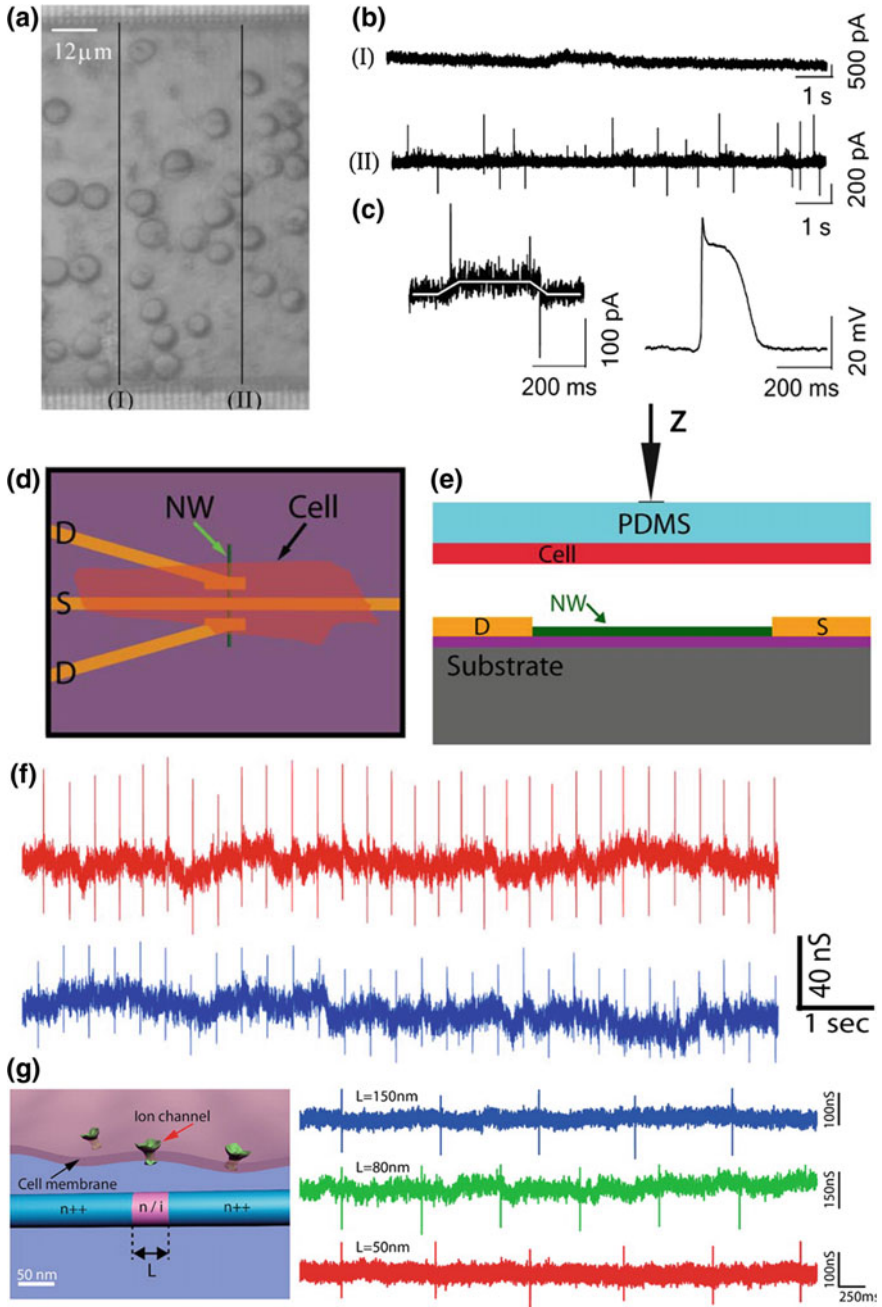
This general approach was used to investigate action potential spike propagation in several multiplexed SiNW-FET/neuron configurations. For example, in the above configuration one SiNW was used as a local input to elicit action potential spikes that were recorded from two other SiNW devices with dendrite junctions while the fourth SiNW, which is not interfaced with either an axon or dendrite, served as a control and showed no action potential signal (Fig. 11.1b). In addition, SiNW/neuron configurations were designed to investigate the spike propagation in axons and dendrites. As shown in Fig. 11.1c, multiple SiNWs forming junctions with a single dendrite and axon revealed signal propagation rates of 0.16 m/s for the dendrite and 0.43 m/s for the axon. The potential to extend this approach to highly integrated systems was also shown with a configuration containing 50 independently addressable NW-axon elements for a single neuron (Fig. 11.1d). Overall, these results showed early on the potential for SiNW-FET sensors to enable multiplexed recording with subcellular spatial resolution from neurons.

### 11.2.2.2 Extracellular Recording from Cardiac Cells

Cardiomyocytes represent another electrogenic cell type that have been extensively studied with bioelectronic devices. The groups of Chen [44] and Lieber [45] carried out extracellular recording from cardiac cells using SiNWs synthesized by top-down and bottom-up approaches, respectively. An advantage of top-down fabricated NWs is the capability to define (during fabrication) their length such that measurements across an entire cell membrane or simultaneous measurement from multiple cells can be made (Fig. 11.2a–c). In the work of Chen and coworkers [44], cultured cardiomyocytes on NW chips exhibited rhythmic transient changes in the device conductance after 1–2 days involving an up-stroke current spike followed by a down-stroke one. The authors attributed the paired spikes to the onset and end of an AP, although this contrasts most other work in the literature [45–48]. Specifically, typical extracellular recordings show only one peak associated with the rapid potential change due to sodium-ion channel opening.

**Fig. 11.1** **a** Optical image of a NW-neuron interface. **b** Neuron stimulation and resulting NW electrical responses. NW4 is not in contact with any neurites. **c** Propagation studies using the multi-NW—neurite structures. *Top* Optical image of the settings. *Bottom* Relation of latency time with distance and histogram of propagation speed. **d** Aligned axon crossing a 50-NW device array and corresponding signal propagation data. Reproduced from [43]. Copyright 2006 the American Association for the Advancement of Science







◀ **Fig. 11.2** Interfacing SiNW-FETs with cardiomyocytes for extracellular recording. **a** Long NWs fabricated by top-down paradigm. Isolated cardiomyocytes are cultured on the NW chip, where the *dark lines* denoted two NWs, I and II. **b** Currents measured by NW I and II. A series of transient current events are observed for NW II because it is covered by a contracting myocyte. **c** Typical results from NW II (*left*) compared to the intracellular action potential recorded with a nanopipette (*right*). Reproduced from [44]. Copyright 2009 John Wiley & Sons, Inc. **d, e** Schematic of a cardiomyocyte on a NW-FET device and the displacement ( $Z$ ) of the PDMS/cell substrate. **f** Two traces recorded with different  $Z$  values. Reproduced from [45]. Copyright 2009 National Academy of Sciences of the United States of America. **g** Point-like recording using a short-channel NW fabricated by bottom-up paradigm. *Left* Schematic of the short-channel FET-cell interface, where the active channel size is comparable to that of a few ion channels. *Right* Typical signals of beating cardiomyocytes from devices with channel lengths of 150 (*blue*), 80 (*green*) and 50 nm (*red*). Reproduced from [49]. Copyright 2012 American Chemical Society

Multiplexed measurements made with bottom-up SiNW-FET device arrays interfaced with cultured embryonic chicken cardiomyocytes showed single biphasic peaks associated with each AP of the beating cells [45] (Fig. 11.2d–f). To investigate the signal propagation within cardiomyocyte monolayers, an average spacing between adjacent SiNW-FETs in the array was set around 300  $\mu\text{m}$ . Multiple SiNW-FETs in contact with cardiomyocytes were simultaneously recorded, and showed stable field potential spikes with high signal-to-noise ratio ( $>10$ ). The large signal magnitude indicates a good junction, and therefore a large seal resistance, exists between SiNW-FETs and cardiomyocytes. Later, the same group [49] synthesized SiNWs encoded with active FET channel lengths of 50, 80, and 150 nm (Fig. 11.2g). These devices were interfaced to cardiomyocytes and the conductance-time response of action potentials was recorded. Significantly, while the peak-to-peak voltage and signal-to-noise ratio showed little variation versus channel length, the deduced peak-to-peak extracellular action potential width of  $\sim 500 \mu\text{s}$  was found to be comparable to the reported time constant for individual sodium ion channels. In longer or large devices, the extracellular action potential widths are typically  $\geq 1 \text{ ms}$ , presumably due to averaging over a number of

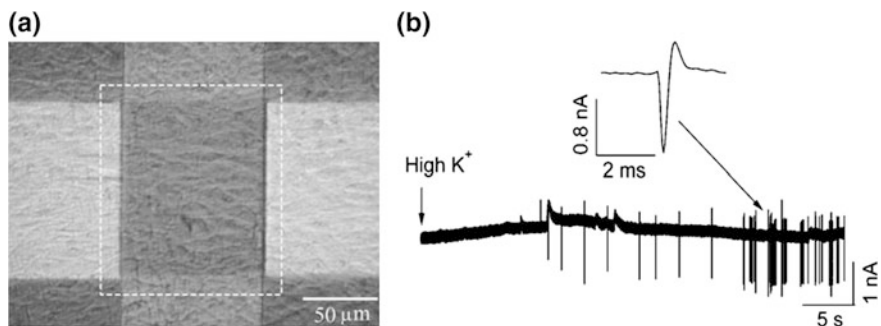


**Fig. 11.3** SiNW interfaced to aortic smooth muscle cells. **a** Rat aortic smooth muscle cells (A7r5) on the NW chip, in which the *dashed square* depicts the sensing area. **b** NW recorded current signals induced by membrane depolarizing in high concentration  $\text{K}^+$  solution. Reproduced from [44]. Copyright 2009 John Wiley & Sons, Inc

channels. These results thus suggest the possibility to monitor ion channel activity using short-channel NW-FET devices. In addition, Eschermann et al. [48] evaluated the signal shape recorded from spontaneous activity of cardiac muscle HL-1 cells with SiNW transistors fabricated by top-down process. It is worth mentioning that they also used diamond transistor array for recording HL-1 and HEK293 cells transfected with potassium channels [50].

### 11.2.2.3 Extracellular Recording from Other Electrogenic Cells

SiNW-FET devices have also been used to investigate electrophysiological properties of other types of electrogenic cells. For example, Chen and coworkers [44] investigated the electrical activities of rat aortic smooth muscle cells (A7r5) as shown in Fig. 11.3, where each NW was in contact with multiple cells. A series of current spikes was recorded by the NW upon introduction of a solution containing a high concentration of potassium ions with each spike having a biphasic signal with durations of  $\sim 1$  ms similar to recording from cardiomyocytes [45, 48] but nearly two orders of magnitude shorter than that of typical intracellular action potential of A7r5 cells [51, 52]. As discussed above this is consistent with the NWs recording the initial rapid inward sodium current, which contributes to the initial depolarization of the action potential recorded with the patch-clamp, but not subsequent slower repolarizing steps.

## 11.2.3 *Intracellular and Intracellular-like Electrophysiological Recording*

### 11.2.3.1 Strengths and Constraints of Intracellular Measurements

In general, noninvasive extracellular recording has advantages for long-term multiplexed measurements. However, extracellular recording sacrifices one-to-one correspondence between cells and electrodes, and also suffers from other fundamental limitations such as reduced signal strength and quality, and difficulty in recording sub-threshold events [53]. Intracellular recording can overcome all of these limitations, although not without other challenges. For example, the patch clamp methodology [54, 55], which is the most widely used intracellular recording technique, requires the formation of direct ionic and/or electrical junctions between the probe tip and the cytosol, which has several limitations. First, the probe tip size needs to be within  $0.2\text{--}5\ \mu\text{m}$ : small enough to ensure penetrating the cell membrane without major damage, but also large enough to produce a low junction impedance needed for recording small cellular signals. Second, irreversible changes occur to the cell when it is directly exposed to external probe surfaces and electrolytes, thus limiting the capability for long-term recording. Third, the relatively large size of the pipettes and associated 3D manipulators limit potential integration for multiplexed

measurements. With these limitations in mind, it is possible to define the characteristics of an ideal electronic device for intracellular recording; this device should possess (i) a small size to minimize invasiveness and potentially allow for direct contact with subcellular structures, (ii) high sensitivity and signal fidelity as size is decreased, and (iii) the capability to achieve multiplexed recording at both single cell and cell network levels. Over the past several years, solid-state nanoFET based devices have demonstrated capabilities that may allow for accurate, fast, and multiplexed intracellular recording [2, 56–58].

### 11.2.3.2 Intracellular-Like Recording with Protruding Metal Electrodes

The existence of an extracellular cleft between the living cell membranes and the planar substrate used to support recording devices can reduce electrical coupling

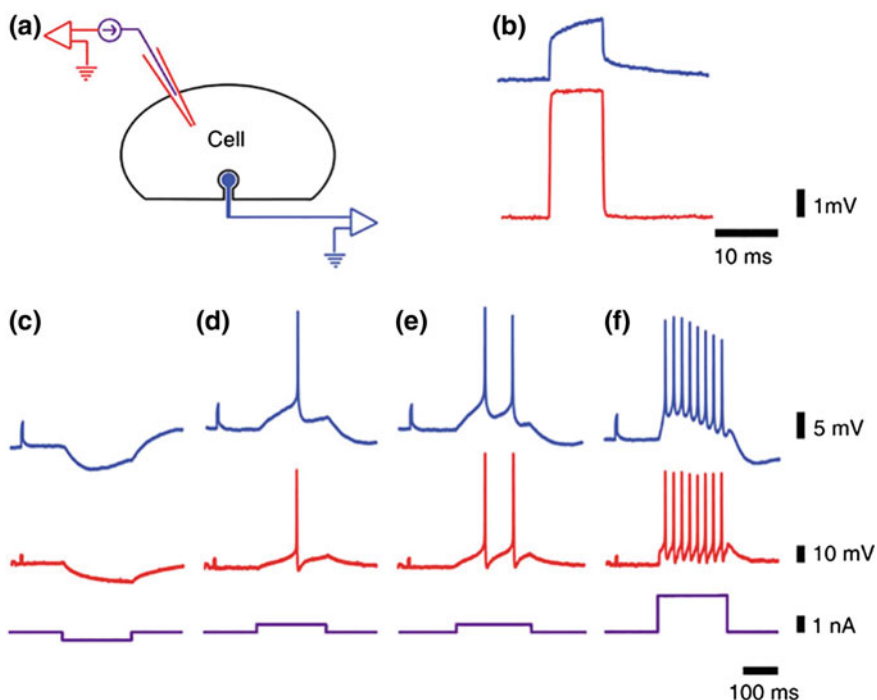
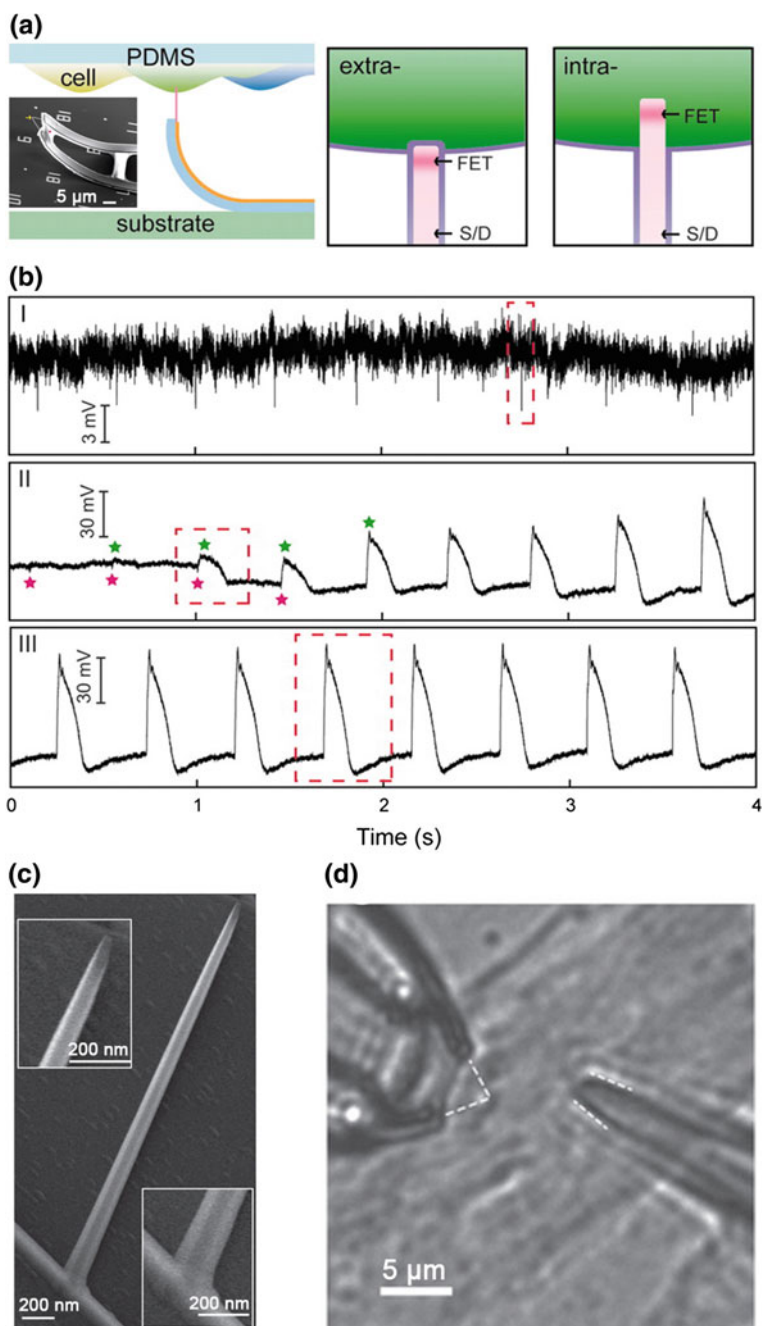


**Fig. 11.4** Intracellular-like recordings with FGSEs. **a** Experimental setup with one cell interfaced to a single glass microelectrode (*red*) and FGSE (*blue*). **b** Calibrated recording from the intracellular microelectrode (*red*) and FGSE (*blue*) for a pulse of 5 mV, 20 ms. **c** A hyperpolarizing current pulse (*purple*) induced hyperpolarization recorded by the intracellular microelectrode (*red*) and the FGSE (*blue*). **d–f** Depolarizing currents generated action potentials with amplitudes of  $\sim 50$  mV (intracellular microelectrode, *red*) and  $\sim 25$  mV (FGSE, *blue*). Reproduced from [61]. Copyright 2010 Nature Publishing Group



◀ **Fig. 11.5** Intracellular recordings with SiNW-FETs. **a** Schematics of cellular recording from a cardiomyocyte monolayer on PDMS support (*left*) and extracellular (*middle*) and intracellular (*right*) NW/cell interfaces. Inset is an SEM image of the kinked nanowire device. Purple lines denote the cell membrane and NW lipid coating. **b** Plots corresponding to (i) extracellular, (ii) extracellular to intracellular transition, and (iii) steady-state intracellular recording. Reproduced from [46]. Copyright 2010 American Association for the Advancement of Science. **c** A branched SiO<sub>2</sub> nanotube integrated on top of a SiNW transistor. Reproduced from [66]. Copyright 2012 Nature Publishing Group. **d** Optical image of a kinked NW probe (*left*) and patch-clamp pipette (*right*) recording from the same cell. Reproduced from [68]. Copyright 2014 Nature Publishing Group

and corresponding signal levels. As discussed above in Sect. 11.2.1.4, a number of approaches have focused on decreasing the cleft size and consequently increasing the seal resistance as a means to enhance signals. Spira and coworkers [42, 59–61] significantly increased the seal resistance by functionalizing micrometre-size mushroom-shaped gold protrusions, thereby forming tight coupling with the cell membrane. This approach was further confirmed by Offenhäusser and coworkers [62]. Systematic investigations of the cleft width between the plasma membrane and protruding gold electrode surfaces reveal that these structures significantly enhance the contact, in particular at the protruding head region. As an example, studies of an *Aplysia* neuron cultured on a chemically functionalized gold-spine electrode (FGSE) and simultaneously interrogated with a patch-clamp microelectrode (Fig. 11.4) showed several key points. First, injection of a hyperpolarizing current with the patch-clamp electrode yielded a 10 and 5 mV recorded polarizations using the patch-clamp and FGSE (Fig. 11.4c). In addition, injection of depolarizing currents led to the observation of intracellular action potentials that were temporally correlated between the patch-clamp and FGSE (Fig. 11.4d–f), although the amplitudes were approximately twofold smaller for the FGSE (25 mV) versus the patch clamp (50 mV). These observations demonstrate that functionalized FGSEs can record intracellular-like responses from electrogenic cells and thus provide significant information beyond that obtained from conventional planar metallic microelectrodes and MEAs.

### 11.2.3.3 Intracellular 3D Nanowire Transistors

The nanoscale dimensions of SiNW-FETs make them potentially ideal as intracellular probes because (i) their small size should allow for minimally-invasive insertion and (ii) the FET device holds the promise for the true intracellular recording since it is nearly independent of interfacial impedance in contrast to passive electrode techniques. Nevertheless, the overall size of all conventional nanoFETs, which have a linear device geometry, is much larger than active FET component due to the source and drain electrical contacts. The necessity of having two contacts makes minimally-invasive insertion of a nanoFET into cells difficult if not impossible.

A break-through that first overcame this geometry-size constraint was achieved with synthesis on nonlinear kinked NWs [63]. The kinked structure allows for localization of a point like FET detector at the kinked NW tip, metal contacts geometrically-removed from this probe tip (Fig. 11.5a) thereby allowing for the realization of bioprobes capable of facile intracellular recordings [46]. An interesting feature of these nanoFET probes was modification with phospholipid bilayers to promote spontaneous cellular internalization without external forces. Indeed, contact of cultured cardiomyocyte cells to a 3D kinked SiNW bioprobe showed three distinguishable recording stages during internalization (Fig. 11.5b). Initially, only an extracellular action potential was observed, and then after ca. 40s, the extracellular signal gradually disappeared with concomitant increase in a new signal consistent with the intracellular action potential. Finally, at steady state an intracellular action potential with average peak amplitude of  $\sim 80$  mV and duration of  $\sim 200$  ms was recorded, which is consistent with true intracellular recording.

Following this pioneering work, 3D FET-based NW-nanotube and kinked  $p$ - $n$  junctions nano-bioprobes were also investigated for intracellular recordings [64–69]. For example, recording using branched nanotube-NWs was reported in 2012 [66]. In this work, a branched SiO<sub>2</sub> nanotube was synthetically integrated on a SiNW transistor (Fig. 11.5c), modified with a phospholipid bilayer, which allowed penetration through cardiomyocyte cell membranes, followed by intracellular action potential recording by the SiNW-FET. The intracellular potential functions as an electrolyte gate through the nanotube, thereby modulating the conductance of the nanoFET. Significantly, by using multiple branched SiNW-FETs, the authors demonstrated multiplexed intracellular electrical recordings from both single cells and cell networks.

A limitation of these chip-based 3D nano-bioprobes has been a difficulty in exploiting the nanometer-scale probe resolution in a deterministic manner to record from specific cell regions and/or subcellular structures. To overcome this limitation, Qing et al. [68] fabricated free-standing probes with a kinked SiNW nanoFET sensors. Under a standard microscope, these probes were manipulated in 3D space to target specific regions and obtain stable, full-amplitude intracellular action potential spikes. Compared to the signal measured from patch-clamp probes on the same cell, the free-standing NW probe showed the same amplitude and temporal properties (Fig. 11.5d), thus demonstrating the capability to record true intracellular (vs. intracellular-like) properties.

The substantial progress in intracellular recording described above was made possible by the availability of nanostructures with similar characteristic length scales to natural biological functional substructures. Semiconductor NW building blocks excel among nanomaterials in their capabilities to be rationally designed and synthesized with complex motifs with near molecular-scale precision. It is worth noting that applications of semiconductor NWs in biology are still at an early stage with future research needed to better understand and ultimately exploit the biochemical mechanisms yield nanoFET-cell interfaces.

### 11.2.3.4 Intracellular MEA-Based Nanopillars

Substantial effort has also been placed on the development of vertical NW electrode arrays. In 2012, Park and coworkers [70] demonstrated parallel electrical interfacing to mammalian neurons using vertical NW electrode arrays (Fig. 11.6a–c). The NWs in the arrays were 150 nm in diameter and 3  $\mu\text{m}$  in height with Ti/Au metallic tips, where each addressable electrode consisted of 9 NWs. To achieve recording it was necessary to apply voltage/current pulses, which can electroporate the cell membrane, although the spike amplitudes was much smaller than true intracellular signals (Fig. 11.6d). In parallel, Cui and coworkers [71] reported using vertical Pt NWs electrodes (150 nm in diameter and 1–2  $\mu\text{m}$  in height) to record extracellular and intracellular action potentials from cultured cardiomyocytes, although the peak amplitudes were less than full-amplitude intracellular action potential. This work also used electroporation to assist short-term penetration of NWs across the cell

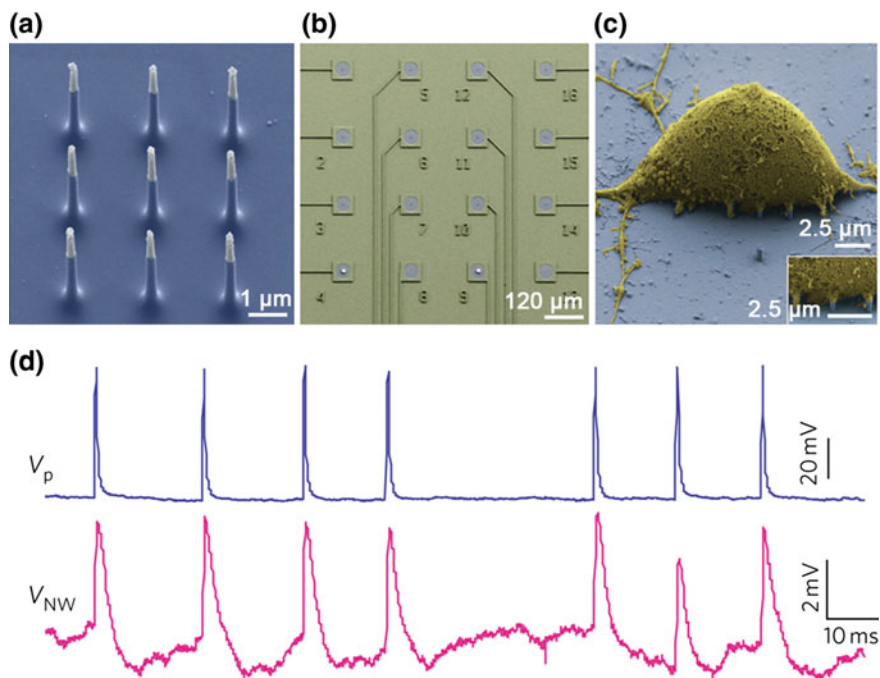


**Fig. 11.6** **a** SEM image of a vertical NW electrode array. **b** Stimulation/recording pads for multi-site interrogation of neuronal circuits. **c** A rat cortical cell on the NW array. **d** Action potentials stimulated using a patch pipette (*blue*) and recorded by the NW array (*magenta*). Reproduced from [70]. Copyright 2012 Nature Publishing Group

membrane. In these two vertical metallic NW studies, the intracellular-like access gained by electroporation was transient, in contrast to the long-term access of lipid-coated SiNW-FETs reported by the Lieber group. Notably, Melosh and coworkers have also shown that proper surface functionalization can help electrodes similar to the Park and Cui studies to gain intracellular access [72–75].

More recently, Cui and coworkers [76] have reported MEA-based nanoelectrodes consisting of iridium oxide ( $\text{IrO}_2$ ) nanotubes. When these  $\text{IrO}_2$  nanotube-based chips were used as a substrate for cardiomyocytes culture, they reported that the cell membrane wrapped around the vertical nanotubes and protruded into the hollow spacing between adjacent nanotubes, thus suggesting that the nanotube array geometry could be beneficial for creating tight cell-electrode junctions similar to that achieved with FGSEs. Consistent with this structural observation, the authors observed larger and more stable intracellular action potentials from the beating cardiomyocytes with amplitudes closer to expected full amplitude measured with patch-clamp micropipettes.

The above results show that vertical NWs can bridge microelectrode-cell interfaces and allow direct access to intracellular information like micron-scale gold spine electrodes [42, 59–61]. However, the current vertical NW MEAs have several limitations, including (i) high electrochemical impedance due to the small contact area, which has generally been overcome by using multiple NWs as a single electrode, and (ii) recorded intracellular potentials that are about ten times lower than the patch-clamp signals. Future research on the effects of NW surface modification should be investigated to improve the internalization of these NW-based MEA electrodes as well as cell sealing, which could improve the stability and signal-to-noise ratio of the observed signals.

### 11.3 Nanowire-Tissue Interfaces and Electrophysiological Recording

Making effective electrode-tissue interfaces requires consideration of the interfacial contact between electrodes and the 3D cell networks comprising functional tissues. In this regard, the position, shape, and size of an electrode with respect to the target tissue are all critical factors determining this contact or coupling. Moreover, given the intrinsic 3D interconnectivity of cells in tissues, consideration of the mechanical properties and connectivity of the nanoelectronic devices will also be critical. These latter factors are typically not considered in recording from single cells for 2D in vitro cell cultures. Previously, several different types of micro- and nanostructures based electrodes have been used as tools for interfacing to tissues [77–80], although they are outside the scope of this book. Below we will introduce cutting-edge studies that have exploited SiNW-FETs for interfacing to brain and heart tissues, and additionally, will summarize how their integration into flexible electronics can open up new opportunities in bioelectronics.

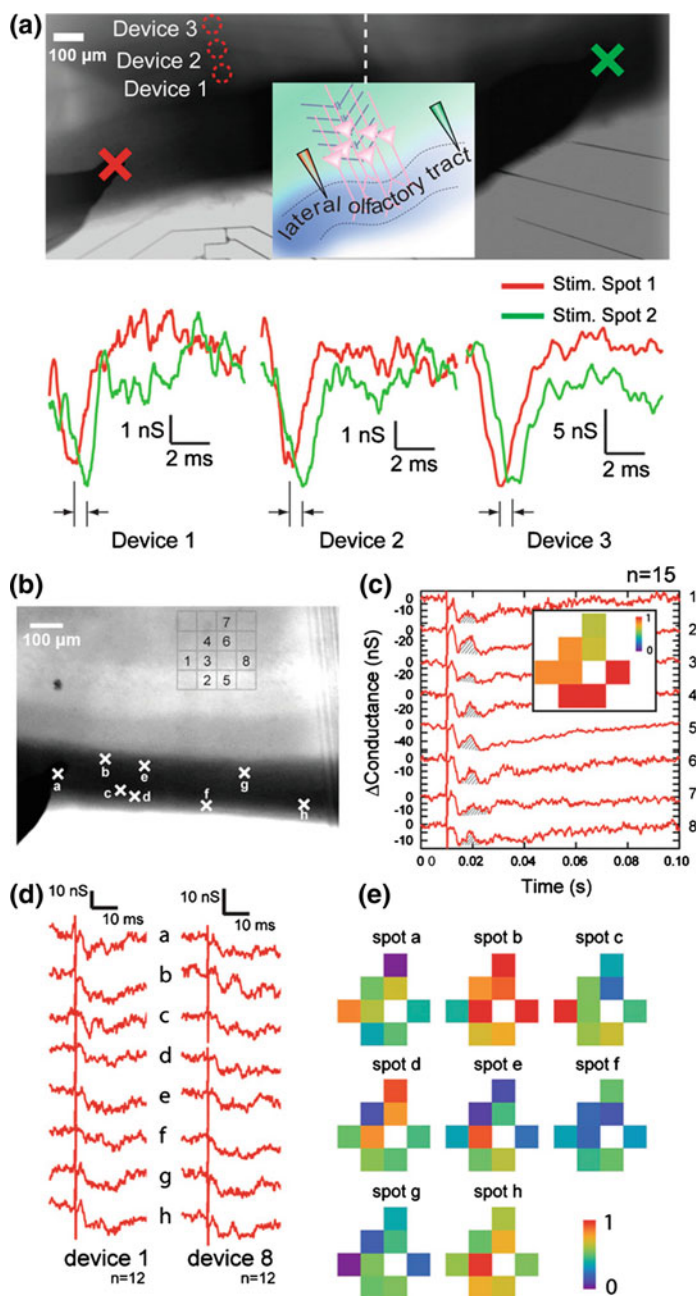


### ***11.3.1 Acute Brain Slice Studies with Nanowire Transistors***

In 2010, Qing et al. [47] reported studies of SiNW-FET arrays fabricated on transparent substrates that were interfaced to acute brain slices to yield sub-millisecond temporal resolution and better than 10  $\mu\text{m}$  spatial resolution. The transparent device chip allowed for imaging of individual cell bodies and identifying areas of healthy neurons on both upper and lower tissue surfaces. The small active device area ( $0.06 \mu\text{m}^2$ ) and array spacing (3  $\mu\text{m}$ ) enable highly localized multiplexed measurements of neuronal activities and, for example, provided information addressing signal propagation in the lateral olfactory tract and functional neural connectivity in the olfactory cortex. Figure 11.7a shows a NW-FET array under an acute brain slice that was stimulated at different locations. Based on the time and distance difference for stimulation, it was possible to estimate a propagation rate 1.6–2 m/s in the lateral olfactory tract. To demonstrate the capability to probe the activity patterns, eight devices within a four-by-four array were simultaneously monitored while stimulating at eight different locations in the lateral olfactory tract (Fig. 11.7b). Similar responses are obtained by each device irrespective to the stimulation positions after a strong stimulation that can activate all axons fibers, as revealed in Fig. 11.7c. Reducing the stimulation intensity, such that only a limited number of axon are activated, yielded data (Fig. 11.7d) that unambiguously revealed device specific features. In this weak stimulation regime, 2D activity maps from all eight devices (Fig. 11.7e) demonstrated clearly heterogeneous activity and unique pairwise activity correlations for different stimulation spots. For example, the signals from devices 1 and 8 showed close correlation for 5/8 stimulation spots while those from devices 3 and 4 show close correlation for only 3/8 stimulation spots. These studies provided the first example of how highly-localized direct electrical recording from intact neural networks using nanoelectronic devices could serve as a powerful approach to visualize the dynamic, functional neural networks and thus provide key information necessary to understand circuits and plasticity.

### ***11.3.2 Cardiac Tissue Studies with Nanowire Transistors***

Spontaneously beating embryonic chicken hearts were also studied using bottom-up SiNW-FETs on planar substrates [81] (Fig. 11.8a, b). The bottom-up fabrication process yields protruding NW-FET channels from the underlying chip, and thus can enhance coupling to heart tissue. Simultaneous recordings from a beating heart using a NW-FET and a conventional glass pipette (Fig. 11.8c) showed close temporal correlation except for a  $\sim 100$  ms delay in the NW-FET peak consistent with the separation of electrodes. Individual signals recorded from FET devices exhibited two characteristic components; that is, initial fast and subsequent slower ones. Further measurement made with and without blebbistatin, which prevents



◀ **Fig. 11.7** **a** *Top* optical image of an acute brain slice covering a linear array of NW-FETs with the array perpendicular to the lateral olfactory tract fiber. *Red circles* denote three devices for recording while the crosses denote the positions of two stimulation electrodes, corresponding to distances ca. 400 (*red*) and 1200  $\mu\text{m}$  (*green*) from the NW array. Inset is a schematic of the experimental configuration. *Bottom* Conductance versus time traces from devices 1–3 following stimulation at *red* and *green crosses*, respectively; the curves correspond to averages of 8 recordings. **b** Optical image of an acute slice covering a  $4 \times 4$  NW-FET array. Numbers 1–8 denote the device positions while the crosses denote the eight stimulation spots. **c** Averaged signals from 15 recordings following stimulation (200  $\mu\text{s}/400 \mu\text{A}$  pulses). Inset is the normalized map of the signal intensity from the 8 devices deduced from the *shaded area* in each trace. **d** Representative recordings (averaged from 12) from devices 1 and 8 for stimulations at spots a–h (200  $\mu\text{s}/100 \mu\text{A}$  pulses). **e** Maps of the relative signal intensity for devices 1–8. Reproduced from [47]. Copyright 2010 National Academy of Sciences of the United States of America

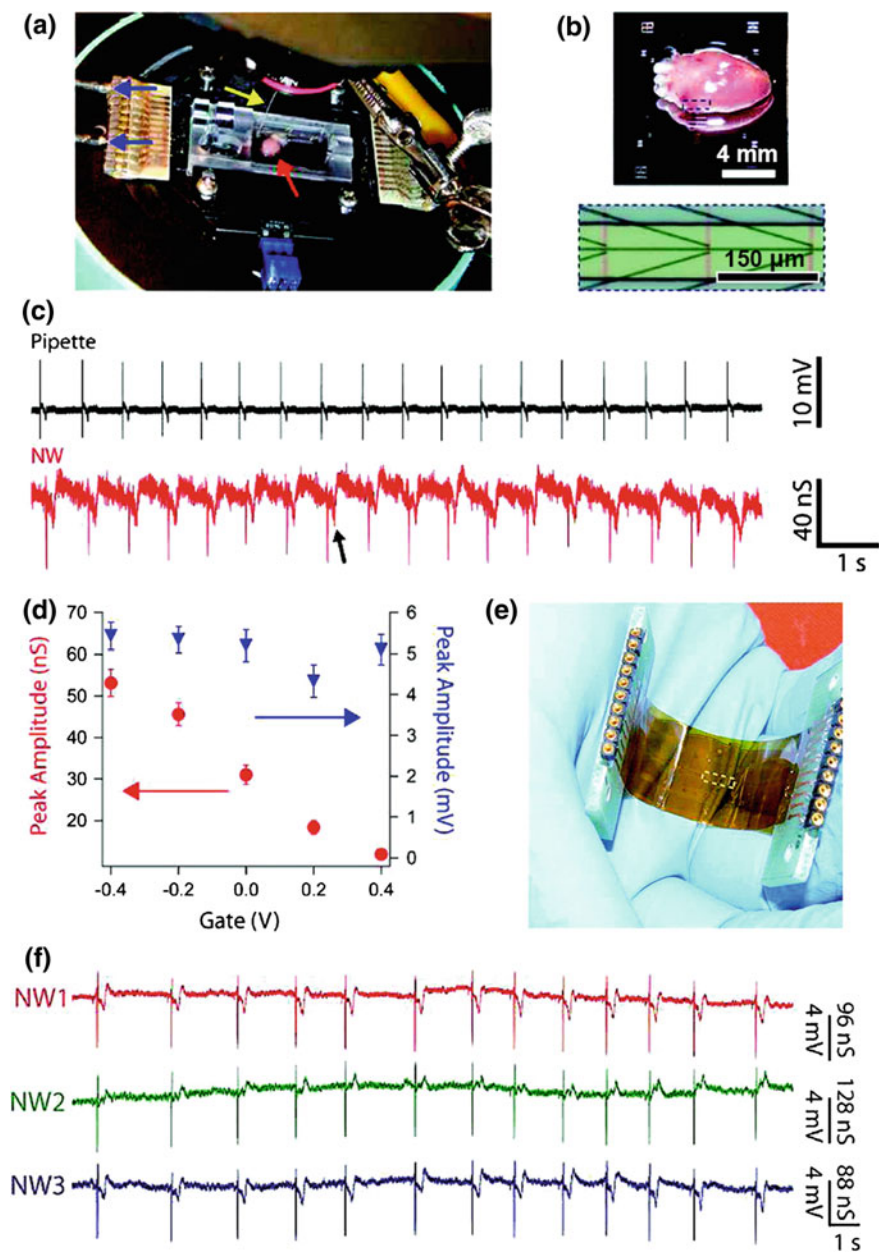
contraction while maintaining ion channels excitability, demonstrated that the fast component was associated with ion-channel current. Studies of the fast transient peak mad as a function of water-gate potential showed a conductance change from ca. 55 to 11 nS while the voltage-calibrated signals were constant,  $5.1 \pm 0.4 \text{ mV}$  (Fig. 11.8d). The relatively constant recorded junction voltage confirmed the robust nanoFET/heart interface.

Last, the authors also fabricated NW-FET devices on a flexible polymer substrate (Fig. 11.8e) which enabled simultaneous recording from an isolated beating heart from multiple devices (Fig. 11.8f). Notably, the calibrated voltages associated with the fast transient for three NW-FET devices,  $5.3 \pm 0.2$ ,  $4.6 \pm 0.1$ , and  $5.3 \pm 0.2 \text{ mV}$ , further highlight the reproducibility of the nanoFET/heart interfaces. Moreover, the significantly larger signal-to-noise ratio for the fast transient implies a tighter interface contact due to the flexible substrate.

### 11.3.3 3D Nano–Bioelectronic Hybrids

An important goal in tissue engineering is to construct culture systems as close as possible to the biological, physical and chemical environment of the natural extracellular matrix (ECM) [82]. 2D bioelectronics have been used in studies of engineered tissues [83], although the recording devices are not capable of mapping the critical 3D behavior of the cells comprising the tissue as a whole. To overcome this basic limitation requires the development of nanoelectronic recording devices in a 3D architecture interpenetrating the tissue. To achieve this goal necessitates the following features: (i) macroporous structures to allow for cell interpenetration during culture; (ii) nanometer to micrometer scale structural features consistent with the ECM or tissue scaffolds; and (iii) mechanical properties similar to ECM for natural tissue development [2, 57, 84].

Tian et al. [85] demonstrated the first example of these new concepts using macroporous NW nanoelectronic scaffolds (nanoES) to develop innervated synthetic tissues. In this new paradigm, SiNW transistors were fabricated into network



◀ **Fig. 11.8** **a** Image of experimental setup for NW-FET/heart interface and recording. *Arrows* denote the positions of heart (*red*), Ag/AgCl reference electrode (*yellow*), and source/drain interconnect wires (*blue*), respectively. **b** *Top* Magnified image of heart on the device. *Bottom* Zoom-in view of the *dotted region* in upper image, showing three pairs of NWs with the orientation along the vertical *red lines*. **c** Parallel recordings made using a glass pipette (*black*) and NW-FET (*red*). **d** Peak conductance amplitude (*red*) and calibrated peak voltage amplitude (*blue*) as a function of gate voltage. **e** Image of a complete chip on a flexible Kapton<sup>TM</sup> substrate, where the central *dashed box* denotes the position of NW-FETs. **f** Measured signals at gate of  $-0.2$  V. Reproduced from [81]. Copyright 2009 American Chemical Society

structures, where the network, which contains electrical interconnects needed to address the nanoFETs, was designed to have feature sizes and porosities similar to conventional passive tissue scaffold. Second, the nanoES was released from the underlying substrate and configured as a 3D macroporous scaffold by either stress-induced self-organization or external forces. The porosity of nanoES can exceed 99 %, which renders the scaffold high flexibility (Fig. 11.9a, b). Last, the nanoES was combined with biodegradable ECMs, seeded with cells and then the assembly was cultured to produce synthetic tissues innervated in 3D with nanoFETs.

The structure of a representative nanoES/cardiac hybrid characterized by confocal fluorescence microscopy and epifluorescence microscopy (Fig. 11.9c, d) highlights the high density of cardiomyocytes in close contact with nanoES components. Clear striations of cardiac tissue, indicative of mature tissue, were also observed. The monitoring capability of 3D nanoES/cariac hybrid was demonstrated by recording from a single-NW-FET located below the construct surface as shown in Fig. 11.9e. The data revealed regularly spaced spikes with a frequency of  $\sim 1$  Hz, calibrated potential change of  $\sim 2$ – $3$  mV, signal-to-noise ratio of  $\geq 3$  and  $\sim 2$  ms width, all of which agree well with expectations for extracellular recordings from cardiomyocytes. Moreover, addition of norepinephrine, a drug that stimulates cardiac contraction, showed a twofold increase of the contraction frequency. Given the capability to resolve action potentials with single-shot submillisecond time resolution in 3D (Fig. 11.9f), this work suggests substantial potential for the nanoES/cardiac hybrids and other tissue hybrids as a new paradigm for 3D monitoring and screening of drugs.

Further development of the nanoES paradigm has been achieved in the seamless incorporation of active nanoelectronic networks within 3D materials, where active monitoring and control of host systems have been exhibited by multifunctional NW electronics. For example, Liu et al. [86] reported the conversion of ordered 2D NW nanoelectronics precursors into ordered, 3D interconnected and addressable macroporous nanoelectronic networks. Hundreds of addressable NW devices, with feature sizes from 10-nm scale (for device elements) to 10- $\mu$ m scale (for electrical and structural interconnections), were incorporated in these 3D networks (Fig. 11.10). Significantly, simultaneous NW photocurrent and confocal microscopy imaging studies demonstrated that it was possible to localize NW positions inside 3D hybrid materials with  $\sim 14$ -nm resolution. This method should prove particularly useful in future for mapping the positions of the nanodevices to

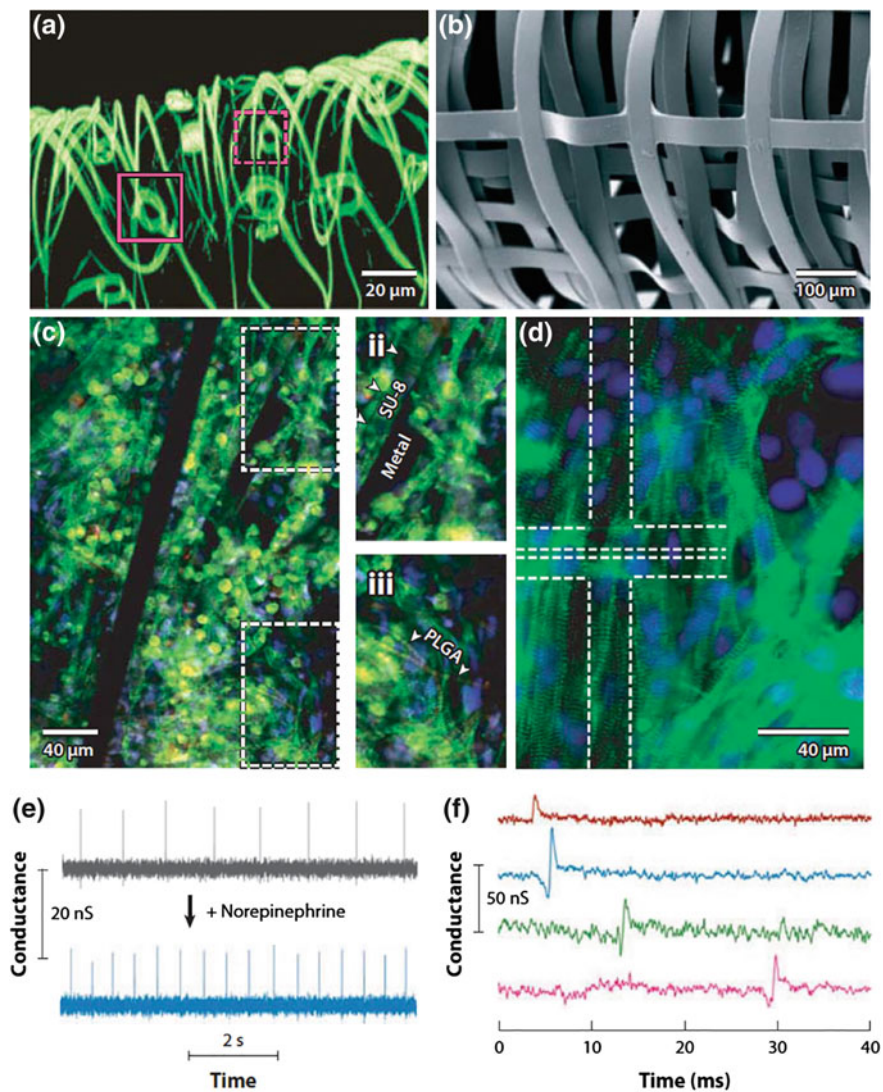


**Fig. 11.9** Nanoelectronic scaffolds (nanoES) and synthetic tissues. **a, b** Confocal fluorescence microscopy and SEM images, respectively, of two nanoES. **c** Confocal fluorescence micrographs of a hybrid nanoES/cardiac synthetic tissue patch. **d** Epifluorescence micrograph of the surface from the same hybrid with the posing of a NW-FET source-drain electrodes highlighted by the *white dashed lines*. **e** Time-evolution of periodic conductance spikes recorded by a NW-FET device in the nanoES/cardiac hybrid before and after addition of noradrenaline. **f** Multiplex recordings from four NW-FETs in a nanoES/cardiac hybrid. Reproduced from [85]. Copyright 2012 Nature Publishing Group

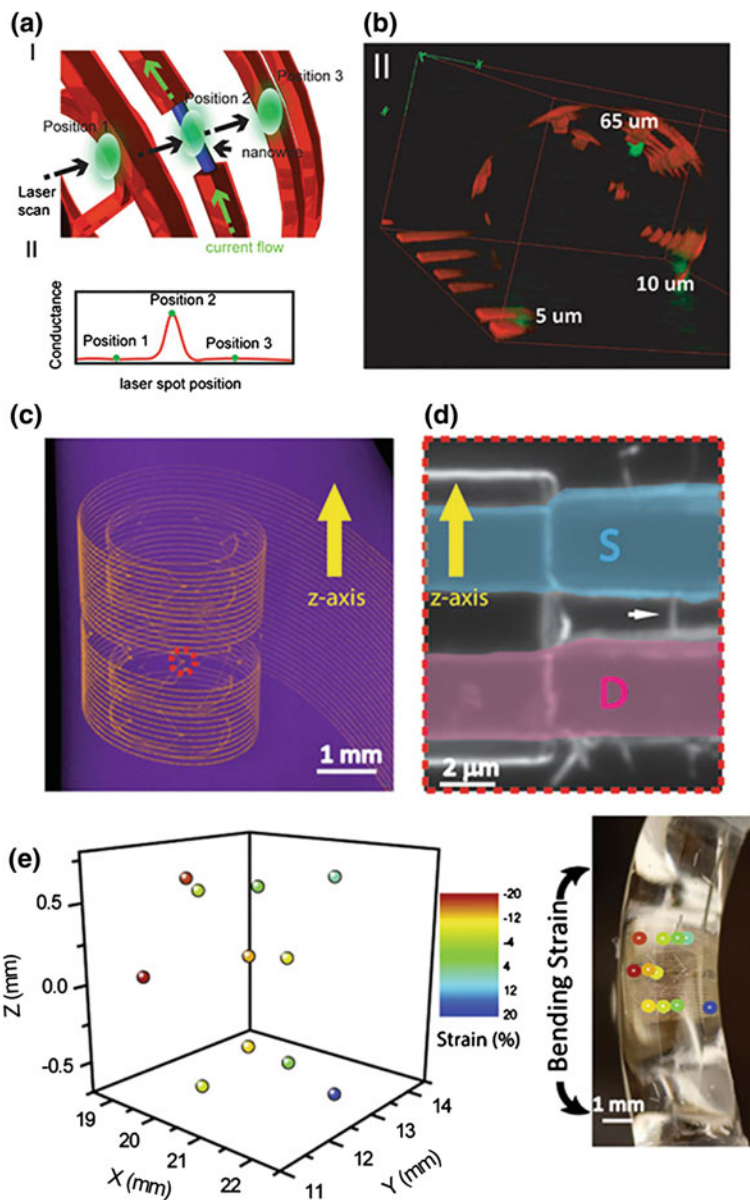


**Fig. 11.10** a Schematic of 3D macroporous NW structure highlighting simultaneous confocal fluorescence and photocurrent imaging to localize the positions of NW-FET devices: blue cylinder NW; orange-red polymer mesh network; green dot laser spot. b 3D reconstructed confocal fluorescence/photocurrent microscopy image of a 3D mesh structure. The polymer mesh structure is red-orange and NW-FET positions are green. c 3D micro-CT image of a strain sensor array embedded in an elastomer, where metal interconnects are visible as yellow-orange lines. d Optical image of a typical NW device. The white arrow points to the NW, and source (S) and drain (D) highlighted with blue and pink coloring, respectively. e 3D strain field mapped by the NW strain sensors, left; and image of elastomer with embedded macroporous NW network, right. Reproduced from [86]. Copyright 2013 National Academy of Sciences of the United States of America

high-resolution with respect to cells. The success of integrating 3D multifunctional nanoelectronics with biological hosts indicates the capability of fabricating truly 3D nanoelectronic circuits and subsequent 3D incorporation of these multifunctional circuits into living systems for smart materials and even “cyborg” tissues, although additional work will be needed before the nanoES-based hybrids can be used as implants *in vivo*. Last, it should be noted that the basic nanoES paradigm is amenable to incorporation of additional types of functional devices, including photonic devices as well as strain and biochemical sensors, and these could further broaden the capabilities and opportunities for *in vitro* and *in vivo* studies of the brain and heart in the future.

### ***11.3.4 Injectable Electronics***

The mismatch of mechanical properties represents an essential challenge at the tissue/electrode interface in living systems. Tissues are soft and flexible, also with interior cell migration while the implanted electronics made, for example, of metal or silicon, have rigid nonporous structures. This difference results in two disadvantages. First, rigidity can yield incomplete and/or ineffective contacts between devices and cells that corresponding lead to weak signals that may be overwhelmed by noise [87–89]. Second and perhaps more important, such rigid probes are known to illicit chronic immune responses that result in the build-up of scar tissue around probes (e.g., glial scarring in the brain), where the biologically inactive scar tissue can diminish or eliminate recorded and/or stimulated signals [90, 91]. To overcome these long-standing limitations of existing implantable electrode probes requires greater attention to the importance of the electrode/tissue interfaces and matching of overall probe/tissue feature sizes and mechanical properties.

Significantly, the Lieber group [92, 93] recently proposed and demonstrated a new paradigm that overcomes these long-standing challenges through syringe injection of centimeter-scale macroporous electronic networks. In this new approach (Fig. 11.11a), the syringe is loaded with the ultra-flexible mesh, inserted into tissue or cavity, and then the mesh is injected while simultaneously retracting the needle. The mesh structure is critical for controlling the bending stiffness and allowing loading/injection. Specifically, the angle  $\alpha$  (Fig. 11.11b) determines the bending stiffness of the unit cell. The authors found that when  $\alpha = 45^\circ$ , the mesh electronics can be smoothly delivered through a needles with inner diameters that were  $>30$  times smaller than the original mesh width ( $W$ ).

Notably, studies of the chronic tissue response following injection of the macroporous mesh into live rodent brains (Fig. 11.11c) demonstrated several new and exciting features, including (i) filling-in of neural tissue through the macroporous network, (ii) minimal or absence of astrocyte proliferation in the vicinity of



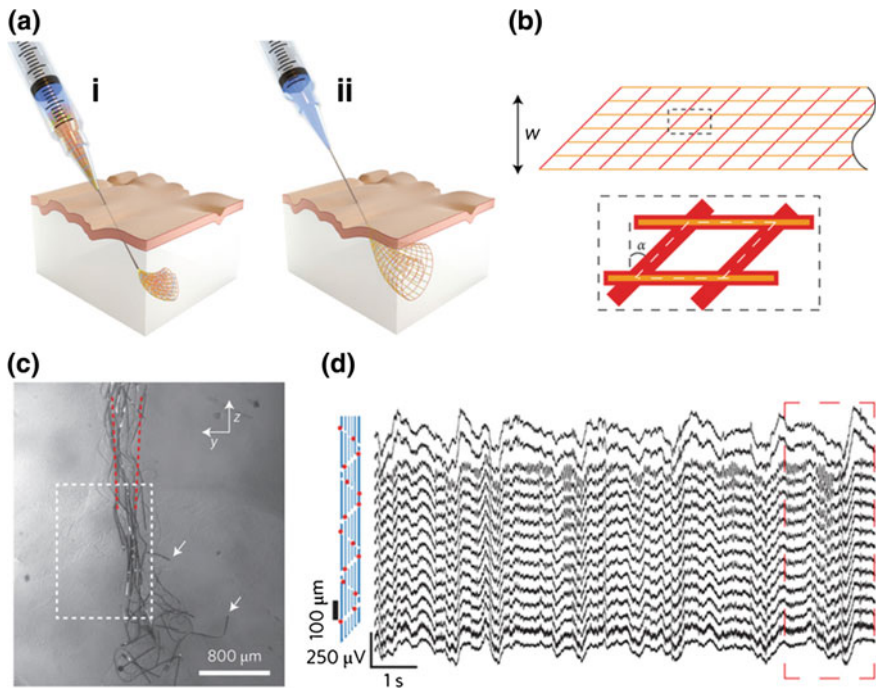


**Fig. 11.11** **a** Schematics for injectable electronics. The needle is inserted (i) and retracted (ii) to leave the mesh electronics in the cavity. **b** Schematic of the mesh design, where  $\alpha$  is the angle with respect to a *rectangular* configuration. **c** Optical image of a longitudinal brain slice taken five weeks after injection into the hippocampus. The mesh is fully extended. **d** 16-channel recording with the mesh electronics following injection into the brain of a live mouse. Reproduced from [92]. Copyright 2015 Nature Publishing Group

the injected probe, and correspondingly, (iii) attractive interactions between the neurons and the macroporous mesh, which lead to the formation of tight electronics/cell junctions that are ideal for recording. Indeed, the mesh electronics have proved to be able to record well-defined neural activity from live mice brains (Fig. 11.11d). In this case, the rigid shell of the syringe allowed placement of the mesh in specific brain regions. In parallel, they also developed another method to implant the ultraflexible 3D macroporous electronic device into rodent brains by rapid freezing in liquid nitrogen and inserting the probe in frozen state [94]. Significantly, the chronic histology studies, which revealed filling-in of neural tissue through the macroporous network and attractive neuron probe interactions, contrast results from other solid and more rigid probe designs and are consistent with a unique long-term stability and biocompatibility of the ultra-flexible mesh probe/tissue interface. Although it will be important in future studies to develop

these probes further, for example by extending the chronic histology studies to shorter and longer times, and increasing the number of sensor elements available for multiplexed recording and/or introducing stimulation capabilities, the new paradigm of syringe injectable macroporous mesh electronics promises to be transformative in capabilities for stable chronic brain activity mapping through the development of implants for next-generation brain machine interfaces.

## 11.4 Future Directions and Challenges

The challenges associated with nanotechnology applications in biomedical sciences are numerous, but their impact on our understanding of how the cardiac and nervous systems work, how they fail in disease, and how one can intervene at a nanoscopic or even molecular level, is significant. For instance, neural developmental factors, such as the cadherins, laminins, and bone morphometric protein families, as well as their receptors, can be manipulated in new ways [14]. Bottom-up NW nanotechnology allows us to explore the functional specificity of these molecules by incorporating them into predefined locations in NW devices to exert highly targeted effects on single cells. Incorporating nanoelectronics or nanoscience in general into synthetic biology and/or systems biology can be highly rewarding. Doing so will represent a great leap forward in materials and biological sciences, especially because of the many nanoelectronic and nanophotonic devices that one can envision building into cellular circuitry and merging with biological information processing systems.

Although great progress has been made in both extracellular and intracellular electrical recording with NW-FETs, many challenges remain. For extracellular studies, there remains a pressing need to further enhance nanoFET S/N so that very weak endogenous biological signals, with an amplitude of  $\sim 100 \mu\text{V}$ , can be readily resolved. This goal may be achieved by a new chemical design and synthesis of high-mobility NW building blocks for nanoFETs, or nanoscale engineering of NW materials to reduce nanoFET noise by, for example, thermal annealing and/or surface passivation. For intracellular studies, more research is needed to advance nanoFET-based intracellular measurement techniques. For example, the S/N of nanoFETs is no better than that of glass micropipette recordings, although the spatial resolution of the former is much higher. Current nanoFET designs allow only potential recordings, but measurements of ionic currents could be performed if other signal transduction mechanisms are combined with nanoFETs. Moreover, nanoFETs are not yet capable of cell stimulation, in addition to recording. Nevertheless, there are many advantages of nanoFET intracellular probes used in these studies, including their sub-10-nm sizes; ease of operation (e.g., no need to compensate or calibrate the probe junction potential and capacitance); lipid fusion-assisted cellular entrance; minimal mechanical and biochemical invasiveness; and potential for large-scale, high-density, multiplexed recordings. These capabilities make nanoFET intracellular probes very attractive

tools for substantially broadening the scope of fundamental and applied electrophysiology studies to regimes that are difficult to access by current methodologies. For nanoelectronics-cyborg tissues, the long-term in vivo biocompatibility of nanoES should be studied in greater depth. In addition, cell or tissue interactions with nanoES and the manipulation of such interactions through modification with cell growth determinants represents a fruitful area for future studies. In addition, it should be possible to develop the nanoES to provide electrical and mechanical stimulation to optimize cell culture and match those of host tissues. Last but not least, exploration of the frontier of nanoelectronics-brain interfaces, including chronic in vivo brain activity mapping and modulation with high spatial and temporal resolution, represents a truly unique opportunity to impact fundamental research and ultimately healthcare with a substantial benefit to society worldwide. More generally, as we take advantage of the uniquely small sizes of nanoelectronic devices organized into arrays and circuits that have similar connectivity, feature sizes and mechanical properties as the cell networks comprising living tissues of interest such as the brain, we begin to blur the distinction between nonliving electronic and living biological systems, and we suggest that this will lead to major and sometimes unexpected opportunities in understanding complex biological systems, diseases and potential new therapeutic directions in the future.

## References

1. N.A. Kotov, J.O. Winter, I.P. Clements, E. Jan, B.P. Timko, S. Campidelli, S. Pathak, A. Mazzatenta, C.M. Lieber, M. Prato, Nanomaterials for neural interfaces. *Adv. Mater.* **21** (40), 3970–4004 (2009)
2. A. Zhang, C.M. Lieber. Nano-bioelectronics. *Chem. Rev.* **116**(1), 215–257 (2016)
3. K. Jain, Nanobiotechnology-based drug delivery to the central nervous system. *Neurodegener. Dis.* **4**(4), 287–291 (2007)
4. S.J. Luck, in *An Introduction to the Event-Related Potential Technique* (MIT Press, Cambridge, 2014)
5. M. Guye, G. Bettus, F. Bartolomei, P.J. Cozzone, Graph theoretical analysis of structural and functional connectivity MRI in normal and pathological brain networks. *Magn. Reson. Mater. Phys. Biol. Med.* **23**(5–6), 409–421 (2010)
6. N.K. Logothetis, What we can do and what we cannot do with fMRI. *Nature* **453**(7197), 869–878 (2008)
7. G. Buzsáki, C.A. Anastassiou, C. Koch, The origin of extracellular fields and currents—EEG, ECoG, LFP and spikes. *Nat. Rev. Neurosci.* **13**(6), 407–420 (2012)
8. M.S. Siegel, E.Y. Isacoff, A genetically encoded optical probe of membrane voltage. *Neuron* **19**(4), 735–741 (1997)
9. C. Stosiek, O. Garaschuk, K. Holthoff, A. Konnerth, In vivo two-photon calcium imaging of neuronal networks. *Proc. Natl. Acad. Sci. USA* **100**(12), 7319–7324 (2003)
10. W. Mittmann, D.J. Wallace, U. Czubayko, J.T. Herb, A.T. Schaefer, L.L. Looger, W. Denk, J. N. Kerr, Two-photon calcium imaging of evoked activity from L5 somatosensory neurons in vivo. *Nat. Neurosci.* **14**(8), 1089–1093 (2011)
11. M. Scanziani, M. Häusser, Electrophysiology in the age of light. *Nature* **461**(7266), 930–939 (2009)

12. M.R. Warden, J.A. Cardin, K. Deisseroth, Optical neural interfaces. *Annu. Rev. Biomed. Eng.* **16**, 103 (2014)
13. J.M. Kralj, A.D. Douglass, D.R. Hochbaum, D. Maclaurin, A.E. Cohen, Optical recording of action potentials in mammalian neurons using a microbial rhodopsin. *Nat. Methods* **9**(1), 90–95 (2012)
14. G.A. Silva, Neuroscience nanotechnology: progress, opportunities and challenges. *Nat. Rev. Neurosci.* **7**(1), 65–74 (2006)
15. A.P. Alivisatos, M. Chun, G.M. Church, R.J. Greenspan, M.L. Roukes, R. Yuste, The brain activity map project and the challenge of functional connectomics. *Neuron* **74**(6), 970–974 (2012)
16. A.P. Alivisatos, A.M. Andrews, E.S. Boyden, M. Chun, G.M. Church, K. Deisseroth, J.P. Donoghue, S.E. Fraser, J. Lippincott-Schwartz, L.L. Looger, Nanotools for neuroscience and brain activity mapping. *ACS Nano* **7**(3), 1850–1866 (2013)
17. M.R. Angle, B. Cui, N.A. Melosh, Nanotechnology and neurophysiology. *Curr. Opin. Neurobiol.* **32**, 132–140 (2015)
18. C. Thomas, P. Springer, G. Loeb, Y. Berwald-Netter, L. Okun, A miniature microelectrode array to monitor the bioelectric activity of cultured cells. *Exp. Cell Res.* **74**(1), 61–66 (1972)
19. A.F. Johnstone, G.W. Gross, D.G. Weiss, O.H.-U. Schroeder, A. Gramowski, T.J. Shafer, Microelectrode arrays: a physiologically based neurotoxicity testing platform for the 21st century. *Neurotoxicology* **31**(4), 331–350 (2010)
20. L. Berdondini, K. Imfeld, A. Maccione, M. Tedesco, S. Neukom, M. Koudelka-Hep, S. Martinoia, Active pixel sensor array for high spatio-temporal resolution electrophysiological recordings from single cell to large scale neuronal networks. *Lab Chip* **9**(18), 2644–2651 (2009)
21. Y. Nam, B.C. Wheeler, In vitro microelectrode array technology and neural recordings. *Crit. Rev. Biomed. Eng.* **39**(1) (2011)
22. R. Huys, D. Braeken, D. Jans, A. Stassen, N. Collaert, J. Wouters, J. Loo, S. Severi, F. Vleugels, G. Callewaert, Single-cell recording and stimulation with a 16 k micro-nail electrode array integrated on a 0.18  $\mu\text{m}$  CMOS chip. *Lab Chip* **12**(7), 1274–1280 (2012)
23. L.R. Hochberg, M.D. Serruya, G.M. Friebs, J.A. Mukand, M. Saleh, A.H. Caplan, A. Branner, D. Chen, R.D. Penn, J.P. Donoghue, Neuronal ensemble control of prosthetic devices by a human with tetraplegia. *Nature* **442**(7099), 164–171 (2006)
24. A. Berényi, Z. Somogyvari, A.J. Nagy, L. Roux, J.D. Long, S. Fujisawa, E. Stark, A. Leonardo, T.D. Harris, G. Buzsáki, Large-scale, high-density (up to 512 channels) recording of local circuits in behaving animals. *J. Neurophysiol.* **111**(5), 1132–1149 (2014)
25. G.W. Gross, B.K. Rhoades, D.L. Reust, F.U. Schwalm, Stimulation of monolayer networks in culture through thin-film indium-tin oxide recording electrodes. *J. Neurosci. Methods* **50**(2), 131–143 (1993)
26. M.E. Spira, A. Hai, Multi-electrode array technologies for neuroscience and cardiology. *Nat. Nanotechnol.* **8**(2), 83–94 (2013)
27. M.J. Nelson, P. Pouget, E.A. Nilsen, C.D. Patten, J.D. Schall, Review of signal distortion through metal microelectrode recording circuits and filters. *J. Neurosci. Methods* **169**(1), 141–157 (2008)
28. J. Pine, Recording action potentials from cultured neurons with extracellular microcircuit electrodes. *J. Neurosci. Methods* **2**(1), 19–31 (1980)
29. J.-H. Kim, G. Kang, Y. Nam, Y.-K. Choi, Surface-modified microelectrode array with flake nanostructure for neural recording and stimulation. *Nanotechnology* **21**(8), 085303 (2010)
30. E.W. Keefer, B.R. Botterman, M.I. Romero, A.F. Rossi, G.W. Gross, Carbon nanotube coating improves neuronal recordings. *Nat. Nanotechnol.* **3**(7), 434–439 (2008)

31. L. Bareket-Keren, Y. Hanein, Carbon nanotube-based multi electrode arrays for neuronal interfacing: progress and prospects. *Front. Neural Circuits* **6**, 122 (2012)
32. P. Fromherz, A. Offenhäusser, T. Vetter, J. Weis, A neuron-silicon junction: a Retzius cell of the leech on an insulated-gate field-effect transistor. *Science* **252**(5010), 1290–1293 (1991)
33. M. Voelker, P. Fromherz, Signal transmission from individual mammalian nerve cell to field-effect transistor. *Small* **1**(2), 206–210 (2005)
34. G. Wrobel, M. Höller, S. Ingebrandt, S. Dieluweit, F. Sommerhage, H.P. Bochem, A. Offenhäusser, Transmission electron microscopy study of the cell–sensor interface. *J. R. Soc. Interface* **5**(19), 213–222 (2008)
35. F. Santoro, S. Dasgupta, J. Schnitker, T. Auth, E. Neumann, G. Panaitov, G. Gompfer, A. Offenhäusser, Interfacing electrogenic cells with 3D nanoelectrodes: position, shape, and size matter. *ACS Nano* **8**(7), 6713–6723 (2014)
36. K. Toma, H. Kano, A. Offenhäusser, Label-free measurement of cell-electrode cleft gap distance with high spatial resolution surface plasmon microscopy. *ACS Nano* **8**(12), 12612–12619 (2014)
37. J. Van Pelt, P.S. Wolters, M. Corner, W.L. Rutten, G.J. Ramakers, Long-term characterization of firing dynamics of spontaneous bursts in cultured neural networks. *IEEE Trans. Biomed. Eng.* **51**(11), 2051–2062 (2004)
38. S. Morefield, E. Keefer, K. Chapman, G. Gross, Drug evaluations using neuronal networks cultured on microelectrode arrays. *Biosens. Bioelectron.* **15**(7), 383–396 (2000)
39. M.E. Ruaro, P. Bonifazi, V. Torre, Toward the neurocomputer: image processing and pattern recognition with neuronal cultures. *IEEE Trans. Biomed. Eng.* **52**(3), 371–383 (2005)
40. H. Craighead, S. Turner, R. Davis, C. James, A. Perez, P.S. John, M. Isaacson, L. Kam, W. Shain, J. Turner, Chemical and topographical surface modification for control of central nervous system cell adhesion. *Biomed. Microdevices* **1**(1), 49–64 (1998)
41. H. Craighead, C. James, A. Turner, Chemical and topographical patterning for directed cell attachment. *Curr. Opin. Solid State Mater. Sci.* **5**(2), 177–184 (2001)
42. A. Hai, J. Shappir, M.E. Spira, Long-term, multisite, parallel, in-cell recording and stimulation by an array of extracellular microelectrodes. *J. Neurophysiol.* **104**(1), 559–568 (2010)
43. F. Patolsky, B.P. Timko, G. Yu, Y. Fang, A.B. Greytak, G. Zheng, C.M. Lieber, Detection, stimulation, and inhibition of neuronal signals with high-density nanowire transistor arrays. *Science* **313**(5790), 1100–1104 (2006)
44. T.-S. Pui, A. Agarwal, F. Ye, N. Balasubramanian, P. Chen, CMOS-compatible nanowire sensor arrays for detection of cellular bioelectricity. *Small* **5**(2), 208–212 (2009)
45. T. Cohen-Karni, B.P. Timko, L.E. Weiss, C.M. Lieber, Flexible electrical recording from cells using nanowire transistor arrays. *Proc. Natl. Acad. Sci. USA* **106**(18), 7309–7313 (2009)
46. B. Tian, T. Cohen-Karni, Q. Qing, X. Duan, P. Xie, C.M. Lieber, Three-dimensional, flexible nanoscale field-effect transistors as localized bioprobes. *Science* **329**(5993), 830–834 (2010)
47. Q. Qing, S.K. Pal, B. Tian, X. Duan, B.P. Timko, T. Cohen-Karni, V.N. Murthy, C.M. Lieber, Nanowire transistor arrays for mapping neural circuits in acute brain slices. *Proc. Natl. Acad. Sci. USA* **107**(5), 1882–1887 (2010)
48. J.F. Eschermann, R. Stockmann, M. Hueske, X.T. Vu, S. Ingebrandt, A. Offenhäusser, Action potentials of HL-1 cells recorded with silicon nanowire transistors. *Appl. Phys. Lett.* **95**(8), 083703 (2009)
49. T. Cohen-Karni, D. Casanova, J.F. Cahoon, Q. Qing, D.C. Bell, C.M. Lieber, Synthetically encoded ultrashort-channel nanowire transistors for fast, pointlike cellular signal detection. *Nano Lett.* **12**(5), 2639–2644 (2012)
50. M. Dankerl, S. Eick, B. Hofmann, M. Hauf, S. Ingebrandt, A. Offenhäusser, M. Stutzmann, J.A. Garrido, Diamond transistor array for extracellular recording from electrogenic cells. *Adv. Funct. Mater.* **19**(18), 2915–2923 (2009)

51. C. Van Renterghem, G. Romey, M. Lazdunski, Vasopressin modulates the spontaneous electrical activity in aortic cells (line A7r5) by acting on three different types of ionic channels. *Proc. Natl. Acad. Sci. USA* **85**(23), 9365–9369 (1988)
52. L.I. Brueggemann, C.J. Moran, J.A. Barakat, J.Z. Yeh, L.L. Cribbs, K.L. Byron, Vasopressin stimulates action potential firing by protein kinase C-dependent inhibition of KCNQ5 in A7r5 rat aortic smooth muscle cells. *Am. J. Physiol. Heart Circ. Physiol.* **292**(3), H1352–H1363 (2007)
53. E. Chorev, J. Epsztein, A.R. Houweling, A.K. Lee, M. Brecht, Electrophysiological recordings from behaving animals—going beyond spikes. *Curr. Opin. Neurobiol.* **19**(5), 513–519 (2009)
54. A.L. Hodgkin, A.F. Huxley, Action potentials recorded from inside a nerve fibre. *Nature* **144** (3651), 710–711 (1939)
55. A. Molleman, *Patch clamping: an introductory guide to patch clamp electrophysiology* (Wiley, Chichester, 2003)
56. B. Tian, C.M. Lieber, Design, synthesis, and characterization of novel nanowire structures for photovoltaics and intracellular probes. *Pure Appl. Chem.* **83**(12), 2153 (2011)
57. B. Tian, C.M. Lieber, Synthetic nanoelectronic probes for biological cells and tissues. *Annu. Rev. Anal. Chem.* **6**, 31–51 (2013)
58. X. Duan, T.-M. Fu, J. Liu, C.M. Lieber, Nanoelectronics-biology frontier: from nanoscopic probes for action potential recording in live cells to three-dimensional cyborg tissues. *Nano Today* **8**(4), 351–373 (2013)
59. A. Hai, A. Dormann, J. Shappir, S. Yitzchaik, C. Bartic, G. Borghs, J. Langedijk, M.E. Spira, Spine-shaped gold protrusions improve the adherence and electrical coupling of neurons with the surface of micro-electronic devices. *J. R. Soc. Interface* **6**, 1153–1165 (2009)
60. A. Hai, D. Kamber, G. Malkinson, H. Erez, N. Mazurski, J. Shappir, M.E. Spira, Changing gears from chemical adhesion of cells to flat substrata toward engulfment of micro-protrusions by active mechanisms. *J. Neural Eng.* **6**(6), 066009 (2009)
61. A. Hai, J. Shappir, M.E. Spira, In-cell recordings by extracellular microelectrodes. *Nat. Methods* **7**(3), 200–202 (2010)
62. F. Santoro, J. Schnitker, G. Panaitov, A. Offenhäusser, On chip guidance and recording of cardiomyocytes with 3D mushroom-shaped electrodes. *Nano Lett.* **13**(11), 5379–5384 (2013)
63. B. Tian, P. Xie, T.J. Kempa, D.C. Bell, C.M. Lieber, Single-crystalline kinked semiconductor nanowire superstructures. *Nat. Nanotechnol.* **4**(12), 824–829 (2009)
64. L. Xu, Z. Jiang, Q. Qing, L. Mai, Q. Zhang, C.M. Lieber, Design and synthesis of diverse functional kinked nanowire structures for nanoelectronic bioprobes. *Nano Lett.* **13**(2), 746–751 (2013)
65. Z. Jiang, Q. Qing, P. Xie, R. Gao, C.M. Lieber, Kinked p–n junction nanowire probes for high spatial resolution sensing and intracellular recording. *Nano Lett.* **12**(3), 1711–1716 (2012)
66. X. Duan, R. Gao, P. Xie, T. Cohen-Karni, Q. Qing, H.S. Choe, B. Tian, X. Jiang, C.M. Lieber, Intracellular recordings of action potentials by an extracellular nanoscale field-effect transistor. *Nat. Nanotechnol.* **7**(3), 174–179 (2012)
67. R. Gao, S. Strehle, B. Tian, T. Cohen-Karni, P. Xie, X. Duan, Q. Qing, C.M. Lieber, Outside looking in: nanotube transistor intracellular sensors. *Nano Lett.* **12**(6), 3329–3333 (2012)
68. Q. Qing, Z. Jiang, L. Xu, R. Gao, L. Mai, C.M. Lieber, Free-standing kinked nanowire transistor probes for targeted intracellular recording in three dimensions. *Nat. Nanotechnol.* **9**, 142–147 (2014)
69. T.-M. Fu, X. Duan, Z. Jiang, X. Dai, P. Xie, Z. Cheng, C.M. Lieber, Sub-10-nm intracellular bioelectronic probes from nanowire–nanotube heterostructures. *Proc. Natl. Acad. Sci. USA* **111**(4), 1259–1264 (2014)

70. J.T. Robinson, M. Jorgolli, A.K. Shalek, M.-H. Yoon, R.S. Gertner, H. Park, Vertical nanowire electrode arrays as a scalable platform for intracellular interfacing to neuronal circuits. *Nat. Nanotechnol.* **7**(3), 180–184 (2012)
71. C. Xie, Z. Lin, L. Hanson, Y. Cui, B. Cui, Intracellular recording of action potentials by nanopillar electroporation. *Nat. Nanotechnol.* **7**(3), 185–190 (2012)
72. B.D. Almquist, N.A. Melosh, Fusion of biomimetic stealth probes into lipid bilayer cores. *Proc. Natl. Acad. Sci. USA* **107**(13), 5815–5820 (2010)
73. B.D. Almquist, N.A. Melosh, Molecular structure influences the stability of membrane penetrating biointerfaces. *Nano Lett.* **11**(5), 2066–2070 (2011)
74. B.D. Almquist, P. Verma, W. Cai, N.A. Melosh, Nanoscale patterning controls inorganic–membrane interface structure. *Nanoscale* **3**(2), 391–400 (2011)
75. X. Xie, A.M. Xu, M.R. Angle, N. Tayebi, P. Verma, N.A. Melosh, Mechanical model of vertical nanowire cell penetration. *Nano Lett.* **13**(12), 6002–6008 (2013)
76. Z.C. Lin, C. Xie, Y. Osakada, Y. Cui, B. Cui, Iridium oxide nanotube electrodes for sensitive and prolonged intracellular measurement of action potentials. *Nat. Commun.* **5**, 3206 (2014)
77. Y. Sun, J.A. Rogers, Inorganic semiconductors for flexible electronics. *Adv. Mater.* **19**(15), 1897–1916 (2007)
78. Z. Yu, O. Graudejus, C. Tsay, S.P. Lacour, S. Wagner, B. Morrison III, Monitoring hippocampus electrical activity in vitro on an elastically deformable microelectrode array. *J. Neurotrauma* **26**(7), 1135–1145 (2009)
79. S.P. Lacour, S. Benmerah, E. Tarte, J. FitzGerald, J. Serra, S. McMahon, J. Fawcett, O. Graudejus, Z. Yu, B. Morrison III, Flexible and stretchable micro-electrodes for in vitro and in vivo neural interfaces. *Med. Biol. Eng. Comput.* **48**(10), 945–954 (2010)
80. Y.-C. Chen, H.-L. Hsu, Y.-T. Lee, H.-C. Su, S.-J. Yen, C.-H. Chen, W.-L. Hsu, T.-R. Yew, S.-R. Yeh, D.-J. Yao, An active, flexible carbon nanotube microelectrode array for recording electrocorticograms. *J. Neural Eng.* **8**(3), 034001 (2011)
81. B.P. Timko, T. Cohen-Karni, G. Yu, Q. Qing, B. Tian, C.M. Lieber, Electrical recording from hearts with flexible nanowire device arrays. *Nano Lett.* **9**(2), 914–918 (2009)
82. T. Dvir, B.P. Timko, D.S. Kohane, R. Langer, Nanotechnological strategies for engineering complex tissues. *Nat. Nanotechnol.* **6**(1), 13–22 (2011)
83. R.F. Fakhru'llin, A.I. Zamaleeva, R.T. Minullina, S.A. Konnova, V.N. Paunov, Cyborg cells: functionalisation of living cells with polymers and nanomaterials. *Chem. Soc. Rev.* **41**(11), 4189–4206 (2012)
84. X. Duan, C.M. Lieber, Nanoelectronics meets biology: from new nanoscale devices for live-cell recording to 3D innervated tissues. *Chem. Asian J.* **8**(10), 2304–2314 (2013)
85. B. Tian, J. Liu, T. Dvir, L. Jin, J.H. Tsui, Q. Qing, Z. Suo, R. Langer, D.S. Kohane, C.M. Lieber, Macroporous nanowire nanoelectronic scaffolds for synthetic tissues. *Nat. Mater.* **11**(11), 986–994 (2012)
86. J. Liu, C. Xie, X. Dai, L. Jin, W. Zhou, C.M. Lieber, Multifunctional three-dimensional macroporous nanoelectronic networks for smart materials. *Proc. Natl. Acad. Sci. USA* **110**(17), 6694–6699 (2013)
87. V.S. Polikov, P.A. Tresco, W.M. Reichert, Response of brain tissue to chronically implanted neural electrodes. *J. Neurosci. Methods* **148**(1), 1–18 (2005)
88. J.P. Seymour, D.R. Kipke, Neural probe design for reduced tissue encapsulation in CNS. *Biomaterials* **28**(25), 3594–3607 (2007)
89. M. HajjHassan, V. Chodavarapu, S. Musallam, NeuroMEMS: neural probe microtechnologies. *Sensors* **8**(10), 6704–6726 (2008)
90. T.D.Y. Kozai, D.R. Kipke, Insertion shuttle with carboxyl terminated self-assembled monolayer coatings for implanting flexible polymer neural probes in the brain. *J. Neurosci. Methods* **184**(2), 199–205 (2009)
91. R. Biran, D.C. Martin, P.A. Tresco, Neuronal cell loss accompanies the brain tissue response to chronically implanted silicon microelectrode arrays. *Exp. Neurol.* **195**(1), 115–126 (2005)

92. J. Liu, T.-M. Fu, Z. Cheng, G. Hong, T. Zhou, L. Jin, M. Duvvuri, Z. Jiang, P. Kruskal, C. Xie, Syringe-injectable electronics. *Nat. Nanotechnol.* **10**, 629–636 (2015)
93. G. Hong, T.-M. Fu, T. Zhou, T.G. Schuhmann, J. Huang, C.M. Lieber, Syringe injectable electronics: precise targeted delivery with quantitative input/output connectivity. *Nano Lett.* **15** (10), 6979–6984 (2015)
94. C. Xie, J. Liu, T.-M. Fu, X. Dai, W. Zhou, C.M. Lieber, Three-dimensional macroporous nanoelectronic networks as minimally invasive brain probes. *Nat. Mater.* **14**(12), 1286–1292 (2015)



## Chapter 12

# Conclusions and Outlook

**Abstract** The development of NW-based materials has led to breakthrough achievements with rapid expanding impact in all areas of nanotechnology, including but not limited to, electronics, optoelectronics, energy science, sensors and the life sciences. In spite of the progresses discussed in this book, substantial room still exists for NW research and development, and the opportunities may be realized by exquisite control of NW synthesis and assembly, as well as large scale production. In this chapter, we will summarize the basic NW research and applications introduced in this book, and challenges and exciting future opportunities will be discussed.

Central to the vision underlying nanotechnology is the idea that developing and following a common intellectual path—the bottom-up paradigm of nanoscale science and technology—will make it possible to build or assemble virtually any kind of device or functional system, ranging from ultrasensitive medical sensors to nanocomputers and brain-machine interfaces. Underpinning this bottom-up paradigm is the controlled growth of nanoscale materials—the building blocks of the bottom-up approach—pursued within the disciplines of materials sciences and chemistry. In this book we have reviewed the remarkable progress made over the past two plus decades in NW research developing this broad vision.

The intimate integration and interplay between growth and fundamental characterization has enabled the field not only to expand the basic understanding of NW science and technology, but also to make rational predictions and define new device concepts unique to these nanoscale building blocks. A key that has been and will continue to be critical to continued scientific advances is expanding the level of rational synthetic control of the powerful NW building blocks with precisely controlled and tunable chemical composition, structure, size, and morphology since these characteristics ultimately determine physical properties. Moreover, the capability to create new NW topologies and assemblies where composition and structure are tuned on multiple length scales has been and will continue to be central to scientific breakthroughs, such as the first demonstrations of intracellular transistors merging key elements of living and nonliving information processors [1–3], that can enable new and potentially transformative future technologies. In this

regard, semiconductor NWs serve as one of the most powerful platform available today in nanoscience given that it is now possible to design structures *ab initio*, and synthetically realize these structures with the structure and composition controlled from the atomic scale and up. This capability to design and synthetically realize complex NW materials is almost unique among nanomaterials, and enables systems or building blocks to be created, which have predictable physical properties and which enable testing fundamental limits of performance [4–9].

To fully exploit this bottom-up paradigm in technologies, it will be important to also build upon rational methods of organizing NWs and other nanomaterials. The building blocks need to be assembled not only in close-packed arrays, which give a very fixed kind of interconnectivity, but the orientation, position and spacing controlled on multiple length scales [10]. It is also possible to assemble hybrid or multi-component functional materials in novel environments using diverse NW building blocks [11], allowing for rational exploration of new architectures and possible applications of multi-component material systems. In addition, advances described in this book have shown how this approach has already enabled new concepts for NW device structures, functional units and systems [12–15], and thus demonstrates unambiguously the potential of creating technologies that might previously have been more the realm of science fiction versus scientific reality.

Over the past two decades, research on NWs has witnessed fast developments, as well as substantial and robust achievements that are synonymous with original ideas put forth in seminal publications [16–18]; that is, the capability to synthetically-control composition, structure, morphology on multiple length scales allows for remarkable advances simply not possible in single component materials. The development of NW-based materials has led to breakthrough achievements with rapid expanding impact in all areas of nanotechnology. The remarkable performance properties of NWs are leading to revolutionary technologies in electronics, optoelectronics, energy science, sensors and the life sciences more generally, and will continue to broadly impact the fields of physics, chemistry, biology, medicine, environmental science, and engineering [19–32]. For example, in the energy studies, especially related to renewable energy conversion and storage, the rational design of SiNW structures and array architectures, together with surface coating and bandgap engineering, has demonstrated significant potentials in increasing light absorption, charge transfer and separation, photoconversion efficiencies, and chemical and catalytic performances [33–35]. In the biological studies, for instance, sensor devices based on SiNW-FETs are emerging as a general and powerful platform for ultrasensitive, direct electrical detection of biological and chemical species, as well as interfacing with live cells and tissues for nonconventional intracellular electrical measurements [9, 22, 23, 28, 29, 32]. The authors believe this latter area has tremendous growth potential from perspectives of both basic research and applications, and expect to see transformative advances impacting medicine and healthcare in the future.

In spite of the remarkable progress discussed in this book, substantial room still exists for basic NW research and development. These opportunities may be realized by tackling several challenges. First, the ultimate understanding and exquisite

control of NW synthesis with atomic accuracy in material morphologies, structures, chemical modulations, and doping profiles, have not been fully realized by current synthetic methods and technologies. Second, the assembly and patterning of NWs into functional device arrays with higher efficiency, accuracy and uniformity will benefit exploration of larger scale integrated systems for research as well commercialization of existing NW devices that do exhibit unique properties, such as in the biological realm [36]. Third, development of efficient large scale NW synthesis/production is ultimately needed to fuel large-scale applications as well as efficient commercialization strategies to realize the most promising technologies. Looking into the future, continued efforts to exploit the unique capabilities that exist today in NW building blocks and will further expand with continued efforts, for example by thinking out of the box to applications not possible with existing planar technologies, promises to be a fruitful direction for creating new NW-based research tools, which may answer long-standing questions or even allow researchers to pose new questions with the advanced capabilities, to transformative and/or disruptive technologies for commercialization. We believe that the future is remarkably bright, with likely revolutionary technologies from NW-based nanosystems that will impact in many ways in areas such as life sciences, health-care, information technology, and energy science, and importantly, in so doing offer a substantial benefit to humankind.

## References

1. B. Tian, T. Cohen-Karni, Q. Qing, X. Duan, P. Xie, C.M. Lieber, Three-dimensional, flexible nanoscale field-effect transistors as localized bioprobes. *Science* **329**(5993), 830–834 (2010)
2. X. Duan, R. Gao, P. Xie, T. Cohen-Karni, Q. Qing, H.S. Choe, B. Tian, X. Jiang, C.M. Lieber, Intracellular recordings of action potentials by an extracellular nanoscale field-effect transistor. *Nat. Nanotechnol.* **7**(3), 174–179 (2012)
3. Q. Qing, Z. Jiang, L. Xu, R. Gao, L. Mai, C.M. Lieber, Free-standing kinked nanowire transistor probes for targeted intracellular recording in three dimensions. *Nat. Nanotechnol.* **9**, 142–147 (2014)
4. C.M. Lieber, Nanoscale science and technology: building a big future from small things. *MRS Bull.* **28**(07), 486–491 (2003)
5. X. Duan, C.M. Lieber, Semiconductor nanowires: rational synthesis, in *Dekker Encyclopedia of Nanoscience and Nanotechnology*, ed. by J.A. Schwarz (Marcel Dekker, Inc., New York, 2005)
6. W. Lu, C.M. Lieber, Semiconductor nanowires. *J. Phys. D Appl. Phys.* **39**(21), R387–R406 (2006)
7. C.M. Lieber, Z.L. Wang, Functional nanowires. *MRS Bull.* **32**(02), 99–108 (2007)
8. Z. Zhong, C. Yang, C.M. Lieber, Silicon nanowires and nanowire heterostructures, in *Nanosilicon*, ed. by V. Kumar (Elsevier, Amsterdam, 2008), pp. 176–216
9. C.M. Lieber, Semiconductor nanowires: a platform for nanoscience and nanotechnology. *MRS Bull.* **36**(12), 1052–1063 (2011)
10. J. Yao, H. Yan, C.M. Lieber, A nanoscale combing technique for the large-scale assembly of highly aligned nanowires. *Nat. Nanotechnol.* **8**(5), 329–335 (2013)
11. A. Javey, S. Nam, R.S. Friedman, H. Yan, C.M. Lieber, Layer-by-layer assembly of nanowires for three-dimensional, multifunctional electronics. *Nano Lett.* **7**(3), 773–777 (2007)

12. J. Yao, H. Yan, S. Das, J.F. Klemic, J.C. Ellenbogen, C.M. Lieber, Nanowire nanocomputer as a finite-state machine. *Proc. Natl. Acad. Sci. USA* **111**(7), 2431–2435 (2014)
13. W. Shim, J. Yao, C.M. Lieber, Programmable resistive-switch nanowire transistor logic circuits. *Nano Lett.* **14**(9), 5430–5436 (2014)
14. H. Yan, H.S. Choe, S. Nam, Y. Hu, S. Das, J.F. Klemic, J.C. Ellenbogen, C.M. Lieber, Programmable nanowire circuits for nanoprocessors. *Nature* **470**(7333), 240–244 (2011)
15. Y. Dong, G. Yu, M.C. McAlpine, W. Lu, C.M. Lieber, Si/a-Si core/shell nanowires as nonvolatile crossbar switches. *Nano Lett.* **8**(2), 386–391 (2008)
16. H. Dai, E.W. Wong, Y.Z. Lu, S. Fan, C.M. Lieber, Synthesis and characterization of carbide nanorods. *Nature* **375**(6534), 769–772 (1995)
17. C. Lieber, A. Morales, P. Sheehan, E. Wong, P. Yang, in *One-Dimensional Nanostructures: Rational Synthesis, Novel Properties and Applications*. Proceedings of the Robert A. Welch Foundation 40th Conference on Chemical Research: Chemistry on the Nanometer Scale (1997), pp. 165–187
18. A.M. Morales, C.M. Lieber, A laser ablation method for the synthesis of crystalline semiconductor nanowires. *Science* **279**(5348), 208–211 (1998)
19. Y. Huang, X. Duan, C.M. Lieber, Semiconductor nanowires: nanoscale electronics and optoelectronics, in *Dekker Encyclopedia of Nanoscience and Nanotechnology*, ed. by J.A. Schwarz (Marcel Dekker, Inc., New York, 2005)
20. R. Agarwal, C.M. Lieber, Semiconductor nanowires: optics and optoelectronics. *Appl. Phys. A* **85**(3), 209–215 (2006)
21. Y. Li, F. Qian, J. Xiang, C.M. Lieber, Nanowire electronic and optoelectronic devices. *Mater. Today* **9**(10), 18–27 (2006)
22. F. Patolsky, G. Zheng, C.M. Lieber, Nanowire sensors for medicine and the life sciences. *Nanomedicine* **1**, 55–65 (2006)
23. F. Patolsky, B.P. Timko, G. Zheng, C.M. Lieber, Nanowire-based nanoelectronic devices in the life sciences. *MRS Bull.* **32**(02), 142–149 (2007)
24. W. Lu, P. Xie, C.M. Lieber, Nanowire transistor performance limits and applications. *IEEE T. Electron. Dev.* **55**(11), 2859–2876 (2008)
25. B. Tian, T.J. Kempa, C.M. Lieber, Single nanowire photovoltaics. *Chem. Soc. Rev.* **38**(1), 16–24 (2009)
26. B. Tian, C.M. Lieber, Design, synthesis, and characterization of novel nanowire structures for photovoltaics and intracellular probes. *Pure Appl. Chem.* **83**(12), 2153 (2011)
27. T. Cohen-Karni, C.M. Lieber, Nanowire nanoelectronics: building interfaces with tissue and cells at the natural scale of biology. *Pure Appl. Chem.* **85**(5) (2013)
28. X. Duan, T.-M. Fu, J. Liu, C.M. Lieber, Nanoelectronics-biology frontier: from nanoscopic probes for action potential recording in live cells to three-dimensional cyborg tissues. *Nano Today* **8**(4), 351–373 (2013)
29. X. Duan, C.M. Lieber, Nanoelectronics meets biology: from new nanoscale devices for live-cell recording to 3D innervated tissues. *Chem. Asian J.* **8**(10), 2304–2314 (2013)
30. X. Duan, C.M. Lieber, Nanoscience and the nano-bioelectronics frontier. *Nano Res.* **8**(1), 1–22 (2015)
31. P.B. Kruskal, Z. Jiang, T. Gao, C.M. Lieber, Beyond the patch clamp: nanotechnologies for intracellular recording. *Neuron* **86**(1), 21–24 (2015)
32. A. Zhang, C.M. Lieber, Nano-bioelectronics. *Chem. Rev.* **116**(1), 215–257 (2016)
33. Y. Wang, T. Wang, P. Da, M. Xu, H. Wu, G. Zheng, Silicon nanowires for biosensing, energy storage, and conversion. *Adv. Mater.* **25**(37), 5177–5195 (2013)
34. K.-Q. Peng, X. Wang, L. Li, Y. Hu, S.-T. Lee, Silicon nanowires for advanced energy conversion and storage. *Nano Today* **8**(1), 75–97 (2013)
35. A.I. Hochbaum, P. Yang, Semiconductor nanowires for energy conversion. *Chem. Rev.* **110**(1), 527–546 (2010)
36. G. Yu, C.M. Lieber, Assembly and integration of semiconductor nanowires for functional nanosystems. *Pure Appl. Chem.* **82**(12), 2295–2314 (2010)

# Curriculum Vitae

## **Anqi Zhang**

Anqi Zhang is currently a Ph.D. student under the supervision of Prof. Charles M. Lieber in the Department of Chemistry and Chemical Biology at Harvard University. She received her bachelor's degree in Materials Chemistry from Fudan University in China in 2014. Her research interests include development of novel nano-bioelectronic tools and their applications in neurophysiology. She has published 10 peer-reviewed papers and one book chapter.

## **Gengfeng Zheng**

Gengfeng Zheng is a Professor of Fudan University, China. He obtained his B.S. degree (2000) at Fudan University in China, and Master (2004) and Ph.D. (2007) degrees in Chemistry at Harvard University in USA, under the guidance of Prof. Charles Lieber. He was a postdoctoral fellow working with Prof. Chad Mirkin at Northwestern University in USA (2007–2009). He became a full professor at Department of Chemistry and Laboratory of Advanced Materials at Fudan University in 2010. Prof. Zheng is also a Co-Editor of the Journal of Colloid and Interface Science, and an Advisory Board member of the Journal of Materials Chemistry A.

The research fields of Prof. Gengfeng Zheng include: (1) Synthesis and self-assembly of low-dimensional semiconducting nanomaterial heterostructures; (2) Fabrication of photoelectrochemical nanodevices for solar energy conversion and electrochemical energy storage; and (3) Development of nanomaterial-biomaterial interfaces for disease diagnosis, imaging and treatment. He has published over 100 peer-reviewed papers in internationally renown journals, with more than 7000 citations.

Prof. Gengfeng Zheng was a recipient of the Bao-Steel Faculty Award (2015), the Shanghai Shu-Guang Project (2015), the Chinese Chemical Society Youth Award (2014), NSFC Excellent Young Scholar Grant (2013), the Shanghai Eastern Scholar Professorship (2012 and 2015), the Chinese Ministry of Education New Century Excellent Talent (2011), the Shanghai Pujiang Talents (2010), the Northwestern University Outstanding Researcher Award (2009), the American Academy of Nanomedicine Young Investigator Award (2006), the Materials

Research Society Graduate Student Gold Award (2006), and Harvard University Distinction in Teaching (2004).

### **Charles M. Lieber**

Charles M. Lieber is a Professor in the Department of Chemistry and Chemical Biology at Harvard University. He attended Franklin and Marshall College for his undergraduate education and graduated with honors in Chemistry. After doctoral studies at Stanford University and postdoctoral research at the California Institute of Technology, he joined Columbia University in 1987 as an Assistant Professor. Here Lieber embarked on a new research program addressing the synthesis and properties of low-dimensional materials. He moved to Harvard University in 1991 and now holds a joint appointment in the Department of Chemistry and Chemical Biology, as the Mark Hyman Professor of Chemistry, and the Harvard John A. Paulson School of Engineering and Applied Sciences. He also serves as Chair of the Department of Chemistry and Chemical Biology. At Harvard, Lieber has pioneered synthesis of a broad range of nanoscale materials, characterization of their unique physical properties, and development of methods of hierarchical assembly of nanoscale wires, together with applications of these materials in nanoelectronics, nanocomputing, biological and chemical sensing, neurobiology and nanophotonics. Lieber has also developed and applied a new chemically sensitive microscopy for probing organic and biological materials at nanometer to molecular scales.

Lieber's research interests include: the chemistry and physics of materials with an emphasis on nanoscale materials; rational synthesis of new nanoscale materials and nanostructured solids; development of methodologies for hierarchical assembly of nanoscale materials into complex and functional systems; investigation of fundamental electronic, optical and optoelectronic properties of nanoscale materials; design and development of nanoelectronics and nanophotonic systems with emphasis on digital and quantum computing, nano-enabled photovoltaics for renewable energy, nanoelectronic-biology interfaces with emphasis on real-time, ultra-sensitive biodetectors, new tools for neuroscience and cell biology, and novel nanoelectronic interfaces to tissue and organs.

Lieber's research has been recognized by numerous awards, including the Remsen Award (2016), Nano Research Award, Tsinghua University Press/Springer (2013); IEEE Nanotechnology Pioneer Award (2013); Willard Gibbs Medal (2013); Wolf Prize in Chemistry (2012); Fred Kavli Distinguished Lectureship in Nanoscience, Materials Research Society (2010); Friendship Award, People's Republic of China (2009); Inorganic Nanoscience Award, ACS Division of Inorganic Chemistry (2009); Pioneer Award, National Institutes of Health (2008); Einstein Award, Chinese Academy of Sciences (2008); NBIC Research Excellence Award, University of Pennsylvania (2007); Nanotech Briefs Nano 50 Award (2005); World Technology Award in Materials (2004); ACS Award in the Chemistry of Materials (2004); Scientific American 50 Award in Nanotechnology and Molecular Electronics (2003); Nelson W. Taylor Award, Pennsylvania State University (2003); World Technology Award in Materials (2003); New York Intellectual Property Law Association Inventor of the Year Award (2003); APS

McGroddy Prize for New Materials (2003); Harrison Howe Award, University of Rochester (2002); MRS Medal (2002); Foresight Institute Feynman Prize in Nanotechnology (2001); NSF Creativity Award (1996); Leo Hendrik Baekeland Award, American Chemical Society (1995); George Ledlie Prize, Harvard University (1994–1995); MRS Outstanding Young Investigator Award (1993); ACS Award in Pure Chemistry (1992); Denkwalter Prize, Loyola University Chicago (1992); Camille and Henry Dreyfus Teacher-Scholar Award (1990–1995); Wilson Prize (1990); NSF Presidential Young Investigator Award (1988–1993); Distinguished New Faculty Award, Dreyfus Foundation (1987); American Institute of Chemists Distinguished Senior Award (1981); Theodore Saulnier Research Award (1981); Pentathlon Medal for Excellence in Chemistry (1981).

Lieber is an Elected Member of the National Academy of Sciences and the American Academy of Arts and Sciences, Elected Foreign Member of the Chinese Academy of Science, Elected Fellow of the Materials Research Society, American Chemical Society (Inaugural Class), and American Physical Society, Honorary Fellow of the Chinese Chemical Society, and Member of the Institute of Electrical and Electronics Engineers, International Society for Optical Engineering and American Association for the Advancement of Science. Lieber is Co-Editor of the nanoscience and nanotechnology journal *Nano Letters*, and serves on the Editorial and Advisory Boards of a large number of science and technology journals.

Lieber has published over 380 papers in peer-reviewed journals and is the principal inventor on more than 40 issued US patents. Based on his citation impact scores, Lieber was ranked #1 in Chemistry for the decade 2000–2010 by Thomson Reuters. In his spare time, Lieber has been active in commercializing nanotechnology, and has founded the nanotechnology company Nanosys, Inc. and the nanosensor company Vista Therapeutics.

# Index

## A

AAO membranes, 94  
Absorption, 233  
Action potentials (APs), 278  
Active node pattern, 132  
Activity maps, 291  
Address coding, 122  
Adenosine triphosphate (ATP), 262  
Adsorption, 79  
Aharonov–Bohm (AB) oscillations, 196  
Alignment, 82, 89  
Alignment angle, 94  
Alloying/dealloying mechanism, 209  
Alloy systems, 162  
Amorphous Si shell, 207  
Amorphous state, 127  
Anchor, 87  
AND gate, 117, 120  
Andreev levels, 196  
Andreev reflection, 192  
Angular momentum, 181  
Anisotropic chemical etching, 83  
Anisotropic etching, 75  
Anisotropic growth, 23  
Annealing, 45  
Anodes, 205  
Anodic aluminum oxide (AAO), 24  
Antielectron, 194  
Anti-reflection property, 232  
Anti-Stokes frequencies, 150  
Applications, 308  
Arithmetic logic unit, 131  
Arrays, 70  
Artificial photosynthesis, 240  
Association/dissociation, 259  
Asymmetric light propagation, 152  
Asymmetric NW heterostructures, 241  
Atomically abrupt interfaces, 45  
Atomic-level, 19

Auger recombination, 236  
Avalanche photodiode, 167  
Axial heterostructures, 107  
Axial junctions, 113  
Axial modulated structures, 42  
Axial modulation, 115

## B

Backbone/branch heterostructures, 115  
Backbone NWs, 56  
Ballistic limit, 110  
Band-edge emission, 154  
Band gaps, 236  
Basic computation, 119  
Batteries, 203  
Bi<sub>2</sub>Se<sub>3</sub> nanoribbons, 196  
Binding/unbinding, 260  
Biocompatible, 242  
Biomolecule detection, 255, 263  
Biosystems, 277  
Bi-stable, 125  
Blown bubble film (BBF), 77  
Boolean functions, 131  
Bottom-up, 5, 16, 103  
Bottom-up NW nanotechnology, 300  
Bottom-up paradigm, 63, 307  
Brain mapping, 278  
Brain slice, 291  
Branched/tree-like structures, 53  
Building blocks, 69, 129, 168, 307

## C

Cancer biomarkers, 259  
Carbide nanorods, 9  
Carbon-based materials, 218  
Carbon-coated SiNWs, 206  
Carbon coating, 240  
Carbon nanotube, 9  
Cardiac cells, 280



- Cardiac tissue, 291
  - Carrier mobility, 110
  - Carrier relaxation, 159
  - Carrier separation, 233, 237
  - Carrier transport, 112
  - Cascaded tiles, 136
  - Catalytic approach, 4
  - Cathodes, 211
  - Cavity modes, 235
  - CdS NW, 159
  - Cellular circuitry, 300
  - Charge/discharge cycles, 206
  - Charged molecule, 256
  - Charge sensing, 187
  - Charge transport, 177, 197, 241
  - Charging energy, 181
  - Chemical/biomolecule detection, 271
  - Chemical interactions, 78
  - Chemically reactive templates, 26
  - Chemical vapor deposition (CVD), 18
  - Chemical vapor transport (CVT), 20
  - Chronic immune responses, 298
  - CMOS, 120, 279
  - Co-assembly, 89
  - Coaxial heterostructured NWs, 237
  - Coaxial modulated structures, 52
  - Cocatalysts, 241
  - Complementary chemical interactions, 71
  - Complex doping profiles, 48
  - Composition-graded NWs, 153
  - Composition grading, 162
  - III-V Compounds, 236
  - Concentration-dependent detection, 259
  - Conducting polymers, 218
  - Configurations, 179
  - Confinement-guided NW growth, 62
  - Contact printing, 85
  - Controlled growth, 40
  - Core/multishell, 50
  - Core/shell, 49, 53, 129
  - Core/shell NW, 207
  - Core/shell NW arrays, 216
  - Core-multishell, 111
  - Coulomb blockade (CB), 181, 192
  - Coulomb oscillation, 185
  - Coupled cavity, 165
  - Coupled quantum dots, 184
  - Covalent binding, 257
  - Crossbar NW array, 126
  - Crossed nanowire (NW), 111, 154
  - Crossed NW configuration, 113
  - Crossed NW-FET array, 117, 121
  - Crossed NW p-n junctions, 117
  - Crystalline state, 127
  - Crystal orientations, 207
  - Crystal phases, 56
  - Cylindrical growth substrates, 86
  - Cystic fibrosis, 260
- D**
- 1-D electron gases, 110
  - 1D hole-gas system, 183
  - 2D electron gases (2DEGs), 178
  - 2D shapes, 62
  - 3D branched nanowires, 263
  - 3D multifunctional nanoelectronics, 298
  - 3D nano-bioelectronic hybrids, 293
  - 3D nano-bioprobes, 288
  - Debye length, 265, 270
  - Debye screening, 261
  - Debye screening effect, 270
  - Defect-induced growth, 23
  - Demultiplexers (Demux), 121, 122
  - Dengue, 261
  - Device noise, 265
  - Dielectric layer, 126
  - Dielectric polarization, 146
  - Dielectrophoresis, 267
  - Dielectrophoretic forces, 82
  - Differential roll printing (DRP), 86
  - Dimension, 1
  - Dimensionality, 2
  - Direct growth, 70
  - Disproportionation reaction, 23
  - D latch, 133
  - DNA detection, 261
  - DNA targets, 260
  - Dopant modulation, 45
  - Doping, 42
  - Double-gate nanowire sensors, 270
  - Double-layer mask, 93
  - Double QDs, 186
  - Dual-band gap, 240
  - Dual-gated, 106
  - Dynamic random access memory (DRAM), 122
- E**
- Effective g-factor, 181, 187
  - Electrical injection, 166
  - Electrically-pumped NW lasers, 166
  - Electric field (E-field)-assisted assembly, 81
  - Electrochemical activity, 219
  - Electrochemical capacitors (ECs), 214
  - Electrochemical energy storage, 219
  - Electrode/cell interfaces, 279
  - Electrode materials, 203
  - Electrodes, 219

Electrogenic cells, 284  
 Electrokinetic effects, 267  
 Electroluminescence (EL), 113, 166  
 Electron and hole mobilities, 107  
 Electron-beam lithography, 90  
 Electron beam metal evaporation, 27  
 Electronic properties, 181  
 Electronic switches, 115  
 Electrophysiology, 278  
 Electroporation, 289  
 Electrostatic force microscopy (EFM), 114  
 Elemental mapping, 50  
 End-to-end registry, 73  
 Energy conversion, 227, 248  
 Energy storage, 203  
 Engineered tissue patches, 272  
 Enhanced capture efficiency, 263  
 Epitaxial growth, 95, 97  
 Equilibrium phase diagrams, 7, 17  
 Equilibrium thermodynamics, 8  
 Evaporation, 22  
 Excitation, 145  
 Extracellular recording, 278, 280, 284, 295

## F

Fabry-Perot cavity, 157  
 Facet-selective growth, 51  
 Ferroelectric memory, 125, 127  
 Field-effect transistors, 104  
 Field-effect transistor sensors, 256, 271  
 Finite-difference-time-domain, 235  
 Finite-state machine (FSM), 133  
 Flash memory, 126, 127  
 Flexibility, 152  
 Flexible substrate, 293  
 Flip-flops, 132  
 Floating gate, 125, 126  
 Flow-assisted alignment, 70  
 Four-wave mixing (FWM), 150  
 Free-standing NW probe, 288  
 Frequency, 150  
 Frequency domain, 267  
 Full-adder logic circuit, 132  
 Full subtractor, 132  
 Fully integrated system, 241  
 Functional device arrays, 97  
 Functional devices, 298  
 FWM signal, 150

## G

GaN NWs, 159  
 Gas flows, 72  
 Gate-all-around structure, 107  
 Gate electrode, 111

Ge/Si core/shell NW heterostructure, 183  
 Ge/Si core/shell NWs, 187  
 Ge/Si core/shell system, 108  
 GeNWs, 107, 115  
 Gleevec, 262  
 Gluing LB technique, 73  
 Gold-spine electrode, 287  
 Growing planes, 30  
 Growth chemistry, 235  
 Growth direction, 7, 19  
 Growth substrate, 56, 62  
 $G^*$  values, 189

## H

HeLa cells, 261  
 Helical, 59  
 Heterobranched growth, 54  
 Heterogeneous activity, 291  
 Heterogeneous nucleation, 61  
 Heterojunction energy barrier, 107  
 Heterostructure, 43, 46, 107, 145, 155, 182, 217  
 Heterostructured NWs, 186  
 Hexagonal pattern, 93  
 Hierarchical organization, 69, 97  
 Hierarchical  $V_2O_5$ NWs, 213  
 High mobility, 110, 112  
 High pressure, 29  
 High temperature, 29  
 Homogeneous nanowires, 40, 144  
 HRTEM, 45  
 Hybrid nanotechnologies, 6  
 Hybrid NW, 217  
 Hybrid semiconductor NW—bacteria system, 242  
 Hybrid structures, 218, 239  
 Hybrid superconductor-semiconductor devices, 192  
 Hydrogen evolution reaction, 238  
 Hydrophilic, 75  
 Hyperbranched, 54  
 Hyperfine interaction, 191  
 Hysteretic resistance switches, 125

## I

Implants, 298  
 Incorporation, 295  
 Influenza A, 261  
 Initial design, 4  
 Injectable electronics, 298  
 In-place planarization, 89  
 Integrated circuits, 115, 136  
 Integrated large-scale arrays, 73  
 Integrated NW sensor arrays, 259

- Integrated systems, 97  
Intercalation/deintercalation mechanism, 209  
Interconnection, 54, 75  
Interfacial kinetics, 49  
Interfacial ordering, 79  
Interfacial tension, 75  
Intracellular measurements, 284  
Intracellular recording, 284, 285, 288  
Inverter, 120
- J**  
Josephson junctions, 192  
Junctionless nanowire transistors, 111  
Junctions, 179
- K**  
Kinetic control, 30  
Kinetics, 19  
Kinked NWs, 60, 288
- L**  
Label-free, 257  
Langmuir-Blodgett method, 72  
Large-scale NW assembly, 97, 136  
Laser ablation, 16  
Laser ablation method, 10  
Laser-assisted catalytic growth, 16  
Lasers, 143  
Lasing mechanisms, 159  
Lasing thresholds, 164  
Latches, 132  
Laterally deterministic assembly, 87  
Lateral olfactory tract, 291  
Lattice matching, 96  
 $\text{Li}_4\text{Mn}_2\text{O}_5$ , 212  
 $\text{Li}_x\text{V}_2\text{O}_5$  phases, 213  
LIB anodes, 209  
 $\text{LiCoO}_2$ , 212  
Light absorption, 229  
Light-emitting diodes (LED), 143, 153  
Light polarization, 149  
Li ion intercalation, 213  
 $\text{LiMn}_2\text{O}_4$ , 212  
Lithiation, 207  
Lithium intercalation, 211  
Lithium intercalation material, 204  
Lithium-ion batteries, 203, 204  
Lithium ion storage capacity, 207  
Lithium metal phosphates, 214  
Lithium transition metal oxides, 211  
Logic, 120  
Logical negation, 132  
Logic circuit, 120  
Logic flow, 134
- Logic gates, 115  
Logic gate structures, 117  
Logic state, 132  
Logic tiles, 129  
Longitudinal NW heterostructures, 42  
Long-term stability, 271  
Lorentzian peak, 267  
Lower diameter limit, 8  
Low-melting-point metal catalysts, 28  
Low temperature, 19  
Low threshold, 159
- M**  
Macroporous nanoelectronic networks, 295, 298  
Macroporous structures, 293  
Magic number structure, 187  
Magnetic field, 82, 182  
Majorana fermions, 178, 194  
Majorana zero modes, 194, 196  
Mass production, 31  
MEA-based nanopillars, 289  
Mechanical properties, 206, 298  
Metallic states, 196  
Metallo-organic precursors, 27  
Metal-organic vapor-phase epitaxy, 10  
Metal oxide nanostructures, 30  
Metal oxides, 208  
Metal-semiconductor heterostructures, 43  
Metal-semiconductor junctions, 42  
Metal silicides, 107  
Microbial systems, 242  
Microelectrode arrays (MEAs), 279  
MicroRNAs, 261  
Millimeter-long SiNWs, 40  
Minimized free energy, 97  
 $\text{MnO}_2$ , 215  
Modulated nanostructures, 42  
Modulation, 48  
Modulation-doped SiNWs, 184  
Molecular beam epitaxy (MBE), 21  
Molecular dimensions, 40  
Molecular-level control, 103  
Molecule-patterned substrate, 79  
Monodispersed Au nanocrystals, 29  
Morphological features, 48  
Multibit full adder, 136  
Multi-component functional materials, 308  
Multifunctional circuits, 298  
Multifunctional nanoelectronics, 136  
Multifunctional NW electronics, 295  
Multi-input binary tree demuxes, 122  
Multiple junction arrays, 117  
Multiplexed measurements, 283

- Multiplexed recording, 280
- Multiplexed sensing, 259
- Multi-quantum-well (MQW), 50, 146
- N**
- Na intercalation materials, 219
- NAND gate, 120
- NAND logic, 120
- Nanocluster catalyzed, 40
- Nanocluster catalyzed VLS, 18, 86
- Nanocombing, 87
- Nanocomputers, 129
- Nanoelectronic devices, 104, 136
- Nanoelectronic scaffolds, 293
- Nanoelectronics-brain interfaces, 301
- Nanoelectronics-cyborg tissues, 301
- NanoFET, 285, 287, 295, 300
- NanoFET-cell interfaces, 288
- NanoFET intracellular probes, 300
- NanoFSM, 133, 134
- Nanogenerator, 246
- Nanoimprint lithography (NIL), 94
- NanoLEDs, 153
- Nanophotonics, 143
- Nanopore, 24, 269
- Nanoprobe manipulation, 165
- Nanoprocessors, 129, 136
- Nano-revolution, 5
- Nanoscale building blocks, 32
- Nanosphere lithography, 91
- Nanostructures, 1, 25
- Nanowire/Cell Interfaces, 278
- Nanowire-tissue interfaces, 290
- Nanowire waveguides, 152
- Near-IR lasers, 160
- Neural networks, 278
- Neuronal activities, 291
- Neurons, 280
- 1/f noise, 267
- Noise spectra, 267
- Non-centrosymmetric structures, 148
- Nonlinear optical (NLO) processes, 147
- Nonvolatile memory, 124
- Nonvolatile RAM devices (NVRAM), 124
- NOR gate, 117, 129, 133
- N-type, 42
- Nucleic acid detection, 260
- Nanowire (NW), 1, 203, 209, 212, 215, 219, 233
- NW arrays, 204, 210, 229
- NW-axon elements, 280
- NW-based crossbar structure, 125
- NW-based FET sensors, 271
- NW-based materials, 308
- NW-based QDs, 179
- NW building blocks, 3, 39, 64, 136
- NW cavity, 151
- NW crossbar arrays, 120
- NW-FET, 105, 111, 255, 260, 300
- NW-FET arrays, 120, 272
- NW-FET devices, 263
- NW-FET integrated circuits, 129
- NW heterostructure, 125, 211
- NW materials, 220
- NW-nanotube, 288
- NW photoelectrodes, 241
- NW p-n junctions, 113
- NW PV devices, 229
- NW science and technology, 307
- NW transistor arrays, 129
- O**
- Off current, 107
- Ohmic contacts, 183
- On/Off current ratio, 107
- On/Off ratios, 125
- On current, 105
- One-dimensional (1D), 39, 51
- Optically-pumped nanowire lasers, 156
- Optical modes, 162
- Optical properties, 144
- Ordered metal nanocluster catalyst arrays, 90
- Oscillations, 183
- Ostwald ripening process, 30
- Oxide-assisted growth (OAG), 23
- Oxide catalyzed NW growth mechanism, 10
- Oxygen evolution reaction, 238
- P**
- Patch clamp, 284
- Patterned printing, 85
- Patterning lines, 75
- Pattern-transfer, 94
- Patterns, 233
- PDMS stamp, 83
- PDMS transfer, 83, 84
- PEC electrodes, 239
- PEG, 266
- Peptide nucleic acids, 260
- Periodic, 45
- Periodicity, 58
- Periodic quantum interference effects, 196
- Periodic shells, 52
- Permeable polymer layer, 265
- Perovskite material, 164
- PET substrate, 84
- Phase-change behavior, 128
- Phase-change memory (PCM), 125, 127

Phase coherence length, 192  
Phase matching, 148  
Phase transition, 56  
Phospholipid bilayers, 288  
Photodetectors, 143, 167, 168  
Photodiodes, 167  
Photoelectrochemical conversion, 238  
Photolithography, 75, 90  
Photoluminescence (PL), 113, 144  
Photon confinement, 144  
Photonic circuits, 152  
Photonic devices, 168  
Phototransistors, 168  
Photovoltaics (PVs), 228  
PH sensing, 257  
Physiological fluids, 270  
Piezoelectric effect, 246  
P-i-n coaxial SiNWs, 53  
P-i-n coaxial structure, 233  
Pitch, 75  
Plateau-Rayleigh instability, 51  
P-n homojunctions, 45  
P-n junction photodiode, 228  
P-n junctions, 42, 113  
Polarizability, 81  
Polarization anisotropy, 145  
Polymeric fluid, 77  
Polymorphic core/multi-shell NWs, 235  
Potential barriers, 184  
Preferential binding, 30  
Printing, 83  
Printing techniques, 82  
Programmable, 129  
Programmable NW-FETs, 126, 129  
Propagation loss, 162  
Protein detection, 258  
Protruding NW-FET channels, 291  
Proximity-induced superconductivity, 192  
PSA, 266, 268  
Pseudo-capacitors, 215  
P-type, 42

## Q

Quantum computers, 198  
Quantum confinement, 145, 181  
Quantum dot (QD), 178  
Quantum electronics, 197  
Quantum information, 146  
Quantum phenomena, 177  
Quantum properties, 197  
Quantum structure, 183  
Quantum yields, 164

## R

Radial/coaxial modulated structures, 48  
Radial heterostructures, 108  
Radial junction nanowires, 233  
Radial structures, 49  
Raman, 151  
Rate of discharge and charge, 214  
Rational control, 63  
Rationally assembled, 4  
Real-time observation, 19  
Recording, 278  
Rectifying behavior, 113  
Redox supercapacitors, 215  
Reduction/oxidation reactions, 210  
Reflection, 229  
Regioselective, 50  
Relative stability, 56  
Renewable energy, 248  
Reprogram, 136  
Resistive memory, 125  
Resistive-switching, 126  
Reversible surface modifications, 259  
Revolutionary technologies, 308  
Ring oscillators, 120  
Ring structure, 159  
RuO<sub>2</sub>, 215

## S

Sandwich-like structure, 72  
Sapphire substrates, 95  
Scalable assembly, 69  
Scalable integration, 75  
Scaling limits, 279  
Scaling strategies, 103  
Scanning gate microscopy (SGM), 46, 114  
Screw dislocation, 58  
Seal resistance, 279, 287  
Secondary building unit (SBU), 60  
Second harmonic generation (SHG), 147, 149  
Selective chemical modification, 121  
Self-assembled nanofilms, 80  
Self-assembled structures, 25  
Self-assembly, 91  
Self-catalytic growth, 58  
Semiconductor heterojunctions, 43  
Semiconductor NW, 3, 105, 147, 227, 229, 248  
Semiconductor NW-based materials, 227  
Semiconductor NW photonic devices, 144  
Semiconductor NW sensors, 255  
Sensitivity enhancement, 265  
Sequential catalyst-assisted method, 54  
Sequential deposition, 44, 70

- Sequential logic circuits, 132  
SET, 182  
Shadow masks, 75  
Shape-controlled nanotunnels, 62  
Shear stress, 77  
Shorter carrier diffusion length, 233  
Short-term penetration, 289  
Si anodes, 206  
Si FETs, 279  
Signal propagation, 291  
Silicide, 45  
Silicon nanowires (SiNWs), 7  
    preparation of, 10  
Single charge tunneling, 177  
Single electron devices, 181  
Single-electron effects, 183  
Single-mode lasing, 165  
Single-molecule DNA sequencing, 269  
Single particle level, 261  
Single quantum dots, 182  
SiNW, 206, 233, 235, 238, 239, 245, 258, 262  
SiNW arrays, 233  
SiNW backbones, 241  
SiNW devices, 261  
SiNW electrodes, 206  
SiNW-FET, 105, 257, 259, 264, 266, 270, 280, 283, 287, 290, 291, 308  
SiNW-FET arrays, 291  
SiNW-FET devices, 284  
SiNW-FET sensor, 268  
SiNW structures, 308  
Small diameter, 29  
Smaller receptors, 265  
Small molecule detection, 262  
Sodium-ion batteries, 219  
Solar cell, 228  
Solar cell characterization, 229  
Solid phase reaction, 45  
Solid-solid transformation, 30  
Solution growth, 56  
Solution-liquid-solid (SLS), 27  
Solution-phase method, 79  
Solution-solution-solid (SSS), 30  
Solvothermal/hydrothermal synthesis, 29  
Specific and selective assembly, 79  
Spin blockade, 190  
Spin coherence time, 187  
Spin manipulation, 187  
Spin-orbit interaction, 182, 187, 189, 194  
Spin states, 189  
Stark effect, 187  
STEM, 50  
Step edges, 95, 97  
Step-flow kinetics, 22  
Sterero configuration, 61  
Stimulated emission, 157  
Stimulated Raman scattering, 150  
Stimulation, 291  
Stokes frequencies, 150  
Strain, 59  
Strain-release based assembly, 89  
Streptavidin, 258  
Stretchable, 89  
Sub-bands, 179  
Subcellular spatial resolution, 280  
Subthreshold regime, 263  
Subwavelength waveguides, 148  
Superconducting electronics, 178  
Superconductor nanowire, 168  
Supercritical fluid-liquid-solid, 28  
Supercurrent, 192  
Superlattice, 43, 49  
Superlattice nanowire pattern transfer (SNAP), 26  
Surface area, 263  
Surface chemical modification, 85  
Surface diffusion, 21  
Surface energy, 19  
Surface functionalization, 255, 257  
Surface molecular patterns, 78  
Surface-programmed assembly, 78  
Surface states, 196  
S-wave superconductor, 194  
Synthetic challenges, 4  
Synthetic methods, 32  
Synthetic tissues, 293  
Syringe injection, 298
- T**  
Tandem junction sequence, 48  
Tapered SiNW arrays, 232  
Temperature gradient, 244  
Template-based growth, 24  
Template mechanism, 9  
Template mediated growth, 4  
    2-terminal, 124  
    3-terminal, 125  
Thermodynamics, 19  
Thermoelectric figure of merit, 244  
Thermoelectrics, 244  
THG signal, 150  
Third-harmonic generation (THG), 147, 150  
Three-phase boundary, 61  
Three-phase interface, 80  
Three-phase interfacial assembly, 79  
Tile, 133  
Tissue engineering, 293  
Top-down, 5, 15, 103

- Top-down lithography, 8
  - Top-down methods, 235
  - Topological insulators (TIs), 178, 196
  - Track-etched polymer, 24
  - Transconductance, 106
  - Transistors, 115
  - Transition, 45
  - Transition metal oxides, 210
  - Translocation, 269
  - Transmission, 229
  - Transmission measurements, 232
  - Triangular array, 93
  - Truth table, 136
  - Tunable band gap quantum well, 155
  - Two-dimensional shapes, 62
- U**
- Ultrafast nanoelectronics, 110
  - Ultra-flexible mesh, 298
  - Ultrahigh-density arrays, 26
  - Ultra-high vacuum, 21
  - Ultrasensitive detection, 271
  - Ultrashort, 48
  - Undersaturation/supersaturation, 60
  - Uniaxially aligned, 75
  - UV lasers, 157
- V**
- V<sub>2</sub>O<sub>5</sub>, 213
  - Vapor phase growth, 16
  - Vapor-phase nanocluster catalyzed growth, 10
  - Vapor-solid (VS), 23
  - Vapor-solid-solid (VSS), 22
  - Various NW structures, 220
  - Virus detection, 261
  - Virus templates, 25
  - Visible lasers, 159
  - VLS growth, 6, 62, 72, 233, 234
  - Volatile organic compounds (VOCs), 263
  - Volume expansion, 207
  - VS growth mechanism, 23
  - VSS mechanism, 48
- W**
- Water-air interface, 72
  - Water splitting, 238, 239
  - Waveguides, 143
  - Wavelength-tunable lasers, 162
  - Wet-chemical etching, 48
  - Wurtzite crystals, 58
- Z**
- Zeeman effect, 195
  - Zeeman energy, 189
  - Zeeman splitting, 182
  - Zero-bias peak (ZBP), 194
  - ZnO NWs, 157, 246
  - Z-scheme, 241